Mathematical and Computational Systems

Theory, Methods, and Applications in Physics, Networking, and Intelligent Modeling

Editors

Professor Dr. Miguel Vivas-Cortez
Dean Chou D.Phil. (Oxon)

Ptolemy Institute of Scientific Research and Technology (PISRT), Lahore 54000, Pakistan.

Mathematical and Computational Systems: Theory, Methods, and Applications in Physics, Networking, and Intelligent Modeling

Mathematical and Computational Systems: Theory and Applications

Professor Dr. Miguel Vivas-Cortez
Pontificia Universidad Católica del Ecuador
Sede Quito, Ecuador

Dean Chou D.Phil. (Oxon)
National Cheng Kung University, Tainan, Taiwan

Published by Ptolemy Science Research Press

List of Authors

Dr. Javed Rashid: Department of Computer Science, University of Okara, Okara, 56300, Pakistan.

Dr. Riaz ul Amin: Department of Computer Science, University of Okara, Okara, 56300, Pakistan.

Dr. Bilal Shabbir Qaisar: Department of Computer Science, University of Okara, Okara, 56300, Pakistan.

Dr. Muhammad Shoaib Saleem: Department of Mathematics, University of Okara, Okara, 56300, Pakistan.

Mr. Ahsan Fareed Shah: Department of Mathematics, University of Okara, Pakistan.

Mr. Abdullah: Department of Mathematics and Statistics, University of Agriculture, Faisalabad,Pakistan.

Dr. Madiha Ghamkhar: Department of Mathematics and Statistics, University of Agriculture, Faisalabad,Pakistan.

Ms. Adeeba Fatima: Department of Mathematics and Statistics, University of Agriculture, Faisalabad, Pakistan.

Ms. Asra Ayub: Department of Mathematics and Statistics, University of Agriculture, Faisalabad, Pakistan.

Ms. Aamna Amer: Department of Mathematics, University of Okara, Okara Pakistan.

Dr. Hamood Ur Rehman: Department of Mathematics, University of Okara, Okara Pakistan.

Ms. Ifrah Iqbal: Department of Mathematics, University of Okara, Okara Pakistan.

Mr. Muhammad Tehseen: Department of Mathematics, University of Okara, Okara Pakistan.

Dr. Mujahid Iqbal: College of Information Science and Technology, Dalian Maritime University, Liaoning, China.

Dr. Muhammad Ashraf : College of Information Science and Technology, Dalian Maritime University, Liaoning, China.

Dr. Hameed Ashraf: Department of Mathematics, University of Okara, Okara Pakistan.

Ms. Ayesha Siddiqa: Department of Mathematics, University of Okara, Okara Pakistan.

Dr. Madeeha Tahir: Department of Mathematics, Government College Women University, Faisalabad, Pakistan.

Prof. Dr. Saima Akram: Department of Mathematics, Government College Women University, Faisalabad, Pakistan.

Dr. Shahla Faisal: Department of Statistics, Government College University, Faisalabad 38000, Pakistan.

Prof. Dr. M. Imran Department of Mathematics, Government College University, Faisalabad 38000, Pakistan.

Mr. Muhammad Abid: Department of Statistics, Government College University, Faisalabad 38000, Pakistan.

Mr. G. A. Danish: Department of Statistics, Government College University, Faisalabad 38000, Pakistan.

Dr. Khadija Tul Kubra: Department of Mathematics, Government College University, Faisalabad, Pakistan.

Mr. Rooh Ali: Department of Mathematics, Government College University, Faisalabad, Pakistan.

Ms. Muniba Nasir: Department of Mathematics, Government College University, Faisalabad, Pakistan.

Ms. Bushra Ujala: Department of Mathematics, Government College University, Faisalabad, Pakistan.

Ms: Samra Gulshan: Department of Mathematics, Government College University, Faisalabad, Pakistan.

Dr. Abdul Malik Sultan: Department of Mathematics, University of Okara, Okara Pakistan.

Dr. Abdul Jawad: Department of Mathematics, COMSATS University Islamabad, Lahore-Campus, Lahore Pakistan.

Dr. Muhammad Irfan: Department of Mathematics, University of Okara, Okara Pakistan.

Ms. Tahreem Ashraf: Department of Mathematics, GC University, Faisalabad, Pakistan.

Dr. Nazeran Idrees: Department of Mathematics, GC University, Faisalabad, Pakistan.

Dr. Farkhanda Afzal: MCS, National University of Sciences and Technology, Islamabad.

Dr. Akhtar Ali: Department of Mathematics, Government College University, Faisalabad, Pakistan.

Mr. Ali Raza: Department of Mathematics, Government College University, Faisalabad, Pakistan.

Ms. Fatima Saeed: Department of Mathematics, Government College University, Faisalabad, Pakistan.

Dr. Fozia Bashir Farooq Department of Mathematics and Statistics, Imam Mohammad Ibn Saud Islamic University, Saudi Arabia.

Prof. Dr. Mohsan Raza: Department of Mathematics, Government College University, Faisalabad, Pakistan.

Prof. Dr. M. Ahsan Binyamin: Department of Mathematics, Government College University, Faisalabad, Pakistan.

Editors

Professor Dr. Miguel Vivas-Cortez
Pontificia Universidad Católica del
Ecuador Sede Quito, Ecuador.
mjvivas@puce.edu.ec

Dean Chou D.Phil. (Oxon)
National Cheng Kung University, Tainan, Taiwan.
dean@gs.ncku.edu.tw

Ptolemy Institute of Scientific Research and Technology (PISRT)
https://pisrt.org/
ISBN: 978-627-7623-05-0

First printing, December 2025

To our Teachers

Contents

List of Tables

List of Figures

Contributors

Dr. Javed Rashid: Department of Computer Science, University of Okara, Okara, 56300, Pakistan.

Dr. Riaz ul Amin: Department of Computer Science, University of Okara, Okara, 56300, Pakistan.

Dr. Bilal Shabbir Qaisar: Department of Computer Science, University of Okara, Okara, 56300, Pakistan.

Dr. Muhammad Shoaib Saleem: Department of Mathematics, University of Okara, Okara, 56300, Pakistan.

Mr. Ahsan Fareed Shah: Department of Mathematics, University of Okara, Okara, Pakistan.

Mr. Abdullah: Department of Mathematics and Statistics, University of Agriculture, Faisalabad,Pakistan.

Dr. Madiha Ghamkhar: Department of Mathematics and Statistics, University of Agriculture, Faisalabad, Pakistan.

Ms. Adeeba Fatima: Department of Mathematics and Statistics, University of Agriculture, Faisalabad, Pakistan.

Ms. Asra Ayub: Department of Mathematics and Statistics, University of Agriculture, Faisalabad,Pakistan.

Ms. Aamna Amer: Department of Mathematics, University of Okara, Okara Pakistan.

Dr. Hamood Ur Rehman: Department of Mathematics, University of Okara, Okara Pakistan.

Ms. Ifrah Iqbal: Department of Mathematics, University of Okara, Okara Pakistan.

Mr. Muhammad Tehseen: Department of Mathematics, University of Okara, Okara Pak-

istan.

Dr. Mujahid Iqbal: College of Information Science and Technology, Dalian Maritime University, Dalian 116026, Liaoning, PR China.

Dr. Muhammad Ashraf : College of Information Science and Technology, Dalian Maritime University, Liaoning, China.

Dr. Hameed Ashraf: Department of Mathematics, University of Okara, Okara Pakistan.

Ms. Ayesha Siddiqa Department of Mathematics, University of Okara, Okara Pakistan.

Dr. Madeeha Tahir: Department of Mathematics, Government College Women University, Faisalabad 38000, Pakistan.

Prof. Dr. Saima Akram: Department of Mathematics, Government College Women University, Faisalabad 38000, Pakistan.

Dr. Shahla Faisal: Department of Statistics, Government College University, Faisalabad 38000, Pakistan.

Prof. Dr. Muhammad Imran: Department of Mathematics, Government College University, Faisalabad 38000, Pakistan.

Mr. Muhammad Abid: Department of Statistics, Government College University, Faisalabad 38000, Pakistan.

Mr. G. A. Danish: Department of Statistics, Government College University, Faisalabad 38000, Pakistan.

Dr. Khadija Tul Kubra: Department of Mathematics, Government College University, Faisalabad, Pakistan.

Mr. Rooh Ali: Department of Mathematics, Government College University, Faisalabad, Pakistan.

Ms. Muniba Nasir: Department of Mathematics, Government College University, Faisalabad, Pakistan.

Ms. Bushra Ujala: Department of Mathematics, Government College University, Faisalabad, Pakistan.

Ms: Samra Gulshan: Department of Mathematics, Government College University, Faisalabad, Pakistan.

Dr. Abdul Malik Sultan: Department of Mathematics, University of Okara, Okara Pakistan.

Dr. Abdul Jawad: Department of Mathematics, COMSATS University Islamabad, Lahore-

Campus, Lahore, Pakistan.

Dr. Muhammad Irfan: Department of Mathematics, University of Okara, Okara Pakistan.

Ms. Tahreem Ashraf: Department of Mathematics, GC University, Faisalabad, Pakistan

Dr. Nazeran Idrees: Department of Mathematics, GC University, Faisalabad, Pakistan.

Dr. Farkhanda Afzal: MCS, National University of Sciences and Technology, Islamabad.

Dr. Akhtar Ali: Department of Mathematics, Government College University, Faisalabad, Pakistan.

Mr. Ali Raza: Department of Mathematics, Government College University, Faisalabad, Pakistan.

Dr. Nazeran Idrees: Department of Mathematics, Government College University, Faisalabad, Pakistan.

Ms. Fatima Saeed: Department of Mathematics, Government College University, Faisalabad, Pakistan.

Dr. Fozia Bashir Farooq: Department of Mathematics and Statistics, Imam Mohammad Ibn Saud Islamic, University, Saudi Arabia.

Prof. Dr. Mohsan Raza: Department of Mathematics, Government College University, Faisalabad, Pakistan.

Prof. Dr. M. Ahsan Binyamin: Department of Mathematics, Government College University, Faisalabad, Pakistan.

Preface

This book, Mathematical and Computational Systems: Theory, Methods, and Applications in Physics, Networking, and Intelligent Modeling, presents a collection of research studies and methodologies bridging mathematical theory and practical applications. It covers diverse topics, including machine learning for disease classification, computational intelligence, optimization algorithms, biofluid modeling, neural network paradigms in epidemiology, cosmology, topological descriptors, and fractional differential equations in HIV–AIDS dynamics. The aim is to provide readers, researchers, academicians, and graduate students, with insights into advanced computational methods and their applications across science and engineering. We hope this volume inspires new research directions and promotes the integration of theory, computation, and real-world problem-solving.

We extend our sincere gratitude to all contributors for their valuable work in making this book possible

Lahore, Pakistan

December. 2025

CHAPTER 1

MODC-SET: A Stacked Ensemble Deep Learning Framework for Classification of Mouth and Oral Diseases

Javed Rashid*, **Riaz ul Amin*** **and Bilal Shabbir Qaisar***

**Department of Computer Science, University of Okara, Okara, 56300, Pakistan*

Corresponding Author: Javed Rashid: RanaJavedRashid@gmail.com

Abstract:

Oral diseases such as leukoplakia, lichen planus, and squamous cell carcinoma pose major public health challenges, and early detection is essential for timely treatment. Traditional diagnostic methods often rely on invasive biopsies and expert interpretation, which are time-consuming and resource-intensive. This chapter introduces MODC-SET, a stacked ensemble deep learning framework integrating MobileNetV2, InceptionResNetV2, and ResNet50 with an XGBoost meta-classifier for robust oral disease classification. Trained on the newly curated MOD dataset of seven clinically significant conditions, the model achieved 99.32% accuracy, substantially outperforming existing approaches. These results demonstrate that ensemble deep learning provides a powerful and scalable tool for non-invasive oral disease detection, offering promising applications in clinical and resource-limited settings.

Keywords: Deep Learning, Stacking Ensemble, Transfer Learning, Oral Disease Classification, Medical Image Analysis, Automated Diagnosis, MODC-SET

1.1 Introduction

Oral illnesses are a significant health issue that can negatively impact individuals and society [1]. Recent years have seen a substantial increase in oral diseases, such as oral cancer, dental caries, periodontal

disease, and dental fluorosis [2]. Research indicates that poor oral hygiene can have systemic effects, such as bacteria from dental plaque entering the bloodstream through the gums, increasing the risk of blood clots and cardiovascular diseases [3]. Untreated periodontal disease can lead to systemic disorders, including diabetes, cardiovascular disease, and metabolic syndrome, leading to tooth loss and reduced quality of life [4, 5].

Public awareness of oral health concerns and preventative care is growing in impoverished places [6]. The global market for titanium dental implants is expected to reach $ 6.3 billion in 2021 due to increased demand for superior dental treatment. Global aging has increased the prevalence of oral disorders, including periodontitis and tooth loss, making them major public health issues [7]. The WHO predicts that oral diseases will impact 3.5 billion people by 2022, highlighting the need for effective diagnostic and preventive measures [8]. Oral cancer is the sixth most prevalent cancer worldwide, with some 300,000 new cases diagnosed annually [9]. In 2021, the American Cancer Society predicted 54,010 new oral cancer cases in the US [8].

Dental caries is one of the most common chronic infectious disorders of dental hard tissues. The Global Burden of Disease Study of 2017 found chronic dental caries to be the most prevalent disease among 328, ranking second globally [10]. Approximately 2.44 billion people experience tooth decay, with a notable rise in children's tooth decay over the past decade [11]. Epidemiological research indicates 178 million Americans have missing teeth, with 40 million entirely edentulous [12]. About 91% of persons aged 20-64 have had dental caries, and 27% have suffered irreversible tooth damage [11]. Dental crises are prevalent in the US, with patients seeking care every 15 seconds [8].

Traditional methods, including periodontal probing depth measurement, bleeding on probing, and radiographic analysis, are crucial for recognizing gingivitis and chronic periodontitis [13]. These procedures are invasive, uncomfortable, and subject to examiner-dependent variances in probing techniques, leading to inconsistent results [14, 15]. The time and effort required to perform these diagnostic tests hinder timely and cost-effective dental care. Nearly 75% of people seek new dentists based on online recommendations, although dental practitioners' knowledge is generally restricted [8]. In Pakistan, almost 50% of the population has never seen a dentist, and only 5% receive complete oral and dental treatment [16]. Given these challenges, an automated deep learning system is essential for accurate, efficient, and cost-effective oral disease identification, especially in remote and disadvantaged areas.

AI and deep learning are revolutionizing medical diagnostics, including CAD applications [17, 18, 19, 20]. CNNs excel in fields such as agriculture, energy predictions, image forgery detection, medical imaging, and Alzheimer's disease diagnosis [21, 22, 23, 24, 25, 26, 27, 28, 29, 30]. CNN-based deep learning for dentistry accurately identifies periodontal bone loss, caries lesions, and apical lesions in periapical radiographs [31]. Previous dental disease classification studies have used invasive methods like microscopy, radiography, and fluorescence imaging, limiting their applicability outside clinical settings [11, 32, 33]. Advancements in intraoral imaging enable early periodontitis diagnosis [6]. Using self-generated data, A Mask R-CNN model was presented by Liu et al. [34] to diagnose dental illnesses like caries, plaque

accumulation, osteoporosis, and periodontal disease. Similarly, Li et al. [35] created a deep learning framework with 86-97% sensitivity for categorizing incisors, canines, premolars, and molars. In a collection of 434 pictures, Askar et al. [5] obtained 84% accuracy in detecting white spots, fluorotic and non-fluorotic lesions.

Despite these developments, deep learning for oral illness classification has significant limitations in the literature. Diagnostics for oral thrush, canker sores, cold sores, gingivostomatitis, mouth cancer, oral cancer, and oral lichen planus have not been thoroughly studied. The absence of publicly available, large-scale mouth and oral disease datasets has further hampered the development of accurate and generic deep-learning models. This paper introduces a deep learning-based oral illness categorization method to fill these shortcomings.

The present study proposes the Mouth and Oral Diseases Classification using the Stack Ensemble Technique (MODC-SET), a novel recognition model designed to classify seven key oral diseases: gingivostomatitis (Gum), canker sores (CaS), cold sores (CoS), oral lichen planus (OLP), oral thrush (OT), mouth cancer (MC), and oral cancer (OC). To enhance diagnostic accuracy, the MODC-SET integrates three state-of-the-art transfer learning models—MobileNetV2, InceptionResNetV2, and ResNet50 at the first level and SGBoost (meta classifier) on the second level. The significant contributions of this research are:

1. **Development of the MOD Dataset:** A newly curated dataset dedicated to oral diseases, encompassing seven diverse conditions previously underrepresented in deep learning research.
2. **Comprehensive Disease Detection:** Unlike prior studies focusing on limited oral conditions, MODC-SET provides an all-encompassing classification framework for multiple oral diseases.
3. **Deep Ensemble Technique Implementation:** The stacking ensemble technique enhances classification accuracy by leveraging the combined predictive power of multiple deep learning models.
4. **State-of-the-Art Performance:** MODC-SET achieves an overall accuracy of 99.32%, significantly outperforming existing models in the literature.
5. **Emphasis on Preventive Healthcare:** The model is particularly relevant for early disease detection in low-resource settings, offering a cost-effective solution for oral health diagnostics.

The rest of this paper is structured as follows: Section 2.2 reviews related work in deep learning-based oral disease classification. Section 2.3 describes the dataset, methodology, and the proposed MODC-SET model architecture. Section 2.4 presents experimental results and discussion, including performance analysis and comparative evaluation. Section 2.5 concludes the paper with suggestions for future research.

1.2 Literature Work

Deep learning (DL) and artificial intelligence (AI) techniques, including oral health, are essential in medical diagnostics. Different machine learning (ML) and deep learning-based methods have been proposed

to improve the precision and efficiency of diagnosing oral and dental diseases. This section reviews the literature on oral disease classification and outlines the research gaps the study seeks to address.

1.2.1 Early Approaches to Oral Disease Diagnosis

Clinical, radiographic, and microscopic tests dominate oral disease diagnosis. Standard periodontal disease detection procedures include probing depth measurement, bleeding on probing, and alveolar bone loss analysis [13]. Inter-examiner variability and instrument sensitivity can lead to unreliable results with these procedures [14, 15]. Additionally, they are invasive, laborious, and need highly experienced practitioners, making them inaccessible to many populations globally.

Researchers have researched ML and DL algorithms to automate oral illness identification and address these issues. Research suggests that ensemble methods and CNNs can effectively diagnose and classify oral disorders [20, 19]. CAD systems have improved detection and have been used in clinics to reduce human error and boost usage.

1.2.2 Deep Learning-Based Approaches in Dental and Oral Disease Classification

Introducing new deep learning architectures, such as CNNs, transfer learning models, and hybrid ensemble techniques, has improved the accuracy of the classification of oral diseases [31]. Different methods of diagnosing dental caries, periodontal diseases, oral cancers, and inflammatory conditions have been studied.

1.2.2.1 Classification of Dental Caries and Periodontal Diseases

Globally, dental caries and periodontal diseases are the most common oral health problems [11]. Deep learning methods have been employed for automated detection and classification in several studies:

1. **SqueezeNet-based Classification:** Askar et al. [5] developed a deep learning model using SqueezeNet to classify fluorotic lesions, white spot lesions, and other carious lesions from a self-generated dataset, achieving an accuracy of 87%.
2. **ResNet50 for Gingivitis Detection:** Alalharith et al. [4] are intrigued by the ResNet50 model to differentiate inflamed teeth from non-inflamed teeth using intraoral images. Despite achieving an accuracy of 77.12% in the classification, the model still has the opportunity to improve classification precision.
3. **Cubic SVM for Dental Restorations:** Abdalla-Aslan et al. [1] applied Cubic Support Vector Machine (SVM) to classify dental restorations, including composite crowns, fillings, amalgam fillings, and root canal treatments. The proposed model achieved an accuracy of 93.6%.
4. **Faster R-CNN for Caries and Internal Root Resorption Detection:** Khan et al. [36]

proposed a Faster R-CNN model to detect caries, auditory brainstem response (ABR), and internal root resorption (IRR) from periapical radiographs, and it obtained an accuracy of 84.76%.

Recent advancements further reinforce the role of deep learning in medical and genomic diagnostics. For example, Can et al. [37] introduced the Common Vector Approach pooling (CVApool) to overcome the limitations of traditional average pooling in CNNs, demonstrating significantly enhanced accuracy (up to 86.4%) in detecting twenty categories of dental diseases from intraoral X-rays. Similarly, Kang et al. [38] developed DOLNet, a hierarchical attention-based framework for diagnosing odontogenic jaw lesions from panoramic radiographs, achieving recall and F1-score improvements of more than 40% compared to prior methods and even outperforming expert clinicians These studies highlight two important trends: (i) the design of novel pooling and attention mechanisms tailored to biomedical imaging tasks, and (ii) the capacity of deep learning to surpass traditional diagnostic methods by addressing challenges such as class imbalance, positional biases, and interpretability. Incorporating these insights into cancer genomics-based detection frameworks underscores the growing importance of specialized architectures and attention-based feature fusion for improving robustness, generalization, and clinical applicability.

These experiments show that deep learning can diagnose dental diseases, although dataset sizes and class imbalances remain issues.

1.2.2.2 Hybrid Deep Learning Approaches for Oral Health Diagnostics

Hybrid deep-learning approaches are gaining popularity to improve oral disease classification performance. Some key contributions are:

1. **Deep CNN for Tooth Classification:** Schwendicke et al. [31] used deep CNNs to classify premolars and molars from periapical radiographs, achieving an accuracy of 82.8%.
2. **MASK R-CNN for Periodontal Disease Identification:** Liu et al. [34] developed a MASK R-CNN model trained on a self-created dataset to classify decayed teeth, plaque accumulation, osteoporosis, and periodontal disease.
3. **VGG16 for Oral Lichen Planus Detection:** Akaike et al. [3] proposed a VGG16-based CNN model trained on whole-slide images (WSIs) to detect oral lichen planus (OLP), achieving an impressive accuracy of 97.38%.
4. **EfficientNet and ResNet-50 for Dental Caries Detection:** Watanabe et al. [39] compared EfficientNet-B0, DenseNet-121, and ResNet-50 for detecting dental and non-dental caries, with ResNet-50 achieving the highest accuracy (92%).

While these models exhibit high classification performance, they often focus on a limited subset of oral diseases, overlooking conditions such as oral thrush, canker sores, and mouth cancer.

1.2.2.3 Oral Cancer and Lesion Detection Using Deep Learning

Oral cancer is one of the most serious and life-threatening oral diseases, necessitating early detection for effective treatment [9]. Several studies have attempted to integrate deep learning models into oral cancer diagnosis:

1. **Fragment Jaya Whale Optimizer with Deep CNN (FJWO-DCNN):** Hemalatha et al. [20] proposed an FJWO-DCNN model for classifying oral cancer from the BAHNO NMDS dataset, achieving an accuracy of 91.96%.
2. **GoogLeNet and Inception-V3 for Dental Caries:** Lee et al. [40] used GoogLeNet Inception-V3 to classify dental and non-dental caries from periapical radiographs, reaching an accuracy of 89%.

Despite these advances, current deep learning models lack comprehensive datasets encompassing multiple oral disease categories, limiting their applicability in real-world clinical settings. Table table 1.1 summarizes the literature review.

Table 1.1: Summary of Methods, Diseases, Datasets, Accuracy, and Limitations

Ref.	Methodology	Target Diseases	Dataset Source	Acc	Limitations
[5]	SqueezeNet (CNN)	Fluorotic lesions, white spot lesions, other lesions	Self-generated dataset	87%	Limited to lesion detection; lacks coverage of broader oral diseases
[4]	ResNet50 (CNN)	Inflamed vs. non-inflamed teeth	Intraoral image dataset	77.12%	Binary classification only; relatively low accuracy
[1]	Cubic SVM	Dental restorations (fillings, crowns, implants, etc.)	Periapical radiographs	93.6%	Limited to specific restorations; not general oral diseases
[36]	Faster R-CNN	Caries, ABR, IRR	Dental periapical radiographs	84.76%	Only three disease categories; accuracy could improve

[31]	Deep CNN	Premolars and molars classification	Periapical radiographs	82.8%	Narrow scope (tooth types only)
[35]	Mask R-CNN	Decayed teeth, plaque, osteoporosis, periodontal disease	Self-created dataset	NR	Unknown dataset size; no benchmark comparison
[3]	VGG-16 (CNN)	Oral Lichen Planus (OLP)	Whole-Slide Images	97.38%	OLP-specific; lacks generalizability
[39]	EfficientNet-B0, DenseNet-121, ResNet-50	Dental caries	Self-created dataset	92% (ResNet-50)	Caries-only focus
[20]	FJWO-DCNN	Oral Cancer	BAHNO NMDS dataset	91.96%	Oral cancer only; not multi-disease

1.2.3 Limitations in Existing Studies

Deep learning applications for oral illness classification have advanced; however, research has significant limitations. Publicly available datasets are scarce, limiting generalization across varied populations [11]. Most studies rely on self-created datasets with limited disease categories. Previous research narrowly focused on dental caries, periodontal diseases, and oral cancer, neglecting oral thrush, canker sores, cold sores, and gingivostomatitis [5, 31]. These models are constrained in real-world clinical settings where a wider spectrum of oral problems must be reliably diagnosed.

Invasive diagnostic methods like radiographic imaging, fluorescence imaging, and microscopic analysis may be inaccessible in underdeveloped regions due to the need for specialized equipment and trained professionals [11, 32, 33]. Although deep learning models show promise, specific disease categories still require more robust approaches for better classification accuracy [4, 36]. Due to class imbalance, misclassification, and poor feature extraction, many models perform inconsistently among oral disease categories.

1.2.4 Research Gaps and Motivation

MODC-SET, a complete deep learning framework, addresses these problems and fills research gaps. This model improves classification accuracy and reliability using deep ensemble learning and three resilient transfer learning architectures—MobileNetV2, InceptionResNetV2, and ResNet50. To overcome dataset limitations, this study provides the Mouth and Oral Disorders (MOD) dataset, including seven oral disorders, for robust model training and validation. MODC-SET predicts oral disease accurately and is scalable, filling gaps in previous studies, especially in resource-limited settings.

The literature review discusses deep learning-based oral sickness categorization improvements, dataset availability, disease coverage, diagnostic methodologies, and accuracy limits. Some studies employ deep learning to detect dental caries, periodontal problems, and oral cancer, although not all. Furthermore, intrusive diagnostic approaches restrict these models to clinical contexts.

MODC-SET, a revolutionary deep-learning framework with transfer learning models to classify oral illnesses, overcomes these challenges. A freshly developed MOD dataset covers more ailments, making MODC-SET a practical, non-invasive, and accessible choice for early diagnosis and preventative treatment. This study surpasses current models with 99.32% accuracy, enhancing dental and oral health research diagnosis. This research may help global healthcare systems identify illnesses, intervene early, and reduce the oral disease burden.

1.3 Materials and Methods

1.3.1 Overview of the Proposed Methodology

Traditional machine learning algorithms such as Support Vector Machines (SVMs) and Random Forests (RFs) often perform well when datasets are relatively small and feature spaces are well-structured. SVMs excel at finding clear decision boundaries between two classes, which makes them effective in binary classification tasks but less scalable in high-dimensional or highly imbalanced data. Random Forests, on the other hand, aggregate multiple decision trees, allowing them to capture complex feature interactions and reduce overfitting, which often results in strong baseline performance for structured biomedical data. However, as the dimensionality and heterogeneity of genomic and medical datasets increase, deep neural networks (DNNs) and hybrid architectures demonstrate superior performance. Their layered representations enable automatic extraction of hierarchical and nonlinear patterns, making them more effective in capturing subtle biological signals and distinguishing between overlapping classes. This explains why traditional algorithms perform competitively in simpler cases, while deep learning models, particularly ensemble and attention-based methods, achieve higher accuracy and robustness in complex multi-class biomedical classification tasks.

Our Mouth and Oral Disease Classification using the Stack Ensemble Technique (MODC-SET) framework classifies oral diseases reliably and robustly, and with generalization improvement, using deep

learning. This framework employs a stacking ensemble technique, combining MobileNetV2, InceptionResNetV2, and ResNet50 to extract hierarchical features and train robust classifiers [40]. A stack ensemble overcame single-model classifier limitations to improve picture representation and detection for numerous oral illnesses. Figure 10.5 illustrates the MODC-SET architecture, where input passes through three basic models before being analyzed by the stacking ensemble meta-classifier for final decision-making.

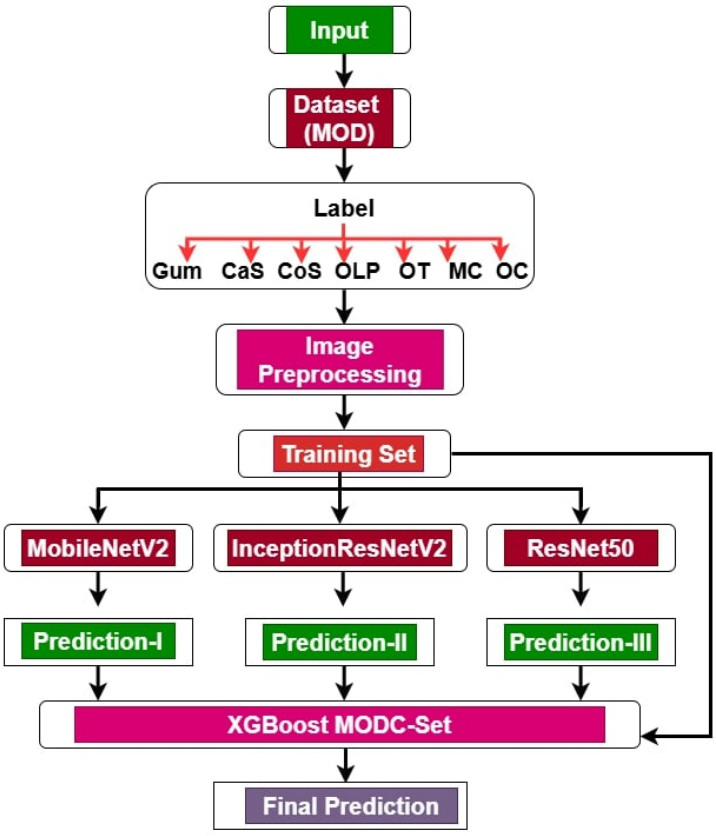

Figure 1.1: Flowchart of the Proposed Method.

1.3.1.1 Objective and Scope

MODC-SET intends to create an AI-powered oral illness classification system. This study intends to enhance early detection and preventive health in low-resource settings with limited access to dental specialists [6]. In contrast, standard diagnostic methods rely on periodontal probing, radiographic imaging, fluorescence, and microscopic inspection [32, 33]. The non-invasive, cost-effective MODC-SET approach classifies oral illnesses using real-time clinical photos.

The proposed MODC-SET classifies the following oral diseases:

1. **Canker Sores (CaS):** Small, painful ulcers in the mouth are often associated with stress or immune reactions.
2. **Cold Sores (CoS):** Viral infections cause painful blisters around the lips and mouth.

3. **Gingivostomatitis (Gum):** A bacterial or viral infection that leads to gum inflammation, affecting oral health.
4. **Mouth Cancer (MC):** A malignant condition affecting various parts of the oral cavity.
5. **Oral Cancer (OC):** A broader classification encompassing multiple cancerous lesions in the mouth.

These disorders were chosen for their prevalence, clinical relevance, and oral health impact. MODC-SET provides a clinically useful diagnostic tool that includes numerous kinds of diseases.

1.3.2 Methodological Framework of MODC-SET

The proposed MODC-SET model framework is divided into the following key stages:

1.3.2.1 Dataset Compilation and Annotation

MOD data is meticulously curated from clinically validated images, open-source medical imaging databases, and real-world clinical case studies. The dataset was obtained from Liaqat Medical and Dental Complex, Okara, Pakistan, under the supervision of Dr Sibtain Liaqat, and is publicly available. This dataset was collected by ethical principles, where the images were anonymized [6]. A panel of senior dental practitioners, radiologists, and AI experts manually labeled and validated each image to ensure accurate disease classification. The MOD dataset covers seven important oral diseases that can occur in the oral cavity. Figure 1.2 shows sample texts of the dataset.

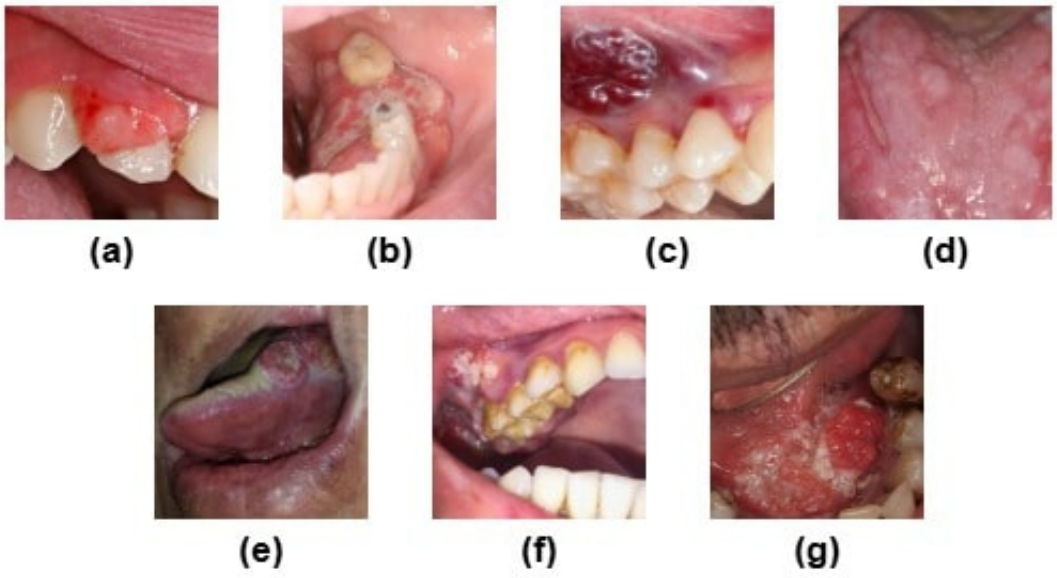

Figure 1.2: (a) CaS, (b) CoS, (c) Gum, (d) MC, (e) OC, (f) OLP, and (g) OT Classes Samples of MOD Dataset.

1.3.2.2 Dataset Composition and Class Distribution

The MOD dataset helps develop and test deep-learning oral disease categorization algorithms. The dataset includes clinical pictures of CaS, CoS, Gum, MC, OC, OLP, and OT. The dataset is annotated and structured to represent disease classifications equally, making it ideal for strong deep-learning models. The collection began with 517 clinical records, an open-access medical library, and case study photographs. The dataset has 5,233 images after adding 4,716 augmented shots to fix class imbalance and improve model generalization. Geometric changes (rotation, flipping, scaling), color tweaks (contrast, brightness normalization), and noise addition boosted intra-class variability and model generalization across real-world situations.

Table 1.2: Distribution of MOD Dataset by Disease Category

Class Label	**Number of Images (Original)**	**Number of Augmented Images**	**Total Images (Final)**
Canker Sores (**CaS**)	78	722	800
Cold Sores (**CoS**)	79	759	838
Gingivostomatitis (**Gum**)	61	539	600
Mouth Cancer (**MC**)	90	810	900
Oral Cancer (**OC**)	54	486	540
Oral Lichen Planus (**OLP**)	93	807	900
Oral Thrush (**OT**)	62	593	655
Total	517	4716	5233

Table 1.2 displays the distribution of original photos per class, augmented images, and total images for training and evaluation. The dataset is balanced, so no disease class dominates, reducing model training biases. Mouth Cancer (900 images) and Oral Lichen Planus (900 images) have the most images, while Oral Cancer (540 images) has the fewest, reflecting real-world prevalence. This dataset provides a comprehensive standard for deep learning research in oral disease categorization, enabling AI-powered diagnostic solutions for non-invasive, scalable, and automated oral healthcare medical picture analysis. Future expansions will add illness categories, multi-modal imaging (radiographic and fluorescence imaging), and larger datasets from varied demographic sources to improve the robustness and clinical application.

1.3.2.3 Image Acquisition and Standardization

The images in the MOD dataset were collected from varied sources, ensuring real-world applicability. The dataset includes:

- High-resolution intraoral photographs captured using DSLR cameras and intraoral scanners from clinical settings.
- Dermoscopic and microscopic images obtained from open-source medical databases for precise disease classification.
- Publicly available datasets, ensuring diversity in sample representation, improving generalization performance.

1.3.2.4 Data Preprocessing

To standardize the dataset, all photos underwent a meticulous preprocessing protocol, which encompassed:

- Resizing: All images were resized to 224 × 224 pixels, the standard input dimension for deep learning models like MobileNetV2, InceptionResNetV2, and ResNet50.
- Normalization: Pixel intensity values were scaled between 0 and 1 using min-max normalization to enhance training efficiency.
- Color Space Adjustment: Images were transformed to RGB format to provide consistency among all samples.
- Noise Reduction: Adaptive median filtering was utilized to mitigate artifacts and enhance image clarity.

1.3.2.5 Data Augmentation Strategy

Rotation, shear transformation, horizontal flipping, and brightness correction promote dataset variety and reduce overfitting [41]. Data augmentation was used to reduce overfitting and increase model generalization across unknown data. These changes were dynamically applied during training using TensorFlow's ImageDataGenerator to ensure model resilience. Augmentation methods increase the dataset, boosting classification accuracy and real-life model generalization. The data augmentation strategy is shown in Table 1.3.

Table 1.3: Data Augmentation Techniques Applied

Augmentation Technique	Purpose	Applied Variations
Rotation	Simulates different orientations of oral images	±25°
Width and Height Shifts	Creates spatial variability	±10%
Shear Transformations	Introduces distortions to improve adaptability	0.2 radians
Horizontal Flipping	Enhances recognition of mirrored structures	Yes

Brightness Adjustments	Adjusts contrast to simulate different lighting conditions	0.5 – 1.0 scale
Zooming	Simulates variations in image focus	±15%
Channel Shifting	Introduces slight intensity variations to improve color consistency	±0.05

1.3.2.6 Dataset Partitioning for Training and Testing

The dataset was randomly shuffled before partitioning to prevent class ordering biases during training. Table 1.4 shows the dataset partitioning details. To ensure a fair and unbiased evaluation, the MOD dataset was split into three subsets:

- Training Set (60%) – Used to train deep learning models.
- Validation Set (20%) – Used for hyperparameter tuning and model optimization.
- Testing Set (20%) – Used for final evaluation to measure model performance.

Table 1.4: MOD Dataset Partitioning

Dataset Split	Number of Images	Percentage (%)
Training Set	3137	60%
Validation Set	1028	20%
Testing Set	1028	20%
Total	5233	100%

1.3.2.7 Deep Learning Model Selection and Training

The MODC-SET framework utilizes three pre-trained deep learning models, each known for its strengths in medical image classification:

- **MobileNetV2 [42]:** A lightweight CNN architecture optimized for mobile applications, offering computational efficiency with depthwise separable convolutions.
- **InceptionResNetV2 [43]:** A hybrid architecture that combines Inception's multi-scale feature extraction with ResNet's residual learning, improving gradient flow during training.
- **ResNet50 [18]:** A deep residual network designed to mitigate the vanishing gradient problem, ensuring efficient learning in deep architectures.
- **Stacking Ensemble Learning Implementation: Stacking ensemble learning combines the predictions from the three base classifiers to improve classification reliability. The final**

decision is computed using a meta-classifier (Logistic Regression), which refines the outputs of the base models [44, 45]. This method ensures that MODC-SET achieves higher classification accuracy than individual deep learning models, reducing misclassification errors [46].

1.3.2.8 The Proposed Methodology

Stacking is an advanced ensemble learning method [47]. Stacking assumes that derivative models of base data can make more accurate predictions. If the models were the same, so would the results. We used multiple models to understand the findings better; each model may have picked up different data features more efficiently. Stacking causes many weak learners [48]. Stacking uses several failing learners to train a meta-model (XGBoost) to make predictions utilizing their enormous number of forecasts.

Figure 1.3 shows two layers of the recommended architecture. The first-layer basic classifiers MobileNetV2, InceptionResNetV2, and ResNet50 were trained using training data. Tang et al. [49] found a variation in stacking representation learning classifiers for distinct features. The first layer's core classifiers need high accuracy and diversity to learn features from raw input. All three base classifiers handle nonlinear challenges well despite their modeling methods.

MobileNetV2, InceptionResNetV2, and ResNet50 make first-level predictions on training and test sets. The three models predict photo features separately on the MOD training set. The XGBoost-based second-level prediction uses feature predictions from the first-level prediction model. To improve results, a new test data analysis algorithm analyzes algorithm performance and training progress. Finally, XGBoost predicts and classifies.

Ensemble classification systems use many classification methods and a combiner to perform the same task. Jaiswal et al. [50] propose a transfer learning picture categorization model. The theory states that a broad dataset can train a generic visual model. We can avoid starting from scratch by training a large model on a large dataset and employing feature maps. Previous network representations can assist in finding key data features. Reuse the dataset feature maps by adding a classifier to the pre-trained model. Classifiers get ensemble model features. Transfer learning enables deep neural network training with less data by reusing models and addressing new challenges [51]. Transfer learning reduces input, speeds up training, and improves neural network performance.

Based on their similarities and differences and positive cross-validation, we created the first layer of the stacking model using all three models. The second layer meta-learner must be good at generalization to correct the learning algorithm's bias toward the training set and prevent over-aggregation. XGBoost [52] was used for second-level meta-learner generalization. This approach estimates parameters using the incredible likelihood method if all data are logical.

A better classification model requires modifying several XGBoost hyperparameters. Changing hyperparameters enhances machine learning model performance and behavior [53]. Choosing this parameter before learning happens outside the model. A lack of hyperparameter tweaking may cause improper

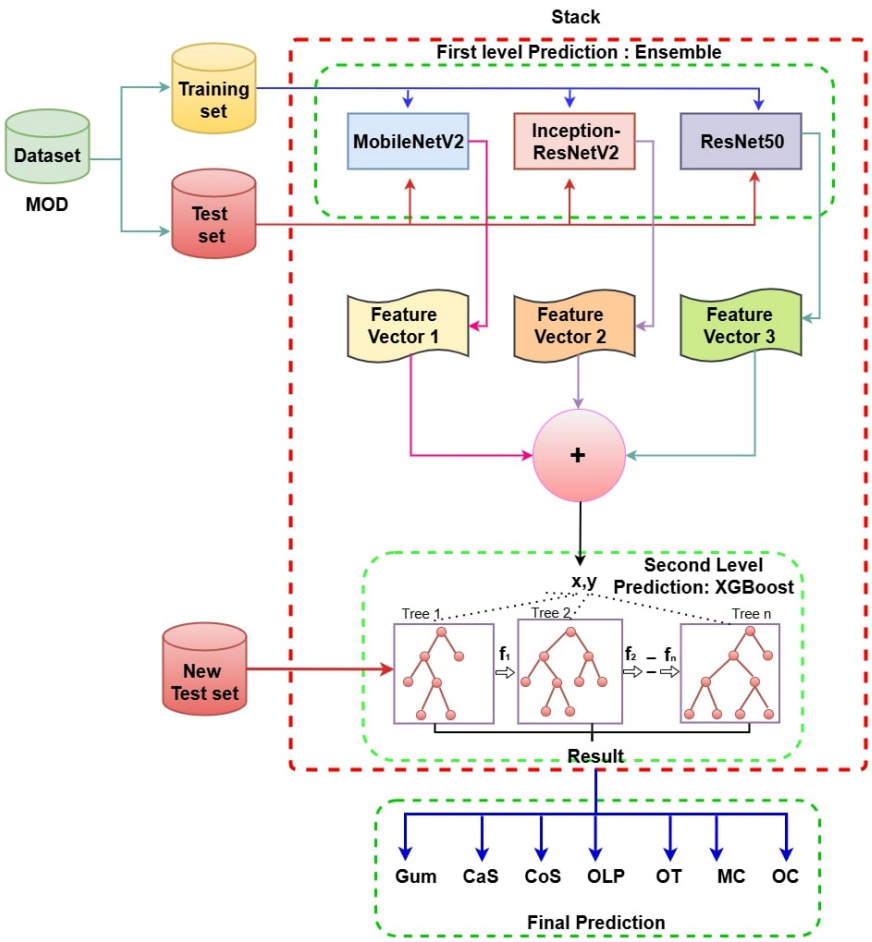

Figure 1.3: The Proposed Method Architectural Diagram.

loss function minimization. Model mistakes should be minimized. The optimal hyperparameter settings improve model performance, reduce loss, and improve outcomes.

1.3.2.9 Justification for Stacking Ensemble Learning

Deep learning models exhibit variations in feature extraction capabilities, leading to performance fluctuations based on the complexity of input images. Due to inherent biases in feature representation, a single deep learning model may fail to generalize well across all disease categories. Therefore, an ensemble learning approach—mainly stacking—is adopted to overcome these challenges. Why Stacking?

- **Feature Diversity:** Different CNN architectures specialize in learning different hierarchical features. By combining three models, MODC-SET leverages multi-scale feature representations, leading to more accurate classification.
- **Reduced Overfitting:** While individual models may overfit to specific disease classes, ensemble learning minimizes this risk by aggregating predictions from multiple architectures.
- **Improved Generalization:** Using Logistic Regression as a meta-classifier refines final predictions, improving generalization across unseen data [44, 45]. Ensemble methods have demonstrated superior

performance in various computer vision tasks, particularly in medical imaging applications [45]. The MOD dataset is a benchmark for oral disease classification, addressing critical gaps in dataset availability, diversity, and standardization. The rigorous data preprocessing pipeline, augmentation strategies, and balanced partitioning ensure that the dataset is suitable for deep learning applications in medical diagnostics.

1.3.3 Experimental Setup and Parameters

We used a Google Colab [41] Pro account with high-powered graphical processing units and no settings to train and test the suggested methods. Our team used transfer deep learning models to achieve this goal. We built a stacking ensemble model with data from the first three experiments. For each test of the proposed MODC-SET, we employed the adaptive moment estimation (Adam) optimizer set to a learning rate of 0.0001. We built our models with the help of the Sparse Categorical Cross-entropy loss function. All models were trained with a batch size of 16, early stopping, keeping only the best val_loss model, and five training iterations. The suggested MODC-SET model included the following specifications: 16 batches, five epochs, early halting, and model saving based on val_loss.

1.3.4 Evaluation Measures

The effectiveness of MODC-SET is evaluated using classification accuracy, precision, recall, F1-score, and AUC-ROC analysis [8, 31]. The model undergoes extensive testing to verify its robustness across different oral disease categories. First, we define and graphically portray four possible outcomes: a true positive (TP), a true negative (TN), a false negative (FN), and a false positive (FP). We then test the proposed method using the testing set with different evaluation measures, such as accuracy, F1 score, precision, and recall, to evaluate the structure's effectiveness. Below, we provide a closer examination of the evaluation criteria used.

1.3.4.1 Classification Accuracy

The accuracy of a classification system can be evaluated by determining the percentage of its predictions that were correct and the percentage that were incorrect.

$$\text{Accuracy} = \frac{TP + TN}{TP + TN + FP + FN} \tag{4}$$

1.3.4.2 Precision

Classification accuracy is not necessarily the best criterion for evaluating a model's performance. It is one situation in which a sizeable socioeconomic divide exists. It is safe to assume that each sample is of the highest possible quality. If the model is not picking up any new information, inferring that all

components belong to the best class would be irrational. Therefore, when discussing accuracy, we refer to the fluctuation in findings received while measuring the same object several times with the same tools. The term precision refers to one of these statistics and can be defined as follows:

$$\text{Precision} = \frac{TP}{TP + FP} \tag{5}$$

1.3.4.3 Recall

Another critical parameter is recall, which refers to the percentage of input samples of a type that the model can accurately predict. The formula for the recall is as follows:

$$\text{Recall} = \frac{TP}{TP + FN} \tag{6}$$

1.3.4.4 F1 Score

The F1 score is a statistic utilized to contrast recall and precision.

$$F_1 \text{ Score} = \frac{2 \times (\text{Precision} \times \text{Recall})}{\text{Precision} + \text{Recall}} \tag{7}$$

1.3.4.5 ROC Curve

The effectiveness of classifiers can be shown over their cutoff value using a receiver operating characteristic(ROC) curve. An excellent model can be evaluated using the widely appreciated ROC curve to determine the optimum threshold. The true positive rate (TPR) is in competition with the false positive rate (FPR) at various limits.

1.4 Results and Discussion

In this section, we report the conclusions of a comprehensive series of tests conducted to evaluate the usefulness of the proposed tool for classifying mouth and oral diseases. The performance of the proposed method is estimated in the following:

1. The efficacy of the proposed MODC-SET method was witnessed on the MOD dataset.
2. In order to compare results obtained on the study of treating cancer with modalities of the MODC-SET, the trials were carried out with and without data augmentation.
3. A comparison study of the proposed model with those available would have been followed.

1.4.1 The Performance Analysis of the Proposed MODC-SET Technique

Figure 1.4 displays the effectiveness of the MODC-SET model during training. Graphs (a) and (b) show the model's accuracy and loss over epochs or training rounds. Graph (a) shows training and validation accuracy lines. Both lines reach the first-starting twentieth epoch. The training accuracy line starts high and stays stable, indicating that the model performs well on the training set. The validation accuracy line starts around the training accuracy and stays close to it, indicating that the model generalizes well to fresh data. Graph (b) shows two lines for the training and validation loss of the model. Both axes start at epoch 1. After a rapid decrease, signals fast learning during training, the training loss line flattens as the model converges. The validation loss line drops sharply and plateaus, indicating that the model is learning generic patterns rather than overfitting, which matches the training loss. Figure 1.4 demonstrates that the MODC-SET model successfully trains machine learning models with high accuracy and minimal loss. The loss and accuracy graphs show good model performance without overfitting because the training and validation lines are close.

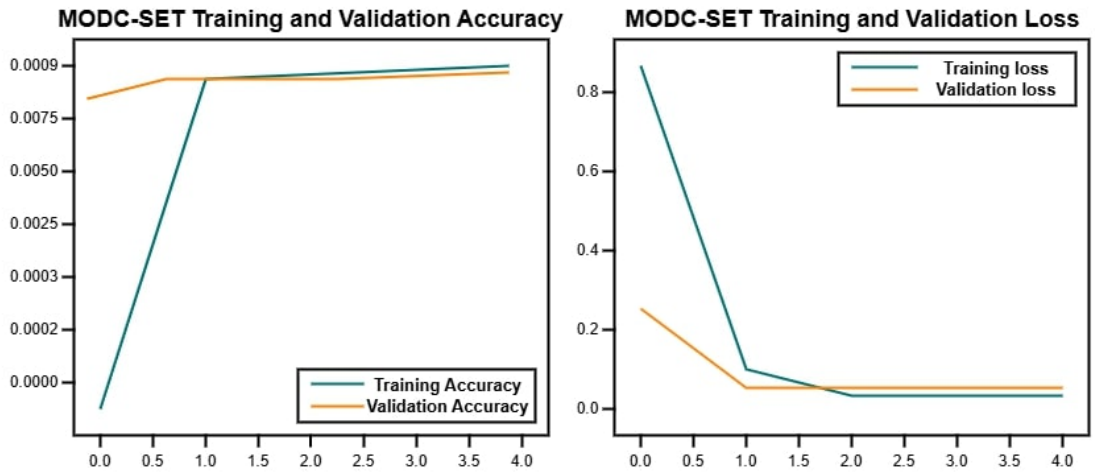

Figure 1.4: The Proposed Method's Accuracy and Loss Graph of Training and Loss.

Table 1.5: Evaluation of the Suggested MODC-SET Method in Terms of Precision, Recall, F1, and Accuracy

Performance Measures	Precision	Recall	F1 Score	Accuracy
CaS	98%	97%	98%	97.0%
CoS	100%	100%	100%	100%
Gum	100%	100%	100%	100%
MC	99%	99%	100%	99.0%
OC	99%	99%	99%	98.9%
OLP	99%	99%	99%	99.0%

OT	100%	100%	100%	100%
	Average Accuracy			**99.32%**

In Table 1.5, the proposed Mouth and Oral Diseases Classification using the Stack Ensemble Technique (MODC-SET) is assessed for precision, recall, F1 score, and accuracy across seven oral illness classes. The precision values represent the percentage of projected affirmative cases appropriately detected. The MODC-SET method eliminates false positives with 98-100% precision across all classes. The MODC-SET technique accurately diagnoses all oral diseases due to its low specificity of 97%. As the MODC-SET model balances precision and recall, its F1 score is 98% or higher for all classes, indicating its disease classification resilience. The average class correctness is 99.32%, with individuals ranging from 97.0% to 100%. It proves MODC-SET's oral disorder expertise. Results show that the MODC-SET model may effectively and reliably identify mouth and oral problems, making it a viable clinical diagnostic tool.

The confusion matrix demonstrates good recall and precision by class for the model. Classifications inside the diagonal are correct, while those outside are incorrect. MODC-SET's confusion matrix has low off-diagonal values, indicating correctness.

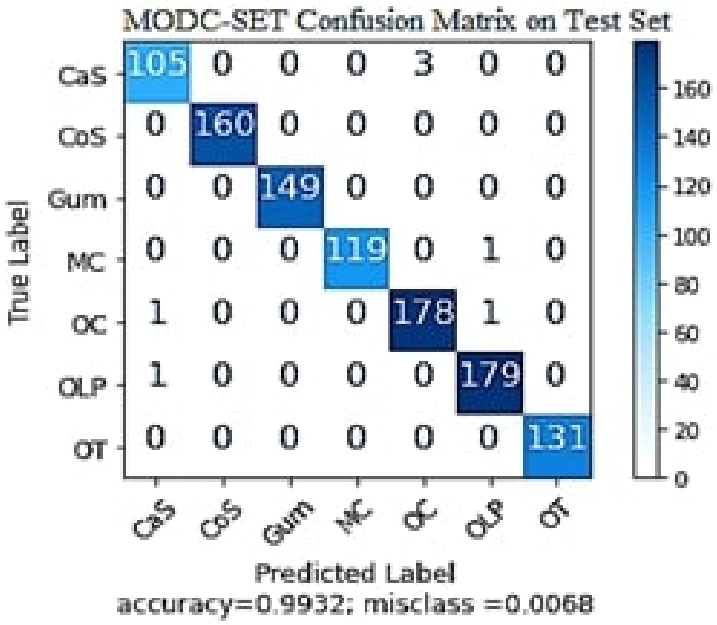

Figure 1.5: The Proposed MODC-SET Model Confusion Matrix on Test Set.

The model accurately classifies oral ailments with few misclassifications. Refer to Figure 2.3 for the confusion matrix of the proposed MODC-SET model for classifying oral diseases. Despite correctly predicting 105 cases, the suggested method mislabeled three. Each of the 160 CoS class forecasts was correct. The technique predicted all 149 GUM cases. It misclassified one of 119 cases as OT. The approach successfully predicted 178 occurrences but mislabeled one CaS and one OLP. The OLP and OT courses'

179 and 131 occurrences were appropriately predicted. Overall, the MODC-SET model is accurate, with 99.32% correct identification of samples across all classes. The misclassification rate of 0.68% highlights the small number of incorrectly categorized cases. Figure 2.3 displays the MODC-SET model's remarkable performance on the test set, with thorough classification results for each oral disorder category. This model's accuracy and low misclassification rate make it effective in clinical diagnosis.

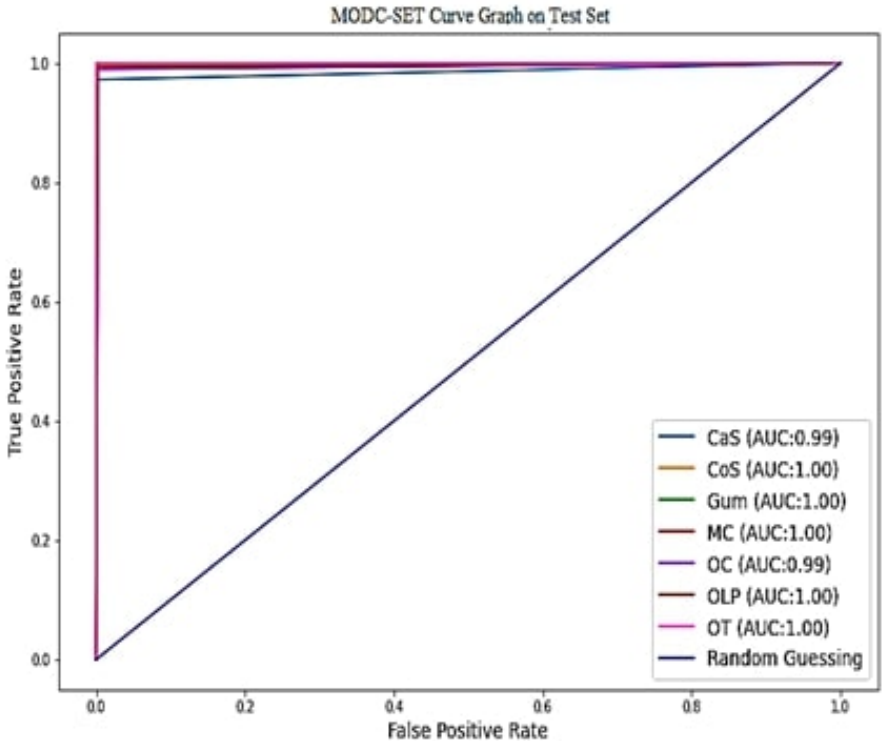

Figure 1.6: The Proposed MODC-SET Model Confusion Matrix on Test Set.

Figure 2.4 shows the ROC curve for the proposed Mouth and Oral Diseases Classification utilizing the Stack Ensemble Technique (MODC-SET) model on the test set. The area and ROC under the curve (AUC) metrics measure the model's oral disease classification ability. The True Positive Rate (TPR) for Canker Sores (CaS) is 99%, showing the model's accurate detection. The AUC is not explicitly given in the extract but is usually a numerical measure of the ROC curve's class performance. For Cold Sores (CoS), the TPR is 100%, indicating complete identification. Given the optimum TPR, this class's AUC should be high. Gingivostomatitis (GUM): 100% TPR indicates accurate diagnosis. AUC, though not reported, may indicate significant discrimination. The TPR for Mouth Cancer (MC) is 100%, indicating precise detection. The AUC is not given but should be high, indicating good discrimination. For Oral Cancer (OC), the TPR is 99%, indicating the model's strong ability to detect cases. The AUC value measures this class's ROC curve performance. For Oral Lichen Planus (OLP), the TPR is 100%, confirming the accurate diagnosis. Although not explicitly stated, the AUC may show the model's discrimination. The TPR of 100% implies that the model accurately predicts oral thrush (OT). AUC, which is not expressly provided, should reflect the ROC curve performance for that class. The ROC curve shows the trade-off between true

and false positive rates, demonstrating the model's discrimination ability at different thresholds. High TPR values across all classes imply accurate oral disease mapping with few false positives. The MODC-SET model AUC evaluations match these results. High AUC values (100%) show the MODC-SET model's ability to classify oral illnesses using testing data accurately. By examining the MODC-SET model as an object detection model, Figure 2.4 shows its effectiveness in discriminating oral illness classes in the test set. The expected high TPR and AUC values confirm the model's clinical diagnostic robustness.

1.4.2 Ablation Study of MODC-SET Model

We evaluate each MODC-SET Model component for ablation comparability. The study examines the contribution of transfer learning models to the ensemble and the effect of data augmentation on classification performance.

1.4.2.1 Impact of Individual Base Models

The MODC-SET model is applied to MobileNetV2, InceptionResNetV2, and ResNet50 transfer learning models. We evaluate the performance of these models trained separately on the MOD dataset.

Table 1.6: *Performance of Individual Base Models*

Model	Precision	Recall	F1 Score	Accuracy
MobileNetV2	93.8%	92.5%	93.1%	92.7%
InceptionResNetV2	95.1%	94.3%	94.7%	94.5%
ResNet50	96.2%	95.5%	95.8%	95.4%
MODC-SET (Ensemble)	**99.3%**	**99.2%**	**99.2%**	**99.32%**

Table 1.6 shows that combining base models as an ensemble enhances classification accuracy. In standalone models, ResNet50 (95.4%) is the most accurate, followed by InceptionResNetV2 (94.5%) and MobileNetV2 (92.7%). Combining these three models in MODC-SET boosts accuracy to 99.32, showing how ensemble learning can use each model's capabilities to exceed any single model. Multimodel stacking enhances recall, precision, and classification robustness. The ensemble approach improves the F1-score and recall compared to the single model, showing that the MODC-SET model reduces misclassification and improves generalizability. While effective, individual models lack generalizability compared to ensemble approaches, which include numerous perspectives.

1.4.2.2 Effect of Data Augmentation

To assess the impact of data augmentation on model performance, we compare MODC-SET with and without data augmentation.

Table 1.7: Effect of Data Augmentation on Model Performance

Model	Precision	Recall	F1 Score	Accuracy
MODC-SET (Without Data Augmentation)	85.7%	83.6%	84.6%	84.2%
MODC-SET (With Data Augmentation)	**99.3%**	**99.2%**	**99.2%**	**99.32%**

The impact of data augmentation is demonstrated in Table 1.7. The MODC-SET model has an accuracy of 84.2% and an F1 score of 84.6% without data augmentation. Data augmentation improves model performance, yielding 99.32% accuracy and 99.2% F1 score. Diversifying the training dataset with data augmentation increases model generalization. Transformations like rotation, scaling, flipping, and brightness help the model represent features well and avoid overfitting.

1.4.2.3 Effect of Data Augmentation

We evaluate model combinations to discover if stacking all three models is essential. Table 1.8 shows that all three models are most effective. Each base model's capabilities are used to maximize classification effectiveness in the stacking ensemble approach. InceptionResNetV2 and ResNet50 extract features are better than those of MobileNetV2 with either of the other two models. The MODC-SET ensemble outperforms all combinations, demonstrating the necessity of integrating all three models.

The ablation study shows that ensemble learning and data augmentation improve classification accuracy with the MODC-SET model. Although each base model contributes significantly, their combination leads to a significant performance improvement, obtaining a phenomenal accuracy of 99.32%. Data augmentation increased precision, recall, and F1 scores, improving model generalization. Classification accuracy and robustness were highest when all three transfer learning models were combined. These findings show that ensemble learning and data augmentation improve deep learning-based classification of mouth and oral disorders, enabling more accurate and efficient diagnostics.

Table 1.8: fPerformance of Different Model Combinations

Model Combination	Precision	Recall	F1 Score	Accuracy
MobileNetV2 + InceptionResNetV2	96.4%	95.9%	96.2%	95.8%
InceptionResNetV2 + ResNet50	97.3%	97.1%	97.2%	97.0%
MobileNetV2 + ResNet50	96.9%	96.5%	96.7%	96.6%
MODC-SET (All Three Models)	**99.3%**	**99.2%**	**99.2%**	**99.32%**

1.4.3 Comparison with State-of-the-Art Models

No published research has combined CaS, CoS, Gum, MC, OC, OLP, and OT. Ensemble approaches in this field require literature. It prevents study comparisons. We chose relevant research to compare our model to existing state-of-the-art oral health diagnosis methods. Table 1.9 shows that the proposed technique beats recent studies' accuracy.

Ekert et al. [14] obtained 96% accuracy using a CNN-based model on panoramic radiographs. Teeth are divided into incisors, canines, premolars, and molars by structure and function. According to Abdalla-Aslan et al., [1], a Cubic SVM model accurately classified dental restorations in a panoramic radiography dataset with 93.6% accuracy. Using a dataset, Askar et al. [5] classified white spots, fluorotic, and other lesions. However, their CNN-based SqueezeNet model was outperformed by the MODC-SET model. Hemalatha et al. [20] developed a Fragment Jaya Whale Optimizer with a Deep Convolutional Neural Network to detect oral cancer patients. The proposed method had 91.96 percent accuracy in tests. The VGG16 model was used by Akaike et al. [3] to detect oral lichen planus (OLP). The proposed method was 97.38 percent accurate. Kuwana R et al. [32] applied the Detect-Net model to periapical radiography data with 96% efficiency. Park et al. [54] classified dental and non-dental caries with 95% accuracy using a CNN-based model on a self-created dataset. Sudha et al. studied pre-trained models for a low-cost, multimodal oral sensing device employing federated learning, MLP, and deep belief networks to identify and classify mouth disorders [55]. Using a preprocessed and supplemented image dataset, the model achieved 85% accuracy, enabling early diagnosis and appropriate treatment. The MODC-SET model outperformed state-of-the-art techniques with a 99.32% success rate. Table 1.9 reveals that the proposed model outperforms previous models in accuracy.

Table 1.9: Proposed Method Comparison with State-of-the-Art Studies

Ref., Year	**Method**	**Disease**	**Dataset**	**Accuracy**
[14], 2019	CNN	Incisors, Canines, Premolars, Molars, Amalgam filling, Dental implant, Composite filling, Crown, Root canal treatment, Core	Periapical radiographs	96%
[1], 2020	Cubic SVM	Same as above	Periapical radiographs	93.6%
[5], 2021	**SqueezeNet**	White spot lesions, Fluorotic lesions, other lesions	Self-created	87%

[32], 2021	**AlexNet**, VGG-16, Detect-Net	Maxillary incisor region	Periapical radiographic	90%, 92%, 96%
[20], 2022	FJWO-DCNN	Oral Cancer (OC)	BAHNO NMDS	91.96%
[3], 2023	VGG16	Oral Lichen Planus (OLP)	Whole-Slide Images (WSIs)	97.38%
[54], 2023	CNN	Periodontal diseases, Dental caries, Dental calculus	Self-Created	ResNet-92%
[55], 2024	MLP, DBN	Mouth and Oral diseases	Self-Created	85% (DBN)
Proposed Method	MODC-SET	**CaS, CoS, Gum, MC, OC, OLP, OT**	MOD	**99.32%**

1.5 Conclusion and Future Work

MODC-SET, a deep learning-based stacking ensemble system, automatically classifies mouth and oral disorders. The model improves classification accuracy and generalization by incorporating MobileNetV2, InceptionResNetV2, and ResNet50. Based on the newly constructed MOD dataset, MODC-SET outperforms existing approaches with an impressive 99.32% accuracy across seven oral illnesses. Stacking ensemble learning, fine-tuning pre-trained models, and data augmentation have created a robust and scalable diagnostic tool with great potential for clinical applications, telemedicine, and automated dental screening in resource-limited environments. The results show that AI-driven diagnostic tools can deliver non-invasive, cost-effective, and reliable oral healthcare early detection and intervention solutions. Despite promising results, some areas need further study to improve the model's generalizability, efficiency, and clinical application. Radiographic, fluorescence, and hyperspectral imaging will be used in future studies to enhance diagnostic accuracy and disease coverage. Additional external validation on multi-center datasets from varied demographics will assure broader applicability. Quantization and pruning will be used to optimize MODC-SET for real-time deployment on mobile and edge devices to improve computing efficiency. Using explainable AI (XAI) strategies will improve model interpretability and build healthcare professionals' trust by offering transparent decision-making insights. Leukoplakia, erythroplakia, and TMDs can be added to MODC-SET to widen its coverage. To assess performance in the real world and incorporate it into the process of clinical practice, hospitals and dental practitioners will be included in shared clinical trials. DC-SET will help to advance AI-based dental diagnostics since it addresses these factors and raises the bar on the automated, scalable, and high-precision analysis of medical images in the oral healthcare sector.

References

Bibliography

[1] R. Abdalla-Aslan, T. Yeshua, D. Kabla, I. Leichter, and C. Nadler, "An artificial intelligence system using machine-learning for automatic detection and classification of dental restorations in panoramic radiography," *Oral surgery, oral medicine, oral pathology and oral radiology*, vol. 130, no. 5, pp. 593–602, 2020.

[2] S. T. A. Aberin and J. C. de Goma, "Detecting periodontal disease using convolutional neural networks," in *2018 IEEE 10th International Conference on Humanoid, Nanotechnology, Information Technology, Communication and Control, Environment and Management (HNICEM)*. IEEE, 2018, pp. 1–6.

[3] Y. Akaike, K.-i. Morita, K. Sakamoto, F. Tsushima, K. Kayamori, N. Maruta, K. Yamazaki, E. Anzai, E. Tonouchi, H. Harada *et al.*, "Automatic detection of spongiosis associated with oral lichenoid lesions using machine learning," *Journal of Oral and Maxillofacial Surgery, Medicine, and Pathology*, vol. 35, no. 4, pp. 368–374, 2023.

[4] D. M. Alalharith, H. M. Alharthi, W. M. Alghamdi, Y. M. Alsenbel, N. Aslam, I. U. Khan, S. Y. Shahin, S. Dianišková, M. S. Alhareky, and K. K. Barouch, "A deep learning-based approach for the detection of early signs of gingivitis in orthodontic patients using faster region-based convolutional neural networks," *International Journal of Environmental Research and Public Health*, vol. 17, no. 22, p. 8447, 2020.

[5] H. Askar, J. Krois, C. Rohrer, S. Mertens, K. Elhennawy, L. Ottolenghi, M. Mazur, S. Paris, and F. Schwendicke, "Detecting white spot lesions on dental photography using deep learning: A pilot study," *Journal of dentistry*, vol. 107, p. 103615, 2021.

[6] A. T. Balaei, P. de Chazal, J. Eberhard, H. Domnisch, A. Spahr, and K. Ruiz, "Automatic detection of periodontitis using intra-oral images," in *2017 39th Annual International Conference of the IEEE Engineering in Medicine and Biology Society (EMBC)*. IEEE, 2017, pp. 3906–3909.

[7] J. Beck, P. Papapanou, K. Philips, and S. Offenbacher, "Periodontal medicine: 100 years of progress," *Journal of dental research*, vol. 98, no. 10, pp. 1053–1062, 2019.

[8] A. S. Becker, M. Marcon, S. Ghafoor, M. C. Wurnig, T. Frauenfelder, and A. Boss, "Deep learning in mammography: diagnostic accuracy of a multipurpose image analysis software in the detection of breast cancer," *Investigative radiology*, vol. 52, no. 7, pp. 434–440, 2017.

[9] H.-J. Chang, S.-J. Lee, T.-H. Yong, N.-Y. Shin, B.-G. Jang, J.-E. Kim, K.-H. Huh, S.-S. Lee, M.-S.

Heo, S.-C. Choi *et al.*, "Deep learning hybrid method to automatically diagnose periodontal bone loss and stage periodontitis," *Scientific reports*, vol. 10, no. 1, p. 7531, 2020.

[10] H. Chen, K. Zhang, P. Lyu, H. Li, L. Zhang, J. Wu, and C.-H. Lee, "A deep learning approach to automatic teeth detection and numbering based on object detection in dental periapical films," *Scientific reports*, vol. 9, no. 1, p. 3840, 2019.

[11] Catharine, "Available online: https://www.medicalnewstoday.com," https://www.medicalnewstoday.com, 2024, accessed on 08 Oct. 2024.

[12] A. Afshin, P. J. Sur, K. A. Fay, L. Cornaby, G. Ferrara, J. S. Salama, E. C. Mullany, K. H. Abate, C. Abbafati, Z. Abebe *et al.*, "Health effects of dietary risks in 195 countries, 1990–2017: a systematic analysis for the global burden of disease study 2017," *The lancet*, vol. 393, no. 10184, pp. 1958–1972, 2019.

[13] M. Dhima, V. Paulusova, C. Lohse, T. J. Salinas, and A. B. Carr, "Practice-based evidence from 29-year outcome analysis of management of the edentulous jaw using osseointegrated dental implants," *Journal of Prosthodontics on Dental Implants*, pp. 121–130, 2015.

[14] T. Ekert, J. Krois, L. Meinhold, K. Elhennawy, R. Emara, T. Golla, and F. Schwendicke, "Deep learning for the radiographic detection of apical lesions," *Journal of endodontics*, vol. 45, no. 7, pp. 917–922, 2019.

[15] J. Rashid, B. S. Qaisar, M. Faheem, A. Akram, R. u. Amin, and M. Hamid, "Mouth and oral disease classification using inceptionresnetv2 method," *Multimedia Tools and Applications*, vol. 83, no. 11, pp. 33 903–33 921, 2024.

[16] V. Gulshan, L. Peng, M. Coram, M. C. Stumpe, D. Wu, A. Narayanaswamy, S. Venugopalan, K. Widner, T. Madams, J. Cuadros *et al.*, "Development and validation of a deep learning algorithm for detection of diabetic retinopathy in retinal fundus photographs," *jama*, vol. 316, no. 22, pp. 2402–2410, 2016.

[17] J. Rashid, I. Khan, I. A. Abbasi, M. R. Saeed, M. Saddique, and M. Abbas, "A hybrid deep learning approach to classify the plant leaf species," *CMC-COMPUTERS MATERIALS & CONTINUA*, vol. 76, no. 3, pp. 3897–3920, 2023.

[18] K. He, X. Zhang, S. Ren, and J. Sun, "Deep residual learning for image recognition," in *Proceedings of the IEEE conference on computer vision and pattern recognition*, 2016, pp. 770–778.

[19] A. F. Hefti, "Periodontal probing," *Critical Reviews in Oral Biology & Medicine*, vol. 8, no. 3, pp. 336–356, 1997.

[20] S. Hemalatha, N. Chidambararaj, and R. Motupalli, "Performance evaluation of oral cancer detection and classification using deep learning approach," in *2022 International Conference on Advances in Computing, Communication and Applied Informatics (ACCAI)*. IEEE, 2022, pp. 1–6.

[21] N. Iqbal, M. U. Shahzad, E.-S. M. Sherif, M. U. Tariq, J. Rashid, T.-V. Le, and A. Ghani, "Analysis of wheat-yield prediction using machine learning models under climate change scenarios," *Sustainability*, vol. 16, no. 16, p. 6976, 2024.

[22] J. Rashid, I. Khan, G. Ali, F. Alturise, T. Alkhalifah *et al.*, "Real-time multiple guava leaf disease detection from a single leaf using hybrid deep learning technique." *Computers, Materials & Continua*, vol. 74, no. 1, 2023.

[23] T. Yan, J. Rashid, M. S. Saleem, S. Ahmad, and M. Faheem, "A hybrid deep learning approach for green energy forecasting in asian countries." *Computers, Materials & Continua*, vol. 81, no. 2, 2024.

[24] Y. Liu, M. S. Saleem, J. Rashid, S. Ahmad, and M. Faheem, "Forecasting shifts in europe's renewable and fossil fuel markets using deep learning methods," *Energy Science & Engineering*, vol. 13, no. 1, pp. 119–139, 2025.

[25] A. Akram, J. Rashid, A. Jaffar, F. Hajjej, W. Iqbal, and N. Sarwar, "Weber law based approach formulti-class image forgery detection." *Computers, Materials & Continua*, vol. 78, no. 1, 2024.

[26] R. Jamil, M. Dong, J. Rashid, M. Orken, Z. S. Pernebaykyzy, and M. K. Ragytovna, "High accuracy microcalcifications detection of breast cancer using wiener lti tophat model," *IEEE Access*, 2024.

[27] A. Akram, J. Rashid, F. Hajjej, S. Yaqoob, M. Hamid, A. Arshad, and N. Sarwar, "Recognizing breast cancer using edge-weighted texture features of histopathology images." *Computers, Materials & Continua*, vol. 77, no. 1, 2023.

[28] J. Rashid, M. Ishfaq, G. Ali, M. R. Saeed, M. Hussain, T. Alkhalifah, F. Alturise, and N. Samand, "Skin cancer disease detection using transfer learning technique," *Applied Sciences*, vol. 12, no. 11, p. 5714, 2022.

[29] A. Akram, J. Rashid, M. A. Jaffar, M. Faheem, and R. u. Amin, "Segmentation and classification of skin lesions using hybrid deep learning method in the internet of medical things," *Skin Research and Technology*, vol. 29, no. 11, p. e13524, 2023.

[30] G. Ali, M. Anwar, M. Nauman, M. Faheem, and J. Rashid, "Lyme rashes disease classification using deep feature fusion technique," *Skin Research and Technology*, vol. 29, no. 11, p. e13519, 2023.

[31] F. Schwendicke, T. Golla, M. Dreher, and J. Krois, "Convolutional neural networks for dental image diagnostics: A scoping review," *Journal of dentistry*, vol. 91, p. 103226, 2019.

[32] R. Kuwana, Y. Ariji, M. Fukuda, Y. Kise, M. Nozawa, C. Kuwada, C. Muramatsu, A. Katsumata, H. Fujita, and E. Ariji, "Performance of deep learning object detection technology in the detection and diagnosis of maxillary sinus lesions on panoramic radiographs," *Dentomaxillofacial Radiology*, vol. 50, no. 1, p. 20200171, 2021.

[33] J.-H. Lee, D.-H. Kim, S.-N. Jeong, and S.-H. Choi, "Detection and diagnosis of dental caries using a deep learning-based convolutional neural network algorithm," *Journal of dentistry*, vol. 77, pp. 106–111, 2018.

[34] L. Liu, J. Xu, Y. Huan, Z. Zou, S.-C. Yeh, and L.-R. Zheng, "A smart dental health-iot platform based on intelligent hardware, deep learning, and mobile terminal," *IEEE journal of biomedical and health informatics*, vol. 24, no. 3, pp. 898–906, 2019.

[35] Z. Li, S.-H. Wang, R.-R. Fan, G. Cao, Y.-D. Zhang, and T. Guo, "Teeth category classification via seven-layer deep convolutional neural network with max pooling and global average pooling," *International Journal of Imaging Systems and Technology*, vol. 29, no. 4, pp. 577–583, 2019.

[36] H. A. Khan, M. A. Haider, H. A. Ansari, H. Ishaq, A. Kiyani, K. Sohail, M. Muhammad, and S. A. Khurram, "Automated feature detection in dental periapical radiographs by using deep learning," *Oral surgery, oral medicine, oral pathology and oral radiology*, vol. 131, no. 6, pp. 711–720, 2021.

[37] Z. Can, S. Isik, and Y. Anagun, "Cvapool: using null-space of cnn weights for the tooth disease classification," *Neural Computing and Applications*, vol. 36, no. 26, pp. 16 567–16 579, 2024.

[38] J. Kang, V. N. T. Le, D.-W. Lee, and S. Kim, "Diagnosing oral and maxillofacial diseases using deep learning," *Scientific Reports*, vol. 14, no. 1, p. 2497, 2024.

[39] H. Watanabe, Y. Ariji, M. Fukuda, C. Kuwada, Y. Kise, M. Nozawa, Y. Sugita, and E. Ariji, "Deep learning object detection of maxillary cyst-like lesions on panoramic radiographs: preliminary study," *Oral radiology*, vol. 37, pp. 487–493, 2021.

[40] J.-H. Lee, D.-h. Kim, S.-N. Jeong, and S.-H. Choi, "Diagnosis and prediction of periodontally compromised teeth using a deep learning-based convolutional neural network algorithm," *Journal of periodontal & implant science*, vol. 48, no. 2, pp. 114–123, 2018.

[41] Google Colaboratory, "Welcome to colaboratory," Available Online: https://colab.research.google.com/notebooks/intro.ipynb?utm_source=scs-index (Accessed on 08 Oct. 2024), 2024.

[42] M. Sandler, A. Howard, M. Zhu, A. Zhmoginov, and L.-C. Chen, "Mobilenetv2: Inverted residuals and linear bottlenecks," in *Proceedings of the IEEE conference on computer vision and pattern recognition*, 2018, pp. 4510–4520.

[43] C. Szegedy, V. Vanhoucke, S. Ioffe, J. Shlens, and Z. Wojna, "Rethinking the inception architecture for computer vision," in *Proceedings of the IEEE conference on computer vision and pattern recognition*, 2016, pp. 2818–2826.

[44] M. Wang, H. Wang, J. Wang, H. Liu, R. Lu, T. Duan, X. Gong, S. Feng, Y. Liu, Z. Cui *et al.*, "A novel model for malaria prediction based on ensemble algorithms," *PloS one*, vol. 14, no. 12, p. e0226910, 2019.

[45] E. L. Ray and N. G. Reich, "Prediction of infectious disease epidemics via weighted density ensembles," *PLoS computational biology*, vol. 14, no. 2, p. e1005910, 2018.

[46] H. Yang and P. A. Bath, "The use of data mining methods for the prediction of dementia: evidence from the english longitudinal study of aging," *IEEE journal of biomedical and health informatics*, vol. 24, no. 2, pp. 345–353, 2019.

[47] Y. Wang, D. Wang, N. Geng, Y. Wang, Y. Yin, and Y. Jin, "Stacking-based ensemble learning of decision trees for interpretable prostate cancer detection," *Applied Soft Computing*, vol. 77, pp. 188–204, 2019.

[48] A. U. Haq, J. P. Li, Z. Ali, I. Khan, A. Khan, M. I. Uddin, B. L. Y. Agbley, and R. U. Khan, "Stacking approach for accurate invasive ductal carcinoma classification," *Computers and Electrical Engineering*, vol. 100, p. 107937, 2022.

[49] J. Tang, J. Liang, C. Han, Z. Li, and H. Huang, "Crash injury severity analysis using a two-layer stacking framework," *Accident Analysis & Prevention*, vol. 122, pp. 226–238, 2019.

[50] A. Jaiswal, N. Gianchandani, D. Singh, V. Kumar, and M. Kaur, "Classification of the covid-19 infected patients using densenet201 based deep transfer learning," *Journal of Biomolecular Structure and Dynamics*, vol. 39, no. 15, pp. 5682–5689, 2021.

[51] M. Iman, H. R. Arabnia, and K. Rasheed, "A review of deep transfer learning and recent advancements," *Technologies*, vol. 11, no. 2, p. 40, 2023.

[52] Z. Shilong *et al.*, "Machine learning model for sales forecasting by using xgboost," in *2021 IEEE International Conference on Consumer Electronics and Computer Engineering (ICCECE)*. IEEE, 2021, pp. 480–483.

[53] B. Zhang, R. Rajan, L. Pineda, N. Lambert, A. Biedenkapp, K. Chua, F. Hutter, and R. Calandra, "On the importance of hyperparameter optimization for model-based reinforcement learning," in *International Conference on Artificial Intelligence and Statistics*. PMLR, 2021, pp. 4015–4023.

[54] S. Park, H. Erkinov, M. A. M. Hasan, S.-H. Nam, Y.-R. Kim, J. Shin, and W.-D. Chang, "Periodontal disease classification with color teeth images using convolutional neural networks," *Electronics*, vol. 12, no. 7, p. 1518, 2023.

[55] G. Sudha, M. M. Hussani, N. Bagyalakshmi, R. Avanthika, M. Saraswathi, and S. Renuka, "Digital diagnosis of mouth disease using deep learning algorithms," in *2024 Tenth International Conference on Bio Signals, Images, and Instrumentation (ICBSII)*. IEEE, 2024, pp. 1–9.

CHAPTER 2

Enhanced Classification of Breast Cancer: A Comparative Analysis of Machine Learning Models with Applied Regression Analysis

Javed Rashid* **and Muhammad Shoaib Saleem†**

*Department of Computer Science, University of Okara, Okara, 56300, Pakistan

dagger Department of Mathematics, University of Okara, Okara, 56300, Pakistan

Corresponding Author: Javed Rashid: RanaJavedRashid@gmail.com

Abstract:

Breast cancer ranks second among cancer-related deaths of women worldwide, thus emphasizing the need to detect cancer at early stages to enhance survival from the disease. This paper is a comparative study of various machine learning (ML) methods that have been used to analyze their efficiency in predicting breast cancer related to the Wisconsin Diagnostic Breast Cancer Dataset (WBCD). Overall evaluation of performance was done through such metrics as accuracy, precision, recall, F1-score, and the area under the ROC curve (AUC). Compared to the other models, the XGBoost algorithm produced the maximum result on the classification based on the testing accuracy performance 99%. Besides, K-means clustering as well as statistical validation (e.g., the Wilcoxon test) were used to analyze the clinical significance of the picked features. The findings draw the conclusion that ensemble and boosting methods can be used as a solution to the development of robust, accurate, and interpretable diagnostic instruments, resulting in timely and evidence-based breast cancer diagnosis in the clinic.

Keywords: Breast Cancer Detection, Machine Learning, Ensemble Methods, XGBoost, Feature Selection, Wisconsin Diagnostic Dataset

2.1 Introduction

Breast cancer is the most lethal kind of cancer in women. Tragically, breast cancer claims the lives of so many people annually. According to a December 2020 report by the International Agency for Research on Cancer (IARC), breast cancer is now the most common chronic cancer among women globally, surpassing even lung cancer. The number of new cases of cancer increased from 10 million in 2000 to 19.3 million in 2015 [1]. One in five people today has cancer. Manually diagnosing breast cancer is a lengthy and laborious process. Thus, cancer diagnosis requires multiple automated methods. Breast cancer can be detected using logistic regression, decision trees, random forests, K-nearest neighbors, support vector machines, ADA boost, gradient boost, and Gaussian naive Bayes.

Investigations based on the detection of breast cancer on the UCI Machine Learning dataset have been emerging in recent years to employ the diversity of machine learning and deep learning algorithms in advancing the correct diagnosis. Popular methods are traditional classifiers, e.g., Support Vector Machines (SVM) [2], k-Nearest Neighbors (k-NN) [3], Decision Trees [4], and Random Forests [5], that have been applied many times due to their readability and ability to process structured data. Other methods, such as gradient boosting and XGBoost [6], have been used by creating more powerful learners using ensemble methods, which fuse several weak learners together. Moreover, various deep learning architectures, in particular Artificial Neural Networks (ANN) [7] and Convolutional Neural Networks (CNN) [8], have been considered in order to learn complex patterns automatically, based on the features. Techniques like Principal Component Analysis (PCA) [9], Recursive Feature Elimination (RFE) [10], and mutual information ranking have been used to select the features and decrease the dimension so that the performance of the classifier can be improved. Most articles pay far more attention to accuracy, precision, recall, and F1-score as measures of identifying the efficacy of models, and they all prove the great prospects of these methods of early and confident breast cancer detection.

Although there is tremendous growth in breast cancer detection using machine learning algorithms, there are several issues that need to be overcome when the UCI Machine Learning dataset is used. One, the data tends to be imbalanced towards the benign, with more data than the malignant, with the tendency to be biased, thus causing low sensitivity of important malignant cases. Second, a high percentage of the existing models are based on hand-designed features, ignoring the fact of feature redundancy and irrelevancy that can lead to the decline of model accuracy and computational complexity. Third, different classifiers have been used, but there is no standardized benchmarking and comparison, and it is very hard to conclude which are the most robust and generalizable models under different clinical situations. All these problems point to the necessity of more moderate, feature-oriented, and intensively tested strategies.

Breast cancer remains one of the leading causes of cancer-related mortality among women worldwide, and early detection plays a pivotal role in improving survival outcomes. Traditional diagnostic techniques, while clinically effective, are often constrained by subjectivity, variability in interpretation, and limited scalability in resource-constrained settings. Recent advances in machine learning and deep learn-

ing have provided promising alternatives, offering automated, accurate, and reproducible methods for breast cancer classification. The motivation behind this study stems from the urgent need to integrate such computational intelligence into clinical workflows, ensuring timely detection, reduced diagnostic errors, and broader accessibility. By leveraging state-of-the-art architectures and addressing challenges such as data imbalance and feature heterogeneity, this work aims to contribute toward building robust, scalable, and clinically reliable models for breast cancer detection.

This research uses the publicly available UCI tumor database for training and testing. Noncancerous tumors are called benign. Research is undertaken to develop more effective early cancer detection and diagnosis methods. Many use early detection to make therapy cheaper and easier; many researchers are still looking for a good cancer diagnosis method. So, treatment can begin sooner, increasing the likelihood of success. This research evaluates and contrasts many machine learning (ML) methods for detecting breast cancer. Many recent advances in technology have led to novel approaches for predicting breast cancer.

Nevertheless, the pursuit of improved accuracy and reliability in early breast cancer detection using algorithmic methods continues to be a problem, even with these developments. This research aims to assess five different machine-learning methods for breast cancer prediction. The following algorithms were found to achieve the highest accuracy on the Wisconsin (diagnostic) breast cancer dataset: gradient boosting, decision tree (DT), support vector machine (SVM), ADA boost (AB), and random forest (RF). A K-means clustering analysis was also conducted to ensure that the variables utilized for categorization are clinically relevant. The main contributions of this study are: :

1. Evaluate and contrast five ML approaches to breast cancer prediction using the Wisconsin (diagnostic) dataset: ADA boost (AB), decision tree (DT), gradient boosting, and random forest (RF).
2. A study comparing various state-of-the-art evaluation parameters applied to ML techniques.
3. To aid medical professionals in understanding and using the results produced by the machine learning model for the early detection and prognosis of breast cancer.

The rest of this paper is structured as follows: Section 2.2 reviews related work in deep learning-based oral disease classification. Section 2.3 describes the dataset, methodology, and the proposed model architecture. Section 2.4 presents experimental results and discussion, including performance analysis and comparative evaluation. Section 2.5 concludes the paper with suggestions for future research.

2.2 Literature Work

Medical detectors, such as breast cancer, have become one of the main topics requiring extensive research in the sphere of medical diagnostics, and machine learning approaches provide strong potential for early and accurate diagnosis. The UCI Breast Cancer Wisconsin dataset has gained wide popularity because

it contains well-structured features and is publicly available, allowing benchmarking and development of diverse classification models. Supervised learning algorithms have been widely utilized to classify benign and malignant tumors, reducing human error in clinical diagnosis.

The UCI dataset has been extensively applied in numerous studies. For instance, Support Vector Machines (SVM) with PCA-based feature selection achieved an accuracy of 97.1% [11]. Recursive Feature Elimination (RFE) using decision trees reached 95.6% accuracy [12], whereas k-NN with distance-weighted voting obtained 94.7% precision [13]. Addressing class imbalance, Singh et al. [14], while logistic regression after feature scaling yielded 93.5% [15], and an ensemble of SVM and k-NN attained 97.4% [16], while Extra Trees Classifier reported 96.7% accuracy [17]. More recent gradient boosting methods, such as LightGBM (97.5%) [18], demonstrated consistent improvements. Stacking ensembles of SVM, RF, and LR achieved 98.4% accuracy [19], highlighting the potential of hybrid strategies.

In addition to structured gene-expression datasets, recent works have investigated advanced imaging- and texture-based frameworks for breast cancer detection. Jamil et al. [20] proposed a Wiener Linear Time-Invariant Filter combined with Tophat transformation for microcalcification detection in mammography images, achieving a 99.5% detection accuracy. Their approach effectively enhanced image clarity and highlighted malignant regions using CLAHE preprocessing and morphological operators, outperforming traditional contrast-based methods. Similarly, Akram et al. [21] developed an edge-weighted texture feature extraction method using wavelet transformation and XGBoost for histopathology images. By incorporating multi-scale magnification levels from the BreakHis dataset and balancing data via SMOTE, their method achieved accuracies up to 99.27%, significantly improving robustness in histology-based classification. These recent studies emphasize the complementary role of texture analysis, advanced filters, and hybrid deep learning in addressing both micro-level (e.g., microcalcifications) and tissue-level (e.g., histopathological structures) breast cancer features.

Collectively, these works illustrate the evolution from traditional single-model pipelines toward ensemble and hybrid approaches that integrate feature engineering, augmentation, and deep neural architectures. The consistent trend of accuracies exceeding 97–99% demonstrates the effectiveness of ensemble, texture-based, and image-processing models in advancing early breast cancer detection. At the same time, the inclusion of recent imaging-based methodologies underscores the importance of extending beyond UCI-style datasets to real-world clinical data modalities, improving generalizability and clinical relevance.

2.3 Materials and Methods

The major purpose of this research is to identify the most accurate and predictive method of diagnosing breast cancer. The proposed layout is depicted in Figure 10.5. After data collection, the pre-processing phase consists of actions including feature extraction, target feature selection, attribute selection, and data purification. Algorithms trained with data are then used to detect breast cancer using novel parameters.

The model is then tested on labeled data for accuracy. Train_test_split is frequently used to divide labeled data into two halves for training and testing purposes. Our machine learning training set contains 80% of the data used for training. Twenty percent of the information is taken out to test the model, known as the "test data" or "test set." The results are compared to choose the best algorithm. RFE and univariate feature selection are used to assess the performance of existing models. We now have the finest method for detecting breast cancer.

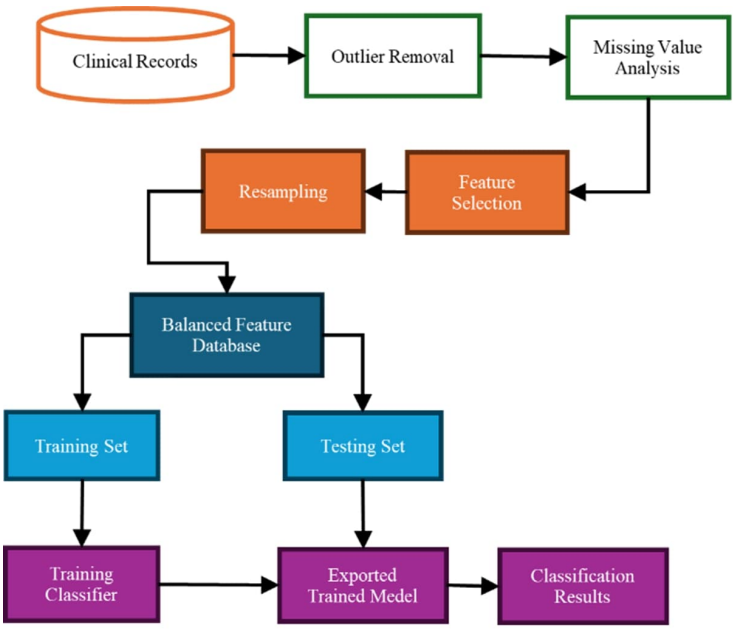

Figure 2.1: The Proposed Architecture of the Breast Cancer Detection.

2.3.1 Machine Learning Library

The Scikit-learn package for Python was utilized to validate the machine-learning techniques presented in this paper. Scikit-learn, more commonly spelled sklearn, is an open-source Python toolkit for machine learning [8]. Scikit-Learn [9], NumPy [10], matplotlib [22], pandas [11], and Seaborn [12] were some of the scientific computing tools that were utilized to bring about the success of this investigation.

2.3.2 Wisconsin Diagnostic Breast Cancer Dataset (WBCD)

In this study, we utilized the Wisconsin Diagnostic Breast Cancer Dataset (WBCD) [15], originally developed by Dr. William H. Wolberg at the University of Wisconsin Hospital, Madison. The dataset was constructed using the XCYT graphical software, which enables digital cytological analysis of fine-needle aspirate (FNA) samples of breast masses. For each sample, ten morphological properties of cell nuclei are computed using curve-fitting techniques, and statistical descriptors (mean, standard deviation, and extreme values) are derived, resulting in a 30-dimensional feature vector. These features represent clini-

cally relevant properties such as radius, texture, perimeter, area, smoothness, concavity, and symmetry, along with higher-order descriptors including fractal dimension and concave points.

The dataset contains a total of 569 patient cases with 33 attributes, of which 30 are diagnostic features, one is the patient identifier, one is the diagnosis label (M = malignant, B = benign), and one is an unnamed column that is excluded in preprocessing. Out of the 569 cases, 212 (37.3%) are malignant and 357 (62.7%) are benign, providing a balanced yet clinically realistic distribution for binary classification tasks.

2.3.3 Data Preprocessing

To prepare the dataset for analysis, the identifier and unnamed columns were removed as they carried no diagnostic information. The categorical diagnostic labels ('M', 'B') were mapped into binary numerical values, where malignant = 1 and benign = 0. All features were standardized to ensure comparable scales using z-score normalization:

$$z = \frac{x - \mu}{\sigma}, \tag{2.1}$$

where x represents the feature value, μ the mean, and σ the standard deviation. Normalization was implemented in Python using the `StandardScaler()` function, with training and testing sets kept separate to avoid data leakage. The training data was fit and transformed, while the test data was only transformed using the parameters of the training distribution.

2.3.4 Feature Selection

Feature selection was applied to improve classifier performance by reducing redundancy and emphasizing the most discriminative features. This process not only speeds up model training but also enhances interpretability.

2.3.4.1 Univariate Feature Selection

Univariate Feature Selection (UFS) was employed using statistical tests such as analysis of variance (ANOVA) to identify the features most strongly associated with the target variable [23]. The test scores were ranked, and the five most relevant features identified were: *perimeter_mean*, *area_mean*, *area_se*, *perimeter_worst*, and *area_worst*. These features, strongly linked to tumor size and morphology, have been widely reported in clinical literature as critical indicators for distinguishing malignant from benign tumors.

2.3.4.2 Correlation Heatmap

Correlation, for instance, can evaluate the dissimilarity between two parameters. The strong correlation between an independent and dependent variable increases the weight of the former. The direction of the change determines whether the correlation value is positive, negative, or zero. A correlation between dependent and independent variables is desirable, but a strong link is not [14]. Variable correlations were displayed in Figure 2.2. It is unnecessary to keep track of two independent variables that are intertwined so closely.

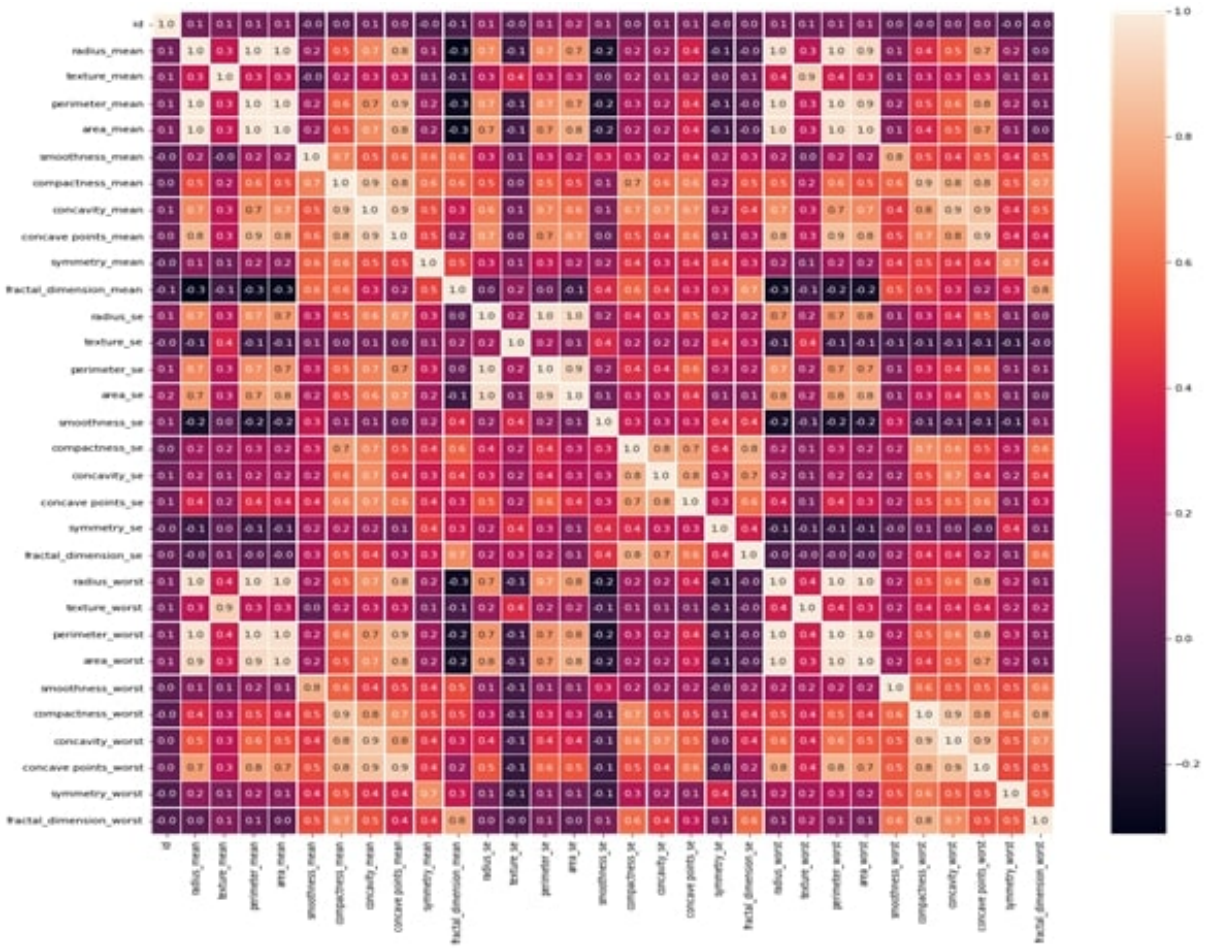

Figure 2.2: A Heatmap Representing the Correlation between All Dependent and Independent Variables.

2.3.5 Proposed Machine Learning Algorithms

This study evaluates and compares multiple machine learning (ML) techniques for breast cancer detection. Both feature-selection-based and non-feature-selection-based algorithms are explored. For a given input feature vector $\mathbf{X} = (X_1, X_2, \ldots, X_n)$, the predicted output $\hat{P}$ can be represented as:

$$\hat{P} = \beta_0 + \sum_{i=1}^{n} \beta_i X_i, \tag{2.2}$$

where β_0 denotes the intercept (bias), and β_i are the feature coefficients associated with the respective inputs X_i. The following classifiers were implemented and are briefly described below.

2.3.5.1 Decision Tree Classifier

A Decision Tree (DT) is a supervised learning algorithm that recursively partitions the feature space into subregions to classify input data. Internal nodes represent decision rules on features, branches represent outcomes of these rules, and leaf nodes correspond to class labels. DTs are constructed by optimizing impurity measures, such as Entropy or the Gini index.

The entropy of a node is defined as:

$$\text{Entropy} = -\sum_{i=1}^{n} p_i \log(p_i), \tag{2.3}$$

where p_i is the probability of class i. Alternatively, the Gini index is widely used as a measure of class inequality:

$$\text{Gini index} = 1 - \sum_{i=1}^{n} p_i^2. \tag{2.4}$$

A lower Gini index or entropy indicates purer nodes. DTs are computationally efficient and interpretable but prone to overfitting on small datasets [24].

2.3.5.2 Random Forest Classifier

Random Forest (RF) is an ensemble learning technique that constructs multiple decision trees on random bootstrap samples of the dataset and averages their predictions to improve generalization. By aggregating results from multiple weak learners, RF mitigates overfitting and achieves robust performance.

Mathematically, for an input $\mathbf{X} = (x_1, \ldots, x_n)$, the ensemble output is given as:

$$\hat{Y} = \frac{1}{B} \sum_{b=1}^{B} h_b(\mathbf{X}), \tag{2.5}$$

where $h_b(\mathbf{X})$ is the prediction of the b-th tree, and B is the number of trees in the forest.

2.3.5.3 AdaBoost (AB) Classifier

Adaptive Boosting (AdaBoost) is a boosting-based ensemble method that combines multiple weak classifiers, typically decision stumps, into a strong classifier. Each subsequent learner is trained to correct the errors of its predecessor by assigning higher weights to misclassified samples.

The final classifier is expressed as:

$$H(x) = \text{sign}\left(\sum_{k=1}^{K} \alpha_k h_k(x)\right), \tag{2.6}$$

where $h_k(x)$ denotes the k^{th} weak classifier, α_k is its weight, and K is the total number of classifiers. AdaBoost adapts iteratively, improving overall accuracy by focusing on difficult-to-classify samples [25].

2.3.5.4 Gradient Boosting Classifier

Gradient Boosting (GB) is another boosting-based ensemble approach that builds models sequentially, with each weak learner attempting to minimize the residual errors of the previous ensemble. Unlike AdaBoost, which adjusts sample weights, GB fits new learners to the negative gradient of the loss function.

The model update at iteration m is defined as:

$$F_m(X) = F_{m-1}(X) + \eta f_m(X), \tag{2.7}$$

where $F_{m-1}(X)$ is the current model, $f_m(X)$ is the new weak learner, and η is the learning rate controlling the contribution of each learner. GB is highly flexible and can optimize various loss functions, such as log loss for classification and mean squared error (MSE) for regression [19, 18].

2.3.5.5 K-means Clustering

Although primarily an unsupervised algorithm, K-means clustering is included here for exploratory data analysis and visualization. The algorithm partitions N data points into K non-overlapping clusters by minimizing the within-cluster sum of squared distances (WCSS).

$$\min_{\mu} \sum_{i=1}^{K} \sum_{x_j \in C_i} \|x_j - \mu_i\|^2, \tag{2.8}$$

where μ_i is the centroid of cluster C_i, and $\|\cdot\|$ denotes the Euclidean distance. The optimal value of K is often determined using the Elbow method, which evaluates the trade-off between clustering quality and model complexity.

2.3.6 Evaluation Measures

The effectiveness of the proposed method is evaluated using classification accuracy, precision, recall, F1-score, and AUC-ROC analysis. The model undergoes extensive testing to verify its robustness across different oral disease categories. First, we define and graphically portray four possible outcomes: a true positive (TP), a true negative (TN), a false negative (FN), and a false positive (FP). We then test the proposed method using the testing set with different evaluation measures, such as accuracy, F1 score, precision, and recall, to evaluate the structure's effectiveness. Below, we provide a closer examination of the evaluation criteria used.

2.3.6.1 Classification Accuracy

The accuracy of a classification system can be evaluated by determining the percentage of its predictions that were correct and the percentage that were incorrect.

$$\text{Accuracy} = \frac{TP + TN}{TP + TN + FP + FN} \tag{4}$$

2.3.6.2 Precision

Classification accuracy is not necessarily the best criterion for evaluating a model's performance. It is one situation in which a sizeable socioeconomic divide exists. It is safe to assume that each sample is of the highest possible quality. If the model is not picking up any new information, inferring that all components belong to the best class would be irrational. Therefore, when discussing accuracy, we refer to the fluctuation in findings received while measuring the same object several times with the same tools. The term precision refers to one of these statistics and can be defined as follows:

$$\text{Precision} = \frac{TP}{TP + FP} \tag{5}$$

2.3.6.3 Recall

Another critical parameter is recall, which refers to the percentage of input samples of a type that the model can accurately predict. The formula for the recall is as follows:

$$\text{Recall} = \frac{TP}{TP + FN} \tag{6}$$

2.3.6.4 F1 Score

The F1 score is a statistic utilized to contrast recall and precision.

$$F_1 \text{ Score} = \frac{2 \times (\text{Precision} \times \text{Recall})}{\text{Precision} + \text{Recall}} \tag{7}$$

2.3.6.5 ROC Curve

A receiver operating characteristic (ROC) curve can show classifiers' effectiveness regarding their cutoff value. The widely used ROC curve can be used to find the optimal cutoff for a great model. The true positive rate (TPR) competes with the false positive rate (FPR) at several different bounds.

2.4 Results and Discussion

A ten-fold cross-validation method was used to assess the study's stability and capacity to be applied to unidentified data. Here, we split the data into ten equal chunks, train the model repeatedly on nine of

them, and then use the remaining chunk for testing. This strategy comprehensively evaluates the model's prediction ability by ensuring that every data point is used exactly at once for training and validation. Using the results of the cross-validation technique, we may gain a deeper understanding of the Random Forest model's performance and potential clinical utility in breast cancer diagnosis. After this quick summary, we get into the data analysis, discussing their significance and how they stack up against other diagnostic methods. Detailed analysis is categorized as:

1. The proposed methods were observed using the MOD dataset to assess their efficacy.
2. To compare the results of the proposed method ablation study.
3. A comparison analysis of the proposed model with existing studies was performed.

2.4.1 Performance Analysis of Testing Results of Machine Learning Algorithms

See how XGBOOST, Decision Tree, Random Forest Classifier, and AdaBoost stack up against each other and against "Benign" and "Malignant" ML algorithms in Table 2.1. F1 Score, Accuracy, Precision, Recall, and AUROC are some of the performance metrics. With a Precision of 0.991, a Recall of 0.956, an F1 Score of 0.973, an AUROC of 0.973, and an Accuracy of 0.972, XGBOOST surpasses the Benign class across the board. All the metrics of this malignant class are better than average, including accuracy, recall, F1 score, and area under the curve (AUROC). Against the alternatives in the Benign and Malignant classes, the Decision Tree performs poorly in the Precision, Recall, and F1 Score. AUROC and accuracy both amount to 0.935 in both cases. Concerning benign and malignant classifications, it seems that the Random Forest Classifier provides the same high results, with the Precision, Recall, F1 Score, and Accuracy being 0.967. The AdaBoost algorithm results in F1 Score, AUROC, and an accuracy of 0.958, with a recall of 0.959 for benign and malignant cases and an overall precision of 0.97. Due to its low values of Precision, Recall, and F1 Score, XGBOOST also exhibits high Accuracy and ranks the highest method regarding the classification of samples with benign or malignant cells. The other algorithms compete successfully, although with lesser ratings. The encouraging signs of all algorithms prove their high capacity to forecast the two groups.

Table 2.1: Comparative analysis of five algorithms

Algorithm	Classes	Precision	Recall	F1-Score	AUROC	Accuracy
XGBOOST	Benign (0)	0.991	0.956	0.973	0.973	0.972
	Malignant (1)	0.953	0.990	0.971	0.973	
Decision Tree	Benign (0)	0.963	0.912	0.936	0.936	0.935
	Malignant (1)	0.907	0.961	0.933	0.936	
Random Forest Classifier	Benign (0)	0.973	0.965	0.969	0.968	0.967

	Malignant (1)	0.961	0.971	0.966	0.968	
ADABOOST	Benign (0)	0.981	0.938	0.959	0.959	0.958
	Malignant (1)	0.935	0.980	0.957	0.959	

Figure 2.3 shows four confusion matrices, i.e., machine learning-based classifiers including AdaBoost, Decision Tree, Random Forest, and XGBoost performed in a supervised learning environment. A confusion matrix is a tabular presentation of how an algorithm performs in terms of the predicted classification and actual target labels. The XGBoost model has a strong performance with the parameters of the true positive (TP) rate, which is 95.58, the true negative (TN) rate, which is 99.02, the false negative (FN) rate, which is 0.92, and the false positive (FP) rate, which is 4.42. These measures demonstrate a strong recall and a high precision, assuring considerable predictive accuracy. Comparatively, the Decision Tree model produces the TP of 91.15% and TN of 96.08%, yet the FN and FP rates are higher than those of the XGBoost, indicating more misclassification. Random Forest model gives roughly the same results as XGBoosts, both in terms of TP and TN. However, it shows a slightly higher rate of FP and FN, meaning that there will be an incidence of type I (FP) error and type II (FN) error. In general, XGBoost performs better than the other models, achieving lower error rates and patterns of alignments with the target classifications.

Finally, the ADABOOST model has reasonable performance with 98.04 TP, 93.81 TN, 1.96 FN faults and 6.19 FP. Its accuracy is comparable to that of XGBOOST and Random Forest. While every model performs admirably, the XGBOOST model is particularly error-free. By revealing both the strengths and weaknesses of a model, matrix analysis aids in both the development of better models and the comprehension of their practical uses.

Figure 2.4 displays the receiver operating characteristic (ROC) curves for two classes predicted by four machine learning classifiers: XGBOOST, Decision Tree, Random Forest, and AdaBoost. ROC curves illustrate the relationship between the discrimination threshold and the diagnostic ability of a binary classifier system. The y-axis displays sensitivity (the number of true positives), and the x-axis displays specificity (the number of false positives) in each subplot containing the ROC curves for Class 0 and Class 1 for a single classifier. An improved actual positive rate and a decreased false positive rate are indicated by a classifier's curve moving closer to the plot's top-left corner. One scalar metric that may be used to quantify the success of the classifier is the area under the ROC curve (AUC), where 1.0 represents an ideal model, and 0.5 means no discriminating capacity (similar to random guessing). The XGBOOST and AdaBoost classifiers provide effective performance with AUC values of 0.97, as seen in the image. Thus, the two classes may be differentiated with great accuracy. An area under the curve (AUC) of 0.94 for both classes indicates that the Decision Tree classifier is not very effective. Both classes were well-served by the Random Forest classifier, which had an AUC of 0.96. Class 0 and Class 1's red and blue lines almost touch, suggesting that XGBOOST and AdaBoost make comparable predictions. Although other

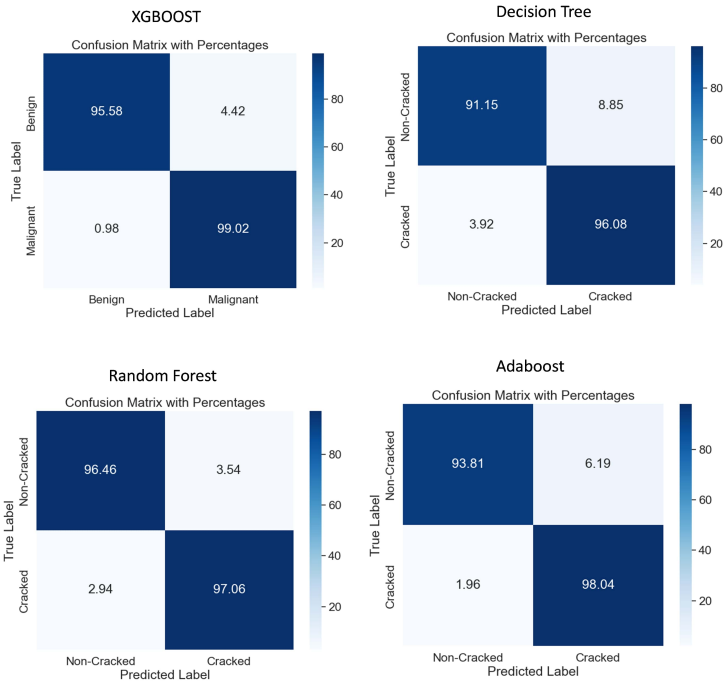

Figure 2.3: The Proposed Models Confusion Matrix on Test Set.

classifiers do well, the figure shows that XGBOOST and AdaBoost do the best in this work.

2.4.2 Performance Analysis of K-Means Clustering to Find Medical Relevance of Variables

In this study, the elbow method has been used to determine the best k value for k-means clustering. Figure 2.5 depicts the elbow approach to finding the optimal number of clusters for a clustering algorithm such as k-means. Data points can be grouped based on commonalities using clustering. The x-axis of the graph indicates the overall number of clusters, while the y-axis shows the distortion, which measures how well the clusters fit the data. An "elbow" point appears on the graph when the distortion abruptly decreases and flattens. You can use it to find a decent number of clusters because adding more after this stage does not significantly enhance the fit. About $k = 2$ is where the graph's elbow points. Consequently, it is reasonable to classify this data into five clusters.

The mean of many variables across four clusters is displayed in Figure [**?**], a clustered line graph. Medical and biological datasets often include variables such as "radius," "texture," "perimeter," and "smoothness" that describe cell or tumor characteristics that can be helpful in cancer diagnosis. The study's findings reveal that the graph shows substantial inter-cluster fluctuation in the mean values of these variables, with the 'area_mean' variable falling precipitously between Clusters 1 and 2 before stabilizing between Clusters 2 and 4. Accordingly, it appears that 'area_mean' differentiates the first two groups more than the third and fourth clusters. The lines for smoothness_mean, compactness_mean, and

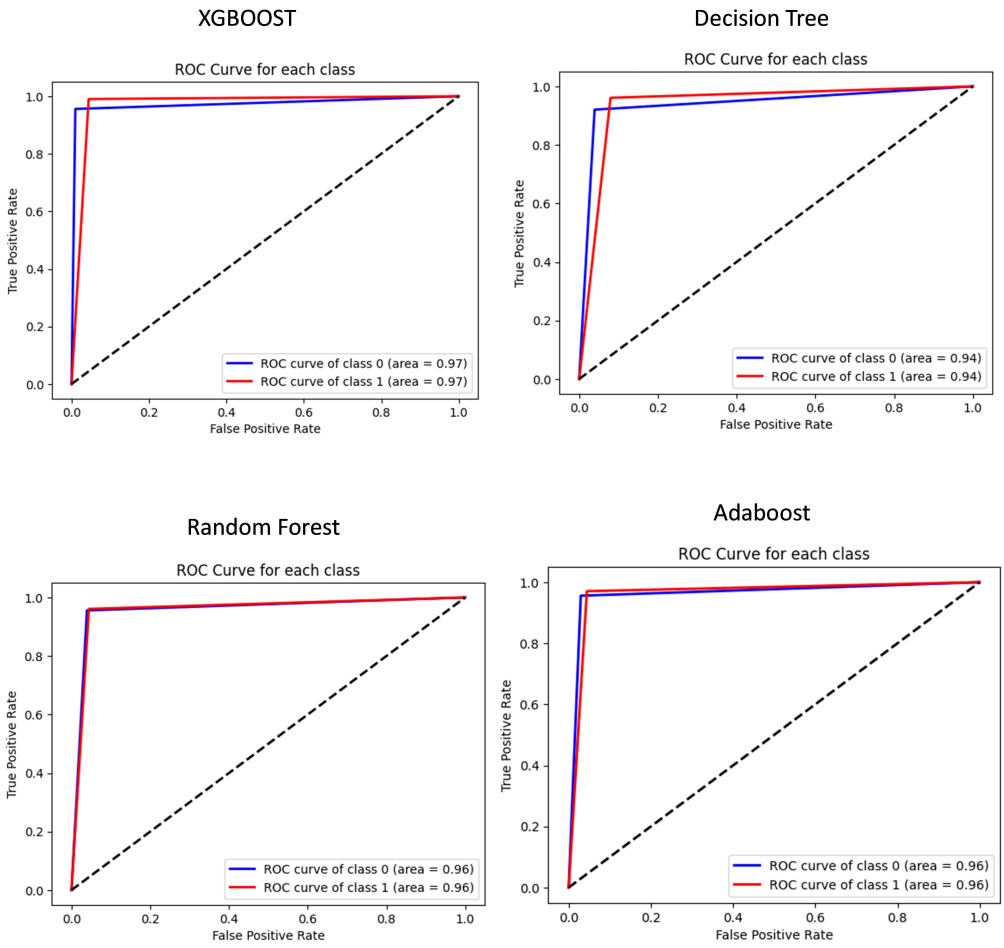

Figure 2.4: The Proposed Models Confusion Matrix on Test Set.

concavity_mean are flat across clusters, in contrast to 'area_mean.' This might suggest that the mean values of these variables are comparable across clusters or that there is less variation in them.

Additional classification of the variables is accomplished using prefixes such as "_mean," "_se" (which might indicate a standard error), and "_worst." Since standard error variables capture the dispersion of sample means from population means—typically smaller—their significantly lower mean values across all clusters are unsurprising. The "_worst" variables do not exhibit any trend between clusters, indicating that the worst-case values do not deviate sufficiently from the mean values to discern the clusters.

It is clear from the visual analysis which attributes are more crucial for cluster membership. Potentially therapeutically useful in clustering patients according to tumor stage or disease subtype, 'area_mean' may distinguish Cluster 1 from the others. Additional statistical analysis is required to validate these results and determine the underlying causes of these clusters.

Several variables in two clusters (Cluster 1 and Cluster 2) are shown in Table 2.2 with their Wilcoxon rank sum test findings. At its worst, each variable is measured using the standard error (SE) and the mean value. The p-values for each potential combination of variables and clusters are displayed in the table. These p-values show the likelihood that the two clusters' distributions would differ under the null

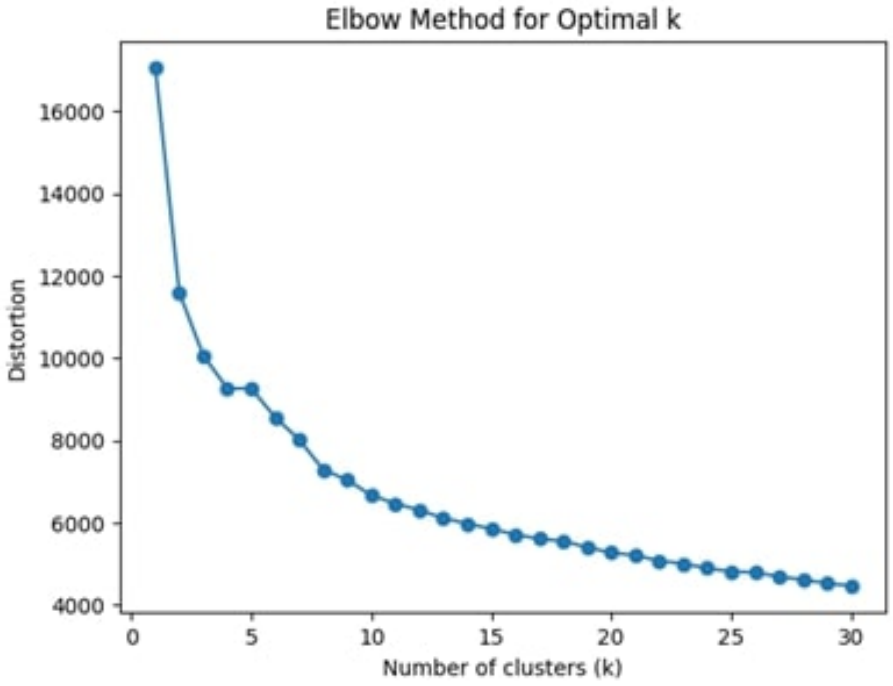

Figure 2.5: Visual Representation of Distortions using Elbow Method to Find Optimal Number of Clusters.

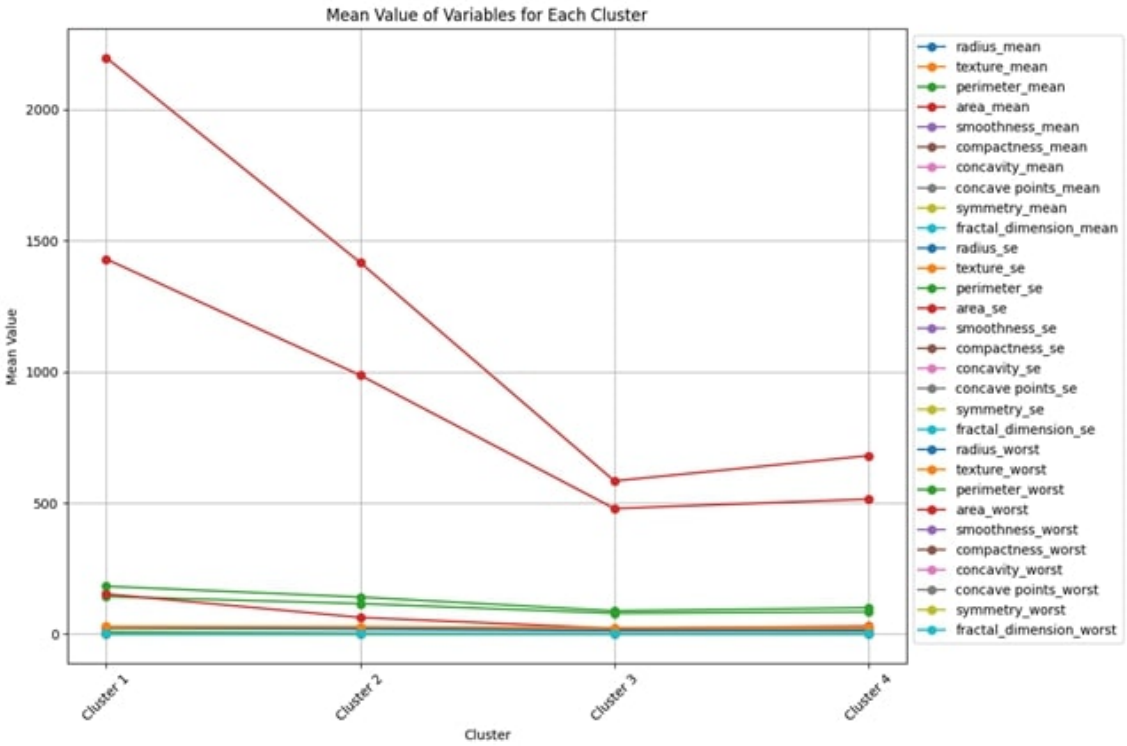

Figure 2.6: Visual Representation of Mean p-Values to Find Relevancy of Variables and Cluster Analysis.

hypothesis. Table p-values for all variables in both clusters are extremely small, approaching zero. This

raises serious doubts about the validity of the null hypothesis by providing strong evidence that the distributions of these variables differ significantly between the two clusters. According to these data, the area, smoothness, compactness, concavity, concave points, symmetry, perimeter, and fractal dimension can be used to differentiate between the two patient groups clinically. The factors in question may effectively differentiate between phenotypes or subtypes in Clusters 1 and 2, as the tiny p-values indicate.

Table 2.2: Wilcoxon Test results show clinical relevance of variables

Variable	Clus.	P-Value	Variable	Clus.	P-Value	Variable	Clus.	P-Value
radius mean	1	1.33E-32	radius se	1	1.33E-32	radius worst	1	1.33E-32
radius mean	2	3.47E-64	radius se	2	3.48E-64	radius worst	2	3.47E-64
texture mean	1	1.33E-32	texture se	1	1.33E-32	texture worst	1	1.33E-32
texture mean	2	3.47E-64	texture se	2	3.48E-64	texture worst	2	3.48E-64
Perimeter mean	1	1.33E-32	Perimeter se	1	1.33E-32	Perimeter worst	1	1.33E-32
Perimeter mean	2	3.48E-64	Perimeter se	2	3.48E-64	Perimeter worst	2	3.48E-64
Area mean	1	1.33E-32	Area se	1	1.33E-32	Area worst	1	1.33E-32
Area mean	2	3.48E-64	Area se	2	3.47E-64	Area worst	2	3.48E-64
Smoothness mean	1	1.33E-32	Smoothness se	1	1.33E-32	Smoothness worst	1	1.33E-32
Smoothness mean	2	3.47E-64	Smoothness se	2	3.48E-64	Smoothness worst	2	3.47E-64
Compactness mean	1	1.33E-32	Compactness se	1	1.33E-32	Compactness worst	1	1.33E-32
Compactness mean	2	3.48E-64	Compactness se	2	3.48E-64	Compactness worst	2	3.48E-64
Concavity mean	1	1.33E-32	Concavity se	1	1.33E-32	Concavity worst	1	1.33E-32
Concavity mean	2	4.63E-62	Concavity se	2	4.63E-62	Concavity worst	2	4.63E-62
Concave points mean	1	1.33E-32	Concave points se	1	1.33E-32	concave points worst	1	1.33E-32
Concave points mean	2	4.63E-62	Concave points se	2	4.63E-62	concave points worst	2	4.63E-62

Symmetry mean	1	1.33E-32	Symmetry se	1	1.33E-32	Symmetry worst	1	1.33E-32
Symmetry mean	2	3.47E-64	Symmetry se	2	3.47E-64	Symmetry worst	2	3.47E-64
Fractal dimension mean	1	1.33E-32	Fractal dimension se	1	1.33E-32	Fractal dimension worst	1	1.33E-32
Fractal dimension mean	2	3.47E-64	Fractal dimension se	2	3.48E-64	Fractal dimension worst	2	3.48E-64

2.4.3 Ablation Study

To further certify the stability and the contribution of varying components within our machine learning training, we need to conduct various ablation experiments. The underlying idea of these experiments was to distill out and evaluate the influence of such factors as preprocessing steps, feature selection methods, and configuration of the algorithm on the overall result of classification performance in breast cancer detection based on the Wisconsin Diagnostic Breast Cancer Dataset (WBCD).

2.4.3.1 Impact of Feature Selection Methods

Table 2.3 illustrates the influences of the type of feature selection on the performance of an XGBoost classifier. When there was no feature selection, the model showed a 96.4% accuracy rate, but the use of Univariate Feature Selection (UFS) gave 97.2%. The optimal results were obtained with Recursive Feature Elimination (RFE): 99.0% accuracy and precision of 0.991, recall of 0.990, and F1-score of 0.990. These findings prove that RFE is efficient enough in boosting the performance of the classification, as it filters out redundancies as well as irrelevant features, thereby being the best approach to increase and improve the robustness of breast cancer prediction in this experiment.

Table 2.3: *Influence of Feature Selection Methods on Proposed Classifiers*

Feature Selection	Algorithm	Accuracy	Precision	Recall	F1-Score	AUC
None	XGBoost	96.4%	0.951	0.949	0.950	0.962
UFS	XGBoost	97.2%	0.961	0.956	0.958	0.968
RFE	XGBoost	99.0%	0.991	0.990	0.990	0.973

2.4.3.2 Influence of Base Estimators in Ensemble Models

Table 2.4 is a comparison of the work done by various base estimators in AdaBoost and Gradient Boosting models. With a decision tree (depth=1), AdaBoost had a high accuracy of 95.8 with an F1-score of 0.958, whereas logistic regression had an accuracy of 94.2 and an F1-score of 0.946. The Gradient Boosting model obtained significant improvements in the increase of depth: the tree with depth 3 showed very high accuracy of 97.3, and further increase of the depth up to 5 led to increased accuracy up to 98.2 and to the F1-score up to 0.979. These findings suggest that decision trees make better base learners with AdaBoost than logistic regression, and that tree depth in gradient boosting should be increased to increase learning capacity, but with the commensurate risk of overfitting and therefore under-optimally increased tree depth.

Table 2.4: Influence of Base Estimators

Model	Base Estimator	Accuracy	F1-Score
AdaBoost	Decision Tree (depth=1)	95.8%	0.958
AdaBoost	Logistic Regression	94.2%	0.946
Gradient Boosting	Tree (depth=3)	97.3%	0.970
Gradient Boosting	Tree (depth=5)	98.2%	0.979

2.4.3.3 Impact of Data Normalization on Classifier Performance

Figure 2.7 shows how data normalization spans the performance of four types of classifiers using 5 major metrics. In general, the use of normalization ("Yes" bars) made every model work better. XGBoost had the best growth, accuracy, precision, recall, and F1-score, which all rose to about 99%, proving it is sensitive to normalization of levels of input. Random Forest did not fare so badly either, improving all measures by approximately 2% to 3%. It was mainly the decision tree that showed small increases in accuracy and F1-score, but a significant improvement in precision. The best results are displayed by AdaBoost, whose precision increased by nearly 98 percent after normalization. These results mean that the normalization of data is an important preprocessing operation that translates to an enormous boost in predictive accuracy, especially in ensemble models, which include XGBoost and AdaBoost, since it stabilizes gradients and centers the scale of features. '

2.4.3.4 Effect of SMOTE Balancing on Classifier Performance (Malignant Class Focus)

Figure 2.8 shows how the performance of all classifiers was affected by SMOTE balancing, where the main area of focus is malignant class detection. In XGBoost, the SMOTE technique produced significantly better results in terms of all metrics, with the accuracy rate elevated to almost 99% and the recall and F1-score of the malignant cases surpassing 98%, which also reinforces the idea of SMOTE being quite

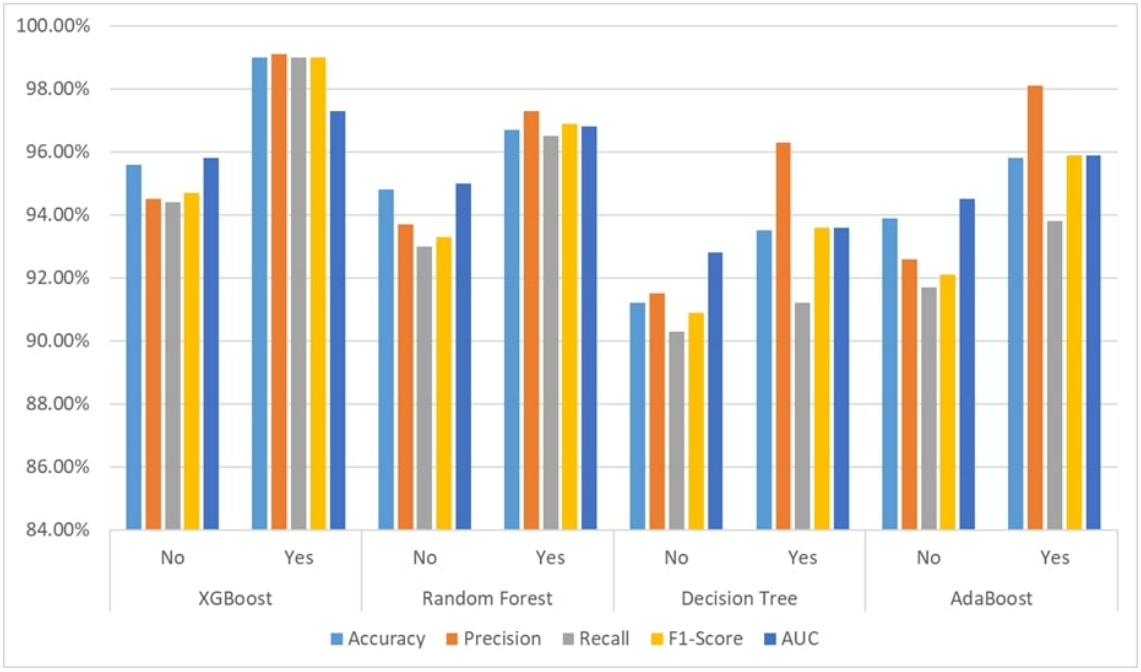

Figure 2.7: Impact of Data Normalization on Classifier Performance.

sensitive to balanced data. Random Forest also became more efficient after SMOTE was used, with the recall and F1-score rising by approximately 2%. Decision Tree performed very well in terms of recall and F1-score, as it was shown to be sensitive to skewing in class distributions. AdaBoost showed a moderate improvement, with correct recognition of malignancy increasing sharply to 98%, which again showed more recognition of the minority class. All of these findings verify the fact that SMOTE is an effective tool in improving the classifier sensitivity and discrimination powers of malignant tumors, and it is an important objective in early cancer detection since the failure to detect such a disease can be extremely detrimental to the patient.

2.4.3.5 Novelty and Strength of the Proposed Work

A distinctive strength of this study lies in the comprehensive ablation experiments, which systematically evaluated the impact of feature selection strategies, normalization, and SMOTE balancing on classifier performance. The inclusion of Recursive Feature Elimination (RFE) demonstrated significant improvements in predictive power by eliminating redundant attributes, yielding near-perfect performance for XGBoost. Similarly, normalization was shown to stabilize gradients and harmonize feature scales, producing measurable gains in ensemble models, while SMOTE balancing enhanced sensitivity toward the malignant class, mitigating the bias introduced by class imbalance. Together, these analyses provide strong empirical evidence of the robustness, generalizability, and practical applicability of the proposed framework. By highlighting how each methodological refinement contributes incrementally to overall performance, this work advances beyond conventional single-model studies and presents a validated, reproducible pipeline for clinically relevant breast cancer detection.

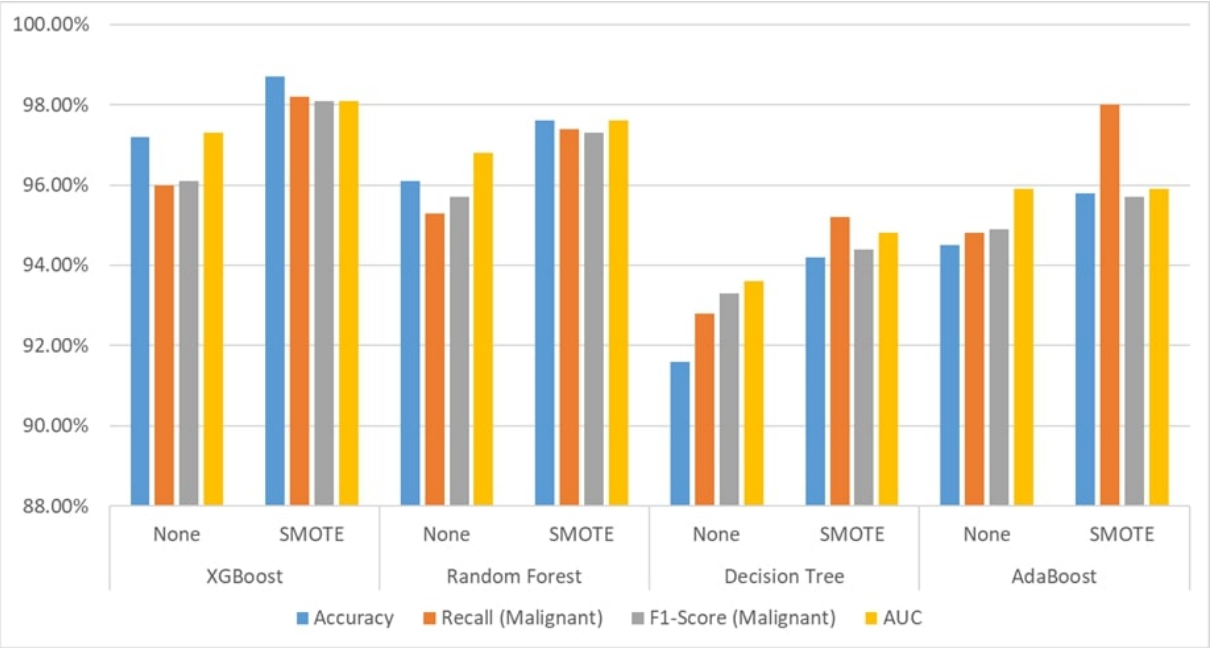

Figure 2.8: Effect of SMOTE Balancing.

2.5 Conclusion and Future Work

This study presented a comparative evaluation of multiple machine learning algorithms for breast cancer detection using the Wisconsin Diagnostic Breast Cancer Dataset (WBCD). The results demonstrated that ensemble and boosting approaches, particularly XGBoost and Random Forest, consistently achieved superior performance across accuracy, precision, recall, F1-score, and AUC metrics. Through ablation studies, the practical advantages of feature selection, normalization, and SMOTE balancing were highlighted, confirming the robustness and reproducibility of the proposed pipeline.

Practical Relevance: Beyond academic benchmarking, the findings hold direct implications for clinical practice. By reducing false negatives and ensuring higher sensitivity in malignant case detection, the proposed framework provides medical professionals with a decision-support tool that complements traditional diagnostic techniques. Such systems can assist pathologists by offering fast, consistent, and evidence-driven predictions, thereby reducing diagnostic errors and supporting early intervention strategies. This integration of computational intelligence into medical workflows has the potential to significantly improve patient outcomes.

Future Work: While the results on WBCD are promising, the study acknowledges the limitations of dataset size and diversity. Future research will focus on validating the proposed models on larger, multi-institutional datasets that include imaging and genomic modalities to enhance generalizability. Additionally, incorporating explainable AI (XAI) mechanisms will improve interpretability for clinicians, enabling transparency in model decision-making. The extension of this framework to real-time clinical settings and the integration with federated learning approaches could further strengthen scalability,

privacy preservation, and adoption in diverse healthcare environments.

In summary, the proposed methodology not only advances academic research in breast cancer classification but also lays the foundation for clinically relevant, scalable, and interpretable diagnostic systems.

References

Bibliography

[1] L. Liao, "Inequality in breast cancer: Global statistics from 2022 to 2050," *The Breast*, vol. 79, p. 103851, 2025.

[2] A. Akram, J. Rashid, A. Jaffar, F. Hajjej, W. Iqbal, and N. Sarwar, "Weber law based approach formulti-class image forgery detection." *Computers, Materials & Continua*, vol. 78, no. 1, 2024.

[3] J. S. S. Adapala, K. V. S. Gontla, V. Koka, S. L. Modugula, R. Mothukuri, and S. Bulla, "Breast cancer classification using svm and knn," in *2023 Second International Conference on Electronics and Renewable Systems (ICEARS)*. IEEE, 2023, pp. 1617–1621.

[4] H.-T. Liu, Z.-X. Gao, F. Li, X.-Y. Guo, C.-L. Li, H. Zhang, R.-N. Zhao, Y. Liu, D.-B. Shi, W.-J. Zhu *et al.*, "Lncrna ly6e-dt and its encoded metastatic-related protein play oncogenic roles via different pathways and promote breast cancer progression," *Cell Death & Differentiation*, vol. 31, no. 2, pp. 188–202, 2024.

[5] M. Minnoor and V. Baths, "Diagnosis of breast cancer using random forests," *Procedia Computer Science*, vol. 218, pp. 429–437, 2023.

[6] T. Chen, X. Zhou, and G. Wang, "Using an innovative method for breast cancer diagnosis based on extreme gradient boost optimized by simplified memory bounded a," *Biomedical Signal Processing and Control*, vol. 87, p. 105450, 2024.

[7] M. A. Bülbül, "Optimization of artificial neural network structure and hyperparameters in hybrid model by genetic algorithm: ios–android application for breast cancer diagnosis/prediction," *The Journal of Supercomputing*, vol. 80, no. 4, pp. 4533–4553, 2024.

[8] M. Kaddes, Y. M. Ayid, A. M. Elshewey, and Y. Fouad, "Breast cancer classification based on hybrid cnn with lstm model," *Scientific Reports*, vol. 15, no. 1, p. 4409, 2025.

[9] S. Laghmati, S. Hamida, K. Hicham, B. Cherradi, and A. Tmiri, "An improved breast cancer disease prediction system using ml and pca," *Multimedia Tools and Applications*, vol. 83, no. 11, pp. 33 785–33 821, 2024.

[10] A. A. Adam and R. Alfred, "Optimizing the classification performance by fine-tuning the machine learning hyperparameters and utilizing pca and rfe feature selection methods," in *International Conference on Advances in Computational Science and Engineering*. Springer, 2023, pp. 435–454.

[11] H.-p. Zhang, R.-y. Jiang, J.-y. Zhu, K.-n. Sun, Y. Huang, H.-h. Zhou, Y.-b. Zheng, and X.-j. Wang, "Pi3k/akt/mtor signaling pathway: an important driver and therapeutic target in triple-negative breast cancer," *Breast Cancer*, vol. 31, no. 4, pp. 539–551, 2024.

[12] P. Patel and J. Shah, "Metformin pretreatment potentiates the antiproliferative action of doxorubicin against breast cancer," in *Annales Pharmaceutiques Françaises*, vol. 81, no. 4. Elsevier, 2023, pp. 636–652.

[13] M. M. Khan, S. S. K. Yalamarty, B. A. Rajmalani, N. Filipczak, and V. P. Torchilin, "Recent strategies to overcome breast cancer resistance," *Critical Reviews in Oncology/Hematology*, vol. 197, p. 104351, 2024.

[14] N. Islam, A. M. R. Bhuiyan, A. Alam, M. K. Chowdhury, J. Biswas, P. C. Banik, M. M. A. Molla, M. M. Kowshik, M. Sarker, and N. Ahmed, "Coping strategy among the women with metastatic breast cancer attending a palliative care unit of a tertiary care hospital of bangladesh," *PLoS One*, vol. 18, no. 1, p. e0278620, 2023.

[15] M. P. Sharma, S. Shukla, and G. Misra, "Recent advances in breast cancer cell line research," *International Journal of Cancer*, vol. 154, no. 10, pp. 1683–1693, 2024.

[16] M. Mehta, C. Zhang, S. Sarrami, V. Mroueh, and C. De La Cruz, "Evaluating breast implant screening guidelines in breast cancer reconstruction," *Annals of Plastic Surgery*, vol. 94, no. 4S, pp. S173–S176, 2025.

[17] S. Das, S. Koley, and T. Saha, "Machine learning approaches for investigating breast cancer," *Biosciences Biotechnology Research Asia*, vol. 20, no. 4, pp. 1109–1131, 2023.

[18] A. Kumar, D. Ghosh, D. Mahto, and J. P. Singh, "Comprehensive examination and comparative analysis of machine learning algorithms for breast cancer prediction," in *Intelligent Computing and Communication Techniques*. CRC Press, 2025, pp. 107–114.

[19] A. Batool and Y.-C. Byun, "Toward improving breast cancer classification using an adaptive voting ensemble learning algorithm," *IEEE Access*, vol. 12, pp. 12 869–12 882, 2024.

[20] R. Jamil, M. Dong, J. Rashid, M. Orken, Z. S. Pernebaykyzy, and M. K. Ragytovna, "High accuracy microcalcifications detection of breast cancer using wiener lti tophat model," *IEEE Access*, 2024.

[21] A. Akram, I. Khan, J. Rashid, M. Saddique, M. Idrees, Y. Y. Ghadi, and A. Algarn, "Enhanced steganalysis for color images using curvelet features and support vectormachine." *Computers, Materials & Continua*, vol. 78, no. 1, 2024.

[22] A. Reddy, "Ai and machine learning in breast cancer: Advancing precision medicine through data-driven models," *International Journal of Innovation in Engineering*, vol. 4, no. 4, pp. 37–42, 2024.

[23] S. Singh, H. Saini, A. Sharma, S. Gupta, V. Huddar, and R. Tripathi, "Breast cancer: mirnas monitoring chemoresistance and systemic therapy," *Frontiers in Oncology*, vol. 13, p. 1155254, 2023.

[24] R. Rani, P. Malik, S. Dhania, and T. K. Mukherjee, "Recent advances in mesoporous silica nanoparticle-mediated drug delivery for breast cancer treatment," *Pharmaceutics*, vol. 15, no. 1, p. 227, 2023.

[25] V. Gupta and R. Sharma, "Enhancing breast cancer prediction with xai-enabled boosting algorithms," in *2024 15th International Conference on Computing Communication and Networking Technologies (ICCCNT)*. IEEE, 2024, pp. 1–5.

CHAPTER 3

Refinements of some Fractional Integral Inequalities for Refined Exponential type (α,m,p)-Pre-invex Function

Muhammad Shoaib Saleem[†], **and Ahsan Fareed Shah**[†*]

[†] *Department of Mathematics, University of Okara, Pakistan.*

[*] *Faculty of Mathematics, FGEID (C/G) MoD, Pakistan.*

Corresponding Author: Ahsan Fareed Shah: ahsaanfareedshah@gmail.com

Abstract: *Hermite-Hadamard inequalities are widely explored in mathematics which are useful in optimization, physics and engineering. Pre-invex functions and generalized fractional integrals are advanced mathematical tools basically used to solve complex real-life problems in mathematics and economics. As a generalization of convex functions, Pre-invex functions are very useful in optimization, signal processing, control theory, finance and medicine. We combine concepts of α-preinvex, m-preinvex, p-preinvex, exponential kind preinvex and introduce a refined class of pre-invex function. This refined exponential kind (α, m, p)-Pre-invex function is used to develop new inequalities for generalized Riemann-Liouville fractional integrals. For exponential kind (m,p)-Pre-invex, exponential kind (α,p)-Pre-invex and related functions, the established results provide refinements of existing results. In addition, using a parameter substitution, the k-fractional variants of certain inequalities are also presented.*

Keywords: Pre-invex function, Refined (α,h-m)-convex function, Refined exponential kind p-convex function, Refined exponential kind m-convex function, Hermite-Hadamard inequality, Riemann-Liouville fractional integrals

3.1 Introduction

Fractional calculus was introduced in the 17^{th} century, as L'Hospital and Leibniz started a debate on derivatives having non-integer orders. This discussion motivated many mathematicians to explore and study about fractional derivatives. The field of fractional calculus was then modified in the end of 19^{th} century. Optimization, physics and engineering, as well as signal processing, control theory, finance and medicine are related to this area of mathematics.

The use of fractional integral inequalities in analysis and applied sciences has increased in previous decades. Many fractional derivatives and integrals, such as Riemann-Liouville, Caputo, Katugampola, and Caputo-Fabrizio, have been discussed in recent years with different inequalities in fuzzy, fractal, quantum and stochastic domains. Researchers have generated several variants of well-known inequalities of Ostrowski, Newton, Fejér, Hardy, Opial, Hadamard, Grüss and Mercer types using these integrals. ([1]-[11]).

Li et al. [7], established Hermite-Hadamard inequalities for Caputo-Fabrizio fractional integral operators with interesting applications in medical, electronics, engineering, robotics, automotive industry and physics. Shah et al [8], established quantum version of Hermite-Hadamard inequalities on finite intervals with applications. Zhou et al. [9], established Hermite-Hadamard inequalities on interval-valued functions using interval valued Riemann-Liouville fractional integrals. Yang et al. [10] and Li et al. [11], established Hermite-Hadamard inequalities on fuzzy interval valued functions. Vivas-Cortez et al. [12] and Chen et al. [13], established Hermite-Hadamard inequalities on fractal sets using local fractional integrals and raina's mapping. Shah et al. [14], established Hermite-Hadamard inequalities on interval-valued stochastic processes with applications in information theory and entropy.

A refined (α,m,p)-preinvex function is used to verify the Hermite-Hadamard inequality for this operator. This inequality also pointed out that several known results are specific examples of this inequality. The established inequalities are also given in k-fractional integral form. In accordance with this, we refine certain previously published results.

We aim to establish some well-known inequalities of Hermite-Hadamard kind via Riemann-Liouville operators applied to the refined class of preinvex functions. We will focus on the Riemann-Liouville fractional integrals with a monotonically increasing function, which are critical in our research. As a modification of convex mappings, Pre-invex mappings are very helpful in optimization, signal processing, control theory, finance and medicine.

- We merge ideas of α-preinvex, m-preinvex, p-preinvex, exponential kind preinvex mappings and introduce a refined class of pre-invex mapping.
- This refined exponential kind (α, m, p)-Pre-invex mapping is utilized to establish generalized inequalities for generalized Riemann-Liouville fractional integrals.
- For exponential kind (m,p)-Pre-invex, exponential kind (α,p)-Pre-invex and related mappings, the introduced results give refinements of existing works.

- Applying a parameter substitution, the k-fractional variants of some inequalities are also established.

We aim to further investigate these kind of inequalities and refined classes of preinvex functions in relation with quantum, fuzzy, interval, stochastic, and fractal calculus ([10]-[13]).

This paper is organized as follows: first, we will provide some background information about our research. In the third section, we will describe our main results, which include fractional integral inequalities of Hermite-Hadamard kind inequalities.

3.2 Preliminaries

A function $\mathsf{T} : [\jmath_1, \jmath_2] \to \mathcal{R}$ is convex for $\imath \in [0,1]$, if the following inequality holds,

$$\mathsf{T}(\jmath_1\imath + (1-\imath)\jmath_2) \leq \imath\, \mathsf{T}(\jmath_1) + (1-\imath)\, \mathsf{T}(\jmath_2). \tag{3.1}$$

We can also define a convex mapping $\mathsf{T} : [\jmath_1, \jmath_2] \to \mathcal{R}$ for $\jmath_1 < \jmath_2$ *and* $\mathsf{T} \in L^1[\jmath_1, \jmath_2]$, by Hermite-Hadamard kind inequality given below:

$$\mathsf{T}\left(\frac{\jmath_1 + \jmath_2}{2}\right) \leq \frac{1}{\jmath_2 - \jmath_1}\int_{\jmath_1}^{\jmath_2} \mathsf{T}(n)dn \leq \frac{\mathsf{T}(\jmath_1) + \mathsf{T}(\jmath_2)}{2}. \tag{3.2}$$

Now, we recall the following definition given in ([23]).

Definition 3.1: A function $\mathsf{T} : [\jmath_1, \jmath_2] \to \mathcal{R}$ is p-convex for $\imath \in [0,1]$, and $p \in \mathcal{R} - \{0\}$, if the following inequality holds,

$$\mathsf{T}\left((\jmath_1^p\imath + (1-\imath)\jmath_2^p)^{\frac{1}{p}}\right) \leq \imath\, \mathsf{T}(\jmath_1) + (1-\imath)\, \mathsf{T}(\jmath_2). \tag{3.3}$$

We can also define p-convex mapping $\mathsf{T} : [\jmath_1, \jmath_2] \to \mathcal{R}$ for $\jmath_1 < \jmath_2$ *and* $\mathsf{T} \in L^1[\jmath_1, \jmath_2]$, by Hermite-Hadamard kind inequality given below:

$$\mathsf{T}\left(\left[\frac{\jmath_1^p + \jmath_2^p}{2}\right]^{\frac{1}{p}}\right) \leq \frac{p}{\jmath_2^p - \jmath_1^p}\int_{\jmath_1}^{\jmath_2} n^{p-1}\, \mathsf{T}(n)dn \leq \frac{\mathsf{T}(\jmath_1) + \mathsf{T}(\jmath_2)}{2}. \tag{3.4}$$

Definition 3.2: ([15]) A set $[0, \jmath_2] \subset \mathcal{R}^n$ according to a vector mapping $\eta : \mathcal{R}^n \times \mathcal{R}^n \to \mathcal{R}^n$, is an invex set when,

$$\jmath_2 + \imath\eta(\jmath_1, \jmath_2) \in [0, \jmath_2], \quad \forall \jmath_1, \jmath_2 \in [0, \jmath_2],\ \imath \in [0,1].$$

Definition 3.3: [15] A mapping T defined on an invex set $[0, \jmath_2]$, according to a vector mapping $\eta : [0, \jmath_2] \times [0, \jmath_2] \to \mathcal{R}^n$ being a pre-invex mapping if,

$$\mathsf{T}(\jmath_2 + \imath\eta(\jmath_1, \jmath_2)) \leq (1-\imath)\, \mathsf{T}(\jmath_2) + \imath\, \mathsf{T}(\jmath_1), \quad \forall \jmath_1, \jmath_2 \in [0, \jmath_2],\ \imath \in [0,1]. \tag{3.5}$$

We recall the definition of refined (α, h-m)-convex function as follows.

Definition 3.4: ([24]) For a positive mapping $h : I \subset \mathcal{R} \to \mathcal{R}$, where $(0,1) \subset I$, a function $\mathsf{T} : [0, \jmath_2] \to \mathcal{R}$ is refined (α-h,m)-convex if, T is positive, and the inequality below holds:

$$\mathsf{T}(\jmath_1\imath + m(1-\imath)\jmath_2) \leq h(\imath^\alpha).h(1-\imath^\alpha)[\mathsf{T}(\jmath_1) + m\,\mathsf{T}\,(\jmath_2)], \tag{3.6}$$

$\forall\ \jmath_1, \jmath_2 \in [0, \jmath_2], (\alpha, m) \in [0,1]^2$ *and* $\imath \in (0,1)$.

Remark 3.1: For $\alpha = m = 1$ *and* $h(\imath) = \imath$ in (3.6), we get tgs-convex function.

Remark 3.2: For $\alpha = h(\imath) = m = 1$ in (3.6), we get P-convex function.

Remark 3.3: For $h(\imath) = \imath$ in (3.6), we get refined (α,m)-convex function.

Remark 3.4: For $h(\imath) = \imath,\ m = 1$ in (3.6), we get refined α-convex function.

Definition 3.5: ([25], [26]) A function T on the set I, is exponential kind convex function if,

$$\mathsf{T}(\jmath_1\imath + (1-\imath)\jmath_2) \leq (e^{(1-\imath)} - 1)\,\mathsf{T}\,(\jmath_2) + (e^{\imath} - 1)\,\mathsf{T}\,(\jmath_1), \tag{3.7}$$

$\forall \jmath_1, \jmath_2 \in I,\ \imath \in [0,1]$.

We can also define an exponential kind convex mapping $\mathsf{T} : [\jmath_1, \jmath_2] \to \mathcal{R}$ for $\jmath_1 < \jmath_2$ *and* $\mathsf{T} \in L^1[\jmath_1, \jmath_2]$, by Hermite-Hadamard kind inequality given below:

$$\frac{1}{2(e^{\frac{1}{2}} - 1)}\,\mathsf{T}\left(\frac{\jmath_1 + \jmath_2}{2}\right) \leq \frac{1}{\jmath_2 - \jmath_1}\int_{\jmath_1}^{\jmath_2} \mathsf{T}(n)dn \leq (e-2)[\mathsf{T}(\jmath_1) + \mathsf{T}(\jmath_2)]. \tag{3.8}$$

The well-known Riemann-Liouville fractional integral is given below.

Definition 3.6: ([5],[17],[21],[22]) Let $\mathsf{T} \in L[\jmath_1, \jmath_2]$ (T is Riemann-Liouville fractional integrable), we can define Riemann-Liouville fractional integrals of order $r > 0$ with $0 \leq \jmath_1$,

$$I^r_{\jmath_1^+}\,\mathsf{T}\,(v) = \frac{1}{\Gamma(r)}\int_{\jmath_1}^{v} (v-n)^{r-1}\,\mathsf{T}\,(n)dn \quad ,(v > \jmath_1), \tag{3.9}$$

$$I^r_{\jmath_2^-}\,\mathsf{T}\,(v) = \frac{1}{\Gamma(r)}\int_{v}^{\jmath_2} (n-v)^{r-1}\,\mathsf{T}\,(n)dn \quad ,(v < \jmath_2). \tag{3.10}$$

Theorem 3.1: *([16],[17]) Let* $\mathsf{T} : [\jmath_1, \jmath_2] \to \mathcal{R}$ *be a convex function on* $[\jmath_1, \jmath_2]$ *and positive function with* $0 \leq \jmath_1 < \jmath_2$. *Also, suppose that,* $\mathsf{T} \in L[\jmath_1, \jmath_2]$. *then the following fractional integral inequality holds:*

$$\mathsf{T}\left(\frac{\jmath_1 + \jmath_2}{2}\right) \leq \frac{\Gamma(r+1)}{2(\jmath_2 - \jmath_1)^r}[I^r_{\jmath_1^+}\,\mathsf{T}\,(\jmath_2) + I^r_{\jmath_2^-}\,\mathsf{T}\,(\jmath_1)] \leq \frac{\mathsf{T}(\jmath_1) + \mathsf{T}(\jmath_2)}{2}. \tag{3.11}$$

3.3 Main Results

First, we will develop our main results using Riemann-Liouville fractional integrals for refined exponential kind (α, m)-p-Pre-invex mappings given below. Inspired by, exponential kind convexity, pre-invexity and p-convexity, we define,

Definition 3.7: A function $\mathsf{T} : [0, \jmath_2] \to \mathcal{R}$ on an invex interval $[0, \jmath_2]$, according to a vector mapping $\eta : [0, \jmath_2] \times [0, \jmath_2] \to \mathcal{R}^n$ is refined exponential kind p-Pre-invex if, T is non-negative, and following inequality holds

$$\mathsf{T}\left(\left[\jmath_2^p + \imath\eta(\jmath_1^p, \jmath_2^p)\right]^{\frac{1}{p}}\right) \leq (e^{\imath} - 1)(e^{(1-\imath)} - 1)[\mathsf{T}(\jmath_1) + \mathsf{T}(\jmath_2)], \tag{3.12}$$

$\forall\ \jmath_1, \jmath_2 \in [0, \jmath_2],\ p \in \mathcal{R} - \{0\}$ *and* $\imath \in (0, 1)$.

Remark 3.5: Taking $p = 1$ in (3.12) we get, refined exponential kind Pre-invex function.

Remark 3.6: Taking $p = -1$ in (3.12) we get, refined exponential kind harmonically Pre-invex function.

Remark 3.7: Taking $p = 3$ in (3.12) we get, refined exponential kind cubic Pre-invex function.

Inspired by, exponential kind convexity, pre-invexity, α, m and p-convexity, we define,

Definition 3.8: A function $\mathsf{T} : [0, \jmath_2] \to \mathcal{R}$ on the invex set $[0, \jmath_2]$, according to a vector mapping $\eta : [0, \jmath_2] \times [0, \jmath_2] \to \mathcal{R}^n$ is refined exponential kind (α,m,p)-Pre-invex if, T is non-negative, and following inequality holds

$$\mathsf{T}\left(\left[m\jmath_2^p + \imath\eta(\jmath_1^p, m\jmath_2^p)\right]^{\frac{1}{p}}\right) \leq (e^{\imath^\alpha} - 1)(e^{(1-\imath^\alpha)} - 1)[\mathsf{T}(\jmath_1) + m\,\mathsf{T}\,(\jmath_2)], \tag{3.13}$$

$\forall\ \jmath_1, \jmath_2 \in [0, \jmath_2], (\alpha, m) \in [0, 1]^2,\ p \in \mathcal{R} - \{0\}$ *and* $\imath \in (0, 1)$.

Remark 3.8: Taking $\alpha = m = 1$ in (3.13) we get, (3.12).

Remark 3.9: Taking $\alpha = 1$ in (3.13) we get, refined exponential kind (m,p)-Pre-invex mapping.

Remark 3.10: Taking $m = 1$ in (3.13) we get, refined exponential kind (α,p)-Pre-invex mapping.

Remark 3.11: Taking $p = 1$ in (3.13) we get, refined exponential kind $(\alpha - m)$ Pre-invex function.

Remark 3.12: Taking $p = -1$ in (3.13) we get, refined exponential kind harmonically $(\alpha - m)$ Pre-invex function.

Remark 3.13: Taking $p = 3$ in (3.13) we get, refined exponential kind cubic $(\alpha - m)$ Pre-invex function.

Remark 3.14: Taking $p = \alpha = 1$ in (3.13) we get, refined exponential kind (m,p) Pre-invex function.

Remark 3.15: Taking $p = m = 1$ in (3.13) we get, refined exponential kind α-Pre-invex mapping.

Theorem 3.2: *Let $\mathsf{T} : [\jmath_1, \jmath_2] \to \mathcal{R}$ being a non-negative mapping with $0 \leq \jmath_1 < m\jmath_2$ and $\mathsf{T} \in L^1[\jmath_1, \jmath_2]$. Assume that T being a refined exponential kind (α,m,p)-Pre-invex mapping on $[\jmath_1, \jmath_2]$ as well. A non-negative monotone mapping g on $(\jmath_1, \jmath_2]$ with a continuous derivative g' on $(\jmath_1, \jmath_2)$. Then, the fractional integral inequality below holds for $(\alpha, m) \in (0, 1]^2$ and $p \in \mathcal{R} - \{0\}$:*

$$\frac{1}{\left(e^{(1/2^\alpha)} - 1\right)\left(e^{(1-(1/2^\alpha))} - 1\right)} \mathsf{T}\left(\left[m\jmath_2^p + \frac{1}{2}\eta(\jmath_1^p, m\jmath_2^p)\right]^{\frac{1}{p}}\right)$$
$$\leq \frac{\Gamma(r+1)}{\eta^r(m\jmath_2^p, \jmath_1^p)}\left[I^{r,g}_{g^{-1}(\jmath_1^p)^+}(\mathsf{T}og)\left(g^{-1}(m\jmath_2^p)\right) + m^{r+1} I^{r,g}_{g^{-1}(\jmath_2^p)^-}(\mathsf{T}og)\left(g^{-1}(\frac{\jmath_1^p}{m})\right)\right]$$
$$\leq rK_1\left[\mathsf{T}(\jmath_1) + 2m\,\mathsf{T}(\jmath_2) + m^2\,\mathsf{T}(\frac{\jmath_1}{m^2})\right], \quad (3.14)$$

$$K_1 = \frac{\mathrm{e}r\,(-1)^{\frac{r}{\alpha}}\,\Gamma\left(\frac{r}{\alpha}, 1\right) + r\,\Gamma\left(\frac{r}{\alpha}, -1\right) + \left(-\mathrm{e}r\,(-1)^{\frac{r}{\alpha}} - r\right)\Gamma\left(\frac{r}{\alpha}\right) + (\mathrm{e}+1)\,\alpha\,(-1)^{\frac{r}{\alpha}}}{\alpha r\,(-1)^{\frac{r}{\alpha}}}. \quad (3.15)$$

Proof: From refined exponential kind (α,m,p)-Pre-invexity of T, we get

$$\mathsf{T}\left(\left[my^p + \frac{1}{2}\eta(x^p, my^p)\right]^{\frac{1}{p}}\right) \leq \left(e^{(1/2^\alpha)} - 1\right)\left(e^{(1-(1/2^\alpha))} - 1\right)[\mathsf{T}(x) + m\,\mathsf{T}(y)],$$

Substituting,

$$x^p = m\jmath_2^p + \imath\eta(\jmath_1^p, m\jmath_2^p) \quad \text{and} \quad y^p = \frac{\jmath_1^p}{m} + \imath\eta\left(\jmath_2^p, \frac{\jmath_1^p}{m}\right),$$

we get,

$$\mathsf{T}\left(\left[m\jmath_2^p + \frac{1}{2}\eta(\jmath_1^p, m\jmath_2^p)\right]^{\frac{1}{p}}\right)$$
$$\leq \left(e^{(1/2^\alpha)} - 1\right)\left(e^{(1-(1/2^\alpha))} - 1\right)\left[\mathsf{T}\left(m\jmath_2^p + \imath\eta(\jmath_1^p, m\jmath_2^p)\right) + m\,\mathsf{T}\left(\frac{\jmath_1^p}{m} + \imath\eta\left(\jmath_2^p, \frac{\jmath_1^p}{m}\right)\right)\right],$$

Multiplying by $\imath^{r-1}$ on both sides, integrating over $[0, 1]$ and using refined exponential kind (α,m,p)-Pre-invexity of T, we get

$$\mathsf{T}\left(\left[m\jmath_2^p + \frac{1}{2}\eta(\jmath_1^p, m\jmath_2^p)\right]^{\frac{1}{p}}\right)\frac{1}{\left(e^{(1/2^\alpha)} - 1\right)\left(e^{(1-(1/2^\alpha))} - 1\right)}\int_0^1 \imath^{r-1}d\imath$$
$$\leq \int_0^1 \imath^{r-1}\left[\mathsf{T}\left(m\jmath_2^p + \imath\eta(\jmath_1^p, m\jmath_2^p)\right) + m\,\mathsf{T}\left(\frac{\jmath_1^p}{m} + \imath\eta\left(\jmath_2^p, \frac{\jmath_1^p}{m}\right)\right)\right]d\imath$$
$$\leq \left[\mathsf{T}(\jmath_1) + 2m\,\mathsf{T}(\jmath_2) + m^2\,\mathsf{T}(\frac{\jmath_1}{m^2})\right]\int_0^1 \imath^{r-1}(e^{\imath^\alpha} - 1)(e^{1-\imath^\alpha} - 1)d\imath,$$

$$\mathsf{T}\left(\left[m\jmath_2^p+\frac{1}{2}\eta(\jmath_1^p,m\jmath_2^p)\right]^{\frac{1}{p}}\right)\frac{1}{r\left(e^{(1/2^\alpha)}-1\right)\left(e^{(1-(1/2^\alpha))}-1\right)}$$
$$\leq\int_0^1\imath^{r-1}\left[\mathsf{T}\left(m\jmath_2^p+\imath\eta(\jmath_1^p,m\jmath_2^p)\right)+m\,\mathsf{T}\left(\frac{\jmath_1^p}{m}+\imath\eta\left(\jmath_2^p,\frac{\jmath_1^p}{m}\right)\right)\right]d\imath$$
$$\leq K_1\left[\mathsf{T}\left(\jmath_1\right)+2m\,\mathsf{T}\left(\jmath_2\right)+m^2\,\mathsf{T}\left(\frac{\jmath_1}{m^2}\right)\right],$$

Substituting,

$$g(y)=m\jmath_2^p+\imath\eta(\jmath_1^p,m\jmath_2^p)\quad and\quad g(z)=\frac{\jmath_1^p}{m}+\imath\eta\left(\jmath_2^p,\frac{\jmath_1^p}{m}\right),$$

We get, respectively

$$\imath=\frac{g(y)-m\jmath_2^p}{\eta(\jmath_1^p,m\jmath_2^p)}\quad and\quad \imath=\frac{g(z)-\frac{\jmath_1^p}{m}}{\eta\left(\jmath_2^p,\frac{\jmath_1^p}{m}\right)},$$

Thus, we get

$$\mathsf{T}\left(\left[m\jmath_2^p+\frac{1}{2}\eta(\jmath_1^p,m\jmath_2^p)\right]^{\frac{1}{p}}\right)\frac{1}{r\left(e^{(1/2^\alpha)}-1\right)\left(e^{(1-(1/2^\alpha))}-1\right)}$$
$$\leq\frac{\Gamma(r)}{\eta^r(m\jmath_2^p,\jmath_1^p)}\left[I^{r,g}_{g^{-1}(\jmath_1^p)+}(\mathsf{T}og)\left(g^{-1}(m\jmath_2^p)\right)+m^{r+1}I^{r,g}_{g^{-1}(\jmath_2^p)-}(\mathsf{T}og)\left(g^{-1}(\frac{\jmath_1^p}{m})\right)\right]$$
$$\leq K_1\left[\mathsf{T}\left(\jmath_1\right)+2m\,\mathsf{T}\left(\jmath_2\right)+m^2\,\mathsf{T}\left(\frac{\jmath_1}{m^2}\right)\right].$$

Simplifying, we get the required result. □

Corollary 3.1: *For g, being identity function, (3.14) becomes,*

$$\frac{1}{\left(e^{(1/2^\alpha)}-1\right)\left(e^{(1-(1/2^\alpha))}-1\right)}\mathsf{T}\left(\left[m\jmath_2^p+\frac{1}{2}\eta(\jmath_1^p,m\jmath_2^p)\right]^{\frac{1}{p}}\right)$$
$$\leq\frac{\Gamma(r+1)}{\eta^r(m\jmath_2^p,\jmath_1^p)}\left[I^r_{(\jmath_1^p)+}\,\mathsf{T}\left(m\jmath_2^p\right)+m^{r+1}I^r_{(\jmath_2^p)-}\,\mathsf{T}\left(\frac{\jmath_1^p}{m}\right)\right]$$
$$\leq rK_1\left[\mathsf{T}\left(\jmath_1\right)+2m\,\mathsf{T}\left(\jmath_2\right)+m^2\,\mathsf{T}\left(\frac{\jmath_1}{m^2}\right)\right].$$

Corollary 3.2: *Using $p=1$ in (3.14), we get the result for refined exponential kind (α,m) Pre-invex function as follows from (3.15);*

$$\frac{1}{\left(e^{(1/2^\alpha)}-1\right)\left(e^{(1-(1/2^\alpha))}-1\right)}\mathsf{T}\left(m\jmath_2+\frac{1}{2}\eta(\jmath_1,m\jmath_2)\right)$$
$$\leq\frac{\Gamma(r+1)}{\eta^r(m\jmath_2,\jmath_1)}\left[I^{r,g}_{g^{-1}(\jmath_1)+}(\mathsf{T}og)\left(g^{-1}(m\jmath_2)\right)+m^{r+1}I^{r,g}_{g^{-1}(\jmath_2)-}(\mathsf{T}og)\left(g^{-1}(\frac{\jmath_1}{m})\right)\right]$$
$$\leq rK_1\left[\mathsf{T}\left(\jmath_1\right)+2m\,\mathsf{T}\left(\jmath_2\right)+m^2\,\mathsf{T}\left(\frac{\jmath_1}{m^2}\right)\right].$$

Corollary 3.3: *Using $\alpha = 1$ in (3.14), we get the result for refined exponential kind (m,p)-Pre-invex mapping as follows;*

$$\frac{1}{\left(e^{(1/2)}-1\right)^2}\,\mathsf{T}\left(\left[m\jmath_2^p+\frac{1}{2}\eta(\jmath_1^p,m\jmath_2^p)\right]^{\frac{1}{p}}\right)$$
$$\leq \frac{\Gamma(r+1)}{\eta^r(m\jmath_2^p,\jmath_1^p)}\left[I^{r,g}_{g^{-1}(\jmath_1^p)+}(\mathsf{T}og)\left(g^{-1}(m\jmath_2^p)\right)+m^{r+1}I^{r,g}_{g^{-1}(\jmath_2^p)-}(\mathsf{T}og)\left(g^{-1}(\frac{\jmath_1^p}{m})\right)\right]$$
$$\leq rK_1\left[\mathsf{T}(\jmath_1)+2m\,\mathsf{T}(\jmath_2)+m^2\,\mathsf{T}(\frac{\jmath_1}{m^2})\right],$$

$$K_2=\frac{\mathrm{e}r\,(-1)^r\,\Gamma(r,1)+r\,\Gamma(r,-1)+(-\mathrm{e}r\,(-1)^r-r)\,\Gamma(r)+(\mathrm{e}+1)\,(-1)^r}{r\,(-1)^r}. \tag{3.16}$$

Corollary 3.4: *Using $m = 1$ in (3.14), we get the result for refined exponential kind (α,p)-Pre-invex mapping as follows from (3.15);*

$$\frac{1}{\left(e^{(1/2^\alpha)}-1\right)\left(e^{(1-(1/2^\alpha))}-1\right)}\,\mathsf{T}\left(\left[\jmath_2^p+\frac{1}{2}\eta(\jmath_1^p,\jmath_2^p)\right]^{\frac{1}{p}}\right)$$
$$\leq \frac{\Gamma(r+1)}{\eta^r(\jmath_2^p,\jmath_1^p)}\left[I^{r,g}_{g^{-1}(\jmath_1^p)+}(\mathsf{T}og)\left(g^{-1}(\jmath_2^p)\right)+I^{r,g}_{g^{-1}(\jmath_2^p)-}(\mathsf{T}og)\left(g^{-1}(\jmath_1^p)\right)\right]$$
$$\leq 2rK_1\left[\mathsf{T}(\jmath_1)+\mathsf{T}(\jmath_2)\right].$$

Corollary 3.5: *Using $m = \alpha = 1$ in (3.14), we get the result for refined exponential kind p-Pre-invex mapping as follows from (3.16);*

$$\frac{1}{\left(e^{(1/2)}-1\right)^2}\,\mathsf{T}\left(\left[\jmath_2^p+\frac{1}{2}\eta(\jmath_1^p,\jmath_2^p)\right]^{\frac{1}{p}}\right)$$
$$\leq \frac{\Gamma(r+1)}{\eta^r(\jmath_2^p,\jmath_1^p)}\left[I^{r,g}_{g^{-1}(\jmath_1^p)+}(\mathsf{T}og)\left(g^{-1}(\jmath_2^p)\right)+I^{r,g}_{g^{-1}(\jmath_2^p)-}(\mathsf{T}og)\left(g^{-1}(\jmath_1^p)\right)\right]$$
$$\leq 2rK_2\left[\mathsf{T}(\jmath_1)+\mathsf{T}(\jmath_2)\right].$$

Corollary 3.6: *Using $m = p = 1$ in (3.14), we get the result for refined exponential kind α-Pre-invex mapping as follows from (3.15);*

$$\frac{1}{\left(e^{(1/2^\alpha)}-1\right)\left(e^{(1-(1/2^\alpha))}-1\right)}\,\mathsf{T}\left(\left[\jmath_2+\frac{1}{2}\eta(\jmath_1,\jmath_2)\right]\right)$$
$$\leq \frac{\Gamma(r+1)}{\eta^r(\jmath_2,\jmath_1)}\left[I^{r,g}_{g^{-1}(\jmath_1)+}(\mathsf{T}og)\left(g^{-1}(\jmath_2)\right)+I^{r,g}_{g^{-1}(\jmath_2)-}(\mathsf{T}og)\left(g^{-1}(\jmath_1)\right)\right]$$
$$\leq 2rK_1\left[\mathsf{T}(\jmath_1)+\mathsf{T}(\jmath_2)\right].$$

Corollary 3.7: *Using $\alpha = p = 1$ in (3.14), we get the result for refined exponential kind m-Pre-invex*

mapping as follows from (3.16);

$$\frac{1}{\left(e^{(1/2)}-1\right)^2}\,\mathsf{T}\left(\left[m\jmath_2+\frac{1}{2}\eta(\jmath_1,m\jmath_2)\right]\right)$$
$$\leq\frac{\Gamma(r+1)}{\eta^r(m\jmath_2,\jmath_1)}\left[I^{r,g}_{g^{-1}(\jmath_1)^+}(\mathsf{T}og)\left(g^{-1}(m\jmath_2)\right)+m^{r+1}I^{r,g}_{g^{-1}(\jmath_2)^-}(\mathsf{T}og)\left(g^{-1}(\frac{\jmath_1}{m})\right)\right]$$
$$\leq rK_2\left[\mathsf{T}(\jmath_1)+2m\,\mathsf{T}(\jmath_2)+m^2\,\mathsf{T}(\frac{\jmath_1}{m^2})\right].$$

Corollary 3.8: *Using $\alpha=p=m=1$ in (3.14), we get the result for refined exponential kind Pre-invex function as follows from (3.16);*

$$\frac{1}{\left(e^{(1/2)}-1\right)^2}\,\mathsf{T}\left(\jmath_2+\frac{1}{2}\eta(\jmath_1,\jmath_2)\right)$$
$$\leq\frac{\Gamma(r+1)}{\eta^r(\jmath_2,\jmath_1)}\left[I^{r,g}_{g^{-1}(\jmath_1)^+}(\mathsf{T}og)\left(g^{-1}(\jmath_2)\right)+I^{r,g}_{g^{-1}(\jmath_2)^-}(\mathsf{T}og)\left(g^{-1}(\jmath_1)\right)\right]$$
$$\leq 2rK_2\left[\mathsf{T}(\jmath_1)+\mathsf{T}(\jmath_2)\right],$$

For g, being identity function we get,

$$\frac{1}{\left(e^{(1/2)}-1\right)^2}\,\mathsf{T}\left(\jmath_2+\frac{1}{2}\eta(\jmath_1,\jmath_2)\right)\leq\frac{\Gamma(r+1)}{\eta^r(\jmath_2,\jmath_1)}\left[I^r_{\jmath_1^+}\,\mathsf{T}(\jmath_2)+I^r_{\jmath_2^-}\,\mathsf{T}(\jmath_1)\right]$$
$$\leq 2rK_2\left[\mathsf{T}(\jmath_1)+\mathsf{T}(\jmath_2)\right].$$

3.3.1 k-Generalizations of Hermite-Hadamard inequalities for Refined Exponential kind (α,m)-p-Pre-invex mappings

For the refined exponential kind (α,m)-p-Pre-invex mapping presented in Section 3, we offer k-fractional versions of Hermite-Hadamard kind inequalities in this section.

Definition 3.9: ([4], [18], [19], [20]) Let $\mathsf{T}\in L^1[\jmath_1,\jmath_2]$. Also let g be an increasing and positive monotone function on $(\jmath_1,\jmath_2]$ having a continuous derivative g' on $(\jmath_1,\jmath_2)$. The left-sided and right-sided fractional integrals of a function T with respect to another function g on $[\jmath_1,\jmath_2]$ of order r, where $\mathcal{R}(r)>0,k>0$, are defined by

$${}_kI^{r,g}_{\jmath_1^+}\,\mathsf{T}(v)=\frac{1}{k\Gamma_k(r)}\int_{\jmath_1}^{v}g'(n)(g(v)-g(n))^{((r/k)-1)}\,\mathsf{T}(n)dn\quad,(v>\jmath_1),\tag{3.17}$$

$${}_kI^{r,g}_{\jmath_2^-}\,\mathsf{T}(v)=\frac{1}{k\Gamma_k(r)}\int_{v}^{\jmath_2}g'(n)(g(n)-g(v))^{((r/k)-1)}\,\mathsf{T}(n)dn\quad,(v<\jmath_2),\tag{3.18}$$

where,

$$\Gamma_k(r) = k^{((r/k)-1)}\Gamma\left(\frac{r}{k}\right) = \int_o^\infty n^{r-1}e^{(n^k/k)}dn, \quad \mathcal{R}(r) > 0. \tag{3.19}$$

$$k^{\frac{-r}{k}} I^{(r/k),g}_{\jmath_1^+}\, \intercal\,(v) =_k I^{r,g}_{\jmath_1^+}\, \intercal\,(v). \tag{3.20}$$

$$k^{\frac{-r}{k}} I^{(r/k),g}_{\jmath_2^-}\, \intercal\,(v) =_k I^{r,g}_{\jmath_2^-}\, \intercal\,(v). \tag{3.21}$$

Theorem 3.3: *Using the same suppositions as for Theorem (3.14) and for $k > 0$, we get k-generalized fractional integral inequality,*

$$\begin{aligned}
&\frac{1}{\left(e^{(1/2^\alpha)}-1\right)\left(e^{(1-(1/2^\alpha))}-1\right)}\, \intercal\left(\left[m\jmath_2^p + \frac{1}{2}\eta(\jmath_1^p, m\jmath_2^p)\right]^{\frac{1}{p}}\right) \\
&\quad \leq \frac{\Gamma_k(r+k)}{\eta^{r/k}(m\jmath_2^p, \jmath_1^p)}\left[\, {}_kI^{r,g}_{g^{-1}(\jmath_1^p)+}(\intercal og)\left(g^{-1}(m\jmath_2^p)\right) + m^{((r/k)+1)}\, {}_kI^{r,g}_{g^{-1}(\jmath_2^p)-}(\intercal og)\left(g^{-1}(\frac{\jmath_1^p}{m})\right)\right] \\
&\quad \leq \frac{r}{k}K_3\left[\, \intercal\,(\jmath_1) + 2m\, \intercal\,(\jmath_2) + m^2\, \intercal\,(\frac{\jmath_1}{m^2})\right].
\end{aligned} \tag{3.22}$$

$$K_3 = \frac{\mathrm{e}r\,(-1)^{\frac{r}{k\alpha}}\,\Gamma\left(\frac{r}{k\alpha}, 1\right) + r\,\Gamma\left(\frac{r}{k\alpha}, -1\right) + \left(-r\mathrm{e}\,(-1)^{\frac{r}{k\alpha}} - r\right)\Gamma\left(\frac{r}{k\alpha}\right) + k\,(\mathrm{e}+1)\,\alpha\,(-1)^{\frac{r}{k\alpha}}}{\alpha r\,(-1)^{\frac{r}{k\alpha}}}. \tag{3.23}$$

Proof: By using $r = (r/k)$ and (3.17-3.21) in (3.14) we get the required result. □

Corollary 3.9: *For g, being identity function we get from (3.22),*

$$\begin{aligned}
&\frac{1}{\left(e^{(1/2^\alpha)}-1\right)\left(e^{(1-(1/2^\alpha))}-1\right)}\, \intercal\left(\left[m\jmath_2^p + \frac{1}{2}\eta(\jmath_1^p, m\jmath_2^p)\right]^{\frac{1}{p}}\right) \\
&\quad \leq \frac{\Gamma_k(r+k)}{\eta^{r/k}(m\jmath_2^p, \jmath_1^p)}\left[\, {}_kI^{r}_{(\jmath_1^p)+}\, \intercal\,(m\jmath_2^p) + m^{((r/k)+1)}\, {}_kI^{r}_{(\jmath_2^p)-}\, \intercal\,(\frac{\jmath_1^p}{m})\right] \\
&\quad \leq \frac{r}{k}K_3\left[\, \intercal\,(\jmath_1) + 2m\, \intercal\,(\jmath_2) + m^2\, \intercal\,(\frac{\jmath_1}{m^2})\right].
\end{aligned}$$

Corollary 3.10: *Using $p = 1$ in (3.22), we get the result for refined exponential kind (α, m) Pre-invex function as follows from (3.23);*

$$\begin{aligned}
&\frac{1}{\left(e^{(1/2^\alpha)}-1\right)\left(e^{(1-(1/2^\alpha))}-1\right)}\, \intercal\left(\left[m\jmath_2 + \frac{1}{2}\eta(\jmath_1, m\jmath_2)\right]\right) \\
&\quad \leq \frac{\Gamma_k(r+k)}{\eta^{r/k}(m\jmath_2, \jmath_1)}\left[\, {}_kI^{r,g}_{g^{-1}(\jmath_1)+}(\intercal og)\left(g^{-1}(m\jmath_2)\right) + m^{((r/k)+1)}\, {}_kI^{r,g}_{g^{-1}(\jmath_2)-}(\intercal og)\left(g^{-1}(\frac{\jmath_1}{m})\right)\right] \\
&\quad \leq \frac{r}{k}K_3\left[\, \intercal\,(\jmath_1) + 2m\, \intercal\,(\jmath_2) + m^2\, \intercal\,(\frac{\jmath_1}{m^2})\right].
\end{aligned}$$

Corollary 3.11: *Using $\alpha = 1$ in (3.22), we get the result for refined exponential kind (m,p)-Pre-invex mapping as follows;*

$$\frac{1}{\left(e^{(1/2)}-1\right)^2}\,\mathsf{T}\left(\left[m\jmath_2^p+\frac{1}{2}\eta(\jmath_1^p,m\jmath_2^p)\right]^{\frac{1}{p}}\right)$$
$$\leq \frac{\Gamma_k(r+k)}{\eta^{r/k}(m\jmath_2^p,\jmath_1^p)}\left[\,{}_kI^{r,g}_{g^{-1}(\jmath_1^p)+}(\mathsf{T}og)\left(g^{-1}(m\jmath_2^p)\right)+m^{((r/k)+1)}\,{}_kI^{r,g}_{g^{-1}(\jmath_2^p)-}(\mathsf{T}og)\left(g^{-1}(\frac{\jmath_1^p}{m})\right)\right]$$
$$\leq \frac{r}{k}K_4\left[\,\mathsf{T}\,(\jmath_1)+2m\,\mathsf{T}\,(\jmath_2)+m^2\,\mathsf{T}\,(\frac{\jmath_1}{m^2})\right],$$

$$K_4=\frac{\mathrm{e}r\,(-1)^{\frac{r}{k}}\,\Gamma\left(\frac{r}{k},1\right)+r\,\Gamma\left(\frac{r}{k},-1\right)+\left(-r\mathrm{e}\,(-1)^{\frac{r}{k}}-r\right)\Gamma\left(\frac{r}{k}\right)+k\,(\mathrm{e}+1)\,(-1)^{\frac{r}{k}}}{r\,(-1)^{\frac{r}{k}}}. \tag{3.24}$$

Corollary 3.12: *Using $m=1$ in (3.22), we get the result for refined exponential kind (α,p)-Pre-invex mapping as follows from (3.23);*

$$\frac{1}{\left(e^{(1/2^\alpha)}-1\right)\left(e^{(1-(1/2^\alpha))}-1\right)}\,\mathsf{T}\left(\left[\jmath_2^p+\frac{1}{2}\eta(\jmath_1^p,\jmath_2^p)\right]^{\frac{1}{p}}\right)$$
$$\leq \frac{\Gamma_k(r+k)}{\eta^{r/k}(\jmath_2^p,\jmath_1^p)}\left[\,{}_kI^{r,g}_{g^{-1}(\jmath_1^p)+}(\mathsf{T}og)\left(g^{-1}(\jmath_2^p)\right)+\,{}_kI^{r,g}_{g^{-1}(\jmath_2^p)-}(\mathsf{T}og)\left(g^{-1}(\jmath_1^p)\right)\right]$$
$$\leq \frac{2r}{k}K_3\left[\,\mathsf{T}\,(\jmath_1)+\mathsf{T}(\jmath_2)\right].$$

Corollary 3.13: *Using $m=\alpha=1$ in (3.22), we get the result for refined exponential kind p-Pre-invex mapping as follows from (3.24);*

$$\frac{1}{\left(e^{(1/2)}-1\right)^2}\,\mathsf{T}\left(\left[\jmath_2^p+\frac{1}{2}\eta(\jmath_1^p,\jmath_2^p)\right]^{\frac{1}{p}}\right)$$
$$\leq \frac{\Gamma_k(r+k)}{\eta^{r/k}(\jmath_2^p,\jmath_1^p)}\left[\,{}_kI^{r,g}_{g^{-1}(\jmath_1^p)+}(\mathsf{T}og)\left(g^{-1}(\jmath_2^p)\right)+\,{}_kI^{r,g}_{g^{-1}(\jmath_2^p)-}(\mathsf{T}og)\left(g^{-1}(\jmath_1^p)\right)\right]$$
$$\leq \frac{2r}{k}K_4\left[\,\mathsf{T}\,(\jmath_1)+\mathsf{T}(\jmath_2)\right].$$

Corollary 3.14: *Using $m=p=1$ in (3.22), we get the result for refined exponential kind α-Pre-invex mapping as follows from (3.23);*

$$\frac{1}{\left(e^{(1/2^\alpha)}-1\right)\left(e^{(1-(1/2^\alpha))}-1\right)}\,\mathsf{T}\left(\left[\jmath_2+\frac{1}{2}\eta(\jmath_1,\jmath_2)\right]\right)$$
$$\leq \frac{\Gamma_k(r+k)}{\eta^{r/k}(\jmath_2,\jmath_1)}\left[\,{}_kI^{r,g}_{g^{-1}(\jmath_1)+}(\mathsf{T}og)\left(g^{-1}(\jmath_2)\right)+\,{}_kI^{r,g}_{g^{-1}(\jmath_2)-}(\mathsf{T}og)\left(g^{-1}(\jmath_1)\right)\right]$$
$$\leq \frac{2r}{k}K_3\left[\,\mathsf{T}\,(\jmath_1)+\mathsf{T}(\jmath_2)\right].$$

Corollary 3.15: *Using $\alpha=p=1$ in (3.22), we get the result for refined exponential kind m-Pre-invex mapping as follows from (3.24);*

$$\frac{1}{\left(e^{(1/2)}-1\right)^2}\,\mathsf{T}\left(\left[m\jmath_2+\frac{1}{2}\eta(\jmath_1,m\jmath_2)\right]\right)$$
$$\leq \frac{\Gamma_k(r+k)}{\eta^{r/k}(m\jmath_2,\jmath_1)}\left[\,{}_kI^{r,g}_{g^{-1}(\jmath_1)+}(\mathsf{T}og)\left(g^{-1}(m\jmath_2)\right)+m^{((r/k)+1)}\,{}_kI^{r,g}_{g^{-1}(\jmath_2)-}(\mathsf{T}og)\left(g^{-1}(\frac{\jmath_1}{m})\right)\right]$$
$$\leq \frac{r}{k}K_4\left[\,\mathsf{T}\,(\jmath_1)+2m\,\mathsf{T}\,(\jmath_2)+m^2\,\mathsf{T}\,(\frac{\jmath_1}{m^2})\right].$$

Corollary 3.16: *Using $\alpha=p=m=1$ in (3.22), we get the result for refined exponential kind Pre-invex function as follows from (3.24);*

$$\frac{1}{\left(e^{(1/2)}-1\right)^2}\,\mathsf{T}\left(\left[\jmath_2+\frac{1}{2}\eta(\jmath_1,\jmath_2)\right]\right)$$
$$\leq \frac{\Gamma_k(r+k)}{\eta^{r/k}(\jmath_2,\jmath_1)}\left[\,{}_kI^{r,g}_{g^{-1}(\jmath_1)+}(\mathsf{T}og)\left(g^{-1}(\jmath_2)\right)+\,{}_kI^{r,g}_{g^{-1}(\jmath_2)-}(\mathsf{T}og)\left(g^{-1}(\jmath_1)\right)\right]$$
$$\leq \frac{2r}{k}K_4\left[\,\mathsf{T}\,(\jmath_1)+\mathsf{T}(\jmath_2)\right].$$

For g, being identity function we get,

$$\frac{1}{\left(e^{(1/2)}-1\right)^2}\,\mathsf{T}\left(\left[\jmath_2+\frac{1}{2}\eta(\jmath_1,\jmath_2)\right]\right)$$
$$\leq \frac{\Gamma_k(r+k)}{\eta^{r/k}(\jmath_2,\jmath_1)}\left[\,{}_kI^{r}_{(\jmath_1)+}\,\mathsf{T}\,(b)+\,{}_kI^{r}_{g^{-1}(\jmath_2)-}\,\mathsf{T}\,(\jmath_1)\right]\leq \frac{2r}{k}K_4\left[\,\mathsf{T}\,(\jmath_1)+\mathsf{T}(\jmath_2)\right].$$

3.4 Conclusion

Inequalities of Hermite-Hadamard type are broadly discussed in mathematics, as they are applicable in optimization, physics and engineering. Pre-invex mappings and generalized fractional integrals are modern mathematical concepts especially applied to solve complex real-life problems in mathematics and economics. As a modification of convex mappings, Pre-invex mappings are very helpful in optimization, signal processing, control theory, finance and medicine. We merge ideas of α-preinvex, m-preinvex, p-preinvex, exponential kind preinvex mappings and introduce a refined class of pre-invex mapping. This refined exponential kind (α,m,p)-Pre-invex mapping is utilized to establish generalized inequalities for generalized Riemann-Liouville fractional integrals. For exponential kind (m,p)-Pre-invex, exponential kind (α,p)-Pre-invex and related mappings, the introduced results give refinements of existing works. Furthermore, applying a parameter substitution, the k-fractional variants of some inequalities are also established. We aim to work in this direction, merging interval analysis, fuzzy calculus, quantum calculus, fractal theory and stochastic processes.

Bibliography

[1] Mohammed, P. O., & Abdeljawad, T. (2020). Opial integral inequalities for generalized fractional operators with nonsingular kernel. *Journal of Inequalities and Applications*, *2020*, 148.

[2] Farid, G., Rehman, A. U., Bibi, S., & Chu, Y. M. (2021). Refinements of two fractional versions of Hadamard inequalities for Caputo fractional derivatives and related results. *Open Journal of Mathematical Sciences*, *5*, 1–10.

[3] Khan, M. A., Begum, S., Khurshid, Y., & Chu, Y. M. (2018). Ostrowski type inequalities involving conformable fractional integrals. *Journal of Inequalities and Applications*, *2018*, 70.

[4] Sarikaya, M. Z., Bilişik, C. C., & Tunç, T. (2020). On Hardy type inequalities via k-fractional integrals. *TWMS Journal of Applied and Engineering Mathematics*, *10*(2), 443–451.

[5] Dahmani, Z., Tabharit, L., & Taf, S. (2010). New generalizations of Grüss inequality using Riemann-Liouville fractional integrals. *Bulletin of Mathematical Analysis and Applications*, *2*(3), 93–99.

[6] Set, E., Akdemir, A. O., & Ozata, F. (2020). Grüss type inequalities for fractional integral operator involving the extended generalized Mittag-Leffler function. *Applied and Computational Mathematics*, *19*(3), 402–414.

[7] Li, J., Lin, Y., Özcan, S., Saleem, M. S., & Shah, A. F. (2025). A study of Hermite-Hadamard inequalities via Caputo-Fabrizio fractional integral operators using strongly (s, m)-convex functions in the second sense. Journal of Inequalities and Applications, 2025(1), 17.

[8] Shah, A.F., Boulaaras, S.M., Wong, P.J.Y., Saleem, M.S., Umair Shahzad, M. (2025), Quantum integral inequalities via different variants of parameterized harmonically convex functions on finite intervals with related applications. Math. Meth. Appl. Sci. 48(8), 9194-9206.

[9] Zhou, H., Saleem, M. S., Nazeer, W., & Shah, A. F. (2022). Hermite-Hadamard type inequalities for interval-valued exponential type pre-invex functions via Riemann-Liouville fractional integrals. *AIMS Mathematics*, *7*(2), 2602–2617. https://doi.org/10.3934/math.2022146

[10] Yang, Y., Saleem, M. S., Nazeer, W., & Shah, A. F. (2021). New Hermite-Hadamard inequalities in fuzzy-interval fractional calculus via exponentially convex fuzzy interval-valued function. *AIMS Mathematics*, *6*(11), 12260–12278. https://doi.org/10.3934/math.2021710

[11] Li, J., Riaz, M. B., Sherif, E. S. M., Shah, A. F., & Jhangeer, A. (2025). Exploring Fractional Hermite-Hadamard Inclusions in Up-Down Fuzzy Mechanism Associated with Multiple Harmonic Convexities. Fractals, 2540158. http://dx.doi.org/10.1142/S0218348X25401589

[12] Vivas-Cortez, M., Saleem, M. S., Shah, A. F., Nazeer, W., Hernandez, J. E. H. (2023). On Generalized Harmonically ψ-MT-Convex Functions via Local Fractional Integrals and some Applications. Appl. Math, 17(3), 417-429.

[13] Chen, L., Radwan, T., Shah, A. F., Vivas-Cortez, M., & Saleem, M. S. (2025). Fractal integral inequalities for generalized harmonically convex functions using local fractional integrals and Raina's mapping with related applications. Fractals, 2540150. https://doi.org/10.1142/S0218348X25401504

[14] Shah, A. F., Özcan, S., Vivas-Cortez, M., Saleem, M. S., & Kashuri, A. (2024). Fractional hermite–hadamard–mercer-type inequalities for interval-valued convex stochastic processes with center-radius order and their related applications in entropy and information theory. Fractal and Fractional, 8(7), 408.

[15] Weir, T., & Mond, B. (1988). Preinvex functions in multiple objective optimization. *Journal of Mathematical Analysis and Applications*, *136*, 29–38.

[16] Sarikaya, M. Z., Set, E., Yaldiz, H., & Başak, N. (2013). Hermite-Hadamard's inequalities for fractional integrals and related fractional inequalities. *Mathematical and Computer Modelling*, *57*(9–10), 2403–2407.

[17] Sarikaya, M. Z., & Yildirim, H. (2017). On Hermite-Hadamard type inequalities for Riemann-Liouville fractional integrals. *Miskolc Mathematical Notes*, *17*(2), 1049–1059.

[18] Agarwal, P., Jleli, M., & Tomar, M. (2017). Certain Hermite-Hadamard type inequalities via generalized k-fractional integrals. *Journal of Inequalities and Applications*, *2017*, 55.

[19] Set, E., Choi, J., & Gözpinar, A. (2017). Hermite-Hadamard type inequalities for the generalized k-fractional integral operators. *Journal of Inequalities and Applications*, *2017*, 206.

[20] Farid, G., Rehman, A. U., & Ain, Q. U. (2019). k-Fractional integral inequalities of Hadamard type for (h–m)-convex functions. *Computational Methods for Differential Equations*, *7*(5), 1–22.

[21] Liu, K., Wang, J., & O'Regan, D. (2019). On the Hermite-Hadamard type inequality for ψ-Riemann-Liouville fractional integrals via convex functions. *Journal of Inequalities and Applications*, *2019*, 27.

[22] Mohammed, P. O. (2021). Hermite-Hadamard inequalities for Riemann-Liouville fractional integrals of a convex function with respect to a monotone function. *Mathematical Methods in the Applied Sciences*, *44*(3), 2314–2324.

[23] Zhang, K. S., & Wan, J. P. (2007). p-convex functions and their properties. *Pure and Applied Mathematics*, *23*(1), 130–133.

[24] Jung, C. Y., Farid, G., Yasmeen, H., Lv, Y. P., & Pecari, J. (2021). Refinements of some fractional integral inequalities for refined (α, h–m)-convex functions. *Advances in Difference Equations*, *2021*, Article 391. https://doi.org/10.1186/s13662-021-03544-0

[25] Vivas-Cortez, M., Kashuri, A., Butt, S. I., Tariq, M., & Nasir, J. (2021). Exponential type p–convex function with some related inequalities and their applications. *Applied Mathematics and Information Sciences*, *15*(3), 253–261.

[26] Mohammed, P. O., Abdeljawad, T., Baleanu, D., Kashuri, A., Hamasalh, F., & Agarwal, P. (2020). New fractional inequalities of Hermite-Hadamard type involving the incomplete gamma functions. *Journal of Inequalities and Applications*, *2020*, 263. https://doi.org/10.1186/s13660-020-02538-y

CHAPTER 4

Computational Intelligence and Optimization Algorithms

Abdullah[†], Madiha Ghamkhar [†], Adeeba Fatima [†] and Asra Ayub [†]

[†] *Department of Mathematics and Statistics, University of Agriculture, Faisalabad,Pakistan .*

Corresponding Author: Madiha Ghamkhar: madiha.ghamkhar@uaf.edu.pk

Abstract: *Computational Intelligence (CI) is an example of convergence of artificial intelligence, nature-inspired computing and complex mathematical modeling. Development of adaptive systems is the subject of CI by definition. This article provides a historical overview, conceptual discussion of CI and the theory of optimization. It explains how principles of adaptation, self-organization and robustness allow building intelligent systems that are fault-tolerant and can scale well. CI deals with the development of systems that can learn and make decisions in uncertain, nonlinear and high-dimensional settings. The most important natural phenomena neural networks, fuzzy systems, and evolutionary computation have their own problem-solving approach. Simultaneously, the optimization theory introduced the mathematical methods of optimal problems with constraints, both single and multi-objective. It includes linear and nonlinear programming and the gradient-based algorithms, as well as non-convexity and search spaces that are high dimensional. The more modern methods that are drawing increasing interest are stochastic optimization techniques, multi-objective systems and constraint-handling heuristics. These technologies have practical applicability which is demonstrated by practical applications in engineering, finance, healthcare, smart cities and cognitive computing.*

Keywords: Neural Network, Fuzzy System, Evolutionary Computation, Gradient-Based Algorithm, Stochastic Optimization Technique.

4.1 Computational Intelligence

4.1.1 Introduction to Computational Intelligence

Computational Intelligence is an emerging field in modern computer science. It deals with the development and analysis of systems that can display intelligent behavior. A system will be known as an intelligent agent if it behaves in an appropriate way given its own situation and goals, exhibits flexibility in dynamic environments, learns from experience and makes choices of action based upon limited perceptual and computational resources. It is the scientific purpose of CI to explain the principles that make a possible intelligent behavior in natural and artificial systems. The main goal of engineering missions is to develop practical methodologies to construct useful and intelligent artifacts. Having both aims in mind, the scientific process in CI is highly important and the iteration of designing, implementing and evaluating the computational systems that perform intelligent tasks. It is the great importance for scientific progress.

4.1.1.1 Definition and Scope of Computational Intelligence

Computational Intelligence is essentially about the way in which systems can be built to behave intelligently in complex environments. [1] studied its relation to the design of intelligent agents that are able to act appropriately in relevant contexts, be flexible in changing goals, learn through experience and act rationally under inherent limitations in both perception and computational resources. The method of research lies in empirical science, which is derived from the iterative cycle of designing, building and testing computational systems that perform tasks are commonly considered to be intelligent agents. Within the study of general hypotheses of intelligence, study cannot exist without building of machines which go beyond the imitation of human or organizational behavior and realize the principles behind the intelligent entities . Nature-inspired techniques are central to this effort. This focus contrasts with symbol-based artificial intelligence (AI), which consists of purely symbol-based approaches as CI solutions are designed by using observed and abstract concepts of nature. Beck expressed this view at an early stage by defining the computationally intelligent system as a system that works with numerical input only and contains some elements of pattern-recognization and does not require any conventional knowledge. The field has grown in many different ways since its roots in classical approaches and now uses more modern breakthroughs including deep learning, computational swarm intelligence, approximate reasoning and learning Bayesian networks.

4.1.1.2 Historical Evolution and Key Milestones

The development of Computational intelligence is a natural expansion of the historical development of computing in general with the continuing expansion of computational techniques by which people can understand and control the world around them. In ancient times, the method of computing was performed by humans with the world-renowned example for prediction of the phenomenon of Halley comet in the

eighteenth century. Mechanical devices appeared as soon as the slide rule was invented in the seventeenth century, which resulted in a considerable advanced automation of computations. The introduction of punch cards to store data was signed on most notably by Herman Hollerith in the 1890, United States Census and by Emile Baud in telegraph systems significantly enhanced the capabilities of information processing and storage. In the 1930s, electrical relays were discovered for suitable arithmetic operations, laying the foundations of electronic computation. The systematic study of machine intelligence came into the limelight from presentation of the Turing test in the year 1950. Further development of machine learning and deep learning has considerably expanded in the domain of CI, proving its dynamic and perpetually changing aspect.

4.1.1.3 Core Principles of Computational Intelligence

CI systems are designed to operate effectively within complex, dynamically changing environments and this ability derives out of three basic principles namely adaptation, self-organization, and robustness. One of the central constructs in CI the intelligent agent is characterized by the responsiveness to changing tasks and environment. Ability to internalize experience and capability to produce adequate decisions in spite of limitations on perceptions. These are not additional features of extra value to systems which must operate in real-world environments with problems that are often poorly defined non-linear, time-varying or stochastic. Where comprehensive knowledge or precise mathematical models are often not feasible. As an example of a paradigmatic demonstration swarm intelligence is one of the prevailing paradigms in CI, shows that complex problem-solving may result through decentralized, self-organizing groups of simple agents with only local crudely beneficial rules. Self -organization produces spontaneously arising order due to local interactions in the context of positive and negative feedback loops, providing in turn its own scalability. In such decentralized control system, the decision-making is distributed among the individual agents build on local information processing and communication. This kind of distributive architecture inherently increases robustness and fault tolerance because performance of the system does not decrease as the individual components fail. These emergent effects are successful in displaying higher intelligence beyond the capability of the individual agents due to the collective behaviors that arise. This emerging capability is especially significant, it suggests that within CI systems of intelligence is rarely programmed in a top-down manner but it arises out of emergence of simple elements and therefore imparts systems with a natural degree of flexibility as well as the capability to solve problems in unanticipated ways that are not specified by the human programmer. In its turn, adaptation of CI systems to react the possible environmental or contextual changes by adjusting their own behavior and maintaining the possibility of effective functioning in a changing environment. This is closely linked with the ability of the system to learn, generalize, abstract, discover and associate which is a faculty that enables the system to use environment-specific behavior change. Adaptation, self-organization and robustness are mutually dependent. It will form a basic framework of successful problem-solving in real-life complex and unpredictable tasks. The concepts of adaptation helps to make sense of dynamic environments and

adaptations to provide the structural foundation of responses which are decentralized and flexible but in turn facilitate robustness of failures and scalability in complex systems. This synergistic correlation makes Computational Intelligence (CI) especially for the values of ill-defined problems. Since it incorporate a natural coping capability that allows systems to run in the face of partial information or imperfect models. The interconnection between fields of CI, Artificial Intelligence (AI) and Machine Learning (ML) with a significant methodological and applications overlap are observed. AI encompasses the general task of creating machines that can behave intelligently. ML and CI techniques play a central role in this field as important techniques and working tools. [2] defined ML as a specifically fundamental area of AI, which is interested in making systems able to understand data and then generate predictions based on the information without explicit programming. CI sometimes creates an ambiguity in the distinction between two related fields. CI is a sub-field of AI that comprises both ML and adaptive techniques such as neural networks, fuzzy systems and evolutionary computation.

4.1.2 Foundational Paradigms of Computational Intelligence

Computational Intelligence is built upon several foundational paradigms. Each offering distinct approaches to problem-solving inspired by natural processes. These include Neural Networks, Fuzzy Systems and Evolutionary Computation. Each paradigm contributes unique mechanisms for learning, adaptation and optimization. Collectively enabling CI to address complex challenges in diverse domains.

4.1.2.1 Neural Networks

Neural Network's mathematical models used for approximate complex, non-linear functions [3]. These are combined layers of nodes where each node performs a weighted summation of its inputs followed by a non-linear activation function. From a mathematical standpoint a neural network can be viewed as a composition of functions, optimization to minimize the error between predicted and actual outputs. The basic structure includes $x = [x_1, x_2, ..., x_n]$, where each node computes

$$z_j^{(l)} = \sum_i w_{ji}^{(l)} a_i^{(l-1)} + b_j^{(l)},$$

$$a_j^{(l)} = \sigma(z_j^{(l)}).$$

where $w_{ji}^{(l)}$, are weights and $b_j^{(l)}$, are bases and σ, is an activation function.

4.1.2.2 Fuzzy Systems

Fuzzy Systems represent a paradigm within Computational Intelligence that excels at handling imprecise, uncertain and incomplete information, a common characteristic of real-world problems [4]. Fuzzy logic is built upon the concept of fuzzy sets, where the membership of an object to a set is not sharply defined

but typically by a real number between 0 and 1.

$$\mu_A(X) : X \to [0, 1].$$

These systems are widely applied in control systems, decision-making processes and pattern recognition. The use of linguistic variables whose values are words or sentences rather than numbers are fundamental concept of approximate reasoning in fuzzy logic. A collection of IF-THEN rules are expressed as linguistic statements that describe the relationships between inputs and outputs.

If-Then rules:

$$R_i : \text{ IF } x_1 \text{ is } A_1^i \text{ AND } x_2 \text{ is } A_2^i \ \ldots \text{ AND } x_n \text{ is } A_n^i \text{ THEN } y \text{ is } B^i.$$

Where:

- R_i = the i^{th} fuzzy rule.
- A_j^i = fuzzy set for the j^{th} input variable in rule i.
- B^i = fuzzy set for the output in rule i.

The Inference Engine processes the fuzzified inputs using these rules, applying fuzzy logic operations to generate fuzzy outputs

$$y^* = \frac{\int y \cdot \mu(y) dy}{\int \mu(y) dy}.$$

This allows for a direct computational representation of semantic meaning and human-centric descriptions, facilitating easier knowledge acquisition from human experts and creating systems that are more intuitive for human interaction and interpretation. The ability of fuzzy logic is to bridge the gap between human cognition and computational models by embracing uncertainty and imprecision. It highlights the unique strength in addressing problems where qualitative human expertise is paramount [5, 6].

4.1.2.3 Evolutionary Computation

Evolutionary Computation (EC) is a family of metaheuristic algorithms designed to perform optimization and problem solving that are based in part on the paradigm of biological evolution. The principle of natural selection was proposed by Charles Darwin. As iteration procedures acting on a set of candidate solutions such algorithms presented as a population-based search process [7]. The power of EC lies in being able to model the key evolutionary processes of variation, selection and inheritance in ways that are computationally feasible and to apply them for a vast general-purpose array of tasks often with little apparent [8, 9].

4.2 Optimization Algorithms

Optimization algorithms are essential tools in various disciplines of science and engineering providing step-by-step effective methods to find optimal solutions satisfying a set of definite constraints. At its core, optimization boils down to picking an option that can produce the most desirable output at the lowest possible cost or give the utmost performance by maximizing what is wanted and minimizing what is unwanted. Although the end goal of the process is an optimal or optimum solution, it is often true that the intricacy of real world problems inevitably require the use of a diverse set of algorithms.

4.2.1 Problem Formulation in Optimization

The effectiveness of optimization methods always depends on how accurate the underlying mathematical description of the problem is, and this invariably consists of three main parts: objective function, the decision variables and constraints. The objective function gives the mathematical expression of the optimization goal and may be either linear or nonlinear depending on the nature of the problem.

Minimize/Maximize:

$$f(\tilde{x}).$$

Where $\tilde{x} = [\tilde{x_1}, \tilde{x_2}, ..., \tilde{x_n}] \in R^n$, are variables. Depending on the problem:

- If linear

$$f(\tilde{x}) = c^T \tilde{x}.$$

- If non-linear

$$f(\tilde{x}) = \tilde{x}^T Q \tilde{x} + c^T \tilde{x}.$$

Decision variables are the unknown real variables whose value the algorithm uses to achieve the objective. These variables exist in certain domain, which can be discrete, or continuous. Represented as a vector $\tilde{x} \in R^n$, where each component $\tilde{x}_i$, lies within a domain. $\tilde{x}_i \in [a_i, b_i]$, or $\tilde{x}_i \in Z$, if discrete. Constraints refers to the set of equalities or inequalities that determine ranges of permissible values of decision variables and is often interpreted as the set of values that are permitted solutions thus defining a subspace of admissible solution, known as a feasible region.

- Equality Constraints

$$h_j(\tilde{x}) = 0, \ j = 1, 2, 3, .., q.$$

- Inequality Constraints

$$g_k(\tilde{x}) \leq 0, \ k = 1, 2, , .., n.$$

Constraints are often thought to represent physical bounds, available resources, performance requirements or a design specification. An optimization problem is said to either be feasible, infeasible or unbounded; most real-life problems are feasible, whereas infeasible or unbounded solutions are often indicative of

an incomplete model [10]. The structure of optimization problem has a strong effect on the efficiency of the algorithm of its solution. In constraint optimization problems (COPs), the feasibility region and its resolvent often span titanic dimensions by constraining the spread across objective and constraint variables. However, extremely efficient constraint propagation may accelerate the progress by establishing promptly whether a solution can possibly pass the constraints which confirms that an insoluble chore can be rendered solvable by a well-designed formulation and ill-structured formulation can obstruct even the best algorithms.

Minimize:

$$f(z).$$

Subject to:

$$h_j(z) = 0, j = 1, 2, 3, .., p.$$

$$g_k(z) \leq 0, k = 1, 2, , .., m.$$

The efficient performance of learning systems is also closely intertwined with the careful selection and tuning of hyperparameters. These parameters are decided on before the learning process, and directly determine convergence, avoidance of overfitting and underfitting, and the ability of the learned model to generalize to new data. As such, their impact points to the importance of hyperparameter tuning as central to achieving effective optimization.

4.2.2 Classical Optimization Techniques

The essence of modern numerical optimization techniques are developed as derivatives of calculus. The main application of these analytical methods minimized nonlinear functions that give assumptions about the functions under consideration are continuous and twice differentiable. It can find solutions by equating the gradient of the objective function to zero for finding local minima, local maxima or saddle points.

4.2.2.1 Gradient-Based Methods

Gradient-based optimization is guided by continual feedback with the gradient vector that indicates the direction of greatest decrease in the objective landscape [11]. The algorithm usually starts at a random point and iteratively improves solutions by increasingly small steps in the direction until a local optimum is reached or some pre-specified criteria have been attained.

$$\tilde{x}^{(k+1)} = \tilde{x}^{(k)} - \alpha_k \cdot \bigtriangledown f(\tilde{x}^{(k)}).$$

Where $\bigtriangledown f,$ is the gradient and $\alpha_k,$ is the learning rate (step size).

These are particularly efficient and effective when the objective function is smooth, convex and differentiable. However, gradient-based techniques are sensitive for the factors such as noise in the function

after choosing step size and the initial starting point. A significant limitation is their susceptibility to getting trapped at saddle points or local optima. It can prevent them from finding the global optimum. Gradient-based methods are key components of neural network training, where they play a crucial role in minimizing loss functions and improving model accuracy.

4.2.2.2 Gradient Descent and Newton-Raphson Optimization

Two prominent gradient-based optimization methods are Gradient Descent and Newton's Method. Each offering distinct approaches to navigating the optimization landscape. Gradient Descent also known as the most intuitive optimization method. Firstly, Augustin-Louis Cauchy proposed in 1847. Its main concept was to continuously move in the reverse direction of gradient of the function at current position. The iterative update rule is typically expressed as

$$\tilde{\tilde{x}}^{(k+1)} = \tilde{\tilde{x}}^{(k)} - \alpha \cdot \bigtriangledown f(\tilde{\tilde{x}}^{(k)}).$$

The choice of α, is a critical step size that is too small can lead to very slow convergence, while one that is too large risks overshooting the minimum and causing divergence. While simple to implement and guaranteed to converge for a local minimum under conditions of convexity and continuity. Classical gradient descent can be extremely slow in practice. Stochastic Gradient Descent (SGD) is a widely used variant that updates parameters by using only a small subset of the data that make it more computationally effectual for large datasets and a cornerstone for training deep neural networks. Enhancements like Momentum further improve SGD's performance by enabling the algorithm to navigate flat areas and noisy gradients more effectively.

$$v^{(k+1)} = \beta v^{(k)} - \alpha_k \cdot \bigtriangledown f(\tilde{\tilde{x}}^{(k)}),$$

$$\tilde{\tilde{x}}^{(k+1)} = \tilde{\tilde{x}}^{(k)} - v^{(k+1)}.$$

where β, is the momentum coefficient. Newton's Method is a classical optimization technique that leverages higher-order information about the objective function's curvature to achieve faster convergence. Unlike gradient descent, which only uses the first derivative, Newton's method utilizes the second derivative to take a more direct path towards the minimum. The method aims to find the roots of the objective function's derivative which correspond to its critical points. Geometrically, at each iteration, Newton's method fits a parabola for graph of function at present spot, matching its slope and curvature, and then moves to the minimum of that approximating parabola. The iterative update rule in higher dimensions is

$$x^{(k+1)} = x^{(k)} - [\bigtriangledown^2 f(x^{(k)})]^{-}1 \bigtriangledown f(x^{(k)}).$$

where $\bigtriangledown f,$ is the gradient and $\bigtriangledown^2 f,$ is the Hessian matrix.

While Newton's method can converge quadratically fast when close to the optimum, its practical application is often limited by the computational expense of calculating and inverting the Hessian matrix,

especially in high-dimensional problems. Furthermore, it may not always converge or can converge to a saddle point instead of a true minimum. Quasi-Newton methods address the computational burden by approximating the Hessian or its inverse, making these methods more practical for larger-scale problems.

$$H_{k+1} = H_k + \frac{y_k y_k^T}{y_k^T s_k} - \frac{H_k s_k s_k^T H_k}{s_k^T H_k s_k}.$$

Where

- $s_k = \tilde{\tilde{x}}^{(k+1)} - \tilde{\tilde{x}}^{(k)}$.
- $y_k = \bigtriangledown f(\tilde{\tilde{x}}^{(k+1)}) - \bigtriangledown f(\tilde{\tilde{x}}^{(k)})$.

4.2.3 Linear Programming and Nonlinear Programming

Optimization problems was categorized on the base of linearity of their objective functions and constraints, leading to the distinct fields of Linear Programming (LP) and Nonlinear Programming (NLP) [12]. Linear Programming (LP) is a mathematical method which is used to gain best possible outcome in situations where all requirements and the objective function are represented by linear relationships. In LP objective function is linear and constraints are system of linear equalities or inequalities. A standard form for LP problems involves

Minimize or Maximize:

$$Z = c^T x.$$

Subject to:

$$Ax = b,\ x \geq 0.$$

Where c, and b, are given vectors, and A, is a given matrix. Various problem formulations can be converted into this standard form by using these techniques. LP is widely applied in diverse fields such as business, economics and engineering. Particularly in areas like transportation, energy and manufacturing for planning, routing, scheduling and resource allocation. Historically, LP has profoundly influenced core concepts in optimization theory, including duality and the significance of convexity. Common solution methods include the simplex method and more recent interior point methods. Nonlinear Programming (NLP) addresses optimization problems where at least one of the objective function or the constraint is nonlinear. This sub-field of mathematical optimization deals with calculating the extrema of nonlinear objective function for a set of unknown real variables.

Minimize:

$$f(\tilde{x}).$$

subject to:

$$g_i(\tilde{x}) \leq 0,$$

$$h_j(\tilde{x}) = 0.$$

where:

- $f(\tilde{x})$, is a nonlinear objective function.
- $g_i(\tilde{x})$, are non linear inequality constraints.
- $h_j(\tilde{x})$, are nonlinear equality constraints.

NLP problems are significantly more difficult than LP problems for their non-linear nature that made it a challenge to find the global optimum.

Special cases of NLP include:

4.2.3.1 Convex Programming

If the objective function is convex or concave and the constraint set is convex, general methods from convex optimization can often be applied

$$\min_{x \in R^n} f(x_1),$$

$$g_i(x_1) \leq 0, i = 1, 2, , .., n.$$

$$h_j(x_1) = 0, j = 1, 2, 3, .., p.$$

where all g_i, are convex and h_j, are affine.

4.2.3.2 Quadratic Programming

Involves a quadratic objective function subject to linear constraints.

$$\min_{x \in R^n} \frac{1}{2} \dot{x}^T Q \dot{x} + c^T \dot{x}.$$

where $Q \in R^{n \times n}$, is positive semi-definite and $c \in R^n$.

$$A\dot{x} \leq b, \ A_{eq}\dot{x} = b_{eq}.$$

Where $A \in R^{n \times m}$, and $b \in R^m$.

$$\pounds(\dot{x}, \lambda) = \frac{1}{2} \dot{x}^T Q \dot{x} + c^T \dot{x} + \lambda^T (A\dot{x} - b),$$

$$f(\lambda \dot{x} + (1 - \lambda) f(y)) \leq \lambda f(\dot{x} + (1 - \lambda) f(y)),$$

$$\forall \dot{x}, y \in C \text{ and } \lambda \in [0, 1].$$

4.2.3.3 Fractional Programming

Fractional programming deals with optimization problems in which the objective function is expressed as the ratio of a concave numerator and a convex denominator. Formally, the problem can be written as:

Objective function

$$\max_{x \in X} \frac{f(x)}{g(x)}.$$

Where $f(x)$, is concave and $g(x)$, is convex.

Transform using Dinkelbach's Method:

At iteration k, the problem is formulated as

$$x^k = \arg\max_{x \in X} [f(x) - \lambda^{(k)} g(x)],$$

with the update rule

$$\lambda^{(k+1)} = \frac{f(x^{(k)})}{g(x^{(k)})}.$$

The iterations are repeated until $f(x^{(k)}) - \lambda^{(k)} g(x^{(k)}) < \epsilon$, is satisfied. This formulation can be transformed into convex optimization problems under certain conditions. For NLP problems, necessary conditions are provided the Karush-Kuhn-Tucker (KKT) conditions for optimal solution and convexity. These conditions are also sufficient for a global optimum. However, solving KKT conditions analytically is often difficult. These methods typically start with an initial point and iteratively move towards a better solution by using update rules that can be zero-order, first-order or second-order. The presence of many local optima in non-convex NLP problems remains a significant challenge, often requiring sophisticated search strategies or multiple restarts to increase the likelihood of finding a good solution.

4.2.4 Challenges in Complex Optimization

Optimizing complex systems particularly in fields like deep learning present significant challenges that often render traditional optimization techniques ineffective. These challenges primarily stem from the inherent characteristics of the optimization objectives and the scale of the problems involved. One of the most pervasive challenges is non-convexity, unlike convex optimization problems, where any local minimum is also a global minimum but non-convex problems feature a loss landscape riddled with numerous local minima, saddle points and flat regions. Local minima are points where the loss function has a lower value than surrounding points but not the absolute lowest possible value. Optimization algorithms can easily converge to these suboptimal solutions, leading to models that perform below their potential. Saddle points are points where the gradient is zero and the function curves upwards in some directions and downwards in others.

Algorithms can get stalled at saddle points, hindering further progress towards better solutions. Flat

regions are areas where the gradient is nearly zero due to extremely slow progress in optimization. Algorithms can struggle to escape these regions, significantly prolonging the training process. These problems are further compounded by the high dimensionality of modern deep learning models. Neural networks may have billions of parameters distributed over many layers. Such high dimensionality exponentially grows the number of possible local minima and saddle points, which makes the optimization process much more cumbersome. An additional parameter brings more degrees of freedom and traps which make the task of finding the global optimum even more challenging. Deep learning models have very non-linear and complex loss landscapes because of their complex architectures, which conventional optimization approaches find it difficult to explore efficiently.

The second-order optimization methods scales quadratically in the number of parameters, which makes it computationally infeasible to be computed in large deep learning models. Gradient descent itself even in a plain form may be computationally expensive in large-scale tasks and perform a complete pass of the training data with each gradient update. The size of current neural networks alone makes them computationally and memory-demanding, making most of the classic or even advanced optimization methods infeasible.

In addition to these structural and dimensional issues, there are also some issues of theoretical guarantees on complex optimization problems. Convergence to a global minimum is not guaranteed and algorithms may converge to sub optimal solutions. Moreover, the real-time adaptation in dynamic situations is a major challenge because systems must be able to quickly react to various conditions, which may be computationally demanding. The sensitivity of these algorithms to parameter tuning is also very high and the task of selecting and setting these parameters to best suit performance of the algorithm is in itself a complicated problem. Lastly, a large number of real-life optimization problems fall into the NP-hard category, which means that the exact solutions cannot be found in a reasonable time, and heuristic or approximate algorithms are to be used instead.

4.2.5 Stochastic Optimization Techniques

Stochastic optimization techniques are iterative methods that are used for random sampling to approximate and optimization of complex objective functions. These techniques are valuable when dealing with large-scale problems or noisy data where traditional methods are computationally expensive. These algorithms can efficiently escape local minima and converge to a good enough solution. Its common examples are Stochastic Gradient Descent (SGD) and evolutionary algorithms.

4.2.6 Advanced Optimization Techniques

The classical optimization algorithms, typically based on relatively straightforward and constrained problems, are quite problematic on the large scale and non-convex settings prevalent in modern data-intensive tasks. A number of more boundary paradigms have been proposed in the domain of Computational Intel-

ligence, which utilizes nature-inspired insights or innovative mathematical designs to explore complicated search spaces. Let the optimization problem be defined as:

Minimize

$$f(\hat{x}).$$

Subject to

$$\hat{x} \in X \subseteq R^n.$$

Where

- $f(x)$, is non convex objective function.
- $\hat{x}$, is a vector of decision variables.
- X, represents the feasible search space.

These algorithms use population-based heuristics, nature-inspired metaheuristics, or surrogate models to handle non-convexity, non-linearity, and multi-modality in $f(x)$.

4.3 High-Dimensional Optimization and Dimensionality Reduction Techniques

Most recent data-driven fields are regularly faced with a problem of high-dimensional optimization where a multivariate dataset has a significant number of features or variables. This phenomenon is referred to as the curse of dimensionality which contributes to the increment of computational complexity, sparsity, and the difficulties in model performance, often leading to overfitting. To eliminate these constraints, dimensionality reduction is applied to map the data into a reduced and lower-dimensional data space but without sacrificing the attributes and data information. The benefits of such methods are diverse. They usually consist of two steps. Firstly, Identify and retain the most important variables from the original dataset.

Select subset

$$S \subseteq x_1, x_2, ..., x_n.$$

such that relevance(S) is maximized and redundancy(S) is minimized. Then create new lower-dimensional variables by combining or transforming the original ones. A common method is Principal Component Analysis (PCA):

Given a data matrix

$$X \in R^{m \times n}.$$

compute its covariance matrix:

$$\Sigma = (\frac{1}{m}) X^T X.$$

Then compute the eigenvectors $v_1, v_2, ...v_k$, corresponding to the k, largest eigen values $\lambda_1, \lambda_2, ..., \lambda_k$, and project:

$$Z = X \cdot [v_1, v_2, ...v_k].$$

This transformation preserves variance and reduces dimensionality from n, to k, where $k < n$. Studies also show that dimensionality reduction algorithms can optimize or maintain classification results and at the same time reduce the computational load e.g. by decreasing the number of needed evaluations, hence their usefulness in those areas where the efficiency is a key factor yet they need the proper precision.

4.3.1 Constraint Handling Techniques

A lot of optimization problems encountered in the real world, especially when it comes to engineering design, are non-linear by their nature and have a number of constraints. These constraints either reflect physical constraints, the maximum allowable values or design space constraints. These constraints make the optimization process much more difficult, since solutions need not only optimize the objective function, but also meet all the set conditions. To allow population-based metaheuristics to efficiently traverse such constrained search spaces, Constraint Handling Techniques (CHTs) have been developed to restrict the search to the feasible domain. Probably the most widely used and general CHT is the penalty function method. A penalty term is introduced to the objective function in a way that when one or more constraints are not met a large penalty is imposed, but when all the constraints are met no penalty is imposed.

Minimize

$$f(x).$$

subject to

$$g(x) \leq 0.$$

A modified function $f_{pen}(x) = f(x) + \alpha \cdot max(0, g(x))^k$,could be used.

where α, is a positive penalty parameter and k, is an exponent.

For equality constraints,

$$f_{pen}(x) = f(x) + \beta \cdot (h(x))^k.$$

The process typically involves minimizing $\tilde{f}(x)$, with an initial set of penalty parameters. [13] Increased these parameters and used the previous solution as a starting point for the next minimization. While increasing the penalty parameters improves the accuracy with which constraints are enforced, it also tends to slow down the convergence of the unconstrained algorithm, as the modified function can develop very large gradients, making the search more challenging.

$$\lim_{\alpha \to \infty} x_\alpha = \dot{x}^*.$$

Where $\dot{x}^*$,is a solution to the original constrained problem. Theoretically, under appropriate assump-

tions, as the penalty parameters are increased without bound, any convergent subsequence of solutions to the unconstrained penalized problems will converge to a solution of the original constrained problem. This highlights a trade-off between solution precision and computational efficiency in penalty function methods. Other CHTs don't provide materials in detailed. It often involve specialized feasibility rules or multi-objective approaches that treat constraint violation as a separate objective to be minimized.

4.3.2 Parallel and Distributed Optimization Algorithms

The increasing complexity and scale of modern optimization problems, particularly in areas like deep learning and large-scale machine learning, necessitate computational approaches that can transcend the limitations of single-processor systems. Parallel and distributed optimization algorithms are designed to address these challenges by leveraging multiple computing resources to accelerate the search for optimal solutions. These paradigms are crucial for handling high computational demands, improving scalability and addressing privacy concerns associated with large datasets and models. The fundamental aim of these algorithms is to achieve global optimization by intelligently coordinating synchronization and data flow across a network of heterogeneous architectures. For an individual x_i, in the population

$$P = x_1, x_2, ..., x_n,$$

$$Fitness(x_i) = f(x_i).$$

Where $f(x)$, is the objective function. A key design principle involves strictly separating the structure of an algorithm from its executed functions, often utilizing a hierarchical decomposition of parallel design patterns, such as an Abstract Pattern Tree (APT), as well-established building blocks for algorithmic structures.

$$F : APT \to R.$$

The optimization goal:

$$\max_{APT \in \varsigma} F(APT).$$

Where ς, is the set of all possible abstract pattern trees within a given depth. Parallel computing in optimization involves distributing computational tasks across multiple processors or cores that work simultaneously. This approach is particularly beneficial for algorithms that can be naturally decomposed into independent subtasks such as the fitness evaluation of individuals in population-based metaheuristics. Graphics Processing Units (GPUs), with their massive parallel processing capabilities, have become essential hardware accelerators for executing AI-based computational workloads, enabling significant speedups in training deep neural networks and other computationally intensive tasks. Parallelization can save computing time by allowing direct database calls or modifying memory operations in function libraries. Distributed optimization extends this concept across networked machines, where data and

computations are spread across multiple nodes.

$$N = N_1, N_2, N_3, ..., N_n,$$

$$f(x) = f_1(x) + f_2(x) + f_3(x) + ... + f_k(x).$$

Where:

- x, is the global variable.
- $f(x)$, is the local objective function.
- N, is the total number of nodes.

This approach is often based on probabilistic and mathematical statistical rules, allowing for the prediction of local optimal solutions within specific timeframes. In large-scale parallelization, resource allocation strategies are employed to ensure similarity and overlap between the numbers of samples obtained across different computing units. Despite their advantages, parallel and distributed optimization algorithms face challenges. Optimal utilization of parallelism across instruction, routine (local), and algorithm (global) levels requires significant expert knowledge. However, frameworks that abstract parallel algorithms into global, structural representations can enable automatic hardware mapping and global optimizations. Studies have demonstrated that these methods can achieve significant speedups in estimated and measured runtime costs, ranging from 1.42 to 3.08 times, by applying complex transformations that utilize specific hardware characteristics. This underscores their role in enhancing developer productivity and promoting performance portability for complex optimization problems.

4.3.3 Multi-Objective Optimization

Multi-objective optimization (MOO)is also known as Pareto optimization is that mathematical optimization problems that involve two or more than two objective functions.

$$\min_{x \in R^n} f(\tilde{x}) = [f_1(\tilde{x}), f_2(\tilde{x}), f_3(\tilde{x}), ..., f_k(\tilde{x})].$$

Subject to:

$$g_i(\tilde{x}) \leq 0,$$

$$h_j(\tilde{x}) = 0.$$

Where:

- $f_1(\tilde{x}), f_2(\tilde{x}), f_3(\tilde{x}), ..., f_k(\tilde{x})$, are multiple objective functions.
- $g_i(\tilde{x})$, and $h_j(\tilde{x})$,are the constraints.

Real-life settings often have these goals competing with each other. This means that in most cases, there is no solution that will optimize the goals simultaneously. The main aim of MOO is not to get one optimal solution but also a set of representative Pareto optimal solutions. A solution is Pareto optimal if no one objective function can make better off without at the same time worsening at least one of the other objective values.

There may be a potentially infinite number of such Pareto optimal solutions when no further subjective preference information is available to a human decision-maker and all are considered equally good mathematically. The set of these Pareto optimal outcomes is referred to as the Pareto front, Pareto frontier or Pareto boundary. It is bounded by the upper bounds and lower bounds of the objective functions of Pareto optimal solutions. Evolutionary algorithms (EAs) are now a common and widely successful way of solving MOO problems due to the ability of evolutionary algorithms to search difficult search spaces and deal with multiple and conflicting objectives. Two well known multi-objective evolutionary algorithms (MOEAs) are:

$$f_i(x) \leq f_i(\tilde{x}^*), \ \forall i.$$

$$f_j(x) \leq f_j(\tilde{x}^*), \ \text{for some } j.$$

There may be a potentially infinite number of such Pareto optimal solutions when no further subjective preference information is available to a human decision-maker and all are considered equally good mathematically. The set of these Pareto optimal outcomes is referred to as the Pareto front, Pareto frontier or Pareto boundary. It is bounded by the nadir objective vector (or upper bounds) and an ideal objective vector (or lower bounds) of the objective functions of Pareto optimal solutions. Evolutionary algorithms (EAs) are now a common and widely successful way of solving MOO problems due to the ability of evolutionary algorithms to search difficult search spaces and deal with multiple and conflicting objectives. Two well known multi-objective evolutionary algorithms (MOEAs) are:

4.3.3.1 Non-Dominated Sorting Genetic Algorithm II (NSGA-II)

It is one of the most popular MOEAs. [14] used non dominated sorting to rank the solutions according to Pareto dominance. The solutions that are not dominated by any other solution are placed in the first rank, then they are eliminated and the procedure is repeated with the remaining solutions. A crowding distance assignment is also used in NSGA-II in order to ensure that solutions on the same Pareto front are diverse, encouraging a good spread of optimal solutions. Crowding distance is a measure of the distance between solutions in the objective space. It is used in NSGA-II to ensure that solutions within a front are diverse. This is calculated by:

$$\text{Crowding Distance}(x) = \sum_{i=1}^{m} \frac{f_i(x_i + 1) - f_i(x_i - 1)}{f_{max}(i) - f_{min}(i)}.$$

Where

- $f_i(x_i + 1)$, and $f_i(x_i - 1)$, are the values of the objective function for the neighboring solutions.
- $f_{max}(i)$, and $f_{min}(i)$, are the maximum and minimum values of thei^{th} objective in the current population.

4.3.3.2 MOEA/D

This algorithm explicitly decomposes a multi-objective optimization problem into numbers of scalar optimization subproblems and then solved simultaneously by evolving a population of solutions.

$$\min_{x \in R^n} \sum_{i=1}^{m} \lambda_i f_i(x).$$

Each sub problem is associated with a specific weight vector and neighborhood relations among these sub problems are defined based on the distances between their aggregation coefficient vectors. Each subproblem is defined as:

$$g^t e(x|\lambda^{(i)}, z^*) = \min_{1 \leq j \leq M} \lambda_j^{(i)} |f_j(x) - z_j^*|.$$

Where

- $\lambda^{(i)}$, is weight vector for sub problem.
- z^*, is an ideal point.

MOEA/D often demonstrates lower computational complexity per generation compared to NSGA-II and can effectively handle issues like fitness assignment and diversity maintenance. Examples include minimizing power loss and cost in advanced power systems or balancing weight and efficiency in aerodynamic shape optimization. A significant challenge in large-scale MOO is used particularly for high-dimensional decision variables and for maintaining of both convergence and diversity.

4.4 Real-World Applications of Computational Intelligence and Optimization

Computational Intelligence (CI) and optimization algorithms have transcended theoretical research to become indispensable tools across a myriad of real-world applications. Their ability to handle complex, non-linear and uncertain data, coupled with their adaptive and self-organizing capabilities, makes them uniquely suited to solve problems that defy traditional analytical methods. This section explores their transformative impact across various critical domains.

4.4.1 Engineering Design and Structural Optimization

A significant application is Aerodynamic Shape Optimization (ASO). It is crucial for improving the aerodynamic performance of aircraft. ASO typically combines Computational Fluid Dynamics (CFD)

simulations with numerical optimization algorithms. Both gradient-based methods and gradient-free optimization approaches are employed. Recent advancements integrate ML technologies to enhance ASO capabilities, particularly in improving the accuracy of end-to-end aerodynamic modeling for rapid prediction of objective functions. For instance, unsupervised isometric feature mapping from manifold learning can capture geometric features that correlate with aerodynamic performance. It allows for the filtering out of poor-performing airfoil shapes before computationally intensive CFD simulations for improving optimization efficiency by over 50 percent compared to original evolutionary algorithms.

4.4.2 Finance

. The finance sector is undergoing a significant transformation driven by the integration of Machine Learning (ML) and Computational Intelligence (CI) techniques in the area of portfolio optimization, risk management and algorithmic trading. These revolutionary computational technologies simplify, optimize and enhance financial operations. It can improves decision-making, fraud detection, efficiency and tailored customer service. Portfolio Optimization is a cornerstone of investment management due to construct a portfolio that maximizes returns while simultaneously minimizing risk. Traditional methods, such as Markowitz's mean-variance optimization often prove insufficient in dynamic and complex market environments. ML algorithms include reinforcement learning, support vector machines and genetic algorithms. Which are increasingly employed to dynamically adjust asset allocations based on real-time market conditions and predictive analytics. The application of CI and optimization in finance not only automates routine tasks, reducing human error and freeing employees for strategic projects, but also processes vast amounts of data to provide insights for better financial planning and investment strategies. This transformation is estimated to contribute significantly to global banking profits through productivity gains.

4.4.3 Smart Cities

Smart cities leverage advanced computational intelligence and optimization techniques to enhance urban living in critical infrastructure domains like traffic management and energy grid optimization. The goal is to create more sustainable, efficient and adaptive urban environments that improve the quality of life for residents. In Traffic Management, smart cities utilize sophisticated systems to address congestion and optimize urban mobility. Traditional traffic control systems often struggle with increasing urban populations and vehicle volumes, necessitating advanced technological interventions. The integration of big data analytics, real-time data processing, machine learning algorithms, sensor data and predictive models is crucial for enhancing traffic flow and overall transportation efficiency. Real-time adaptive signal control has demonstrated significant reductions in travel times by achieving 15-25 Percent improvements in high-traffic areas. Fuzzy logic-based energy management systems are proving effective in incorporating renewable energy sources into smart grids. These systems can adjust control actions in real-time to

accommodate fluctuations in renewable energy generation, changes in consumption patterns and variations in battery storage status. [15] applied advanced deep learning algorithms to optimize overall energy usage in smart cities. leveraging massive datasets to predict energy demand and enable dynamic load balancing by reducing waste and promoting energy-efficient urban environments [16]. These applications underscore the critical role of CI and optimization in building resilient, efficient, and sustainable urban infrastructures.

4.5 Emerging Trends and Future Directions

The field of Computational Intelligence (CI) and optimization is in a state of continuous evolution, driven by advancements in underlying technologies and the increasing complexity of real-world problems. Several key trends are shaping the future of this domain, promising more sophisticated, efficient, and ethically responsible intelligent systems. The increasing reliance on complex deep learning models necessitates advancements in hardware accelerators, with GPUs and FPGAs becoming essential for achieving low-latency, energy-efficient inference, especially in edge applications. A notable shift in research focus is moving beyond more architectural innovations to emphasize the fundamental bottleneck of AI: data quality and efficiency, recognizing that the internet's vast data resources have been pivotal for scaling AI models. The growing complexity and impact of AI systems underscore the critical importance of Explainable AI (XAI). XAI aims to provide interpretability and transparency in AI models, fostering trust and confidence in their predictions and decisions. Techniques like SHAP (Shapley Additive Explanations) and LIME, along with rule-based models, offer insights into the decision-making process of black-box in AI systems. While XAI introduces computational overhead and presents a trade-off between interpretability and accuracy, future research will explore hybrid models and real-time XAI to enhance unstably and reliability in high-stakes environments like cybersecurity, finance and healthcare .The quest for more efficient problem-solving methodologies had led to the exploration of Quantum-Inspired Optimization Algorithms (QIAs) [17]. These algorithms mimic the principles of quantum computing but run on classical hardware, offering significant performance improvements over traditional methods and serving as a bridge between classical and quantum computing paradigms. QIAs leverage quantum mechanics concepts to efficiently explore vast solution spaces and escape local optima to find applications in hyper-parameter tuning, route optimization, resource allocation in logistics and drug discovery. Despite challenges related to scalability for extremely complex problems, QIAs represent a promising avenue for revolutionizing AI optimization.

4.6 Discussion of Limitations

However, it is crucial to discuss the limitations of the criteria and methodologies presented.

- **Sensitivity to Parameters and Hyperparameters:** The performance of many CI algorithms in metaheuristics and deep learning models is highly sensitive to the choice of parameters. parameters can lead to slow convergence, premature convergence to suboptimal solutions or overfitting. This often necessitates computationally expensive tuning processes.
- **Computational Complexity:** Complex models like deep neural networks or running population-based algorithms for many generations requires significant processing power and time. It can be a barrier to real-time application or deployment on resource-constrained devices.
- **Theoretical Guarantees:** Many CI algorithms, especially evolutionary algorithms have lack strong theoretical convergence guarantees. Their effectiveness is often demonstrated empirically rather than mathematically, which can be a limitation in safety-critical applications.
- **Interpretability and Black-Box Nature:** In neural networks, the decision-making process can be opaque that make it difficult to understand why a specific solution was generated or a prediction was made. This limits trust and accountability, especially in domains like healthcare and finance.
- **Generalization and Overfitting:** There is always a risk that a highly optimized model will overfit to the training data or the specific formulation of the objective function that can give poor performance on unseen data or in slightly different scenarios. Robustness to distribution shifts remains a challenge.

These limitations include the development of more robust auto-tuning frameworks and the use of surrogate models to reduce function evaluation costs.

4.7 Conclusions

Computational Intelligence (CI) and optimization algorithms is a new discipline that is transforming the problems solving approaches into a large range of fields. CI has its own origin in the adaptive and self-organizing paradigms and encompasses major models namely Neural Networks, Fuzzy Systems and Evolutionary Computation. which are equipped with specific abilities to deal with complexity, uncertainty and dynamism. Even though it is positioned separately and addition to Artificial Intelligence and Machine Learning. CI combines data-driven learning with the stability of flexible modeling approaches. Structuring of the problem is achieved by specification of objective functions, decision variables and constraints by using optimization algorithms at the same time addressing non-convexity and scalability by sophisticated techniques including dimensionality reduction, parallel processing and multi-objective optimization. Engineering, financial, smart-cities and cognitive-computing applications demonstrate the effectiveness and versatility that can be achieved through CI, although they also highlight implementation issues such as overfitting and sensitivity to parameters. New trends of deep reinforcement learning, explainable AI and quantum-inspired algorithms are indicators of even more autonomous and transparent intelligent systems. However, such developments should be ethically driven-fairness, accountable and sustainable resource steward-to ensure responsible and societally profitable integration of CI.

Bibliography

[1] Kruse, R., Borgelt, C., Klawonn, F., Moewes, C., Steinbrecher, M., & Held, P. (2011). *Computational intelligence*. Springer.

[2] Garfinkel, S. L., & Grunspan, R. H. (2019). *The computer book: From the abacus to artificial intelligence, 250 milestones in the history of computer science*. Union Square and Company.

[3] Cohen, Y., Kohn, A., & Dailey, M. (2022). Recent advances at the interface of neuroscience and artificial neural networks. *Journal of Neuroscience*, *42*(45), 8514–8523. https://doi.org/10.1523/JNEUROSCI.1505-22.2022

[4] Pal, S. K., & Mandal, D. P. (1991). Fuzzy logic and approximate reasoning: An overview. *IETE Journal of Research*, *37*(5-6), 548–560. https://doi.org/10.1080/03772063.1991.11437013

[5] Sabri, N., Puteh, M., & Mahmood, M. R. (2013). Fuzzy inference system: Short review and design. *International Review of Automatic Control*, *6*(4), 441–449.

[6] Muir, D. R. (2018). Feedforward approximations to dynamic recurrent network architectures. *Neural Computation*, *30*(2), 546–567. https://doi.org/10.1162/neco_a_01046

[7] Fortin, F.-A., De Rainville, F.-M., Gardner, M.-A., Parizeau, M., & Gagné, C. (2012). DEAP: Evolutionary algorithms made easy. *Journal of Machine Learning Research*, *13*(1), 2171–2175.

[8] Lagani, G., Falchi, F., Gennaro, C., & Amato, G. (2022). Comparing the performance of Hebbian against backpropagation learning using convolutional neural networks. *Neural Computing and Applications*, *34*(8), 6503–6519. https://doi.org/10.1007/s00521-021-06800-2

[9] Tolk, A., Adams, K. M., & Keating, C. B. (2011). Towards intelligence-based systems engineering and system of systems engineering. In A. Tolk & L. Jain (Eds.), *Intelligence-based systems engineering* (pp. 1–22). Springer.

[10] Cheng, K. C., & Yap, R. H. (2008, September). Search space reduction for constraint optimization problems. In D. A. Cohen (Ed.), *Proceedings of the 14th International Conference on Principles and Practice of Constraint Programming* (pp. 654–658). Springer. https://doi.org/10.1007/978-3-540-85958-1_53

[11] Sakovich, N., Petlenkov, E., Vesselko, J., & Nõmm, S. (2024). MAMGD: Gradient-based optimization method using exponential decay. *Technologies*, *12*(9), 154. https://doi.org/10.3390/technologies12090154

[12] Luenberger, D. G., & Ye, Y. (1984). *Linear and nonlinear programming* (Vol. 2). Springer.

[13] Bryan, K., & Shibberu, Y. (2005). Penalty functions and constrained optimization. *Department of Mathematics, Rose-Hulman Institute of Technology*, *4*(1), 1–5.

[14] Acerce, A., & Denizhan, B. (2025). Application of the Non-Dominated Sorting Genetic Algorithm II (NSGA-II) in a Two-Echelon Cold Supply Chain. *Systems*, *13*(3), 206. https://doi.org/10.3390/systems13030206

[15] Miftah, M., Alghamdi, A., Khan, I., & Li, X. (2025). Big data analytics for smart cities: Optimizing urban traffic management using real-time data processing. *Journal of Computer Science and Technology Application*, *2*(1), 14–23.

[16] Rajasekaran, S., & Pai, G. V. (2017). *Neural networks, fuzzy systems and evolutionary algorithms: Synthesis and applications*. PHI Learning Pvt. Ltd.

[17] Ganguli, R. (2001). A fuzzy logic system for ground based structural health monitoring of a helicopter rotor using modal data. *Journal of Intelligent Material Systems and Structures*, *12*(6), 397–407. https://doi.org/10.1106/XJVV-8X2E-JVEA-BK0L

CHAPTER 5

Soliton-Driven Signal Enhancement in Optical Amplifiers Using the Concatenation Model

Aamna Amer[†], Hamood Ur Rehman[†], Ifrah Iqbal[†], and Muhammad Tehseen Saleem[†]

[†] *Department of Mathematics, University of Okara, Okara Pakistan.*

Corresponding Author: Aamna Amer: aamna_amer@yahoo.com

Abstract: *This chapter introduces optical soliton solutions for the concatenation model, which is a concatenated form of the familiar nonlinear Schrödinger's equation, Lakshmanan-Porsezian-Daniel equation and the Sasa-Satsuma equation. The solutions are obtained using the modified extended tanh method with the Riccati equation and* $(\frac{1}{\vartheta(\eta)}, \frac{\vartheta^{'}(\eta)}{\vartheta(\eta)})$ *method. The proposed methods work by adding a new variable to the equation to convert its form into a non-linear equation with ordinary derivatives. A comparative analysis of the solutions is carried out at distinct temporal values. The novelty of this work lies in the fact that no previous articles have identified the new solutions obtained through the application of these two analytical methods. The acquired solutions include dark, bright, periodic, and singular wave solutions, which are illustrated using several 3D and 2D graphs. The adopted approaches demonstrate notable performance and are suitable for solving other non-linear partial differential equations that arise in the natural sciences.*

Keywords: Concatenation model, Traveling wave solutions, Optical solitons, Modified extended tanh method with the Riccati equation, Nonlinear equations

5.1 Introduction

The study of optical solitons is a significant non-linear phenomena that arises in optical fibers when dispersion is precisely balanced by non-linearity. In the realm of telecommunication networks, optical solitons facilitate rapid data transmission [1, 2]. Optical solitons have been detected experimentally in various physical systems, including bulk optical materials [3], single-mode fibers [4], and femtosecond lasers [5]. The integrity of communication networks relies on the analysis of traveling wave propagation in optical fibers. Numerous models illustrating the behavior of soliton propagation have facilitated researchers comprehension of solitons, including the non-linear Schrödinger equation (NLSE) [6], Schrödinger-Hirota equation [7], Lakshmanan-Porsezian-Daniel model (LPD) [8], Kudryashov's model [9], Triki-Biswas model [10], Manakov model [11], Ginzburg-Landau model [12], Fokas-Lenells model [13], and Sasa-Satsuma (SS) model [14], among others [15, 16].

Studying and deriving soliton solutions for non-linear partial differential equations (NLPDEs) is essential for understanding numerous real phenomena. Thereby, several exact approaches have been formulated to derive soliton solutions for NLPDEs, including, extended hyperbolic function method [17], the tanh-function expansion and its several modifications [18], the (G'/G)-expansion method [19], the variational iteration technique [20], the extended rational sine-cosine and rational sinh-cosh method [21], the modified Khater method [22], the sine-Gordon expansion (SGE) method [23], the extended Tanh-Coth method [24], the first integral method [25], the Sardar sub-equation method [26], the Jacobi elliptic function (JEF) method [27], and much more [28, 29, 30].

Despite the existence of numerous theories elucidating the transmission of solitons over transcontinental and transoceanic distances via optical fibers, the concatenation model, introduced by Ankiewicz *et al.* in 2014, remains particularly compelling [31, 32]. In this article, concatenated model is considered, which is a concatenation of LPD equation, SS equation and NLS equation [40, 33]. Through the coupling of various physical processes, this model behaves as a foundation for examining intricate interactions in nonlinear optical systems. It comprises Kerr nonlinearity, which denotes the intensity-dependent refractive index that leads to self-phase modulation (SPM), and nonlinear chromatic dispersion (CD), which deals with wavelength-dependent variations in refractive index. A more thorough illustration of the dynamics in a non-linear optical medium is produced by concatenating these effects. Due to a balance between non-linearity and dispersion, this model helps researchers understand the evolution and transmission of solitons-localized wave packets that retain their structure. A wide range of physical phenomena observed in experimental context can be represented by the concatenation model's mathematical foundation, which offers a versatile foundation for both analytical and numerical solutions.

Multiple studies have been reported using this model. Researchers have recently paid close attention to the concatenated model, which has been examined in numerous research works. Using Jacobi's elliptic function, Kudryashov *et al.* [34] investigated the Painlevè analysis and optical solitons for a concatenated model. Yildirim *et al.* [35] acquired the quiescent optical solitons for the concatenation model

with non-linear CD by means of the F-expansion procedure, the extended Jacobi's elliptic function expansion approach, the sine-Gordon equation scheme, and the Riccati equation method. Biswas *et al.* [36] constructed the optical solitons and conservation laws for the concatenation model by employing an undetermined coefficients and multipliers approach. Using the trial equation approach, Wang *et al.* [37] derived optical solitons for a concatenation model. The exact soliton solutions of the concatenation model are acquired by Khan *et al.* [38] using two effective techniques. With numerous Hamiltonian perturbation terms, spatio-temporal dispersion, and Kerr law nonlinearity, utilizing the two integration techniques, the concatenation model is studied by Zayed *et al.* [39].

5.2 Governing Model:

The concatenation model considered in this study is formulated as [40]:

$$i\psi_t + a\psi_{xx} + b|\psi|^2\psi + c_1\left[\sigma_1\psi_{xxxx} + \sigma_2(\psi_x)^2\psi^* + \sigma_3|\psi_x|^2\psi + \sigma_4|\psi|^2\psi_{xx} + \sigma_5\psi^2\psi^*_{xx} + \sigma_6|\psi|^4\psi\right]$$
$$+ic_2\left[\sigma_7\psi_{xxx} + \sigma_8|\psi|^2\psi_x + \sigma_9\psi^2\psi^*_x\right] = 0. \tag{5.1}$$

The complex function $\psi(x,t)$ describes wave patterns, including its spatial and temporal derivatives and $\psi^*(x,t)$ depicts its conjugate. In Eq. (5.1), the first term depicts the linear temporal evolution. The coefficient a in the second term denotes the linear CD, while the Kerr nonlinearity through the SPM effect is governed by the coefficient b. Additionally, $i = \sqrt{-1}$ denotes the imaginary unit. Furthermore, the fourth-order dispersion coefficient is σ_1, while the perturbation terms with the non-linear dispersion characteristics are σ_2, σ_3, σ_4, and σ_5. Moreover, two-photon absorption is taken into consideration with σ_6, the third-order dispersion is indicated by σ_7, and the effects of nonlinear dispersion are reflected by σ_8 and σ_9.

Let's look at the effects of setting particular values for the parameters c_1 and c_2, as well as the consequent simplified models, in order to give a thorough explanation of Eq. (5.1). When $c_1 = 0$, Eq. (5.1) is simplified to the renowned SS equation, a prominent model that incorporates higher-order non-linear phenomena, such as third-order dispersion, which are critical in non-linear optics. When high-order dispersion effects are taken into consideration, this equation provides information about how ultrashort pulses behave in optical fibers. One of the basic models in nonlinear wave propagation, the NLSE, which represents the evolution of wave envelopes in dispersive and non-linear media, collapses when $c_1 = c_2 = 0$. The NLSE addressed optical solitons, steady pulse solutions that retain their shape due to a balance between dispersion and non-linearity. Further while taking $c_2 = 0$, (5.1) shrinks to the familiar LPD model. By including second-order dispersion and other nonlinearities, this model extends its application in systems with non-trivial dispersion control by capturing intermediary effects between the SS equation and the NLSE. We have studied in this paper the Eq. (5.1) with $c_1 \neq 0$ and $c_2 \neq 0$ to retrieve optical solitons.

To construct the optical soliton solutions of Eq. (5.1), we have applied two efficient techniques, namely,

the modified extended tanh method (METM) with the Riccati equation (RE) and $(\frac{1}{\vartheta(\eta)}, \frac{\vartheta'(\eta)}{\vartheta(\eta)})$ method. These two innovative techniques are used for the first time to derive optical soliton solutions of the suggested model. Through the application of these two techniques, certain novel soliton solutions have been generated that have not yet been published anywhere else. These proposed methods generate dark, bright, periodic, and singular solutions. The study conducts a comparative analysis at distinct temporal values, offering new insights into solution dynamics and stability behavior. Moreover, the inclusion of 2D and 3D graphical illustrations provides a deeper physical interpretation of the obtained results, making the theoretical outcomes more transparent and applicable to optical communication contexts. The validity and efficacy of these procedures are demonstrated by their capacity to yield more exact solutions than current methodologies.

5.3 General Methodology

Consider the nonlinear PDE

$$\Psi(p, p_x, p_t, p_{xx}, p_{xt}, ...) = 0, \tag{5.2}$$

where the polynomial of $p(x,t)$ and its partial derivatives are indicated by Ψ. We introduce the wave transformation $p(x,t)$ to $\mathcal{P}(\Omega)$ as

$$p(x,t) = \mathcal{P}(\Omega), \qquad \Omega = x - kt, \tag{5.3}$$

where k is for wave speed. By plugging the transformation (15.17) into Eq. (15.10), the PDE can be reduced to an integer-order ODE

$$\Lambda(\mathcal{P}, \mathcal{P}', \mathcal{P}'', \mathcal{P}''', ...) = 0, \tag{5.4}$$

here the derivative w.r.t. Ω is indicated by primes.

5.4 Traveling Wave Solution:

To solve Eq. (5.1), we suppose the non-linear waveform as:

$$\psi(x,t) = u(\eta)e^{i\phi(x,t)}. \tag{5.5}$$

Here $\eta = x - \gamma t$ and $\phi(x,t) = -kx + \omega t + \theta_0$ is the phase component of the wave. Here γ is the soliton's speed, k depicts the frequency of soliton, ω is the wave number and θ_0 represents the phase constant. In addition, the wave's amplitude is indicated by $u(\eta)$. Eq. (5.1) is converted into an ODE using the

transformations from Eq. (15.12), after separating, the real part is:

$$c_1\sigma_1 u^{(4)} + [a + 3k(c_2\sigma_7 - 2kc_1\sigma_1)]u'' + c_1(\sigma_4 + \sigma_5)u^2u'' + c_1(\sigma_1 + \sigma_3)uu'^2 + c_1\sigma_6 u^5 \tag{5.6}$$
$$+[b - c_1k^2(\sigma_2 - \sigma_3 + \sigma_4 + \sigma_5) + kc_2(\sigma_8 - \sigma_9)]u^3 - [(a - c_1k^2\sigma_1 + c_2k\sigma_7)k^2 + \omega]u = 0,$$

while the imaginary part is:

$$(4kc_1\sigma_1 - c_2\sigma_7)u''' + [(2a - 4k^2c_1\sigma_1 + 3kc_2\sigma_7)k + \gamma]u' \tag{5.7}$$
$$+[2(\sigma_2 + \sigma_4 - \sigma_5)kc_1 - (\sigma_8 + \sigma_9)c_2]u^2u' = 0.$$

From Eq. (5.7), the following constraints are extracted:

$$(4kc_1\sigma_1 - c_2\sigma_7) = 0, \tag{5.8}$$

$$[2kc_1(\sigma_2 + \sigma_4 - \sigma_5) - (\sigma_8 + \sigma_9)c_2] = 0, \tag{5.9}$$

$$[k(2a - 4k^2c_1\sigma_1 + 3kc_2\sigma_7) + \gamma] = 0. \tag{5.10}$$

Now the Eq. (5.6) reduces to

$$c_1\sigma_1 u^{(4)} + \left(a + 6c_1k^2\sigma_1\right)u'' + c_1\left(\sigma_2 + \sigma_3\right)uu'^2 + c_1\left(\sigma_4 + \sigma_5\right)u^2u'' \tag{5.11}$$
$$+c_1\sigma_6 u^5 + Au^3 - Bu = 0,$$

where

$$A = b - c_1k^2(\sigma_2 - \sigma_3 + \sigma_4 + \sigma_5) + \frac{4c_1k^2\sigma_1(\sigma_8 - \sigma_9)}{\sigma_7},$$

and

$$B = -[k^2(a + 3k^2c_1\sigma_1) + \omega].$$

5.5 Methodologies

This section will employ two distinct approaches; the modified extended tanh method (METM) with the Riccati equation (RE) and $(\frac{1}{\vartheta(\zeta)}, \frac{\vartheta'(\zeta)}{\vartheta(\zeta)})$ method to solve Eq. (5.11).

5.5.1 The METM with the RE

The present section addresses the steps to implanting the METM with RE, a promising analytical method, in order to construct specific solitonic expressions for the governing concatenation model [41].

Therefore, this implemented method starts by presuming that Eq. (5.11) admits the following predicted solution:

$$\psi(x,t) = u(\eta) = \sum_{i=0}^{\varrho} a_i \varphi^i(\eta) + \sum_{i=1}^{\varrho} b_i \varphi^{-i}(\eta), \tag{5.12}$$

where a_i and b_i are free constants, which will be obtained. In addition, the function $\varphi = \varphi(\eta)$ a solution of the Riccati equation, gratifies the nonlinear ordinary differential equation (NODE) that follows

$$\frac{d\varphi}{d\eta} = \lambda + \varphi^2. \tag{5.13}$$

The latter NODE possesses the following exact solutions;

If $\lambda < 0$, then

$$\begin{aligned} \varphi(\eta) &= -\sqrt{-\lambda}\ tanh(\sqrt{-\lambda}\eta), \\ \varphi(\eta) &= -\sqrt{-\lambda}\ coth(\sqrt{-\lambda}\eta). \end{aligned} \tag{5.14}$$

If $\lambda = 0$, then

$$\varphi(\eta) = -\frac{1}{\eta}. \tag{5.15}$$

If $\lambda > 0$, then

$$\begin{aligned} \varphi(\eta) &= \sqrt{\lambda}\ tan(\sqrt{\lambda}\eta), \\ \varphi(\eta) &= -\sqrt{\lambda}\ cot(\sqrt{\lambda}\eta). \end{aligned} \tag{5.16}$$

The solution to Eq. (5.1), can be obtained by solving these equations using Mathematica.

In this regard, by the homogenous balancing rule, we get the value of $\varrho = 1$, from Eq. (5.11). By substituting the derived value of ϱ into Eq. (5.12), we get

$$u(\eta) = a_0 + a_1\varphi(\eta) + \frac{b_1}{\varphi(\eta)}. \tag{5.17}$$

To construct the algebraic system, we plug Eq. (5.17) into Eq. (5.11) by making use of Eq. (5.13) and set the coefficients of all powers of $\varphi^i(\eta)$ equal to zero. Using Mathematica, we solved the resulting system

and obtained the following solutions:

$$
\begin{aligned}
&a_0 = 0,\ a_1 = -\sqrt{\frac{-(P_1+P_2)}{2}},\ b_1 = 0, \\
&A = \frac{1}{24\sigma_1}\left(\sigma_2\left(a+2c_1\sigma_1\left(3k^2-14\lambda\right)\right)+\sigma_3\left(a+2c_1\sigma_1\left(3k^2-14\lambda\right)\right)\right. \\
&\left.+2\left(\sigma_4+\sigma_5\right)\left(a+2c_1\sigma_1\left(3k^2-2\lambda\right)\right)-aP_1-6c_1k^2\sigma_1P_1-20c_1\lambda\sigma_1P_1\right), \\
&B = \frac{\lambda\left(4a\sigma_6-c_1\left(\lambda\left(\left(\sigma_2+\sigma_3\right)\left(P_1+\sigma_2+\sigma_3+2\left(\sigma_4+\sigma_5\right)\right)-32\sigma_1\sigma_6\right)-24k^2\sigma_1\sigma_6\right)\right)}{2\sigma_6}.
\end{aligned}
\tag{5.18}
$$

Here, the following substitutions are used for simplifications.

$$P_1 = \sqrt{\left(\sigma_2+\sigma_3+2\left(\sigma_4+\sigma_5\right)\right)^2-96\sigma_1\sigma_6},$$

$$P_2 = \frac{\sigma_2+\sigma_3+2\left(\sigma_4+\sigma_5\right)}{\sigma_6}.$$

Plugging Eq. (5.18) into Eq. (5.17) and utilizing Eq. (5.13), the solution of Eq. (5.1) is given as;

When $\lambda < 0$,

$$\psi_1(x,t) = \sqrt{\frac{\lambda(P_1+P_2)}{2}}\left[\tanh\left(\sqrt{-\lambda}\eta\right)\right]e^{i(-kx+\omega t+\theta_0)}, \tag{5.19}$$

and

$$\psi_2(x,t) = \sqrt{\frac{\lambda(P_1+P_2)}{2}}\left[\coth\left(\sqrt{-\lambda}\eta\right)\right]e^{i(-kx+\omega t+\theta_0)}. \tag{5.20}$$

When $\lambda > 0$,

$$\psi_3(x,t) = -\sqrt{\frac{-\lambda(P_1+P_2)}{2}}\left[\tan\left(\sqrt{\lambda}\eta\right)\right]e^{i(-kx+\omega t+\theta_0)}, \tag{5.21}$$

and

$$\psi_4(x,t) = \sqrt{\frac{-\lambda(P_1+P_2)}{2}}\left[\cot\left(\sqrt{\lambda}\eta\right)\right]e^{i(-kx+\omega t+\theta_0)}. \tag{5.22}$$

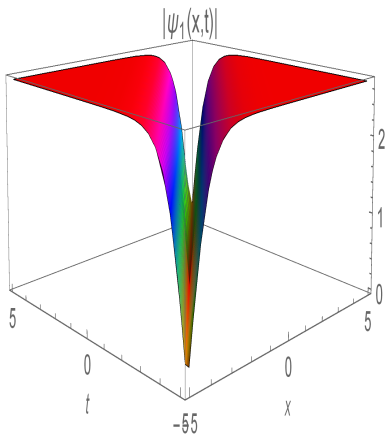

(a) 3D plot for $|\psi_1(x,t)|$.

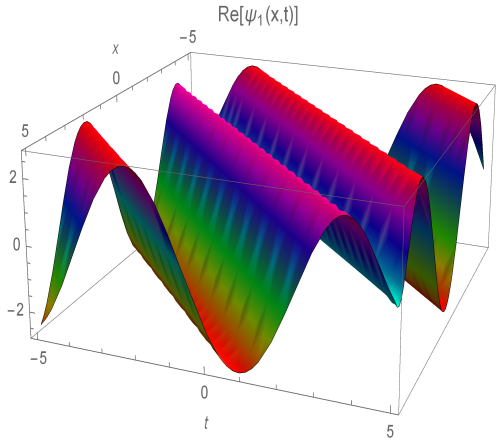

(b) 3D plot for $Re(\psi_1(x,t))$.

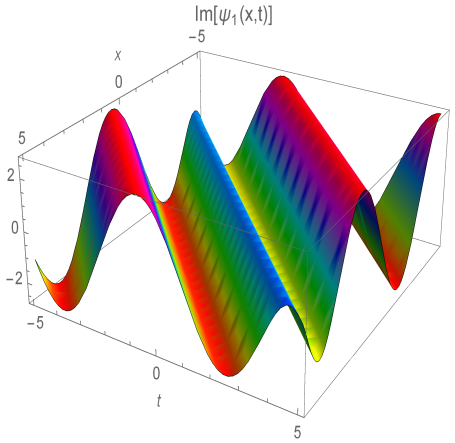

(c) 3D plot for $Im(\psi_1(x,t))$.

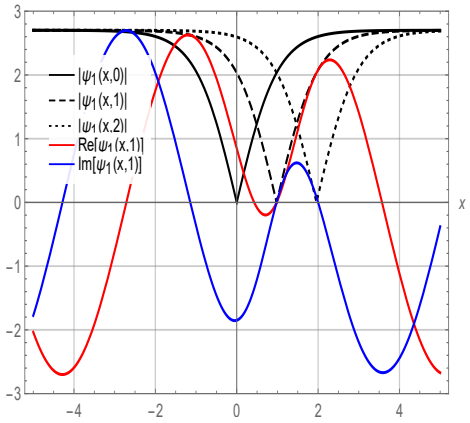

(d) 2D plots

Figure 5.1: Dark soliton solution of $\psi_1(x,t)$, with $\gamma = 0.98$, $\theta = 1$, $\lambda = -1$, $k = 1$, $\sigma_1 = 1$, $\sigma_2 = 0.95$, $\sigma_3 = 1$, $\sigma_4 = -0.97$, $\sigma_5 = 2$, $\sigma_6 = -1$, and $\omega = 1$.

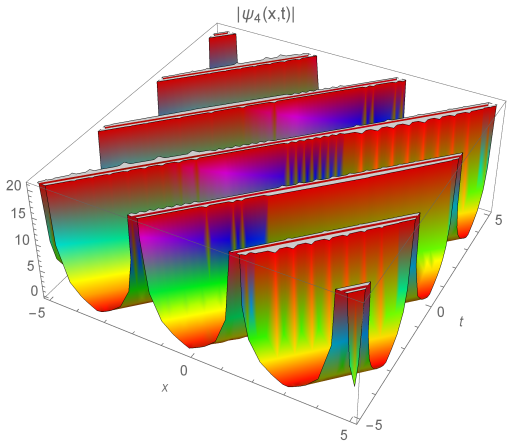

(a) 3D plot for $|\psi_4(x,t)|$.

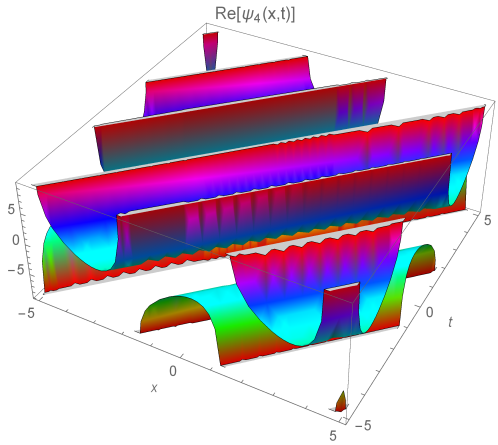

(b) 3D plot for $Re(\psi_4(x,t))$.

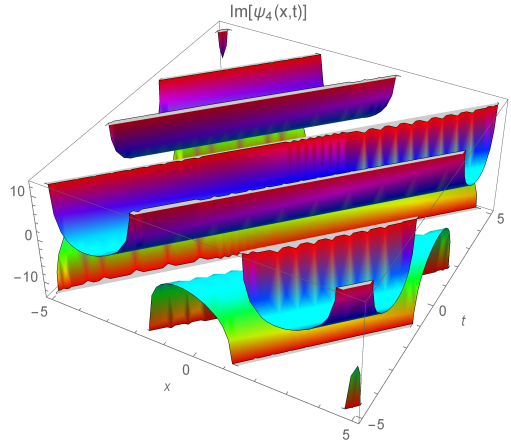

(c) 3D plot for $Im(\psi_4(x,t))$.

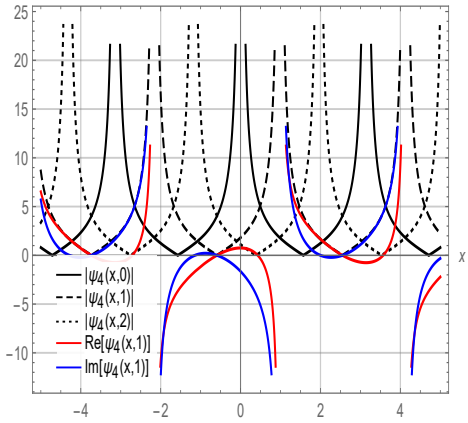

(d) 2D plots

Figure 5.2: Periodic soliton solution of $\psi_4(x,t)$, with $\gamma = 0.98$, $\theta = 1$, $\lambda = 1$, $k = 1$, $\sigma_1 = 1$, $\sigma_2 = 0.95$, $\sigma_3 = 1$, $\sigma_4 = -0.97$, $\sigma_5 = 2$, $\sigma_6 = -1$, and $\omega = 1$.

5.5.2 $(\frac{1}{\vartheta(\eta)}, \frac{\vartheta'(\eta)}{\vartheta(\eta)})$ method

Based on this approach [42], it is presumed that the solution to Eq. (5.11) can be written as:

$$u(\eta) = \omega_0 + \sum_{\sigma=1}^{\epsilon} \frac{\omega_\sigma + \beta_\sigma \vartheta'(\eta)^\sigma}{\vartheta(\eta)^\sigma}. \tag{5.23}$$

Discovering the values of ω_0, ω_σ, and β_σ (where $\sigma = 1, 2, ..., \epsilon$) allows one to solve equation (5.11), and the function $\vartheta(\eta)$ fulfills the subsequent evolution equation:

$$\vartheta'(\eta)^2 = \vartheta(\eta)^2 - \tau. \tag{5.24}$$

One can solve (5.24) to obtain the solution:

$$\vartheta(\eta) = he^{\eta} + \frac{\tau}{4he^{\eta}}, \tag{5.25}$$

Here τ and h are any constant value.

From Eq. (5.11) we get $\epsilon = 1$, which results in

$$u(\eta) = \omega_0 + \frac{\omega_1 + \beta_1 \vartheta'(\eta)}{\vartheta(\eta)}. \tag{5.26}$$

Plugging Eq. (5.26) and the necessary derivatives in to Eq. (5.11), and after solving the algebraic system we get the following set of values:

$$\begin{aligned} &\omega_0 = 0,\ \beta_1 = 0,\ \omega_1 = \sqrt{\frac{P_4 - P_3}{2}}, \\ &A = \frac{1}{24\sigma_1\tau}\left(\sigma_2\tau\left(a + 2c_1\left(3k^2 - 7\right)\sigma_1\right) + \sigma_3\tau\left(a + 2c_1\left(3k^2 - 7\right)\sigma_1\right)\right. \\ &\left.+2\left(\sigma_4 + \sigma_5\right)\tau\left(a + 2c_1\left(3k^2 - 1\right)\sigma_1\right) + aP_3 + 6c_1k^2\sigma_1P_3 + 10c_1\sigma_1P_3\right), \\ &B = a + c_1\left(6k^2 + 1\right)\sigma_1. \end{aligned} \tag{5.27}$$

Here, the following substitutions are used for simplifications.

$$P_3 = \sqrt{\left(\left(\sigma_2 + \sigma_3 + 2\left(\sigma_4 + \sigma_5\right)\right)^2 - 96\sigma_1\sigma_6\right)\tau^2},$$

and

$$P_4 = \frac{\left(\sigma_2 + \sigma_3 + 2\left(\sigma_4 + \sigma_5\right)\right)\tau}{\sigma_6}.$$

Consequently, given Eq. (5.11), the wave profile can be expressed as:

$$u(x,t) = \frac{2he^{\eta}\sqrt{2(P_4 - P_3)}}{4h^2e^{2\eta} + \tau}, \tag{5.28}$$

Plugging $\tau = \pm 4h^2$, we get following solutions

$$\psi_5(x,t) = \frac{\sqrt{P_4 - P_3}}{2\sqrt{2}h}\left[\operatorname{sech}(\eta)\right]\ e^{i(-kx+\omega t+\theta_0)}, \tag{5.29}$$

and

$$\psi_6(x,t) = \frac{\sqrt{P_4 - P_3}}{2\sqrt{2}h}\left[\operatorname{csch}(\eta)\right]\ e^{i(-kx+\omega t+\theta_0)}. \tag{5.30}$$

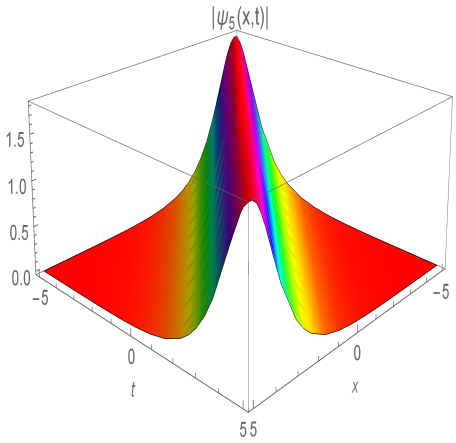

(a) 3D plot for $|\psi_5(x,t)|$.

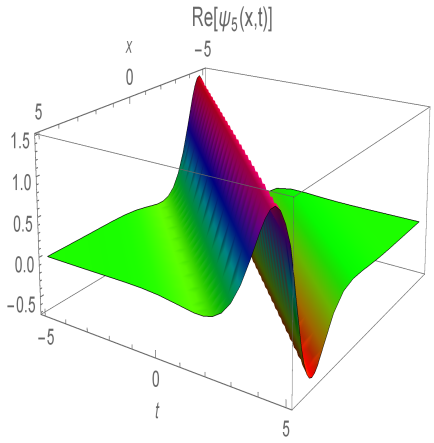

(b) 3D plot for $Re(\psi_5(x,t))$.

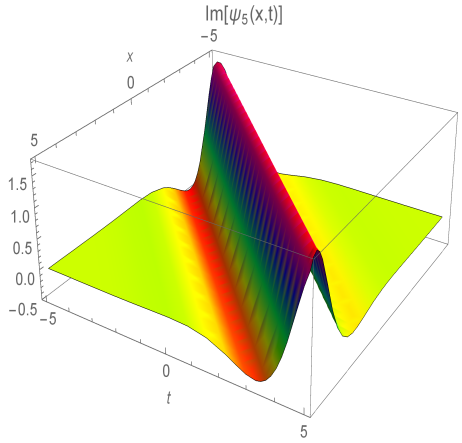

(c) 3D plot for $Im(\psi_5(x,t))$.

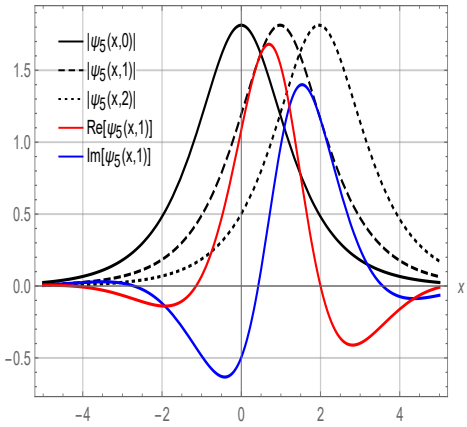

(d) 2D plots

Figure 5.3: Bright soliton of $\psi_5(x,t)$, with $\gamma = 0.98$, $h = 1$, $k = 1$, $\sigma_1 = 1$, $\sigma_2 = 0.95$, $\sigma_3 = 1$, $\theta_0 = 1$, $\sigma_4 = -0.97$, $\sigma_5 = 2$, $\sigma_6 = -1$, and $\omega = 1$.

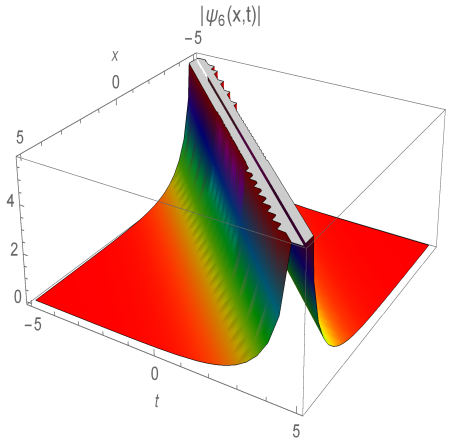

(a) 3D plot for $|\psi_6(x,t)|$.

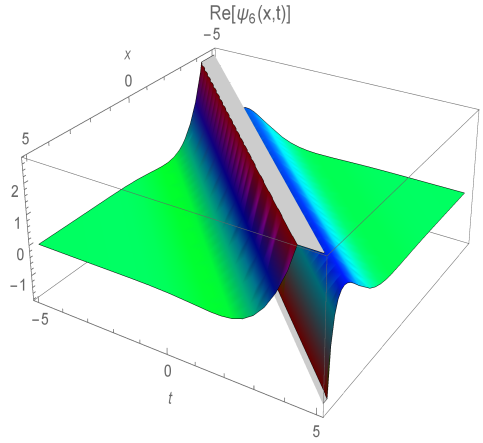

(b) 3D plot for $Re(\psi_6(x,t))$.

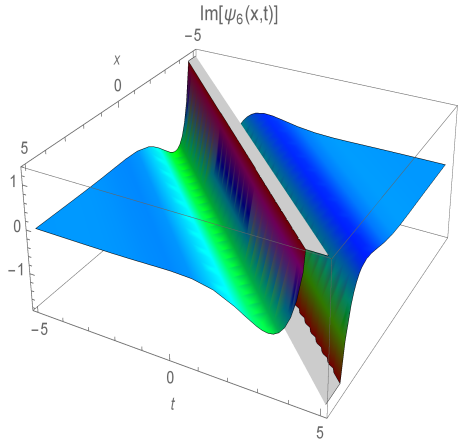

(c) 3D plot for $Im(\psi_6(x,t))$.

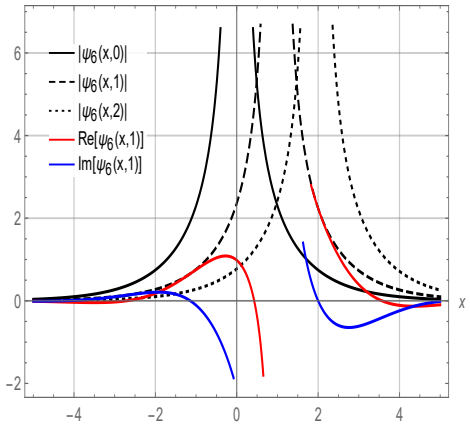

(d) 2D plots

Figure 5.4: Singular soliton behavior of $\psi_6(x,t)$, with $\gamma = 0.98$, $h = 1$, $k = 1$, $\sigma_1 = 1$, $\sigma_2 = 0.95$, $\sigma_3 = 1$, $\theta_0 = 1$, $\sigma_4 = -0.97$, $\sigma_5 = 2$, $\sigma_6 = -1$, and $\omega = 1$.

5.6 Graphical Illustration and Discussion

The propagation of a pulse in optical fiber is a significant structure in optical events and high speed optical communications have become necessary in global information transmission networks. Therefore, it becomes essential to illustrate the physical view of an optical fiber pulse. This section delves into the visual representation of specific solution functions that were obtained in sections 3, as well as some interpretations of those functions. As a general approach, the graphs presented in all figures represent the solutions $\psi(x,t)$ derived by utilizing appropriate methods. The 3D simulation of the $|\psi(x,t)|$ form is shown in subgraph (a) of these graphs, while the components of $Re(\psi(x,t))$ and $Im(\psi(x,t))$ are displayed in (b) and (c), respectively, in the other two graphics. Moreover, the 2D representations of the specified 3D shapes are reflected in the (d) graphs. These representations demonstrate a cross-section for $Re(\psi(x,t))$ and $Im(\psi(x,t))$ at just $t = 1$, as well as a traveling wave representation for the $|\psi(x,t)|$ form at $t = 0,\ 1,$ and 2, respectively. In order to incorporate the given soliton forms, the parameter selections have been made taking into account the problem's definition and constraints as well as the methods that have been

applied. To avoid degeneracy in the produced soliton form, additional parameter values can be used for drawing in this context, although the chosen parameter values are limited to the presented values.

Upon closer inspection of the graphics produced in compliance with the above-mentioned aspects, it can be observed that figure (13.2) depicts the solution function $\psi_1(x,t)$ as defined by Eq. (5.19), with parametric values; $\gamma = 0.98,\ \theta = 1,\ \lambda = -1,\ k = 1,\ \sigma_1 = 1,\ \sigma_2 = 0.95,\ \sigma_3 = 1,\ \sigma_4 = -0.97,\ \sigma_5 = 2,\ \sigma_6 = -1$, and $\omega = 1$. Where fig. (5.1a) depicting the 3D view of $|\psi_1(x,t)|$, depicting the dark soliton, while figs. (5.1b) and (5.1c) present the 3D representations of the real and imaginary components of the solution in Eq. (5.19), respectively. In fig. (5.1d), a 2D format of $|\psi_1(x,t)|$ is depicted, with black lines illustrating its appearance at various times $(t = 0, 1, 2)$. This graph demonstrates that as t rises, the dark soliton shifts to the right. The wave representations depicted in red and blue signify the $Re(\psi_1(x,t))$ and $Im(\psi_1(x,t))$, respectively, illustrating the periodic soliton configurations at varying amplitudes. Dark solitons, owing to their stable localized dips, are advantageous in high-bit-rate transmission and wavelength-division multiplexing (WDM) systems, where they minimize cross-talk and maintain channel separation. The extraordinary stability and resistivity to loss of the dark soliton make it an ideal material for fiber lasers [43, 44].

Figure (14.2) presents the soliton solution of $\psi_4(x,t)$ from Eq. (5.22) with values $\gamma = 0.98,\ \theta = 1,\ \lambda = 1,\ k = 1,\ \sigma_1 = 1,\ \sigma_2 = 0.95,\ \sigma_3 = 1,\ \sigma_4 = -0.97,\ \sigma_5 = 2,\ \sigma_6 = -1$, and $\omega = 1$. Where fig. (5.2a) represents the 3D view of $|\psi_4(x,t)|$, depicting the periodic soliton, while figs. (5.2b) and (5.2c) present the 3D representations of the $Re(\psi_4(x,t))$ and $Im(\psi_4(x,t))$ components of the solution in Eq. (5.22), respectively. To observe the movement of soliton over time, the wave profiles of $|\psi_4(x,t)|$ at $t = 0,\ 1,\ 2$ with black lines, and $Re(\psi_4(x,t))$ and $Im(\psi_4(x,t))$ in red and blue line respectively, are illustrated in 2D view in fig. (5.2d). Advanced signal processing methods make extensive use of periodic solutions. Visual representations show that these solutions are oscillatory, which can be used for different signal operations in optical communication systems, such as pulse shaping and wavelength conversion [45].

In figure (8.3), graphical illustrations in 3D and 2D view of $\psi_5(x,t)$ by defined by Eq. (5.29) with values $\gamma = 0.98,\ h = 1,\ k = 1,\ \sigma_1 = 1,\ \sigma_2 = 0.95,\ \sigma_3 = 1,\ \theta_0 = 1,\ \sigma_4 = -0.97,\ \sigma_5 = 2,\ \sigma_6 = -1$, and $\omega = 1$. Fig. (5.3a) represents the 3D view of $|\psi_5(x,t)|$, showing a bright soliton solution. While figs. (5.3b) and (5.3c) present the 3D representations of the $Re(\psi_5(x,t))$ and $Im(\psi_5(x,t))$ components of the solution in Eq. (5.29), respectively. In fig. (5.3d), a 2D format of $|\psi_5(x,t)|$ is depicted, with black lines illustrating its appearance at various times $(t = 0, 1, 2)$. As seen in this graph, the bright soliton moves to the right as t grows. The wave representations depicted in red and blue signify the $Re(\psi_5(x,t))$ and $Im(\psi_5(x,t))$, respectively, illustrating the periodic soliton configurations at varying amplitudes. The characteristic feature of bright solitons is a central peak of maximum intensity. Optical communication systems rely on these solitons because of their distortion-free long-distance propagation, which allows for efficient high-speed data transmission. The stable propagation of bright solitons is highlighted in the 2D and 3D graphs, which highlight their importance in enabling high-performance optical communication networks and ensuring signal integrity [45].

Figure (8.4) exhibits the plotted results for the solution $\psi_6(x,t)$ as defined by Eq. (5.30) in 3D and 2D form, with values $\gamma = 0.98,\ h = 1,\ k = 1,\ \sigma_1 = 1,\ \sigma_2 = 0.95,\ \sigma_3 = 1,\ \theta_0 = 1,\ \sigma_4 = -0.97,\ \sigma_5 = 2,\ \sigma_6 = -1$, and $\omega = 1$. Fig. (5.4a) illustrates the 3D view of $|\psi_6(x,t)|$, depicting the singular soliton. The 3D graphics of real and imaginary components of the solution in Eq. (5.30) are depicted in figs. (5.4b) and (5.4c) respectively. Figure (5.4d) illustrates the 2D view of $|\psi_6(x,t)|$ with black lines illustrating its appearance at various times ($t = 0, 1, 2$). This graph depicts that the singular soliton shifts to the right as t rises. The wave representations drawn in red and blue signify the $Re(\psi_6(x,t))$ and $Im(\psi_6(x,t))$, respectively. Singular soliton structures, though less common in standard communication systems, suggest pathways for signal reshaping and novel amplification mechanisms. When investigating extreme wave phenomena, singular solitons are useful for developing realistic models due to their centered infinite amplitude [45]. More generally, soliton-driven signal enhancement is crucial in all-optical signal processing, fiber sensor networks, and emerging quantum communication technologies, where the preservation of signal stability and coherence is vital. The variety of solutions derived from this study enhances the practical significance of the concatenation model, demonstrating its potential applicability in numerous photonic applications.

5.7 Conclusion

In this study, we successfully developed a broad class of novel optical soliton solutions for the concatenation model. Utilizing the modified extended tanh method with the Riccati equation and the $(\frac{1}{\vartheta(\eta)}, \frac{\vartheta'(\eta)}{\vartheta(\eta)})$ method, we extracted numerous types of solutions, encompassing dark soliton, periodic wave soliton solutions, bright solitons, and singular soliton solutions. The parameter constraints guarantee the existence of the derived soliton solutions, while the graphical representations elucidate the physical attributes of these solutions. The results of this research possess considerable ramifications for the domain of optical meta-materials, potentially influencing the design and engineering of next-generation technology across multiple industries. Our results indicate that the proposed methodologies are exceptionally effective, offering robust solutions to various nonlinear partial differential equations. This enhances our comprehension of the fundamental physics and establishes a foundation for future improvements in the design and utilization of advanced optical meta-materials.

Bibliography

[1] Biswas, A., Ekici, M., Sonmezoglu, A., & Belic, M. R. (2019). Solitons in optical fiber Bragg gratings with dispersive reflectivity by extended trial function method. Optik, 182, 88–94..

[2] Chou, D., Rehman, H. U., Amer, A., & Osman, M. (2024). Optical soliton dynamics of the con-

formable nonlinear evolution equation in Bose–Einstein condensates. Rendiconti Lincei. Scienze Fisiche e Naturali, 35, 1–12.

[3] Aitchison, J. S., Weiner, A., Silberberg, Y., Oliver, M., Jackel, J., Leaird, D., Vogel, E., & Smith, P. (1990). Observation of spatial optical solitons in a nonlinear glass waveguide. Optics Letters, 15(9), 471–473.

[4] Mollenauer, L. F., Stolen, R. H., & Gordon, J. P. (1980). Experimental observation of picosecond pulse narrowing and solitons in optical fibers. Physical Review Letters, 45(13), 1095–1098.

[5] Salin, F., Grangier, P., Roger, G., & Brun, A. (1986). Observation of high-order solitons directly produced by a femtosecond ring laser. Physical Review Letters, 56(11), 1132–1135.

[6] Savaissou, N., Gambo, B., Rezazadeh, H., Bekir, A., & Doka, S. Y. (2020). Exact optical solitons to the perturbed nonlinear Schrödinger equation with dual-power law of nonlinearity. Optical and Quantum Electronics, 52, 1–16.

[7] Akinyemi, L., Rezazadeh, H., Shi, Q.-H., Inc, M., Khater, M. M., Ahmad, H., Jhangeer, A., & Akbar, M. A. (2021). New optical solitons of perturbed nonlinear Schrödinger–Hirota equation with spatio-temporal dispersion. Results in Physics, 29, 104656.

[8] El-Sheikh, M., Ahmed, H. M., Arnous, A. H., Rabie, W. B., Biswas, A., Alshomrani, A. S., Ekici, M., Zhou, Q., & Belic, M. R. (2019). Optical solitons in birefringent fibers with Lakshmanan–Porsezian–Daniel model by modified simple equation. Optik, 192, 162899.

[9] Kudryashov, N. A. (2020). Optical solitons of mathematical model with arbitrary refractive index. Optik, 224, 165391.

[10] Yildirim, Y. (2019). Sub pico-second pulses in mono-mode optical fibers with Triki–Biswas model using trial equation architecture. Optik, 183, 463–466.

[11] Yildirim, Y. (2019). Optical soliton molecules of Manakov model by trial equation technique. Optik, 185, 1146–1151.

[12] Chou, D., Amer, A., Rehman, H. U., & Li, M.-L. (2025). Unravelling quiescent optical solitons: An exploration of the complex Ginzburg–Landau equation with nonlinear chromatic dispersion and self-phase modulation. Nonlinear Engineering, 14(1), 20240043.

[13] Li, Z., & Huang, C. (2023). Bifurcation, phase portrait, chaotic pattern and optical soliton solutions of the conformable Fokas–Lenells model in optical fibers. Chaos, Solitons & Fractals, 169, 113237.

[14] Samir, I., Ahmed, H. M., Mirzazadeh, M., & Triki, H. (2023). Derivation of new solitons and other solutions for higher-order Sasa–Satsuma equation by using the improved modified extended tanh scheme. Optik, 274, 170592.

[15] Akinyemi, L. (2023). Shallow ocean soliton and localized waves in extended (2+1)-dimensional nonlinear evolution equations. Physics Letters A, 463, 128668.

[16] Rehman, H. U., Said, G. S., Amer, A., Ashraf, H., Tharwat, M., Abdel-Aty, M., Elazab, N. S., & Osman, M. (2024). Unravelling the (4+1)-dimensional Davey–Stewartson–Kadomtsev–Petviashvili equation: Exploring soliton solutions via multiple techniques. Alexandria Engineering Journal, 90, 1723–1735.

[17] Shang, Y. (2008). The extended hyperbolic function method and exact solutions of the long–short wave resonance equations. Chaos, Solitons & Fractals, 36(3), 762–771.

[18] Elwakil, S. A., El-Labany, S., Zahran, M., & Sabry, R. (2002). Modified extended tanh-function method for solving nonlinear partial differential equations. Physics Letters A, 299(2–3), 179–188.

[19] Wang, M., Li, X., & Zhang, J. (2008). The (G'/G)-expansion method and travelling wave solutions of nonlinear evolution equations in mathematical physics. Physics Letters A, 372(4), 417–423.

[20] He, J. (1997). Variational iteration method for delay differential equations. Communications in Nonlinear Science and Numerical Simulation, 2(4), 235–236.

[21] Vahidi, J., Zekavatmand, S. M., Rezazadeh, H., Inc, M., Akinlar, M. A., & Chu, Y.-M. (2021). New solitary wave solutions to the coupled Maccari system. Results in Physics, 21, 103801.

[22] Khater, M. M., Inc, M., Attia, R. A., Lu, D., & Almohsen, B. (2020). Abundant new computational wave solutions of the GM-DP-CH equation via two modified recent computational schemes. Journal of Taibah University for Science, 14(1), 1554–1562.

[23] Ablowitz, M. J., Kaup, D. J., Newell, A. C., & Segur, H. (1973). Method for solving the sine-Gordon equation. Physical Review Letters, 30(25), 1262–1264.

[24] Savaissou, N., Gambo, B., Rezazadeh, H., Bekir, A., & Doka, S. Y. (2020). Exact optical solitons to the perturbed nonlinear Schrödinger equation with dual-power law of nonlinearity. Optical and Quantum Electronics, 52, 1–16.

[25] Akbar, M. A., Ali, N. H. M., & Hussain, J. (2019). Optical soliton solutions to the (2+1)-dimensional Chaffee–Infante equation and the dimensionless form of the Zakharov equation. Advances in Difference Equations, 2019, 118.

[26] Chou, D., Rehman, H. U., Amer, A., & Amer, A. (2023). New solitary wave solutions of generalized fractional Tzitzeica-type evolution equations using Sardar sub-equation method. Optical and Quantum Electronics, 55(13), 1148.

[27] Az-Zobi, E. A., Alzoubi, W. A., Akinyemi, L., Senol, M., & Masaedeh, B. S. (2021). A variety of wave amplitudes for the conformable fractional (2+1)-dimensional Ito equation. Modern Physics Letters B, 35(15), 2150254.

[28] Houwe, A., Abbagari, S., Saliou, Y., Inc, M., Doka, S. Y., Bouetou, T. B., & Bayram, M. (2021). Attitude of the modulation instability gain in oppositely directed coupler with the effects of the intrapulse Raman scattering and saturable function. Results in Physics, 31, 104851.

[29] Biswas, A., Yildirim, Y., Yasar, E., Zhou, Q., Moshokoa, S. P., & Belic, M. R. (2018). Optical solitons for Lakshmanan–Porsezian–Daniel model by modified simple equation method. Optik, 160, 24–32.

[30] Yao, S.-W., Akinyemi, L., Mirzazadeh, M., Inc, M., Hosseini, K., & Senol, M. (2021). Dynamics of optical solitons in higher-order Sasa–Satsuma equation. Results in Physics, 30, 104825.

[31] Ankiewicz, A., & Akhmediev, N. (2014). Higher-order integrable evolution equation and its soliton solutions. Physics Letters A, 378(4), 358–361.

[32] Ankiewicz, A., Wang, Y., Wabnitz, S., & Akhmediev, N. (2014). Extended nonlinear Schrödinger equation with higher-order odd and even terms and its rogue wave solutions. Physical Review E, 89(1), 012907.

[33] Akram, U., Tang, Z., Althobaiti, S., & Althobaiti, A. (2024). Dynamics of optical dromions in concatenation model. Nonlinear Dynamics, 112(16), 14321–14341.

[34] Kudryashov, N. A., Biswas, A., Borodina, A. G., Yildirim, Y., & Alshehri, H. M. (2023). Painlevé analysis and optical solitons for a concatenated model. Optik, 272, 170255.

[35] Yildirim, Y., Biswas, A., Moraru, L., & Alghamdi, A. A. (2023). Quiescent optical solitons for the concatenation model with nonlinear chromatic dispersion. Mathematics, 11(7), 1709.

[36] Biswas, A., Vega-Guzman, J., Kara, A. H., Khan, S., Triki, H., Gonzalez-Gaxiola, O., Moraru, L., & Georgescu, P. L. (2022). Optical solitons and conservation laws for the concatenation model: Undetermined coefficients and multipliers approach. Universe, 9(1), 15.

[37] Wang, M.-Y., Biswas, A., Yildirim, Y., Moraru, L., Moldovanu, S., & Alshehri, H. M. (2022). Optical solitons for a concatenation model by trial equation approach. Electronics, 12(1), 19.

[38] Khan, M. A. U., Akram, G., & Sadaf, M. (2024). Dynamics of novel exact soliton solutions of concatenation model using effective techniques. Optical and Quantum Electronics, 56(3), 385.

[39] Zayed, E. M., Arnous, A. H., Biswas, A., Yildirim, Y., & Asiri, A. (2024). Optical solitons for the concatenation model with multiplicative white noise. Journal of Optics, 53(4), 3098–3107.

[40] Khan, M. A. U., Akram, G., & Sadaf, M. (2024). Dynamics of novel exact soliton solutions of concatenation model using effective techniques. Optical and Quantum Electronics, 56(3), 385.

[41] Amer, A., Boulaaras, S. M., Althobaiti, A., Althobaiti, S., & Rehman, H. U. (2025). Unveiling soliton dynamics: Innovative methods and numerical insights for the Shynaray-IIA equation. International Journal of Modern Physics B, 39(25), 2550203.

[42] Bashan, A. (2023). Solitary wave, undular-bore and wave-maker solutions of the cubic, quartic and quintic nonlinear generalized equal width (GEW) wave equation. The European Physical Journal Plus, 138(1), 53.

[43] Ge, Y., Luo, J., Li, L., Jin, X., Tang, D., Shen, D., Zhang, S., & Zhao, L. (2014). Initial conditions for dark soliton generation in normal-dispersion fiber lasers. Applied Optics, 54(1), 71–75.

[44] Ma, C., Gao, B., Wu, G., Zhang, T., & Tian, X. (2016). Observation of dissipative bright soliton and dark soliton in an all-normal dispersion fiber laser. International Journal of Optics, 2016, 3946525.

[45] Kamel, N. M., Ahmed, H. M., & Rabie, W. B. (2025). Solitons unveilings and modulation instability analysis for sixth-order coupled nonlinear Schrödinger equations in fiber Bragg gratings. AIMS Mathematics, 10(3), 6952–6980.

CHAPTER 6

Solitary Wave Solutions of Nonlinear Kudryashov-Sinelshchikov Equation Through a New Generalized Analytical Method

Mujahid Iqbal[†*], and Muhammad Ashraf[‡]

[†] *College of Information Science and Technology, Dalian Maritime University, Dalian 116026, Liaoning, PR China.*

[‡] *Department of Mathematics, National College of Business Administration & Economics Lahore, Sub–Campus Multan 66000, Pakistan.*

Corresponding Author: Mujahid Iqbal: mujahidiqbal399@gmail.com

Abstract: *The nonlinear Kudryashov–Sinelshchikov equation is investigated using the auxiliary equation method. This equation plays a significant role in studying pressure wave processes in mixtures of liquid and gas bubbles, while accounting for heat conduction and viscosity. In this work, we derive exact analytical wave solutions that exhibit diverse physical structures, including solitons and several types of solitary waves such as kink waves, peakon bright solitons, peakon dark solitons, singular solitons, periodic solitons, anti-kink waves, mixed solitons, and other solitary wave structures. These solutions enhance our understanding of wave propagation in nonlinear media and contribute to the broader class of exact solutions for nonlinear evolution equations (NLEEs). The physical properties of the obtained solutions are demonstrated graphically through contour plots, as well as two– and three–dimensional visualizations, all supported by computational simulations. The soliton structures identified in this study are expected to play an important role across various domains of science and engineering, including nonlinear dynamics, nonlinear optics, mathematical physics, and optical fiber research. Overall, the presented research highlights that the proposed method is efficient, precise, and powerful, making it a valuable tool for studying a wide range of nonlinear evolution equations.*

Keywords: Nonlinear Kudryashov–Sinelshchikov equation, Auxiliary equation method, Solitary wave structure, Analytical solutions, Solitons.

6.1 Introduction

Nonlinear evolution equations (NLEEs) are crucial for understanding the dynamics of physical sciences and are widely applied in disciplines such as neural networks, solid-state physics, fiber optics, economics, communication systems, and nonlinear mechanics to study complex phenomena over time [1, 2, 3, 4, 5, 6]. The discovery of soliton solutions for previously studied phenomena has been both fascinating and significant. Expanding soliton results for a broad range of NLEEs remains an important area of research.

The study of solitons in nonlinear dynamical equations is a vital topic in fluid dynamics and nonlinear science. Solitons are stable, self-reinforcing wave-like solutions that appear in various physical systems, such as liquid–gas bubble mixtures. They provide unique insights into system dynamics and have practical applications in oceanography, fluid mechanics, and materials science, with engineering implications for water wave control and heat exchanger optimization [7, 8, 9, 10, 11].

Several analytical methods have been proposed for solving nonlinear problems, including the Sardar subequation method [12], first integral scheme [13], the Φ^6-expansion scheme [14], Jacobian elliptic method [15], extended hyperbolic function scheme [16], extended simple equation technique [17, 18], Bäcklund transformation [19], $\exp(-\Psi(\eta))-$expansion approach [20], improved extended fan sub equation technique [21], modified Sardar sub equation method [22], extended auxiliary equation mapping scheme [23, 24, 25], Laplace transformation method [26], modified tanh function approach [27], new mapping approach [28], extended modified rational expansion technique [29, 30, 31, 32], extended direct algebraic equation mapping approach [33, 34], the $(G^{'}/G)$-expansion approach [35], modified auxiliary equation approach [36, 37], among many others.

Most physical models admit a variety of solitary wave structures. The analysis of dynamical solutions to NLEEs demonstrates their importance in mathematical physics. In 2010, Kudryashov and Sinelshchikov derived a more general NLEE to describe pressure waves in a liquid–gas mixture, taking into account heat transfer and liquid viscosity [38, 39]. The Kudryashov–Sinelshchikov equation (KS equation) is therefore an important framework for modeling soliton behavior in such systems, as it incorporates fluid interactions, heat transfer, and viscosity factors essential for a realistic description of soliton dynamics.

This research aims to construct and analyze novel soliton structures governed by the nonlinear Kudryashov–Sinelshchikov (NLKS) equation for liquid–gas mixtures. Using both analytical techniques and numerical simulations, we visualize and characterize the obtained solutions. The NLKS equation is given by

$$u_t + \alpha_1 u u_x + u_{xxx} - \alpha_2 (u u_{xx}) x - \alpha 3 u_x u_{xx} - \alpha_4 u_{xx} - \alpha_5 (u u_x) x = 0, \tag{6.1}$$

where $u(x,t)$ denotes the physical quantities related to heat transfer, density, and viscosity, and $\alpha 1, \alpha_2, \alpha_3, \alpha_4, \alpha_5$ are real constants. Special cases of Eq. (15.8) reduce to well-known equations. For instance:
If $\alpha_2 = \alpha_3 = \alpha_4 = \alpha_5 = 0$, Eq. (15.8) reduces to the KdV equation [40]:

$$u_t + \alpha_1 u u_x + u_{xxx} = 0. \tag{6.2}$$

If $\alpha_2 = \alpha_3 = \alpha_5 = 0$, Eq. (15.8) becomes the Korteweg de Vries–Burgers (KdVB) equation:

$$u_t + \alpha_1 u u_x + u_{xxx} - \alpha_4 u_{xx} = 0. \tag{6.3}$$

If $\alpha_1 = \alpha_2 = 1$ and $\alpha_4 = \alpha_5 = 0$, Eq. (15.8) takes the form:

$$u_t + u_{xxx} + u u_x - (u u_{xx})\, x - \alpha 4 u u_{xx} = 0. \tag{6.4}$$

Ryabov et al. examined solitary wave solutions of Eq. (15.17) using a modified truncated expansion technique under specific parameter conditions $\alpha = -3, \alpha = -4$ [41]. Many researchers have since explored various solution methods for the NLKS equation under different parameter settings. For example, Randruut et al. derived phase curves, solitary, and periodic wave solutions; He et al. obtained smooth and non-smooth solitary and periodic waves using the bifurcation method [42]; Yang et al. applied Lie symmetry analysis to secure exact solutions for the three–dimensional NLKS equation [43]; Zhao et al. employed the F–expansion technique [44]; Ryabov et al. used truncated expansion methods [45]; Gupta et al. developed fractional NLKS solutions via the radial basis function (RBF) method [46]; Hubert et al. applied the $(G^{'}/G)-$expansion scheme [47]; Seadawy et al. used the modified auxiliary equation method [48]; Kudryashov et al. derived solitary waves through the extended simple equation approach [49]; Kumar et al. employed the generalized exponential rational function approach[50]; Bruzon et al. explored exact and symmetric solutions via Lie group methods [51]; Ray et al. applied the improved sub-equation method [52]. These studies have revealed diverse solitary wave solutions with different physical structures, including kink wave solitons, mixed bright and dark solitons, peakon bright solitons, periodic solitons, anti-kink wave solitons, peakon dark solitons, and other solitary wave solutions. To the best of our knowledge, such a variety of results for the NLKS equation has not been systematically reported before.
This chapter is organized as follows: Section 1 provides the introduction and literature review of the proposed equation. Section 2 describes the methodology. Section 3 presents the soliton solutions of the NLKS equation. Section 4 compares the constructed results. Finally, Section 5 concludes the study.

6.2 Auxiliary equation method

The proposed approach is one of the powerful and efficient methods for obtaining exact soliton solutions to nonlinear partial differential equations (NLPDEs). It has been successfully applied

to investigate various types of solutions to NLPDEs, including the nonlinear third-order Klein–Fock–Gordon equation[53], the nonlinear Schrödinger equation[54], and nonlinear ionic current microtubule and Mikhailov–Novikov–Wang dynamical equations[55]. Previous studies have also demonstrated important considerations about this method and noted that it can be regarded as a specific form of the simple equation method.

The general form of nonlinear partial differential equations is given as

$$\nabla\left(u_t,\ uu_x,\ u_{xxx},\ u_xu_{xx},...\right)=0. \tag{6.5}$$

Where ∇ called polynomial function of u and its partial derivatives.

Step 1.

Let us wave transform given as

$$u(x,t)=W(\vartheta),\qquad \vartheta=x-\mu t. \tag{6.6}$$

Inserting Eq.(15.19) in Eq.(15.18), the nonlinear equation with ordinary derivatives obtained as

$$\eth(-\mu W^{'},\ WW^{'},\ W^{'''},\ W^{'}W^{''},...)=0. \tag{6.7}$$

Step 2.

The generalized solution of Eq.(8.7) mentioned as

$$W\left(\vartheta\right)=\sum_{i=0}^{\aleph}b_i\phi^i(\vartheta). \tag{6.8}$$

The value of $\phi(\vartheta)$ verify the following auxiliary equation.

$$\left(\phi^{'}(\vartheta)\right)^2=\varpi_1\phi^2(\vartheta)+\varpi_2\phi^3(\vartheta)+\varpi_3\phi^4\left(\vartheta\right). \tag{6.9}$$

Here $\varpi_1,\ \varpi_2$, and ϖ_3, are real constants. Exact solutions to the Eq.(8.9) are mentioned as

Case – I

$$\phi\left(\vartheta\right)=-\frac{\varpi_1\varpi_2\mathrm{sech}\left(\frac{\sqrt{\varpi_1}\vartheta}{2}\right)^2}{\varpi_2^2-\varpi_1\varpi_3\left(1-\tanh\left(\frac{\sqrt{\varpi_1}\vartheta}{2}\right)\right)^2},\quad \text{when}\quad \varpi_1>0.$$

Case – II

$$\phi\left(\vartheta\right)=\frac{2\varpi_1\mathrm{sech}(\sqrt{\varpi_1}\vartheta)}{\sqrt{\varpi_2^2-4\varpi_1\varpi_3}-\varpi_2-\mathrm{sech}(\sqrt{\varpi_1}\vartheta)}\quad \text{when } \varpi_2^2-4\varpi_1\varpi_3>0,\quad \varpi_1>0.$$

Step 3.

Utilizing the homogeneous balance scheme on Eq.(8.7) to secure the positive integer$\aleph$.

Step 4.

Setting Eq.(8.8) in Eq.(8.9) and collect every factors to the $\phi(\vartheta)$, and make them equal to zero. We

secured the algebraic equations and solving them utilizing the any computational simulation to secure the unknown values of parameters. Setting the secured values with $\phi(\vartheta)$ in Eq.(8.9) then we extract the essential solutions for Eq.(15.18).

6.3 Solitary wave solutions of NLKS equation

In this section, we examine the solitary wave solutions for the NLKS equation through auxiliary equation method. The NLKS equation given as

$$u_t + \alpha_1 u u_x + u_{xxx} - \alpha_2 (u u_{xx})_x - \alpha_3 u_x u_{xx} - \alpha_4 u_{xx} - \alpha_5 (u u_x)_x = 0. \tag{6.10}$$

Wave transformation taken as

$$u(x,t) = W(\vartheta), \qquad \vartheta = x - \mu t. \tag{6.11}$$

Inserting Eq.(8.11) into Eq.(8.10) and integrate the resulting equation with respect to ϑ, finally we obtained the nonlinear ODE of Eq.(8.10) as

$$-\mu W + \frac{\alpha_1}{2} W^2 + W^{''} - \alpha_2 W W^{''} - \frac{\alpha_3}{2} (W^{'})^2 - \alpha_4 W^{'} - \alpha_5 W W^{'} = 0. \tag{6.12}$$

By using the homogeneous balance approach on Eq.(10.12), secured $\aleph = 2$. The general solution to the Eq.(10.12) consider as

$$W(\vartheta) = b_0 + b_1 \phi(\vartheta) + b_2 \phi^2(\vartheta). \tag{6.13}$$

Setting Eq.(10.13) into Eq.(10.12), and collect each factor of $\phi(\vartheta)$ and make them equal to zero. We secured the algebraic equations and solving them utilizing the computational simulation mathematica and secured these values of parameters as

Family–I

$$\begin{aligned} \mu =& \varpi_1, \quad b_0 = 0, \quad b_1 = b_1, \quad b_2 = b_2, \quad \alpha_1 = \frac{1}{2}\varpi_1 \left(-\alpha_2 - \frac{20 b_2}{b_1^2} \right), \\ \alpha_3 =& -\frac{1}{2}(5\alpha_2), \quad \varpi_2 = \frac{2 b_2 \varpi_1}{b_1}, \quad \varpi_3 = \frac{b_2^2 \varpi_1}{b_1^2}. \end{aligned} \tag{6.14}$$

We secured the exact solutions to the Eq.(8.10) in solitons form by inserting the Eq.(8.14) into Eq.(10.13).

$$u_1(x,t)=\left(\operatorname{sech}^4\left(\frac{1}{2}\sqrt{\varpi_1}(x-\mu t)\right)\right)\varpi_1\varpi_2\left(2b_2\varpi_1\varpi_2-\ b_1\left(\varpi_2^2\left(\cosh\left(\sqrt{\varpi_1}(x-\mu t)\right)+1\right)\right.\right.$$
$$\left.+2\varpi_1\varpi_3\left(\sinh\left(\sqrt{\varpi_1}(x-\mu t)\right)-\cosh\left(\sqrt{\varpi_1}(x-\mu t)\right)\right)\right)\Big)\Big/$$
$$2\left(\varpi_2^2-\varpi_1\varpi_3\left(\tanh\left(\frac{1}{2}\sqrt{\varpi_1}(x-\mu t)\right)-1\right)^2\right)^2, \tag{6.15}$$

$$u_2(x,t)=2\operatorname{sech}\left(\sqrt{\varpi_1}(x-\mu t)\right)\varpi_1\left(2b_2\varpi_1\operatorname{sech}\left(\sqrt{\varpi_1}(x-\mu t)\right)+\right.$$
$$\left.+b_1\left(-\varpi_2+\sqrt{\varpi_2^2-4\varpi_1\varpi_3}-\operatorname{sech}\left(\sqrt{\varpi_1}(x-\mu t)\right)\right)\right)\Big/$$
$$\left(\varpi_2-\sqrt{\varpi_2^2-4\varpi_1\varpi_3}+\operatorname{sech}\left(\sqrt{\varpi_1}(x-\mu t)\right)\right)^2. \tag{6.16}$$

Family–II

$$b_0=\frac{5\alpha_2b_1^2-\sqrt{5}\sqrt{5\alpha_2^2b_1^4-24\alpha_2b_2b_1^2+80b_2^2}+20b_2}{40\alpha_2b_2},\quad b_1=b_1,\quad b_2=b_2,$$
$$\alpha_1=-\frac{\varpi_1\left(-3\alpha_2b_1^2+\sqrt{5}\sqrt{5\alpha_2^2b_1^4-24\alpha_2b_2b_1^2+80b_2^2}+20b_2\right)}{4b_1^2},\quad \alpha_3=-\frac{1}{2}\left(5\alpha_2\right),$$
$$\mu=-\frac{\varpi_1\left(-5\alpha_2b_1^2+\sqrt{5}\sqrt{5\alpha_2^2b_1^4-24\alpha_2b_2b_1^2+80b_2^2}+20b_2\right)}{40b_2},\quad \varpi_2=\frac{2b_2\varpi_1}{b_1},\quad \varpi_3=\frac{b_2^2\varpi_1}{b_1^2}. \tag{6.17}$$

We secured the exact solutions to the Eq.(10.16) in solitary waves form by inserting the Eq.(8.14) into Eq.(10.13).

$$u_3(x,t)=\frac{b_1^2}{8b_2}+\frac{\frac{1}{2}-\frac{\sqrt{\alpha_2^2b_1^4-\frac{24}{5}\alpha_2b_2b_1^2+16b_2^2}}{8b_2}}{\alpha_2}+\frac{b_2\varpi_1^2\varpi_2^2\operatorname{sech}^4\left(\frac{1}{2}\sqrt{\varpi_1}(x-\mu t)\right)}{\left(\varpi_2^2-\varpi_1\varpi_3\left(\tanh\left(\frac{1}{2}\sqrt{\varpi_1}(x-\mu t)\right)-1\right)^2\right)^2}$$
$$+\frac{b_1\varpi_1\varpi_2\operatorname{sech}^2\left(\frac{1}{2}\sqrt{\varpi_1}(x-\mu t)\right)}{\varpi_1\varpi_3\left(\tanh\left(\frac{1}{2}\sqrt{\varpi_1}(x-\mu t)\right)-1\right)^2-\varpi_2^2}, \tag{6.18}$$

$$u_4(x,t)=\frac{b_1^2}{8b_2}+\frac{\frac{1}{2}-\frac{\sqrt{\alpha_2^2b_1^4-\frac{24}{5}\alpha_2b_2b_1^2+16b_2^2}}{8b_2}}{\alpha_2}+\frac{4b_2\varpi_1^2\operatorname{sech}^2\left(\sqrt{\varpi_1}(x-\mu t)\right)}{\left(\varpi_2-\sqrt{\varpi_2^2-4\varpi_1\varpi_3}+\operatorname{sech}\left(\sqrt{\varpi_1}(x-\mu t)\right)\right)^2}$$
$$-\frac{2b_1\varpi_1\operatorname{sech}\left(\sqrt{\varpi_1}(x-\mu t)\right)}{\varpi_2-\sqrt{\varpi_2^2-4\varpi_1\varpi_3}+\operatorname{sech}\left(\sqrt{\varpi_1}(x-\mu t)\right)}. \tag{6.19}$$

Family–III

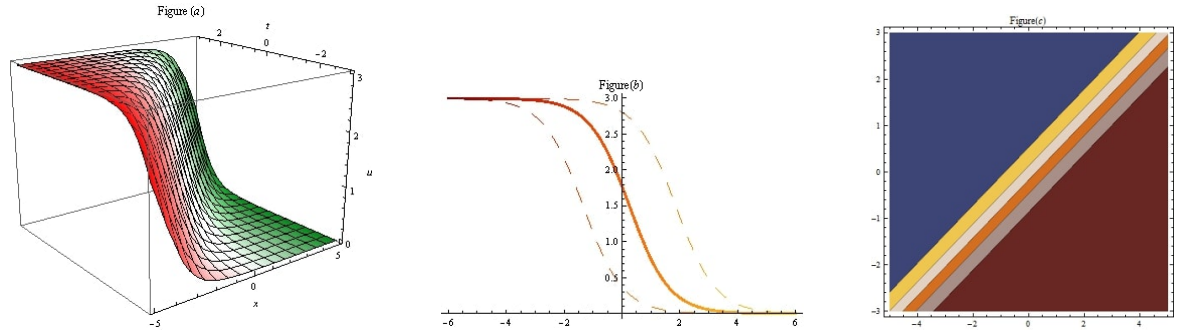

Figure 6.1: Graphical analysis to the $u_1(x,t)$ representing to kink wave soliton by three–dim, two–dim, and contour plotting with $\varpi_1 = 2,\ \varpi_2 = 4,\ \varpi_3 = 2,\ \mu = 1.6,\ b_1 = -2,\ b_2 = 1$

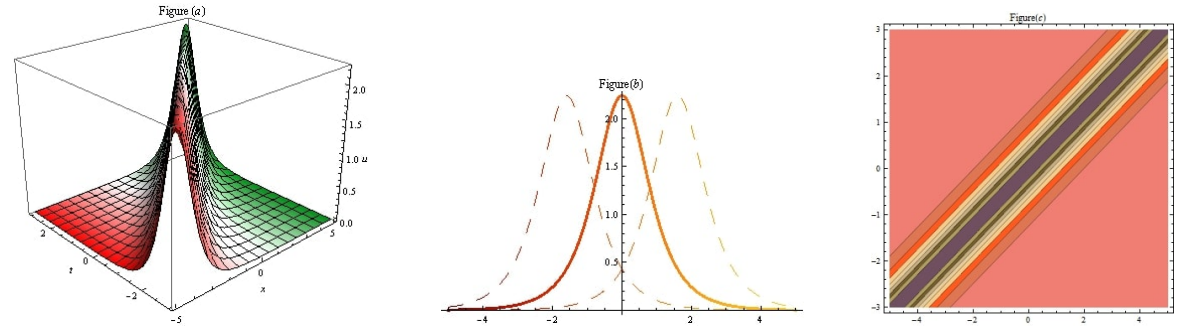

Figure 6.2: Graphical analysis to the $u_2(x,t)$ representing to peakon bright soliton by three–dim, two–dim, and contour plotting with $\varpi_1 = 2,\ \varpi_2 = 4,\ \varpi_3 = 2,\ \mu = 1.6,\ b_1 = -2,\ b_2 = 1$

$$\mu = \frac{3}{2}\left(-\frac{3\alpha_2}{\alpha_3} - 2\right)\varpi_1, \quad b_0 = -\frac{3}{2\alpha_3}, \quad b_1 = 0, \quad b_2 = b_2, \quad \alpha_1 = 2\left(3\alpha_2 + 2\alpha_3\right)\varpi_1. \tag{6.20}$$

We secured the exact solutions to the Eq.(8.10) in solitary waves form by inserting the Eq.(8.20) into Eq.(10.13).

$$u_5(x,t) = \frac{b_2\varpi_1^2\varpi_2^2\mathrm{sech}^4\left(\frac{1}{2}\sqrt{\varpi_1}(x-\mu t)\right)}{\left(\varpi_2^2 - \varpi_1\varpi_3\left(\tanh\left(\frac{1}{2}\sqrt{\varpi_1}(x-\mu t)\right) - 1\right)^2\right)^2} - \frac{3}{2\alpha_3}, \tag{6.21}$$

$$u_6(x,t) = \frac{4b_2\varpi_1^2\mathrm{sech}^2\left(\sqrt{\varpi_1}(x-\mu t)\right)}{\left(\varpi_2 - \sqrt{\varpi_2^2 - 4\varpi_1\varpi_3} + \mathrm{sech}\left(\sqrt{\varpi_1}(x-\mu t)\right)\right)^2} - \frac{3}{2\alpha_3}. \tag{6.22}$$

Family–IV

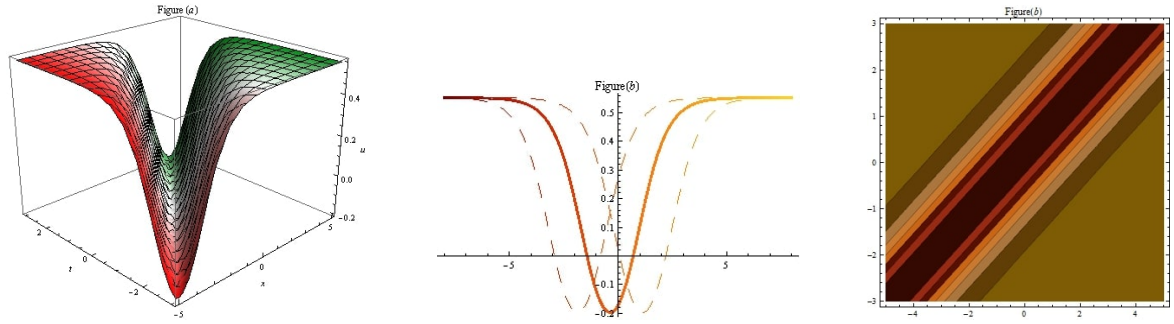

Figure 6.3: Graphical analysis to the $u_3(x,t)$ representing to peakon dark soliton by three–dim, two–dim, and contour plotting with $\varpi_1 = 2,\ \varpi_2 = 5,\ \varpi_3 = 2,\ \mu = 1.5,\ b_1 = 2,\ b_2 = 1,\ \alpha_2 = 1$

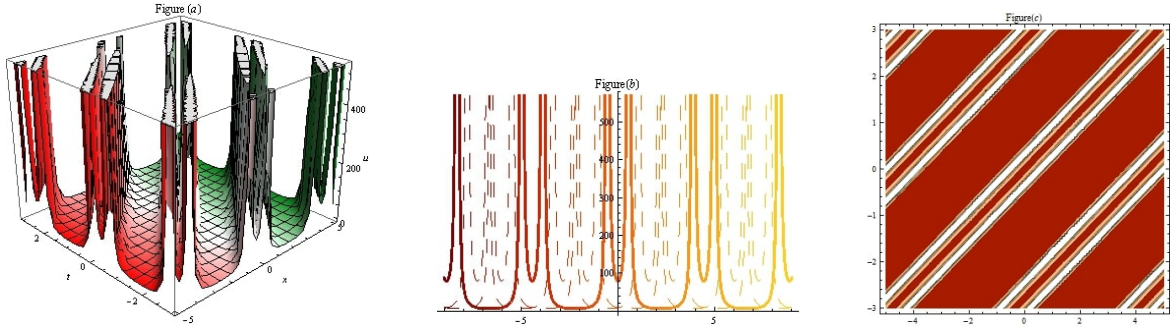

Figure 6.4: Graphical analysis to the $u_4(x,t)$ representing to periodic soliton by three–dim, two–dim, and contour plotting with $\varpi_1 = -2,\ \varpi_2 = 5,\ \varpi_3 = 2,\ \mu = 1.6,\ b_1 = 2,\ b_2 = 1,\ \alpha_2 = 1$

$$\begin{aligned}\mu =&\varpi_1\left(\alpha_2 b_0 - 1\right),\quad b_0 = b_0,\quad b_1 = b_1,\quad b_2 = 0,\quad \alpha_1 = \frac{2\varpi_1\left(\alpha_2 b_0 - 1\right)}{b_0},\\ \alpha_3 =& -4\alpha_2,\quad \varpi_2 = \frac{2b_1\varpi_1\left(2\alpha_2 b_0 - 1\right)}{3b_0\left(\alpha_2 b_0 - 1\right)}.\end{aligned} \tag{6.23}$$

We secured the exact solutions to the Eq.(8.10) in solitary waves form by inserting the Eq.(8.23) into Eq.(10.13).

$$u_7(x,t) = \frac{b_1\varpi_1\varpi_2 \mathrm{sech}^2\left(\frac{1}{2}\sqrt{\varpi_1}(x-\mu t)\right)}{\varpi_1\varpi_3\left(\tanh\left(\frac{1}{2}\sqrt{\varpi_1}(x-\mu t)\right)-1\right)^2 - \varpi_2^2} + b_0, \tag{6.24}$$

$$u_8(x,t) = b_0 - \frac{2b_1\varpi_1 \mathrm{sech}\left(\sqrt{\varpi_1}(x-\mu t)\right)}{\varpi_2 - \sqrt{\varpi_2^2 - 4\varpi_1\varpi_3} + \mathrm{sech}\left(\sqrt{\varpi_1}(x-\mu t)\right)}. \tag{6.25}$$

Family–V

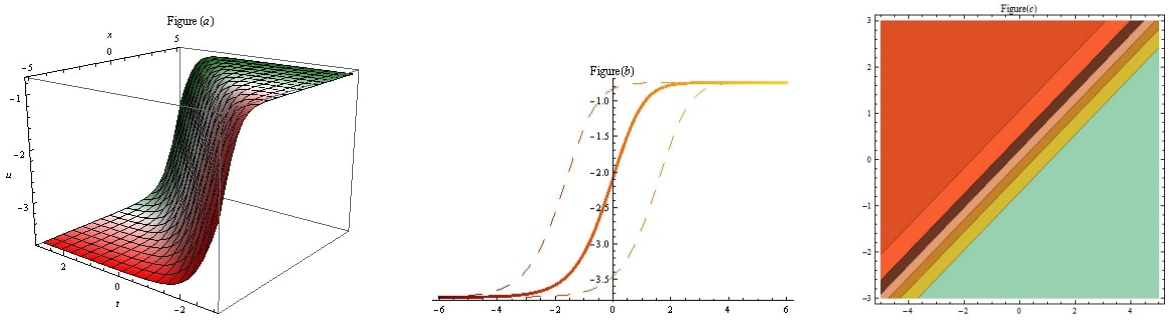

Figure 6.5: Graphical analysis to the $u_5(x,t)$ representing to anti–kink wave soliton by three–dim, two–dim, and contour plotting with $\varpi_1 = 2,\ \varpi_2 = 4,\ \varpi_3 = 2,\ \mu = 1.6,\ b_2 = -3,\ \alpha_3 = 2$

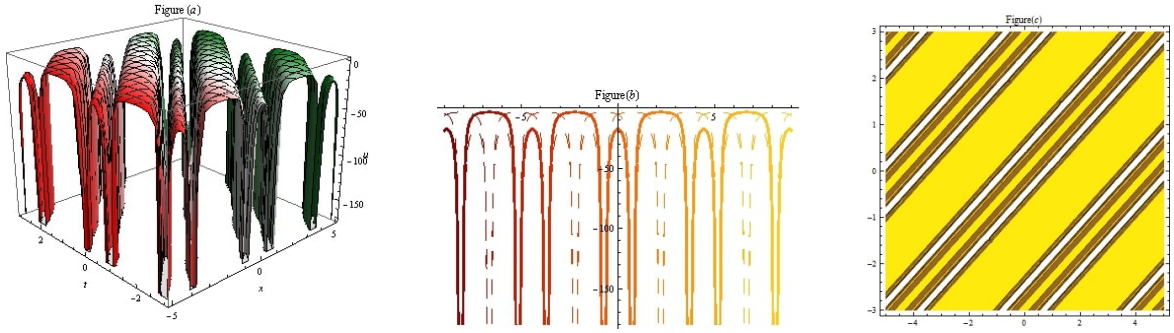

Figure 6.6: Graphical analysis to the $u_6(x,t)$ representing to periodic soliton by three–dim, two–dim, and contour plotting with $\varpi_1 = -2,\ \varpi_2 = 3,\ \varpi_3 = 2,\ \mu = 1.5,\ b_2 = 1,\ \alpha_3 = 1$

$$\begin{aligned} b_0 =& 0, \quad b_1 = b_1, \quad b_2 = b_2, \quad \alpha_1 = -\frac{10 b_2 \varpi_1}{b_1^2}, \\ \varpi_2 =& \frac{2 b_2 \varpi_1}{b_1}, \quad \varpi_3 = \frac{b_2^2 \varpi_1}{b_1^2}, \quad \mu = \varpi_1. \end{aligned} \tag{6.26}$$

We secured the exact solutions to the Eq.(8.10) in solitary waves form by inserting the Eq.(10.33) into Eq.(10.13).

$$\begin{aligned} u_9(x,t) = & \left(\operatorname{sech}^4\left(\frac{1}{2}\sqrt{\varpi_1}(x-\mu t)\right)\right) \varpi_1 \varpi_2 \left(2 b_2 \varpi_1 \varpi_2 - \ b_1 \left(\varpi_2^2 \left(\cosh\left(\sqrt{\varpi_1}(x-\mu t)\right)\right) + 1\right) + \right. \\ & \left. 2 \varpi_1 \varpi_3 \left(\sinh\left(\sqrt{\varpi_1}(x-\mu t)\right) - \cosh\left(\sqrt{\varpi_1}(x-\mu t)\right)\right)\right)\Big)\Big/ \\ & 2\left(\varpi_2^2 - \varpi_1 \varpi_3 \left(\tanh\left(\frac{1}{2}\sqrt{\varpi_1}(x-\mu t)\right) - 1\right)^2\right)^2, \end{aligned} \tag{6.27}$$

$$u_{10}(x,t) = 2\operatorname{sech}\left(\sqrt{\varpi_1}(x-\mu t)\right) \varpi_1 \left(2 b_2 \varpi_1 \operatorname{sech}\left(\sqrt{\varpi_1}(x-\mu t)\right) + \right.$$

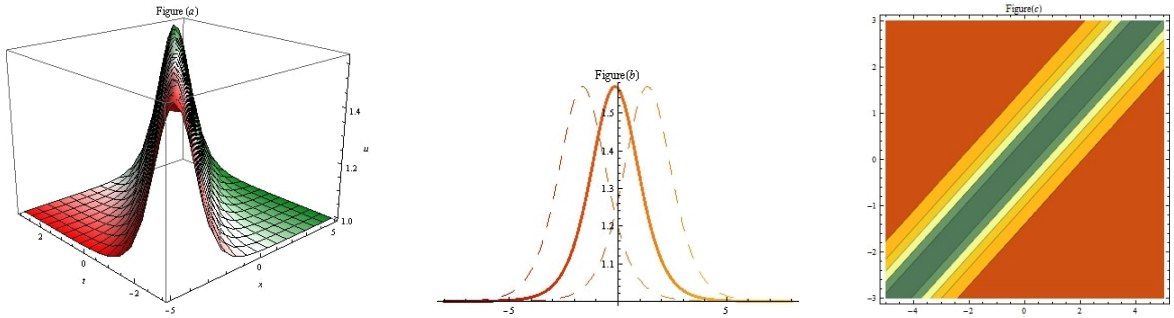

Figure 6.7: Graphical analysis to the $u_7(x,t)$ representing to bright soliton by three–dim, two–dim, and contour plotting with $\varpi_1 = 2,\ \varpi_2 = -5,\ \varpi_3 = 1,\ \mu = 1.5,\ b_0 = 1,\ b_1 = 1.3$

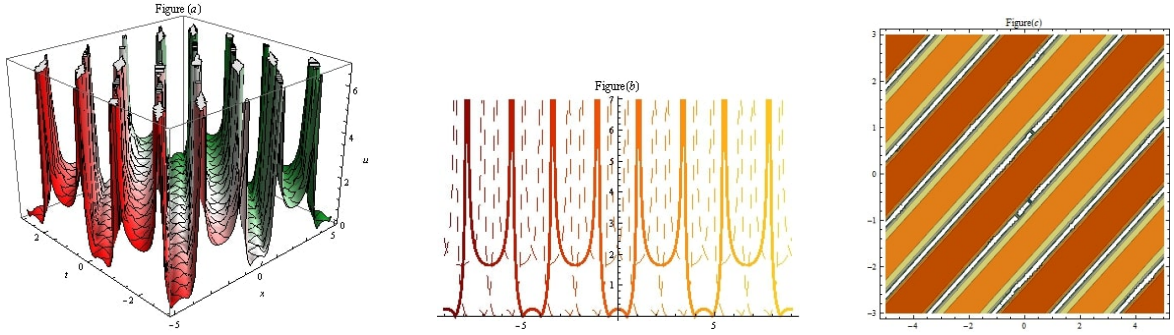

Figure 6.8: Graphical analysis to the $u_8(x,t)$ representing to periodic soliton by three–dim, two–dim, and contour plotting with $\varpi_1 = -2,\ \varpi_2 = -5,\ \varpi_3 = 2,\ \mu = 1.5,\ b_0 = 1,\ b_1 = 2$

$$b_1\left(-\varpi_2 + \sqrt{\varpi_2^2 - 4\varpi_1\varpi_3} - \operatorname{sech}\left(\sqrt{\varpi_1}(x-\mu t)\right)\right)\Big/ \left(\varpi_2 - \sqrt{\varpi_2^2 - 4\varpi_1\varpi_3} + \operatorname{sech}\left(\sqrt{\varpi_1}(x-\mu t)\right)\right)^2. \tag{6.28}$$

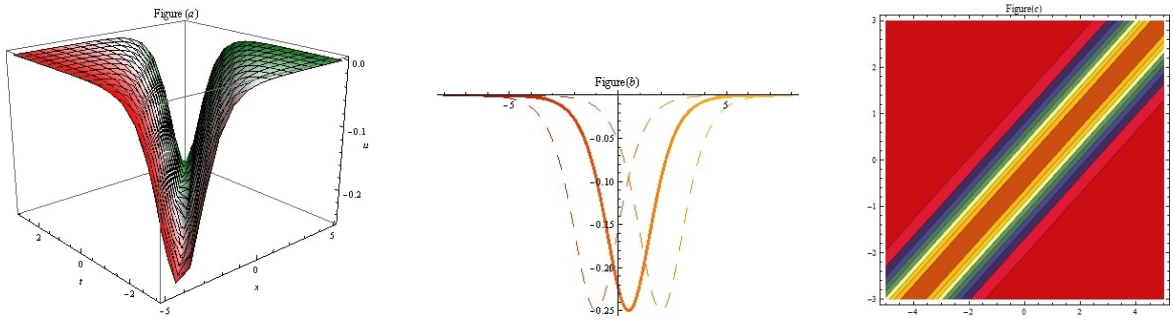

Figure 6.9: Graphical analysis to the $u_9(x,t)$ representing to dark soliton by three–dim, two–dim, and contour plotting with $\varpi_1 = 2,\ \varpi_2 = 4,\ \varpi_3 = 2,\ \mu = 1.5,\ b_1 = 1,\ b_2 = 1$

Family–VI

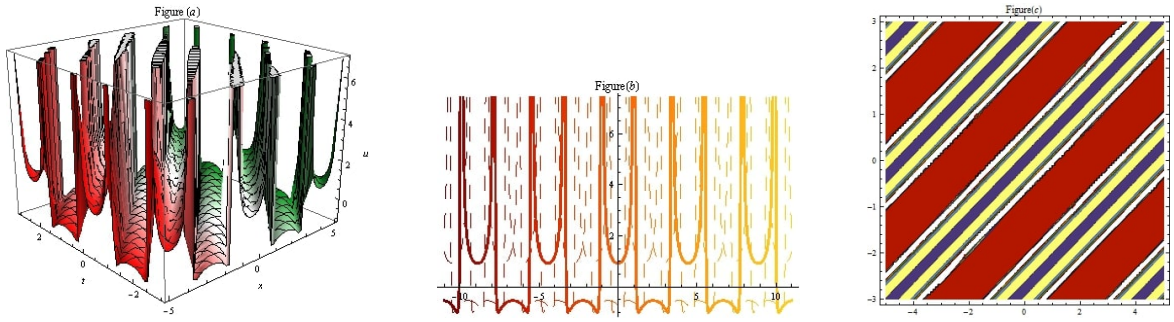

Figure 6.10: Graphical analysis to the $u_9(x,t)$ representing to periodic soliton by three–dim, two–dim, and contour plotting with $\varpi_1 = -2,\ \varpi_2 = -5,\ \varpi_3 = 2,\ \mu = 1.6,\ b_1 = -2,\ b_2 = 1$

$$\begin{aligned} \mu =& \varpi_1, \quad b_0 = 0, b_1 = b_1, \quad b_2 = b_2, \quad \alpha_1 = -\frac{8b_2\ \varpi_1}{b_1^2}, \\ \alpha_2 =& -\frac{4b_2}{b_1^2}, \quad \alpha_3 = \frac{4b_2}{b_1^2}. \end{aligned} \tag{6.29}$$

We secured the exact solutions to the Eq.(8.10) in solitary waves form by inserting the Eq.(10.36) into Eq.(10.13).

$$\begin{aligned} u_{11}(x,t) =& \left(\operatorname{sech}^4\left(\frac{1}{2}\sqrt{\varpi_1}(x-\mu t)\right)\varpi_1\varpi_2\left(2b_2\varpi_1\varpi_2 - b_1\left(\varpi_2^2\left(\cosh\left(\sqrt{\varpi_1}(x-\mu t)\right)+1\right)+\right.\right.\right. \\ & \left.\left.\left.2\varpi_1\varpi_3\left(\sinh\left(\sqrt{\varpi_1}(x-\mu t)\right)-\cosh\left(\sqrt{\varpi_1}(x-\mu t)\right)\right)\right)\right)\Big/ \\ & 2\left(\varpi_2^2 - \varpi_1\varpi_3\left(\tanh\left(\frac{1}{2}\sqrt{\varpi_1}(x-\mu t)\right)-1\right)^2\right)^2, \end{aligned} \tag{6.30}$$

$$\begin{aligned} u_{12}(x,t) =& 2\operatorname{sech}\left(\sqrt{\varpi_1}(x-\mu t)\right)\varpi_1\left(2b_2\varpi_1\operatorname{sech}\left(\sqrt{\varpi_1}(x-\mu t)\right)+\right. \\ & \left. b_1\left(-\varpi_2+\sqrt{\varpi_2^2-4\varpi_1\varpi_3}-\operatorname{sech}\left(\sqrt{\varpi_1}(x-\mu t)\right)\right)\right)\Big/ \\ & \left(\varpi_2-\sqrt{\varpi_2^2-4\varpi_1\varpi_3}+\operatorname{sech}\left(\sqrt{\varpi_1}(x-\mu t)\right)\right)^2. \end{aligned} \tag{6.31}$$

6.4 Results and discussion

In previous studies, researchers have obtained different types of solutions to the NLKS equation in trigonometric, rational, and elliptic functional forms. These include dark and bright solitons, kink and anti-kink solitons, singular solitons, and exact traveling waves, derived using methods such as the bifurcation method [42], Lie symmetry analysis [43], F–expansion method [44], truncated expansion technique

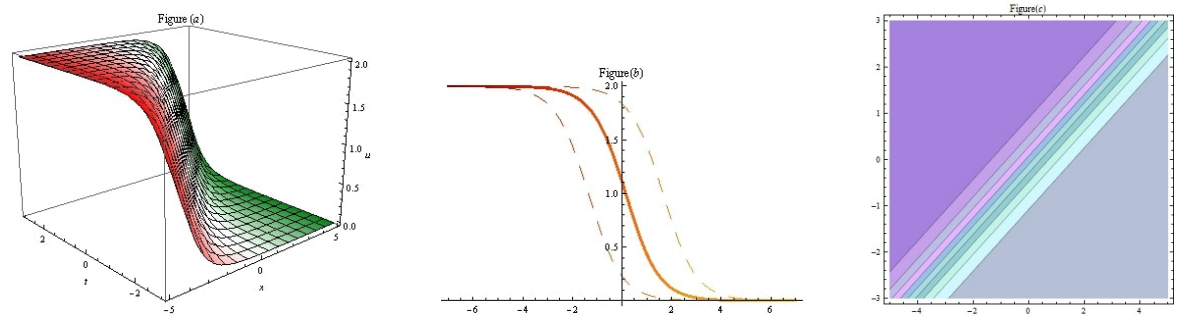

Figure 6.11: Graphical analysis to the $u_{11}(x,t)$ representing to kink wave soliton by three–dim, two–dim, and contour plotting with $\varpi_1 = 2,\ \varpi_2 = -4,\ \varpi_3 = 2,\ \mu = 1.5,\ b_1 = 1,\ b_2 = 1$

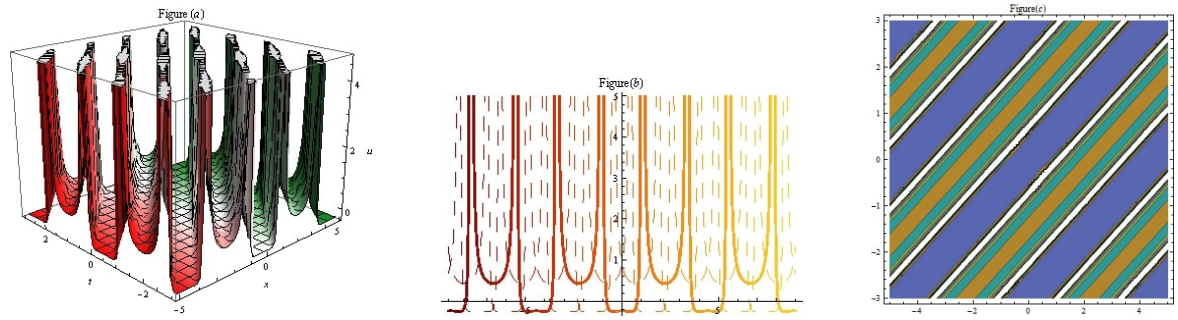

Figure 6.12: Graphical analysis to the $u_{12}(x,t)$ representing to periodic soliton by three–dim, two–dim, and contour plotting with $\varpi_1 = -2,\ \varpi_2 = -5,\ \varpi_3 = 2,\ \mu = 1.5,\ b_1 = 1,\ b_2 = 1$

[45], radial basis function method [46], the $G^{'}/G-$expansion technique [47], modified auxiliary equation mapping approach [48], extended simple equation approach [49], generalized exponential rational function approach [50], Lie group method [51], and improved sub equation method [52]. In this work, we apply the auxiliary equation approach to the NLKS equation with the aid of mathematical software and explore a variety of soliton solutions. However, the constructed solutions obtained here exhibit novel structures. As shown in Figures 13.2–6.12, the results include kink waves, peakon bright solitons, peakon dark solitons, periodic wave solitons with new structural forms, singular bright solitons, anti-kink waves, and several other soliton structures.

Through detailed analysis and discussion, new results have been obtained for investigating various NLEEs, demonstrating that the applied approach is more efficient, reliable, simple, precise, and powerful compared to previous methods.

6.5 Conclusion

This study investigates novel soliton solutions to the NLKS equation using the auxiliary equation technique. The successful application of this method produced a variety of soliton structures, including kink solitons, mixed bright and dark solitons, peakon bright solitons, periodic solitons, anti–kink solitons,

peakon dark solitons, and several other solitary wave forms. The results demonstrate the effectiveness of the applied approach in generating diverse solitary wave solutions and highlight its potential for exploring a wide range of nonlinear models. The obtained solutions are illustrated graphically through contour plots, as well as two– and three–dimensional visualizations. These newly derived solutions are expected to be valuable in various domains, including quantum mechanics, nonlinear optics, soliton theory, optical fibers, ocean dynamics, and other branches of physical sciences. Overall, the technique proves to be a powerful and reliable tool for solving nonlinear models.

Bibliography

[1] Seadawy, A. R., Iqbal, M., & Lu, D. Applications of propagation of long-wave with dissipation and dispersion in nonlinear media via solitary wave solutions of generalized Kadomtsev–Petviashvili modified equal width dynamical equation. Computers & Mathematics with Applications, 2019; 78(11), 3620-3632.

[2] Chou, D., Rehman, H. U., Awan, A. U., Bashir, U., Ashraf, H., & Sultan, A. M. (2025). Investigating soliton phenomena in incompressible fluids: Study of the (2+ 1)–dimensional Boiti–Leon–Manna–Pempinelli equation. Modern Physics Letters A, 40(15n16), 2550049.

[3] Lu, D., Seadawy, A. R., & Iqbal, M. (2018). Mathematical methods via construction of traveling and solitary wave solutions of three coupled system of nonlinear partial differential equations and their applications. Results in Physics, 11, 1161-1171.

[4] Iqbal, M., Seadawy, A. R., Lu, D., & Xianwei, X. (2020). Construction of a weakly nonlinear dispersion solitary wave solution for the Zakharov–Kuznetsov–modified equal width dynamical equation. Indian Journal of Physics, 94(9), 1465-1474.

[5] Seadawy, A. R., Iqbal, M., & Lu, D. (2019). Analytical methods via bright-dark solitons and solitary wave solutions of the higher-order nonlinear Schrödinger equation with fourth-order dispersion. Modern Physics Letters B, 33(35), 1950443.

[6] Iqbal, M., Liu, J., Seadawy, A. R., Alrashdi, H. D., Algethamie, R., Aljohani, A., & Fu, C. (2025). Analysis of periodic wave soliton structure for the wave propagation in nonlinear low–pass electrical transmission lines through analytical technique. Ain Shams Engineering Journal, 16(9), 103506.

[7] Seadawy, A. R., Zahed, H., & Iqbal, M. (2022). Solitary Wave Solutions for the Higher Dimensional Jimo–Miwa Dynamical Equation via New Mathematical Techniques. Mathematics, 10(7), 1011.

[8] Seadawy, A. R., Iqbal, M., Althobaiti, S., Sayed, S. (2021). Wave propagation for the nonlinear modified Kortewege–de Vries Zakharov–Kuznetsov and extended Zakharov–Kuznetsov dynamical equations arising in nonlinear wave media. Optical and Quantum Electronics, 53, 1-20.

[9] Iqbal, M., Seadawy, A. R., Lu, D., & Zhang, Z. (2023). Computational approach and dynamical analysis of multiple solitary wave solutions for nonlinear coupled Drinfeld–Sokolov–Wilson equation. Results in Physics, 54, 107099.

[10] Faridi, W. A., Asjad, M. I., Toseef, M., & Amjad, T. (2022). Analysis of propagating wave structures of the cold bosonic atoms in a zig–zag optical lattice via comparison with two different analytical techniques. Optical and Quantum Electronics, 54(12), 773.

[11] Rehman, H. U., Akber, R., Wazwaz, A. M., Alshehri, H. M., & Osman, M. S. (2023). Analysis of Brownian motion in stochastic Schrödinger wave equation using Sardar sub-equation method. Optik, 289, 171305.

[12] Rehman, H. U., Inc, M., Asjad, M. I., Habib, A., & Munir, Q. (2022). New soliton solutions for the space-time fractional modified third order Korteweg–de Vries equation. Journal of Ocean Engineering and Science.

[13] Tariq, H., & Akram, G. New traveling wave exact and approximate solutions for the nonlinear Cahn–Allen equation: evolution of a nonconserved quantity. Nonlinear Dynamics, 2017; 88, 581-594.

[14] Faridi, W. A., Asjad, M. I., & Jarad, F. Non-linear soliton solutions of perturbed Chen–Lee–Liu model by Φ^6–model expansion approach. Optical and Quantum Electronics, (2022); 54(10), 664.

[15] Ali, A. T. New generalized Jacobi elliptic function rational expansion method. Journal of computational and applied mathematics, 2011; 235(14), 4117-4127.

[16] Ur Rehman, H., Boulaaras, S. M., Althobaiti, S., Althobaiti, A., & Haseeb, M. (2025). Dynamics in (2+ 1)-dimensional complex coupled Maccari system: Bifurcation analysis, phase portraits and optical solitons. Modern Physics Letters B, 39(30), 2550179.

[17] Iqbal, M., Lu, D., Seadawy, A. R., & Zhang, Z. (2024). Nonlinear behavior of dust acoustic periodic soliton structures of nonlinear damped modified Kortewege-de Vries equation in dusty plasma. Results in Physics, 107533.

[18] Iqbal, M., Lu, D., Seadawy, A. R., Alomari, F. A., Umurzakhova, Z., Alsubaie, N. E., & Myrzakulov, R. (2024). Exploration of unexpected optical mixed, singular, periodic and other soliton structure to the complex nonlinear Kuralay–IIA equation. Optik, 171694.

[19] Li, J., Xu, T., Meng, X. H., Zhang, Y. X., Zhang, H. Q. & Tian, B. (2007). Lax pair, Bäcklund transformation and N–soliton–like solution for a variable-coefficient Gardner equation from nonlinear lattice, plasma physics and ocean dynamics with symbolic computation. Journal of Mathematical Analysis and Applications, 336(2), 1443-1455.

[20] Qin, C. Y., Tian, S. F., Wang, X. B., Zhang, T. T., & Li, J. (2018). Rogue waves, bright-dark solitons and traveling wave solutions of the (3+ 1)–dimensional generalized Kadomtsev–Petviashvili equation. Computers & Mathematics with Applications, 75(12), 4221-4231.

[21] Seadawy, A. R., & Manafian, J. (2018). New soliton solution to the longitudinal wave equation in a magneto–electro–elastic circular rod. Results in Physics, 8, 1158-1167.

[22] Ibrahim, S., Ashir, A. M., Sabawi, Y. A., & Baleanu, D. (2023). Realization of optical solitons from nonlinear Schrödinger equation using modified Sardar sub–equation technique. Optical and Quantum Electronics, 55(7), 617.

[23] Iqbal, M., Seadawy, A. R., & Lu, D. (2019). Applications of nonlinear longitudinal wave equation in a magneto–electro–elastic circular rod and new solitary wave solutions. Modern Physics Letters B, 33(18), 1950210.

[24] Iqbal M, Seadawy A R, Lu D. (2018). Construction of solitary wave solutions to the nonlinear modified Kortewege–de Vries dynamical equation in unmagnetized plasma via mathematical methods, Modern Physics Letters A, 33(32), 1850183.

[25] Iqbal M, Seadawy A R, Lu D. (2018). Dispersive solitary wave solutions of nonlinear further modified Kortewege–de Vries dynamical equation in a unmagnetized dusty plasma via mathematical methods, Modern Physics Letters A, 33(37), 1850217.

[26] Arda, A., & Sever, R. (2012). Exact solutions of the Morse-like potential, step–up and step–down operators via Laplace transform approach. Communications in Theoretical Physics, 58(1), 27.

[27] Seadawy, A. R., & El–Rashidy, K. (2016). Nonlinear Rayleigh-Taylor instability of the cylindrical fluid flow with mass and heat transfer. Pramana, 87(2), 1-9.

[28] Iqbal, I., & Rehman, H. U. (2025). Optical soliton solutions via the Biswas–Milovic equation: Quasi-periodic behavior, sensitivity, and bifurcation. Nonlinear Dynamics, 1-26.

[29] Iqbal, M., Seadawy, A.R., Lu, D. & Zhang, Z. (2023). Structure of analytical and symbolic computational approach of multiple solitary wave solutions for nonlinear Zakharov–Kuznetsov modified equal width equation. Numerical Methods for Partial Differential Equations, 39(5), 3987–4006.

[30] Iqbal, M., Seadawy, A. R., Khalil, O. H., & Lu, D. (2020). Propagation of long internal waves in density stratified ocean for the (2+1)–dimensional nonlinear Nizhnik–Novikov–Vesselov dynamical equation. Results in Physics, 16, 102838.

[31] Iqbal, M., Seadawy, A. R., Lu, D., & Zhang, Z. (2023). Physical structure and multiple solitary wave solutions for the nonlinear Jaulent–Miodek hierarchy equation. Modern Physics Letters B, 2341016.

[32] Iqbal, M., Seadawy, A. R., Lu, D., & Zhang, Z. (2024). Multiple optical soliton solutions for wave propagation in nonlinear low-pass electrical transmission lines under analytical approach. Optical and Quantum Electronics, 56(1), 35.

[33] Zahed, H., Seadawy, A. R., & Iqbal, M. (2022). Structure of analytical ion–acoustic solitary wave solutions for the dynamical system of nonlinear wave propagation. Open Physics, 20(1), 313-333.

[34] Seadawy, A. R., & Iqbal, M. (2021). Propagation of the nonlinear damped Korteweg–de Vries equation in an unmagnetized collisional dusty plasma via analytical mathematical methods. Mathematical Methods in the Applied Sciences, 44(1), 737-748.

[35] Alam, M. N., Iqbal, M., Hassan, M., Fayz-Al-Asad, M., Hossain, M. S., & Tunç, C. (2024). Bifurcation, phase plane analysis and exact soliton solutions in the nonlinear Schrodinger equation with Atangana's conformable derivative. Chaos, Solitons & Fractals, 182, 114724.

[36] Seadawy, A. R., & Iqbal, M. Optical soliton solutions for nonlinear complex Ginzburg–Landau dynamical equation with laws of nonlinearity Kerr law media. International Journal of Modern Physics B, 34(19), 2050179.

[37] Seadawy, A. R., Iqbal, M., & Lu, D. (2019). Nonlinear wave solutions of the Kudryashov–Sinelshchikov dynamical equation in mixtures liquid-gas bubbles under the consideration of heat transfer and viscosity. Journal of Taibah University for Science, 13(1), 1060-1072.

[38] Kudryashov, N. A., & Sinelshchikov, D. I. (2010). Nonlinear waves in bubbly liquids with consideration for viscosity and heat transfer. Physics Letters A, 374(19-20), 2011-2016.

[39] Korteweg, D. J., & De Vries, G. (1895). On the change of form of long waves advancing in a rectangular canal, and on a new type of long stationary waves. The London, Edinburgh, and Dublin Philosophical Magazine and Journal of Science, 39(240), 422-443.

[40] Shu, J. J. (2014). The proper analytical solution of the Korteweg-de Vries-Burgers equation. arXiv preprint arXiv:1403.3636.

[41] Ryabov, P. N., Sinelshchikov, D. I., & Kochanov, M. B. (2011). Application of the Kudryashov method for finding exact solutions of the high order nonlinear evolution equations. Applied Mathematics and Computation, 218(7), 3965-3972.

[42] He, B., Meng, Q., & Long, Y. (2012). The bifurcation and exact peakons, solitary and periodic wave solutions for the Kudryashov–Sinelshchikov equation. Communications in Nonlinear Science and Numerical Simulation, 17(11), 4137-4148.

[43] Tu, J. M., Tian, S. F., Xu, M. J., & Zhang, T. T. (2016). On Lie symmetries, optimal systems and explicit solutions to the Kudryashov–Sinelshchikov equation. Applied Mathematics and Computation, 275, 345-352.

[44] Zhao, Y. M. (2013). F-Expansion Method and Its Application for Finding New Exact Solutions to the Kudryashov-Sinelshchikov Equation. Journal of Applied Mathematics, 2013(1), 895760.

[45] Ryabov, P. N. (2010). Exact solutions of the Kudryashov–Sinelshchikov equation. Applied Mathematics and Computation, 217(7), 3585-3590.

[46] Gupta, A. K., & Ray, S. S. (2017). On the solitary wave solution of fractional Kudryashov–Sinelshchikov equation describing nonlinear wave processes in a liquid containing gas bubbles. Applied Mathematics and Computation, 298, 1-12.

[47] Hubert, M. B., Betchewe, G., Doka, S. Y., & Crepin, K. T. (2014). Soliton wave solutions for the nonlinear transmission line using the Kudryashov method and the $(G^{'}/G)$–expansion method. Applied Mathematics and Computation, 239: 299-309.

[48] Seadawy, A. R., Iqbal, M., & Lu, D. (2019). Nonlinear wave solutions of the Kudryashov–Sinelshchikov dynamical equation in mixtures liquid-gas bubbles under the consideration of heat transfer and viscosity. Journal of Taibah University for Science, 13(1), 1060-1072.

[49] Khater, M. M., Seadawy, A. R., & Lu, D. (2018). Solitary traveling wave solutions of pressure equation of bubbly liquids with examination for viscosity and heat transfer. Results in physics, 8, 292-303.

[50] Kumar, S., Niwas, M., & Dhiman, S. K. (2022). Abundant analytical soliton solutions and different wave profiles to the Kudryashov–Sinelshchikov equation in mathematical physics. Journal of Ocean Engineering and Science, 7(6), 565-577.

[51] Bruzón, M. S., Recio, E., de la Rosa, R., & Gandarias, M. L. (2018). Local conservation laws, symmetries, and exact solutions for a Kudryashov–Sinelshchikov equation. Mathematical Methods in the Applied Sciences, 41(4), 1631-1641.

[52] Ray, S. S., & Singh, S. (2017). New exact solutions for the Wick-type stochastic Kudryashov–Sinelshchikov equation. Communications in Theoretical Physics, 67(2), 197.

[53] Iqbal, M., Lu, D., Seadawy, A. R., Mustafa, G., Zhang, Z., Ashraf, M., & Ghaffar, A. (2024). Dynamical analysis of soliton structures for the nonlinear third-order Klein–Fock–Gordon equation under explicit approach. Optical and Quantum Electronics, 56(4), 651.

[54] Iqbal, M., Lu, D., Seadawy, A. R., Ashraf, M., Albaqawi, H. S., Khan, K. A., & Chou, D. (2024). Investigation of solitons structures for nonlinear ionic currents microtubule and Mikhaillov–Novikov–Wang dynamical equations. Optical and Quantum Electronics, 56(3), 361.

[55] Iqbal, M., Nur Alam, M., Lu, D., Seadawy, A. R., Alsubaie, N. E., & Ibrahim, S. (2024). On the exploration of dynamical optical solitons to the modify unstable nonlinear Schrödinger equation arising in optical fibers. Optical and Quantum Electronics, 56(5), 765.

CHAPTER 7

Mathematical Modeling of Biofluids: An Application to Peristaltic-Ciliary Transport in Human Oviduct in the Context of Hydrosalpinx

Hameed Ashraf[a,†] **and Ayesha Siddiqa**[a]

[a] *Department of Mathematics, University of Okara, Okara, Pakistan.*

Corresponding Author: [a,†]: hameedashraf09@uo.edu.pk

Abstract: *Mathematical modeling of biofluids plays a crucial role in understanding the complex transport processes that occur in various physiological systems within the human body. This chapter deals with the peristaltic-ciliary transport mechanism in the context of oviductal hydrosalpinx. A mathematical model is developed based on the hypothesis that oviductal fluid accumulation in the oviduct of a patient with hydrosalpinx forms a porous medium, whose pore spaces are filled with oviductal fluid. Conservation of mass and linear momentum, along with Darcy's law, govern the flow of fluids. A linearly viscous fluid characterized the oviductal fluid and the growing embryo. Subsequently, the formulated partial differential equations are solved to determine exact solutions. Analytic expressions for axial and radial velocity components, residence time, pressure gradient, and stream functions, are derived. The varying effects of pertinent parameters are delineated on flow variables such as residence time and axial velocity. The relevance of the current findings provides useful insight into peristaltic-ciliary transport in the human oviduct affected by hydrosalpinx.*

Keywords: Peristaltic-ciliary flow, Hydrosalpinx, Linearly viscous fluid, Human oviduct, Embryo transport

7.1 Introduction

In humans, oviducts serve as a critical component of the reproductive system, marking the initial stage of life development. The female abdominal cavity contains a pair of elongated, muscular, and narrow structures known as the oviducts, also referred to as Fallopian tubes or uterine tubes. The oviduct consists of four regions: intramural, isthmus, ampulla, and infundibulum. Each oviduct is 0.5 cm to 1.2 cm in width and 10 cm to 13 cm in length. Its principal role is to allow spermatozoa to pass through during the preovulatory phase, to help the ovum exit the ovaries during ovulation, and, if fertilization takes place at the ampulla, to transfer the embryo in the oviductal fluid to the fundus, the upper portion of the uterus, where it can develop into a pregnancy [1, 2, 3, 4, 5]. A mucus membrane lining and peristaltic contractions form the wall of the oviduct. Secretory goblet cells and ciliated cells are densely packed onto the mucus membrane. The goblet cells secrete a little amount of fluid through the oviduct. The viability of the embryo, ovum, and sperm is supported by this fluid. The oviductal fluid also offers an ideal setting for the embryo's early stages of growth. The embryo is propelled from the ampulla to the uterus by means of the peristaltic contractions of the oviduct wall and the swaying movements of the cilia tips, as opposed to sperm, which possess a self-propelling mechanism. Being in a continuous state, these two systems combine to form a traveling wave. Consequently, during the first stages of human reproduction, this traveling wave is the only one responsible for delivering the growing embryo to the uterus that is not pregnant in order to deposit it [6, 7, 8, 9, 10, 11].

Hydrosalpinx is an oviductal pathology which occurs due to the occlusion at three different areas: proximal, near the oviduct, at the fundus, mid-tubal, middle portion of the oviduct *i. e.*, in the ampullar region, and distal, at the end of the oviduct *i. e.*, in the infundibulum region. Occlusion can be found at one or more of these three places. These types of occlusions may be due to some injury or infection, as a result of which the oviduct becomes swollen and engorged with oviductal fluid. A hydrosalpinx that occurs due to occlusion at the fundus (near the oviduct) has adverse effects on the implantation of a developing embryo. Such a situation gives rise to a mechanical obstacle by inducing fluid reflux, which compels the developing embryo to adopt a direction opposite to the direction in which the travelling waves propagate along the oviducts' surfaces [12, 13, 14]. This situation in biomechanics is modelled by treating the tissue as a porous medium and employing Darcy's law. A porous media is one in which the whole volume is divided into solid matrix and pore spaces. The oviductal fluid fills the pore spaces. In its original formulation, the Darcy law is based on the Newtonian flow assumptions [15, 16, 17, 18].

Ashraf et al. [6, 7, 8, 9, 10] developed a mathematical model for peristaltic-cilia dynamics. The model asserts that the mechanisms facilitating the transportation of the embryo within the oviductal fluid in the human oviduct are peristalsis-cilia and the pressure gradient condition. Subsequently, Wang et al. [11] employed this model. The researchers employed linearly viscous fluid, third-grade fluid, Johnson-Segalman fluid, Carreau fluid, shear-rate-dependent viscoelastic fluid, and Phan–Thien–Tanner (PTT) to characterize the properties of the developing embryo and oviductal fluid. The original biological prob-

lem was modeled by approximating the converging human oviduct as a two-dimensional, narrow, uniform tube of finite length. The effects of variations in involved parameters on flow variables, including velocity and residence/residue time, were discussed. To the best of the authors' knowledge, no previous research has modelled the peristalsis-cilia and pressure gradient at the oviductal channel entrench induced fluid flow in the context of hydrosalpinx. This indicates a significant gap in the existing literature, emphasizing the need for further research to develop an accurate mathematical model that effectively investigates peristaltic-ciliary transport in the human oviduct relating to hydrosalpinx and to enhance our understanding of the phenomena associated with this condition.

The objective of this chapter is to theoretically provide the analysis that focuses attention on the biomechanics of hydrosalpinx and the transport characteristics of a developing embryo in the human oviduct. We shall consider a mathematical model based on the hypothesis that the fundus near the oviduct is occluded, due to which the oviduct is swollen and engorged with oviductal fluid in a patient with hydrosalpinx, forming a porous medium within the oviduct whose pore spaces are filled with oviductal fluid. To do this, we will examine the flow of an incompressible linearly viscous fluid through a porous medium whose pore spaces are filled with linearly viscous fluid. The fluid flow within the oviductal channel is driven by the traveling wave and pressure gradient conditions at the entrance. We obtain the expressions for the velocity components and pressure gradient by solving the system of partial differential equations for exact solutions. Through graphical analysis, we will see how changes in the pertinent parameters affect axial velocity at various sagittal cross-sections. We will calculate residence time numerically in MATHEMATICA and use graphical analysis at different sagittal cross-sections to see how the parameters involved affect it. In the context of hydrosalpinx, the results will provide physical insight into the peristaltic-ciliary transfer.

7.2 Problem Formulation & Mathematical Modelling

We consider the transport of a developing embryo in a woman, a patient with hydrosalpinx in which oviductal fluid is accumulated in the oviduct. We propose a mathematical model for the flow of an incompressible, linearly viscous fluid in a two-dimensional, narrow, finite, and symmetric channel of mean half-width a through a porous medium. The pore spaces of this porous medium are filled with oviductal fluid. The peristaltic contractions of the walls of the channel are of cyclic nature and the swaying movements of the tips of cilia that line the interior surfaces of the channel work together to generate the travelling waves. These travelling waves propagate along the two walls W_1 and W_2 at a speed c and drive the fluid through the oviductal fluid that fills the pore spaces of the porous medium. We assume Newtonian fluid as oviductal fluid. The origin is chosen at the midplane of the symmetric channel. The geometries of the walls W_1 and W_2 respectively are defined by the following equations:

$$\bar{H}\left(\bar{X},\bar{t}\right) = a + bsin\frac{2\pi}{\lambda}\left(\bar{X}-c\bar{t}\right) + Ab\frac{2\pi}{\lambda}cos\frac{2\pi}{\lambda}\left(\kappa\left(\bar{X}-c\bar{t}\right)\right)sin\frac{2\pi}{\lambda}\left(\bar{X}-c\bar{t}\right), \tag{7.1}$$

where we represent the sinusoidal wave amplitude with b, wavelength with λ, the material points maximum displacement with Ab, wave speed with c, the constant with κ and metachronal wave amplitude with A [6, 7, 8, 9, 10, 11].

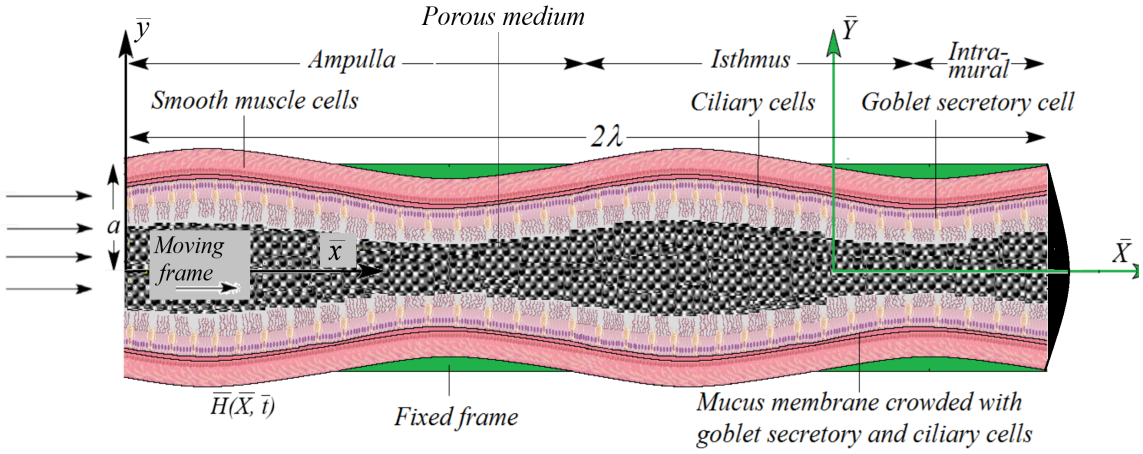

Figure 7.1: Schematic diagram of the human oviduct.

In the laboratory frame of reference, the fundamental two-dimensional governing equations that govern the flow of an incompressible linearly viscous fluid through a porous medium, while eliminating temperature effects and without body force, are [6, 7, 8, 9, 10]:

$$\frac{\partial \bar{U}}{\partial \bar{X}} + \frac{\partial \bar{V}}{\partial \bar{Y}} = 0, \tag{7.2}$$

$$\frac{\partial \bar{U}}{\partial \bar{t}} + \bar{U}\frac{\partial \bar{U}}{\partial \bar{X}} + \bar{V}\frac{\partial \bar{U}}{\partial \bar{Y}} = -\frac{1}{\rho}\frac{\partial \bar{P}}{\partial \bar{X}} + \nu\left[\frac{\partial^2 \bar{U}}{\partial \bar{X}^2} + \frac{\partial^2 \bar{U}}{\partial \bar{Y}^2}\right] - \frac{\nu}{K}\bar{U}, \tag{7.3}$$

$$\frac{\partial \bar{V}}{\partial \bar{t}} + \bar{U}\frac{\partial \bar{V}}{\partial \bar{X}} + \bar{V}\frac{\partial \bar{V}}{\partial \bar{Y}} = -\frac{1}{\rho}\frac{\partial \bar{P}}{\partial \bar{Y}} + \nu\left[\frac{\partial^2 \bar{V}}{\partial \bar{X}^2} + \frac{\partial^2 \bar{V}}{\partial \bar{Y}^2}\right] - \frac{\nu}{K}\bar{V}, \tag{7.4}$$

where we denote the laboratory frame coordinates with $(\bar{X},\ \bar{Y})$, velocity components with $(\bar{U},\ \bar{V})$ respectively in the directions $\bar{X}$ and $\bar{Y}$, fluid constant density with ρ, pressure with $\bar{P}$, instant of time with $\bar{t}$, kinematic viscosity with ν, and permeability of the porous medium with K.

The coordinates $(\bar{X},\ \bar{Y})$, the velocity components $(\bar{U},\ \bar{V})$, the pressure $\bar{P}$, and the travelling wave $\bar{H}$ in the laboratory frame of reference are related to the normalized coordinates x and y, the components of velocity u and v, the pressure p, and the travelling wave h in the moving frame of reference through the following relations:

$$x = \frac{2\pi(\bar{X} - c\bar{t})}{\lambda},\ y = \frac{\bar{Y}}{a},\ u = \frac{\bar{U} - c}{c},\ v = \frac{\bar{V}\lambda}{2\pi a c},\ p = \frac{\bar{P}2\pi a^2}{\mu\lambda c},\ h = \frac{\bar{H}}{a}. \tag{7.5}$$

When we make use of normalized relations (15.18) into Eqs. (15.8)-(15.17), in turn utilizing the low

Reynolds number and long wavelength assumptions in the subsequent equations, we finally get

$$\frac{\partial u}{\partial x}+\frac{\partial v}{\partial y}=0, \tag{7.6}$$

$$\frac{\partial^2 u}{\partial y^2}-\beta u=\frac{dp}{dx}+\beta, \tag{7.7}$$

$$h\left(x\right)=1+\phi Sin\left(x\right)+\epsilon\phi Cos\left(\kappa x\right)Sin\left(x\right), \tag{7.8}$$

where we represent amplitude ratio with $\phi=\frac{b}{a}$, metachronal wave parameter with $\epsilon=\frac{2\pi A}{\lambda}$, and $\beta=\frac{1}{Da}$ in which $Da=\frac{K}{a^2}$ is the Darcy number. The physical boundary conditions associated with the Eq. (15.19) and Eq. (7.7) are of the following form:

$$\frac{\partial u(x,0)}{\partial y} = 0, \tag{7.9}$$

$$u(x,h) = -1, \tag{7.10}$$

$$v(x,0) = 0, \tag{7.11}$$

$$v(x,h) = -\frac{dh}{dx}, \tag{7.12}$$

$$\frac{dp(0)}{dx} = -\xi. \tag{7.13}$$

Here, ξ is the value of pressure gradient with which ovum enters from infundibulum region to ampullar region in the oviductal channel. This condition in literature is termed as "pressure gradient condition at the oviductal channel entrance" [6].

Eq. (7.7) is a second-order nonhomogeneous and linear partial differential equation, while Eq. (15.19) is a first-order homogeneous and linear partial differential equation. In the next section, we will solve this system subject to the boundary conditions (8.8)-(10.12) to seek the closed-form solutions to have expressions for velocity components, pressure gradient, and residence time.

7.3 Solution of the problem

Eq. (7.7) upon solving for closed-form solution subject to boundary conditions (8.8) and (8.9), we finally have

$$u(x,y)=-1+\beta^{-1}\frac{dp}{dx}\left[\frac{\cosh\left(\sqrt{\beta}\,y\right)}{\cosh\left(\sqrt{\beta}\left(1+\phi\sin\left(x\right)+\epsilon\phi\cos\left(\kappa x\right)\sin\left(x\right)\right)\right)}-1\right], \tag{7.14}$$

which represents the axial velocity of the linearly viscous fluid within oviductal fluid through porous medium.

Using Eq. (7.14) into the Eq. (15.19), in turn integrating with respect to 'y', one gets

$$v(x,y)=-\beta^{-1}\frac{d^2p}{dx^2}\left[\frac{\sinh\left(\sqrt{\beta}\,y\right)}{\sqrt{\beta}\,\cosh\left(\sqrt{\beta}\left(1+\phi\sin\left(x\right)+\epsilon\phi\cos\left(\kappa x\right)\sin\left(x\right)\right)\right)}-y\right]$$

$$+\beta^{-1}\frac{dp}{dx}\frac{(\phi\cos(x)+\epsilon\phi\cos(x)\cos(kx)-k\epsilon\phi\sin(x)\sin(kx))}{\cosh^2\left(\sqrt{\beta}\,(1+\phi\sin(x)+\epsilon\phi\cos(\kappa x)\sin(x))\right)}$$
$$\times\sinh\left(\sqrt{\beta}\,(\phi\cos(x)+\epsilon\phi\cos(x)\cos(kx)-k\epsilon\phi\sin(x)\sin(kx))\right)\sinh\left(\sqrt{\beta}\,y\right)$$
$$+C(x), \tag{7.15}$$

where $C(x)$ denotes for arbitrary function.

Making use of boundary condition (8.10) into Eq. (7.15), we get

$$v(x,y)=-\beta^{-1}\frac{d^2p}{dx^2}\left[\frac{\sinh\left(\sqrt{\beta}\,y\right)}{\sqrt{\beta}\,\cosh\left(\sqrt{\beta}\,(1+\phi\sin(x)+\epsilon\phi\cos(\kappa x)\sin(x))\right)}-y\right]$$
$$+\beta^{-1}\frac{dp}{dx}\frac{(\phi\cos(x)+\epsilon\phi\cos(x)\cos(kx)-k\epsilon\phi\sin(x)\sin(kx))}{\cosh^2\left(\sqrt{\beta}\,(1+\phi\sin(x)+\epsilon\phi\cos(\kappa x)\sin(x))\right)}$$
$$\times\sinh\left(\sqrt{\beta}\,(\phi\cos(x)+\epsilon\phi\cos(x)\cos(kx)-k\epsilon\phi\sin(x)\sin(kx))\right)\sinh\left(\sqrt{\beta}\,y\right). \tag{7.16}$$

Eq, (7.16) represents the vertical velocity of the linearly viscous fluid within oviductal fluid through porous medium. Invoking boundary condition (8.11) into Eq. (7.16), after solving the resultant equation for pressure gradient $\frac{dp}{dx}$, one gets after simplification

$$\frac{dp}{dx}=\frac{\beta\sqrt{\beta}\,(A_0+1+\phi\sin(x)+\epsilon\phi\cos(\kappa x)\sin(x))}{tanh(\sqrt{\beta}(1+\phi\sin(x)+\epsilon\phi\cos(\kappa x)\sin(x)))-\sqrt{\beta}(1+\phi\sin(x)+\epsilon\phi\cos(\kappa x)\sin(x))}, \tag{7.17}$$

where we denote the arbitrary constant with A_0. Using pressure gradient condition at the oviductal channel entrance (10.12) into Eq. (7.17), we get the value of this arbitrary constant as follows:

$$A_0=-1-\frac{\xi}{\beta\sqrt{\beta}}\left[tanh(\sqrt{\beta})-\sqrt{\beta}\right]. \tag{7.18}$$

The residence time refers to the period during which a developing embryo remains in the human oviduct. During this time, complete and proper mitotic divisions occur in the embryo. This residence time is crucial for ensuring that these mitotic divisions are complete and proper. The residence time $t_{residence}$ in dimensionless form is defined as [7, 8, 9, 10]:

$$t_{residence}=\int_0^L\frac{1}{u(x,y)}dx. \tag{7.19}$$

Eq. (7.19) with the help of Eq. (7.14) will yield the $t_{residence}$. We will solve the resultant equation numerically in MATHEMATICA.

Remark: We recovered the expressions for velocity components $(u,\ v)$ and pressure gradient $\frac{dp}{dx}$ in the absence of porous medium when we make $\beta\to 0$ respectively into Eqs. (7.14), (7.16) and (7.17):

$$u(x,y)=-1+\frac{1}{2}\frac{dp}{dx}\left[y^2-(1+\phi\sin(x)+\epsilon\phi\cos(\kappa x)\sin(x))^2\right], \tag{7.20}$$

$$v(x,y) = -\frac{1}{6}\frac{d^2p}{dx^2}\left[y^3 - 3y(1+\phi\sin(x)+\epsilon\phi\cos(\kappa x)\sin(x))^2\right] + \frac{dp}{dx}(\phi\cos(x)+\epsilon\phi\cos(x)\cos(kx)-k\epsilon\phi\sin(x)\sin(kx)) \times (1+\phi\sin(x)+\epsilon\phi\cos(\kappa x)\sin(x))y, \tag{7.21}$$

$$\frac{dp}{dx} = \frac{3\left[1-(1+\phi\sin(x)+\epsilon\phi\cos(\kappa x)\sin(x))\right]-\xi}{(1+\phi\sin(x)+\epsilon\phi\cos(\kappa x)\sin(x))^3}. \tag{7.22}$$

7.4 Results and Discussion

A hypothetical model of fluid flow through a porous medium within a finite, symmetric, two-dimensional channel of narrow width is proposed. The proposed model is implemented in a woman, a patient of hydrosalpinx in which oviductal fluid is accumulated in the oviduct due to occlusion at the fundus, near the oviduct. We choose $a = 1.0$ and $L = 2\lambda$ (where $\lambda = 2\pi$), respectively, as the averaged value for the mean half-width and length of the oviduct (from ampullar region to intramural region). In the previous section, the expressions for velocity components and pressure gradient are determined.

The quantitative impacts of the amplitude ratio ϕ, metachronal wave parameter ϵ, Darcy number Da, and pressure gradient at the oviductal channel entrance ξ that emerged in the current analysis are estimated in this section. As shown in graphs (see Figs. 2-5), we developed numerical codes using MATHEMATICA to obtain numerical assessments of the analytical results presented in the preceding section. Additionally, we will use numerical computation to calculate the residence time in this section (refer to Fig. 6).

7.4.1 Velocity Profile

The travelling wave (10.13) induces fluid flow through the pore spaces of the porous medium filled with oviductal fluid. The induced flow alternates forward and backward through these pore spaces. The backward flow mainly occurs in a region with a local maximum in channel width, while the forward flow occurs in a region with a local minimum in channel width. As the channel's cross-section widens, the flow direction shifts in the opposite direction of the traveling waves' propagation. Wang et al. [11] determined that to comprehend the variation effects of involved parameters, it is better to consider different sagittal-cross sections. Therefor, in this analysis, we choose five sagittal-cross sections ($\frac{2\pi}{3}$, y), ($\frac{4\pi}{3}$, y) and (2π, y), ($\frac{8\pi}{3}$, y), and ($\frac{10\pi}{3}$, y) and will observe the variations effects of Da, ϕ, ϵ, and ξ on axial velocity. For this purpose, we plotted Figs. 2-5. Fig. 2 shows the variation effects of Da on axial velocity at the chosen sagittal-cross sections. We perceive that with an increase in Da, the axial velocity increases at all chosen sagittal-cross sections. With an increase in Da, the permeability of the porous media increases. In turn, higher permeability results in less resistance to flow. In Fig. 3, we delineated the variation effects of ϕ on axial velocity at the chosen sagittal cross-section. From this figure, it is delineated that by the increase in ϕ, the overall axial velocity increases at the sagittal-cross sections ($\frac{4\pi}{3}$, y) and ($\frac{10\pi}{3}$, y). On the other

hand, it diminishes by the increase in ϕ at the sagittal-cross sections ($\frac{2\pi}{3}$, y) and ($\frac{8\pi}{3}$, y). The variation effects in ϕ make no impact on axial velocity at the sagittal-cross section (2π, y). We display Fig. 4 to elucidate the variation effects of ϵ on axial velocity at the chosen sagittal-cross sections. It is elucidated from this figure that there are minute effects of the variations in ϵ on axial velocity. The axial velocity increases minutely at the sagittal-cross sections ($\frac{2\pi}{3}$, y) and ($\frac{4\pi}{3}$, y) whereas it decreases at the sagittal-cross sections ($\frac{8\pi}{3}$, y), ($\frac{10\pi}{3}$, y) with an increase in ϵ. Likewise, the effect of ϕ, the variation in ϵ also makes no impact on the axial velocity at the sagittal-cross section (2π, y). The variation effects of both ϕ and ϵ are consistent with the results of Wang et al. [11]. The purpose of Fig. 5 is to note the variation effects of ξ on the axial velocity at the chosen sagittal-cross sections. We noted that at all sagittal-cross sections the axial velocity increases by the increase in ξ. The greater the value of the pressure gradient at the oviductal channel entrance, the linearly viscous the fluid within the oviductal fluid flow, with a higher velocity in the porous medium.

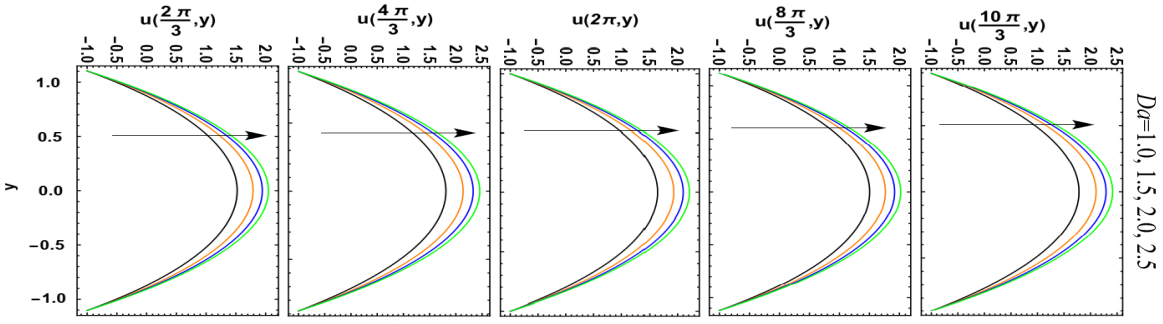

Figure 7.2: Axial velocity plots for variation effects of Da on axial velocity distribution at five different sagittal-cross sections.

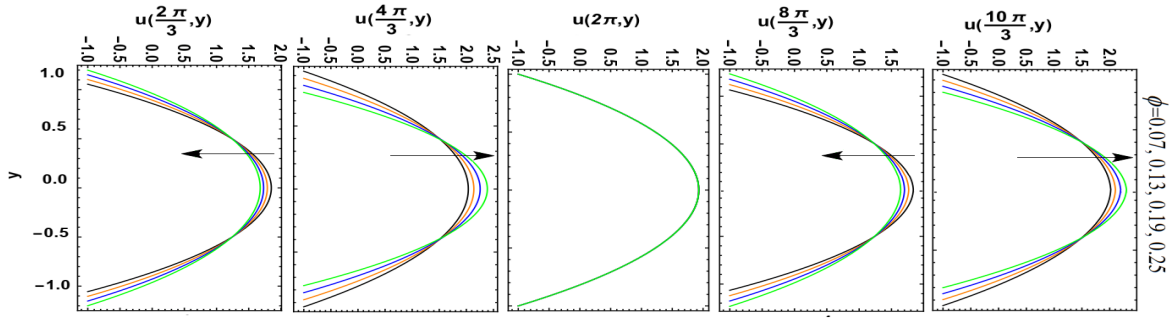

Figure 7.3: Axial velocity plots for variation effects of ϕ on axial velocity distribution at five different sagittal-cross sections.

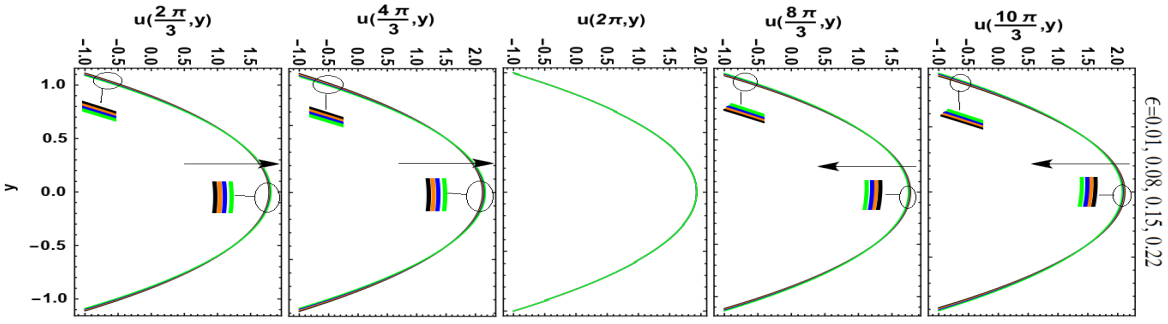

Figure 7.4: Axial velocity plots for variation effects of ϵ on axial velocity distribution at five different sagittal-cross sections.

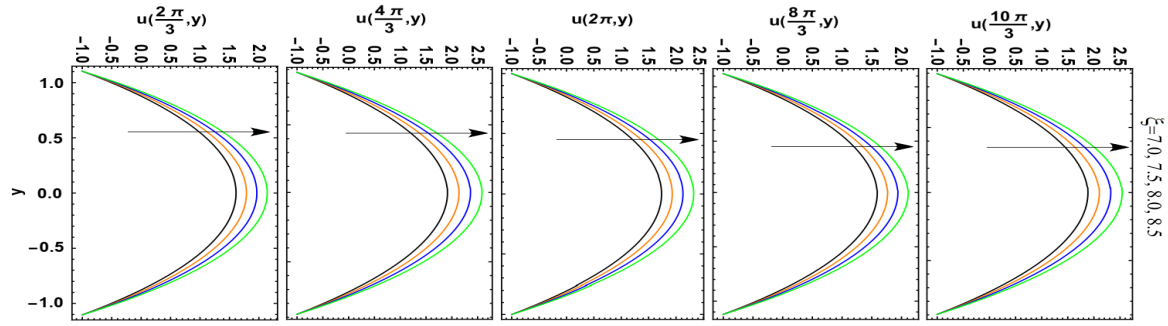

Figure 7.5: Axial velocity plots for variation effects of ξ on axial velocity distribution at five different sagittal-cross sections.

7.4.2 Residence Time

In order to perceive the variation effects of Da, ϕ, ϵ, and ξ on residence time we chosen frontal-cross section $(x, 0.3)$ and displayed Fig. 6. We perform numerical integration of Eq. (7.19) by developing computer codes in MATHEMATICA to plot residence time against oviductal channel length graph. Fig. 6(a) indicates a decrease in residence time with increasing values of Da. In other words, we can say that with an increase in Da, the permeability of the porous media increases, $i.\ e.$ the pore size of the media increases. In turn, resistance to flow decreases, as a result of which the fluid residence decreases. As ϕ and ϵ increase, the residence time increases, as seen in Fig. 6(b) and Fig. 6(c). We find a relationship between the amplitudes of the sinusoidal and metachronal waves and this increase in residence time. The residence time increases in conjunction with the amplitudes of the sinusoidal and metachronal waves. As both waves advance with larger amplitudes, the residence time increases. Fig. 6(d) shows that residence time decreases when ξ increases. It means the relation of the pressure gradient at the oviductal channel entrance with residence time is inversely proportional.

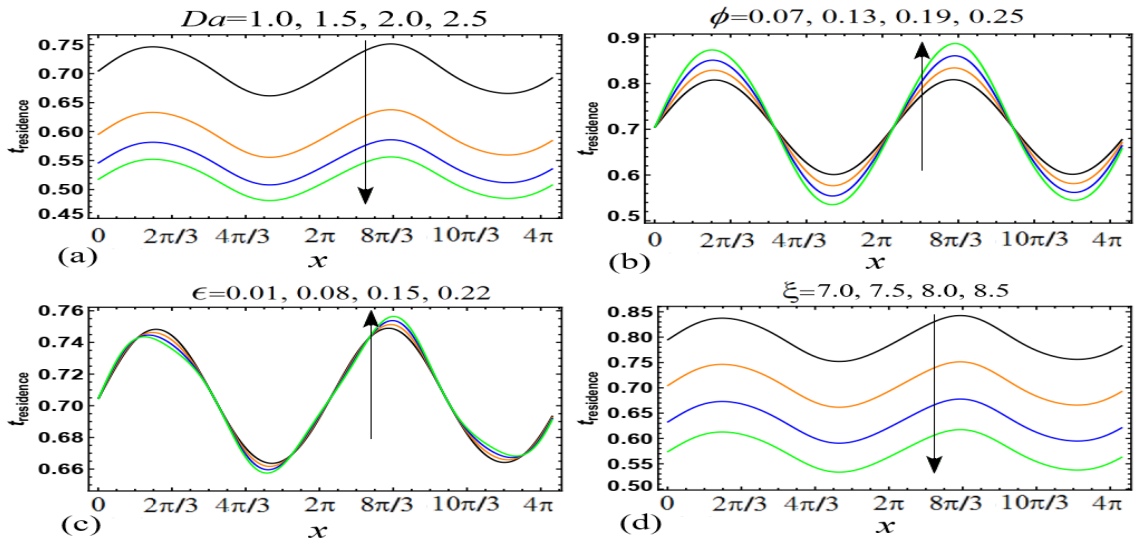

Figure 7.6: Plots of residence time against oviductal channel length for variation effects of (a) Da, (b) ϕ, (c) ϵ and (d) ξ on residence time distribution.

7.5 Transport of a Developing Embryo in the Oviduct

This model of fluid flow in a finite symmetric two-dimensional oviductal channel of narrow width demonstrates the transport of the embryo within the oviductal fluid in humans, particularly in the context of hydrosalpinx [1, 2, 3, 4, 5]. The results obtained in the present theoretical analysis showed that both the axial velocity and the residence time are strongly dependent on Da, ϕ, ϵ, and ξ. The primary concern of the present analysis was to observe the variation effects of emerging parameters at five different sagittal cross-sections on axial velocity and one frontal-cross section on residence. Enhancement in the axial flow velocity with the increase in Da and ξ was evident. With that said, the variation effects of ϕ and ϵ vary and depend mainly on the choice of sagittal-cross sections. Increasing the amplitude of both the sinusoidal wave and the metachronal wave enhances the residence time. These patterns of fluid flow may be applied to the transport of a developing embryo within the oviductal fluid in a moving frame of reference in the human oviduct in the context of hydrosalpinx.

7.6 Concluding Remarks

In the present chapter, we have addressed the problem of peristalsis-cilia and pressure gradient at the oviductal entrance, inducing linearly viscous fluid within oviductal fluid flow in a finite symmetric two-dimensional narrow channel. The purpose of this problem has been to analyze the transportation of a developing embryo within the oviductal fluid in the human oviduct in the context of hydrosalpinx. We used the mathematical model proposed by Ashraf et al. [6, 7, 8, 9, 10]. We have solved the system of partial differential equations for closed-form solutions. We have observed the variation effects of involved

parameters like amplitude ratio ϕ, metachronal wave parameter ϵ, Darcy number Da, and pressure gradient at the oviductal channel entrance ξ on axial velocity and residence time. We have choose five different sagittal-cross sections. We summarized the main findings of the analysis as follows:

- The variation effects of ϕ and ϵ on axial velocity are diverse when we seek the variations in these parameters at the chosen sagittal cross-sections. The effects of ϵ on axial velocity are minute. When the values of Da and xi increase, the axial velocity at all chosen sagittal cross-sections also increases.
- The residence time decreases with an increase in the Da and ξ, whilst it increases with an increase in the ϵ and ϕ.
- The porous medium is better treated as a porous medium and employs Darcy's law. The greater the permeability of the porous media, the lower the resistance to the fluid within the oviductal fluid.

The findings of the present analysis suggest that higher permeability causes less resistance for the fluid, according to Darcy's law, which aids in understanding how flow behaves within porous medium. This knowledge is essential for researching how a developing embryo is transported through the oviductal fluid, particularly in patients with hydrosalpinx, where fluid dynamics are essential.

Bibliography

[1] Croxatto, H. B. (2002). Physiology of gamete and embryo transport through the fallopian tube. Reproduction, Biomedicine Online, 4(2), 160–169.

[2] Fauci, L. J., & Dillon, R. (2006). Biofluidmechanics of reproduction. Annual Review of Fluid Mechanics, 38, 371–394.

[3] Eytan, O., & Elad, D. (1999). Analysis of intra-uterine fluid motion induced by uterine contractions. Bulletin of Mathematical Biology, 61(2), 221–236.

[4] Eytan, O., Jaffa, A. J., & Elad, D. (2005). Peristaltic flow in a tapered channel: application to embryo transport within the uterine cavity. Medical Engineering & Physics, 23(5), 473–482.

[5] Ashraf, H., Siddique, I., Siddiqa, A., Tawfiq, F. M., Tchier, F., Zulqarnain, R. M., ⋯ & Rehman, A. (2024). Analysis of two layered peristaltic-ciliary transport of Jeffrey fluid and in vitro preimplantation embryo development. Scientific Reports, 14(1), 1469.

[6] Ashraf, H., Siddiqui, A. M., & Rana, M. A. (2018). Fallopian tube assessment of the peristaltic-ciliary flow of a linearly viscous fluid in a finite narrow tube. Applied Mathematics and Mechanics, 39(3), 437-454.

[7] Ashraf, H., Siddiqui, A. M., & Rana, M. A. (2018). Fallopian tube analysis of peristaltic flow of third grade fluid in a finite tube. Chinese Journal of Physics, 56(2), 605–621.

[8] Ashraf, H., Siddiqui, A. M., & Rana, M. A. (2018). Analysis of the peristaltic-cilia flow of Johnson-Segalman fluid induced by metachronal cilia of the human fallopian tube. Applied Mathematics and Computation, 308, 305–615.

[9] Ashraf, H., Siddiqui, A. M., & Rana, M. A. (2021). Flow analysis of Carreau fluid model induced by the ciliary cells, smooth muscle cells and pressure gradient at the ampullar region entrance. Theory in Biosciences, 140(3), 249-263.

[10] Ashraf, H., Siddiqui, A. M., Rana, M. A., & Gawo, G. A. (2021). Flow assessment of the shear rate dependent viscoelastic fluid: Application of biomechanics in growing human embryo transport. Alexandria Engineering Journal, 60(6), 5921-5934.

[11] Wang, J., Ashraf, H., Siddiqa, A., Shah, N. A., & Yook, S. J. (2025). Heat transfer analysis of Phan Thien Tanner peristaltic-ciliary fluid flow at distinct sagittal cross-sections in a narrow heated tube. International Communications in Heat and Mass Transfer, 162, 108640.

[12] Halbert, S. A., & Patton, D. L. (1981). Hydrosalpinx: effect of oviductal dilatation on egg transport. Fertility and Sterility, 35(1), 69-73.

[13] Eytan, O., Azem, F., Gull, I., Wolman, I., Elad, D., & Jaffa, A. J. (2001). The mechanism of hydrosalpinx in embryo implantation. Human reproduction, 16(12), 2662-2667.

[14] Bao, H., Qu, Q., Huang, X., Wang, M., Wang, X., & Hao, C. (2017). Impact of hydrosalpinx fluid on early human embryos. Systems Biology in Reproductive Medicine, 63(4), 279-284.

[15] Whitaker, S. (1986). Flow in porous media I: A theoretical derivation of Darcy's law. Transport in porous media, 1(1), 3-25.

[16] Preziosi, L., & Farina, A. (2002). On Darcy's law for growing porous media. International Journal of Non-Linear Mechanics, 37(3), 485-491.

[17] Simintiras, C. A., Fröhlich, T., Sathyapalan, T., Arnold, G. J., Ulbrich, S. E., Leese, H. J., & Sturmey, R. G. (2017). Modelling aspects of oviduct fluid formation in vitro. Reproduction, 153(1), 23-33.

[18] Asghar, Z., Javid, K., Waqas, M., Ghaffari, A., & Khan, W. A. (2020). Cilia-driven fluid flow in a curved channel: effects of complex wave and porous medium. Fluid Dynamics Research, 52(1), 015514.

CHAPTER 8

Rotational flow of fractional second grade fluid through a pipe under time dependent stress on the boundary

Madeeha Tahir[†], Shahla Faisal[‡], Saima Akram[†] Muhammad Imran[*] Muhammad Abid[*] and G. A. Danish[*],

[†] *Department of Mathematics, Government College Women University, Faisalabad 38000, Pakistan*

[‡] *Department of Statistics, Government College University, Faisalabad 38000, Pakistan.*

[*] *Department of Mathematics, Government College University, Faisalabad 38000, Pakistan*

Corresponding Author: M. Imran: drmimranchaudhry@gcuf.edu.pk

Abstract: *Rotational flow of second grade fluid with fractional derivative is analyzed in a infinite circular cylinder. An innovative idea of using shear stress in governing equations instead of velocity field has been used. Initially, the cylinder and fluid with in it are at rest. The motion has been produced because of time dependent stress on the boundary of the cylinder. The aim of present work is to determine stress and velocity field by using integral transform techniques. Final solutions are given in the form of Generalized G and Bessel functions. For the purpose of validity and authenticity, some previous results are recovered. Finally pictorial analysis is made by using Mathcad software to observe the behaviour of physical parameters.*

Keywords: Second grade fluid; Fractional derivative; Exact solution; Shear stress; Velocity field.

8.1 Introduction

Fluid motion in cylindrical domain has vast application in pharmaceutical engineering, civil engineering, agri engineering and also in petroleum industry [1]. In reality it is one of the most worth able problem

related to translational or rotational objects. In our daily life we have to face many fluids around us. On the basis of stress –strain relationship these fluids are categorized into two types i.e. Newtonian fluids (have constant dynamic viscosity) and non-Newtonian fluids (have not constant dynamic viscosity).

In literature there are mainly two sorts of solution are used, those are exact and numerical solutions. Exact solutions are more authentic and reliable as compared to numerical one. Numerical solutions are the approximations of analytical, which are employed to justify the exact results or to solve problem which have no analytic solution. The first exact solution related to motions of non-Newtonian fluids suchlike second grade,Maxwell and Oldroyd–B fluids in cylindrical domains were studied by Ting [2], Srivastava [3] also Waters and King [4] respectively. Fetecau *et. al* [5] studied motion of circular cylinder filled by generalized oldroyed B fluid. Rotational motion of same fluid situated in an annulus are studied by Tong *et. al* [8], Sadiq *et. al* [10] and Tahir *et. al* [11]. Translational flow of an Oldroyd B fluid under different circumstances studied by Tong *et. al* [9]. Burgers' fluid in an annular pipe, analyzed by Khan *et. al* [7]. Detailed study about viscoelastic fluid has been made by Fetecau *et. al* [6].

In the recent times, fractional calculus has attained great achievements for the explanation of complex dynamics e.g. relaxation, oscillation and also for viscoelastic behaviour. Germat [12] suggested firstly the application of fractional derivatives in perspective of viscoelasticity. After this Bagley and Torvic [13] validated the theory of viscoelasticity of coiling polymers by the use of fractional derivatives . Markis *et al.* [14] obtained better approximations for experimental statistics by the use of fractional Maxwell model.

Since last few decays non-Newtonian fluids (milk, juices, tomato-ketchup, cooking-oil, tooth pastes, perfumes, spray, hair oil, butter and custard etc.) has attained great importance from researchers due to their broad applications in practical life. Therefore, the study of non-Newtonian fluids particularly second grade fluid is very vital and significant. Jamil *et al.* [15] studied longitudinal and torsional motions of second grade fluid along with fractional derivative in cylindrical domain. Amir and Gulzman [16], analyzed the motion of second grade fluid, situated in permeable space. They obtained general solutions were represented in terms of Fox H-functions. Nehad [17] examined the thermal analysis for second grade fluid over circular cylinder with the help of Caputo-Febrazio fractional derivative technique while Nauman *et al.* [18] assessed the velocity field and shear stress for non-Newtonian flow i.e. fractional second grade fluid over a circular cylinder.

In present work we develop governing equations in terms of shear stress; however the classical way to study the fluid problem was taking governing relations in terms of velocity field. Non-differential form of boundary condition instead of differential form is taken. Only few researchers [19,20] were employing this new innovative approach to solve the fluid problem with the help of fractional derivatives. The current flow model is investigated in terms of Laplace and Hankel transforms. In the end, graphical analysis also given.

8.2 Governing equations

Consider an infinite circular cylinder of radius R in which an incompressible fractional second grade fluid is in rest position initially. At time $t > 0$, the it starts rotating about its axis under the influence of time dependent stress on the boundary. Due to shear stress, fluid also start rotational motion and velocity is of the form [19, 20]

$$\mathbf{V} = \mathbf{V}(\epsilon, t) = \omega(\epsilon, t)e_\theta, \tag{8.1}$$

where e_θ is unit vector in the θ direction, the constraint of incompressibility for above flow model is satisfied ultimately. At the start whole system is at rest so

$$\tau(\epsilon, 0) = 0, \qquad \mathbf{S}(\epsilon, 0) = 0. \tag{8.2}$$

The constitutive equation of second grade fluid, purpose that only non zero stress $\tau(\epsilon, t) = S_{\epsilon\theta}(\epsilon, t)$ and it also leads to significant partial differential equation

$$\tau(\epsilon, t) = \left(\mu + \alpha_1 \frac{\partial}{\partial t}\right)\left(\frac{\partial}{\partial \epsilon} - \frac{1}{\epsilon}\right)\omega(\epsilon, t). \tag{8.3}$$

In the absence of body forces, the relation for linear momentum becomes

$$\rho \frac{\partial \omega(\epsilon, t)}{\partial t} = \left(\frac{\partial}{\partial \epsilon} + \frac{2}{\epsilon}\right)\tau(\epsilon, t) \tag{8.4}$$

Since we are dealing with a problem in which the shear stress is taken on the boundary so we adopt the procedure [22] and to get rid of the velocity field from Eqs. (15.10) and (15.17), we obtain

$$\frac{\partial \tau(\epsilon, t)}{\partial t} = (\nu + \alpha \tfrac{\partial}{\partial t})\left[\tfrac{\partial^2 \tau(\epsilon,t)}{\partial \epsilon^2} + \tfrac{1}{\epsilon}\tfrac{\partial \tau}{\partial \epsilon} - 4\tfrac{\tau(\epsilon,t)}{\epsilon^2}\right]. \tag{8.5}$$

By apply fractional operator [23]

$$D_t^\varphi \chi(t) = \begin{cases} \frac{1}{\Gamma(1-\varphi)} \frac{d}{dt} \int_0^t \frac{\chi(\tau)}{(t-\tau)^\varphi} d\tau, & 0 \le \varphi < 1; \\ \\ \frac{d}{dt}\chi(t), & \varphi = 1, \end{cases} \tag{8.6}$$

where $\Gamma(\cdot)$ is the Gamma function, the Eq. (15.18) becomes

$$\frac{\partial \tau(\epsilon, t)}{\partial t} = (\nu + \alpha^\varphi D^\varphi)\left[\frac{\partial^2 \tau(\epsilon, t)}{\partial \epsilon^2} + \frac{1}{\epsilon}\frac{\partial \tau}{\partial \epsilon} - 4\frac{\tau(\epsilon, t)}{\epsilon^2}\right], \tag{8.7}$$

and suggestive boundary conditions are

$$\tau(\epsilon,t)|_{\epsilon=R} = ft^m; \qquad t>0, \qquad d\geq 0 \tag{8.8}$$

$$\tau(\epsilon,t)|_{t=0} = 0 = \frac{\partial\tau(\epsilon,t)}{\partial t}|_{t=0}, \qquad \epsilon\in[0,R]. \tag{8.9}$$

8.3 Solution of the flow problem

8.3.1 Calculation of the Stress field

Now firstly we apply Laplace transformation to Eqs. (8.7) and (8.8)

$$q\bar{\tau}(\epsilon,q) = [\nu+\alpha^{\varphi}q^{\varphi}]\left[\frac{\partial^2\bar{\tau}(\epsilon,q)}{\partial\epsilon^2}+\frac{1}{\epsilon}\frac{\partial\bar{\tau}(\epsilon,q)}{\partial\epsilon}-\frac{4\bar{\tau}(\epsilon,q)}{\epsilon^2}\right], \tag{8.10}$$

$$\bar{\tau}(R,q) = f\frac{m!}{q^{m+1}}. \tag{8.11}$$

Finite Hankel and inverse Hankel transformation are [24]

$$\chi_H(\epsilon_n) = \int_0^R \epsilon\chi(\epsilon)J_2(\epsilon\epsilon_n)d\epsilon \tag{8.12}$$

$$\chi(\epsilon) = \frac{2}{R^2}\sum_{n=1}^{\infty}\frac{J_2(\epsilon\epsilon_n)}{[J_2'(R\epsilon_n)]^2}\chi_H(\epsilon_n), \tag{8.13}$$

where

$$\acute{J}_2(R\epsilon_n) = J_1(R\epsilon_n), \tag{8.14}$$

here $J_2(-)$ is the Bessel function of first kind and of 2nd order also ϵ_n are the positive distinct roots of $J_2(R\epsilon_n)=0$. Multiplying Eq. (10) with $rJ_2(\epsilon\epsilon_n)$ then integrating from 0 to R and by using identity [25] we have,

$$\int_0^R \epsilon J_2(\epsilon\epsilon_n)\left[\frac{\partial^2}{\partial\epsilon^2}+\frac{1}{\epsilon}\frac{\partial}{\partial\epsilon}-\frac{4}{\epsilon^2}\right]\bar{\tau}(\epsilon,q) = -R\epsilon_n J_2'(R\epsilon_n)\bar{\tau}(R,q)-\epsilon_n^2\bar{\tau}_H(\epsilon_n,q). \tag{8.15}$$

Now by applying Hankel transformation and using Eqs. (8.11), (8.14) and (10.14)

$$\bar{\tau}_H(\epsilon_n,q) = -R\epsilon_n J_1(R\epsilon_n)\frac{fm!}{q^{m+1}}\left[\nu+\alpha^{\varphi}q^{\varphi}\right]\left[\frac{1}{q+\nu\epsilon_n^2+\epsilon_n^2\alpha^{\varphi}q^{\varphi}}\right], \tag{8.16}$$

above equation can be written as

$$\bar{\tau}_H(\epsilon_n, q) = \frac{-RJ_1(R\epsilon_n)fm!}{\epsilon_n q^{m+1}} + \frac{RJ_1(R\epsilon_n)fm!}{\epsilon_n} \frac{1}{q^m[q + \nu\epsilon_n^2 + \epsilon_n^2\alpha^\varphi q^\varphi]}. \tag{8.17}$$

By using inverse Hankel Transformation on Eq. (10.16) and considering identity

$$\epsilon^2 = -2R\sum_{n=1}^{\infty} \frac{J_2(\epsilon\epsilon_n)}{\epsilon_n J_1(R\epsilon_n)}, \tag{8.18}$$

we get

$$\bar{\tau}(\epsilon, q) = \left(\frac{\epsilon}{R}\right)^2 \frac{fm!}{q^{m+1}} + \frac{2fm!}{R}\sum_{n=1}^{\infty} \frac{J_2(\epsilon\epsilon_n)}{\epsilon_n J_1(R\epsilon_n)} \frac{1}{q^m(q + \nu\epsilon_n^2 + \epsilon_n^2\alpha^\varphi q^\varphi)}. \tag{8.19}$$

By applying the relation

$$\frac{1}{a-b} = \sum_{k=0}^{\infty} \frac{b^k}{a^{k+1}} \tag{8.20}$$

we obtain

$$\frac{q^{-m}}{q + \nu\epsilon_n^2 + \epsilon_n^2 q^\varphi} = \sum_{k=0}^{\infty} (-\nu\epsilon_n^2)^k \frac{q^{-\varphi k - m - \varphi}}{(q^{1-\varphi} + \alpha^\varphi \epsilon_n^2)^{k+1}}. \tag{8.21}$$

Substituting Eq. (8.21) in Eq. (8.19), the result is

$$\bar{\tau}(\epsilon, q) = \left(\frac{\epsilon}{R}\right)^2 \frac{fm!}{q^{m+1}} + \frac{2fm!}{R}\sum_{n=1}^{\infty} \frac{J_2(\epsilon\epsilon_n)}{\epsilon_n J_1(R\epsilon_n)} \sum_{k=0}^{\infty} (-\nu\epsilon_n^2)^k \frac{q^{-\varphi k - m - \varphi}}{(q^{1-\varphi} + \alpha^\varphi \epsilon_n^2)^{k+1}}. \tag{8.22}$$

Now we apply inverse Laplace Transformation to (8.22) and using generalize $G_{\ell,\, j,\, \zeta}(\gamma\,,\, t)$ function [26]

$$G_{b,\, c,\, \sigma}(\gamma\,, t) = L^{-1}\left\{\frac{s^c}{(s^b - \gamma)^\sigma}\right\} = \sum_{\kappa=0}^{\infty} \frac{\gamma^\kappa\, \Gamma(\sigma + \kappa)}{\Gamma(\sigma)\Gamma(\kappa + 1)} \frac{t^{(\sigma+\kappa)b - c - 1}}{\Gamma[(\sigma + \kappa)b - c]}\,;\ \mathrm{Re}(b\sigma - c) > 0,\ \mathrm{Re}(s) > 0, \quad \left|\frac{\gamma}{s^b}\right| < 1, \tag{8.23}$$

$$\tau(\epsilon, t) = \left(\frac{\epsilon}{R}\right)^2 ft^m + \frac{2fm!}{R}\sum_{n=1}^{\infty} \frac{J_2(\epsilon\epsilon_n)}{\epsilon_n J_1(R\epsilon_n)} \sum_{k=0}^{\infty} (-\nu\epsilon_n^2)^k G_{1-\varphi, -\varphi k - \varphi - m, k+1}(-\alpha^\varphi \epsilon_n^2, t). \tag{8.24}$$

8.3.2 Calculation of the velocity field

To find velocity field, the obtained shear stress given in Eq. (10.31), will be used.

Eq. (15.17) can be written as

$$\frac{\partial\omega(\epsilon, t)}{\partial t} = \frac{1}{\rho}\frac{\partial\tau(\epsilon, t)}{\partial\epsilon} + \frac{2\tau(\epsilon, t)}{\rho\epsilon}. \tag{8.25}$$

By Using (10.31) and (10.32), we get

$$\frac{\partial\omega(\epsilon,t)}{\partial t}=\frac{1}{\rho}\frac{ft^m}{R^2}(4R)+\frac{2fm!}{\rho R}\sum_{n=1}^{\infty}\frac{J_1(\epsilon\epsilon_n)}{J_1(R\epsilon_n)}\sum_{k=0}^{\infty}(-\nu\epsilon_n^2)^k G_{1-\varphi},-\varphi k-\varphi-m,k+1(-\alpha^{\varphi}\epsilon_n^2,t). \quad (8.26)$$

Integrating above relation with respect to time

$$\omega(\epsilon,t)=\frac{4f\epsilon t^{m+1}}{\rho R^2(m+1)}+\frac{2fm!}{\rho R}\sum_{n=1}^{\infty}\frac{J_1(\epsilon\epsilon_n)}{J_1(R\epsilon_n)}\sum_{k=0}^{\infty}(-\nu\epsilon_n^2)^k G_{1-\varphi},-\varphi k-\varphi-m-1,k+1(-\alpha^{\varphi}\epsilon_n^2,t). \quad (8.27)$$

8.4 Limiting cases

8.4.1 Ordinary Second Grade Fluid

For $\varphi\to 1$, Eqs. (10.31) and (10.34) implies that

$$\tau(\epsilon,t)=(\frac{\epsilon}{R})^2 ft^m+\frac{2fm!}{R}\sum_{n=1}^{\infty}\frac{J_2(\epsilon\epsilon_n)}{\epsilon_n J_1(R\epsilon_n)}\{\sum_{k=0}^{\infty}(-\nu\epsilon_n^2)^k G_0,-k-m-1,k+1(-\alpha\epsilon_n^2,t)\}, \quad (8.28)$$

$$\omega(\epsilon,t)=\frac{4f\epsilon t^{m+1}}{\rho R^2(m+1)}+\frac{2fm!}{\rho R}\sum_{n=1}^{\infty}\frac{J_1(\epsilon\epsilon_n)}{J_1(R\epsilon_n)}\sum_{k=0}^{\infty}(-\nu\epsilon_n^2)^k G_0,-k-m-2,k+1(-\alpha\epsilon_n^2,t), \quad (8.29)$$

which are the stress and velocity fields for ordinary second grade fluid performing similar motion. By using identity

$$\sum_{k=0}^{\infty}(-\nu\epsilon_n^2)^k\, G_{0,\,-k-m-1,\,k+1}(-\alpha\epsilon_n^2,t)=\Big(-\frac{1}{\nu}\Big)^m\frac{(1+\alpha\epsilon_n^2)^{m-1}}{\epsilon_n^{2m}}$$

$$\times\left[\exp\left(\frac{-\nu\epsilon_n^2 t}{1+\alpha\epsilon_n^2}\right)-\sum_{j=0}^{m-1}\frac{1}{j\,!}\left(\frac{-\nu\epsilon_n^2 t}{1+\alpha\epsilon_n^2}\right)^j\right]\quad m=1,2,3,..., \quad (8.30)$$

Eqs. (10.35) and (10.36)can be written as

$$\tau(\epsilon,t)=(\frac{\epsilon}{R})^2 ft^m+\frac{2fm!}{R}\sum_{n=1}^{\infty}\frac{J_2(\epsilon\epsilon_n)}{\epsilon_n J_1(R\epsilon_n)}$$

$$\times\Big(-\frac{1}{\nu}\Big)^m\frac{(1+\alpha\epsilon_n^2)^{m-1}}{\epsilon_n^{2m}}\left[\exp\left(\frac{-\nu\epsilon_n^2 t}{1+\alpha\epsilon_n^2}\right)-\sum_{j=0}^{m-1}\frac{1}{j\,!}\left(\frac{-\nu\epsilon_n^2 t}{1+\alpha\epsilon_n^2}\right)^j\right]\quad m=1,2,3,..., \quad (8.31)$$

$$\omega(\epsilon,t)=\frac{4f\epsilon t^{m+1}}{\rho R^2(m+1)}+\frac{2fm!}{\rho R}\sum_{n=1}^{\infty}\frac{J_1(\epsilon\epsilon_n)}{J_1(R\epsilon_n)}$$

$$\times\Big(-\frac{1}{\nu}\Big)^m\frac{(1+\alpha\epsilon_n^2)^{m+1}}{\epsilon_n^{2(m+1)}}\left[\exp\left(\frac{-\nu\epsilon_n^2 t}{1+\alpha\epsilon_n^2}\right)-\sum_{j=0}^{m}\frac{1}{j\,!}\left(\frac{-\nu\epsilon_n^2 t}{1+\alpha\epsilon_n^2}\right)^j\right]\quad m=1,2,3,..., \quad (8.32)$$

By choosing $m=0$ in Eq. (8.31), we get

$$\tau(\epsilon,t)=f\left(\frac{\epsilon}{R}\right)^2+\frac{2f}{R}\sum_{n=1}^{\infty}\frac{J_2(\epsilon\epsilon_n)}{\epsilon_n J_1(R\epsilon_n)}\left[\frac{1}{1+\alpha\epsilon_n^2}\exp\left(\frac{-\nu\epsilon_n^2 t}{1+\alpha\epsilon_n^2}\right)\right] \quad (8.33)$$

The Eq. (8.33) was derived by Fetecau *et al.* [27, Eq.(4.7)]

8.4.2 Newtonian fluid

By taking $\alpha \to 0$ in Eqs. (10.35), (10.36) and (8.33) we get

$$\tau(\epsilon,t) = (\frac{\epsilon}{R})^2 f t^m + \frac{2fm!}{R}\sum_{n=1}^{\infty}\frac{J_2(\epsilon\epsilon_n)}{\epsilon_n J_1(R\epsilon_n)}\sum_{k=0}^{\infty}\frac{(-\nu\epsilon_n^2)^k t^{k+m}}{(k+m)!}, \tag{8.34}$$

,

$$\omega(\epsilon,t) = \frac{4f\epsilon t^{m+1}}{\rho R^2(m+1)} + \frac{2fm!}{\rho R}\sum_{n=1}^{\infty}\frac{J_1(\epsilon\epsilon_n)}{J_1(R\epsilon_n)}\sum_{k=0}^{\infty}\frac{(-\nu r_n^2)^k t^{k+m}}{(k+m)!}, \tag{8.35}$$

$$\tau(\epsilon,t) = f\left(\frac{\epsilon}{R}\right)^2 + \frac{2f}{R}\sum_{n=1}^{\infty}\frac{J_2(\epsilon\epsilon_n)}{\epsilon_n J_1(Rr\epsilon_n)}e^{-\nu\epsilon_n^2 t}. \tag{8.36}$$

. These are the outcomes for Newtonian fluid for both velocity and stress fields . The solution obtained by Fetecau *et al.* [27, Eq.(4.11)] recovered as Eq. (8.36).

8.5 Numerical Results and discussion

In the present study, rotational motion of fractional second grade fluid in a circular pipe is studied. Initially the fluid and cylinder both are at rest. The motion is developed by the influence of the non differential shear stress on the surface of the cylinder. The fluid gradually set in its rotational motion due to couple applied by the cylinder on the fluid. The exact solution represented by Eqs. (10.31) and (10.34) are derived by means of finite Hankel and Laplace transforms. The obtained solutions are represented in terms og generalized function to increase the productivity of results. We also find solution for both cases i.e. ordinary second grade and Newtonian fluids. To enhance the understanding of the results, graphical analysis also given in the end.

The impact of time on velocity and shear stress is represented by Fig. 13.2. It is clear that both are increasing functions of time. Fig. 8.4 represent the impact of constant f on stress and velocity functions. The behaviour of both functions is similar to time. The effect of fractional parameter φ on velocity and stress fields is represented by Fig. 8.3. It is noted that velocity is decreasing but stress is increasing function of φ. Fig. 14.2 depicts the effect of α on velocity and tangential stress which is exactly opposite to φ. Fig. 8.5 show the comparison of different fluid model. In all figures, value of velocity nd stress fields are zero at the center of the cylinder and very smoothly increase up to maximum at the boundary of the pipe. All the graphs satisfied all initial and boundary conditions.

In graphical explanation we note following aspects

- It is observed that both fields(velocity and stress) are increasing function of time.Also noted that the value of both fields goes on decreasing from maximum (on the boundary) to minimum value (zero)

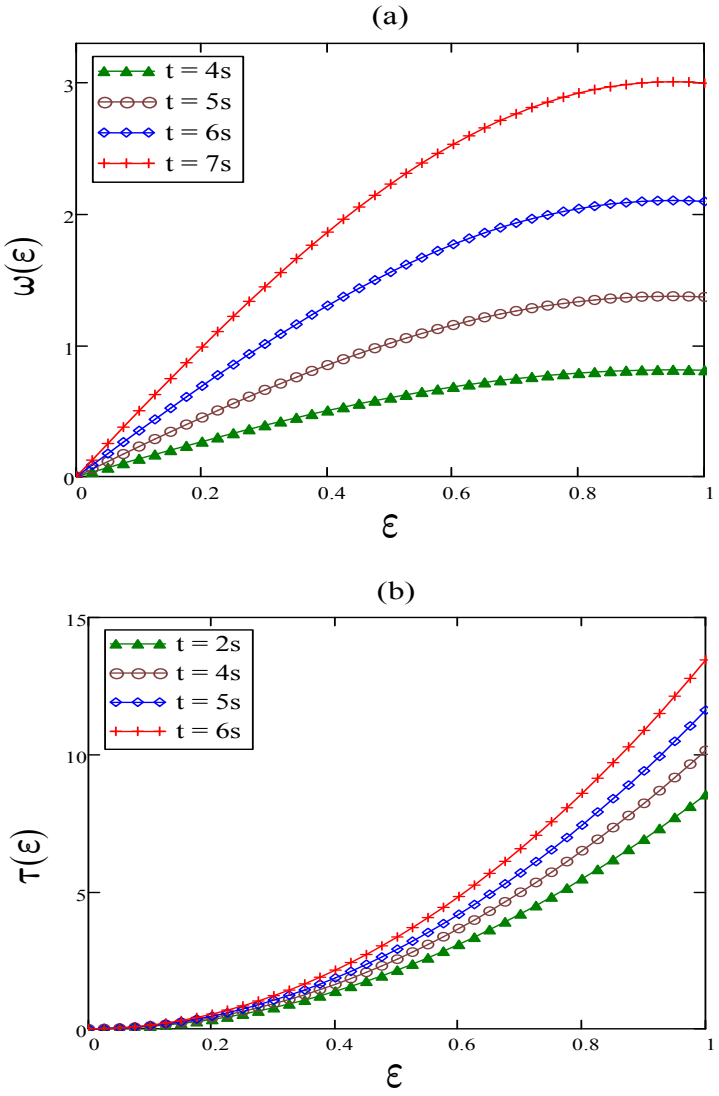

Figure 8.1: Variation in velocity field $\omega(r,t)$ and shear stress $\tau(r)$ given by Eqs. (10.31) and (10.34), for different values of t and $R=1, m=1, \nu=0.003, f=2, \alpha=0.88, \varphi=0.5, \rho=900$

smoothly inside the cylinder up to center.

- Increasing the value of fractional parameter the stress increases but velocity decreases.
- The impact of material constant α on velocity and stress functions is exactly opposite to fractional parameter.
- The influence of constant f is opposite to time.
- It is clear that Newtonian fluid is quickest as compared to current model i.e. fractional second grade.
- The outcomes results for ordinary second grade and Newtonian fluids obtained by Fetecau *et al.* [27, Eq.(4.7), (4.11)] are recovered.
- In all figures, SI units are used.
- All the roots are approximated by $\epsilon_n = (4n-3)\frac{\pi}{4R}$.

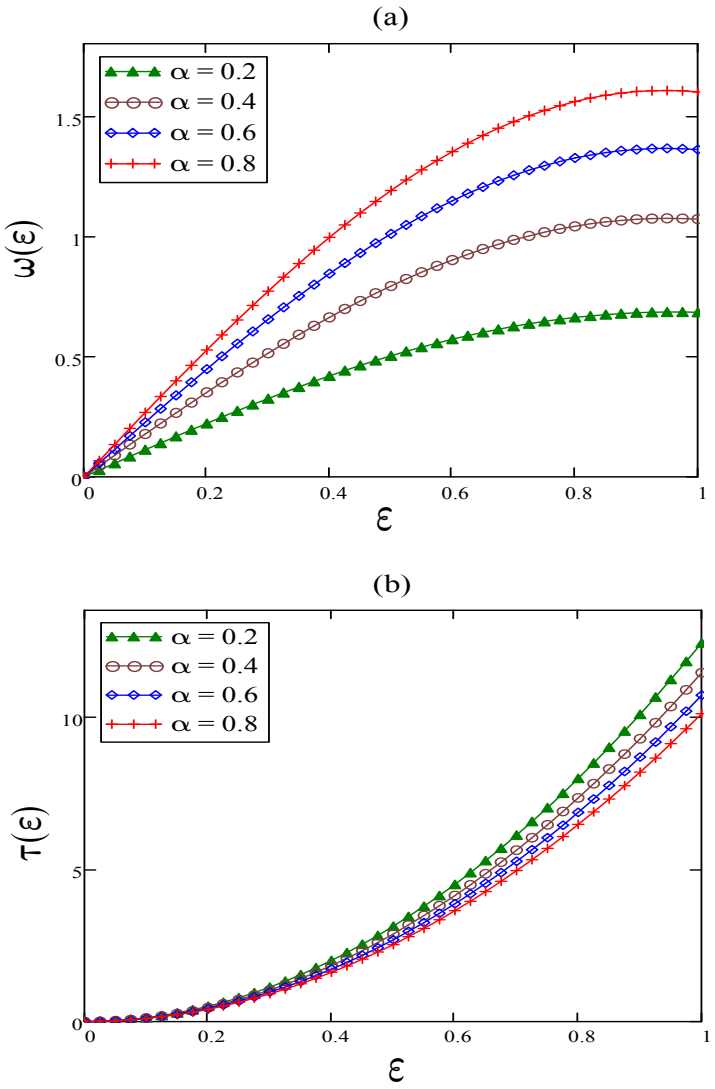

Figure 8.2: Variation in velocity field $\omega(r,t)$ and shear stress $\tau(r)$ given by Eqs.(10.31) and (10.34, for different values of α and $R=1, m=1, \nu=0.003, f=2, \varphi=0.45, \rho=900, t=5$

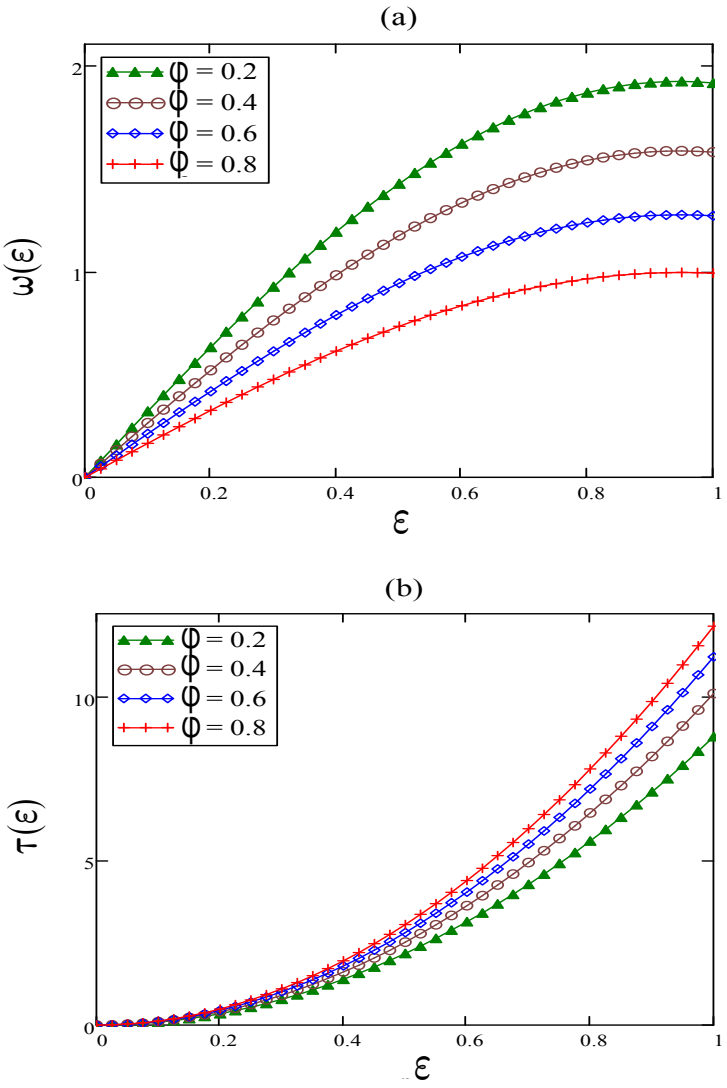

Figure 8.3: Variation in velocity field $\omega(r,t)$ and shear stress $\tau(r)$ given by Eqs.(10.31) and (10.34, for different values of φ and $R=1, m=1, \nu=0.003, f=2, \alpha=0.71, \rho=900, t=2$

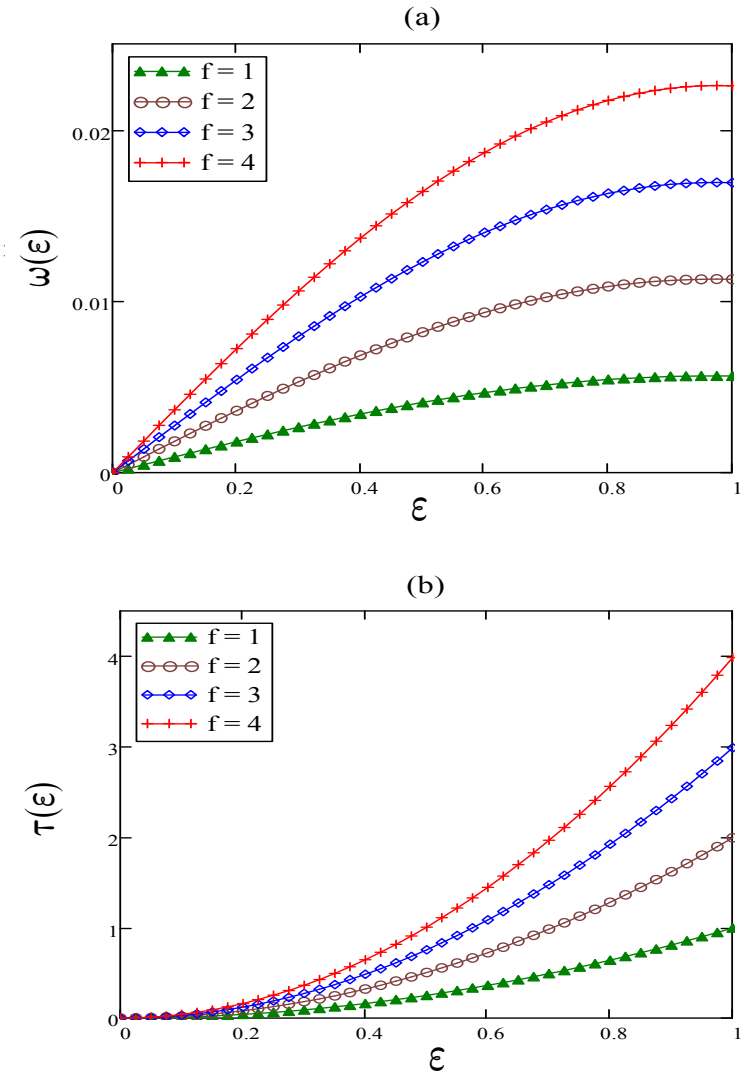

Figure 8.4: Variation in velocity field $\omega(r,t)$ and shear stress $\tau(r)$ given by Eqs.(10.31) and (10.34, for different values of f and $R=1, m=1, \nu=0.003, \alpha=0.88, \varphi=0.5, \rho=900, t=1$

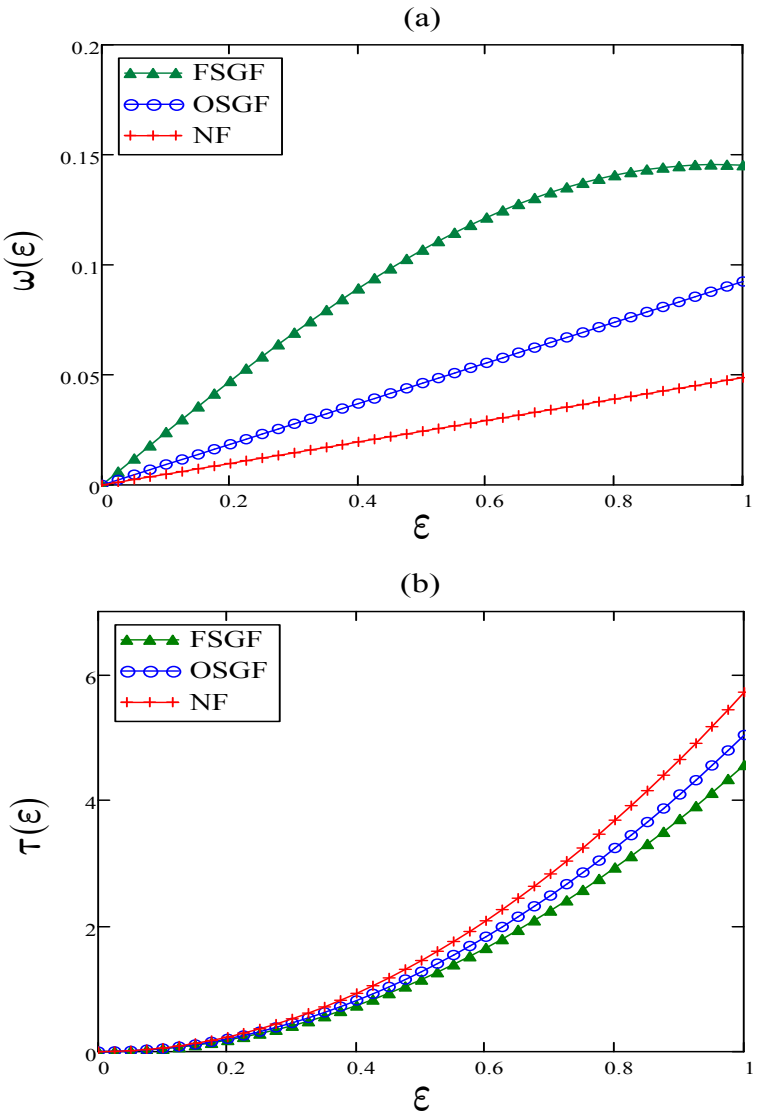

Figure 8.5: Comparison of different non-Newtonian fluids for $R = 1, m = 1, \nu = 0.0035, f = 2, \alpha = 0.88, \varphi = 0.5, \rho = 900, 2.2$

Bibliography

[1] Zhaosheng, Y. & Jianzhong, L. (1998). Numerical research on the coherent structure in the viscoelastic second-order mixing layers. *Applied Mathematics and Mechanics, 19*(8), 717-723.

[2] Ting, T. W. (1963). Certain non-steady flows of second-order fluids. *Archive for Rational Mechanics and Analysis*, 14(1), 1-26.

[3] Srivastava, P. N. (1966). non-steady helical flow of a visco-elastic liquid(nonsteady helical flow of viscoelastic liquid contained in circular cylinder, noting occurrence of oscillations in fluid decaying exponentially with time). *Archiwum Mechaniki Stosowanej, 18*(2), 145-150.

[4] Waters, N. D. & King, M. J. (1971). The unsteady flow of an elastico-viscous liquid in a straight pipe of circular cross section. Journal of Physics D: Applied Physics, 4(2), 204.

[5] Tong, D. & Liu, Y. (2005). Exact solutions for the unsteady rotational flow of non-Newtonian fluid in an annular pipe", *Internat. J. Engrg. Sci. 43* 281-289.

[6] Tong, D., Wang, R. & Yang,H. (2005). Exact solutions for the flow of non-Newtonian fluid with fractional derivative in an annular pipe, *Sci. China Ser. G 48,* 485-496.

[7] Fetecau, C. Mahmood, A.& Vieru, D. (2008). Some exact solutions for the helical flow of a generalized Oldroyd-B fluid in a circular cylinder, *Comput. Math. Appl. 56*, 3096-3108.

[8] Khan, M. Hyder A. S. & Qi, H. (2009.)Exact solutions of starting flows for a fractional Burgers fluid between coaxial cylinders, *Nonlinear Anal. Real World Appl. 10* 1775-1783.

[9] C. Fetecau, A. Mahmood & M. Jamil, Exact solutions for the flow of a viscoelastic fluid induced by a circular cylinder subject to a time dependent shear stress, *Commun. nonlinear Sci. Numer. Simul. 15* (2010) 3931-3938.

[10] Sadiq, N., Imran, M., Safdar, R., Tahir, M., Javaid, M. and Younas, M. (2018). Exact Solution for Some Rotational Motions of Fractional Oldroyd-B Fluids Between Circular Cylinders. *Punjab Univ. J. Math, 50*, 39-59.

[11] Tahir, M., Naeem, M. N., Javaid, M., Younas, M., Imran, M., Sadiq, N., & Safdar, R. (2018). Unsteady flow of fractional Oldroyd-B fluids through rotating annulus. *Open Physics, 16*(1), 193-200.

[12] A. Germant, On fractional differentials, *Philos. Mag. 25* (1938) 540-549.

[13] Bagley R. L. & Torvik, P. J. (1983). A theoretical basis for the application of fractional calculus to viscoelasticity, *J. Rheol. 27* 201-210.

[14] Makris, N., Dargush, G. F. Constantinou, M. C. (1993). Dynamic analysis of generalized viscoelastic fluids. *Journal of Engineering Mechanics, 119*(8), 1663-1679.

[15] Jamil, M., Khan, N. A., & Rauf, A. (2012). Oscillating flows of fractionalized second grade fluid. *ISRN Mathematical Physics,* 2012.

[16] Khan, A. and Zaman, G. (2015). Unsteady magnetohydrodynamic flow of second grade fluid due to impulsive motion of plate. *Electronic Journal of Mathematical Analysis and Applications, 3*(1), 215-227.

[17] Shah, N. A. &Khan, I. (2016). Heat transfer analysis in a second grade fluid over and oscillating vertical plate using fractional Caputo–Fabrizio derivatives. *The European Physical Journal C, 76*(7), 362.

[18] Raza, N., Abdullah, M., Butt, A. R., Awan, A. U., & Haque, E. U. (2018). Flow of a second grade fluid with fractional derivatives due to a quadratic time dependent shear stress. *Alexandria engineering journal, 57*(3), 1963-1969.

[19] Jamil, M., & Fetecau, C. (2010). Helical flows of Maxwell fluid between coaxial cylinders with given shear stresses on the boundary. *Nonlinear Analysis: Real World Applications, 11*(5), 4302-4311.

[20] Kamran, M., Imran, M., Athar,M. & Imran, M. A. (2012). On the unsteady rotational flow of fractional Oldroyd-B fluid in cylindrical domains, *Meccanica 47*(3) 573-584.

[21] Imran, M., Athar, M., & Kamran, M. (2011). On the unsteady rotational flow of a generalized Maxwell fluid through a circular cylinder. *Archive of Applied Mechanics, 8*1(11), 1659-1666.

[22] Fetecau, C., Rubbab, Q., Akhter, S. & Fetecau, C. (2016). New methods to provide exact solutions for some unidirectional motions of rate type fluids. *Thermal Science, 20*(1) 7-20.

[23] Podlubny, I. (1999)., Fractional Differential Equations, Academic Press, San Diego.

[24] Debnath, L. & Bhatta, D. (2007). Integral transfroms and their applications, Second Ed., Chapman and Hall/CRC Press, Boca Raton.

[25] Fetecau, C., Rana M., Nigar N., & Fetecau, C. (2014), First exact solutions for flows of rate type fluids in a circular duct that applies a constant couple to the fluid, *Z. Naturforsch. 69a* 232-238

[26] Lorenzo,C.F. & Hartley, T.T. (1999).Generalized functions for the fractional calculus, NASA/TP

[27] Fetecau, C., Imran, M., Fetecau, C., & Burdujan, I. (2010). Helical flow of an Oldroyd-B fluid due to a circular cylinder subject to time-dependent shear stresses. *Zeitschrift für angewandte Mathematik und Physik, 61*(5), 959-969.

CHAPTER 9

Physics-Informed Neural Networks for Multi-Scale Hepatitis Modeling

Khadija Tul Kubra[†,], **Rooh Ali**[†,*,], **Muniba Nasir**[†], **Bushra Ujala**[‡], **Samra Gulshan**[†,*,], **Muhammad Abid**[†]

[†] *Department of Mathematics, Government College University, Faisalabad 38000, Pakistan.*

[‡] *Department of Radiology, Faisalabad medical University, Allied Hospital Faisalabad 38000, Pakistan.*

[*]**Corresponding Author(s):** **Rooh Ali:** roohali@gcuf.edu.pk; **Samra Gulshan:** samragulshan@gcuf.edu.pk

Abstract: *Hepatitis infections pose a persistent global health challenge, demanding advanced modeling techniques to understand their complex dynamics. This chapter introduces a novel framework that integrates a multi-scale, mechanistic model of hepatitis transmission with the power of Deep Neural Networks (DNNs). We move beyond traditional solvers by employing Physics-Informed Neural Networks (PINNs) to solve the system of nonlinear ordinary differential equations. This approach uses automatic differentiation to ensure the learned solutions strictly adhere to the underlying biological laws described by the model. Our DNN-based solver demonstrates remarkable accuracy and robustness, efficiently handling noisy synthetic and clinical data where classical methods may struggle. We leverage this framework not only for simulation but also for sensitivity analysis and parameter estimation, identifying key drivers of disease spread and persistence, such as transmission rate and viral production. The primary novelty of this work is the successful application of PINNs to multi-scale infectious disease modeling, specifically for hepatitis. This chapter provides a scalable, data-efficient toolkit that bridges mechanistic understanding with data-driven learning, offering significant potential for improving clinical intervention strategies and public health policy planning.*

Keywords: Hepatitis Dynamics; Deep Neural Networks (DNNs); Neural Network Solvers; Parameter Estimation; Sensitivity Analysis; AI-Assisted Disease Modeling; Multi-Scale Modeling.

9.1 Introduction

The global burden of hepatitis remains a critical public health challenge, with chronic and acute infections affecting millions worldwide, leading to severe liver diseases and significant mortality [1, 2, 3, 4, 5, 6]. The complex nature of hepatitis transmission and progression, involving multiple biological scales–from within-host viral dynamics to population-level disease spread–necessitates advanced modeling approaches to better understand and control the disease. Traditional mathematical model, particularly compartmental ordinary differential equation (ODE) systems, have provided foundational insights into hepatitis dynamics by categorizing populations into susceptible, exposed, infected, and recovered classes [7, 8, 9, 10, 11, 12, 13]. However, these models often face challenges when dealing with non-linearities, parameter uncertainties, and computational inefficiencies, especially when integrating multiscale biological processes and real-world data.

There is an increasing interest in using data-driven techniques to complement and enhance mechanistic models in infectious disease epidemiology, with the rapid advancement of artificial intelligence, particularly deep learning. Recent advances in deep learning have significantly enhanced the modeling and interpretation of complex dynamical systems across diverse domains. Explainability in deep neural networks (DNNs) has been extensively studied, with methods like feature attribution and surrogate models enabling transparency in high-dimensional applications, as surveyed by Samek *et al.* [14]. In dynamical systems, physics-guided deep learning has emerged as a powerful framework, integrating domain knowledge with data-driven approaches to improve generalizability, as highlighted by Wang *et al.* [15]. Similarly, Huang *et al.* [16] explore the synergy between partial differential equations (PDEs) and DNNs, demonstrating their efficacy in solving high-dimensional PDEs with nonlinear dynamics. Applications extend to epidemiology, where Mustafa *et al.* [17] employ DNNs to model Marburg virus dynamics, showcasing their utility in predictive healthcare analytics. The intersection of machine learning and nonlinear dynamics is further emphasized by Tang *et al.* [18], who discuss how DNNs capture chaotic and network-driven phenomena. Koopman operator theory, combined with DNNs, offers a data-driven paradigm for global linearization of nonlinear systems, as investigated by Yeung *et al.* [19], while Ogunmolu *et al.* [20] leverage deep dynamic networks for nonlinear system identification. Beyond engineering, Durstewitz *et al.* [21] illustrate the transformative role of DNNs in psychiatry, modeling complex neural and behavioral data. Collectively, these studies underscore the versatility of deep learning in deciphering and predicting nonlinear behaviors, motivating their adoption in interdisciplinary research.

Deep learning and neural networks have made it much easier to model and analyze complex nonlinear dynamical systems. Wang *et al.* [22] demonstrated the efficacy of deep neural networks (DNNs) in functional data analysis, highlighting their capability to capture intricate patterns in high-dimensional data. Similarly, Shobana *et al.* [23] proposed a novel recurrent neural network (RNN) architecture for system identification, providing a comparative study on stability and performance in nonlinear dynamics. The application of DNNs in model order reduction has been explored by Eivazi *et al.* [24], who success-

fully reduced the computational complexity of unsteady flow simulations while preserving dynamical features. Further extending these approaches, Aprile [25] employed deep learning-based Koopman analysis for model reduction and linearization of physiological systems, emphasizing the role of data driven methods in simplifying high-dimensional dynamics. Huynh [26] contributed to this domain by integrating domain-specific knowledge into machine learning frameworks, enhancing interpretability and robustness in multi-scale modeling. Additionally, Guo *et al.* [27] reviewed dynamic neural network structures, underscoring their adaptability in real-time applications and complex system modeling. Collectively, these studies illustrate the transformative potential of deep learning in addressing challenges related to nonlinear dynamics, model reduction, and system identification, providing a strong foundation for further research in this field.

Our study proposes a hybrid modeling framework that combines the interpretability of mechanistic SEIR-type hepatitis models with the flexibility of deep neural networks (DNNs), leveraging automatic differentiation for efficient parameter estimation and sensitivity analysis [28]. This approach captures viral load kinetics and treatment effects, offering a multi-scale perspective to improve hepatitis research [29]. Clinically, it enables personalized treatment strategies, while public health applications include evaluating outbreak containment and vaccination programs. The integration of mechanistic modeling with machine learning also advances scientific machine learning, with potential applications to other infectious diseases [30]. Overall, this framework bridges biology, mathematics, and AI to enhance hepatitis control efforts.

This work introduces a novel multi-scale mathematical model for hepatitis that integrates population-level SEIR dynamics with within-host viral load progression, and develops a pioneering Physics-Informed Neural Network (PINN) framework to solve the resulting complex, nonlinear system. [31] Our approach leverages deep learning's universal approximation capabilities to handle dynamics where classical solvers may fail, while maintaining interpretability through embedded physical constraints. The methodology demonstrates exceptional robustness in handling real-world data imperfections, successfully assimilating noisy clinical data while maintaining predictive accuracy. Furthermore, the research provides practical tools for public health decision-making by identifying critical intervention points through sensitivity analysis and enabling rapid scenario testing for emerging strains and treatment strategies.

This chapter is organized as follows: In Section 9.2, we propose a new mathematical model by incorporating the viral load effect. In Section 9.3, we analyze our proposed mathematical model qualitatively, establishing the positivity and feasibility of the model. The next Section 9.4, presents the deep neural network approximation framework, highlighting the data loss, total loss, and neural network architecture including the network topology under the physics informed neural network (PINN) paradigm. Section 9.5 provides further qualitative analysis, including the disease-free equilibrium point, the basic reproduction number, and the endemic equilibrium point. In Section 9.6, the PINN is trained by minimizing a composite loss function that integrates model dynamics and data constraints. Finally, Section 9.7 presents the graphical results along with a discussion and interpretation of the outcomes. At the end, Section 9.8 describes the concluding remarks and future directions.

9.2 Mathematical Model Formulation

In this chapter we introduced a new mathematical model of hepatitis including susceptible, exposed, infected, recovered and viral load in host populations. The model incorporates both direct and indirect transmission routes, allowing for a more comprehensive understanding of disease dynamics. Additionally, our framework introduces three key innovations to hepatitis modeling, including a hybrid mechanistic-data-driven approach that combines traditional compartmental modeling with deep neural networks, enabling both interpretability and flexibility. End-to-end differentiability through automatic differentiation, permitting efficient parameter estimation and sensitivity analysis without finite-difference approximation. Universal function approximation capabilities of neural networks to handle complex, non-linear dynamics where classical solvers may fail or require restrictive assumptions. The hepatitis transmission dynamics are governed by the coupled nonlinear system:

$$\left.\begin{aligned} \frac{dS}{dt} &= \Lambda - \beta SI - \mu S \\ \frac{dE}{dt} &= \beta SI - (\alpha + \mu)E \\ \frac{dI}{dt} &= \alpha E - (\gamma + \mu + \delta)I - pI \\ \frac{dR}{dt} &= \gamma I + pI - \mu R \\ \frac{dV}{dt} &= kI - cV \end{aligned}\right\} \tag{9.1}$$

With initial conditions, $S(0) = S_o$, $E(0) = E_o$, $I(0) = I_o$, $R(0) = R_o$, and $V(0) = V_o$. Where $(S(0) = S_o, E(0), I(0), R(0), V(0)) \in \mathbb{R}^6_+$. Here, it is assumed that the functions $(B(t), Y(t), N(t), I(t), R(t), D(t))$ and their derivatives are continuous for $t \geq 0$.

9.2.1 Parameter Analysis and Dynamical Flow

The parameters in the proposed hepatitis model play a crucial role in governing the dynamic flow of the population across different compartments. The transmission rate (β) determines the steepness of infection waves, directly influencing how quickly susceptible individuals (S) transition to the exposed class (E). The average latency period (α) regulates the delay before exposed individuals become infectious (I), while the recovery rate (γ) dictates the duration of infectiousness before transitioning to the recovered compartment (R). Treatment interventions, represented by the parameter (p), accelerate recovery, effectively reducing the infectious pool and altering the natural progression of the disease. Additionally, the viral load dynamics (V) are governed by the production rate (k) and clearance rate (c), where the ratio k/c determines the equilibrium viral concentration in infected hosts. These parameters collectively shape the disease trajectory, influencing peak infection times, endemic stability, and the effectiveness of control measures. The interplay between population-level transmission and within-host viral dynamics highlights the multi-scale nature of hepatitis progression, with each parameter contributing to the overall

epidemiological behavior. Sensitivity analysis of these parameters can reveal critical intervention points for mitigating disease spread and optimizing treatment strategies. The model parameters (Table 9.1) exhibit distinct roles in the disease progression:

Symbol	Name	Description	Units
State Variables			
$S(t)$	Susceptible	Individuals capable of contracting hepatitis	Individuals
$E(t)$	Exposed	Infected but not yet infectious individuals	Individuals
$I(t)$	Infectious	Infected and capable of transmitting hepatitis	Individuals
$R(t)$	Recovered	Individuals who have recovered with immunity	Individuals
$V(t)$	Viral Load	Concentration of virus within host population	Viral particles/mL
$N(t)$	Total Population	Sum of all compartments: $S + E + I + R$	Individuals
Model Parameters			
Λ	Recruitment Rate	Rate of new susceptible individuals	individuals·time^{-1}
β	Transmission Rate	Disease transmission rate	(individuals·time)$^{-1}$
μ	Natural Mortality Rate	Background mortality rate	time^{-1}
α	Progression Rate	Transition from exposed to infectious	time^{-1}
γ	Natural Recovery Rate	Recovery rate without treatment	time^{-1}
δ	Disease-Induced Death Rate	Mortality rate due to infection	time^{-1}
p	Treatment Rate	Recovery rate due to treatment	time^{-1}
k	Viral Production Rate	Viral production per infected individual	particles·ind^{-1}·time^{-1}
c	Viral Clearance Rate	Rate of viral clearance from host	time^{-1}

Table 9.1: Core Epidemiological Model Parameters and State Variables.

9.2.2 Biological Interpretations

The model captures three biological scales:

- **Population-level** (S, E, I, R): Traditional SEIR structure modified for hepatitis B/C characteristics
- **Within-host** (V): Viral load dynamics coupled to infectious population
- **Intervention effects**: Treatment term pI directly reduces infectious pool while antiviral effects are implicitly modeled through k reduction

9.3 Qualitative Analysis

The given hepatitis ODE model ensures that all state variables remain non-negative for all $t \geq 0$ time provided that the initial conditions are non-negative. It is easily seen that if any compartment approaches zero, its derivative becomes non-negative, preventing negative solutions. For instance, when $S \to 0$, then $\frac{dS}{dt} = \Lambda$, ensuring $S(t) \geq 0$. Similarly, the other compartments E, I, R, and V remain non-negative due to their respective governing equations. Furthermore, the total population $N = S + E + I + R$ is bounded, is shown by the inequality $\frac{dN}{dt} \leq \Lambda - \mu N$, which converges to $N \leq \frac{\Lambda}{\mu}$. The viral load V is also bounded,

since $\frac{dV}{dt} = kI - cV$ implies that $V \leq \frac{k\Lambda}{c\mu}$. Thus, the biologically feasible region

$$\Omega = \left\{ (S, E, R, I, V) \in \mathbb{R}_5^+ \quad \middle| \quad 0 \leq N(t) \leq \frac{\Lambda}{\mu} \quad \text{and} \quad 0 \leq V(t) \leq \frac{k\Lambda}{c\mu} \right\}, \tag{9.2}$$

is positively invariant. This confirms that the model is well-posed and epidemiologically meaningful for analysis.

9.4 Deep Neural Network Approximation

Here, we defines the physics-informed loss function, $\mathcal{L}_{physics}$, which is the cornerstone of the Physics-Informed Neural Network (PINN) methodology. This term ensures that the neural network's solution, $\mathcal{NN}_\theta(t) = [\hat{S}(t), \hat{E}(t), \hat{I}(t), \hat{R}(t), \hat{V}(t)]$, does not merely fit data but also strictly adheres to the underlying biological laws described by the system (9.1). The physics loss enforces that the DNN satisfies the ODE dynamics:

$$\mathcal{L}_{physics} = \left\| \begin{array}{l} \dfrac{d\hat{S}}{dt} - (\Lambda - \beta\hat{S}\hat{I} - \mu\hat{S}) \\ \dfrac{d\hat{E}}{dt} - (\beta\hat{S}\hat{I} - (\alpha + \mu)\hat{E}) \\ \dfrac{d\hat{I}}{dt} - (\alpha\hat{E} - (\gamma + \mu + \delta)\hat{I} - p\hat{I}) \\ \dfrac{d\hat{R}}{dt} - (\gamma\hat{I} + p\hat{I} - \mu\hat{R}) \\ \dfrac{d\hat{V}}{dt} - (k\hat{I} - c\hat{V}) \end{array} \right\|^2 \tag{9.3}$$

Where all derivatives are computed via automatic differentiation of $\mathcal{NN}_\theta(t)$. The loss is computed as the squared L_2-norm of the residuals of each governing equation. In essence, for each state variable, we calculate the difference between its time derivative (computed via automatic differentiation of the DNN) and the right-hand side of the corresponding ODE. By minimizing $\mathcal{L}_{physics}$, we train the DNN to become a continuous, differentiable function that inherently satisfies the dynamics of the hepatitis transmission model. This approach encodes the "physics" or "biology" of the system directly into the learning process, guaranteeing that the neural network's predictions are physically plausible and consistent with the mechanistic model, even in regions where data is sparse or absent.

9.4.1 Data Loss (if measurements available)

For any observed data points $(t_i, [S_i, E_i, I_i, R_i, V_i])$:

$$\mathcal{L}_{data} = w_S|\hat{S}(t_i) - S_i|^2 + w_E|\hat{E}(t_i) - E_i|^2 + w_I|\hat{I}(t_i) - I_i|^2 + w_R|\hat{R}(t_i) - R_i|^2 + w_V|\hat{V}(t_i) - V_i|^2 \tag{9.4}$$

Where w_* are optional weighting factors. Equation (9.4) defines the data fidelity loss, $\mathcal{L}_{data}$, which anchors the neural network's predictions to empirical observations. This component of the total loss

function is critical for calibrating the model to real-world scenarios. It measures the mean squared error between the DNN's output and available measurement data at specific time points t_i. These data points $(S_i, E_i, I_i, R_i, V_i)$ could originate from clinical reports, historical outbreak records, or synthetic data generated for validation.

The inclusion of optional weighting factors $w_S, w_E, \ldots, w_V$ allows the model to account for variables with different scales (e.g., population size vs. viral concentration) or to express greater confidence in certain measurements over others. In the proposed hybrid framework, $\mathcal{L}_{data}$ ensures that the solution is not only physically consistent but also empirically accurate, effectively bridging the gap between theoretical modeling and observed phenomena.

9.4.1.1 Total Loss

$$\mathcal{L}_{total} = \mathcal{L}_{physics} + \lambda \mathcal{L}_{data} \tag{9.5}$$

With λ controlling the data fidelity term (set $\lambda = 0$ for purely physics-informed learning).

9.4.2 Neural Network Architecture

The proposed Physics-Informed Neural Network (PINN) architecture for approximating solutions to the hepatitis model (Eq. 9.1) consists of the following components:

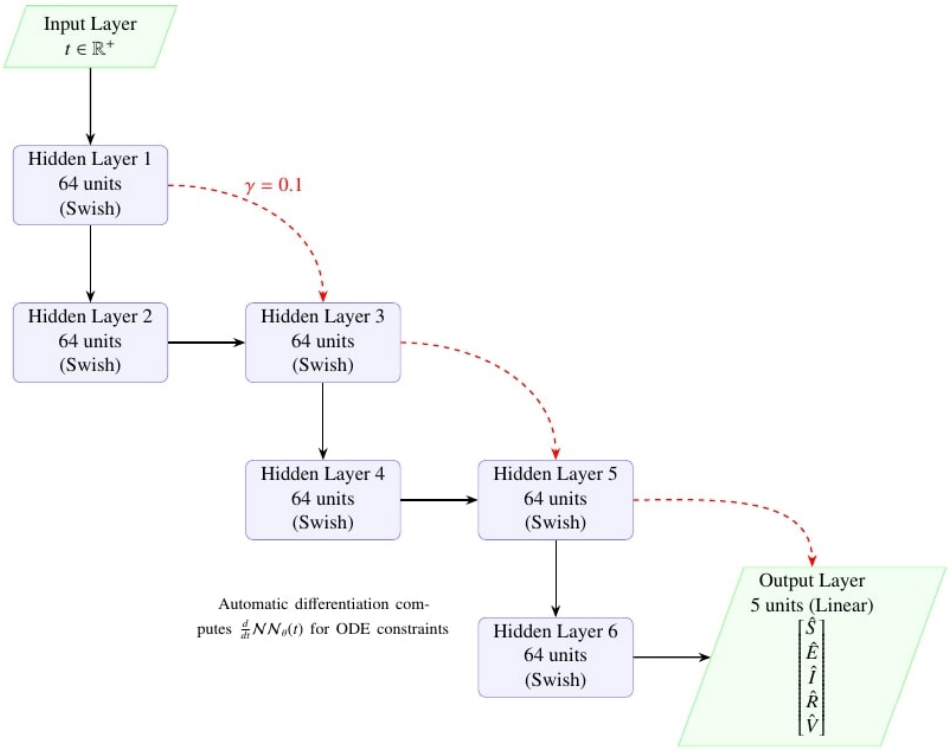

Figure 9.1: Physics-Informed Neural Network (PINN) architecture with six hidden layers and skip connections for solving the hepatitis ODE system.

9.4.2.1 Network Topology

Input Layer: Single input node: $t \in [0, T_{max}]$, normalized to $[0, 1]$ range for numerical stability

Hidden Layers: 6 fully-connected layers with Swish activation ($\beta = 1$):

$$\phi(z) = z \cdot \sigma(z), \quad \sigma(z) = \frac{1}{1 + e^{-z}} \tag{9.6}$$

Layer widths: $[64, 64, 64, 64, 64, 64]$

- Skip connections every 2 layers as $h^{(\ell+2)} = h^{(\ell)} + 0.1 \cdot \mathcal{F}(h^{(\ell+1)})$, where $\mathcal{F}$ represents the layer transformation

Output Layer: Linear transformation to 5 output units:

$$\left[\hat{S}(t)\ \hat{E}(t)\ \hat{I}(t)\ \hat{R}(t)\ \hat{V}(t)\right] = W^{(out)} h^{(6)} + b^{(out)} \tag{9.7}$$

9.5 Equilibria, Basic Reproduction Number

To find the equilibria the proposed hepatitis model is written as:

$$\left.\begin{aligned} \Lambda - \beta SI - \mu S &= 0, \\ \beta SI - (\alpha + \mu)E &= 0, \\ \alpha E - (\gamma + \mu + \delta)I - pI &= 0, \\ \gamma I + pI - \mu R &= 0, \\ kI - cV &= 0, \end{aligned}\right\} \tag{9.8}$$

Equation (9.8) represents the steady-state formulation of the dynamic hepatitis model (Eq. 9.1), obtained by setting all time derivatives to zero ($\frac{dS}{dt} = \frac{dE}{dt} = \cdots = 0$). This system of algebraic equations is solved to find the equilibrium points of the model—the constant solutions where the state variables no longer change over time.

Analyzing these equilibria is fundamental to understanding the long-term behavior of the disease. The solutions to this system yield two critical states: the Disease-Free Equilibrium (DFE), where the infection is entirely absent from the population, and the Endemic Equilibrium (EE), where the infection persists at a constant level. The stability of these points, determined by the basic reproduction number $\mathcal{R}_0$ derived from this system, predicts whether the disease will die out or become an ongoing public health concern, providing vital insights for planning intervention strategies.

9.5.1 Disease-Free Equilibrium (DFE)

The DFE occurs when $E = I = V = 0$. Setting the derivatives to zero $\frac{dS}{dt} = \Lambda - \mu S = 0$ implies that $S = \frac{\Lambda}{\mu}$. Thus, the DFE is:

$$\text{DFE} = \left(S^0, E^0, I^0, R^0, V^0\right) = \left(\frac{\Lambda}{\mu}, 0, 0, 0, 0\right). \tag{9.9}$$

9.5.2 Basic Reproduction Number

The basic reproduction number is computed using the next-generation matrix method. We consider the infected compartments E, I, V.Then, the new infections matrix $\boldsymbol{F}$ and transitions matrix $\boldsymbol{V}$ are given as:

$$\boldsymbol{F} = \begin{pmatrix} \beta SI \\ 0 \\ 0 \end{pmatrix}, \qquad \boldsymbol{V} = \begin{pmatrix} (\alpha+\mu)E \\ -\alpha E + (\gamma+\mu+\delta+p)I \\ -kI + cV \end{pmatrix}. \tag{9.10}$$

At the DFE $(S^0, 0, 0, 0, 0)$, the Jacobians are:

$$F = \begin{pmatrix} 0 & \beta S^0 & 0 \\ 0 & 0 & 0 \\ 0 & 0 & 0 \end{pmatrix}, \qquad V = \begin{pmatrix} \alpha+\mu & 0 & 0 \\ -\alpha & \gamma+\mu+\delta+p & 0 \\ 0 & -k & c \end{pmatrix}. \tag{9.11}$$

The inverse of V is:

$$V^{-1} = \begin{pmatrix} \frac{1}{\alpha+\mu} & 0 & 0 \\ \frac{\alpha}{(\alpha+\mu)(\gamma+\mu+\delta+p)} & \frac{1}{\gamma+\mu+\delta+p} & 0 \\ \frac{\alpha k}{c(\alpha+\mu)(\gamma+\mu+\delta+p)} & \frac{k}{c(\gamma+\mu+\delta+p)} & \frac{1}{c} \end{pmatrix}. \tag{9.12}$$

$$FV^{-1} = \begin{pmatrix} \frac{\alpha\beta S^0}{(\alpha+\mu)(\gamma+\mu+\delta+p)} & \frac{\beta S^0}{\gamma+\mu+\delta+p} & 0 \\ 0 & 0 & 0 \\ 0 & 0 & 0 \end{pmatrix}. \tag{9.13}$$

The basic reproduction number $\mathcal{R}_0$ is the spectral radius (Dominant Eigenvalue) of FV^{-1}:

$$\mathcal{R}_0 = \frac{\alpha\beta S^0}{(\alpha+\mu)(\gamma+\mu+\delta+p)}. \tag{9.14}$$

Substituting $S^0 = \frac{\Lambda}{\mu}$:

$$\mathcal{R}_0 = \frac{\alpha\beta\Lambda}{\mu(\alpha+\mu)(\gamma+\mu+\delta+p)}. \tag{9.15}$$

9.5.3 Endemic Equilibrium (EE)

The EE occurs when $I \neq 0$. Solving the steady-state system (9.8) we obtained the unique endemic equilibrium points which is given as:

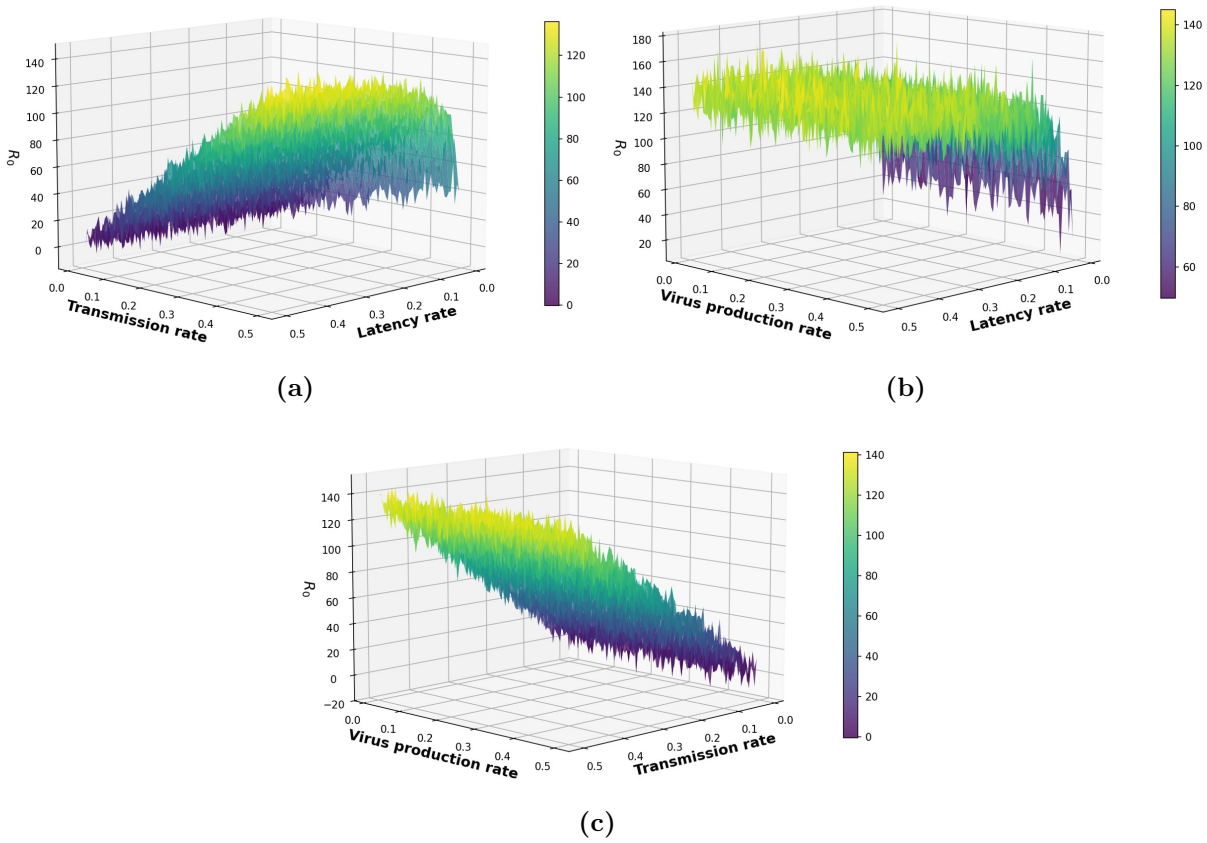

Figure 9.2: Sensitivity analysis of the basic reproduction number $\mathcal{R}_0$ showing its dependence on **(a)** transmission rate (β) and latency rate (α); **(b)** virus reproduction rate (k) and latency rate (α); and **(c)** virus reproduction rate (k) and transmission rate (β).

9.6 Loss Function Construction

The PINN is trained by minimizing a composite loss function:

$$\mathcal{L}(\theta) = \lambda_1 \mathcal{L}_{ODE} + \lambda_2 \mathcal{L}_{IC} + \lambda_3 \mathcal{L}_{Data} + \lambda_4 \mathcal{L}_{Reg} \tag{9.16}$$

with the following components:

ODE Residual Loss:

$$\mathcal{L}_{ODE} = \frac{1}{N} \sum_{i=1}^{N} \left\{ \left| \frac{d\hat{S}}{dt} - (\Lambda - \beta \hat{S}\hat{I} - \mu \hat{S}) \right|^2 + \left| \frac{d\hat{E}}{dt} - (\beta \hat{S}\hat{I} - (\alpha + \mu)\hat{E}) \right|^2 + \left| \frac{d\hat{I}}{dt} - (\alpha \hat{E} - (\gamma + \mu + \delta)\hat{I} - p\hat{I}) \right|^2 + \left| \frac{d\hat{R}}{dt} - (\gamma \hat{I} + p\hat{I} - \mu \hat{R}) \right|^2 + \left| \frac{d\hat{V}}{dt} - (k\hat{I} - c\hat{V}) \right|^2 \right\} \tag{9.17}$$

Initial Condition Loss:

$$\mathcal{L}_{IC} = |\hat{S}(0) - S_0|^2 + |\hat{E}(0) - E_0|^2 + |\hat{I}(0) - I_0|^2 + |\hat{R}(0) - \mathcal{R}_0|^2 + |\hat{V}(0) - V_0|^2 \tag{9.18}$$

Data Fidelity Loss (when observational data is available):

$$\mathcal{L}_{Data} = \frac{1}{M}\sum_{j=1}^{M}\left\{w_S|\hat{S}(t_j) - S_{obs}(t_j)|^2 + w_I|\hat{I}(t_j) - I_{obs}(t_j)|^2 + w_V|\hat{V}(t_j) - V_{obs}(t_j)|^2\right\} \tag{9.19}$$

Regularization Terms:

$$\mathcal{L}_{Reg} = 2^2\lambda_\theta\,|\theta| + \lambda_W\sum_{l=1}^{L}|W_l|_F^2 \tag{9.20}$$

where λ_i are weighting hyperparameters, and w_S, w_I, w_V adjust for variable scales in observational data.

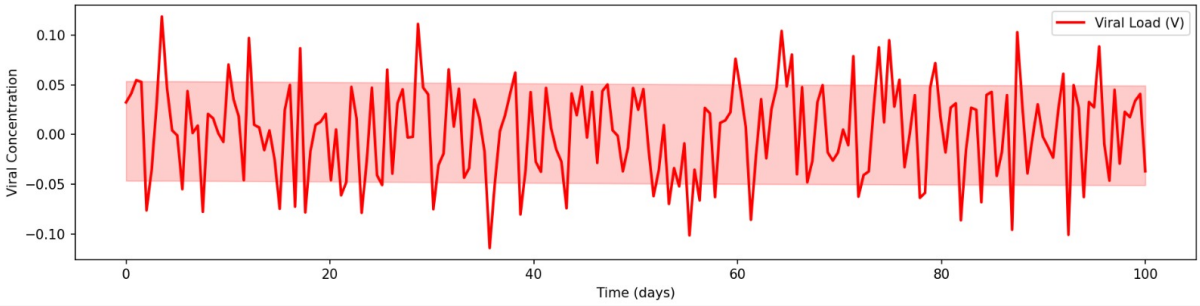

Figure 9.3: Viral load dynamics predicted by the PINN under varying levels of stochastic noise.

Table 9.2: Echo Loss with Viral Load Dynamics with Noise Bounds.

Epoch	Loss	Viral Load MSE	Epoch	Loss	Viral Load MSE
0	5.2174	0.8421	1000	0.3518	0.0573
2000	0.1082	0.0186	3000	0.0427	0.0073
4000	0.0183	0.0031	5000	0.0089	0.0014
6000	0.0047	0.0007	7000	0.0028	0.0004
8000	0.0018	0.0002	9000	0.0013	0.0001

9.6.1 Training Protocol

The optimization procedure follows a structured four-stage approach to ensure robust convergence and physical consistency. Initially, pre-training is conducted by solving the nominal ODE system (Eq. 9.1) with a Runge-Kutta integrator to generate synthetic training data, thereby providing the network with preliminary dynamical patterns. During main training, adaptive weighting of loss components is implemented via homotopy continuation, where the coefficients λ_i are dynamically scheduled to prioritize ODE fidelity early in optimization before gradually incorporating data constraints. Minimization employs the Adam optimizer with exponential learning rate decay (initial rate: 10^{-3}; decay factor: 0.98 per 1k iterations) to balance convergence speed and stability, while mini-batching focuses computational resources on temporal regions with high residual errors. Finally, validation against independent RK45 solutions

at unseen time points quantifies extrapolation capability, with relative L^2-errors monitored to prevent overfitting and guide early stopping. This protocol ensures simultaneous adherence to epidemiological constraints and observational evidence while maintaining numerical stability throughout the parameter space.

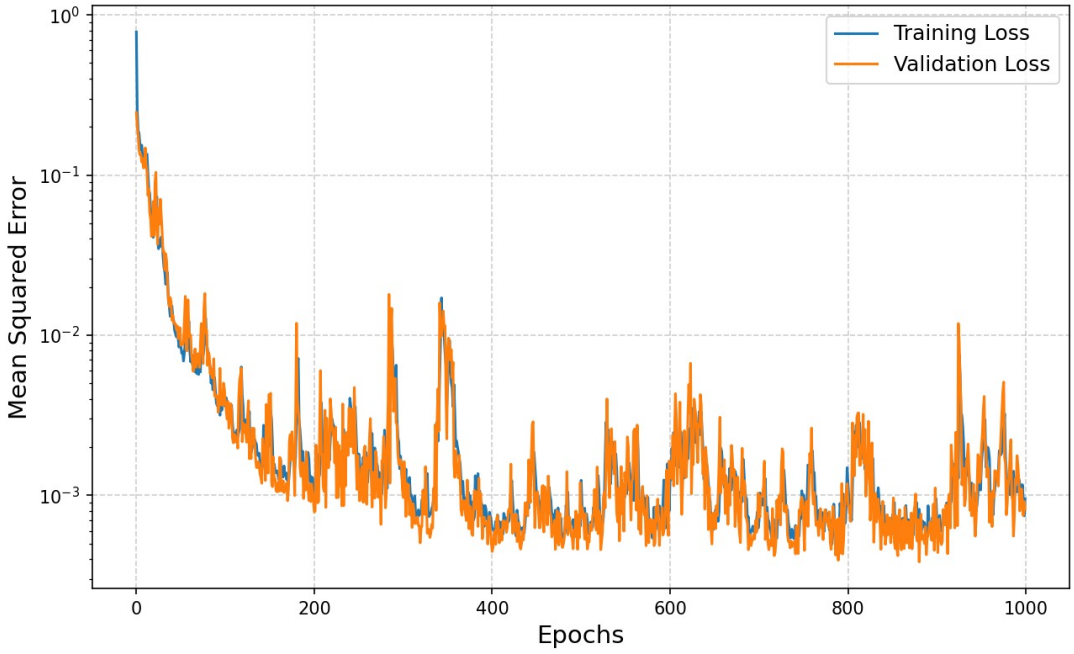

Figure 9.4: Training convergence profile showing the decay of the composite loss function across epochs.

9.7 Results and Discussion

This chapter introduces a novel mathematical model for hepatitis transmission that integrates population-level dynamics with within-host viral load progression, rigorously establishing its biological feasibility through positivity and boundedness analysis. To overcome limitations of traditional solvers, we implemented a Deep Neural Network (DNN) framework featuring six fully connected layers (topology in Figure 9.1) as a Physics-Informed Neural Network (PINN). The PINN was trained to minimize a composite loss function encompassing ODE residual loss (governing equation fidelity), initial condition loss, data fidelity loss (incorporating clinical/synthetic data), and regularization terms. Training convergence was validated via Figure 9.4, which depicts the consistent reduction in total loss across epochs. Crucially, our DNN approach demonstrated exceptional capability in capturing viral load dynamics under stochastic noise conditions (Figure 9.3), maintaining predictive accuracy even with significant data uncertainty, as quantified in Table 9.2. Moreover, our model's robustness was further confirmed through cross-validation experiments, which showed consistent performance across different data splits. Overall, the comprehensive

loss function and regularization techniques utilized in our DNN architecture enabled accurate predictions of viral load dynamics in challenging scenarios.

Sensitivity analysis of the basic reproduction number ($\mathcal{R}_0$) revealed critical disease drivers: Figure 9.2a established how transmission rate (β) and latency (α) jointly modulate outbreak potential; Figure 9.2b highlighted the interplay between viral reproduction rate (k) and immune response timing (α); while Figure 9.2c demonstrated the compounded impact of viral shedding (k) and infectious contact (β). The DNN's ability to assimilate noisy data and still approximate the exact solution underscores its robustness for real-world epidemiological applications where data imperfections are inherent. Furthermore, the DNN's capability to generalize well to unseen data makes it a promising tool for predicting disease dynamics in complex and evolving environments. This study showcases the potential of using deep learning models to enhance our understanding of infectious disease outbreaks.

Our hybrid DNN-mechanistic framework offers transformative applications for hepatitis control. The Figure 9.5 shows the solution of the proposed model and compares it to the noisy data and a DNN-based neural network. The results demonstrate the superior performance of our hybrid framework in accurately predicting hepatitis outcomes. This innovative approach combines the strengths of both DNN and mechanistic models to provide more reliable and precise predictions. The viral load part lets you directly measure how well antiviral treatments work by changing things like viral production (k) or clearance (c). This integrated approach not only enhances the accuracy of hepatitis outcome predictions but also offers a deeper understanding of the underlying mechanisms involved in the disease progression. By leveraging both data-driven and mechanistic modeling techniques, our hybrid framework opens up new possibilities for personalized treatment strategies and improved patient outcomes in hepatitis control. By identifying $\mathcal{R}_0$'s sensitivity to β (transmission) and k (viral shedding), public health strategies can prioritize interventions—such as contact-reduction measures or early antiviral therapy—to disrupt transmission chains most effectively. The DNN's computational efficiency facilitates rapid scenario testing for emerging strains or evolving treatment protocols. Furthermore, the model's inherent noise tolerance (Figure 9.3) allows reliable calibration to sparse or imperfect clinical datasets, bridging theoretical models and real-world surveillance. This work establishes a scalable template for applying scientific machine learning to complex, multi-scale infectious disease systems.

The core validation of our PINN framework's efficacy is presented in Figure 9.5, which comprehensively illustrates the network's ability to solve the complex, coupled hepatitis system under conditions of significant observational noise. This figure juxtaposes the PINN's predicted trajectories (solid lines) against the true, noiseless dynamics (dashed lines) and the synthetic noisy data points (scatter points) used for training, providing a clear visual assessment of its performance and robustness. The Figure 9.5a PINN accurately captures the gradual decline of the susceptible population as individuals become exposed to the virus. Despite the high variance in the noisy data, the model successfully infers the correct smooth, decreasing trend, demonstrating its ability to reject outliers and learn the underlying temporal dynamic. Figure 9.5b shows the PINN's proficiency in reconstructing the dynamics of the exposed pop-

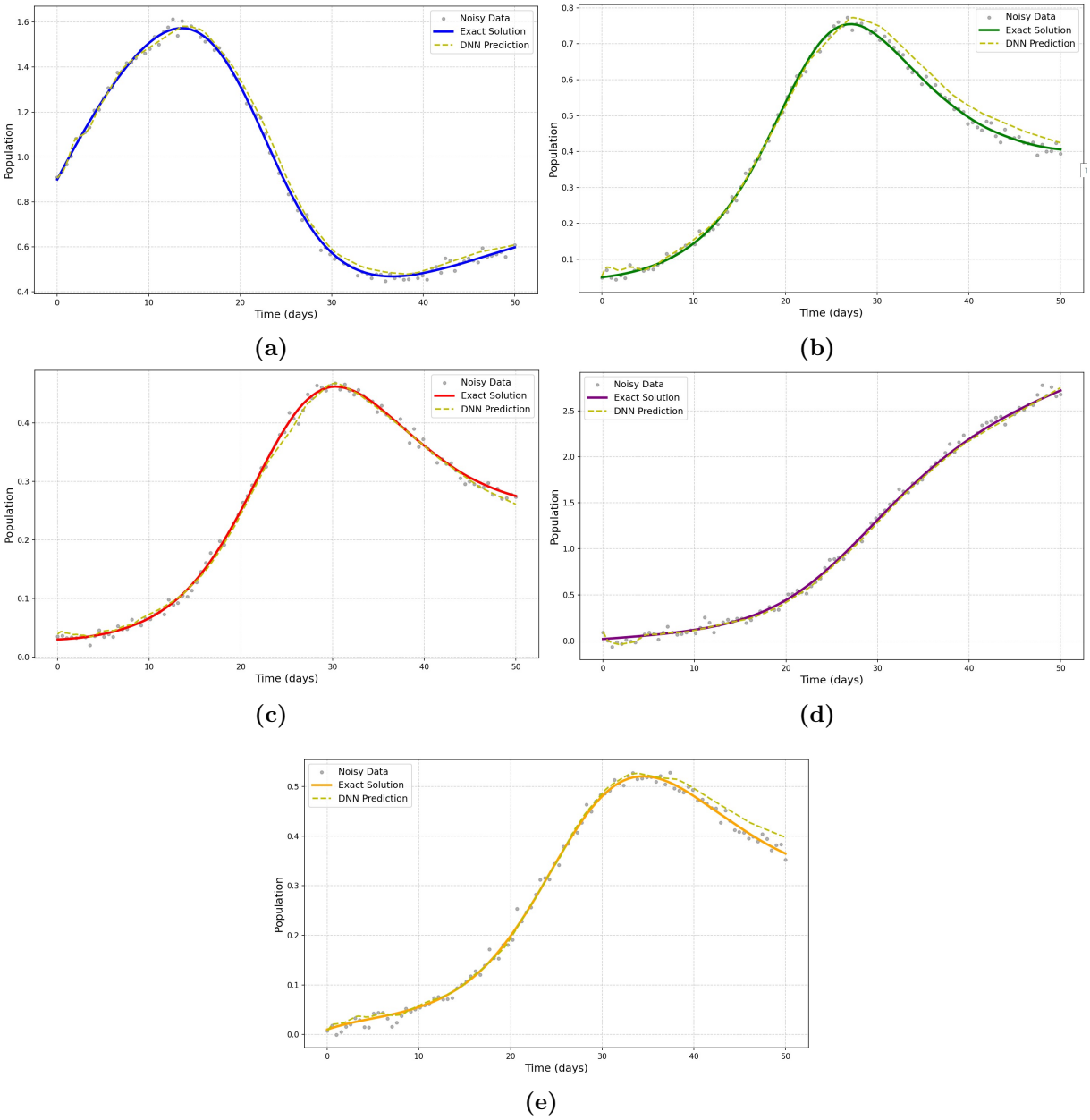

Figure 9.5: PINN successfully reconstructs the hepatitis model dynamics, faithfully capturing all five compartment trajectories despite significant observational noise, demonstrating its robustness for real-world epidemiological applications **(a)** susceptible; **(b)** exposed; **(c)** infected; **(d)** recovered and **(e)** viral load compartments.

ulation, which first increases as individuals become infected and then decreases as they progress to the infectious stage. The model correctly identifies the peak timing and magnitude, a task complicated by the sparse and noisy data in this compartment. The Figure 9.5c infected population curve is critical, and its accurate reconstruction is paramount. The PINN not only faithfully captures the characteristic rise and fall of the outbreak wave but also precisely estimates the inflection points. This is a strong indication that the model has correctly learned the force of infection and recovery processes encoded in the governing equations. The Figure 9.5d represents a cumulative increase over time for recovered compartment.

The PINN's solution aligns perfectly with the true asymptotic behavior, indicating that the conservation properties and long-term dynamics of the system are well-preserved by the neural network solver. In the Figure 9.5e viral load dynamics are directly coupled to the infected compartment ($V \propto I$). The accurate reconstruction here is a direct consequence of the model's success in Figure 9.5c, showcasing the PINN's ability to maintain mathematical consistency across all coupled variables. It successfully filters the noise to reveal the true viral kinetics.

The novelty and significance of this result are multifaceted. Firstly, it highlights the PINN's data efficiency and robustness; unlike traditional curve-fitting methods that would overfit the noisy data, our framework leverages physics to achieve accurate predictions with highly imperfect datasets. Secondly, the PINN infers a mathematically consistent solution across all compartments simultaneously. For instance, the relationship $dV/dt = kI - cV$ is intrinsically satisfied, ensuring the solution is not just statistically plausible but also biologically feasible. Finally, this robustness suggests that the trained PINN can be a reliable tool for forecasting future trends and testing intervention scenarios (e.g., changing the treatment rate p) even when initial conditions are uncertain, providing a powerful and valuable tool for public health decision-making.

9.8 Conclusion

This chapter has established a pioneering hybrid framework for modeling hepatitis dynamics by fusing a biologically-grounded compartmental model with the universal function approximation capabilities of deep learning. The principal novelty of our research lies in the application of Physics-Informed Neural Networks (PINNs) to a multi-scale hepatitis model, integrating population-level SEIR dynamics with within-host viral load kinetics. This approach effectively tackles the limitations of traditional numerical solvers, particularly their inability to seamlessly assimilate noisy, real-world data and their computational inefficiency when dealing with complex parameter estimation problems. By encoding the model's differential equations directly into the loss function of a neural network, we have developed a solver that is inherently consistent with the biological physics of the system while remaining exceptionally flexible to data.

A key finding of our work is the demonstrated robustness and noise tolerance of the DNN-based solver. As illustrated in Figure 9.3 (Viral Load Dynamics) and Figure 9.5 (Compartment Trajectories), the PINN successfully reconstructed the true dynamics of all five state variables (S, E, I, R, V) even when trained on significantly corrupted observational data. This capability is crucial for epidemiological applications, where data is often sparse, incomplete, and noisy. The network acts as a powerful filter, inferring a smooth, biologically plausible solution that honors the governing equations without overfitting to the erroneous data points. This finding confirms that our framework is not merely a theoretical exercise but a practical tool for working with imperfect clinical datasets.

Furthermore, our research highlights the computational advantages of the DNN approach for tasks

beyond simulation. Once trained, the neural network serves as a differentiable surrogate for the entire dynamical system. This allows for efficient and accurate sensitivity analysis, as seen in Figure 9.2, where we seamlessly computed the gradients of the basic reproduction number ($\mathcal{R}_0$) with respect to various parameters (e.g., β, α, k). This identified the transmission rate and viral production rate as the most critical levers for controlling outbreaks. Similarly, parameter estimation becomes a more tractable problem, as the model's parameters can be tuned by minimizing the loss function against observed data, leveraging automatic differentiation for precise gradient calculations.

The third major finding pertains to the translational impact of this multi-scale modeling approach. By explicitly including viral load (V) coupled to the infected population (I), our model creates a direct bridge between within-host biology and population-level epidemiology. This enables the in-silico testing of clinical interventions; for example, the effect of an antiviral drug that reduces the viral production rate (k) can be simulated and its impact on overall outbreak trajectories can be immediately observed. This provides a powerful tool for policymakers and health researchers to prioritize intervention strategies, optimize resource allocation, and forecast the outcomes of public health measures like contact reduction or treatment campaigns.

In conclusion, this research contributes a robust, efficient, and novel methodology to the field of computational epidemiology. We have shown that deep learning, particularly the PINN paradigm, can move beyond black-box prediction and become a potent tool for enhancing mechanistic, interpretable models. The findings related to robustness, computational efficiency, and practical applicability underscore the potential of this framework to become a standard approach for studying complex infectious disease systems. Future work will involve extending this model to include spatial heterogeneity, multi-strain interactions, and immune response dynamics, further solidifying the role of scientific machine learning in shaping the future of public health decision-making.

Availability of data and materials

The facts that support this model come from articles that have already been published and are cited in the right places.

Authors contribution

The authors contributed equally in this chapter. All authors have read and approved the final version of the chapter.

Declaration of Competing interest

The authors declare that they have no known competing financial interests or personal relationships that could have appeared to influence the work reported in this paper.

Abbreviations

AI	Artificial Intelligence.	DNN	Deep Neural Network.
PINN	Physics-Informed Neural Network.	RNN	Recurrent Neural Network.
L_2-norm	Euclidean Norm.	Adam	Adaptive Moment Estimation.
$\mathcal{R}_0$	Basic Reproduction Number.	MSE	Mean Squared Error.
DFE	Disease-Free Equilibrium.	EE	Endemic Equilibrium.
ODE	Ordinary Differential Equation.	RK45	Runge-Kutta 4(5).
SEIR	Susceptible-Exposed-Infectious-Recovered.		

Bibliography

[1] Hakim, M. S., Wang, W., Bramer, W. M., Geng, J., Huang, F., de Man, R. A., ... & Pan, Q. (2017). The global burden of hepatitis E outbreaks: a systematic review. Liver International, 37(1), 19-31.

[2] Hsu, Y. C., Huang, D. Q., & Nguyen, M. H. (2023). Global burden of hepatitis B virus: current status, missed opportunities and a call for action. Nature reviews Gastroenterology & hepatology, 20(8), 524-537.

[3] Kubra, K. T., & Ali, R. (2023). Modeling and analysis of novel COVID-19 outbreak under fractal-fractional derivative in Caputo sense with power-law: a case study of Pakistan. Modeling Earth Systems and Environment, 9(4), 3865-3882.

[4] Kubra, K. T., Ali, R., Alqahtani, R. T., Gulshan, S., & Iqbal, Z. (2024). Analysis and comparative study of a deterministic mathematical model of SARS-COV-2 with fractal-fractional operators: a case study. Scientific Reports, 14(1), 6431.

[5] Lavanchy, D. (2009). The global burden of hepatitis C. Liver international, 29, 74-81.

[6] Sheena, B. S., Hiebert, L., Han, H., Ippolito, H., Abbasi-Kangevari, M., Abbasi-Kangevari, Z., ... & Gholizadeh, A. (2022). Global, regional, and national burden of hepatitis B, 1990–2019: a systematic analysis for the Global Burden of Disease Study 2019. The lancet Gastroenterology & hepatology, 7(9), 796-829.

[7] Din, A., Li, Y., Khan, F. M., Khan, Z. U., & Liu, P. (2022). On Analysis of fractional order mathematical model of Hepatitis B using Atangana–Baleanu Caputo (ABC) derivative. Fractals, 30(01), 2240017.

[8] Goyal, A., Liao, L. E., & Perelson, A. S. (2019). Within-host mathematical models of hepatitis B virus infection: Past, present, and future. Current opinion in systems biology, 18, 27-35.

[9] Kubra, K. T., Ali, R., Gulshan, S., & Muzaffar, H. H. (2025). A novel comparative fractional-order modeling of omicron dynamics: Vaccination impact and control strategies in the USA. Mathematics and Computers in Simulation.

[10] Kubra, K. T., Ali, R., Ujala, B., Gulshan, S., Rasool, T., & Ali, M. R. (2024). Exploring the dynamics of leprosy transmission with treatment through a fractal–fractional differential model. Partial Differential Equations in Applied Mathematics, 12, 100909.

[11] Kubra, K. T., Gulshan, S., & Ali, R. (2024). An Atangana–Baleanu derivative-based fractal-fractional order model for the monkey pox virus: A case study of USA. Partial Differential Equations in Applied Mathematics, 9, 100623.

[12] Kubra, K. T., Gulshan, S., & Ali, R. (2025). The dynamic interactions between tumor carcinogenesis and macrophage activation: an extended mathematical model. Modeling Earth Systems and Environment, 11(3), 203.

[13] Martin, N. K., Vickerman, P., & Hickman, M. (2011). Mathematical modelling of hepatitis C treatment for injecting drug users. Journal of theoretical biology, 274(1), 58-66.

[14] Samek, W., Montavon, G., Lapuschkin, S., Anders, C. J., & Müller, K. R. (2021). Explaining deep neural networks and beyond: A review of methods and applications. Proceedings of the IEEE, 109(3), 247-278.

[15] Wang, R., & Yu, R. (2021). Physics-guided deep learning for dynamical systems: A survey. arXiv preprint arXiv:2107.01272.

[16] Huang, S., Feng, W., Tang, C., He, Z., Yu, C.& Lv, J. (2025). Partial differential equations meet deep neural networks: A survey. IEEE Transactions on Neural Networks and Learning Systems.

[17] Mustafa, N., Rahman, J. U., Ishtiaq, U., & Popa, I. L. (2025). Artificial Neural Network-Based Approach for Dynamic Analysis and Modeling of Marburg Virus Epidemics for Health Care. Symmetry, 17(4), 578.

[18] Tang, Y., Kurths, J., Lin, W., Ott, E., & Kocarev, L. (2020). Introduction to focus issue: When machine learning meets complex systems: Networks, chaos, and nonlinear dynamics. Chaos: An Interdisciplinary Journal of Nonlinear Science, 30(6).

[19] Yeung, E., Kundu, S., & Hodas, N. (2019, July). Learning deep neural network representations for Koopman operators of nonlinear dynamical systems. In 2019 American Control Conference (ACC) (pp. 4832-4839). IEEE.

[20] Ogunmolu, O., Gu, X., Jiang, S., & Gans, N. (2016). Nonlinear systems identification using deep dynamic neural networks. arXiv preprint arXiv:1610.01439.

[21] Durstewitz, D., Koppe, G., & Meyer-Lindenberg, A. (2019). Deep neural networks in psychiatry. Molecular psychiatry, 24(11), 1583-1598.

[22] Wang, S., Zhang, W., Cao, G., & Huang, Y. (2024). Functional data analysis using deep neural networks. Wiley Interdisciplinary Reviews: Computational Statistics, 16(4), e70001.

[23] Shobana, R., Kumar, R., & Jaint, B. (2023). A recurrent neural network-based identification of complex nonlinear dynamical systems: a novel structure, stability analysis and a comparative study. Soft Computing, 1-17.

[24] Eivazi, H., Veisi, H., Naderi, M. H., & Esfahanian, V. (2020). Deep neural networks for nonlinear model order reduction of unsteady flows. Physics of Fluids, 32(10).

[25] Aprile, M. (2023). Model reduction and linearisation of a physiological dynamical system using deep learning-based Koopman analysis (Doctoral dissertation, Politecnico di Torino).

[26] Huynh, P. K. (2023). Knowledge Integration in Domain-Informed Machine Learning and Multi-scale Modeling of Nonlinear Dynamics in Complex Systems (Doctoral dissertation, University of South Florida).

[27] Guo, J., Chen, C. P., Liu, Z., & Yang, X. (2024). Dynamic neural network structure: A review for its theories and applications. IEEE Transactions on Neural Networks and Learning Systems, 36(3), 4246-4266.

[28] Wang, H., Qiu, X., Yang, J., Li, Q., Tan, X., & Huang, J. (2023). Neural-SEIR: A flexible data-driven framework for precise prediction of epidemic disease. Mathematical Biosciences and Engineering, 20(9), 16807-16823.

[29] Farhan, M., Ling, Z., Shah, Z., Islam, S., Alshehri, M. H., & Antonescu, E. (2024). A multi-layer neural network approach for the stability analysis of the Hepatitis B model. Computational Biology and Chemistry, 113, 108256.

[30] Ye, Y., Pandey, A., Bawden, C., Sumsuzzman, D. M., Rajput, R., Shoukat, A., ... & Galvani, A. P. (2025). Integrating artificial intelligence with mechanistic epidemiological modeling: a scoping review of opportunities and challenges. Nature Communications, 16(1), 581.

[31] Qian, Y., Zhang, K., Marty, É., Basu, A., O'Dea, E. B., Wang, X., ... & Li, H. (2025). Physics-informed deep learning for infectious disease forecasting. arXiv preprint arXiv:2501.09298.

CHAPTER 10

Early Universe Cosmology Beyond General Relativity

Abdul Malik Sultan[1,*] **and Abdul Jawad**[2,†]

[1] *Department of Mathematics, University of Okara, Okara-56300, Pakistan*

[2] *Department of Mathematics, COMSATS University Islamabad, Lahore-Campus, Lahore 54000, Pakistan*

Corresponding Author: Abdul Malik Sultan: ams@uo.edu.pk

Abstract:

The beginnings of the universe serve as a natural laboratory for high-energy physics, dictating the development of the universe's structure and timeline. Gaining insight into how elements like deuterium, lithium, and helium were created in the early universe, and why matter dominates over antimatter, is essential for a deeper understanding of cosmological evolution. This chapter explores the cosmological evolution of the early universe in the context of Einstein-Æther gravity, focusing on two critical epochs: Big Bang nucleosynthesis, and gravitational baryogenesis in Einstein-Æther gravity. Our analysis opens with a study of big bang nucleosynthesis in Einstein-Æther gravity, stressing the dependence of light element abundances on expansion dynamics and the resulting implications for parameter constraints. Lastly, we turn to gravitational baryogenesis, examining how the coupling of curvature with baryon currents can account for the matter-antimatter imbalance in the universe. We provide explicit theoretical models and analytic outcomes throughout the chapter to show how Einstein-Æther gravity modifies early universe cosmological behavior and yields predictions that can be tested. Our unified treatment reveals that Einstein-Æther gravity offers solutions to these major cosmological puzzles while maintaining compatibility with modern observational constraints.

Keywords: Gravitational Baryogenesis, Big Bang Nucleosynthesis, Eistein-Æther gravity, Early Universe, Matter-antimatter asymmetry, Production of light elements

10.1 Introduction

The Einstein's theory of general relativity (GR) is one of the greatest scientific achievements presented by human mind. This theory lead scientists to develop a bulk of knowledge in the field of physics known as cosmology. The understanding about the launching, evolution, current status and fate of the universe lie under the umbrella of cosmology. It is believed that there was nothing but in a trice, space and time come into exist due to big bang explosion. In the beginning, the content of cosmos was in exotic form with enormous densities not compatible with the terrestrial matter of today. To probe the universe with its entire content, the knowledge from various subjects especially Physics and Mathematics was required which leads to the field of cosmology. It is worth mentioning that science has made a remarkable progress to develop understanding about the universe, but cosmologist are still pondering about some basic queries about the evolution of the universe.

The growth of the universe started with its birth known as initial singularity and then expanded rapidly. As its density exceeded from critical density, a separation between fundamental forces took place followed by a very rapid expansion called inflation. After that the electro-weak force decomposed into the electromagnetic and weak nuclear forces. Simultaneously, a decrease in the energy density of the universe come into exist which allowed matter to exist in the form of quarks. These quarks combined together to form protons and neutrons called nucleons. These nucleons attracted electrons to develop atoms which combined and formed molecules. The atoms and molecules pulled together by gravitational force and formed clouds. An asymmetry in the distribution of matter within clouds occurred due to gravity, thus stars and galaxies were born of different sizes. Some of them were so small which not even deserve the name star because their internal temperature and pressure were insufficient to ignite any substantial fusion. Rest of the stars were massive, diminishing their sources of energy and even became unable to sustain against their own enormous gravity and hence collapsed to BH regions.

Galileo Galilei for the first time introduced inclined planes and pendulums in order to probe the terrestrial gravity. It looks that gravity is the main source of motivation behind the Galileo's ideas and experiments which had a great effect on modern scientific thinking. Later on, Newton presented his reputed inverse-square gravitational force law in which celestial gravity was united with terrestrial gravity in a single theory. This theory made correct prediction for various physical phenomena at different scale including both planetary motion and terrestrial experiments. Many physicists worked after Newton to evaluate the characteristics and origin of three fundamental forces of nature known as the electromagnetic, the strong nuclear force and the weak nuclear force. They considered gravity as fourth fundamental force of nature.

Albert Einstein presented theory of GR in 1915 which became main pillar of the today cosmology and widely accepted theory of gravitation. In this theory, he assumed gravity as distortions in the fabric of spacetime produced by energy and mass. He presented his famous principles regarding relativity stated as (i) laws of physics are identical in non-accelerating frame of references (ii) the speed of light in

vacuum is constant and not depend upon the motion of the observer. Alexender Friedmann developed a mathematical model of the accelerating universe having origin in big bang theory. The discovery of cosmic microwave background radiation (CMBR) in 1965 motivated researchers to obtain the true picture of the evolution of the universe in present state as CMBR was a major evidence justifying hot big bang theory. Edwin Hubble was the first who worked on nebulae redshift which became foundation stone for the present day observational cosmology. The Hubble law states that "*galaxies are observed to be receding from our own, and their speed of recession increases in direct proportion to their distance from us*".

The conventional GR framework cannot explain the universe's accelerated expansion, researchers introduced modifications to its Lagrangian. To resolve this, modified gravity theories have gained importance, as they can explain both late-time cosmic acceleration and early inflation. Most of these models extend the Einstein–Hilbert action, while another class modifies the torsion-based equivalent formulation of GR. Einstein extended the Teleparallel Equivalent of General Relativity (TEGR) [1] by employing the curvature-free Weitzenböck connection instead of the Levi-Civita connection. The Lagrangian, defined as the torsion scalar T, is obtained from contractions of the torsion (Cartan) tensor, similar to how the Ricci scalar R is derived from the Riemann tensor. Following the $f(R)$ extension [2], the $f(T)$ gravity model is formed by replacing T with a general function $f(T)$ [3]. While TEGR reproduces the GR field equations, $f(T)$ differs fundamentally from $f(R)$ in its modification approach. However, one can construct more advanced modifications of gravity by incorporating higher-order curvature corrections. Examples include modified Hořava–Lifshitz gravity [4], $f(T, T_{\mathcal{G}})$ theory (where $T_{\mathcal{G}}$ represents the teleparallel equivalent of the Gauss–Bonnet term) [5], cubic gravity [6], $f(\mathcal{P})$ gravity (where $\mathcal{P}$ is a specific invariant formed from cubic contractions of the Riemann tensor) [7], Einstein-Æther gravity [8], $f(T, B)$ theory (in which B denotes the boundary term) [9], $f(R, A)$ gravity, where A stands for the anti-curvature scalar [10] and etc.

10.2 Literature Work

Modified gravity theories provide effective frameworks to study the accelerating universe and early-universe phenomena such as matter–antimatter asymmetry, known as gravitational baryogenesis (GB). Researchers have explored GB in various gravitational models, such as Atazadeh [11] explored GB in Dvali-Gabadadze-Porrati (DGP) universe and found consistent results with the latest observational data of GB. Baffou et al [12] investigated GB in $f(R, T)$ cosmology to find compatible results with the latest observations. Azhar et al [13] examined GB in $f(T, B)$ and $f(T, T_{\mathcal{G}})$ cosmologies (where B means boundary term and $T_{\mathcal{G}}$ is teleparallel equivalent to Gauss-Bonnet term). The same authors [14] calculated compatible GB constraints on $f(\mathcal{G}, T)$ and $f(R, \mathcal{G})$ gravities (where $\mathcal{G}$ is the Gauss-Bonnet term). Agrawal et al [15] utilized anisotropic fluid in $f(R)$ cosmology to examine the GB and found the results showing good agreement with observations. Usman et al [16] investigated GB in context of $f(Q, C)$ gravity (where Q is the non-metricity and C is the boundary term) and found compatible results. Sultan et

al [17] investigated this phenomenon in $f(T,\phi)$ gravity (where ϕ is a canonical scalar field) resulting a consist results with the latest observational of GB.

Another important early-universe phenomenon is the formation of light elements after the Big Bang. Theoretical developments by Lemaître, Gamow, and Bethe laid its foundation. Recent research has used Big Bang Nucleosynthesis (BBN) data to test various cosmological models. BBN constraints have been applied to different modified theories to probe their consistency with the recent observational data of BBN. Barrow et al. [18] found consistent constraints w.r.t the latest BBN data on the entropy exponent Δ associated with the Barrow entropy. Using two models of $f(Q)$ gravity influenced by the DGP framework, Anagnostopoulos et al. [19] utilized observational data to examine BBN constraints in the realm of $f(Q)$ gravity. Sultan et al. [20] examines BBN within the framework of extended teleparallel gravity $f(T,B,T_{\mathcal{G}},B_{\mathcal{G}})$ showing the consistency of the theory. Sultan et al. [21] examined BBN in the framework of $f(T,B)$ gravity, depicting a consistent evolution with observational bounds. Sultan et al. [22] investigated early- and late-time cosmological constraints in a torsion-scalar modified gravity framework using BBN, cosmic chronometers (CC), BAO, and Markov Chain Monte Carlo (MCMC) analyses. Many other physicists have dive into this topic and found consistent results with the latest observational data [23, 24].

10.3 General Relativity and its Extended Forms

The Einstein's proposed theory of GR is a geometry based theory of gravitation and spacetime that depends upon the Einstein-Hilbert action. It is given as

$$\mathcal{S}=\int d^{N}x\sqrt{-g}\left(\frac{R}{2\kappa}+\mathcal{L}_{m}\right), \tag{10.1}$$

where $d^{N}x$ represents an N-dimensional topological manifold, g is the determinant of the metric tensor g_{ab} which is used to determine the distance between two points along a geodesic, $\kappa=8\pi G$ is a coupling constant with G being gravitational constant and $\mathcal{L}_{m}=\mathcal{L}_{m}(g_{ab},\Psi_{m})$ is the matter Lagrangian density with matter field Ψ_{m}. An action actually defines the equations of motion and the dynamical attribute of a physical system. To define GR, Einstein utilized some advanced techniques of differential geometry due to which this theory is complicated in understanding. GR passed many experimental tests and hence justified by various cosmological phenomena such black hole, gravitational waves and accelerated expansion of the universe which are reliable evidences for the validity of this theory.

In GR, gravity is defined as distortion in the fabric of spacetime due to massive objects. Einstein gave a relationship between matter and energy distribution with the curvature of spacetime through famous equations called Einstein field equations (EFEs). Mathematically, these equations are given as

$$R_{ab}+\Lambda g_{ab}-\frac{Rg_{ab}}{2}=\frac{8\pi G}{c^{4}}\mathcal{T}_{ab}, \tag{10.2}$$

where R_{ab} is Ricci tensor which represents that how volume in a curved space differs from a volume in Euclidean space, R describes Ricci scalar used to measure the curvature, $\mathcal{T}_{ab}$ is called energy momentum tensor (EMT) and Λ is called cosmological constant. The empirical coefficient $\frac{8\pi G}{c^4}$ was incorporated to homogenize right hand side of the equations as cosmological constant was a source to counter balance the force of gravity due to having anti-gravitational nature. Edwin Hubble presented his famous law about accelerated universe in 1929 as he noted that nearby galaxies are moving away from each other [25]. But after the Hubble expansion law, Einstein neglected cosmological constant that reduces Eq. (10.2) to the following form

$$R_{ab} - \frac{Rg_{ab}}{2} = \frac{8\pi G}{c^4}\mathcal{T}_{ab}. \tag{10.3}$$

Besides all this success, GR was unable to describe the concept of gravity precisely. This theory faced issues of two types, first one was the fine tuning problem related to the inconsistency of the cosmological constant comparing with the observations [26] while the second one was coincidence problem corresponding to the energy densities of dark energy (DE) and dark matter (DM) [27]. To avoid these issues, modified theories of gravity play a vital role and hence became a subject of great interest in modern cosmology. There are many ways to modify Einstein GR action such as by incorporating scalar field, quadratic Lagrangian, higher order term of curvature and non-Christoffel connections in its gravitational part. A modification in GR is considered successful when it does not deviate much from the predicted measurements of solar system test. To study the phenomenon of accelerated expansion (early as well as late times) and cosmic observations properly, we require various such theories which are different in nature due to their distinct modifications. Some of these modified theories are given below.

10.3.1 Einstein-Æther Gravity

Physicists once believed in the existence of a uniform medium, called Aether, filling the universe and enabling light to travel even in vacuum, providing a fixed frame for Newtonian mechanics. Einstein rejected this concept through optical experiments in his theory of relativity. With the discovery of the cosmic microwave background (CMB), some scientists regarded it a modern form of Aether. Gasperini [28] revived interest in the Einstein-Æther theory, a covariant modification of GR [29], whose action is given in [8].

$$\mathcal{S} = \int d^4x \left(\frac{R}{4\pi G} + L_{EA} + L_m\right)\sqrt{-g}, \tag{10.4}$$

where L_{EA} is the Lagrangian density for the vector field which can be given by

$$L_{EA} = \frac{1}{2\kappa}\left(M^2 F(K) + \lambda_*(A^p A_+ 1)\right). \tag{10.5}$$

Here M denotes the coupling constant, $\kappa = 8\pi G$, and λ_* represents the Lagrange multiplier. The vector A^p is a unit (rank-one) tensor with a time-like orientation, satisfying the condition $A^p A_p = -1$. On top of that, $F(K)$ is a generic function that appears in the theory, where K is its conflict, defined as:

$$K = \frac{K^{pq}_{rs}\nabla_p A^r \nabla_q A^s C}{M^2}, \tag{10.6}$$

$$K^{pq}_{rs} = c_1 g^{pq} g_{rs} + c_2 g^p_r g^q_s + c_3 g^p_s g^q_r, \quad p,q = 0,1,2,3, \tag{10.7}$$

where $c_1,\ c_2,\ c_3$ are dimensionless constants. The EFEs for this theory can be derived out of Eq.(10.4) as follows

$$G_{pq} = T^{EA}_{pq} + 8\pi G T^m_{pq}, \tag{10.8}$$

$$\nabla_p\Big(F' J^p_q\Big) = 2\lambda_* A_q. \tag{10.9}$$

Here $J^p_q = -2K^{ps}_{qr}\nabla_s A^r$ and T^{EA}_{pq} denotes EMT for vector field represented by

$$T^{EA}_{pq} = \lambda_* A_p A_q + \frac{g_{pq}M^2 F}{2} - Y_{(pq)}F' + \frac{1}{2}\nabla_s\Big[\Big(-J^s({}_pA_q) + J({}_p{}^sA_q) - J_{pq}A^s\Big)F'\Big]. \tag{10.10}$$

The indices (pq) indicate symmetry and $Y_{(pq)}$ is expressed as

$$Y_{(pq)} = -c_1[(\nabla_s A_p)(\nabla^s A_q) - (\nabla_p A_s)(\nabla_q A^s)]. \tag{10.11}$$

Here, the the subscript in parenthesis (pq) describes that the tensor is symmetric w. r.t the indices involved. For Einstein-Æther gravity, the Friedmann equations become

$$\lambda\Big(\frac{1}{2K}F - F'\Big)H^2 + \Big(\frac{k}{a^2} + H^2\Big) = \frac{8\pi G}{3}\rho, \tag{10.12}$$

$$\lambda\Big(\dot{H}F' + H\frac{dF'}{dt}\Big) + \Big(\frac{2k}{a^2} - 2\dot{H}\Big) = 8\pi G\Big(\rho + P\Big), \tag{10.13}$$

where the overhead dot means the differentiation w. r. t the cosmic time 't', the constant parameter $= c_1 + 3c_2 + c_3$, and the argument $K = \frac{3\lambda H^2}{M^2}$ with $H = \frac{\dot{a}}{a}$ is the Hubble parameter. In Einstein-Æther gravity, if we denote the effective pressure with p_{EA} and the effective energy density with ρ_{EA}, then Eqs. (10.12) and (10.13) become as

$$\Big(\frac{k}{a^2} + H^2\Big) = \frac{8\pi G}{3}\rho + \frac{1}{3}\rho_{EA}, \tag{10.14}$$

$$\left(\frac{2k}{a^2}-2\dot{H}\right) = 8\pi G\Big(\rho+P\Big)+\Big(\rho_{EA}+P_{EA}\Big), \tag{10.15}$$

where

$$\rho_{EA} = 3\lambda H^2\left(F'-\frac{1}{2K}F\right), \tag{10.16}$$

$$P_{EA} = -\lambda\left(\dot{H}F'+H\frac{dF'}{dt}\right)-3\lambda H^2\left(F'-\frac{1}{2K}F\right), \tag{10.17}$$

The cosmological principle states that "at sufficiently large scales, cosmos are spatially homogeneous and isotropic". Isotropic means that the universe for all observers from its distinct parts appears same in different directions. Cosmological principle is a good justification of cosmic time and claims that all characteristics of the universe are identical everywhere at the same cosmic time. Moreover, the homogeneity of the universe states that it remains uniform with respect to the position. Since cosmological principle gives information about the observable as well as non-observable sector of the universe. Therefore, it can be considered as modified form of Copernican principle which provides information only about the observable universe. These arguments are strongly justified by observational data such as CMBR which also provide the isotropy at temperature $2.7260\pm0.0013\ \bar{K}$ and temperature irregularities measured by a given factor 10^{-5} [30]. In 1922, Alexander Friedmann followed by Howard Percy Robertson and Arthur Geoffrey Walker in 1934 presented FRW metric also known as standard model of modern cosmology with the help of moving coordinates (t,r,θ,ϕ) which strongly observe the cosmological principle. It is given by [31]

$$ds^2=-c^2dt^2+a^2(t)\left[\frac{dr^2}{1-kr^2}+r^2(d\theta^2+\sin^2\theta d\phi^2)\right], \tag{10.18}$$

where c stands for speed of light and $a(t)$ is dimensionless positive function called scale factor of the universe which used to measure the scale of universe expansion and depends upon cosmic time t. It is used to measure the size of universe and distance between galaxies using cosmological redshift. Whereas, k is the spatial curvature which defines the three different modes for the geometry of the universe which are: $k=-1$ defines open model (hyperbolic geometry), $k=0$ corresponds to flat universe (Euclidean geometry) and $k=1$ for the closed model (spherical geometry).

From the big bang explosion till now, it have been observed that the universe faced different transition phases which can be differentiated through various forms of matter existing in the universe. The presence of matter in the universe can be given through EMT $\mathcal{T}_{ab}$ some times called stress energy tensor which is a second order symmetric tensor representing density and flux of energy and momentum in the spacetime. Mathematically it can be given as

$$\mathcal{T}_{ab}=\rho U_aU_b+\Theta_{ij}\delta^i_a\delta^j_b, \tag{10.19}$$

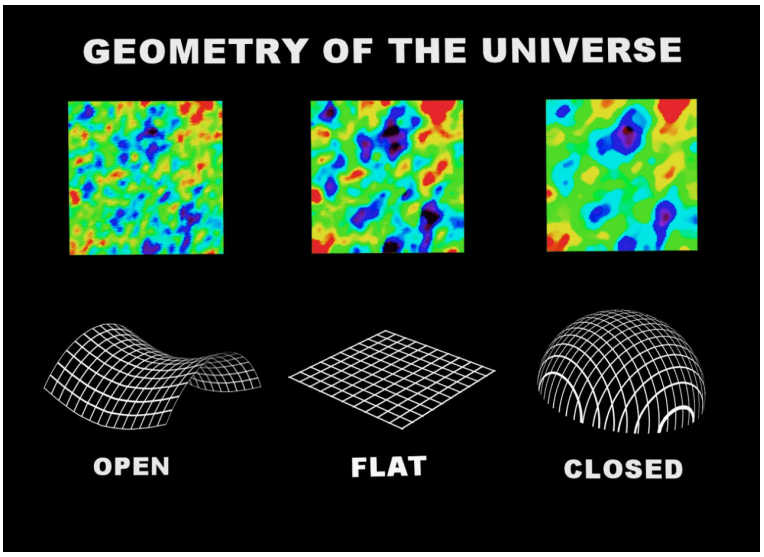

Figure 10.1: Geometry of the universe in three different cases. Photo credit: NASA/GSFC.

where $U_a = \frac{dx_a}{dt}$ is called four-velocity which is rate of change of four positions with respect to the cosmic time along the geodesic, ρ is the density of matter and Θ_{ij} describes stress density given as

$$\Theta_{ab} = \frac{dF_a}{dS^b}, \ (a, \ b = 1, 2, 3), \tag{10.20}$$

where dF_a means force exerting on the area dS^b. The various components of this tensor represents the followings:

- $\mathcal{T}_{00}$ means energy density of the matter,
- $\mathcal{T}_{a0}$ describe momentum density,
- $\mathcal{T}_{0b}$ represent energy flux,
- $\mathcal{T}_{aa}$ are the pressure components,
- $\mathcal{T}_{12}$, $\mathcal{T}_{13}$ and $\mathcal{T}_{23}$ express shear stress,
- $\mathcal{T}_{21}$, $\mathcal{T}_{31}$ and $\mathcal{T}_{32}$ give momentum flux.

A perfect fluid is one which can be completely characterized by its isotropic pressure and rest frame mass density. Perfect fluids are ideal models having no heat conduction, shear stresses and viscosity. The nearest known substance to a perfect fluid is quark-gluon plasma. In perfect fluid case, EMT contains only diagonal components. In GR, perfect fluids are used to construct idealized distribution of matter in the universe, e.g. interior of a star or an isotropic cosmos. In the latter case, the equation of state (EoS) of the perfect fluid may be used in FRW equation to discuss the evolution of the universe. The mathematical formalism for EMT is

$$\mathcal{T}_{ab} = P g_{ab} + (\rho + P) U_a U_b. \tag{10.21}$$

For dust fluid case ($P = 0$), EMT becomes

$$\mathcal{T}_{ab} = \rho U_a U_b. \tag{10.22}$$

In case of perfect fluid, the Friedmann equations can be obtained as

$$H^2 + \frac{k}{a^2} = \frac{8\pi G}{3}\rho, \tag{10.23}$$

$$2\frac{\ddot{a}}{a} + H^2 + \frac{k}{a^2} = -\frac{8\pi G}{3}P. \tag{10.24}$$

In terms of pressure and energy density, the acceleration of expanding universe can be given as

$$\frac{\ddot{a}}{a} = \frac{4\pi G}{3}(\rho + 3P). \tag{10.25}$$

10.4 Baryogenesis

In particle physics and cosmology, baryogenesis (or baryosynthesis) refers to an early-universe process that generated the observed baryonic asymmetry, an excess of matter over antimatter. But everything around us which we can see is made up of matter that contributes about 31.7% of the total budget of the universe (both visible and invisible). First suggested by Paul Dirac in 1928 through his work combining quantum mechanics and special relativity, this asymmetry remains a central puzzle in modern physics.

10.4.1 Sakharov Criteria

In 1967, a Russian physicist Sakharov [32] listed for the first time three essential requirements for the development of a baryon asymmetry. He proposed these matter-asymmetry conditions, drawing inspiration from CMB detection and the evidence of charge Parity (CP) violation in the neutral kaon system. Such requirements are

1 Braking of net baryon/ lepton quantity,

2 Braking of charge and CP transformation uniformity,

3 interactions that deviate from thermal equilibrium conditions.

The conditions listed by Sakharov can be more easily recognized by considering a hypothetical particle decay process.

10.4.2 Gravitational Baryogenesis

Davoudiasl et al. [33] proposed a supergravity-based mechanism that achieves the necessary baryon asymmetry using only the first two Sakharov conditions. This approach, involving violation of CP, arises from the interaction between the derivative of the curvature scalar R and the baryon current J^i, expressed

as:

$$\frac{1}{M_*^2}\int (\partial_i R) J^i d^4x\sqrt{g}, \tag{10.26}$$

where M_* represents the cutoff scale of the effective theory [34]. In GR with the FRW metric, the baryon-to-entropy ratio $\frac{\eta_B}{S}$ depends on $\frac{dR}{dt}$ and vanishes in the radiation-dominated era ($\omega = \frac{1}{3}$). Although theory predicts balanced matter–antimatter creation, observations [35] and minimal annihilation signatures [36] point to a matter excess. With η_β and $\eta_{\bar{\beta}}$ as baryon and anti-baryon densities, $\eta_B = \eta_\beta - \eta_{\bar{\beta}}$. The GB framework relates by the ratio of net baryon number to entropy S

$$\eta = \frac{\eta_B}{S} = \frac{\eta_\beta - \eta_{\bar{\beta}}}{S}. \tag{10.27}$$

Various observational schemes reported this asymmetry of the universe such as BBN [37] reported this value as $\frac{\eta_B}{S} = (5.80 - 6.50) \times 10^{-10}$. According to CMB [35], this asymmetry has value $\frac{\eta_B}{S} = (6.04 - 6.20) \times 10^{-10}$. According to recent data presented by Ade et al. [38] reported value of this asymmetry as

$$\frac{\eta_B}{S} \simeq 9.42 \times 10^{-11}. \tag{10.28}$$

When the temperature of universe dropped below the critical value $\mathcal{T}$D, representing the point where baryon asymmetry interactions become significant (written as $\mathcal{T}|\mathcal{T}_{\rm D}$), the asymmetry present in the universe can be estimated as [33].

$$\frac{\eta_B}{S} \simeq -\frac{15 g_b}{g_{*s}} \frac{\dot{R}}{M_*^2 \mathcal{T}}\bigg|_{\mathcal{T}_{\rm D}}, \tag{10.29}$$

here g_b represents the number of intrinsic degrees of freedom of baryons, while $g{*}s$ corresponds to those of massless particles.Assuming the system remains in thermal equilibrium, the energy density at any cosmic state with temperature $\mathcal{T}$ is given by

$$\rho(\mathcal{T}) = \frac{\pi^2}{30} g_{*s} \mathcal{T}^4. \tag{10.30}$$

10.5 Gravitational Baryogenesis in Einstein-Æther Gravity

By studying baryogenesis within Einstein-Æther gravity, one can assess how the Æther field influences matter formation and the fundamental structure of the universe, providing fresh insight into gravitational effects and the origins of the cosmos. This study explores GB in Einstein-Æther gravity through four models linear, nonlinear, radical, and logarithmic to understand how the Æther field influences matter, antimatter asymmetry and early universe dynamics. We examined the Hubble parameter H for each model using recent observational data (cosmic chronometers and Pantheon+SH0ES), expanding earlier

studies. This work broadens GB research and deepens insight into how various gravity models influence baryon asymmetry. The models are outlined below.

10.5.1 Model 1

First, we consider a linear model to investigate GB in the context of Einstein-Æther gravity. The mathematical formalism for the assumed model can be given as [39]

$$F(K) = \alpha K + \beta, \tag{10.31}$$

where α and β are real constants. In this model, we derive the BER in terms of the decoupling temperature, τ_D. Using the cosmic decoupling time t_D the energy density ρ has been calculated. Initially, we develop the relevant expressions for F, F', which can be calculated as:

$$K = \frac{3\lambda H^2}{M^2}. \tag{10.32}$$

Considering the power lawa scale factor model which can be given as

$$a = a_o t^p, \tag{10.33}$$

$$H = \frac{p}{t}. \tag{10.34}$$

Substituting the values of argument K and Hubble parameter H from Eqs. (10.32) and (10.34), into Eq. (10.31), we get

$$F = \beta + \frac{3\alpha\lambda p^2}{M^2 t^2}. \tag{10.35}$$

Differentiating Eq. (10.31) and substituting the values of K and H from Eq. (10.32), (10.34) in it, we obtain

$$F' = \alpha. \tag{10.36}$$

Inserting the values of $K,\ H,\ F,\ F'$ from Eqs. (10.32), (10.34), (10.35), (10.36), into Eq.(10.16), we get

$$\rho_{EA} = \frac{3\alpha\lambda p^2}{2t^2} - \frac{\beta M^2}{2} \tag{10.37}$$

Comparing Eq. (10.30) and Eq. (10.37), we obtain t_D as a function of τ_D which can be given as

$$t_D = -\frac{3\sqrt{5}\sqrt{\alpha}\sqrt{\lambda}p}{\sqrt{\pi^2 g_* T_D^4 + 15\beta M^2}}. \tag{10.38}$$

The net BER for the underlying model can be obtained by simplifying the Eqs. (10.29) and (10.38), as

$$\frac{\eta_B}{s} = \frac{g_b\left(\pi^2 g_* T_D^4 + 15\beta M^2\right)^2}{90\pi^2\alpha^2 g_* \lambda M^2 M_*^2 p^2}. \tag{10.39}$$

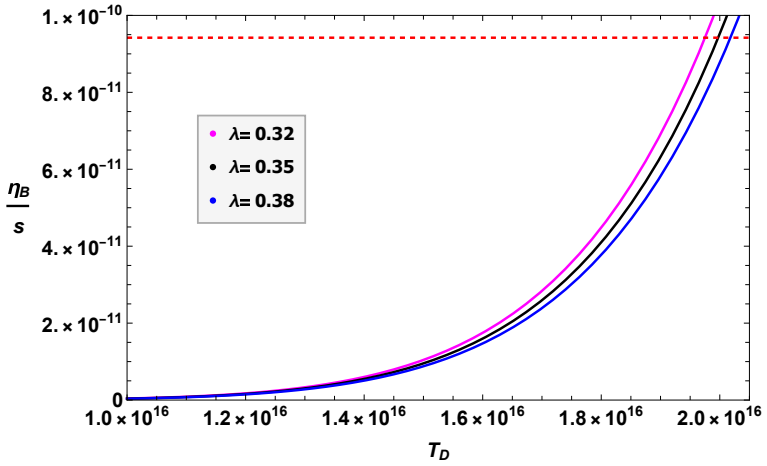

Figure 10.2: Variation of $\frac{\eta_B}{s}$ against T_D considering three different values of parameter λ.

FIG. 1.2 represents BER $\frac{\eta_B}{s}$ in three different curves against T_D for three different values of parameter λ as mentioned in the panel. Following the outcomes of Davoudiasl et al [5] we choose $M_* = 10^{12}$, M_I means upper bound restriction on fluctuation of tensor mode on the inflationary scale which has been obtained in the form of gravitational waves by LIGO. We choose $g_b \sim \mathcal{O}(1)$, $g_* = 106$ and by setting other parameters such as $m = 0.971, M = 1.5,\ \alpha = 0.3$ and $\beta = 0.7$. We obtained a BER which is compatible and consistent with recent observational data.

10.5.2 Model 2

We consider a non-linear model in the second choice to explore the gravitational baryogenesis in the context of Einstein-Æther gravity, the second model of our choice is [40]

$$F(K) = \alpha K + \beta K^2, \tag{10.40}$$

where $\alpha,\ \beta$ are real constants. We derive the BER w. r. t the decoupling temperature τ_D and hence calculate the energy density ρ by utilizing the cosmic time of decoupling t_D. Initially, we derive the corresponding expressions for F, F'. By inserting the value of K and H from Eq. (10.32), (10.34), into (10.40), we get

$$F = \frac{3\lambda p^2\left(\alpha M^2 t^2 + 3\beta\lambda p^2\right)}{M^4 t^4}. \tag{10.41}$$

Differentiating Eq. (10.40) and substituting the required values of H and K from Eq. (10.32), (10.34), we get

$$F' = \alpha + \frac{6\beta\lambda p^2}{M^2 t^2}. \tag{10.42}$$

Inserting the values of $K,\ H,\ F,\ F'$ from Eqs. (10.32), (10.34), (10.41), (10.42) into (10.16) and we get

$$\rho_{EA} = \frac{3\lambda p^2\left(\alpha M^2 t^2 + 9\beta\lambda p^2\right)}{2M^2 t^4}. \tag{10.43}$$

Equating (10.30) and (10.43), we obtained t_D as a function of τ_D, which can be given as

$$t_D = -3\sqrt{\frac{5\alpha\lambda M^2 p^2 - \sqrt{5}\sqrt{\lambda^2 M^2 p^4\left(4\pi^2\beta g T_D^4 + 5\alpha^2 M^2\right)}}{2g\pi^2 M^2 T_D^4}}. \tag{10.44}$$

The net BER for the underlying model can be obtained by simplifying the Eqs. (10.29) and (10.44) which is

$$\frac{\eta_B}{s} = \frac{10\pi^2 g_* g_b \lambda M^2 p^2 T_D^8}{9\left(\sqrt{5}M_*\sqrt{\lambda^2 M^2 p^4\left(4\pi^2\beta g_* T_D^4 + 5\alpha^2 M^2\right)} - 5\alpha\lambda M^2 M_* p^2\right)^2}, \tag{10.45}$$

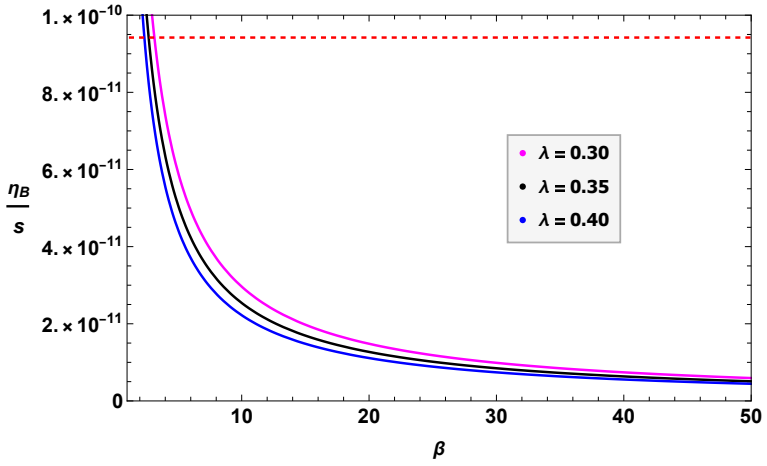

Figure 10.3: Plot of $\frac{\eta_B}{s}$ versus model parameter β for Model 2 considering different values of λ; additional parameters are $g_b = 1, \tau_D = 2 \times 10^{16}, M_* = 10^{12}, g_* = 106$.

FIG. 1.3 represents the BER for assumed model 2 against the model parameter β, for the various values of $\lambda = 0.3$ (pink), $\lambda = 0.35$ (black), $\lambda = 0.4$ (blue). The dotted line represents the value of the observational constraint.

10.6 Big Bang Nucleosynthesis

In cosmology, BBN also known as primordial nucleosynthesis refers to the formation of atomic nuclei, dense cores containing protons and neutrons, leading to the creation of early universe light isotopes. Following GB, it occurred around ten to twenty seconds after the big bang and ended in approximately 20 minutes. The cooling of the universe at that time allowed the creation of isotopes such as Hydrogen ${}^1H$ and Helium ${}^4He$, accounting for the significant Helium content we observe today.

The Primordial ${}^4He$ was produced when the universe had a temperature of about $\mathbf{T} \sim 100$ MeV. During this period, fast moving subatomic particles like electrons, protons, neutrinos and photons determined the energy and number densities, with protons and neutrons contributing negligibly. The particles remained in thermal equilibrium via collisions, and protons and neutrons continued to interact with leptons.

$$\nu_e + n^* \leftrightarrow p + e^-, \tag{10.46}$$

$$e^+ + n^* \leftrightarrow p + \bar{\nu}_e, \tag{10.47}$$

$$n^* \leftrightarrow p + e^- + \bar{\nu}_e. \tag{10.48}$$

These interactions keep the particles in thermal equilibrium, where e denotes electrons, p protons, n^* neutrons, and ν_e neutrinos. During cosmic acceleration, neutron abundance is determined from the proton–neutron conversion rate. The BBN era is significant because it produced almost all primordial hydrogen and helium via fusion, leaving only a small percentage of matter for large-scale structures.

10.6.1 Big Bang Nucleosynthesis Constraints: Basic Scenario

Since BBN is being noticed in radiation era [36], the first Friedmann equation can be simplified to the form below

$$H^2 \approx \frac{\rho_r}{3M_p^2} = H_{GR}^2, \tag{10.49}$$

where $M_p = \frac{1}{\sqrt{8\pi G}}$ is reduced Planck mass, ρ_r is energy density of a relativistic particle filling the universe and is written as

$$\rho \simeq \rho_r = \frac{\pi^2 g_* \mathcal{T}^4}{30}. \tag{10.50}$$

Here $g_* = g(\mathcal{T})$ is the effective number of the degree of freedom usually approximated as $g_* \sim 10$. Substituting the values of ρ_r and M_p in Eq.(10.49), we obtained

$$H(\mathcal{T}) = \left(\frac{4\pi^3 g_*}{45}\right)^{\frac{1}{2}} \frac{\mathcal{T}^2}{M_{p\ell}}, \tag{10.51}$$

The Planck mass is defined as $M_{p\ell} = \sqrt{8\pi}, M_P$. For a radiation-dominated universe, the scale factor follows $a(t) \sim \sqrt{t}$, and the Hubble parameter is $H = \frac{1}{2t}$. This leads to the time-temperature relation

$$\frac{1}{t} = \left(\frac{16\pi^3 g_*}{45}\right)^{\frac{1}{2}} \frac{\mathcal{T}^2}{M_{p\ell}} (or \mathcal{T}(t) \simeq (t/sec)^{-1/2} MeV).$$

or equivalently $\mathcal{T}(t) \simeq (t/\text{sec})^{-1/2}, \text{MeV}$. During BBN, neutrons are produced from the conversion of some protons at a specific proton–neutron rate [41], given as:

$$\Lambda_{pn}(\mathcal{T}) = \Lambda_{(n+\nu_e \to p+e^-)} + \Lambda_{(n+e^+ \to p+\bar{\nu}_e)} + \Lambda_{(n \to p+e^- + \bar{\nu}_e)}, \tag{10.52}$$

and its inverse $\Lambda_{np}(\mathcal{T})$ determines that the total rate can take the form $\Lambda_{tot}(\mathcal{T}) = \Lambda_{pn}(\mathcal{T}) + \Lambda_{np}(\mathcal{T})$, which can be calculated as

$$\Lambda_{tot}(\mathcal{T}) \;=\; 8(12\mathcal{T}^2 + 6Q_*\mathcal{T} + Q_*^2)\bar{A}\;\mathcal{T}^3, \tag{10.53}$$

where Q_* is the mass difference between neutron and proton given as $Q_* = m_n - m_p = 1.29 \times 10^{-3}\text{GeV}$ and $\bar{A} = 1.02 \times 10^{-11}\ \text{GeV}^{-4}$.

The helium mass fraction, $Y_p = \bar{\lambda}\frac{2x(\mathcal{T}_f)}{1+x(\mathcal{T}_f)}$, where $\bar{\lambda} = e^{(\mathcal{T}_f - \mathcal{T}_n)/\tau}.\bar{\lambda}(\mathcal{T}_f)$. Here $\mathcal{T}_f$ denotes the freeze-out time of weak interactions and $\mathcal{T}_n$ corresponds to the freeze-out of nucleosynthesis. The quantity $x(\mathcal{T}_f) = e^{-\frac{Q_*}{\tau(\mathcal{T}_f)}}$ represents the neutron-to-proton equilibrium ratio, while $\tau = 8803 \pm 1.1\text{s}$ is the mean lifetime of a neutron [42]. The function measures the fraction of neutrons that decay into protons during the interval $[\mathcal{T}_f, \mathcal{T}_n]$. We compare the universe expansion rate H^{-1} with the function $\Lambda_{tot}(\mathcal{T})$ from (10.53) to determine the freeze-out temperature $\mathcal{T}_f$. A system remains in thermal equilibrium when the interaction time exceeds the expansion time, $H^{-1} \ll \Lambda_{tot}(\mathcal{T})$ [36], whereas particle decoupling occurs when the expansion time exceeds the interaction time, $H^{-1} \gg \Lambda_{\text{tot}}(\mathcal{T})$. The temperature at which decoupling occurs, known as the freeze-out temperature $\mathcal{T}_f$, corresponds to

$$H(\mathcal{T}_f) = \Delta(\mathcal{T}_f) \simeq c_q \mathcal{T}_f^5,$$

where $c_q \equiv 96\bar{A} \simeq 9.8 \times 10^{-10}\ \text{GeV}^{-4}$ [18]. This expression is applied to determine the change in the Hubble parameter at the freeze-out temperature, giving $\Delta H_{\mathcal{T}_f} = 5c_q T_f^4\, \Delta\mathcal{T}_f$ which shows a direct link

between the variations in $H_{\mathcal{T}_f}$ and $\Delta\mathcal{T}_f$ as

$$\frac{\Delta H\mathcal{T}_f}{H\mathcal{T}_f} = 5\frac{\Delta\mathcal{T}_f}{\mathcal{T}_f}.$$

Using Eqs.(10.51) and (10.53), above requirement leads to the relation

$$\mathcal{T}_f \;=\; \left(\frac{4\pi^3 g_*}{45c_q^2 M_{p\ell}^2}\right)^{1/6}. \tag{10.54}$$

In modified cosmology, the Hubble parameter H will deviate from H_{GR}, leading to a corresponding shift in the freeze-out temperature $\Delta\mathcal{T}_f$ from (10.49).This change results in a deviation in the fractional mass, expressed as Y_p

$$\Delta Y_p \;=\; Y_p\left[\left(1-\frac{Y_p}{2\bar{\lambda}}\right)\ln\left(\frac{2\bar{\lambda}}{Y_p}-1\right)-\frac{2\mathcal{T}_f}{\tau}\right]\frac{\Delta\mathcal{T}_f}{\mathcal{T}_f}, \tag{10.55}$$

where $\Delta\mathcal{T}(\mathcal{T}_n)=0$ as $\mathcal{T}_n$ is fixed by deuterium binding energy [43]. During BBN era, the observational estimation of mass fraction is [44]

$$Y_p \;=\; 0.2476, \qquad |\Delta Y_p| < 10^{-4}. \tag{10.56}$$

In modified gravity theories, an additional term can appear in the Friedmann equations, which must remain much smaller than the radiation component of standard cosmology during the BBN era to preserve consistency with observational evidence. Thus, from the general modified Friedmann equation, $3M_p^2H^2 = \rho_m+\rho_r+\rho_{DE}$, we can obtain

$$H = H_{GR}\left(1+\frac{\rho_{DE}}{\rho_r}\right)^{1/2} = \Delta H + H_{GR}. \tag{10.57}$$

In this case, $\rho_r \gg \rho_m$ indicates how dark energy modifies the expansion rate H compared to standard general relativity, where $H_{GR} = M_p\sqrt{\frac{\rho_r}{2}}$ is the rate at which universe expands in standard cosmology. Thus, we get

$$\Delta H = H_{GR}\left(\sqrt{1+\frac{\rho_{DE}}{\rho_r}}-1\right). \tag{10.58}$$

This variation from standard cosmology results in a change in the freeze-out temperature, denoted by $\Delta\mathcal{T}_f$. Since $H_{GR}=\Lambda_{tot}\approx c_q\mathcal{T}_f^5$, this relation along with (10.54) leads to the relation

$$H_{GR}\left(\sqrt{1+\frac{\rho_{DE}}{\rho_r}}-1\right) = 5c_q\mathbf{T}_f^4\Delta\mathbf{T}_f. \tag{10.59}$$

In this phase $\rho_{DE} \ll \rho_r$, as a result, it is obtained as

$$\frac{\Delta \mathcal{T}_f}{\mathcal{T}_f} \simeq \frac{\rho_{DE}}{\rho_r} \frac{H_{GR}}{10 c_q \mathcal{T}_f^5}. \tag{10.60}$$

The relation derived above theoretically should be contrasted with the corresponding observational constraint.

$$\left| \frac{\Delta \mathcal{T}_f}{\mathcal{T}_f} \right| < 4.7 \times 10^{-4}, \tag{10.61}$$

which is found by using observational estimation of the baryon mass fraction converted into ^4He [44] which is given in Eq.(10.56).

10.6.2 BBN in Einstein-Aether Gravity

The Friedmann equations for Einstein-Aether gravity take the form

$$\gamma\left(\frac{1}{2}FK^{-1} - F'\right)H^2 + \left(\frac{k}{a^2} + H^2\right) = \frac{8\pi G}{3}\rho, \tag{10.62}$$

$$\gamma\left(\dot{H}F' + H\frac{dF'}{dt}\right) + \left(\frac{2k}{a^2} - 2\dot{H}\right) = 8\pi G(\rho + P), \tag{10.63}$$

where the constant parameter $\gamma = c_1 + 3c_2 + c_3$ and the argument $K = \frac{3\gamma H^2}{M^2}$. Taking ρ_{EA} as the effective energy density and P_{EA} as the effective pressure in Einstein–Aether gravity, equations (10.62) and (10.63) can be expressed as follows.

$$\left(\frac{k}{a^2} + H^2\right) = \frac{8\pi G}{3}\rho + \frac{1}{3}\rho_{EA}, \tag{10.64}$$

$$\left(\frac{2k}{a^2} - 2\dot{H}\right) = 8\pi G(\rho + P) + (\rho_{EA} + P_{EA}), \tag{10.65}$$

where

$$\rho_{EA} = 3\gamma H^2\left(F' - \frac{1}{2}FK^{-1}\right), \tag{10.66}$$

$$P_{EA} = -\gamma\left(\dot{H}F' + H\frac{dF'}{dt}\right) - 3\gamma H^2\left(F' - \frac{F}{2K}\right). \tag{10.67}$$

In the following subsections, the framework from Section **2.5** is used to determine the BBN constraints within Einstein–Aether gravity. Using the DE relation (10.66), valid in this context, we evaluate both the BBN constraints and the Hubble parameter H for a flat FRW universe, considering three distinct models.

10.6.3 Model 3: $F(K) = \alpha K^n + \beta\sqrt{K}$

Our initial focus for examining BBN constraints within the framework of Einstein–Aether gravity is on the first proposed model.

$$F(K) = \alpha K^n + \beta\sqrt{K}, \tag{10.68}$$

here $\alpha,\ \beta \neq 0$ are real constants and n is free parameter. By inserting Eq. (10.68) in Eq. (10.66), the mathematical expression for α is obtained.

$$\alpha = \frac{2 \times 3^{1-n} H0^2 M_p^2 \left(\frac{H0^2\gamma}{M^2}\right)^{-n} \Omega_{DEO}}{M^2(-1+2n)} \tag{10.69}$$

By inserting Eqs. (10.68) and (10.69) in Eq. (10.66), we determine the value of ρ_{EA}, which leads to Eq. (10.60).

$$\left|\frac{\Delta\mathcal{T}_f}{\mathcal{T}_f}\right| = \frac{H_0^2 \left(\frac{H_0^2\gamma}{M^2}\right)^{-n} \left(\frac{\mathcal{T}_f^4 \gamma \xi^2}{M^2}\right)^{n} \Omega_{DEO}}{10\, {c_q}^7\, \mathcal{T}_f^4 \xi} \tag{10.70}$$

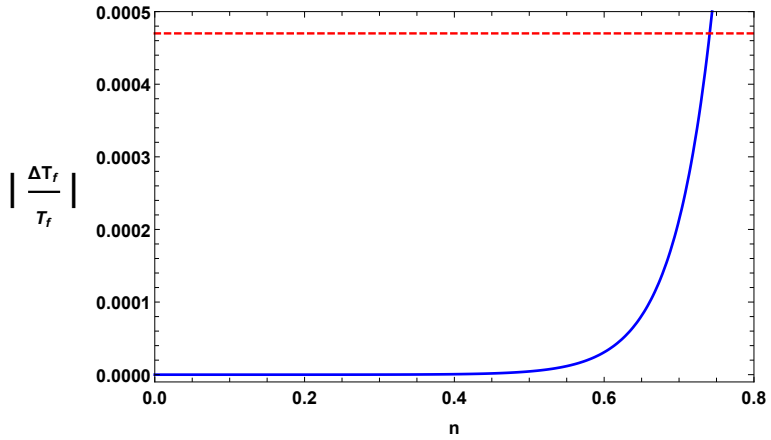

Figure 10.4: Plot of BBN constraint $\left|\frac{\Delta\mathcal{T}_f}{\mathcal{T}_f}\right|$ against model parameter n for **Model IV** in Einstein-Aether gravity.

In **Figure 1.4**, we present the plot of $\left|\frac{\Delta\mathcal{T}_f}{\mathcal{T}_f}\right|$ against n, using the upper bound from Eq. (10.61) and fixing the constants as $H_0 = 70$, $\Omega_{DEO} = 0.7$, $\gamma = 0.05$ and $M = 0.1$. The results show that the relation in Eq. (10.70) remains within the bound of Eq. (10.61) for $n \leq 0.7444$. Furthermore, when the free parameter n is taken to be close to zero, the bound in Eq. (10.60) becomes constant, which is consistent with the ΛCDM scenario.

10.6.4 Model 4: $F(K) = b_0 K^n + Log[K]$

The second model considered for examining BBN constraints within the framework of Einstein–Aether gravity is formulated in a more general form is given as

$$F(K) = b_0 K^n + Log[K], \tag{10.71}$$

here b_0 is constant and n is a free parameter. Hence, the mathematical expression for the constant b_0 during the BBN era can be derived as follows.

$$b_0 = \frac{3^{-n}\left(\frac{H_0^2\gamma}{M^2}\right)^{-n}\left(-2M^2 + 6H_0^2 M_p^2 \Omega_{DEO} + M^2 \log\left[\frac{3H_0^2\gamma}{M^2}\right]\right)}{M^2(-1+2n)} \tag{10.72}$$

Substituting Eqs.(10.71) and (10.72) into (10.66), we obtained the value of ρ_{EA} which gives Eq.(10.60) as

$$\left|\frac{\Delta\mathcal{T}_f}{\mathcal{T}_f}\right| = \frac{1}{60\, c_q\, M_p^2\, \mathcal{T}_f^7\, \xi}\left(M^2\left[2 + \frac{\left(\frac{H_0^2\gamma}{M^2}\right)^{-n}\left(\frac{\mathcal{T}_f^4\gamma\,\xi^2}{M^2}\right)^{n}\left(-2M^2 + 6H_0^2M_p^2\Omega_{DEO} + M^2\log\left(\frac{3H_0^2\gamma}{M^2}\right)\right)}{M^2} - \log\left(\frac{3\mathcal{T}_f^4\gamma\,\xi^2}{M^2}\right)\right]\right). \tag{10.74}$$

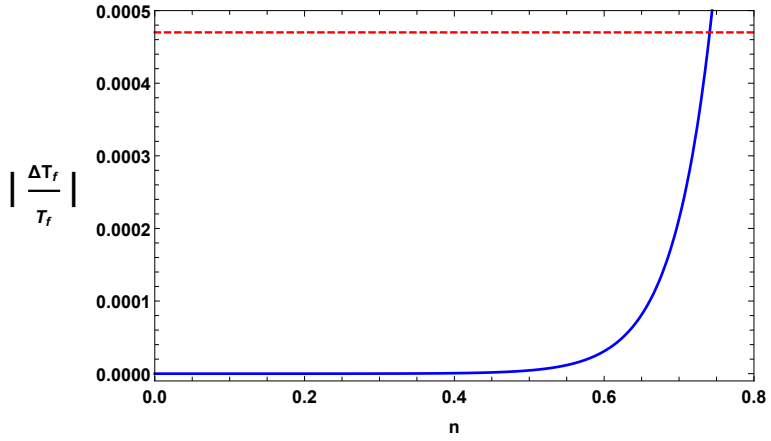

Figure 10.5: Plot of BBN constraint $\left|\frac{\Delta\mathcal{T}_f}{\mathcal{T}_f}\right|$ against model parameter n for **Model V** in Einstein-Aether gravity.

Figure 1.5 illustrates the plot of the above equation with respect to the parameter n, considering an upper bound of 4.7×10^{-4}. It is evident that the absolute value of the given relation remains below

this limit for $n \leq 0.7393$. The fixed parameters used in this analysis are $H_0 = 70$, $\gamma = 0.05$, $\Omega_{DEO} = 0.7$, $M_p = 1$ and $M = 0.1$. Furthermore, when the parameter n is taken close to zero, the bound from Eq. (10.60) becomes constant, which is consistent with the ΛCDM framework.

10.7 Conclusions

The exploration of the universe's fundamental nature has led to various cosmological theories, including Einstein-Æther gravity, which explains late-time cosmic expansion without disturbing early-universe behavior such as GB and BBN. Our analysis focuses on these aspects, highlighting that despite observational progress, the baryon asymmetry problem persists. We examined GB and BBN within the framework of Einstein-Æther gravity. The baryon-to-entropy ratio was computed using fixed parameters $M_* = 10^{12}$ GeV, **TD** $= 2 \times 10^{16}$ GeV, $g_b = 1$, and $g*s = 106$. BBN was further analyzed for two Einstein-Æther models under observational limits on the primordial abundance of ^4He, yielding the bound $\left|\frac{\Delta T_f}{T_f}\right| < 4.7 \times 10^{-4}$. Interestingly, both models of BBN constraints are satisfied up to some particular value of the free parameter n as shown in **Figures 1.4, 1.5** respectively.

Our analysis shows that Einstein-Æther gravity aligns well with the mechanisms of GB and BBN across various models. The observational analysis supports their validity and provides a foundation for further research in modified gravity cosmology. Future studies can extend this work by exploring other cosmological epochs under Einstein-Æther gravity. A detailed comparison with upcoming observational data may further refine model parameters. Additionally, incorporating quantum and thermodynamic effects could offer deeper insight into early-universe dynamics.

Bibliography

[1] Maluf, J. W. (2013). The teleparallel equivalent of general relativity, *Ann. Phys.* **525**, 339.

[2] Nojiri, S., Odintsov, S. D. and Oikonomou, V. K. (2022). Integral $F(R)$ gravity and saddle point condition as a remedy for the H_0-tension, *Nucl. Phys. B* **980**, 115850.

[3] Ferraro, R. and Fiorini, F. (2007). Modified teleparallel gravity: inflation without an inflaton, *Phys. Rev. D* **75**, 084031.

[4] Carloni, S. et al. (2012). Modified first-order Hořava-Lifshitz gravity: Hamiltonian analysis of the general theory and accelerating FRW cosmology in a power-law $F(R)$ model, *Phys. Rev. D* **85**, 129904.

[5] Kofinas, G. and Saridakis, E. N. (2014). Teleparallel equivalent of Gauss-Bonnet gravity and its modifications, *Phys. Rev. D* **90**, 084044.

[6] Bueno, P. and Cano, P. A. (2016). Einsteinian cubic gravity, *Phys. Rev. D* **94**, 104005.

[7] Erices, C. , Papantonopoulos, E. and Saridakis, E. N. (2019). Cosmology in cubic and $f(P)$ gravity, *Phys. Rev. D* **99**, 123527.

[8] Rani, S. et al. (2019). Cosmological consequences of new dark energy models in Einstein-Aether gravity, *Symmetry* **11**, 509.

[9] Capozziello, S., Capriolo, M. and Caso, L. (2020). Weak field limit and gravitational waves in $f(T, B)$ teleparallel gravity, *Eur. Phys. J. C* **80**, 156.

[10] Amendola, L., Giani, L. and Laverda, G. (2020). Ricci-inverse gravity: a novel alternative gravity, its flaws, and how to cure them, *Phys. Lett. B* **811**, 135923.

[11] Atazadeh, K. (2018). Gravitational baryogenesis in DGP brane cosmology, *Eur. Phys. J. C* **78**, 455.

[12] Baffou, E. H. et al. (2019). $f(R, T)$ models applied to baryogenesis, *Eur. Phys. J. C* **79**, 112.

[13] Azhar, N., Jawad, A. and Rani, S. (2020). Generalized gravitational baryogenesis of well-known $f(T, T_G)$ and $f(T, B)$ models, *Phys. Dark Univ.* **30**, 100724.

[14] Azhar, N., Jawad, A. and Rani, S. (2021). Impact of $f(\mathcal{G}, T)$ and $f(R, \mathcal{G})$ on gravitational baryogenesis and observational bounds, *Phys. Dark Univ.* **32**, 100815.

[15] Agrawal, A. S., Tripathy, S. K. and Mishra, B. (2021). Gravitational baryogenesis models comparison in $f(R)$ Gravity, *Chinese J. Phys.* **71**, 333.

[16] Usman, M. Jawad, A. and Sultan, A. M. (2024). Compatibility of gravitational baryogenesis in $f(Q, C)$ gravity, *Eur. Phys. J.C*, **84**, 868.

[17] Sultan, A. M., Mushtaq, A., Jawad, A., Shaymatov, S., and Saleem, M. S. (2025).Gravitational baryogenesis analysis of observationally favored $f(T, \phi)$ models, *Phys. Dark Univ*, **48**, 101936.

[18] Barrow, J. D., Basilakos, S. and Saridakis, E. N. (2021).Big Bang Nucleosynthesis constraints on Barrow entropy, *Phys. Lett. B*, **815**, 136134.

[19] Anagnostopoulos, F. K., Gakis, V., Saridakis, E. N., and Basilakos, S. (2023). New models and big bang nucleosynthesis constraints in $f(Q)$ gravity. *Eur. Phys. J. C* **83**, 58.

[20] Sultan, A. M., Ali, M., Rani, S., Azhar, N., Myrzakulov, N., and Shaymatov, S. (2025) Constraining Big Bang nucleosynthesis in $f(T, B, T_{\mathcal{G}}, B_{\mathcal{G}})$ gravity. *Nucl. Phys. B* **1018**, 117023.

[21] Sultan, A. M., Fatima, M., Said, J. L., and Batool, A. (2025). Constraining big bang nucleosynthesis on $f(T, B)$ gravity through observational analysis. *Physics of the Dark Universe* **49**, 102023.

[22] Sultan, A. M., Fatima, M., and Said, J. L. (2025). BBN in Constrained $f(T, \varphi)$ Gravity Through Various Observational Schemes. *Class. Quan. Grav.* **42**, 175009.

[23] Bhattacharjee, S. (2022). BBN constraints on $f(Q,T)$ gravity, *Int. J.Mod.Phys. A* **37**, 2250017.

[24] Asimakis, P., Basilakos, S., Mavromatos, N. E. and Saridakis, E. N. (2022). Big bang nucleosynthesis constraints on higher-order modified gravities, *Phys. Rev. D* **105**,084010.

[25] Hubble, E. (1929). A relation between distance and radial velocity among extra-galactic nebulae, *Astronomy* **15**, 168.

[26] Urban, F. R. and Zhitnitsky, A. R. (2010). The Cosmological Constant from the QCD Veneziano Ghost, *Phys. Lett. B* **688**, 9.

[27] Percival, W. J. et al. (2010). Baryon Acoustic Oscillations in the Sloan Digital Sky Survey Data Release 7 Galaxy Sample, *Mon. Not. Roy. Astron.Soc.* **401**, 2148.

[28] Gasperini, M. (1998). Repulsive gravity in the very early Universe, *Gen. Relativ. Gravit.* **30**, 1703.

[29] Jacobson, T. and D. Mattingly. (2001). Gravity with a dynamical preferred frame. *Phys. Rev. D* **64**, 024028.

[30] Fixsen, D. J. (2009). The Temperature of the Cosmic Microwave Background, *Astrophys. J.* **707**, 916.

[31] Walker, A. G. (1934). The principle of least action in Milne's kinematical relativty, *Pro. Royal soc. A* **147**, 478.

[32] Sakharov, A. D. (1967). Violation of CP-invariance, C-asymmetry, and Baryon Asymmetry of the Universe, *J. Exp. Theor. Phys. Lett.* **5**, 24.

[33] Davoudiasl, H. et al. (2004). Gravitational baryogenesis, *Phys. Rev. Lett.* **93** 201301.

[34] Nozari, K. and Rajabi, F. (2018). Baryogenesis in $f(R,T)$ Gravity, *Commun. Theor. Phys.* **70**, 451.

[35] Spergel, D. N. et al. (2003). First-Year Wilkinson Microwave Anisotropy Probe (WMAP)* Observations: Determination of Cosmological Parameters, *Astrophys. J. Suppl* **148**, 175.

[36] Cohen, A. G., De Rujula A. and Glashow S. L. (1998). A matter-antimatter universe?, *Astrophys. J.* **495**, 539.

[37] Burles, S. et al. (2001). What is the big-bang-nucleosynthesis prediction for the baryon density and how reliable is it?, *Phys. Rev. D* **63**, 063512.

[38] Ade, P. A. R. et al. (2016). Planck Collaboration,*A & A* **594**, A13.

[39] Caruana, M., Farrugia, G. and Said, J. L. (2020). Cosmological bouncing solutions in $f(T,B)$ gravity, *Eur. Phys. J. C* **80**, 640.

[40] Novello, M. and Bergliaffa, S. E. P. (2008). Bouncing cosmologies, *Phys. Rep.* **463**, 127.

[41] Olive, K. A., Steigman, G. and Walker, T. P. (2000).Primordial nucleosynthesis: theory and observations, *Phys. Rep.***333**, 389.

[42] Olive, K.A. et al. (2014). Review of particle physics, *Chin. Phys. C* **38**, 0900001.

[43] Lambiase, G. (2011). Dark matter relic abundance and big bangnucleosynthesis in Hóravas gravity, *Phys. Rev. D***83**, 107501.

[44] Olive, K. A., Skillman, E. and Steigman, G. (1997). The primordial abundance of ^4He: an update, *Astrophys. J.* **483**, 788.

CHAPTER 11

Topological Descriptors of Chemical Networks: A Case Study of M-Carbon via Entropy Measures and Regression Modeling

Muhammad Irfan

Department of Mathematics, University of Okara, Okara, Pakistan.

Corresponding Author: m.irfan@uo.edu.pk

Abstract: *This chapter presents a detailed characterization of M-carbon, a superhard hypothetical carbon allotrope with a monoclinic crystal structure (C2/m), using a suite of degree-based topological indices. We compute and compare several well-known indices, including the forgotten index, augmented Zagreb index, redefined Zagreb indices, sum connectivity index, arithmetic geometric index, Somber index, and reduced Somber index. In addition to calculating these indices, we determine their corresponding entropy measures. To explore the relationship between the indices and entropy, we analyze power, rational, and logarithmic models to identify the best-fit representation. Furthermore, we investigate the correlation between the various indices and their associated entropy to elucidate how these topological features influence one another.*

This analysis provides a comprehensive topological profile of M-carbon, contributing to a deeper understanding of its structural properties, which are critical for potential applications in ultra-hard materials, cutting tools, and wear-resistant coatings.

Keywords: M-carbon, topological indices, entropy, best fit model, correlation

11.1 Introduction

Diamond is one of the hardest carbon structures. A great deal of superhard allotropes, which are as hard as diamonds, were created in 2011 by Andriy and Artem. Lyakhov and Oganov in [17] searched 9500 structures with various system sizes. M-carbon was one of the superhard carbon allotropes they examined. Li et al. in [18] and Umemoto et al. in [27] suggest that cold compression of graphite can produce carbon allotropes like M-carbon.

Several variations, including graphite, diamond, lonsdaleite (a hexagonal diamond), carbynes, nanotubes, fullerences, and amorphous carbon, are possible for carbon. This is due to the fact that carbon may create hybridised bonds with sp, sp^2, and sp^3. We have discovered a new monoclinic structure with $C2/m$ symmetry as a metastable low-energy polymorph that is distinct from diamond and hexagonal diamond better than graphite at pressures exceeding $13.4GPa$. This monoclinic polymorph is known as M-carbon.

M-carbon exhibits sixfold rings that create twisted "layers." One way to describe this fascinating structure is as warped graphite: Sp^3 bonds between the planes occur when the planes compress against graphite, causing the planes to slide and buckle. XRD (X-ray diffraction) pattern is a graphical representation of the diffraction of X-rays by the atoms in a structure. When X-rays are directed at a structure, they are scattered in specific directions that depend on the structure. The anticipated graphite experimental XRD patterns show changes at 14 GPa, which is in perfect agreement with the M-carbon transition pressure of 13.4 GPa. M-carbon XRD accurately replicates the main experimental results in [19, 30], which show that the high pressure phase's strongest line arises between peaks 100 and 110. The M-carbon diffraction peaks become more pronounced as pressure rises. Observe that the comparatively weaker M-carbon peaks in the 11°–14° range have also blended into the background, much like that in pure graphite. The peaks at ~ 9 and ~ 17 also had a role in the peak broadening. Thus, examination of the XRD patterns adds to the evidence supporting the formation of M-carbon from the cold compression of graphite.

While numerous carbon allotropes exist, M-carbon presents a uniquely compelling subject for topological analysis due to its distinct, anisotropic structure that emerges from the cold compression of graphite. Unlike the isotropic frameworks of diamond or graphite, M-carbon's orthorhombic lattice, composed of fused C_4 and C_6 rings, creates a complex and highly interconnected network. This specific architecture poses critical structural questions regarding its bond connectivity, network robustness, and the influence of its unique ring distribution on overall stability and electronic properties. By applying a suite of topological indices—such as the Randić index to quantify branching complexity, the Zagreb indices to assess molecular stability, and the harmonic index to correlate with energetic properties—we can decode the underlying structural code of M-carbon. The computed indices will provide quantitative, structure-derived predictors for properties like bond strength, lattice energy, and potential chemical reactivity, offering a novel, mathematical lens through which to understand and predict the behavior of this high-pressure

phase, which is difficult to probe experimentally.

11.2 Literature

In mathematical chemistry, we use mathematical methods to explain and analyse some properties of a chemical structure. Chemistry has benefited greatly from the many tools that graph theory has given us, including topological indices. The field of chemical sciences greatly benefits from the study of graph theory. The use of molecular descriptors makes it possible to manipulate and examine chemical structure data. The study of molecular structure benefits from the application of graph theory to the mathematical modelling of molecular events, which is made possible by chemical graph theory.

Molecular descriptors are important tools in mathematical chemistry, particularly when it comes to modelling quantitative structure activity relationships and property relationships. A remarkable space is allotted among them for the well-known topological indices, also known as graph invariants. Topological indices are the term used to refer to the graph invariants in mathematical chemistry. Some familiar topological indices are Wiener index, Randić index, connectivity indices, Zagreb indices etc. The concept of topological indices was first introduced in 1947 when renowned scientist Harold Wiener discovered the Wiener index [29], the first topological index for finding alkane boiling points. The Zagreb indices are linked to the most widely used molecular descriptors among the topological indices developed in the early stages. It was firstly presented by Gutman and Trinajestić [7, 8], where it was acknowledged on [9] that they looked at how the structure of molecules affects the total energy of ϕ-electron. M.C. Shanmukha and co-authors compute anticancer Zagreb indices in 2020.(Refer to [25] article)

Other well-known and frequently used degree-based topological indices to model various structure property/structure-activity relationships include the symmetric division degree index [28], the forgotten topological index [6], the Randić index [23], and the sum connectivity index [31]. B. Basavanagoud and co-authors in [4] introduces zagreb indices and forgotten index of C- product of graph. Chemical graph theory is heavily dependent on degree based and neighborhood based topological indices, particularly in the discipline of chemistry. The edge version of the degree base topological indices of boron triangular nanotubes are calculated by Amna Amer, M. Irfan, and Hamood ul Rehman in [2] and Amna Amer, et al. in [3]. According to [14], the nanotube's neighbourhood degree base topological indices were determined in 2024. Degree-base topological indices, such as entropy and M-polynomial, can be used to compute various formulas. Using degree based topological indices of certain networks, M-polynomials and entropy were computed in [13, 21]. Neighborhood forgotten index of graphene structure calculated in 2019[20]. In 2010, scientists concentrated on creating increasingly intricate indices and using them with polymers, particularly those utilised in the material sciences. In 2020, chemical graph theory had spread to novel fields such as drug design and nanotechnology, with a rising focus on new indices like sum-connectivity and the harmonic index that have found use in materials and pharmaceutical research. F. Afzal et al.

in [1] calculate some new degree base topological indices of polyhex graphs. Researchers from various fields began exploring this novel approach to study the chemical and physical properties of molecules, compounds, and chemical structures.

While topological indices are well-established for characterizing stable carbon allotropes, a significant gap exists in their application to metastable, high-pressure phases like M-carbon, whose unique anisotropic structure remains topologically unexplored. This work fills this gap by performing a comprehensive computational analysis of M-carbon using a suite of advanced degree-based indices. We then extend this analysis by computing the corresponding entropy measures to quantify structural complexity and employing regression modeling to uncover fundamental index-entropy relationships. This integrated approach provides a novel topological descriptor set that deciphers the underlying structural code of M-carbon, enabling the prediction of its properties and bridging a critical divide between mathematical chemistry and the design of advanced superhard materials.

Chemical graph theory is a branch of mathematics that applies graph theory to study molecular structures in chemistry. In this context, atoms are represented as vertices (nodes) and chemical bonds as edges in a graph. This abstraction allows chemists to analyze molecular structures using graph theoretical concepts. Let $G(V, E)$ be a graph with vertex set V and edge set E. If a is a vertex then the number of edges connected to a is called its degree, denoted as h_a.

In this study, we calculated degree based topological indices and their corresponding entropy of M-carbon structure. The structural aspects of the graphs are calculated using a wide range of topological index and their entropy. They are classified into degree based, distance-based, eccentric based and counting related indices of graphs. Topological indices that we shall discuss in this article include harmonic index, sum connectivity index, arithmetic geometric index, redefined zagreb indices, somber index, reduced somber index, augmented Zagreb index and forgotten index.

In 2013 I. Gutman[12] introduced harmonic index is defined as:

$$H(G) = \sum_{ab \in E(G)} \frac{2}{h_a + h_b} \tag{11.1}$$

Trinajstic, Zhou[31] Discussed the characteristics of the sum connectivity index for graphs and provided the sum-connectivity index for a graph G in 2009. The sum-connectivity index SCI of graph G is defined as follows:

$$SCI(G) = \sum_{ab \in E(G)} \frac{1}{\sqrt{h_a + h_b}} \tag{11.2}$$

In 2015, Shegehalli and Kanabur[24] introduced the arithmetic–geometric index AGI of a graph G. Some fundamental properties of the arithmetic–geometric index have been found in Refs [10].

$$AGI(G) = \sum_{ab \in E(G)} \frac{h_a + h_b}{2\sqrt{h_a \times h_b}} \tag{11.3}$$

In 2013 [22] Ranjini et al. defined the redefined first, second, and third zagreb indices for a graph as follows.

$$ReZG_1(G) = \sum_{ab \in E(G)} \frac{h_a + h_b}{h_a \times h_b} \tag{11.4}$$

$$ReZG_2(G) = \sum_{ab \in E(G)} \frac{h_a \times h_b}{h_a + h_b} \tag{11.5}$$

$$ReZG_3(G) = \sum_{ab \in E(G)} (h_a \times h_b)(h_a + h_b) \tag{11.6}$$

The somber index and the reduced somber index are degree-based topological indices that are based on a vertex degree. These indices introduced by Gutman[11]. The following definition of somber index and reduced somber index.

$$SO(G) = \sum_{ab \in E(G)} \sqrt{(h_a)^2 + (h_b)^2} \tag{11.7}$$

$$SO_red(G) = \sum_{ab \in E(G)} \sqrt{(h_a - 1)^2 + (h_b - 1)^2} \tag{11.8}$$

The augmented zagreb index was introduced by Furtula et al. in 2010 [5] and was described as follows:

$$AZI(G) = \sum_{ab \in E(G)} [\frac{h_a \times h_b}{h_a + h_b - 2}]^3 \tag{11.9}$$

F. Gutman presented the F-index or forgotten topological index in 2015[6] was described as follows:

$$F(G) = \sum_{a \in V(G)} (h_a)^3 = \sum_{ab \in E(G)} [(h_a)^2 + (h_b)^2] \tag{11.10}$$

The entropy of a graph expressing a chemical molecule can be used to measure the complexity and structural diversity of that graph. One common entropy metric is the Shannon entropy, which is determined by studying the distribution of particular structural properties in a set of chemical graphs. Shannon entropy can be computed from the distribution of atom and bond types, from topological features like connection patterns and ring diameters, and from other sources as well. In 1948, Shannon also established the idea of entropy, which assesses the molecular disorder of the system [26]. A greater entropy number indicates that there is more structural variety within the set of molecules. In the context of chemical graph theory, the Shannon entropy measures applied to topological indices do not represent thermodynamic entropy but rather informational entropy or structural complexity. It quantifies the degree of uncertainty, heterogeneity, or "surprise" in the distribution of a specific structural property across the entire network. The entropy in nanostructures with Y-junctions was investigated by Koam [15]. The idea of the Nirmala indices based entropy was recently suggested by Virendra Kumar et al. in [16].

$$ENT = -\sum_{i=1}^{r} U_i \frac{f(h_a h_b)}{TI} log \frac{f(h_a h_b)}{TI} = log(TI) - \frac{1}{TI} \sum_{i=1}^{r} U_i f(h_a h_b) log f(h_a h_b) \tag{11.11}$$

In this context, $TI = \sum_{i=1}^{r} U_i f(h_a h_b)$ represents the topological index, where U_i is the frequency, r is the number of edges, and $f(h_a h_b)$ is the weight of the edge $h_a h_b$.

Construction of M-carbon $M[l, m, n]$

We will discuss our key findings on the M-carbon structure, which is represented by the notation $M[l, m, n]$. Firstly, we must briefly describe the variables l, m, n in the notation $M[l, m, n]$.

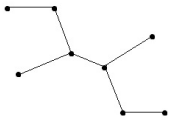

Figure 11.1: Unit Cell

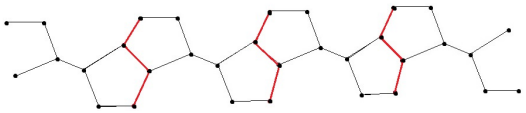

Figure 11.2: Chain of Three Unit Cells

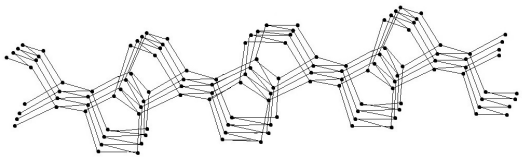

Figure 11.3: $M[4, 4, 1]$

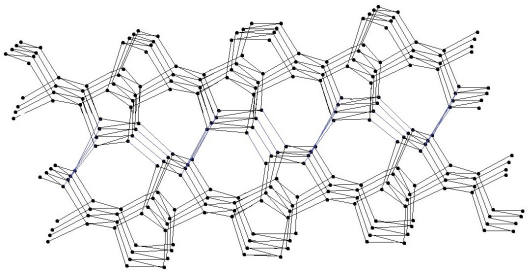

Figure 11.4: Structure of $M[4, 4, 2]$

In this section, we shall present our main results about the M-carbon structure denoted as $M[l, m, n]$. First, we need to give a brief explanation of the variables l, m, n in the notation $M[l, m, n]$. To find and compute the topological indices of the M-carbon structure, we have introduced a way of constructing its structure by the means of these three variables, where l represents the unit as shown in Figures 11.1 and 11.2 represents a chain containing four units, where the connection (bond) is shown in red color. The variable m represents the number of connected chains with each having l numbers of units, Figure 11.3 represents four connected chains. The variable n represents the number of connected layers, the Figure 11.4 represents two layers of four connected chains with four units in each chain.

11.3 The counts, topological invariants and entropies of M-carbon

Using the construction of $M[l,m,n]$ the numbers of vertices and edges in $M[l,m,n]$ are $8lmn$ and $16lmn-4ln-5mn-2lm+n+m$, respectively for $l \geq 2$, $m \geq 2$, and $n \geq 2$.

$M[l,m,n]$ have $2(m+1)n$, $4l-2+2(m-1)n$, $2lmn+2lm+6ln-mn-6l-m-3n+3$, and $6lmn-2lm-6ln-3mn+2l+m+3n-1$ vertices of degrees 1, 2, 3, and 4, respectively. The degree base edge partition of $M[l,m,n]$ is given in Table 11.1. Table 11.2 and 11.3 show the numerical comparison of degree based indices and Figures 11.5 and 11.6 shows their graphical representations. Table 11.4 and 11.5 show the numerical comparison of degree based entropies and Figures 11.7 and 11.8 shows their graphical representations.

Table 11.1: Degree-Based Edge Partition of M carbon $M[l,m,n]$ for $l,m,n \geq 2$

(h_a,h_b)	Frequency
(1,3)	$2n+2$
(1,4)	$2mn-2$
(2,2)	2
(2,3)	$8l+2m+2n-8$
(2,4)	$4mn-4m-6n+6$
(3,3)	$6ln+2lm-4l-2m-3n+5$
(3,4)	$4lm+4ln-2m-4n+2$
(4,4)	$16lmn-8lm-14ln-11mn-4l+7m+10n-7$

11.3.1 Degree-Based Topological Invariants

The degree based indices of M-carbon structure can be computed by using Table 11.1 and equations 11.1,11.2,11.3,11.4,11.5,11.6,11.7,11.8,11.9,11.10.

- **Harmonic Index**

$H(M[l,m,n]) = (2n+2)(\frac{2}{1+3}) + (2mn-2)(\frac{2}{1+4}) + 2(\frac{2}{2+2}) + (8l+2m+2n-8)(\frac{2}{2+3}) + (4mn-4m-6n+6)(\frac{2}{2+4}) + (6ln+2lm-4l-2m-3n+5)(\frac{2}{3+3}) + (4lm+4ln-2m-4n+2)(\frac{2}{3+4}) + (16lmn-8lm-14ln-11mn-4l+7m+10n-7)(\frac{2}{4+4})$,

$H(M[l,m,n]) = 4lmn-0.19lm-0.35ln-0.61mn+0.86l-0.02m+0.15n-0.71.$

- **Sum Connectivity Index**

$SCI(M[l,m,n]) = (2n+2)\frac{1}{\sqrt{1+3}} + (2mn-2)\frac{1}{\sqrt{1+4}} + 2\frac{1}{\sqrt{2+2}} + (8l+2m+2n-8)\frac{1}{\sqrt{2+3}} + (4mn-4m-6n+6)\frac{1}{\sqrt{2+4}} + (6ln+2lm-4l-2m-3n+5)\frac{1}{\sqrt{3+3}} + (4lm+4ln-2m-4n+2)\frac{1}{\sqrt{3+4}} + (16lmn-8lm-14ln-11mn-4l+7m+10n-7)\frac{1}{\sqrt{4+4}}$,

$SCI(M[l,m,n]) = 5.65lmn-0.50lm-0.98ln-1.36mn+0.53l+0.16m+0.24n+0.29.$

- **Arithmetic Geometric Index**

$AGI(M[l,m,n]) = (2n+2)(\frac{1+3}{2\sqrt{1\times 3}}) + (2mn-2)(\frac{1+4}{2\sqrt{1\times 4}}) + 2(\frac{2+2}{2\sqrt{2\times 2}}) + (8l+2m+2n-8)(\frac{2+3}{2\sqrt{2\times 3}}) + (4mn - 4m - 6n + 6)(\frac{2+4}{2\sqrt{2\times 4}}) + (6ln + 2lm - 4l - 2m - 3n + 5)(\frac{3+3}{2\sqrt{3\times 3}}) + (4lm + 4ln - 2m - 4n + 2)(\frac{3+4}{2\sqrt{3\times 4}}) + (16lmn - 8lm - 14ln - 11mn - 4l + 7m + 10n - 7)(\frac{4+4}{2\sqrt{4\times 4}})$,

$AGI(M[l,m,n]) = 16lmn - 1.95lm - 9.95ln - 4.25mn + 0.16l + 0.77m + 0.94n + 0.02.$

- **Redefined First Zagreb Index**

$ReZG_1(M[l,m,n]) = (2n+2)(\frac{1+3}{1\times 3}) + (2mn-2)(\frac{1+4}{1\times 4}) + 2(\frac{2+2}{2\times 2}) + (8l+2m+2n-8)(\frac{2+3}{2\times 3}) + (4mn - 4m - 6n + 6)(\frac{2+4}{2\times 4}) + (6ln + 2lm - 4l - 2m - 3n + 5)(\frac{3+3}{3\times 3}) + (4lm + 4ln - 2m - 4n + 2)(\frac{3+4}{3\times 4}) + (16lmn - 8lm - 14ln - 11mn - 4l + 7m + 10n - 7)(\frac{4+4}{4\times 4})$,

$ReZG_1(M[l,m,n]) = 8lmn - 0.33lm - 0.66ln + 2l - 0.33m + 0.5n + 1.$

- **Redefined Second Zagreb Index**

$ReZG_2(M[l,m,n]) = (2n+2)(\frac{1\times 3}{1+3}) + (2mn-2)(\frac{1\times 4}{1+4}) + 2(\frac{2\times 2}{2+2}) + (8l+2m+2n-8)(\frac{2\times 3}{2+3}) + (4mn - 4m - 6n + 6)(\frac{2\times 4}{2+4}) + (6ln + 2lm - 4l - 2m - 3n + 5)(\frac{3\times 3}{3+3}) + (4lm + 4ln - 2m - 4n + 2)(\frac{3\times 4}{3+4}) + (16lmn - 8lm - 14ln - 11mn - 4l + 7m + 10n - 7)(\frac{4\times 4}{4+4})$,

$ReZG_2(M[l,m,n]) = 32lmn - 6.14lm + 43.85ln - 15.06mn - 4.4l + 5.90m + 4.54n - 2.77.$

- **Redefined Third Zagreb Index**

$ReZG_3(M[l,m,n]) = (2n+2)(1\times 3)(1+3) + (2mn-2)(1\times 4)(1+4) + 2(2\times 2)(2+2) + (8l+2m+2n-8)(2\times 3)(2+3) + (4mn - 4m - 6n + 6)(2\times 4)(2+4) + (6ln + 2lm - 4l - 2m - 3n + 5)(3\times 3)(3+3) + (4lm + 4ln - 2m - 4n + 2)(3\times 4)(3+4) + (16lmn - 8lm - 14ln - 11mn - 4l + 7m + 10n - 7)(4\times 4)(4+4)$,

$ReZG_3(M[l,m,n]) = 2048lmn - 580lm - 1132ln - 1176mn - 488l + 488m + 578n - 394.$

- **Somber Index**

$SO(M[l,m,n]) = (2n+2)(\sqrt{1^2+3^2}) + (2mn-2)(\sqrt{1^2+4^2}) + 2(\sqrt{2^2+2^2}) + (8l+2m+2n-8)(\sqrt{2^2+3^2}) + (4mn - 4m - 6n + 6)(\sqrt{2^2+4^2}) + (6ln + 2lm - 4l - 2m - 3n + 5)(\sqrt{3^2+3^2}) + (4lm + 4ln - 2m - 4n + 2)(\sqrt{3^2+4^2}) + (16lmn - 8lm - 14ln - 11mn - 4l + 7m + 10n - 7)(\sqrt{4^2+4^2})$,

$SO(M[l,m,n]) = 90.50lmn - 18.43lm - 35.40ln - 36.09mn - 10.75l + 11.27m - 59.91n - 7.49.$

- **Reduced Somber Index**

$SO_{red}(M[l,m,n]) = (2n+2)(\sqrt{(1-1)^2+(3-1)^2}) + (2mn-2)(\sqrt{(1-1)^2+(4-1)^2}) + 2(\sqrt{(2-1)^2+(2-1)^2}) + (8l+2m+2n-8)(\sqrt{(2-1)^2+(3-1)^2}) + (4mn - 4m - 6n + 6)(\sqrt{(2-1)^2+(4-1)^2}) + (6ln + 2lm - 4l - 2m - 3n + 5)(\sqrt{(3-1)^2+(3-1)^2}) + (4lm + 4ln - 2m - 4n + 2)(\sqrt{(3-1)^2+(4-1)^2}) + (16lmn - 8lm - 14ln - 11mn - 4l + 7m + 10n - 7)(\sqrt{(4-1)^2+(4-1)^2})$,

$SO_{red}(M[l,m,n]) = 67.88lmn - 13.86lm - 28.00ln - 28.01mn - 10.39l + 8.65m + 9.01n - 6.43.$

- **Augmented Zagreb Index**

$AZI(M[l,m,n]) = (2n+2)(\frac{1\times3}{1+3-2})^3 + (2mn-2)(\frac{1\times4}{1+4-2})^3 + 2(\frac{2\times2}{2+2-2})^3 + (8l+2m+2n-8)(\frac{2\times3}{2+3-2})^3 + (4mn-4m-6n+6)(\frac{2\times4}{2+4-2})^3 + (6ln+2lm-4l-2m-3n+5)(\frac{3\times3}{3+3-2})^3 + (4lm+4ln-2m-4n+2)(\frac{3\times4}{3+4-2})^3 + (16lmn-8lm-14ln-11mn-4l+7m+10n-7)(\frac{4\times4}{4+4-2})^3,$

$AZI(M[l,m,n]) = 303.40lmn - 73.62lm - 141.84ln - 171.85mn - 57.41l + 66.31m + 74.91n - 46.13.$

- **Forgotten Index**

$F(M[l,m,n]) = (2n+2)(1^2+3^2) + (2mn-2)(1^2+4^2) + 2(2^2+2^2) + (8l+2m+2n-8)(2^2+3^2) + (4mn-4m-6n+6)(2^2+4^2) + (6ln+2lm-4l-2m-3n+5)(3^2+3^2) + (4lm+4ln-2m-4n+2)(3^2+4^2) + (16lmn-8lm-14ln-11mn-4l+7m+10n-7)(4^2+4^2),$

$F(M[l,m,n]) = 512lmn - 120lm - 240ln - 238mn - 96l + 84m + 92n - 66.$

Table 11.2: Numerical Comparison of Degree-Based Indices for $M[l,m,n] l,m,n \geq 2$

$[l,m,n]$	$H(G)$	$SCI(G)$	$AGI(G)$	$RezG_1(G)$	$RezG_2(G)$
$[2,2,2]$	29.8357	36.0304	91.1074	65.3333	129.3810
$[3,3,3]$	101.0167	130.1982	346.1232	214.5000	575.4000
$[4,4,4]$	241.8690	320.4891	868.7901	505.6667	1530.7143
$[5,5,5]$	476.3929	640.8442	1755.1081	986.8333	3187.3238
$[6,6,6]$	828.5881	1125.2047	3101.0771	1706.0000	5737.2286
$[7,7,7]$	1322.4548	1807.5116	5002.6973	2711.1667	9372.4286
$[8,8,8]$	1981.9929	2721.7061	7555.9685	4050.3333	14284.9238
$[9,9,9]$	2831.2024	3901.7294	10856.8909	5771.5000	20666.7143
$[10,10,10]$	3894.0833	5381.5225	15001.4643	7922.6667	28709.8000

Table 11.3: Numerical Comparison of Degree-Based Indices for $M[l,m,n]$ $l,m,n \geq 2$

$[l,m,n]$	$RezG_3(G)$	$SO(G)$	$SO_{red}(G)$	$AZI(G)$	$F(G)$
$[2,2,2]$	5594	391.4652	271.16	999.4665	1798
$[3,3,3]$	30644	1688.3725	1219.31	4911.4160	8616
$[4,4,4]$	86782	4441.2532	3249.05	13510.0587	23454
$[5,5,5]$	186296	9193.1653	6768.17	28615.8391	49384
$[6,6,6]$	341474	16487.1669	12183.95	52049.2017	89478
$[7,7,7]$	564604	26866.3158	19903.67	85630.5908	146808
$[8,8,8]$	867974	40873.6702	30334.61	131180.4510	224446
$[9,9,9]$	1263872	59052.2881	43884.05	190519.2267	325464
$[10,10,10]$	1764586	81945.2274	60959.27	265467.3623	452934

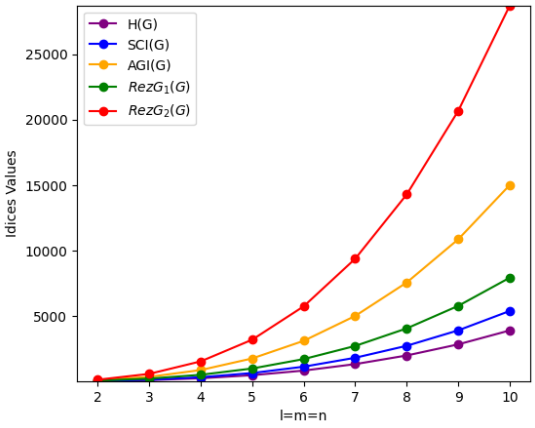

Figure 11.5: Numerical Comparison of $H(G)$,$SCI(G)$,$AGI(G)$,$RezG_1(G)$, $RezG_2(G)$

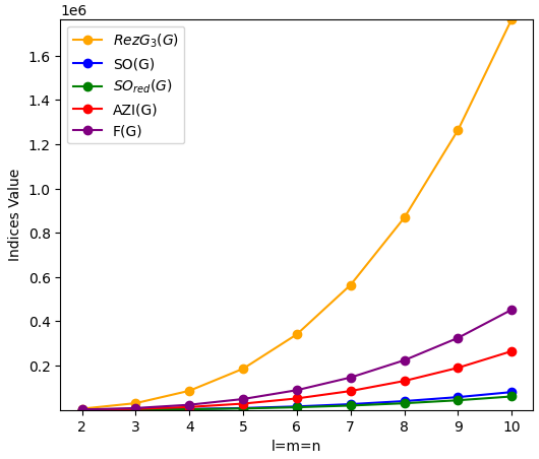

Figure 11.6: Numerical Comparison of $RezG_3(G)$,$SO(G)$,$SO_{red}(G)$,$AZI(G)$,$F(G)$

11.3.2 Degree-Based Entropies

The degree based entropy of M-carbon structure can be computed by using above topological indices, equations 11.11 and Table 11.1.

- **Harmonic Entropy**

$$ENT_{H(M[l,m,n])} = log(4lmn - 0.19lm - 0.35ln - 0.61mn + 0.86l - 0.02m + 0.15n - 0.71) - \frac{1}{4lmn-0.19lm-0.35ln-0.61mn+0.86l-0.02m+0.15n-0.71}\Big[(2n+2)(\tfrac{2}{1+3})log(\tfrac{2}{1+3})+(2mn-2)(\tfrac{2}{1+4})log(\tfrac{2}{1+4})+2(\tfrac{2}{2+2})log(\tfrac{2}{2+2}) + (8l+2m+2n-8)(\tfrac{2}{2+3})log(\tfrac{2}{2+3}) + (4mn-4m-6n+6)(\tfrac{2}{2+4})log(\tfrac{2}{2+4}) + (6ln+2lm-4l-2m-3n+5)(\tfrac{2}{3+3})log(\tfrac{2}{3+3}) + (4lm+4ln-2m-4n+2)(\tfrac{2}{3+4})log(\tfrac{2}{3+4}) + (16lmn-8lm-14ln-11mn-4l+7m+10n-7)(\tfrac{2}{4+4})log(\tfrac{2}{4+4})\Big].$$

- **Sum Connectivity Entropy**

$$ENT_{SCI(M[l,m,n])} = log(5.65lmn - 0.50lm - 0.98ln - 1.36mn + 0.53l + 0.16m + 0.24n + 0.29) - \frac{1}{5.65lmn-0.50lm-0.98ln-1.36mn+0.53l+0.16m+0.24n+0.29}\Big[(2n+2)\tfrac{1}{\sqrt{1+3}}log\tfrac{1}{\sqrt{1+3}} + (2mn-2)\tfrac{1}{\sqrt{1+4}}log\tfrac{1}{\sqrt{1+4}} + 2\tfrac{1}{\sqrt{2+2}}log\tfrac{1}{\sqrt{2+2}} + (8l+2m+2n-8)\tfrac{1}{\sqrt{2+3}}log\tfrac{1}{\sqrt{2+3}} + (4mn-4m-6n+6)\tfrac{1}{\sqrt{2+4}}log\tfrac{1}{\sqrt{2+4}} + (6ln+2lm-4l-2m-3n+5)\tfrac{1}{\sqrt{3+3}}log\tfrac{1}{\sqrt{3+3}} + (4lm+4ln-2m-4n+2)\tfrac{1}{\sqrt{3+4}}log\tfrac{1}{\sqrt{3+4}} + (16lmn-8lm-14ln-11mn-4l+7m+10n-7)\tfrac{1}{\sqrt{4+4}}log\tfrac{1}{\sqrt{4+4}}\Big].$$

- **Arithmetic Geometric Entropy**

$$ENT_{AGI(M[l,m,n])} = log(16lmn - 1.95lm - 9.95ln - 4.25mn + 0.16l + 0.77m + 0.94n + 0.02) - \frac{1}{16lmn-1.95lm-9.95ln-4.25mn+0.16l+0.77m+0.94n+0.02}\Big[(2n+2)(\tfrac{1+3}{2\sqrt{1\times3}})log(\tfrac{1+3}{2\sqrt{1\times3}}) + (2mn-2)(\tfrac{1+4}{2\sqrt{1\times4}})log(\tfrac{1+4}{2\sqrt{1\times4}}) + 2(\tfrac{2+2}{2\sqrt{2\times2}})log(\tfrac{2+2}{2\sqrt{2\times2}}) + (8l+2m+2n-8)(\tfrac{2+3}{2\sqrt{2\times3}})log(\tfrac{2+3}{2\sqrt{2\times3}}) + (4mn-4m-6n+6)(\tfrac{2+4}{2\sqrt{2\times4}})log(\tfrac{2+4}{2\sqrt{2\times4}}) + (6ln+2lm-4l-2m-3n+5)(\tfrac{3+3}{2\sqrt{3\times3}})log(\tfrac{3+3}{2\sqrt{3\times3}}) + (4lm+4ln-2m-4n+2)(\tfrac{3+4}{2\sqrt{3\times4}})log(\tfrac{3+4}{2\sqrt{3\times4}}) +$$

$(16lmn - 8lm - 14ln - 11mn - 4l + 7m + 10n - 7)(\frac{4+4}{2\sqrt{4\times4}})log(\frac{4+4}{2\sqrt{4\times4}})\Big]$.

- **Redefined First Zagreb Entropy**

$ENT_{RezG_1(M[l,m,n])} = log(8lmn - 0.33lm - 0.66ln + 2l - 0.33m + 0.5n + 1) - \frac{1}{8lmn-0.33lm-0.66ln+2l-0.33m+0.5n+1}\Big[(2n+2)(\frac{1+3}{1\times3})log(\frac{1+3}{1\times3}) + (2mn-2)(\frac{1+4}{1\times4})log(\frac{1+4}{1\times4}) + 2(\frac{2+2}{2\times2})log(\frac{2+2}{2\times2}) + (8l + 2m + 2n - 8)(\frac{2+3}{2\times3})log(\frac{2+3}{2\times3}) + (4mn - 4m - 6n + 6)(\frac{2+4}{2\times4})log(\frac{2+4}{2\times4}) + (6ln + 2lm - 4l - 2m - 3n + 5)(\frac{3+3}{3\times3})log(\frac{3+3}{3\times3}) + (4lm + 4ln - 2m - 4n + 2)(\frac{3+4}{3\times4})log(\frac{3+4}{3\times4}) + (16lmn - 8lm - 14ln - 11mn - 4l + 7m + 10n - 7)(\frac{4+4}{4\times4})log(\frac{4+4}{4\times4})\Big]$.

- **Redefined Second Zagreb Entropy**

$ENT_{RezG_2(M[l,m,n])} = log(32lmn - 6.14lm + 43.85ln - 15.06mn - 4.4l + 5.90m + 4.54n - 2.77) - \frac{1}{32lmn-6.14lm+43.85ln-15.06mn-4.4l+5.90m+4.54n-2.77}\Big[(2n + 2)(\frac{1\times3}{1+3})log(\frac{1\times3}{1+3}) + (2mn - 2)(\frac{1\times4}{1+4})log(\frac{1\times4}{1+4}) + 2(\frac{2\times2}{2+2})log(\frac{2\times2}{2+2}) + (8l + 2m + 2n - 8)(\frac{2\times3}{2+3})log(\frac{2\times3}{2+3}) + (4mn - 4m - 6n + 6)(\frac{2\times4}{2+4})log(\frac{2\times4}{2+4}) + (6ln + 2lm - 4l - 2m - 3n + 5)(\frac{3\times3}{3+3})log(\frac{3\times3}{3+3}) + (4lm + 4ln - 2m - 4n + 2)(\frac{3\times4}{3+4})log(\frac{3\times4}{3+4}) + (16lmn - 8lm - 14ln - 11mn - 4l + 7m + 10n - 7)(\frac{4\times4}{4+4})log(\frac{4\times4}{4+4})\Big]$.

- **Redefined Third Zagreb Entropy**

$ENT_{RezG_3(M[l,m,n])} = log(2048lmn - 580lm - 1132ln - 1176mn - 488l + 488m + 578n - 394) - \frac{1}{2048lmn-580lm-1132ln-1176mn-488l+488m+578n-394}\Big[(2n+2)(1\times3)(1+3)log(1\times3)(1+3) + (2mn-2)(1\times4)(1+4)log(1\times4)(1+4) + 2(2\times2)(2+2)log(2\times2)(2+2) + (8l + 2m + 2n - 8)(2\times3)(2+3)log(2\times3)(2+3) + (4mn - 4m - 6n + 6)(2\times4)(2+4)log(2\times4)(2+4) + (6ln + 2lm - 4l - 2m - 3n + 5)(3\times3)(3+3)log(3\times3)(3+3) + (4lm + 4ln - 2m - 4n + 2)(3\times4)(3+4)log(3\times4)(3+4) + (16lmn - 8lm - 14ln - 11mn - 4l + 7m + 10n - 7)(4\times4)(4+4)log(4\times4)(4+4)\Big]$.

- **Somber Entropy**

$ENT_{SO(M[l,m,n])} = log(90.50lmn - 18.43lm - 35.40ln - 36.09mn - 10.75l + 11.27m - 59.91n - 7.49) - \frac{1}{90.50lmn-18.43lm-35.40ln-36.09mn-10.75l+11.27m-59.91n-7.49}\Big[(2n + 2)(\sqrt{1^2+3^2})log(\sqrt{1^2+3^2}) + (2mn - 2)(\sqrt{1^2+4^2})log(\sqrt{1^2+4^2}) + 2(\sqrt{2^2+2^2})log(\sqrt{2^2+2^2}) + (8l + 2m + 2n - 8)(\sqrt{2^2+3^2})log(\sqrt{2^2+3^2}) + (4mn - 4m - 6n + 6)(\sqrt{2^2+4^2})log(\sqrt{2^2+4^2}) + (6ln + 2lm - 4l - 2m - 3n + 5)(\sqrt{3^2+3^2})log(\sqrt{3^2+3^2}) + (4lm + 4ln - 2m - 4n + 2)(\sqrt{3^2+4^2})log(\sqrt{3^2+4^2}) + (16lmn - 8lm - 14ln - 11mn - 4l + 7m + 10n - 7)(\sqrt{4^2+4^2})log(\sqrt{4^2+4^2})\Big]$.

- **Reduced Somber Entropy**

$$ENT_{SO_{red}(M[l,m,n])} = log(67.88lmn - 13.86lm - 28.00ln - 28.01mn - 10.39l + 8.65m + 9.01n - 6.43) - \frac{1}{67.88lmn-13.86lm-28.00ln-28.01mn-10.39l+8.65m+9.01n-6.43}\Big[(2n+2)(\sqrt{(1-1)^2+(3-1)^2})$$
$$log(\sqrt{(1-1)^2+(3-1)^2}) + (2mn-2)(\sqrt{(1-1)^2+(4-1)^2})log(\sqrt{(1-1)^2+(4-1)^2}) +$$
$$2(\sqrt{(2-1)^2+(2-1)^2})log(\sqrt{(2-1)^2+(2-1)^2}) + (8l+2m+2n-8)(\sqrt{(2-1)^2+(3-1)^2})$$
$$log(\sqrt{(2-1)^2+(3-1)^2})+(4mn-4m-6n+6)(\sqrt{(2-1)^2+(4-1)^2})log(\sqrt{(2-1)^2+(4-1)^2})+(6ln+$$
$$2lm-4l-2m-3n+5)(\sqrt{(3-1)^2+(3-1)^2})log(\sqrt{(3-1)^2+(3-1)^2}) + (4lm+4ln-2m-4n+$$
$$2)(\sqrt{(3-1)^2+(4-1)^2})log(\sqrt{(3-1)^2+(4-1)^2}) + (16lmn-8lm-14ln-11mn-4l+7m+10n-$$
$$7)(\sqrt{(4-1)^2+(4-1)^2})log(\sqrt{(4-1)^2+(4-1)^2})\Big].$$

- **Augmented Zagreb Entropy**

$$ENT_{AZI(M[l,m,n])} = log(303.40lmn-73.62lm-141.84ln-171.85mn-57.41l+66.31m+74.91n-46.13) - \frac{1}{303.40lmn-73.62lm-141.84ln-171.85mn-57.41l+66.31m+74.91n-46.13}\Big[(2n+2)(\frac{1\times3}{1+3-2})^3log(\frac{1\times3}{1+3-2})^3 + (2mn-2)$$
$$(\frac{1\times4}{1+4-2})^3log(\frac{1\times4}{1+4-2})^3 + 2(\frac{2\times2}{2+2-2})^3log(\frac{2\times2}{2+2-2})^3 + (8l+2m+2n-8)(\frac{2\times3}{2+3-2})^3log(\frac{2\times3}{2+3-2})^3 + (4mn-4m-$$
$$6n+6)(\frac{2\times4}{2+4-2})^3log(\frac{2\times4}{2+4-2})^3 + (6ln+2lm-4l-2m-3n+5)(\frac{3\times3}{3+3-2})^3log(\frac{3\times3}{3+3-2})^3 + (4lm+4ln-2m-$$
$$4n+2)(\frac{3\times4}{3+4-2})^3log(\frac{3\times4}{3+4-2})^3 + (16lmn-8lm-14ln-11mn-4l+7m+10n-7)(\frac{4\times4}{4+4-2})^3log(\frac{4\times4}{4+4-2})^3\Big].$$

- **Forgotten Entropy**

$$ENT_{F(M[l,m,n])} = log(512lmn - 120lm - 240ln - 238mn - 96l + 84m + 92n - 66) - \frac{1}{512lmn-120lm-240ln-238mn-96l+84m+92n-66}\Big[(2n+2)(1^2+3^2)log(1^2+3^2) + (2mn-2)(1^2+4^2)log(1^2+$$
$$4^2)+2(2^2+2^2)log(2^2+2^2)+(8l+2m+2n-8)(2^2+3^2)log(2^2+3^2)+(4mn-4m-6n+6)(2^2+4^2)log(2^2+$$
$$4^2) + (6ln+2lm-4l-2m-3n+5)(3^2+3^2)log(3^2+3^2) + (4lm+4ln-2m-4n+2)(3^2+4^2)log(3^2+$$
$$4^2) + (16lmn-8lm-14ln-11mn-4l+7m+10n-7)(4^2+4^2)log(4^2+4^2)\Big].$$

Table 11.4: Numerical Comparison of Degree-Based Entropy for $M[l,m,n]$ $l,m,n \geq 2$

$[l,m,n]$	$ENT_{H(G)}$	$ENT_{SCI(G)}$	$ENT_{AGI(G)}$	$ENT_{RezG_1(G)}$	$ENT_{RezG_2(G)}$
$[2,2,2]$	4.4092	4.4236	4.8439	4.6423	5.0965
$[3,3,3]$	5.8036	5.7911	6.1936	5.9280	6.5637
$[4,4,4]$	6.7566	6.7270	7.1202	6.8325	7.5339
$[5,5,5]$	7.4795	7.4391	7.8268	7.5285	8.2632
$[6,6,6]$	8.0618	8.0140	8.3981	8.0938	8.8486
$[7,7,7]$	8.5493	8.4963	8.8778	8.5695	9.3377
$[8,8,8]$	8.9686	8.9116	9.2912	8.9802	9.7580
$[9,9,9]$	9.3364	9.2763	9.6545	9.3415	10.1264

$[10, 10, 10]$	9.6640	9.6014	9.9785	9.6640	10.4544

Table 11.5: Numerical Comparison of Degree-Based Entropy for $M[l, m, n]$ $l, m, n \geq 2$

$[l, m, n]$	$ENT_{RezG_3(G)}$	$ENT_{SO(G)}$	$ENT_{SO_{red}(G)}$	$ENT_{AZI(G)}$	$ENT_{F(G)}$
$[2, 2, 2]$	8.6349	6.0471	5.7158	6.9375	7.5112
$[3, 3, 3]$	10.3341	7.5026	7.2044	8.5238	9.0753
$[4, 4, 4]$	11.3747	8.4678	8.1805	9.5339	10.0759
$[5, 5, 5]$	12.1385	9.1943	8.9124	10.2836	10.8201
$[6, 6, 6]$	12.7443	9.7778	9.4991	10.8813	11.4142
$[7, 7, 7]$	13.2471	10.2657	9.9892	11.3788	11.9092
$[8, 8, 8]$	13.6771	10.6850	10.4100	11.8051	12.3335
$[9, 9, 9]$	14.0528	11.0527	10.7789	12.1781	12.7051
$[10, 10, 10]$	14.3865	11.3802	11.1072	12.5097	13.0355

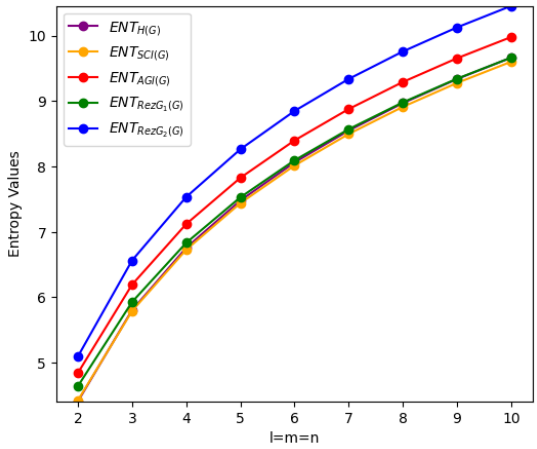

Figure 11.7: Numerical Comparison of $ENT_{H(G)}$,$ENT_{SCI(G)}$,$ENT_{AGI(G)}$,$ENT_{RezG_1(G)}$, $ENT_{RezG_2(G)}$

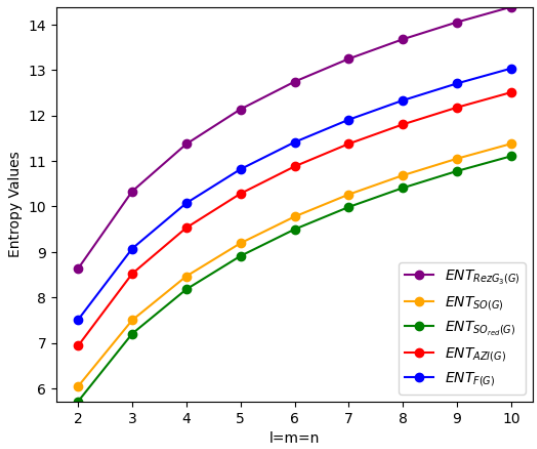

Figure 11.8: Numerical Comparison of $ENT_{RezG_3(G)}$,$ENT_{SO(G)}$,$ENT_{SO_{red}(G)}$, $ENT_{AZI(G)}$,$ENT_{F(G)}$

11.4 Comparative Analysis of Regression Models for Best Fit

In this section, We used three regression models logarithmic, power, and rational to investigate the link between degree based topological indices and the associated entropy measures. The selection of logarithmic, power, and rational models for our regression analysis was motivated by the fundamental nature of the relationship between topological indices and entropy. Topological indices (TIs) are aggregate sums of functions of local vertex degrees, while entropy measures the overall structural complexity and

information content of the entire network. The logarithmic regression model, in which the effect of the predictor variable reduces as values rise, is employed to evaluate nonlinear relationships. The equation is as follows:

$$Y = aln(X) + b$$

Here, the independent variable is the topological index (X), and the dependent variable is the entropy measure (Y).

When the dependent variable vary corresponding to a power of the independent variable, the power regression model is suitable. It works best in systems where small changes to X result in major adjustments to Y. The equation is:

$$Y = aX^2$$

Here, X is the independent variable, Y is the dependent variable , and a and b are constants that define the strength of the relationship. This model is ideal for data that exhibits exponential growth or decay.

The rational regression model is applied when a ratio provides the most effective summary of the relationship between variables. A greater increase in the result from the denominator and the numerator increases its effectiveness. The equation is:

$$Y = \frac{aX + b}{cX + X}$$

where X is the independent variable and Y is the dependent variable, and a, b, c, and d are constants. This method is effective when the result is affected by a number of connected variables with a more complex and fractional impact.

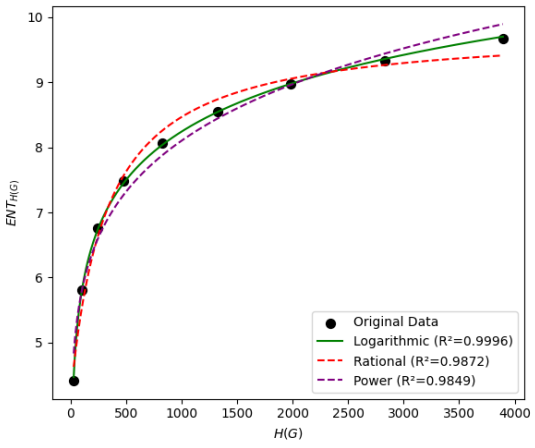

Figure 11.9: Model Between $H(G)$ and $ENT_{H(G)}$

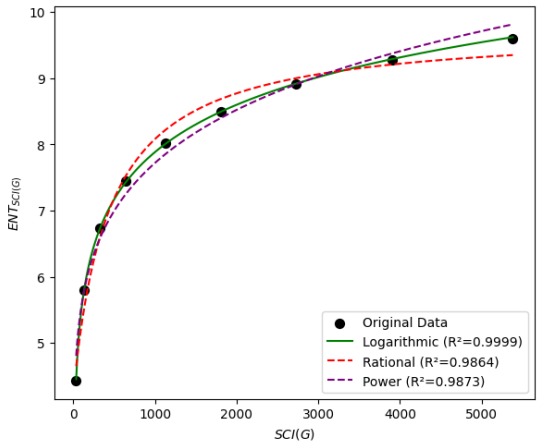

Figure 11.10: Model Between $SCI(G)$ and $ENT_{SCI(G)}$

Table 11.6: Statistical Values for Logarithmic Model of $H(G)$ and $SCI(G)$

Logarithmic Model	R^2	$RMSE$	S_E	F	$P-value$
$ENT_H = 0.8247 \ln H + 1.0736$	0.9996	0.0325	0.0525	17916.3954	0.00
$ENT_{SCI} = 0.7547 \ln SCI + 1.0317$	0.9999	0.0156	0.0256	76021.2960	0.00

Figures 11.9 and 11.10 graphically depict the logarithmic, power, and rational of the regression model, while Table 11.6 displays the statistical values for the logarithmic model of harmonic index and sum connectivity index. Logarithmic, rational, and power regression models were used to analyze the harmonic index and sum connection index. The logarithmic model was the most appropriate for both indices; the harmonic index had a R^2 of 0.9996 and the sum connectivity index 0.9999, demonstrating almost perfect correlations between the topological indices and entropy measurements. For the power model R^2 value for harmonic index is 0.9849 and for the sum connectivity index is 0.9873 indicate that performed better. On the other hand, the rational model showed a less robust match with greater RMSE and P-values. In terms of model's, the logarithmic model frequently outperformed the other.

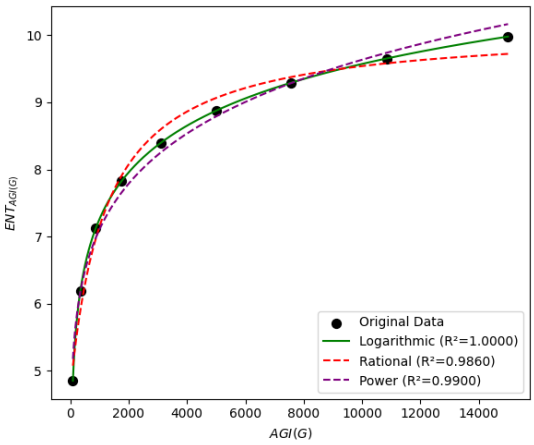

Figure 11.11: Model Between $AGI(G)$ and $ENT_{AGI(G)}$

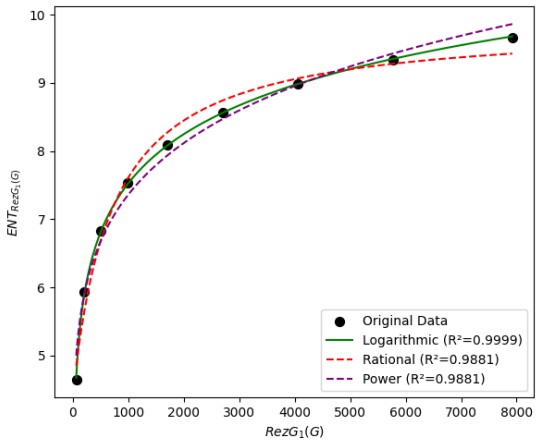

Figure 11.12: Model Between $RezG_1(G)$ and $ENT_{RezG_1(G)}$

Table 11.7: Statistical Values for Logarithmic Model of $AGI(G)$ and $RezG_1(G)$

Logarithmic Model	R^2	$RMSE$	S_E	F	$P-value$
$ENT_{AGI} = 0.3118 \ln AGI + 1.0055$	1.0000	0.0028	0.0051	2362038.8521	0.00
$ENT_{RezG_1} = 0.3115 \ln RezG_1 + 1.0440$	0.9999	0.0175	0.0318	56654.6241	0.00

Table 11.7 display the statistical data for the logarithmic model of the arithmetic geometric index and the first redefined Zagreb index, while Figures 11.11 and 11.12 show the regression models (logarithmic, power, and rational). Three models were used to analyze both indices. Logarithmic model fitting best of R^2 is 1.0000 for arithmetic geometric index and 0.9999 for first redefined Zagreb index indicate practically

perfect correlation between topological indices and entropy metrics. The power model outperformed the rational model with R^2 values of 0.9900 and 0.9881, respectively. Rational model indicating weaker fit its RMSE and P-values are higher. Logarithmic models scored highest for both indices.

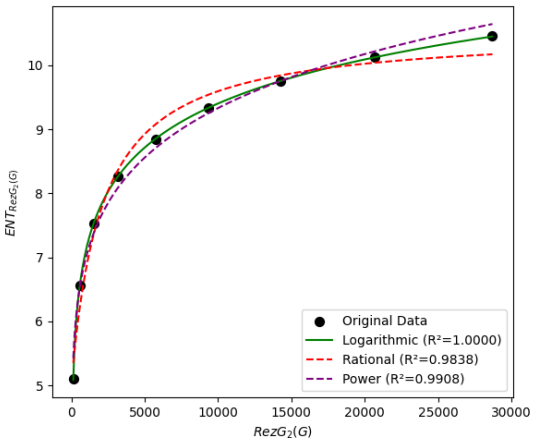

Figure 11.13: Model Between $RezG_2(G)$ and $ENT_{RezG_2(G)}$

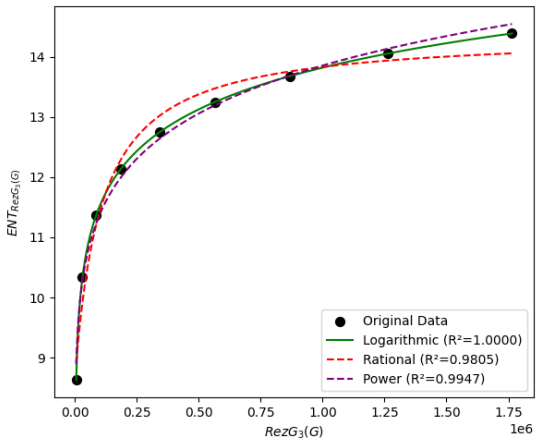

Figure 11.14: Model Between $RezG_3(G)$ and $ENT_{RezG_3(G)}$

Table 11.8: Statistical Values for Logarithmic Model of $RezG_2(G)$ and $RezG_3(G)$

Logarithmic Model	R^2	$RMSE$	S_E	F	$P-value$
$ENT_{RezG_2} = 0.2607 \ln RezG_2 + 0.9925$	1.0000	0.0048	0.0090	857262.6260	0.00
$ENT_{RezG_3} = 0.0080 \ln RezG_3 + 0.9996$	1.0000	0.0003	7.60×10^{-4}	266398765.7769	0.00

The statistical values for the logarithmic model of second redefined Zagreb index and third redefined Zagreb index are shown in Table 11.8, while the logarithmic, power, and rational of the regression model are graphically shown in Figures 11.13 and 11.14, respectively. Logarithmic, rational, and power regression models were used to examine the second and third redefined Zagreb indices. The value of R^2 is 1.0000 for the second redefined Zagreb index and R^2 is 1.0000 for the third redefined index, the logarithmic model was the best fit for both indices, suggesting that the topological indices and entropy measurements are nearly perfectly related. R^2 values is 0.9908 for the power model and 0.9947 for the rational model indicate that the former fared better. The rational model, on the other hand, fit not as well due to its larger RMSE and P-values. In general, the logarithmic model always performed better on both indices.

Table 11.9: Statistical Values for Logarithmic Model of $SO(G)$ and $SO_{red}(G)$

Logarithmic Model	R^2	$RMSE$	S_E	F	$P-value$
$ENT_{SO} = 0.0859 \ln SO + 0.9981$	1.000	0.0012	0.002	14268356.9467	0.00
$ENT_{SO_{red}} = 0.1293 \ln SO_{red} + 0.9961$	1.0000	0.0029	0.0059	2376176.1156	0.00

Figures 11.15 and 11.16 display the graphical representation of the logarithmic, power, and rational

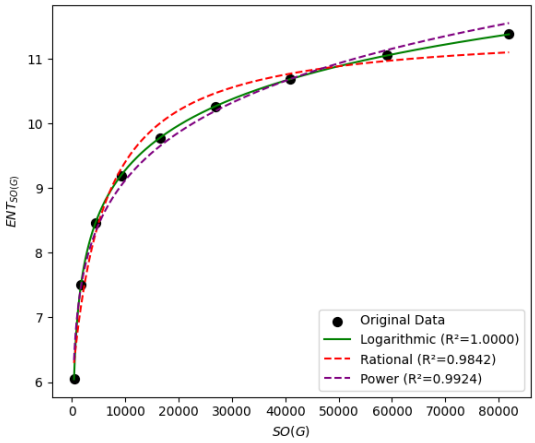

Figure 11.15: Model Between $SO(G)$ and $ENT_{SO(G)}$

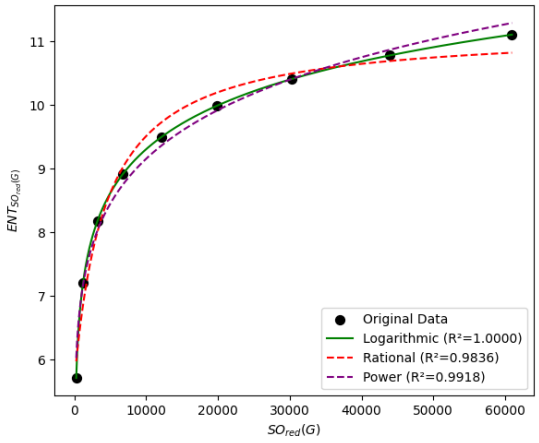

Figure 11.16: Model Between $SO_{red}(G)$ and $ENT_{SO_{red}(G)}$

regression models, while Table 11.9 presents statistical values for the Logarithmic Model of somber index and reduced sombre index. The Somber index and the reduced somber index were best fitted by the logarithmic model, which showed a near perfect association with entropy measures ($\mathbf{R^2}$ values of 1.0000). While the rational model displayed higher RMSE and P-values, suggesting a weaker fit, the power model performed better with value of $\mathbf{R^2}$ is 0.9924 and 0.9918 of both indices.

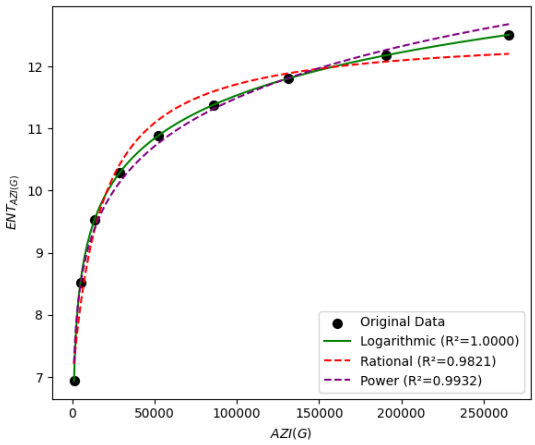

Figure 11.17: Model Between $AZI(G)$ and $ENT_{AZI(G)}$

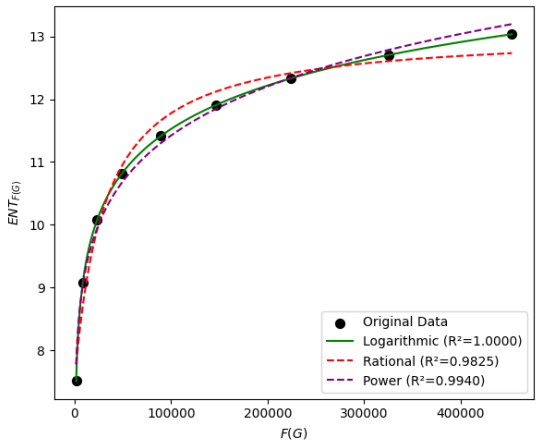

Figure 11.18: Model Between $F(G)$ and $ENT_{F(G)}$

Table 11.10: Statistical Values for Logarithmic Model of $F(G)$ and $AZI(G)$

Logarithmic Model	R^2	$RMSE$	S_E	F	$P-value$
$ENT_{AZI} = 0.0391 \ln AZI + 1.9984$	1.0000	0.0011	0.0025	17575021.0407	0.00
$ENT_F = 0.0215 \ln F + 0.9992$	1.0000	0.0005	0.0013	72535468.1319	0.00

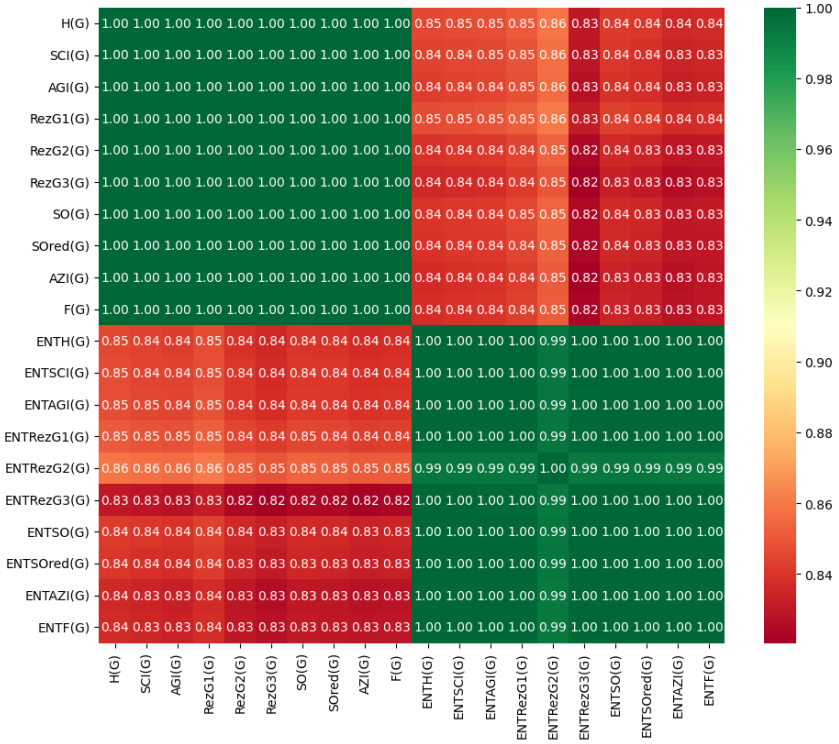

Figure 11.19: Correlation Between Indices and Entropies

Logarithmic, power, and rational regression models are illustrated graphically in Figures $F(G)$ and $AZI(G)$, while statistical data for the logarithmic model of the forgotten index and the Augmented Zagreb index are presented in Table 11.10. The logarithmic model, with an R^2 of 1.0000, was the best fit for both the Augmented Zagreb index and the forgotten index. The power model outperformed the rational model, with R^2 values of 0.9932 and 0.9940, respectively. However, the rational model showed higher RMSE and p-values, indicating a weaker fit. Moreover, the primacy of the logarithmic model is theoretically justified by the functional form of the entropy definition itself equation 11.11. This establishes an intrinsic logarithmic relationship, where the leading term dominates the scaling behavior. The second term acts as a bounded corrective sum, ensuring that the fundamental dependence of entropy on the topological index is inherently logarithmic, thus providing a rigorous a priori rationale for the model's superiority over purely empirical power or rational fits.

11.4.1 Correlation Between Indices and Entropies

This heatmap depicts the correlation between entropy metrics and topological indices in Figure 11.19. The Pearson correlation coefficient for each cell indicates the extent of linear association between the two variables. A perfect positive correlation is represented by a value of +1, a total absence of connection by a value of 0, and a perfect negative correlation by a value of -1. In contrast, red shows a weak negative correlation, while green denotes a strong positive correlation. The correlation between RezG1(G) and ENTRezG1(G) is week, whereas the correlation between F(G) and ENTF(G) is strong. This study

identifies variables with robust patterns for data analysis or modeling.

11.5 Conclusion

This study provides a comprehensive topological profile of the M-carbon structure using a suite of degree-based indices and their corresponding entropy measures. Our analysis revealed that the logarithmic regression model demonstrates a superior, near-perfect correlation ($R^2 \approx 1$) between these indices and their entropies.

The profound predictive power of this logarithmic model has significant broader implications for materials science. It establishes a powerful mathematical framework to predict the properties of larger, as-yet-unsynthesized M-carbon structures directly from their topological descriptors. By extrapolating our models, one can estimate key indicators of stability, connectivity, and complexity for massive systems without resorting to prohibitively expensive experimental or full-scale computational methods. This approach enables the in-silico screening and design of superhard carbon allotropes by targeting specific topological indices that correlate with desired macroscopic properties, such as extreme hardness and wear resistance.

Consequently, this work bridges a critical gap between mathematical chemistry and advanced material design, offering a robust, computationally efficient tool to guide the future exploration and application of M-carbon and related superhard materials in cutting tools, abrasives, and protective coatings.

11.6 Future Work

The methodological framework established in this chapter opens several promising avenues for future research. The immediate next step involves applying this integrated approach—calculating topological indices, their entropies, and identifying best-fit models—to other superhard carbon allotropes (e.g., bct-carbon, W-carbon) and related nanomaterials. A comparative analysis across different allotropes would elucidate how subtle differences in network connectivity manifest in their topological and entropy profiles, helping to identify key structural descriptors for extreme hardness.

Furthermore, the computed indices provide a rich dataset for Quantitative Structure-Property Relationship (QSPR) modeling. Future work will focus on correlating these topological descriptors with experimentally determined physicochemical properties of superhard materials, such as bulk modulus, hardness, and thermal conductivity. Developing such predictive QSPR models could ultimately accelerate the virtual design and discovery of novel materials with tailored mechanical properties, reducing the reliance on trial-and-error experimentation in the lab.

Bibliography

[1] Afzal, F., Zeeshan, M., Afzal, D., Munawar, S., Thapa, D. K., & Mirza, A. (2022). New degree-based topological indices of toroidal polyhex graph by means of M-polynomial. *Journal of Mathematics,* 2, 1-5.

[2] Amer, A., Irfan, M., & Rehman, H. (2021). Computational aspects of line graph of boron triangular nanotubes. *Mathematical Methods in the Applied Sciences*, 1–7.

[3] Amer, A., Naeem, M., Rehman, H., Irfan, M., Saleem, M. S., & Yang, H. (2020). Edge version of topological degree-based indices of Boron triangular nanotubes. *Journal of Information and Optimization Sciences*, 41(4), 973–990.

[4] Basavanagoud, B., Gao, W., Patil, S., Desai, V. R., Mirajkar, K. G., & Pooja, B. (2017). Computing first Zagreb index and F-index of new C-products of graphs. *Applied Mathematics and Nonlinear Sciences,* 2(2), 285–298.

[5] Furtula, B., Graovac, A., & Vukićević, D. (2010). Augmented Zagreb Index. *Journal of Mathematical Chemistry,* 48(2), 370-380.

[6] Furtula, B., & Gutman, I. (2015). A forgotten topological index. *Journal of Mathematical Chemistry, 53*(4), 1184–1190.

[7] Gutman, I., & Das, K. C. (2004). The first Zagreb index 30 years after. *MATCH Communications in Mathematical and in Computer Chemistry*, 50, 83-92.

[8] Gutman, I., & Trinajstić, N. (1972). Graph theory and molecular orbitals. Total ϕ-electron energy of alternant hydrocarbons. *Journal of Chemistry and Physics Letters*, 17, 535-538.

[9] Gutman, I., Rucić, B., Trinajstić, N., & Wilcox, C.F. (1975). Graph theory and molecular orbitals. XII. Acyclic polyenes. *Journal of Chemical Physics*, 62, 3399–3405.

[10] Gutman, I. (2021). Relation between geometric–arithmetic and arithmetic–geometric indices. *Journal of Mathematical Chemistry*, 59(6), 1520–1525.

[11] Gutman, I. (2021). Geometric approach to degree-based topological indices: Sombor indices. *Match Communications in Mathematical and in Computer Chemistry,* 86, 11–16.

[12] Gutman, I. (2013). Degree based topological indices. *Croatica Chemica Acta*, 86, 351-361.

[13] Irfan, M., Rehman, H., Almusawa, H., Rasheed, S., & Baloch, I. A. (2021). M-Polynomials and topological indices for line graphs of chain silicate network and H-naphtalenic nanotubes. *Journal of Mathematics*, 1-11.

[14] Irfan, M., Yasmeen, F., Aziz, S., & M. Mukhtar, M. (2024) Neighborhood Degree Based Topological Indices of Nanotube via Direct and NM-Polynomial. *International Journal of Quantum Chemistry,* 124(17) e27474,.

[15] Koam, A. N., Azeem, M., Jamil, M. K., Ahmad, A., & Hakami, K. H. (2023). Entropy measures of Y-junction based nanostructures. *Ain Shams Engineering Journal*, 14(4), 101–123.

[16] Kumar, V., & Das, S. (2023). On Nirmala indices based entropy measures of silicon carbide network. *Iranian Journal of Mathematical Chemistry*, 14, 271–288.

[17] Lyakhov, A. O., & Oganov, A. R. (2011). Evolutionary search for superhard materials: methodology and applications to forms of carbon and TiO_2. *Physical Review Letters*, 84.

[18] Li, Q., Ma, Y., Oganov, A. R., Wang, H., Wang, H., Xu, Y., Cui, T., Mao, H., & Zou, G. (2009). Superhard monoclinic polymorph of carbon. *Physical Review Letters,* 102(17).

[19] Mao, W. L., Mao, H., Eng, P. J., Trainor, T. P., Newville, M., Kao, C., Heinz, D. L., Shu, J., Meng, Y., & Hemley, R. J. (2003). Bonding changes in compressed superhard graphite. *Science*, 302-427.

[20] Mondal, S., De, N., & A. Pal. (2019). Topological properties of graphene using some novel neighborhood degree-based topological indices. *International Journal of Mathematics for Industry*, 11(1), 1-14.

[21] Ovais, A., Yasmeen, F., Irfan, M., Rasheed, M. W., & Kousar, S. (2024). Entropy measures of dendrimers using degree based indices. *South African Journal of Chemical Engineering*, 50, 168-181.

[22] Ranjini, P. S., Lokesha, V., & Usha, A. (2013). Relation between phenylene and hexagonal squeeze using harmonic index. *International Journal of Graph Theory,* 1, 116–121.

[23] Randić, M. (1975). Characterization of molecular branching. *Journal of the American Chemical Society*, 97, 6609–6615.

[24] Shegehalli, V. S., & Kanabur, R. (2015). Arithmetic-geometric indices of path graph. *Journal of Computer Mathematical Sciences,* 16, 19–24.

[25] Shanmukha, M. C., Basavarajappa, N. S., Shilpa, K. C., & Usha, A. (2020). Degree-based topological indices on anticancer drugs with QSPR analysis. *Heliyon*, 6(6), e04651.

[26] Shannon, C. E. (1948). A mathematical theory of communication. *The Bell system technical journal*, 27(3), 379-423.

[27] Umemoto, K., Wentzcovitch, R. M., Saito, S., & Miyake, T. (2010). Body-centered tetragonal C_4: A viable sp^3 carbon allotrope. *Physical Review Letters*, 104(12).

[28] Vukicevic, D. (2010). Bond additive modeling 2 mathematical properties of max-min rodeg index. *Croatica Chemica Acta*, 54, 261–273.

[29] Wiener, H. (1947). Structural determination of paraffin boiling points. *Journal of the American Chemical Society*, 69(1), 17–20.

[30] Yagi, T., Utsumi, W., Yamakata, M., Kikegawa, T., & Shimomura, O. (1992). High-pressure in situ x-ray-diffraction study of the phase transformation from graphite to hexagonal diamond at room temperature. *Journal of Physics. Review B*, 46(10), 6031-6039.

[31] Zhou, B., & Trinajstić, N. (2009). On a novel connectivity index. *Journal of Mathematical Chemistry,* 46(6), 1252–1270.

CHAPTER 12

Neural Network Insights: Calculating M-Polynomials and Topological Indices in Cellular and Kohonen Models

Tahreem Ashraf[†], Nazeran Idrees [†], Farkhanda Afzal [‡] and Madeeha Tahir[*]

[†] *Department of Mathematics, Government College University, Faisalabad, Pakistan*

[‡] *MCS, National University of Sciences and Technology, Islamabad .*

[*] *Department of Mathematics, Government College Women, University, Faisalabad, Pakistan.*

Corresponding Author: Nazeran Idrees: nazeranidrees@gcuf.edu.pk

Abstract: *Neural networks are a process of deep learning used in artificial intelligence which enables computers to process information like human brain. Artificial Intelligence techniques are based on set of methods and algorithms used to develop intelligent systems, one of those techniques is neural networks. It enables data processing machines to work in humanoid way. It is deep learning, that uses interconnected nodes or neurons in a layered structure that duplicates the human brain. It develops a flexible system that enables machines to learn from their mistakes and improve continuously. In this article, Cellular Neural Network(CNN) and Kohonen Neural Network (KNN) are studied for their structural behavior. Degree based computations of M-polynomials are done and by using these M-polynomials, some particular degree based topological indices are acquired. These indices will provide underlying topology of CNN and KNN. A comprehensive comparison of M-polynomials is done and 3-D models of M-polynomials are also presented.*

Keywords: M-polynomial,Topological Index, Neural Networks, Cellular Neural Network, Kohonen Neural Network

12.1 Introduction

Artificial intelligence is in golden age for its progress where it has magnificently transformed every walk of science. Neural networks, also known as artificial neural networks (ANNs) or simulated neural networks (SNNs). These networks mimic the signals of biological neurons. Neural networks are of immense importance in the domains of neural chemistry and molecular modeling, offering unique capabilities to unravel complex relationships within vast datasets [1]. Cellular neural networks, inspired by biological systems, simulate local interactions and are valuable in spatially distributed processes within cells or tissues, aiding in understanding complex cellular mechanisms and spatial arrangements of molecules. On the other hand, Kohonen neural networks, specifically useful in unsupervised learning, excel in pattern recognition and clustering, allowing for the identification of similarities or differences within molecular structures. The adaptability and pattern recognition capacities of both cellular neural networks and Kohonen networks make them integral in understanding the intricate behaviors of molecules and cellular processes [2].

Cellular neural networks (CNNs) and Kohonen neural networks (KNNs)(also known as self-organizing maps) are interconnected concepts in computational and neural sciences [3]. CNNs are inspired by biological neural networks, consist of interconnected cells governed by local rules and interactions. KNNs utilize unsupervised learning to cluster and organize data, with their architecture represented as a graph. In neural chemistry, these networks aid in predicting molecular properties, understanding chemical reactions, and exploring drug interactions which is crucial in drug development and material science.

Graph theory is a valuable mathematical field in which we study the graphs. It provides a mathematical framework to study complex networks and understand the relationships and structures within them. Its principles are employed to model and analyze the dynamics and information processing capabilities of neural networks [4]. Recently it has emerged as one of the most applicable mathematical discipline, as it has wide range of applications from chemistry to linguistics, from computer science to electrical and from geography to architecture. It contributes in both social and scientific research and has gain a lot of attention [5]. Graph theory concepts like connectivity and distance metrics play a vital role in training and adapting Kohonen networks, enabling effective mapping of input data onto the network's topology. Graph theory acts as a foundation to comprehend and analyze the mechanisms of cellular neural networks and Kohonen neural networks, enhancing their modeling and learning abilities [6]. Topological descriptors is a single value that represents an entire graph [7]. They are utilized in chemical graph theory to estimate biological activities and atomic movements [8]. The Wiener index, introduced by Wiener in 1947, is the first topological descriptor [9]. Other well-known topological descriptors include the Hosoya polynomial, Schultz index, atom-bond connectivity, and geometric-arithmetic index [10]. These descriptors can be categorized based on the calculation method used. In applied sciences, vertex-edge topological descriptors are currently gaining significance.

This study's insights into the topological indices of Cellular Neural Networks (CNN) and Kohonen

Neural Networks (KNN) have practical implications in real-world applications, particularly in fields such as pattern recognition, control systems, and robotics. By understanding and calculating M-polynomials and associated topological indices, we provide a structural framework that could be applied to optimize network architectures, enhancing both stability and resilience. For example, CNNs are extensively used in image processing tasks, where insights into network topology can help improve feature recognition accuracy, critical in quality control applications in manufacturing [11]. Similarly, KNNs play a pivotal role in control systems and robotics, where efficient network configurations can enhance the adaptability and robustness of robotic systems [12]. Future studies could further validate these indices through empirical simulations, comparing topological variations against network performance metrics to demonstrate their practical value.

12.2 Related Works

In reference [13], the authors concentrate on the computation of M-polynomials and entropy, specifically for the allotropic form of carbon known as diamond. The manuscript [14] derives universal expressions for distance-based topological indices, including those of Szeged, Mostar, and Padmakar-Ivan, utilizing SMP-polynomials. Reference [15] explores the geometric index (GA) and atom bond connectivity (ABC) index within diverse CP graphs, constructed from paths, cycles, and complete graphs. After introducing topological indices in neutrosophic graphs (NG), the authors calculate these indices for various well-known graphs such as cycles, paths, stars, wheels, complete graphs, and bipartite complete neutrosophic graphs [16]. In [17], the authors shift their focus to the 2D allotrope structure, carbon nanotubes, and dominating oxide and silicate chemical networks.

Likewise, in reference [18], the authors computed diverse topological descriptors for both fractal and Cayley-type dendrimer trees. Furthermore, entropy values predicted by these indices were determined. In the article [19], an investigation was conducted on the recently developed Sombor indices for various nanotube Y-junctions. Reference [20] involves the calculation of three neighborhood number-based topological indices, the Mostar index, PI index, and Szeged index, for the graphene structure. The objective of the paper [21] is to ascertain degree-based topological indices, specifically the atom-bond connectivity (ABC), ABC4, geometric-arithmetic (GA) and GA5 indices, for cellular neural networks (CNN).

Table 12.1: Related Works.

Ref. No.	Graph Type	M-Polynomial	Degree-based Topological Indices	General Formula for Indices
[11]	Diamond structure	✓		

Table 12.1 (continued): Related Works.

Ref. No.	Graph Type	M-Polynomial	Degree-based Topological Indices	General Formula for Indices
[12]	Polyacenes	✓	✓	✓
[13]	Corona Product graphs		✓	✓
[14]	Neutrosophic graphs		✓	
[15]	Chemical graphs		✓	✓
[16]	Fractal-type molecular graphs			✓
[17]	Nano-structures			✓
[18]	Graphene			✓
[19]	Cellular Neural Networks		✓	
This paper	Cellular Neural Networks and Kohonen Neural Network	✓	✓	✓

12.2.1 Motivations and contributions

An exhaustive examination of prior research and the information presented in Table 12.1 leads to the observation that researchers have not yet generalized the degree-based topological indices of CNN and KNN utilizing the M-polynomial.

- In [14], [15], [16], and [21], researchers exclusively explored degree-based topological indices. Meanwhile, in [13] and [14], researchers delved into topological indices utilizing the M-polynomial. Additionally, in [14], [15], [17], [18], [19], and [20], researchers generalized the formulas for topological indices across various structures.
- The combination of degree-based topological indices employing the M-polynomial and the derivation of a generalized formula for topological indices remains unexplored.
- To the best of our knowledge, there has been no exploration by researchers into the simultaneous consideration of degree-based topological indices, M-polynomial-based topological indices, and the derivation of a generalized formula for topological indices specifically for CNN and KNN.

This study investigates the combined utilization of degree-based topological indices, M-polynomial-based topological indices, and the derivation of a generalized formula for topological indices specific to

CNN and KNN. The key contributions of this paper are outlined as follows:

- This paper introduces a novel mathematical model for computing topological indices of CNN and KNN.
- The combined usage of degree-based topological indices, M-polynomial-based topological indices, and the derivation of a generalized formula for topological indices specific to CNN and KNN.

The assumption of representing neural networks as simple, finite, and undirected graphs provides a solid foundation for calculating M-polynomials and topological indices with clear interpretability. This approach effectively captures core structural insights, which can be valuable in various practical applications. For instance, in analyzing social networks, where connections between individuals (nodes) often require more complex, weighted representations to capture varying interaction strengths, the simplified model may serve as a starting point before introducing these nuances. Additionally, in brain network studies, neural pathways are frequently directed and weighted to reflect asymmetrical information flow and connectivity strength between brain regions, adding complexity to accurately modeling cognitive processes [22]. While these real-world systems involve additional dimensions, the foundational insights offered here could inform future adaptations to such complex, weighted, and directed networks. This study, therefore, provides a robust base that can be extended to more detailed analyses in applied network structures.

The sequence of the remaining paper is as follows. Section 3 includes the Preliminaries. The proposed results of CNN and KNN are in section 4, and section 5 respectively. Section 6 concludes the paper.

12.3 Preliminaries

12.3.1 Neural Networks

In this research , the network considered particularly is simple, finite and undirected. If there is no special explanation, the terminology and notation we mainly use come from [23, 24, 25]. This paper deals with the computation of degree-based topological indices of special classes of neural networks. A network is a set of vertices that are connected together considering some pattern and a neural networks means a network of artificial neurons and nodes [26].

Definition 1: (Cellular Neural Network)

A cellular neural network is shown in Figure 12.1. It contains of $Q \times Q$ cells. Cells can be arranged in several configurations; however, the most common is the two-dimensional CNNs organized in an eight-neighbor rectangular grid. Each cell has an input, a state, and an output, and it interacts directly only with the cells within its radius of neighborhood r: when $r = 1$, which is a common assumption, the neighborhood includes the cell itself and its eight nearest neighboring cells.

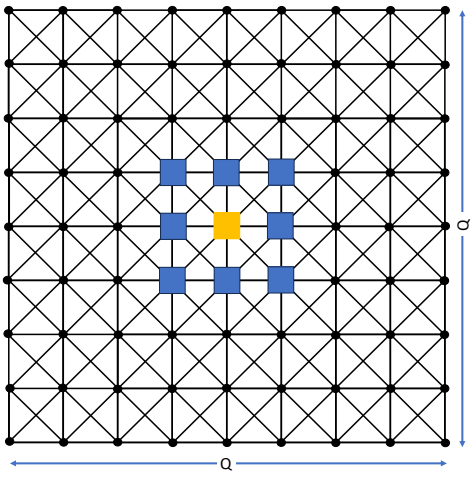

Figure 12.1: Graphical Representation of C_4

Definition 2: (Kohonen Neural Network)

Figure 12.2 represents a Kohonen neural network, which is also called self-organizing map. It has two layers, one is the input layer and the other one is the output layer. The structure wise difference between CNN and KNN is that, each cell in the later one is further connected to n vertices.

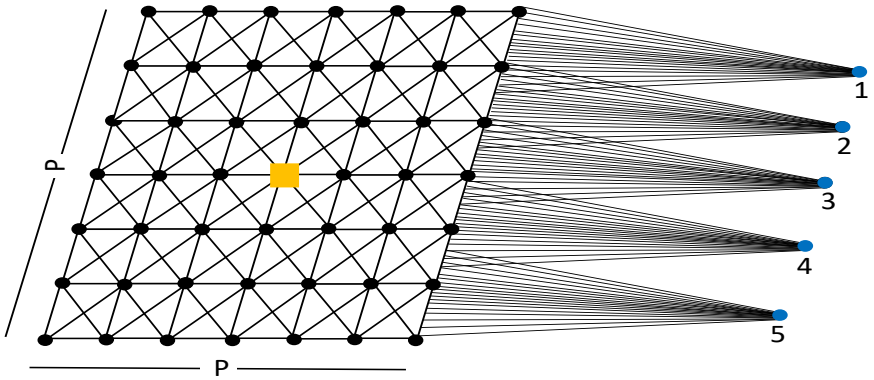

Figure 12.2: Graphical Representation of K_3^5

12.3.2 Topological Indices

Let $\eth = \eth(\mathtt{V}, \mathtt{E})$ be a simple connected graph, where $\mathtt{V} = \{v_1, v_2, ..., v_u\}$ and $\mathtt{E} = \{e_1, e_2, ..., e_u\}$ represent the set of vertices and edges of the graph. Degree of vertex v_i is symbolic as d_{v_i}, which is number of connected edges to the vertex v_i. Topological indices are numerical values that describe and interpret crucial characteristics of the graph [27]. By using M-polynomial we compute some special indices based on degree [28]. The M-polynomial is a contemporary polynomial, that will open to us crucial results and brilliant ideas in our study of degree-based topological descriptors.

Definition 3: (Zegreb Indices)

[30, 31, 32] defined the most expensive topological indices namely, Zegreb indices. For a graph $\eth$ the first, second and second modified Zegreb indices are denoted by $\mathtt{M}_1$, $\mathtt{M}_2$ and $\mathtt{M}_2^m$ respectively and formulated as follows:

$$\mathtt{M}_1(\eth) = \sum_{v_iv_j \in \mathtt{E}(\eth)} \left(d_{v_i} + d_{v_j}\right),$$

$$\mathtt{M}_2(\eth) = \sum_{v_iv_j \in \mathtt{E}(\eth)} \left(d_{v_i}\, d_{v_j}\right),$$

$$\mathtt{M}_2^m(\eth) = \sum_{v_iv_j \in \mathtt{E}(\eth)} \frac{1}{d_{v_i}\, d_{v_j}}.$$

Definition 4: (Augmented Zegreb index)

$\mathcal{A}(\eth)$ is known as Augmented Zegreb index [32] defined as:

$$\mathtt{A}(\eth) = \sum_{v_iv_j \in \mathtt{E}(\eth)} \left(\frac{d_{v_i}\, d_{v_j}}{d_{v_i} + d_{v_j} - 2}\right)^3.$$

Definition 5: (Symmetric Division Degree Index)

The significant index for a graph $\eth$, denoted by

$$\mathtt{SDD}(\eth) = \sum_{v_iv_j \in \mathtt{E}(\eth)} \left(\frac{\min\left(d_{v_i}, d_{v_j}\right)}{\max\left(d_{v_i}, d_{v_j}\right)} + \frac{\max\left(d_{v_i}, d_{v_j}\right)}{\min\left(d_{v_i}, d_{v_j}\right)}\right).$$

Definition 6: (Inverse Sum Index)

For a graph $\eth$, a toplogical index known as Inverse sum index [34, 35] is denoted by $\mathcal{I}(\eth)$ and defined as:

$$\mathtt{I}(\eth) = \sum_{v_iv_j \in \mathtt{E}(\eth)} \frac{d_{v_i} d_{v_j}}{d_{v_i} + d_{v_j}}.$$

Definition 7: (Randić Indices)

For a given graph $\eth$ Randić index is denoted by $\mathtt{R}_{-\frac{1}{2}}(\eth)$, and defined as:

$$\mathtt{R}_{-\frac{1}{2}}(\eth) = \sum_{v_iv_j \in \mathtt{E}(\eth)} \frac{1}{\sqrt{d_{v_i} d_{v_j}}}.$$

The general form of Randić index was designed by Bollobás *et al.* [28] and revisited by Amić *et al.* [29]. General Randić index and inverse Randić index for a given graph $\eth$ are denoted by $\mathtt{R}_\alpha(\eth)$ and $\mathtt{RR}_\alpha(\eth)$ respectively and formulated as:

$$\mathtt{R}_\alpha(\eth) = \sum_{v_iv_j \in \mathtt{E}(\eth)} (d_{v_i} d_{v_j})^\alpha,$$

$$\mathtt{RR}_\alpha(\eth) = \sum_{v_iv_j \in \mathtt{E}(\eth)} \frac{1}{(d_{v_i} d_{v_j})^\alpha}.$$

Definition 8: (Harmonic Index) There is another version of Randić index known as Harmonic index introduced by [30] and defined as:

$$\mathtt{H}(\eth) = \sum_{v_i v_j \in \mathtt{E}(\eth)} \frac{2}{d_{v_i} + d_{v_j}}.$$

Definition 9: (M-Polynomial)

For a graph $\eth$, the M-polynomial is denoted by $\mathtt{M}(\eth; x, y)$ and defined as:

$$\mathtt{M}(\eth; x, y) = \sum_{\alpha \leq i \leq j \leq \beta} \omega_{ij}(\eth) x^i y^j$$

$\omega_{ij}(\eth)$ symbolize the number of total edges $v_i v_j \in \mathtt{E}(\eth)$ such that $(d_{v_i}, d_{v_j}) = (i, j)$, $\alpha = min\ d_{v_i} : v_i \in \mathtt{V}(\eth)$, and $\beta = max\ d_{v_i} \in \mathtt{V}(\eth)$.

Remark 12.3.1. (Relation between topological indices and M-polynomial)

All the above defined indices can also be feasibly computed using M-polynomial.

Let

$$\mathtt{D}_x = x\frac{\partial(f(x,y))}{\partial x},$$
$$\mathtt{D}_y = y\frac{\partial(f(x,y))}{\partial y},$$
$$\mathtt{S}_x = \int_0^x \frac{f(t,y)}{t}dt,$$
$$\mathtt{S}_y = \int_0^y \frac{f(x,t)}{t}dt,$$

$$\mathtt{J}(f(x,y)) = f(x,x), \mathrm{Q}_\alpha f(x,y) = x^\alpha f(x,y)$$

then

$$\mathtt{M}_1(\eth) = (\mathtt{D}_x + \mathtt{D}_y)(f(x,y))|_{x=y=1},$$

$$\mathtt{M}_2(\eth) = (\mathtt{D}_x\mathtt{D}_y)(f(x,y))|_{x=y=1},$$

$$\mathtt{M}_2^m(\eth) = (\mathtt{S}_x\mathtt{S}_y)(f(x,y))|_{x=y=1}.$$

$$\mathtt{A}(\eth) = \mathtt{S}_x^3\mathrm{Q}_{-2}\mathtt{J}\mathtt{D}_x^3\mathtt{D}_y^3(f(x,y))|_{x=1},$$

$$\mathtt{SDD}(\eth) = (\mathtt{D}_x\mathtt{S}_y + \mathtt{S}_x\mathtt{D}_y)(f(x,y))|_{x=y=1}.$$

$$\mathtt{I}(\eth) = \mathtt{S}_x\mathtt{J}\mathtt{D}_x\mathtt{D}_y(f(x,y))|_{x=y=1}.$$

$$\mathtt{R}_\alpha(\eth) = (\mathtt{D}_x^\alpha\mathtt{D}_y^\alpha)(f(x,y))|_{x=y=1},$$

$$\mathtt{RR}_\alpha(\eth) = (\mathtt{S}_x^\alpha\mathtt{S}_y^\alpha)(f(x,y))|_{x=y=1},$$

$$\mathtt{H}(\eth) = 2\mathtt{S}_x\mathtt{J}(f(x,y))|_{x=1},$$

12.4 Topological Indices of CNN

Table 12.2 contains partitioning of the edges of cellular neural networks. This division is degree-based of end vertices of each edge. Figure 12.3 represents the $3D$ plot of M- polynomial of CNN.

$(d_{v_i}d_{v_j})$	$(3,5)$	$(3,8)$	$(5,5)$	$(5,8)$	$(8,8)$
$Frequency$	8	4	$8r-4$	$24r-20$	$16r^2-28r+12$

Table 12.2: Edge partitioning of CNN based on degree vertices

Theorem 12.4.1: Let $\mathcal{C}_r$ be a cellular neural networks. Then M-polynomial of $\mathcal{C}_r, r>0$ is

$$\mathtt{M}(\mathcal{C}_r;x,y)=(8)x^3y^5+(4)x^3y^8+(8r-4)x^5y^5+(24r-20)x^5y^8+(16r^2-28r+12)x^8y^8 \tag{12.1}$$

Proof: Let $\mathcal{C}_r$ be a cellular neural network. The main five edge sets are:

$$E_1(\mathcal{C}_r)=\{v_iv_j\in \mathtt{E}(\ni): d_{v_i}=3,\ d_{v_j}=5\},$$
$$E_2(\mathcal{C}_r)=\{v_iv_j\in \mathtt{E}(\ni): d_{v_i}=3,\ d_{v_j}=8\},$$
$$E_3(\mathcal{C}_r)=\{v_iv_j\in \mathtt{E}(\ni): d_{v_i}=5,\ d_{v_j}=5\},$$
$$E_4(\mathcal{C}_r)=\{v_iv_j\in \mathtt{E}(\ni): d_{v_i}=5,\ d_{v_j}=8\},$$
$$E_5(\mathcal{C}_r)=\{v_iv_j\in \mathtt{E}(\ni): d_{v_i}=8,\ d_{v_j}=8\}.$$

$$|E_1(\mathcal{C}_r)|=8, |E_2(\mathcal{C}_r)|=4, |E_3(\mathcal{C}_r)|=8r-4, |E_4(\mathcal{C}_r)|=24r-20, |E_5(\mathcal{C}_r)|=16r^2-28r+12.$$

Now by applying the definition of M- polynomial on cellular neural network we have:

$$\begin{aligned}
\mathtt{M}(\mathcal{C}_r;x,y) &= \sum_{i\leq j}\omega_{ij}(\mathcal{C}_{\mathrm{r}})x^iy^j=\sum_{v_iv_j\in E_1(\ni)}\omega_{35}(\mathcal{C}_{\mathrm{r}})x^3y^5+\sum_{v_iv_j\in E_2(\ni)}\omega_{38}(\mathcal{C}_{\mathrm{r}})x^3y^8\\
&+\sum_{v_iv_j\in E_3(\ni)}\omega_{55}(\mathcal{C}_{\mathrm{r}})x^5y^5+\sum_{v_iv_j\in E_4(\ni)}\omega_{58}(\mathcal{C}_{\mathrm{r}})x^5y^8+\sum_{v_iv_j\in E_5(\ni)}\omega_{88}(\mathcal{C}_{\mathrm{r}})x^8y^8\\
&= |E_1(\mathcal{C}_r)|x^3y^5+|E_2(\mathcal{C}_r)|x^3y^8+|E_3(\mathcal{C}_r)|x^5y^5+|E_4(\mathcal{C}_r)|x^5y^8+|E_5(\mathcal{C}_r)|x^8y^8\\
\mathtt{M}(\mathcal{C}_r;x,y) &= (8)x^3y^5+(4)x^3y^8+(8r-4)x^5y^5+(24r-20)x^5y^8+(16r^2-28r+12)x^8y^8.
\end{aligned}$$

□

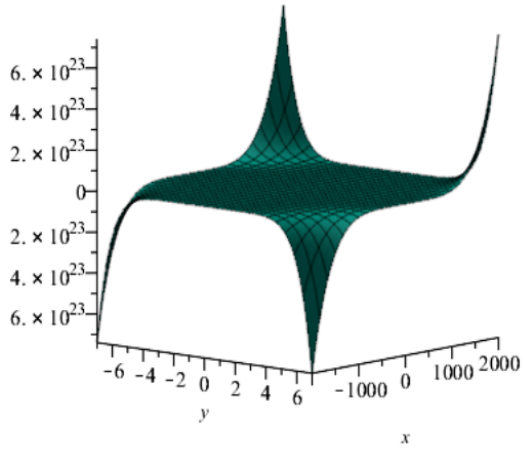

Figure 12.3: The $3D$ plot of M- polynomial of CNN

Proposition 12.4.2: Let $\mathcal{C}_r$ be a cellular neural networks. Then following are the topological indices of $\mathcal{C}_r, r > 0$ based on degree :

1. $\mathtt{M}_1(\supset) = 256r^2 - 56r$
2. $\mathtt{M}_2(\supset) = 1024r^2 - 632r + 84$
3. $\mathtt{M}_2^m(\supset) = \frac{1}{4}r^2 + \frac{193}{400}r + \frac{91}{400}$
4. $\mathtt{SDD}(\supset) = 16r^2 - 5r + \frac{9}{5}$
5. $\mathtt{H}(\supset) = 2r^2 + \frac{233}{130}r + \frac{501}{1430}$
6. $\mathtt{I}(\supset) = 64r^2 - \frac{236}{13}r + \frac{27}{143}$
7. $\mathtt{A}(\supset) = \frac{524288}{343}r^2 - \frac{5329294373}{4174016}r + \frac{415745977553}{1577778048}$
8. $\mathtt{RR}_\alpha(\supset) = \frac{(8)}{15^\alpha} + \frac{(4)}{24^\alpha} + \frac{(8r-4)}{5^{2\alpha}} + \frac{(24r-20)}{40^\alpha} + \frac{(16r^2-28r+12)}{8^{2\alpha}}$
9. $\mathtt{R}_\alpha(\supset) = (8)15^\alpha + (4)(24^\alpha) + (8r-4)5^{2\alpha} + (24r-20)40^\alpha + (16r^2-28r+12)8^{2\alpha}$.

Proof: Let $\mathcal{C}_r, r > 0$ be a cellular neural networks, its M-polynomial is computed in last theorem.

$$\mathtt{M}(\mathcal{C}_r; x, y) = (8)x^3y^5 + (4)x^3y^8 + (8r-4)x^5y^5 + (24r-20)x^5y^8 + (16r^2-28r+12)x^8y^8.$$

By using the formulas defined in *Remark* 3.10, some computations are collected:

$$\begin{aligned} \mathtt{D}_x[(f(x,y)] &= 3x^3y^5(8) + 3x^3y^8(4) + 5x^5y^5(8r-4) + (24r-20)5x^5y^8 \\ &+ (16r^2-28r+12)8x^8y^8, \end{aligned} \tag{12.2}$$

$$\begin{aligned} \mathtt{D}_y[(f(x,y)] &= x^35y^5(8) + x^38y^8(4) + 5x^5y^5(8r-4) + (24r-20)8x^5y^8 \\ &+ (16r^2-28r+12)8x^8y^8, \end{aligned} \tag{12.3}$$

$$\begin{aligned} \mathtt{D}_x\mathtt{D}_y[(f(x,y)] &= 15x^35y^5(8) + 24x^38y^8(4) + 25x^5y^5(8r-4) \\ &+ 40x^5y^8(24r-20) + 64(16r^2-28r+12)x^8y^8, \end{aligned} \tag{12.4}$$

$$\begin{aligned}
\mathtt{S}_x[(f(x,y)] &= \frac{x^3y^5}{3}(8)+\frac{x^3y^8}{3}(4)+\frac{x^5y^5}{5}(8r-4)+\frac{x^5y^8}{5}(24r-20) \qquad (12.5)\\
&+ (16r^2-28r+12)\frac{x^8y^8}{8},\\
\mathtt{S}_y[(f(x,y)] &= \frac{x^3y^5}{5}(8)+\frac{x^3y^8}{8}(4)+\frac{x^5y^5}{5}(8r-4)+\frac{x^5y^8}{8}(24r-20) \qquad (12.6)\\
&+ 7(16r^2-28r+12)\frac{x^8y^8}{8},\\
\mathtt{S}_x\mathtt{S}_y[(f(x,y)] &= \frac{x^3y^5}{15}(8)+\frac{x^3y^8}{24}(4)+\frac{x^5y^5}{25}(8r-4)+\frac{x^5y^8}{40}(24r-20) \qquad (12.7)\\
&+ \frac{x^8y^8}{64}(16r^2-28r+12),\\
\mathtt{S}_x\mathtt{D}_y[(f(x,y)] &= \frac{5}{3}x^3y^5(8)+\frac{8}{3}x^3y^8+x^5y^5(8r-4)+\frac{8}{5}x^5y^8(24r-20) \qquad (12.8)\\
&+ (16r^2-28r+12)x^8y^8,\\
\mathtt{D}_x\mathtt{S}_y[(f(x,y)] &= \frac{3}{5}x^3y^5(8)+\frac{3}{8}x^3y^8+x^5y^5(8r-4)+\frac{5}{8}x^5y^8(24r-20) \qquad (12.9)\\
&+ (16r^2-28r+12)x^8y^8,
\end{aligned}$$

$$\begin{aligned}
\mathtt{D}_x^\alpha\mathtt{D}_y^\alpha[(f(x,y)] &= 15^\alpha x^3y^5(8)+24^\alpha x^3y^8(4)+5^{2\alpha}x^5y^5(8r-4) \qquad (12.10)\\
&+ 40^\alpha x^5y^8(24r-20)+8^{2\alpha}x^8y^5(16r^2-28r+12),\\
\mathtt{S}_x^\alpha\mathtt{S}_y^\alpha[(f(x,y)] &= \frac{x^3y^5}{15^\alpha}(8)+\frac{x^3y^8}{24^\alpha}(4)+\frac{x^5y^5}{5^{2\alpha}}(8r-4)+\frac{x^5y^8}{40^{2\alpha}}(24r-20) \qquad (12.11)\\
&+ \frac{x^8y^8}{8^{2\alpha}}(16r^2-28r+12),\\
\mathtt{J}[(f(x,y)] &= x^8(8)+x^{11}(4)+x^{10}(8r-4)+x^{13}(24r-20) \qquad (12.12)\\
&+ x^{16}(16r^2-28r+12)
\end{aligned}$$

by using above expression we have,

$$\begin{aligned}
\mathtt{S}_x\mathtt{J}[(f(x,y)] &= (8)\frac{x^8}{8}+(4)\frac{x^{11}}{11}+(8r-4)\frac{x^{10}}{10}+(24r-20)\frac{x^{13}}{13} \qquad (12.13)\\
&+ (16r^2-28r+12)\frac{x^{16}}{16}\\
\mathtt{S}_x\mathtt{J}(\mathtt{D}_x\mathtt{D}_y)[(f(x,y)] &= \frac{15}{8}x^8(8)-\frac{24}{11}x^{11}(4)+\frac{25}{10}x^{10}(8r-4) \qquad (12.14)\\
&+ \frac{40}{13}x^{13}(24r-20)+\frac{64}{16}x^{16}(16r^2-28r+12).
\end{aligned}$$

In consequence of the values from the equation (12.1) to (12.14) and M-polynomial, following topological indices are obtained, Figure 12.4 represents the $3D$ plot of M- polynomial of CNN.

$$\mathtt{M}_1(\supset) = 256r^2-56r$$

$$\mathtt{M}_2(\supset) = 1024r^2-632r+84$$

$$\mathtt{M}_2^m(\supset) = \frac{1}{4}r^2+\frac{193}{400}r+\frac{91}{400}$$

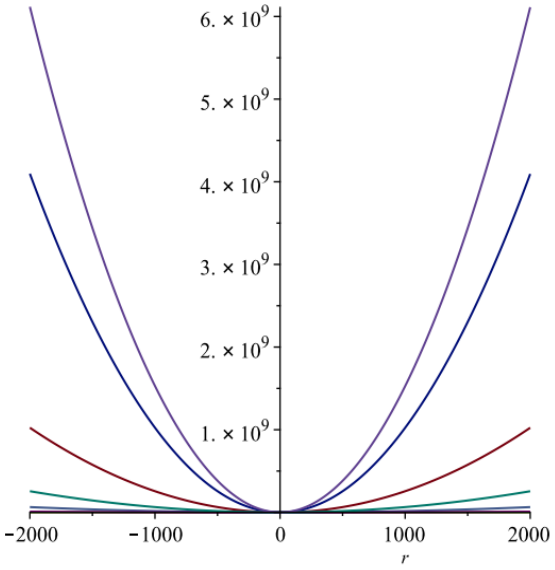

Figure 12.4: $2D$ plot of topological indices of CNN

$$\mathtt{SDD}(\eth) = 16r^2 - 5r + \frac{9}{5}$$

$$\mathtt{H}(\eth) = 2r^2 + \frac{233}{130}r + \frac{501}{1430}$$

$$\mathtt{I}(\eth) = 64r^2 - \frac{236}{13}r + \frac{27}{143}$$

$$\mathtt{A}(\eth) = \frac{415745977553}{1577778048} - r\frac{5329294373}{4174016} + r^2\frac{524288}{343}$$

$$\mathtt{RR}_\alpha(\eth) = \frac{8}{15^\alpha} + \frac{4}{24^\alpha} + \frac{(8r-4)}{5^{2\alpha}} + \frac{(24r-20}{40^\alpha} + \frac{(16r^2-28r+12}{8^{2\alpha}}$$

$$\mathtt{R}_\alpha(\eth) = 15^\alpha(8) + (4)(24^\alpha) + (8r-4)5^{2\alpha} + (24r-20)40^\alpha + (16r^2-28r+12)8^{2\alpha}.$$

□

12.5 Topological Indices of KNN

Table 14.3 contains the edge partition of Kohonen Neural Network networks $\mathcal{K}_r^n$ networks based on degrees of end vertices of each edge. Figure 12.5 represents the $3D$ plot of $\mathtt{M}$- polynomial of KNN.

$(d_{v_i}d_{v_j})$	$((2r+1)^2), n+3)$	$((2r+1)^2), n+5)$	$((2r+1)^2), n+8)$	$(n+3, n+5)$
$Frequency$	$4n$	$4n(2r-1)$	$n(2r-1)^2)$	8
$(d_{v_i}d_{v_j})$	$(n+3, n+8)$	$(n+5, n+5)$	$(n+5, n+8)$	$(n+8, n+8)$
$Frequency$	4	$8r-4$	$24r-20$	$16r^2-28r+12$

Table 12.3: Edge partitioning of KNN based on degree vertices

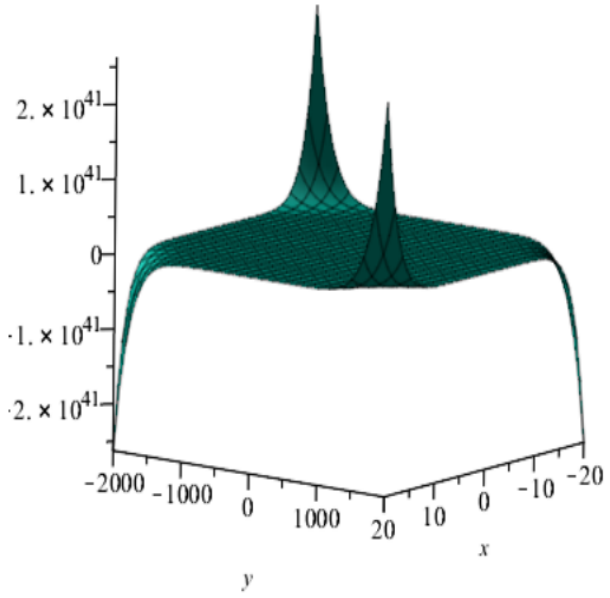

Figure 12.5: The $3D$ plot of M- polynomial of KNN

Theorem 12.5.1: Let $\mathcal{K}_r^n$ be a Kohonen Neural networks. Then M-polynomial of $\mathcal{K}_r^n$ is

$$\begin{aligned}\mathtt{M}(\mathcal{K}_r^n;x,y) &= (4n)x^{(2r+1)^2}y^{n+3}+(4n(2r-1))x^{(2r+1)^2}y^{n+5}+(n(2r-1)^2)x^{(2r+1)^2}y^{n+8}\\ &+ (8)x^{n+3}y^{n+5}+(4)x^{n+3}y^{n+8}+(8r-4)x^{n+5}y^{n+5}+(24r-20)x^{n+5}y^{n+8}\\ &+ (16r^2-28r+12)x^{n+8}y^{n+8} \qquad (12.15)\end{aligned}$$

Proof: Let $\mathcal{K}_r^n$ be a neural network. The edge partitions have following edge sets:

$$\begin{aligned}E_1(\mathcal{K}_r^n)&=\{v_iv_j\in \mathtt{E}(\ni):d_{v_i}=(2r+1)^2,\ d_{v_j}=n+3\},\\ E_2(\mathcal{K}_r^n)&=\{v_iv_j\in \mathtt{E}(\ni):d_{v_i}=(2r+1)^2,\ d_{v_j}=n+5\},\\ E_3(\mathcal{K}_r^n)&=\{v_iv_j\in \mathtt{E}(\ni):d_{v_i}=(2r+1)^2,\ d_{v_j}=n+8\},\\ E_4(\mathcal{K}_r^n)&=\{v_iv_j\in \mathtt{E}(\ni):d_{v_i}=3,\ d_{v_j}=5\},\\ E_5(\mathcal{K}_r^n)&=\{v_iv_j\in \mathtt{E}(\ni):d_{v_i}=3,\ d_{v_j}=8\},\\ E_6(\mathcal{K}_r^n)&=\{v_iv_j\in \mathtt{E}(\ni):d_{v_i}=5,\ d_{v_j}=5\},\\ E_7(\mathcal{K}_r^n)&=\{v_iv_j\in \mathtt{E}(\ni):d_{v_i}=5,\ d_{v_j}=8\},\\ E_8(\mathcal{K}_r^n)&=\{v_iv_j\in \mathtt{E}(\ni):d_{v_i}=8,\ d_{v_j}=8\}.\end{aligned}$$

then

$$|E_1(\mathcal{K}_r^n)|=4n, |E_2(\mathcal{K}_r^n)|=4n(2r+1), |E_3(\mathcal{K}_r^n)|=n(2r-1)^2, |E_4(\mathcal{K}_r^n)|=8,$$

$$|E_5(\mathcal{K}_r^n)| = 4, |E_6(\mathcal{K}_r^n)| = 8r-4, |E_7(\mathcal{K}_r^n)| = 24r-20, |E_8(\mathcal{K}_r^n)| = 16r^2-28r+12.$$

Now by applying the definition of M- polynomial on Kohonen Neural Network network we have:

$$\begin{aligned}
\mathtt{M}(\mathcal{K}_r^n;x,y) &= \sum_{i\leq j}\omega_{ij}(\mathcal{K}_{\mathrm{r}}^{\mathrm{n}})x^iy^j\\
\mathtt{M}(\mathcal{K}_r^n;x,y) &= \sum_{v_iv_j\in E_1(\supset)}\omega_{((2r+1)^2)(n+3)}(\mathcal{K}_{\mathrm{r}}^{\mathrm{n}})x^{(2r+1)^2}y^{n+3}\\
&+ \sum_{v_iv_j\in E_2(\supset)}\omega_{((2r+1)^2)(n+5)}(\mathcal{K}_{\mathrm{r}}^{\mathrm{n}})x^{(2r+1)^2}y^{n+5}\\
&+ \sum_{v_iv_j\in E_3(\supset)}\omega_{((2r+1)^2)(n+8)}(\mathcal{K}_{\mathrm{r}}^{\mathrm{n}})x^{(2r+1)^2}y^{n+8}\\
&+ \sum_{v_iv_j\in E_4(\supset)}\omega_{35}(\mathcal{K}_{\mathrm{r}}^{\mathrm{n}})x^3y^5 + \sum_{v_iv_j\in E_5(\supset)}\omega_{38}(\mathcal{K}_{\mathrm{r}}^{\mathrm{n}})x^3y^8 + \sum_{v_iv_j\in E_6(\supset)}\omega_{55}(\mathcal{K}_{\mathrm{r}}^{\mathrm{n}})x^5y^5\\
&+ \sum_{v_iv_j\in E_7(\supset)}\omega_{58}(\mathcal{K}_{\mathrm{r}}^{\mathrm{n}})x^5y^8 + \sum_{v_iv_j\in E_8(\supset)}\omega_{88}(\mathcal{K}_{\mathrm{r}}^{\mathrm{n}})x^8y^8
\end{aligned}$$

$$\begin{aligned}
\mathtt{M}(\mathcal{K}_r^n;x,y) &= |E_1(\mathcal{K}_r^n)|x^{(2r+1)^2}y^{n+3} + |E_2(\mathcal{K}_r^n)|x^{(2r+1)^2}y^{n+5} + |E_3(\mathcal{K}_r^n)|x^{(2r+1)^2}y^{n+8}\\
&+ |E_4(\mathcal{K}_r^n)|x^3y^5 + |E_5(\mathcal{K}_r^n)|x^3y^8 + |E_6(\mathcal{K}_r^n)|x^5y^5 + |E_7(\mathcal{K}_r^n)|x^5y^8\\
&+ |E_8(\mathcal{K}_r^n)|x^8y^8\\
\mathtt{M}(\mathcal{K}_r^n;x,y) &= (4n)x^{(2r+1)^2}y^{n+3} + (4n(2r-1))x^{(2r+1)^2}y^{n+5} + (n(2r-1)^2)x^{(2r+1)^2}y^{n+8}\\
&+ (8)x^{n+3}y^{n+5} + (4)x^{n+3}y^{n+8} + (8r-4)x^{n+5}y^{n+5} + (24r-20)x^{n+5}y^{n+8}\\
&+ (16r^2-28r+12)x^{n+8}y^{n+8}
\end{aligned}$$

□

Proposition 12.5.2: Let $\mathcal{K}_n^r$ be a Kohonen Neural Network networks. Then following are the topological indices of $\mathcal{K}_n^r$ based on degree:

1. $\mathtt{M}_1(\supset) = n(2r+1)^4 + 4(n+8)^2r^2 + (4n^2+16n-56)r + n^2$
2. $\mathtt{M}_2(\supset) = 4(2r+1)^2((r+1/2)^2n + 8r^2 + 2r)n + 84 + 16(n+8)^2r^2 + (4n^2-56n-632)r$
3. $\mathtt{M}_2^m(\supset) = \frac{4n((r+1/2)^2n^2+(8r^2+14r+4)n+15r^2+33r+79/4)}{(n+3)(n+5)(n+8)(2r+1)^2} + \frac{(16r^2+4r)n^3+(208r^2+172r)n^2+(880r^2+1252r+204)n+1200r^2+2316r+1092}{(n+3)(n+5)^2(n+8)^2}$
4. $\mathtt{SDD}(\supset) = \frac{4n(r+1/2)^2n+8r^2+2r}{n(2r+1)^2} + \frac{(16r^4+32r^3+56r^2+16r+1)n^3+(128r^4+352r^3+832r^2+248r+16)n^2+(240r^4+768r^3+3432r^2+1296r+31)n+3840r^2+1608r+216}{(n+3)(n+5)(n+8)}$
5. $\mathtt{H}(\supset) = \frac{8n(16r^6+48r^5+(8n+92)r^4+(16n+128)r^3+(n^2+20n+110)r^2+(n^2+18n+66)r+(1/4)n^2+(9/2)n+24)}{(4r^2+n+4r+4)(4r^2+n+4r+6)(4r^2+n+4r+9)}$
6. $\mathtt{I}(\supset) = 4n(2r+1)^2(r+1/2)^2\frac{((16n+128)r^4+(32n+160)r^3+(8n^2+120n+320)r^2+(8n^2+80n+192)r+n^3+18n^2+96n+120)}{(4r^2+n+4r+4)(4r^2+n+4r+6)(4r^2+n+4r+9)}$
7. $\mathtt{A}(\supset) = (4n)\frac{(n+3)^3(2r+1)^6}{(n+1+(2r+1)^2)^3}+(4n(2r-1))\frac{(n+5)^3(2r+1)^6}{(n+3+(2r+1)^2)^3}+(n(2r-1)^2)\frac{(n+8)^3(2r+1)^6}{(n+6+(2r+1)^2)^3}+(8)\frac{(n+3)^3(n+5)^3}{(2(n+3))^3}+(4)\frac{(n+3)^3(n+8)^3}{(2n+9)^3} + (8r-4)\frac{(n+5)^6}{(2(n+4))^3} + (24r-20)\frac{(n+5)^3(n+8)^3}{(2n+11)^3} + (16r^2-28r+12)\frac{(n+8)^6}{(2(n+7))^3}$
8. $\mathtt{RR}_\alpha(\supset) = (2r+1)^{2\alpha}[\frac{(4n)}{(n+3)^\alpha} + \frac{(4n(2r-1)}{(n+5)^\alpha} + \frac{(n(2r-1)^2)}{(n+8)^\alpha}] + \frac{1}{(n+3)^\alpha}[\frac{(8)}{(n+5)^\alpha} + \frac{(4)}{(n+8)^\alpha}] + \frac{1}{(n+5)^\alpha}[\frac{(8r-4)}{(n+5)^\alpha} + \frac{(24r-20)}{(n+8)^\alpha}] + \frac{(16r^2-28r+12)}{(n+8)^{2\alpha}}$
9. $\mathtt{R}_\alpha(\supset) = (2r+1)^{2\alpha}[((n+3)^\alpha + (n+5)^\alpha + (n+8)^\alpha] + (n+3)^\alpha[(n+5)^\alpha + (n+8)^\alpha] + (n+5)^\alpha[(n+5)^\alpha + (n+8)^\alpha] + (n+8)^{2\alpha}$.

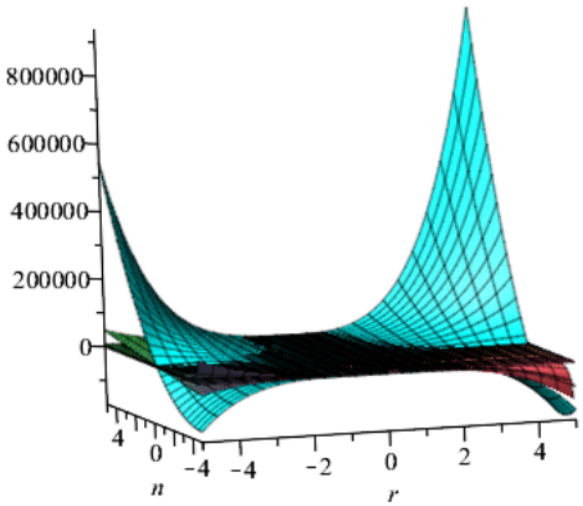

Figure 12.6: $3D$ plot of topological indices of KNN

Proof: M-polynomial of $\mathcal{K}_r^n$ is computed in last theorem is as follows:

$$\begin{aligned}\mathtt{M}(\mathcal{K}_r^n;x,y) &= (4n)x^{(2r+1)^2}y^{n+3} + (4n(2r-1))x^{(2r+1)^2}y^{n+5} + (n(2r-1)^2)x^{(2r+1)^2}y^{n+8}\\ &+ (8)x^{n+3}y^{n+5} + (4)x^{n+3}y^{n+8} + (8r-4)x^{n+5}y^{n+5} + (24r-20)x^{n+5}y^{n+8}\\ &+ (16r^2-28r+12)x^{n+8}y^{n+8}\end{aligned}$$

Some of the following results are computed using M-polynomial defined as in *Remark* 3.10,

$$\begin{aligned}
\mathtt{D}_x[(f(x,y)] &= (4n)(2r+1)^2x^{(2r+1)^2}y^{n+3} + (4n(2r-1))(2r+1)^2x^{(2r+1)^2}y^{n+5} \\
&+ (n(2r-1)^2)(2r+1)^2x^{(2r+1)^2}y^{n+8} + (8)(n+3)x^{n+3}y^{n+5} + (4)(n+3)x^{n+3}y^{n+8} \\
&+ (8r-4)(n+5)x^{n+5}y^{n+5} + (24r-20)(n+5)x^{n+5}y^{n+8} \\
&+ (16r^2-28r+12)(n+8)x^{n+8}y^{n+8}
\end{aligned} \tag{12.16}$$

$$\begin{aligned}
\mathtt{D}_y[(f(x,y)] &= (4n)(n+3)x^{(2r+1)^2}y^{n+3} + (4n(2r-1))(n+5)x^{(2r+1)^2}y^{n+5} \\
&+ (n(2r-1)^2)(n+8)x^{(2r+1)^2}y^{n+8} + (8)(n+5)x^{n+3}y^{n+5} + (4)(n+8)x^{n+3}y^{n+8} \\
&+ (8r-4)(n+5)x^{n+5}y^{n+5} + (24r-20)(n+8)x^{n+5}y^{n+8} \\
&+ (16r^2-28r+12)x^{n+8}y^{n+8}(n+8)
\end{aligned} \tag{12.17}$$

$$\begin{aligned}
\mathtt{D}_x\mathtt{D}_y[(f(x,y)] &= (4n)(2r+1)^2(n+3)x^{(2r+1)^2}y^{n+3} \\
&+ (4n(2r-1))(2r+1)^2(n+5)x^{(2r+1)^2}y^{n+5} \\
&+ (n(2r-1)^2)(2r+1)^2(n+8)x^{(2r+1)^2}y^{n+8} + (8)(n+3)(n+5)x^{n+3}y^{n+5} \\
&+ (4)(n+3)(n+8)x^{n+3}y^{n+8} + (8r-4)(n+5)^2x^{n+5}y^{n+5} \\
&+ (24r-20)(n+5)(n+8)x^{n+5}y^{n+8} + (16r^2-28r+12)(n+8)^2x^{n+8}y^{n+8}
\end{aligned} \tag{12.18}$$

$$\begin{aligned}
\mathtt{S}_x[(f(x,y)] &= (4n)\frac{x^{(2r+1)^2}}{(2r+1)^2}y^{n+3} + (4n(2r-1))\frac{x^{(2r+1)^2}}{(2r+1)^2}y^{n+5} \\
&+ (n(2r-1)^2)\frac{x^{(2r+1)^2}}{(2r+1)^2}y^{n+8} + (8)\frac{x^{n+3}}{(n+3)}y^{n+5} + (4)\frac{x^{n+3}}{(n+3)}y^{n+8} \\
&+ (8r-4)\frac{x^{n+5}}{(n+5)}y^{n+5} + (24r-20)\frac{x^{n+5}}{(n+5)}y^{n+8} + (16r^2-28r+12)\frac{x^{n+8}}{(n+8)}y^{n+8}
\end{aligned} \tag{12.19}$$

$$\begin{aligned}
\mathtt{S}_y[(f(x,y)] &= (4n)x^{(2r+1)^2}\frac{y^{n+3}}{(n+3)} + (4n(2r-1))x^{(2r+1)^2}\frac{y^{n+5}}{(n+5)} \\
&+ (n(2r-1)^2)x^{(2r+1)^2}\frac{y^{n+8}}{(n+8)} + (8)x^{n+3}\frac{y^{n+5}}{(n+5)} + (4)x^{n+3}\frac{y^{n+8}}{(n+8)} \\
&+ (8r-4)x^{n+5}\frac{y^{n+5}}{(n+5)} + (24r-20)x^{n+5}\frac{y^{n+8}}{(n+8)} + (16r^2-28r+12)x^{n+8}\frac{y^{n+8}}{(n+8)}
\end{aligned} \tag{12.20}$$

$$\begin{aligned}
\mathtt{S}_x\mathtt{S}_y[(f(x,y)] &= (4n)\frac{x^{(2r+1)^2}y^{n+3}}{(2r+1)^2(n+3)} + (4n(2r-1))\frac{x^{(2r+1)^2}y^{n+5}}{(2r+1)^2(n+5)} \\
&+ (n(2r-1)^2)\frac{x^{(2r+1)^2}y^{n+8}}{(2r+1)^2(n+8)} + (8)\frac{x^{n+3}y^{n+5}}{(n+3)(n+5)} + (4)\frac{x^{n+3}y^{n+8}}{(n+3)(n+8)} \\
&+ (8r-4)\frac{x^{n+5}y^{n+5}}{(n+5)^2} + (24r-20)\frac{x^{n+5}y^{n+8}}{(n+5)(n+8)} \\
&+ (16r^2-28r+12)\frac{x^{n+8}y^{n+8}}{(n+8)^2}
\end{aligned} \tag{12.21}$$

$$\begin{aligned}
\mathtt{S}_x\mathtt{D}_y[(f(x,y)] &= (4n)\frac{(n+3)}{(2r+1)^2}x^{(2r+1)^2}y^{n+3} + (4n(2r-1))\frac{(n+5)}{(2r+1)^2}x^{(2r+1)^2}y^{n+5} \\
&+ (n(2r-1)^2)\frac{(n+8)}{(2r+1)^2}x^{(2r+1)^2}y^{n+8} + (8)\frac{(n+5)}{x}^{n+3}(n+3)y^{n+5} \\
&+ (4)\frac{(n+8)}{(n+3)}x^{n+3}y^{n+8} + (8r-4)x^{n+5}y^{n+5} + (24r-20)\frac{(n+8)}{(n+5)}x^{n+5}y^{n+8} \\
&+ (16r^2-28r+12)x^{n+8}y^{n+8}
\end{aligned} \tag{12.22}$$

$$\begin{aligned}
\mathtt{D}_x\mathtt{S}_y[(f(x,y)] &= (4n)\frac{(2r+1)^2}{(n+3)}x^{(2r+1)^2}y^{n+3} + (4n(2r-1))\frac{(2r+1)^2}{(n+5)}x^{(2r+1)^2}y^{n+5} \\
&+ (n(2r-1)^2)\frac{(2r+1)^2}{(n+8)}x^{(2r+1)^2}y^{n+8} + (8)\frac{(n+3)}{(n+5)}x^{n+3}y^{n+5} \\
&+ (4)\frac{(n+3)}{(n+8)}x^{n+3}y^{n+8} + (8r-4)x^{n+5}y^{n+5} + (24r-20)\frac{(n+5)}{(n+8)}x^{n+5}y^{n+8} \\
&+ (16r^2-28r+12)x^{n+8}y^{n+8}
\end{aligned} \tag{12.23}$$

$$\begin{aligned}
\mathtt{D}_x^\alpha\mathtt{D}_y^\alpha[(f(x,y)] &= (4n)x^{(2r+1)^2}y^{n+3}(2r+1)^{2\alpha}(n+3)^\alpha \\
&+ (4n(2r-1))x^{(2r+1)^2}y^{n+5}(2r+1)^{2\alpha}(n+5)^\alpha \\
&+ (n(2r-1)^2)x^{(2r+1)^2}y^{n+8}(2r+1)^{2\alpha}(n+8)^\alpha + (8)x^{n+3}y^{n+5}(n+3)^\alpha(n+5)^\alpha \\
&+ (4)x^{n+3}y^{n+8}(n+3)^\alpha(n+8)^\alpha + (8r-4)x^{n+5}y^{n+5}(n+5)^{2\alpha} \\
&+ (24r-20)x^{n+5}y^{n+8}(n+5)^\alpha(n+8)^\alpha + (16r^2-28r+12)x^{n+8}y^{n+8}(n+8)^{2\alpha}
\end{aligned} \tag{12.24}$$

$$\begin{aligned}
\mathtt{S}_x^\alpha\mathtt{S}_y^\alpha[(f(x,y)] &= (4n)\frac{x^{(2r+1)^2}y^{n+3}}{(2r+1)^{2\alpha}(n+3)^\alpha} + (4n(2r-1))\frac{x^{(2r+1)^2}y^{n+5}}{(2r+1)^{2\alpha}(n+5)^\alpha} \\
&+ (n(2r-1)^2)\frac{x^{(2r+1)^2}y^{n+8}}{(2r+1)^{2\alpha}(n+8)^\alpha} + (8)\frac{x^{n+3}y^{n+5}}{(n+3)^\alpha(n+5)^\alpha} \\
&+ (4)\frac{x^{n+3}y^{n+8}}{(n+3)^\alpha(n+8)^\alpha} + (8r-4)\frac{x^{n+5}y^{n+5}}{(n+5)^{2\alpha}} \\
&+ (24r-20)\frac{x^{n+5}y^{n+8}}{(n+5)^\alpha(n+8)^\alpha} + (16r^2-28r+12)\frac{x^{n+8}y^{n+8}}{(n+8)^{2\alpha}}
\end{aligned} \tag{12.25}$$

$$\begin{aligned}
\mathtt{J}[(f(x,y)] &= (4n)x^{(2r+1)^2+(n+3)} + (4n(2r-1))x^{(2r+1)^2+(n+5)} \\
&+ (n(2r-1)^2)x^{(2r+1)^2+(n+8)} + (8)x^{2n+8} + (4)x^{2n+11} + (8r-4)x^{2n+10} \\
&+ (24r-20)x^{2n+13} + (16r^2-28r+12)x^{2n+16}
\end{aligned} \tag{12.26}$$

by using the above expression we have,

$$\begin{aligned}
\mathtt{S}_x\mathtt{J}[(f(x,y)] &= (4n)\frac{x^{(2r+1)^2+(n+3)}}{(2r+1)^2+(n+3)} + (4n(2r-1))\frac{x^{(2r+1)^2+(n+5)}}{(2r+1)^2+(n+5)} \\
&+ (n(2r-1)^2)\frac{x^{(2r+1)^2+(n+8)}}{(2r+1)^2+(n+8)} + (8)\frac{x^{2n+8}}{2n+8} + (4)\frac{x^{2n+11}}{2n+11} \\
&+ (8r-4)\frac{x^{2n+10}}{2n+10} + (24r-20)\frac{x^{2n+13}}{2n+13} + (16r^2-28r+12)\frac{x^{2n+16}}{2n+16} \\
\mathtt{S}_x\mathtt{J}(\mathtt{D}_x\mathtt{D}_y)[(f(x,y)] &= (4n)\frac{(2r+1)^2(n+3)}{(2r+1)^2+(n+3)}x^{(2r+1)^2+(n+3)} \\
&+ (4n(2r-1))x^{(2r+1)^2+(n+5)}\frac{(2r+1)^2(n+5)}{(2r+1)^2+(n+5)} \\
&+ (n(2r-1)^2)x^{(2r+1)^2+(n+8)}\frac{(2r+1)^2(n+8)}{(2r+1)^2+(n+8)} \\
&+ (8)x^{2n+8}\frac{(n+3)(n+5)}{2n+11} + (4)x^{2n+8}\frac{(n+3)(n+8)}{2n+11} + (8r-4)x^{2n+10}\frac{(n+5)^2}{2n+10} \\
&+ (24r-20)x^{2n+13}\frac{(n+5)(n+8)}{2n+13} + (16r^2-28r+12)x^{2n+16}\frac{(n+8)^2}{2n+16}
\end{aligned}$$

In consequence of the values from the equation 12.15 to 12.26 and M-polynomial, the topological

indices are obtained

$\mathtt{M}_1(\supset) = n(2r+1)^4 + 4(n+8)^2r^2 + (4n^2+16n-56)r + n^2$

$\mathtt{M}_2(\supset) = 4(2r+1)^2((r+1/2)^2n + 8r^2 + 2r)n + 84 + 16(n+8)^2r^2 + (4n^2-56n-632)r$

$\mathtt{M}_2^m(\supset) = \frac{4n((r+1/2)^2n^2+(8r^2+14r+4)n+15r^2+33r+79/4)}{(n+3)(n+5)(n+8)(2r+1)^2} +$
$\frac{(16r^2+4r)n^3+(208r^2+172r)n^2+(880r^2+1252r+204)n+1200r^2+2316r+1092}{(n+3)(n+5)^2(n+8)^2}$

$\mathtt{SDD}(\supset) = \frac{4n(r+1/2)^2n+8r^2+2r}{n(2r+1)^2} +$
$\frac{(16r^4+32r^3+56r^2+16r+1)n^3+(128r^4+352r^3+832r^2+248r+16)n^2+(240r^4+768r^3+3432r^2+1296r+31)n+3840r^2+1608r+216}{(n+3)(n+5)(n+8)}$

$\mathtt{H}(\supset) = \frac{8n(16r^6+48r^5+(8n+92)r^4+(16n+128)r^3+(n^2+20n+110)r^2+(n^2+18n+66)r+(1/4)n^2+(9/2)n+24)}{(4r^2+n+4r+4)(4r^2+n+4r+6)(4r^2+n+4r+9)}$

$\mathtt{I}(\supset) = 4n(2r+1)^2(r+1/2)^2\frac{((16n+128)r^4+(32n+160)r^3+(8n^2+120n+320)r^2+(8n^2+80n+192)r+n^3+18n^2+96n+120)}{(4r^2+n+4r+4)(4r^2+n+4r+6)(4r^2+n+4r+9)}$

$\mathtt{A}(\supset) = (4n)\frac{(n+3)^3(2r+1)^6}{(n+1+(2r+1)^2)^3} + (4n(2r-1))\frac{(n+5)^3(2r+1)^6}{(n+3+(2r+1)^2)^3} + (n(2r-1)^2)\frac{(n+8)^3(2r+1)^6}{(n+6+(2r+1)^2)^3} + (8)\frac{(n+3)^3(n+5)^3}{(2(n+3))^3} +$
$(4)\frac{(n+3)^3(n+8)^3}{(2n+9)^3} + (8r-4)\frac{(n+5)^6}{(2(n+4))^3} + (24r-20)\frac{(n+5)^3(n+8)^3}{(2n+11)^3} + (16r^2-28r+12)\frac{(n+8)^6}{(2(n+7))^3}$

$\mathtt{RR}_\alpha(\supset) = (2r+1)^{2\alpha}[\frac{(4n)}{(n+3)^\alpha} + \frac{(4n(2r-1)}{(n+5)^\alpha} + \frac{(n(2r-1)^2)}{(n+8)^\alpha}] + \frac{1}{(n+3)^\alpha}[\frac{(8)}{(n+5)^\alpha} + \frac{(4)}{(n+8)^\alpha}] + \frac{1}{(n+5)^\alpha}[\frac{(8r-4)}{(n+5)^\alpha} + \frac{(24r-20)}{(n+8)^\alpha}] +$
$\frac{(16r^2-28r+12)}{(n+8)^{2\alpha}}$

$\mathtt{R}_\alpha(\supset) = (2r+1)^{2\alpha}[((n+3)^\alpha + (n+5)^\alpha + (n+8)^\alpha] + (n+3)^\alpha[(n+5)^\alpha + (n+8)^\alpha] + (n+5)^\alpha[(n+5)^\alpha +$
$(n+8)^\alpha] + (n+8)^{2\alpha}$. □

12.6 Conclusions

This paper delves into the intricate realm of neural networks, where we meticulously computed degree-based topological indices. Our methodology commenced with the calculation of the m-polynomials for both CNN and KNN. Subsequently, we rigorously determined a suite of advanced topological metrics, encompassing the Zagreb Indices ($\mathtt{M1}(\supset), \mathtt{M2}(\supset), \mathtt{M2}^m(\supset)$), Augmented Zegreb index ($\mathtt{A}(\supset)$), Symmetric Division Degree Index ($\mathtt{SDD}(\supset)$), Inverse Sum Index($\mathtt{I}(\supset)$), Randić Indices ($\mathtt{RR}\alpha(\supset)$, $\mathtt{R}\alpha(\supset)$) and Harmonic Index $\mathtt{H}(\supset)$. This rigorous analytical approach illuminates the intricate structural characteristics of neural networks, providing valuable insights into their topological properties. Future work could extend these methods by incorporating directed and weighted edges or exploring topological indices in dynamic networks to enhance their relevance to real-world applications in fields like pattern recognition and autonomous systems.

Bibliography

[1] Kulichenko, M., Smith, J. S., Nebgen, B., Li, Y. W., Fedik, N., Boldyrev, A. I., ... & Tretiak, S. (2021). The rise of neural networks for materials and chemical dynamics. *The Journal of Physical Chemistry Letters*, *12*(26), 6227–6243.

[2] Brandi, J., Robotti, E., Manfredi, M., Barberis, E., Marengo, E., Novelli, E., & Cecconi, D. (2021).

Kohonen artificial neural network and multivariate analysis in the identification of proteome changes during early and long aging of bovine Longissimus dorsi muscle using SWATH mass spectrometry. *Journal of Agricultural and Food Chemistry*, *69*(38), 11512–11522.

[3] Linka, K., & Kuhl, E. (2023). A new family of Constitutive Artificial Neural Networks towards automated model discovery. *Computer Methods in Applied Mechanics and Engineering*, *403*, 115731.

[4] Zambrano-Luna, B. A., & Zuniga-Galindo, W. A. (2023). p-Adic cellular neural networks. *Journal of Nonlinear Mathematical Physics*, *30*(1), 34–70.

[5] Ding, Y., Wang, Q., Tian, Z., Lyu, Y., Li, F., Yan, Z., & Xia, X. (2023). A graph-theory-based dynamic programming planning method for distributed energy system planning: Campus area as a case study. *Applied Energy*, *329*, 120258.

[6] Zhou, G., Miao, F., Tang, Z., Zhou, Y., & Luo, Q. (2023). Kohonen neural network and symbiotic-organism search algorithm for intrusion detection of network viruses. *Frontiers in Computational Neuroscience*, *17*, 1079483.

[7] Telek, M. L., & Feliu, E. (2023). Topological descriptors of the parameter region of multistationarity: Deciding upon connectivity. *PLOS Computational Biology*, *19*(3), e1010970.

[8] Turaci, M. Ö. (2020). On vertex and edge eccentricity-based topological indices of a certain chemical graph that represents bidentate ligands. *Journal of Molecular Structure*, *1207*, 127766.

[9] Dinar, J., Hussain, Z., Zaman, S., & Rehman, S. U. (2023). Wiener index for an intuitionistic fuzzy graph and its application in water pipeline network. *Ain Shams Engineering Journal*, *14*(1), 101826.

[10] Bomfim, D. S., Soares, R. L., Bez, L. F., Lopes, P. C., Pereira, A. M., & Martha, L. F. (2023). HETOOL: A Half-Edge Topological Object-Oriented Library for generic 2-D geometric modeling. *SoftwareX*, *21*, 101307.

[11] Kohonen, T. (2001). *Self-Organizing Maps*. Springer Science & Business Media.

[12] Yegnanarayana, B. (2009). *Artificial Neural Networks*. PHI Learning Pvt. Ltd.

[13] Ishfaq, F., Nadeem, M. F., & El-Bahy, Z. M. (2023). On topological indices and entropies of diamond structure. *International Journal of Quantum Chemistry*, *123*(21), e27207.

[14] Rajabinejad, Z., & Mohammadian-Semnani, S. (2023). Calculation of Topological Indices Based on the Distance of Polyacenes Without Edge Counting. *Polycyclic Aromatic Compounds*, 1–12.

[15] Ali, N., Kousar, Z., Safdar, M., Tolasa, F. T., & Suleiman, E. (2023). Mapping Connectivity Patterns: Degree-Based Topological Indices of Corona Product Graphs. *Journal of Applied Mathematics*, 2023.

[16] Majeed, A. S., & Arif, N. E. (2023, September). Topological indices of certain neutrosophic graphs. In *AIP Conference Proceedings* (Vol. 2845, No. 1). AIP Publishing.

[17] Aqib, M., Ali Malik, M., Usman Afzal, H., Fatima, T., & Ali, Y. (2023). On topological indices of some chemical graphs. *Molecular Physics*, e2276386.

[18] Malik, M. A., Imran, M., & Adeel, M. (2023). On distance-based topological indices and co-indices of fractal-type molecular graphs and their respective graph entropies. *PLOS ONE*, *18*(11), e0290047.

[19] Imran, M., Ismail, R., Azeem, M., Jamil, M. K., & Al-Sabri, E. H. A. (2023). Sombor topological indices for different nanostructures. *Heliyon*, *9*(10).

[20] PM, S., TK, M. V., Vincent, L., John, T. L., & TJ, R. K. (2023). Neighborhood Number-Based Topological Indices of Graphene. *Polycyclic Aromatic Compounds*, 1–19.

[21] Imran, M., Siddiqui, M. K., Baig, A. Q., Khalid, W., & Shaker, H. (2019). Topological properties of cellular neural networks. *Journal of Intelligent and Fuzzy Systems*, *37*(3), 3605–3614.

[22] Newman, M. E. J. (2018). *Networks*. Oxford University Press.

[23] Alharbi, R., Ahmad, A., Azeem, M., & Koam, A. N. (2023). Probabilistic neural network with the concept of edge weight-based entropy. *Molecular Physics*, e2226773.

[24] Imran, M., Siddiqui, M. K., Ahmad, A., Ali, U., & Hanif, N. (2018). On the degree-based topological indices of the Tickysim SpiNNaker model. *Axioms*, *7*(4), 73.

[25] Augustine, T., & Santiago, R. (2023). On Neighborhood Degree-Based Topological Analysis over Melamine-Based TriCF Structure. *Symmetry*, *15*(3), 635.

[26] Emambocus, B. A. S., Jasser, M. B., & Amphawan, A. (2023). A survey on the optimization of artificial neural networks using swarm intelligence algorithms. *IEEE Access*, *11*, 1280–1294.

[27] Dyer, A. J., & Griffin, L. D. (2023). Inferring the location of neurons within an artificial network from their activity. *Neural Networks*, *157*, 160–175.

[28] Ghani, M. U., Campena, F. J. H., Pattabiraman, K., Ismail, R., Karamti, H., & Husin, M. N. (2023). Valency-Based Indices for Some Succinct Drugs by Using M-Polynomial. *Symmetry*, *15*(3), 603.

[29] Ali, A., Selvaraj, B., Elumalai, S., & Mansour, T. (2023). On n-vertex chemical graphs with a fixed cyclomatic number and minimum general Randic index. *Mathematical Reports*, *25*(8).

[30] Alsinai, A., Saleh, A., Ahmed, H., Mishra, L. N., & Soner, N. D. (2023). On fourth leap Zagreb index of graphs. *Discrete Mathematics, Algorithms and Applications*, *15*(2), 2250077.

[31] Chu, Y. M., Khan, A. R., Ghani, M. U., Ghaffar, A., & Inc, M. (2023). Computation of Zagreb polynomials and Zagreb indices for benzenoid triangular and hourglass system. *Polycyclic Aromatic Compounds*, *43*(5), 4386–4395.

[32] Raza, Z., Akhter, S., & Shang, Y. (2023). Expected value of first Zagreb connection index in random cyclooctatetraene chain, random polyphenyls chain, and random chain network. *Frontiers in Chemistry*, *10*, 1067874.

[33] Rajpoot, A., & Selvaganesh, L. (2023). Comparative Analysis and Predictability of Symmetric Division Degree Index on PCB Congeners.

[34] Kulli, V. R. (2023). Sum augmented and multiplicative sum augmented indices of some nanostructures. *Journal of Mathematics and Informatics*, *24*, 27–31.

[35] Ali, A., Furtula, B., Gutman, I., & Vukičević, D. (2021). Augmented Zagreb index: extremal results and bounds. *MATCH Communications in Mathematical and in Computer Chemistry*.

CHAPTER 13

Mathematical Modelling of HIV–AIDS: Incorporating Antiretroviral Treatment Dynamics for Comprehensive Analysis

Akhtar Ali[†], and Ali Raza [†]

[†] *Department of Mathematics, Government College University, Faisalabad, Pakistan .*

Corresponding Author: Akhtar Ali: utm.akhtar@gmail.com

Abstract: *The lentivirus known as HIV (human immune deficiency) virus is the root cause of AIDS (acquired immune deficiency syndrome). This deadly illness weakens a person's immune system, which leads to potentially fatal opportunistic infections. Antiretroviral therapy's inauguration has transformed HIV from an incurable disease to a curable one. We developed a mathematical model with two different stages of infectious population induced for analyzing the dynamics of HIV infection transmission and incorporating ART. This study concentrated on the analysis and creation of the best control plan by using integer order and fractional order model of the HIV-AIDS pandemic. The use of the Caputo Fabrizio fractional order aims to address the singularity problem often encountered in modelling real-world systems. The study concerned with preventing singularities in the HIV-AIDS model, making it more applicable to real-world scenarios. The existence and uniqueness of problem investigated. The Adam Bashforth method used to solve the system of equations. Finally, simulation of results demonstrated by using MATLAB, we have illustrated the obtained numerical results through graphs.*

Keywords: HIV-AIDS, Equilibrium point, Reproduction number, Adam Bashforth, Caputo Fabrizio.

13.1 Introduction

Human actions that alter the environment are the primary source of epidemics. Devastating diseases including AIDS, Ebola, malaria, and COVID-19 have emerged as a result of microorganisms' adaptation and changes, also they have claimed a significant number of deaths. Despite significant advancements in science and effective health intervention techniques, HIV-AIDS remains one of the most devastating diseases in human history [1]. HIV is the virus that causes HIV infection, and it may be passed from person to person through genitals, nursing, and sharing injecting supplies like needles with HIV positive individuals. AIDS is the most advanced stage of HIV infection and is caused by the HIV infectious virus [2]. According to forecasts, there will be 1.2 million fatalities and 37.9 million individuals living with HIV-AIDS worldwide in 2018. Around 62% of patients with infections had diagnoses and were on antiretroviral therapy (ART) [3]. Despite progress made globally in implementing treatment-as-prevention programs, certain 2 million new HIV infections occur annually [4]. In retrospect, evaluations of the HIV burden are essential to the evaluation of control strategies. Future HIV load estimates are crucial for directing resource allocation and optimizing policy in the long haul. HIV Collaborators for the global burden of disease (GBD) 2017 in the British medical journal 'The Lancet' HIV [5] appraise changes in 195 nations and possessions' HIV incidence, prevalence, mortality, and treatment coverage between 1980 and 2017. In addition to assessing treatment penetration and current HIV loads, the GBD 2017 HIV peers forecast scenarios to 2030 [6]. One crucial area that has to be reinforced in order to meet the worldwide goal of ending AIDS by 2030 is the dynamics of HIV-AIDS transmission. The prevention of the HIV-AIDS epidemic is a critical goal that can only be fulfilled by putting into practice realistic and effective measures, chief among them the provision of HIV-AIDS treatment [7]. Antiretroviral therapy (ART) is one of such significant treatment that infected people may undergo [8]. These therapy interventions are essential because they stop the disease from spreading between sexual partners. Consequently, early access to antiretroviral therapy (ART) is strongly advised, since it not only improves the health condition of those who are living with HIV-AIDS but also acts as a deterrent to the virus's spread [9]. Currently, modeling approaches are essential for controlling and minimizing the spread of viral diseases, both in theory and in execution. This breakthrough has left a substantial impact on how disease epidemiology-related policy is made in many different nations around the world [10]. In the process of understanding the fundamental variables that affect the transmission of disease, mathematical modeling in epidemiology offers suggestions for prevention initiatives [11]. Predictions, parameters, and variables are clarified throughout the model formulation. Additionally, models offer conceptual outcomes like replacement numbers, contact numbers, basic reproduction numbers, and milestones. For the sake of developing and testing theories, evaluating quantitative speculations, providing reliable answers, identifying parameter sensitivity, and estimating the important parameters from statistics, mathematical models and computer simulations are helpful experimental instruments [12]. In order to comprehend the transmission and containment tactics, several researchers worldwide are focusing on HIV-AIDS models. Jan, et al. [13] suggested a mathematical model.

For the chaotic and dynamic behavior they offered a unique numerical method. The fundamental concept of fractional calculus was illustrated by them inside the Atangana–Baleanu framework. Singh, H. Dubey. R.S, et al. [14] proposed HIV-1 infection model to a fractional mathematical model by employing the fractional derivative techniques of Caputo-Fabrizio and Atangana-Baleanu. Which fractional derivative operator was more efficient was demonstrated by a graphical comparison of the results obtained for the Caputo-Fabrizio and the Atangana-Baleanu operator. Cheneke, et al. [15] investigated dynamic analysis of the HIV-AIDS fractional-order model. The endemic equilibrium point arose and was unconditionally asymptotically stable worldwide if the fundamental reproduction number R_0 was greater than one. They used the Predictor-Corrector approach to do some numerical simulations to demonstrate the dynamical analysis. The impact of medication therapy on an HIV infected model examined by Rids. et al. [16]. Bachar and Dorfmayr [17] demonstrated that treating a condition without reducing perilous behavior may potentially cause the proportion of infected individuals to rise. Khalaf and Lazim. [18] suggested an in-vivoven dimensional fractional model for the dynamics of HIV to evaluate Caputo fractional model to HIV infection. The next-generation matrix technique was also used to calculate each HIV strain's fundamental reproduction rate. Khan M.A, et al. [19] investigated the dynamics of HIV utilizing a Caputo-type fractional operator in this work. With the use of a novel technique and a Newton polynomial method, they solved the fractional mathematical model of HIV to visually obtain the numerical solution. The significant parameter was displayed graphically in some cases. When R_0 less or larger than 1, the model was displayed locally asymptotical. Okosun K.O, et al. [20] evaluated the effectiveness of HIV-AIDS treatment and prevention tactics in the context of careless susceptible and therapy. They also extract the prerequisites for the best possible management of the illness. They also studied the reproductive number (R_0) sensitivity analysis. By utilizing the model parameters defined by Moore, E.J. et al. [21] along with we modified model given in [22]. The current study's primary goal is to create and evaluate a Caputo-Fabrizio fractional derivative model for the HIV-AIDS pandemic, which comprises the infected-1 populations receiving ART therapy and infected-2 populations to whom the therapy is not suitable with incorporating ART. To confirm the theoretical conclusions and show the impacts of changing the fractional order model, numerical simulations are performed over a variety of fractional orders by implementing three-step Adams–Bashforth predictor approach. The definitions of Caputo Fabrizio derivative along with its some properties are illustrated in Section 2. The fractional model of HIV-AIDS along two different stages of infected people and including treatment compartment is given in Section 3. Section 4 exhibits the existence and uniqueness of the fractional model. In Section 5 the equilibrium and basic reproduction number for the model is defined. Section 6 comprises the numerical technique for the model's solution and graphical results of numerical simulation. At last, in Section 7 the conclusions have been discussed.

13.2 Preliminaries

13.2.1 Caputo–Fabrizio Fractional Derivative and Integration

The definitions and characteristics of Caputo–Fabrizio (CF) derivative and integration have been streamlined in this section and fractional operators required.

Let $H^1(c,d) = \{g/g \in X^2(c,d) \text{ and } g \in X^2(c,d)\}$, where $X^2(c,d)$ is the space of square integrable functions on the interval (c,d).

Definition 1. Let $g \in H^1(c,d)$ and $\gamma \in (0,1)$. Next *Caputo–Fabrizio fractional derivative* is described as

$$^{CF}D_t^{\gamma} g(t) = \frac{E(\gamma)}{1-\gamma}\int_0^t g'(\omega)\exp\left(-\frac{\gamma}{1-\gamma}(t-\omega)\right)d\omega, \tag{13.1}$$

where, $E(\gamma)$ is a normalization function such that $E(0) = E(1) = 1$. However, if $g(t) \notin H^1(a,b)$, then the derivative is defined as

$$^{CF}D_t^{\gamma} g(t) = \frac{\gamma E(\gamma)}{(1-\gamma)}\int_0^t g(t) - g(\omega)\exp\left(-\frac{\gamma}{1-\gamma}((t-\omega))\right)d\omega. \tag{13.2}$$

Remark 13.1: If we let $\nu = \dfrac{1-\gamma}{\gamma} \in (0,\infty)$, then $\gamma = \dfrac{1}{1+\nu} \in (0,1)$. As consequences, Eq.(13.1) can be assume to form

$$^{CF}D_t^{\gamma}(g(\hat{t})) = \frac{N(\nu)}{\nu}\int_{\rho}^t \exp\left[-\frac{\hat{t}-\omega}{\nu}\right]g'(\omega)d\omega, \tag{13.3}$$

where, in Eq.(13.3), $N(\nu)$ is a term used for normalization that relates to $E(\gamma)$ such that $N(0) = N(\infty) = 1$.

Remark 13.2: The following property holds:

$$\lim_{\nu\to 0}\frac{1}{\nu}\exp\left[-\frac{t-\omega}{\nu}\right] = \delta(\omega - t), \quad \text{where } \delta(\cdot) \text{ denotes the Dirac delta function.} \tag{13.4}$$

Losada and Nieto subsequently modified the Caputo–Fabrizio fractional derivative as follows:

$$^{CF}D_t^{\gamma}(g(t)) = \frac{E(\gamma)(2-\gamma)}{(1-\gamma)^2}\int_{\rho}^t g'(\omega)\exp\left[-\frac{t-\omega}{1-\gamma}\gamma\right]d\omega, \tag{13.5}$$

Nieto and Losada defined the fractional integral corresponding to the derivative in Eq.(13.5) as follows.

Definition 13.1: Let $0 < \gamma < 1$. The following integer of order γ of a function g is described by

$$^{CF}D_t^{\gamma}(g(t)) = \frac{(1-\gamma)2}{E(\gamma)(2-\gamma)}g(t) + \frac{2\gamma}{E(\gamma)(2-\gamma)}\int_0^t g(\omega)d\omega, \quad t \geq 0. \tag{13.6}$$

Remark 13.3: According to the definition given in Eq.(13.1), the function's mean and its integral of order one represent the fractional integral of Caputo-Fabrizio type for a function of order $0 < \gamma < 1$, i.e.,

$$\frac{2(1-\gamma)}{(2-\gamma)E(\gamma)} + \frac{2\gamma}{(2-\gamma)E(\gamma)} = 1, \tag{13.7}$$

And therefore, $E(\gamma) = \dfrac{2}{2-\gamma}, \quad 0 < \gamma < 1.$

Using $E(\gamma) = \dfrac{2}{2-\gamma}$, the new Caputo derivative and its associated integral were proposed by Losada and Nieto as given.

Definition 13.2: Let $0 < \gamma < 1$. The order γ of a function g of fractional Caputo-Fabrizio derivative is given by

$${}^{CF}D_t^{\gamma}(g(t)) = \frac{1}{1-\gamma}\int_{\rho}^{t} \exp\left[-\frac{t-\omega}{1-\gamma}\right]\gamma g'(\omega)d\omega, \quad t \geq 0, \tag{13.8}$$

moreover, its fractional integral is described as

$${}^{CF}D_t^{\gamma}(g(t)) = g(t)(1-\gamma) + \gamma\int_{0}^{t} g(\omega)d\omega, \quad t \geq 0. \tag{13.9}$$

13.3 HIV–AIDS Model Formulation Including Treatment Compartment with CF Fractional Derivative

In this section, we formulate an HIV–AIDS epidemic model that incorporates an ART treatment compartment. The entire population at time t is divided into six compartments, namely $S(t)$, $I_1(t)$, $I_2(t)$, $A(t)$, $T(t)$, $R(t)$ Hence, the total population is given by $N(t) = S(t) + I_1(t) + I_2(t) + A(t) + T(t) + R(t)$.

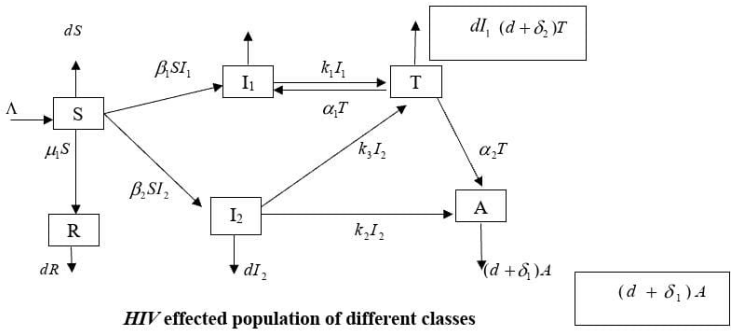

Figure 13.1: Dynamics of HIV infection in different population classes.

The governing system of ordinary differential equations is given by

$$\begin{aligned}
\frac{dS}{dt} &= \Lambda - \beta_1 S I_1 - \beta_2 S I_2 - (\mu + d)S, \\
\frac{dI_1}{dt} &= \beta_1 S I_1 - \alpha I_1 - (\mu + d) I_1, \\
\frac{dI_2}{dt} &= \alpha I_1 - (k_1 + k_2 + \mu + d) I_2, \\
\frac{dA}{dt} &= k_1 I_2 + \alpha_1 T - (\mu + d) A, \\
\frac{dT}{dt} &= k_2 I_2 - (d_1 + \alpha_1 + \delta + \mu) T, \\
\frac{dR}{dt} &= \delta T - dR.
\end{aligned} \tag{13.10}$$

In this model, six compartments constitute the overall population at time t, namely: $S(t)$ represents the number of susceptible patients, $I_1(t)$ represents the HIV-positive population with ART consumption so that this population can survive longer, $I_2(t)$ represents the HIV-positive population without ART consumption, $A(t)$ indicates the number of patients with advanced AIDS who are not responding well to treatment or are not receiving ART at all, $T(t)$ shows the total number of individuals receiving ART treatment and the number of patients for whom the treatment is effective, and $R(t)$ represents the number of people whose sexual behaviors have sufficiently changed to make them resistant to contracting HIV through intercourse.

The initial conditions are specified as

$$S(0) = S_0, \quad I_1(0) = I_{10}, \quad I_2(0) = I_{20}, \quad A(0) = A_0, \quad T(0) = T_0, \quad R(0) = R_0.$$

To incorporate memory effects and hereditary properties of the disease dynamics, we replace the classical first-order derivatives in Eq. (13.10) with the Caputo–Fabrizio fractional derivative defined in Eq. (13.5). The resulting fractional-order HIV–AIDS model with therapy compartments is given by

$$\begin{aligned}
{}^{CF}D_t^{\gamma_1} S &= \Lambda - \beta_1 S I_1 - \beta_2 S I_2 - (\mu + d)S, \\
{}^{CF}D_t^{\gamma_2} I_1 &= \beta_1 S I_1 - \alpha I_1 - (\mu + d) I_1, \\
{}^{CF}D_t^{\gamma_3} I_2 &= \alpha I_1 - (k_1 + k_2 + \mu + d) I_2, \\
{}^{CF}D_t^{\gamma_4} A &= k_1 I_2 + \alpha_1 T - (\mu + d) A, \\
{}^{CF}D_t^{\gamma_5} T &= k_2 I_2 - (d_1 + \alpha_1 + \delta + \mu) T, \\
{}^{CF}D_t^{\gamma_6} R &= \delta T - dR,
\end{aligned} \tag{13.11}$$

with initial conditions

$$(S(0), I_1(0), I_2(0), A(0), T(0), R(0)) = (S_0, I_{10}, I_{20}, A_0, T_0, R_0). \tag{13.12}$$

where the fractional orders satisfy $0 < \gamma_i < 1$ for $i = 1, 2, \ldots, 6$.

13.4 Existence and uniqueness of the *HIV-AIDS* model

In the present part, we examine the uniqueness and existence of the solutions to the Caputo-Fabrizio fractional model for *HIV-AIDS* in Eq. 13.11 under prescribed I.C's (13.12). By imposing the fixed point theory. In this way, we can demonstrate the model's existence and uniqueness. Apply the Caputo Fabrizio fractional integral operator in Eq.(13.1) to each side of Eq.(13.11), and after applying fractional integral we attain

$$\begin{aligned}
S(t) - S(0) &= {}^{CF}I_t^{\gamma_1}\big[\Lambda - \beta_1 I_1 S - \beta_2 I_2 S - (\mu + d)S\big],\\
I_1(t) - I_1(0) &= {}^{CF}I_t^{\gamma_2}\big[\beta_1 I_1 S + \alpha T - (k_1 + d)I_1\big],\\
I_2(t) - I_2(0) &= {}^{CF}I_t^{\gamma_3}\big[\beta_2 I_2 S - (k_2 + k_3 + d)I_2\big],\\
A(t) - A(0) &= {}^{CF}I_t^{\gamma_4}\big[k_2 I_2 + \alpha_2 T - (\delta_1 + d)A\big],\\
T(t) - T(0) &= {}^{CF}I_t^{\gamma_5}\big[k_1 I_1 + k_3 I_2 - (\alpha_1 + \alpha_2 + \delta_2 + d)T\big],\\
R(t) - R(0) &= {}^{CF}I_t^{\gamma_6}\big[\mu_1 S - dR\big].
\end{aligned} \tag{13.13}$$

Next, we define the subsequent Kernels for computational convenience:

$$\begin{aligned}
M_1(t,S) &= \Lambda - \beta_1 I_1(t)S(t) - \beta_2 I_2(t)S(t) - \mu S(t) - dS(t),\\
M_2(t,I_1) &= \beta_1 I_1(t)S(t) + \alpha T(t) - k_1 I_1(t) - dI_1(t),\\
M_3(t,I_2) &= \beta_2 I_2(t)S(t) - (k_2 + k_3 + d)I_2(t),\\
M_4(t,A) &= k_2 I_2(t) + \alpha_2 T(t) - (\delta_1 + d)A(t),\\
M_5(t,T) &= k_1 I_1(t) + k_3 I_2(t) - (\alpha_1 + \alpha_2 + \delta_2 + d)T(t),\\
M_6(t,R) &= \mu_1 S(t) - dR(t).
\end{aligned} \tag{13.14}$$

and the functions

$$\Omega(\gamma) = \frac{(1-\gamma)2}{E(\gamma)(2-\gamma)}, \quad \sigma(\gamma) = \frac{2\gamma}{E(\gamma)(2-\gamma)}. \tag{13.15}$$

The following theorems will be proved under the assumption that and are nonnegative bounded functions. i.e.,

$$|S(t)| \le \theta_1, \quad |I_1(t)| \le \theta_2, \quad |I_2(t)| \le \theta_3, \quad |A(t)| \le \theta_4, \quad |T(t)| \le \theta_5, \quad |R(t)| \le \theta_6,$$

where $\theta_1, \theta_2, \theta_3, \theta_4, \theta_5, \theta_6$ are some positive constants. Denote

$$\begin{aligned}
\lambda_1 &= \beta_1\theta_2 + \beta_2\theta_3 + \mu + d, \quad \lambda_2 = \beta_1\theta_1 + \alpha + k_1 + d,\\
\lambda_3 &= \beta_2\theta_1 + k_2 + k_3 + d, \quad \lambda_4 = \alpha_2 + \delta_1 + d,\\
\lambda_5 &= \alpha_1 + \alpha_2 + \delta_2 + d, \quad \lambda_6 = d.
\end{aligned} \tag{13.16}$$

Now, we impose the Caputo Fabrizio fractional integral definition given in Eq.(13.1) to Eq.(13.13),

then we have

$$\begin{aligned}
S(t) - S(0) &= \Omega(\gamma_1) M_1(t, S) + \sigma(\gamma_1) \int_0^t M_1(\xi, S(\xi))\, d\xi, \\
I_1(t) - I_1(0) &= \Omega(\gamma_2) M_2(t, I_1) + \sigma(\gamma_2) \int_0^t M_2(\xi, I_1(\xi))\, d\xi, \\
I_2(t) - I_2(0) &= \Omega(\gamma_3) M_3(t, I_2) + \sigma(\gamma_3) \int_0^t M_3(\xi, I_2(\xi))\, d\xi, \\
A(t) - A(0) &= \Omega(\gamma_4) M_4(t, A) + \sigma(\gamma_4) \int_0^t M_4(\xi, A(\xi))\, d\xi, \\
T(t) - T(0) &= \Omega(\gamma_5) M_5(t, T) + \sigma(\gamma_5) \int_0^t M_5(\xi, T(\xi))\, d\xi, \\
R(t) - R(0) &= \Omega(\gamma_6) M_6(t, R) + \sigma(\gamma_6) \int_0^t M_6(\xi, R(\xi))\, d\xi.
\end{aligned} \tag{13.17}$$

Theorem 4: If the following inequality holds:

$$0 \leq Z = \max\{\lambda_1, \lambda_2, \lambda_3, \lambda_4, \lambda_5, \lambda_6\} < 1, \tag{13.18}$$

then kernels M_1, M_2, M_3, M_4, M_5 and M_6 accomplish Lipschitz conditions and are contraction mappings.

Proof: We have the Kernel M_1. Let S and $\bar{S}$ be any two functions, then we have

$$\begin{aligned}
|M_1(t, S) - M_1(t, \bar{S})| &= |(-S(t) - \bar{S}(t))(\beta_1 I_1(t) + \beta_2 I_2(t) + \mu + d)| \\
&= |(S(t) - \bar{S}(t))|(\beta_1 I_1(t) + \beta_2 I_2(t) + \mu + d).
\end{aligned} \tag{13.19}$$

Utilizing the triangle inequality for norm on the right side of above equation we arrive at

$$|M_1(t, S) - M_1(t, \bar{S})| \leq |S(t) - \bar{S}(t)| \cdot |\beta_1 I_1(t) + \beta_2 I_2(t) + \mu + d| \leq \lambda_1 |S(t) - \bar{S}(t)|. \tag{13.20}$$

Hence the Kernel M_1 satisfy the Lipschitz condition. Similarly, results for kernels M_2, M_3, M_4, M_5 and M_6 can be derived by using I_1, I_2, A, T, R, as follows:

$$\begin{aligned}
|M_2(t, I_1) - M_2(t, \bar{I}_1)| &\leq \lambda_2 |I_1(t) - \bar{I}_1(t)|, \\
|M_3(t, I_2) - M_3(t, \bar{I}_2)| &\leq \lambda_3 |I_2(t) - \bar{I}_2(t)|, \\
|M_4(t, A) - M_4(t, \bar{A})| &\leq \lambda_4 |A(t) - \bar{A}(t)|, \\
|M_5(t, T) - M_5(t, \bar{T})| &\leq \lambda_5 |T(t) - \bar{T}(t)|, \\
|M_6(t, R) - M_6(t, \bar{R})| &\leq \lambda_6 |R(t) - \bar{R}(t)|.
\end{aligned} \tag{13.21}$$

As $\lambda_1, \lambda_2, \lambda_3, \lambda_4, \lambda_5$ and λ_6 are defined in Eq. (13.16). Therefore, the Lipschitz prerequisites have been satisfied for M_1, M_2, M_3, M_4, M_5 and M_6. In addition, since

$$0 \leq Z = \max\{\lambda_1, \lambda_2, \lambda_3, \lambda_4, \lambda_5, \lambda_6\} < 1,$$

contractions compose up the Kernels. The following is a depiction of the state variables in terms of Kernels derived from Eq.(13.17):

$$\begin{aligned}
S(t) &= S(0) + \Omega(\gamma_1)M_1(t,S) + \sigma(\gamma_1)\int_0^t M_1(\xi, S(\xi))\,d\xi,\\
I_1(t) &= I_1(0) + \Omega(\gamma_2)M_2(t,I_1) + \sigma(\gamma_2)\int_0^t M_2(\xi, I_1(\xi))\,d\xi,\\
I_2(t) &= I_2(0) + \Omega(\gamma_3)M_3(t,I_2) + \sigma(\gamma_3)\int_0^t M_3(\xi, I_2(\xi))\,d\xi,\\
A(t) &= A(0) + \Omega(\gamma_4)M_4(t,A) + \sigma(\gamma_4)\int_0^t M_4(\xi, A(\xi))\,d\xi,\\
T(t) &= T(0) + \Omega(\gamma_5)M_5(t,T) + \sigma(\gamma_5)\int_0^t M_5(\xi, T(\xi))\,d\xi,\\
R(t) &= R(0) + \Omega(\gamma_6)M_6(t,R) + \sigma(\gamma_6)\int_0^t M_6(\xi, R(\xi))\,d\xi.
\end{aligned} \tag{13.22}$$

We now present the following recursive formulae on interval $[S_n, S_{n+1}]$ using Eq.(13.22):

$$\begin{aligned}
S_n(t) &= \Omega(\gamma_1)M_1(t,S_{n-1}) + \sigma(\gamma_1)\int_0^t M_1(\xi, S_{n-1}(\xi))\,d\xi,\\
I_{1_n}(t) &= \Omega(\gamma_2)M_2(t,I_{1_{n-1}}) + \sigma(\gamma_2)\int_0^t M_2(\xi, I_{1_{n-1}}(\xi))\,d\xi,\\
I_{2_n}(t) &= \Omega(\gamma_3)M_3(t,I_{2_{n-1}}) + \sigma(\gamma_3)\int_0^t M_3(\xi, I_{2_{n-1}}(\xi))\,d\xi,\\
A_n(t) &= \Omega(\gamma_4)M_4(t,A_{n-1}) + \sigma(\gamma_4)\int_0^t M_4(\xi, A_{n-1}(\xi))\,d\xi,\\
T_n(t) &= \Omega(\gamma_5)M_5(t,T_{n-1}) + \sigma(\gamma_5)\int_0^t M_5(\xi, T_{n-1}(\xi))\,d\xi,\\
R_n(t) &= \Omega(\gamma_6)M_6(t,R_{n-1}) + \sigma(\gamma_6)\int_0^t M_6(\xi, R_{n-1}(\xi))\,d\xi.
\end{aligned} \tag{13.23}$$

Based on the specified beginning circumstances, the following I.C's of the recursive formulae above are established:

$$S_0(t) = S(0), \quad I_{1_0}(t) = I_1(0), \quad I_{2_0}(t) = I_2(0), \quad A_0(t) = A(0), \quad T_0(t) = T(0), \quad R_0(t) = R(0). \tag{13.24}$$

By evaluating the difference between succeeding values, we attain the following expressions:

$$
\begin{aligned}
\phi_n(t) &= S_n(t) - S_{n-1}(t) = \Omega(\gamma_1)(M_1(t, S_{n-1}) - M_1(t, S_{n-2})) \\
&\quad + \sigma(\gamma_1) \int_0^t (M_1(\xi, S_{n-1}) - M_1(\xi, S_{n-2}))\, d\xi, \\
\psi_n(t) &= I_{1_n}(t) - I_{1_{n-1}}(t) = \Omega(\gamma_2)(M_2(t, I_{1_{n-1}}) - M_2(t, I_{1_{n-2}})) \\
&\quad + \sigma(\gamma_2) \int_0^t (M_2(\xi, I_{1_{n-1}}) - M_2(\xi, I_{1_{n-2}}))\, d\xi, \\
\varphi_n(t) &= I_{2_n}(t) - I_{2_{n-1}}(t) = \Omega(\gamma_3)(M_3(t, I_{2_{n-1}}) - M_3(t, I_{2_{n-2}})) \\
&\quad + \sigma(\gamma_3) \int_0^t (M_3(\xi, I_{2_{n-1}}) - M_3(\xi, I_{2_{n-2}}))\, d\xi, \\
\xi_n(t) &= A_n(t) - A_{n-1}(t) = \Omega(\gamma_4)(M_4(t, A_{n-1}) - M_4(t, A_{n-2})) \\
&\quad + \sigma(\gamma_4) \int_0^t (M_4(\xi, A_{n-1}) - M_4(\xi, A_{n-2}))\, d\xi, \\
\chi_n(t) &= T_n(t) - T_{n-1}(t) = \Omega(\gamma_5)(M_5(t, T_{n-1}) - M_5(t, T_{n-2})) \\
&\quad + \sigma(\gamma_5) \int_0^t (M_5(\xi, T_{n-1}) - M_5(\xi, T_{n-2}))\, d\xi, \\
\eta_n(t) &= R_n(t) - R_{n-1}(t) = \Omega(\gamma_6)(M_6(t, R_{n-1}) - M_6(t, R_{n-2})) \\
&\quad + \sigma(\gamma_6) \int_0^t (M_6(\xi, R_{n-1}) - M_6(\xi, R_{n-2}))\, d\xi.
\end{aligned} \tag{13.25}
$$

Assuming that:

$$
\begin{aligned}
S_n(t) &= \sum_{i=0}^{n} \phi_i(t), \quad I_{1_n}(t) = \sum_{i=0}^{n} \psi_{1_i}(t), \quad I_{2_n}(t) = \sum_{i=0}^{n} \psi_{2_i}(t), \\
A_n(t) &= \sum_{i=0}^{n} \xi_i(t), \quad T_n(t) = \sum_{i=0}^{n} \chi_i(t), \quad R_n(t) = \sum_{i=0}^{n} \eta_i(t).
\end{aligned} \tag{13.26}
$$

Next, we create the inequality that recursively determines the differences $\phi_1(t), \psi_1(t), \psi_2(t), \xi(t), \zeta(t)$ and $\eta(t)$ as follows:

$$
\begin{aligned}
\|\phi_n(\bar{t})\| &= \|S_n(\bar{t}) - S_{n-1}(\bar{t})\| \\
&= \Big\| \Omega(\gamma_1)(M_1(\bar{t}, S_{n-1}) - M_1(\bar{t}, S_{n-2})) \\
&\quad + \omega(\gamma_1) \int_0^{\bar{t}} \big(M_1(y, S_{n-1}) - M_1(y, S_{n-2})\big)\, dy \Big\|
\end{aligned} \tag{13.27}
$$

Apply the triangular inequality for norms to Eq.(13.27):

$$
\begin{aligned}
\|S_n(\bar{t}) - S_{n-1}(\bar{t})\| &\leq \Omega(\gamma_1)\|M_1(\bar{t}, S_{n-1}) - M_1(\bar{t}, S_{n-2})\| \\
&\quad + \omega(\gamma_1) \int_0^{\bar{t}} \|M_1(y, S_{n-1}) - M_1(y, S_{n-2})\|\, dy
\end{aligned} \tag{13.28}
$$

Consequently, since the kernel M_1 uses the Lipschitz constant λ_1 to satisfy the Lipschitz condition, we

have

$$\|S_n(\bar{t}) - S_{n-1}(\bar{t})\| \leq \Omega(\gamma_1)\lambda_1\|S_{n-1} - S_{n-2}\| + \omega(\gamma_1)\lambda_1 \int_0^{\bar{t}} \|S_{n-1} - S_{n-2}\|\, dy \tag{13.29}$$

Thus, we obtain

$$\|\phi_n(\bar{t})\| \leq \Omega(\gamma_1)\lambda_1\|\phi_{n-1}(\bar{t})\| + \omega(\gamma_1)\lambda_1 \int_0^{\bar{t}} \|\phi_{n-1}(y)\|\, dy \tag{13.30}$$

In similar manner we obtain the following results:

$$\begin{aligned}
\|\psi_n(\bar{t})\| &\leq \Omega(\gamma_2)\lambda_2\|\psi_{n-1}(\bar{t})\| + \omega(\gamma_2)\lambda_2 \int_0^{\bar{t}} \|\psi_{n-1}(y)\|dy,\\
\|\varphi_n(\bar{t})\| &\leq \Omega(\gamma_3)\lambda_3\|\varphi_{n-1}(\bar{t})\| + \omega(\gamma_3)\lambda_3 \int_0^{\bar{t}} \|\varphi_{n-1}(y)\|dy,\\
\|\xi_n(\bar{t})\| &\leq \Omega(\gamma_4)\lambda_4\|\xi_{n-1}(\bar{t})\| + \omega(\gamma_4)\lambda_4 \int_0^{\bar{t}} \|\xi_{n-1}(y)\|dy,\\
\|\chi_n(\bar{t})\| &\leq \Omega(\gamma_5)\lambda_5\|\chi_{n-1}(\bar{t})\| + \omega(\gamma_5)\lambda_5 \int_0^{\bar{t}} \|\chi_{n-1}(y)\|dy,\\
\|\eta_n(\bar{t})\| &\leq \Omega(\gamma_6)\lambda_6\|\eta_{n-1}(\bar{t})\| + \omega(\gamma_6)\lambda_6 \int_0^{\bar{t}} \|\eta_{n-1}(y)\|dy,
\end{aligned} \tag{13.31}$$

Theorem 5: If there exist a time $\bar{t}_0 > 0$ such that the following inequalities holds:

$$\Omega(\gamma_j)\lambda_j + \omega(\gamma_j)\lambda_j t_0 < 1, \tag{13.32}$$

Then a system of solutions exists for the fractional *HIV* model Eq.(13.11) and Eq.(13.12).

Proof: Since the functions $S(\bar{t}), I_1(\bar{t}), I_2(\bar{t}), A(\bar{t}), T(\bar{t})$ and $R(\bar{t})$ are assumed to be bounded assuming every Kernel fulfills a Lipschitz requirement, the ensuing relations have obtained.

$$|\phi_n(\bar{t})| \leq \|S(0)\|\,[\Omega(\gamma_1)\lambda_1 + \omega(\gamma_1)\lambda_1\bar{t}]^n, \tag{13.33}$$

$$|\psi_n(\bar{t})| \leq \|I_1(0)\|\,[\Omega(\gamma_2)\lambda_2 + \omega(\gamma_2)\lambda_2\bar{t}]^n, \tag{13.34}$$

$$|\varphi_n(\bar{t})| \leq \|I_2(0)\|\,[\Omega(\gamma_3)\lambda_3 + \omega(\gamma_3)\lambda_3\bar{t}]^n, \tag{13.35}$$

$$|\xi_n(\bar{t})| \leq \|A(0)\|\,[\Omega(\gamma_4)\lambda_4 + \omega(\gamma_4)\lambda_4\bar{t}]^n, \tag{13.36}$$

$$|\chi_n(\bar{t})| \leq \|T(0)\|\,[\Omega(\gamma_5)\lambda_5 + \omega(\gamma_5)\lambda_5\bar{t}]^n, \tag{13.37}$$

$$|\eta_n(\bar{t})| \leq \|R(0)\| \left[\Omega(\gamma_6)\lambda_6 + \omega(\gamma_6)\lambda_6\bar{t}\right]^n. \tag{13.38}$$

Eq.(13.33) to Eq.(13.38) show the presence and reliability of the functions listed in Eq.(13.26). We demonstrate that the function $S_n(\bar{t}), I_1(\bar{t}), I_2(\bar{t}), A_n(\bar{t}), T_n(\bar{t}), R_n(\bar{t})$ eventually settle a system of solutions of Eq.(13.11) and Eq.(13.12). We define $B_n(\bar{t}), C_n(\bar{t}), D_n(\bar{t}), E_n(\bar{t}), F_n(\bar{t})$, and after n iterations, as the remaining conditions i.e.,

$$S(\bar{t}) - S(0) = S_1(\bar{t}) - B_n(\bar{t}), \tag{13.39}$$

$$I_1(\bar{t}) - I_1(0) = I_1(\bar{t}) - C_n(\bar{t}), \tag{13.40}$$

$$I_2(\bar{t}) - I_2(0) = I_2(\bar{t}) - D_n(\bar{t}), \tag{13.41}$$

$$A(\bar{t}) - A(0) = A_n(\bar{t}) - E_n(\bar{t}), \tag{13.42}$$

$$T(\bar{t}) - T(0) = T_n(\bar{t}) - F_n(\bar{t}), \tag{13.43}$$

$$R(\bar{t}) - R(0) = R_n(\bar{t}) - G_n(\bar{t}). \tag{13.44}$$

Now, the Lipschitz condition and the triangle inequality are used for M_1, we have

$$\|B_n(\bar{t})\| = \left\|\Omega(\gamma_1)(M_1(\bar{t}, S) - M_1(\bar{t}, S_{n-1})) + \omega(\gamma_1)\int_0^{\bar{t}} (M_1(y, S) - M_1(y, S_{n-1}))dy\right\|, \tag{13.45}$$

$$\leq \Omega(\gamma_1)\|M_1(\bar{t}, S) - M_1(\bar{t}, S_{n-1})\| + \omega(\gamma_1)\int_0^{\bar{t}} \|(M_1(y, S) - M_1(y, S_{n-1}))\|dy, \tag{13.46}$$

$$\leq \Omega(\gamma_1)\lambda_1\|S - S_{n-1}\| + \omega(\gamma_1)\lambda_1\|S - S_{n-1}\|\bar{t}. \tag{13.47}$$

Recursively, using the preceding process, we get

$$\|B_n(\bar{t})\| \leq \left[(\Omega(\gamma_1) + \omega(\gamma_1)\bar{t})\lambda_1\right]^{n+1}\theta_1. \tag{13.48}$$

Then at $\bar{t}_0$, we gain

$$\|B_n(\bar{t})\| \leq \left[(\Omega(\gamma_1) + \omega(\gamma_1)\bar{t}_0)\lambda_1\right]^{n+1}\theta_1. \tag{13.49}$$

After utilizing condition Eq.(13.32) and putting the limit on Eq.(13.49), we obtain $\|B_n(\bar{t})\| \to 0$. Using similar process as done above, we obtain the following relations:

$$\|C_n(\bar{t})\| \leq [(\Omega(\gamma_2) + \omega(\gamma_2)\bar{t}_0)\lambda_2]^{n+1}\theta_2, \tag{13.50}$$

$$\|D_n(\bar{t})\| \leq [(\Omega(\gamma_3) + \omega(\gamma_3)\bar{t}_0)\lambda_3]^{n+1}\theta_3, \tag{13.51}$$

$$\|E_n(\bar{t})\| \leq [(\Omega(\gamma_4) + \omega(\gamma_4)\bar{t}_0)\lambda_4]^{n+1}\theta_4, \tag{13.52}$$

$$\|F_n(\bar{t})\| \leq [(\Omega(\gamma_5) + \omega(\gamma_5)\bar{t}_0)\lambda_5]^{n+1}\theta_5, \tag{13.53}$$

$$\|G_n(\bar{t})\| \leq [(\Omega(\gamma_6) + \omega(\gamma_6)\bar{t}_0)\lambda_6]^{n+1}\theta_6. \tag{13.54}$$

Similarly taking limit on Eq.(13.49) as $n \to \infty$ and applying the condition Eq. 13.32, we have

$$\|C_n(\bar{t})\| \to 0, \quad \|D_n(\bar{t})\| \to 0, \quad \|E_n(\bar{t})\| \to 0, \quad \|F_n(\bar{t})\| \to 0, \quad \text{and} \quad \|G_n(\bar{t})\| \to 0.$$

Therefore, it indicates that the system of solutions for the system Eq.(13.11)–(Eq. 13.12) exists.

Now, we establish specifications for the system of solutions to be singular.

Theorem 6: Coupled with the IC's Eq.(13.12), system Eq.(13.11) has a distinct set of solutions in the instance that the given below conditions satisfied:

$$(1 - \Omega(\gamma_i)\lambda_i - \omega(\gamma_i)\lambda_i\bar{t}) > 0, \quad \text{for } i = 1, 2, \ldots, 6. \tag{13.55}$$

Proof: Assuming that $\{S(\bar{t}), I_1(\bar{t}), I_2(\bar{t}), A(\bar{t}), T(\bar{t}), R(\bar{t})\}$ be an array of equation's solution (1.11)–(1.12) in regarding to solutions set $\{S(\bar{t}), I_1(\bar{t}), I_2(\bar{t}), A(\bar{t}), T(\bar{t}), R(\bar{t})\}$ existence have derived in theorem 4 and 5. Then we have equation

$$S(\bar{t}) - S_1(\bar{t}) = \Omega(\gamma_1)(M_1(\bar{t}, S) - M_1(\bar{t}, S_1)) + \omega(\gamma_1)\int_0^{\bar{t}} (M_1(y, S) - M_1(y, S_1))dy. \tag{13.56}$$

Implementing norms on both ends of Eq.(13.56)

$$\|S(\bar{t}) - S_1(\bar{t})\| = \left\|\Omega(\gamma_1)(M_1(\bar{t}, S) - M_1(\bar{t}, S_1)) + \omega(\gamma_1)\int_0^{\bar{t}} (M_1(y, S) - M_1(y, S_1))dy\right\|. \tag{13.57}$$

By employing property of triangular inequality, we have

$$\|S(\bar{t}) - S_1(\bar{t})\| \leq \Omega(\gamma_1)\|M_1(\bar{t}, S) - M_1(\bar{t}, S_1)\| + \omega(\gamma_1)\int_0^{\bar{t}} \|(M_1(y, S) - M_1(y, S_1))\|dy. \tag{13.58}$$

Using Lipschitz condition for M_1, we find

$$\|S(\bar{t}) - S_1(\bar{t})\| - \|S(\bar{t}) - S_1(\bar{t})\|(\Omega(\gamma_1)\lambda_1 + \omega(\gamma_1)\lambda_1\bar{t}) \leq 0. \tag{13.59}$$

Then rearranging/taking common values of Eq.(13.59), we obtain

$$\|S(\bar{t}) - S_1(\bar{t})\|(1 - \Omega(\gamma_1)\lambda_1 + \omega(\gamma_1)\lambda_1\bar{t}) \leq 0. \tag{13.60}$$

Finally applying condition $(1 - \Omega(\gamma_i)\lambda_i - \omega(\gamma_i)\lambda_i\bar{t}) > 0$ for $i = 1$ to Eq.(13.60) we have

$$\|S(\bar{t}) - S_1(\bar{t})\| = 0, \tag{13.61}$$

And therefore $S(\bar{t}) = S_1(\bar{t})$. Applying the similar process to each of the following pairs $(I_1(\bar{t}), I_{1_1}(\bar{t}))$, $(I_2(\bar{t}), I_{2_1}(\bar{t}))$, $(A(\bar{t}), A_1(\bar{t}))$, $(T(\bar{t}), T_1(\bar{t}))$ and $(R(\bar{t}), R_1(\bar{t}))$, with inequality Eq.(13.55) for $i = 2, 3, 4, 5, 6$, respectively. We have

$$I_1(\bar{t}) = I_{1_1}(\bar{t}), \quad I_2(\bar{t}) = I_{2_1}(\bar{t}), \quad A(\bar{t}) = A_1(\bar{t}), \quad T(\bar{t}) = T_1(\bar{t}), \quad R(\bar{t}) = R_1(\bar{t}). \tag{13.62}$$

It is demonstrated that the fractional order system's solution is unique.

13.5 Equilibration points of the model and basic reproduction number

By equating the fractional order system Eq.(13.11)'s right side equal to zero, we obtained the equilibrium locations. After the corresponding algebraic system solved, we are left with two different equilibrium points: one under endemic conditions and another for lack of illness. The equilibrium point free from illness is $E^0 = (S^0, I_1^0, I_2^0, A^0, T^0, R^0)$. This equilibrium points free from sickness means we have the number of susceptible population with zero the infected population which *AIDS* treatment populations and the highly effected *AIDS* population are equal to zero. It indicates that there isn't any population-wide infection transmission.

We are provided the disease-free equilibration point as

$$E^0 = (S^0, I_1^0, I_2^0, A^0, T^0, R^0) = \left(\frac{\Lambda}{(\mu_1 + d)}, 0, 0, 0, 0, \frac{\mu_1\Lambda}{(d + \mu_1)d}\right). \tag{13.63}$$

Endemic Equilibrium and Parameter Definitions. The endemic equilibrium point arises when both $I_1 \neq 0$ and $I_2 \neq 0$, yielding $E^* = (S^*, I_1^*, I_2^*, A^*, T^*, R^*)$. The corresponding equilibrium values are obtained as

$$\begin{aligned} I_1^* &= \frac{\alpha_1 T^*}{(k_1 + d - \beta_1 S^*)}, \\ I_2^* &= \frac{(\alpha_1 + \alpha_2 + \delta_2 + d)\beta_2(k_1 + d) - (\alpha_1 + \alpha_2 + \delta_2 + d)\beta_1(k_2 + k_3 + d) - \alpha_1 k_1 \beta_2}{\alpha_1 k_3 \beta_2} I_1^*, \end{aligned} \tag{13.64}$$

and

$$\begin{aligned} S^* &= \frac{\Lambda}{\beta_1 I_1^* + \beta_2 I_2^* + \mu_1 + d}, \\ A^* &= \frac{k_3 I_2^* + \alpha_2 T^*}{\delta_1 + d}, \\ T^* &= \frac{k_1 I_1^* + k_3 I_2^*}{\alpha_1 + \alpha_2 + \delta_2 + d}, \\ R^* &= \frac{\mu_1 \Lambda}{\left(\beta_1 I_1^* + \beta_2 I_2^* + \mu_1 - d\right) d}. \end{aligned} \tag{13.65}$$

Here, the parameters are defined as follows: Λ denotes the recruitment rate of susceptible individuals, d is the natural mortality rate, and μ_1 is the recovery rate associated with immune response. The transmission coefficients are represented by β_1 and β_2 for infection through classes I_1 and I_2, respectively. The progression parameters α_1 and α_2 govern the transition from treatment and asymptomatic stages into subsequent compartments, while δ_1 and δ_2 represent disease-induced death rates in the asymptomatic and treated classes. The parameters k_1, k_2, k_3 are therapy-related rates corresponding to treatment initiation and modification across compartments. Finally, S^*, I_1^*, I_2^*, A^*, T^*, and R^* denote the steady-state populations of susceptible individuals, primary infected class, secondary infected class, asymptomatic class, treated class, and recovered class, respectively.

The fundamental reproduction number R_0, which oftenly computed by employing the next-generation matrix technique. We have system of equations in Eq.(13.11). Let $x = (I_1, I_2, A, T, S, R)^T$, then system of equation can be written as:

$$R_0 = \frac{\beta_2 \Lambda}{(\mu_1 + d)(k_2 + k_3 + d)}. \tag{13.66}$$

It is evident that a specific endemic equilibration point E^* exists if $R_0 > 1$. The developed activation function is characterized by two sets of parameters: (α_1, μ_1) and (α_2, μ_2). In this model, the parameter α denotes the progression rate from the primary infected class I_1 to the secondary infected class I_2. The parameter α_1 represents the transition rate of infected individuals receiving antiretroviral therapy (ART) into the treatment class T, while α_2 denotes the transition rate from treatment to the asymptomatic class A. The parameter μ corresponds to the natural mortality rate applicable to all population classes, whereas μ_1 denotes the recovery rate associated with behavioral change that transfers individuals from

the susceptible class S to the resistant class R.

13.6 Adams-Bashforth scheme via three steps and Numerical Simulations

The vast range of nonlinear fractional derivative models that have served as real world issues has led to the development of several innovative analytical techniques in recent years. The novel analytical techniques include the local fractional homotopy perturbation Laplace transform method (**LFH-PLTM**), the homotopy analysis transform method (**HATM**), and the homotopy analysis Sumudu transform technique (**HASTM**). Furthermore, a variety of numerical techniques have been developed to relent approximations for fractional differential equation solutions. These techniques, which are usually based on discretizing the independent variable, include finite difference, finite element, and Adams-Bashforth Moulton type predictor-corrector approaches, among other variants of the integer order techniques. In this paper, we derived numerical approaches for the fractional model Eq.(13.11) of Caputo-Fabrizio using a three step fractional Adams-Bashforth approach. In order to establish First, we introduce the three-step fractional Adams-Bashforth technique in this section, which provides Quantitative explanations for the fractional *HIV-AIDS* framework provided in Eq.(13.11) for various values of fractional orders and a range of realistic parameter values.

Rather using the Losada and Nieto formulation defined in Eq.(13.1), we described the numerical strategies using applying the authentic Eq.(13.5) formulation of the Caputo-Fabrizio fractional derivative. Analyze the differential equation for fractions of Caputo-Fabrizio:

$$^{CF}D_t^{\gamma}(v(t)) = g(t, v(t)), \tag{13.67}$$

Where $^{CF}D_t^{(*)}$ defined in Eq.(13.1) is the Caputo-Fabrizio fractional derivative. The integral in fractional terms defined as:

$$^{FC}I_t^{\gamma}(g(t)) = \frac{1-\gamma}{E(\gamma)}g(t) + \frac{\gamma}{E(\gamma)}\int_0^t g(\omega)\,d\omega, \tag{13.68}$$

by imposing the integral in fractional terms on either side of Eq. (1.49), we obtain

$$^{FC}I_t^{\gamma}(^{CF}D_t^{\gamma}(v(t))) = {}^{FC}I_t^{\gamma}(g(t, v(t))),$$

$$v(t) - v(0) = {}^{FC}I_t^{\gamma}(g(t, v(t))),$$

$$v(t) - v(0) = \frac{1-\gamma}{E(\gamma)}g(t, v(t)) + \frac{\gamma}{E(\gamma)}\int_0^t g(s, v(s))\,ds. \tag{13.69}$$

Next, we divide the period of time span into discrete halves $[0, t]$ in step of order h and acquired the sequence $t_0 = 0$, $t_j = t_{j-1} + h$, $j = 0, 1, 2, \ldots, n-1$, $t_n = t$. By Eq.(13.69), the recursive formulae that have developed shown below:

$$v(t_{j+1}) - v(0) = \frac{1-\gamma}{E(\gamma)} g(t_j, v(t_j)) + \frac{\gamma}{E(\gamma)} \int_0^{t_{j+1}} g(t, v(t))\, dt, \tag{13.70}$$

and

$$v(t_j) - v(0) = \frac{1-\gamma}{E(\gamma)} g(t_{j-1}, v(t_{j-1})) + \frac{\gamma}{E(\gamma)} \int_0^{t_j} g(t, v(t))\, dt, \tag{13.71}$$

now, we subtract Eq. 13.71 from Eq. 13.70, we obtain

$$v(t_{j+1}) - v(t_j) = \frac{1-\gamma}{E(\gamma)} [g(t_j, v_j) - g(t_{j-1}, v_{j-1})] + \frac{\gamma}{E(\gamma)} \int_{t_j}^{t_{j+1}} g(t, v(t))\, dt. \tag{13.72}$$

We derive a three-step predictor method of the Adams-Bashforth by approximating the integral $\int_{t_j}^{t_{j+1}} g(t, v(t))\, dt$, using the approximation in the equation above $\int_{t_j}^{t_{j+1}} B_2(t)\, dt$, where $B_2(t)$ is Lagrange polynomial with a degree of two that traverses these three locations $(t_{j-2}, g(t_{j-2}, v(t_{j-2})))$, $(t_{j-1}, g(t_{j-1}, v(t_{j-1})))$, $(t_j, g(t_j, v(t_j)))$. That is,

$$B_2(t) = \sum_{i=0}^{2} g(t_{j-i}, v_{j-i}) L_i(t), \tag{13.73}$$

as, $L_i(t)$ are the basis polynomials for Lagrange at three-point (t_{j-2}, t_{j-1}, t_j). Using the variable's change $s = \dfrac{t_j - t_i}{h}$, $sh = t_{j+1} - t$, after integrating and replacing the Lagrange basis polynomials, we have

$$\begin{aligned} \int_{t_j}^{t_{j+1}} g(t, v(t))\, ds = h \Bigg[& \frac{(s-2)(s-3)}{(1-2)(1-3)} g(t_j, v_j) \\ & + \frac{(s-1)(s-3)}{(2-1)(2-3)} g(t_{j-1}, v_{j-1}) + \frac{(s-2)(s-1)}{(3-2)(3-1)} g(t_{j-2}, v_{j-2}) \Bigg]_0^1 \end{aligned} \tag{13.74}$$

$$\int_{t_j}^{t_{j+1}} g(t, v(t))\, ds = h \left[\frac{23}{4!} g(t_j, v_j) - \frac{4}{3} g(t_{j-1}, v_{j-1}) + \frac{5}{4!} g(t_{j-2}, v_{j-2}) \right], \tag{13.75}$$

as, $v_{j-2} = v(t_{j-2})$, $v_{j-1} = v(t_{j-1})$, $v_j = v(t_j)$. By inserting Eq.(13.75) into Eq. Eq.(13.73), the iterative formula obtained is as follows:

$$\begin{aligned} v(t_{j+1}) = v(t_j) & + \frac{1}{E(\gamma)} \left[\frac{23h\gamma}{12} + (1-\gamma) \right] g(t_j, v_j) - \frac{1}{E(\gamma)} \left[\frac{4h\gamma}{3} + (1-\gamma) \right] g(t_{j-1}, v_{j-1}) \\ & + \frac{5h}{12} \frac{\gamma}{E(\gamma)} g(t_{j-2}, v_{j-2}), \end{aligned} \tag{13.76}$$

for a particular situation $\gamma = 1$, Eq.(13.76) demonstrates to the three-step, classic Adams-Bashforth predictor formula

$$v(t_{j+1}) = v(t_j) + \frac{1}{E(\gamma)}\left[\frac{23h}{12}g(t_j, v_j) - \frac{4h}{3}g(t_{j-1}, v_{j-1}) + \frac{5h}{12}g(t_{j-2}, v_{j-2})\right]. \tag{13.77}$$

The Lagrange interpolating polynomial error estimate may be used to estimate the truncation error for the three-step formula, namely

$$g(t, v(t)) = B_2(t) + X_2(t), \tag{13.78}$$

$$X_2(t) = \frac{g^{(3)}(\zeta, u(\zeta))}{3!}(t-t)(t-t_j)(t-t_{j-2}), \quad \zeta_j \in (t_{j-2}, t). \tag{13.79}$$

then we have,

$$\int_{t_j}^{t_j} X_2(t)dt = \int_{t_j}^{t_j} \frac{f^{(3)}(\zeta, u(\zeta))}{3!}(t-t_j)(t-t_{j-1})(t-t_{j-2})dt, \tag{13.80}$$

$$\approx \frac{h^4 g^{(3)}(\nu(\mu_j), \mu_j)}{6(3!)} \int_0^1 (s-1)(3-2)(s-3)\, ds, \tag{13.81}$$

$$= \frac{3}{8}h^4 g^{(3)}(\nu(\mu_j), \mu_j), \tag{13.82}$$

However, $\mu_j \in (t_{j-2}, t_{j+1})$, and to approximate the integral, we have applied the mean value theorem. Signifying the complete right-hand side of Eq.(13.76) by that value, we have

$$v_{j+1} = v_j + (\nu(\mu_j), \mu_j)\frac{3}{8}h^4 g^{(3)}.$$

Consequently, the local truncation error resulting from using the formula Eq.(13.76) is ascertained by

$$\frac{v_{j+1} - v_j}{h} = \frac{\frac{3}{8}h^4 g^{(3)}(\nu(\mu_j), \mu_j)}{h} \cdot \frac{\gamma}{E(\gamma)}, \tag{13.83}$$

$$= \frac{3}{8E(\gamma)}\gamma h^3 g^{(3)}(\mu_j, \nu(\mu_j)). \tag{13.84}$$

Next, Numerical solutions for the fractional model Eq.(13.11)– Eq.(13.12), are derived via the fractional Adam Bashforth method, three steps in Eq.(13.76),. We assumed for the numerical simulations that each fractional derivative in the system Eq.(13.11), possesses same order, i.e.,

$$\gamma_1 = \gamma_2 = \gamma_3 = \gamma_4 = \gamma_5 = \gamma_6 = \gamma. \tag{13.85}$$

After that, we mentioned the system's right-hand side:

$${}^{CF}D_t^{\gamma}(v(t)) = g(t, v(t)), \quad 0 < \gamma < 1. \tag{13.86}$$

Where,

$$v(t) = \begin{bmatrix} S(t) \\ I_1(t) \\ I_2(t) \\ A(t) \\ T(t) \\ R(t) \end{bmatrix}, \qquad g(t, v(t)) = \begin{bmatrix} g_1(t, v(t)) \\ g_2(t, v(t)) \\ g_3(t, v(t)) \\ g_4(t, v(t)) \\ g_5(t, v(t)) \\ g_6(t, v(t)) \end{bmatrix} \tag{13.87}$$

The scalar function $g_i, i = 1, 2, \ldots, 6$, we stated the system's Eq.(13.11), right side as,

$$\begin{aligned} g_1(t, v(t)) &= \Lambda - \beta_1 I_1 S - \beta_2 I_2 S - (\mu_1 + d)S, \\ g_2(t, v(t)) &= \beta_1 I_1 S + \alpha T - (k_1 + d)I_1, \\ g_3(t, v(t)) &= \beta_2 I_2 S - (k_2 + k_3 + d)I_2, \\ g_4(t, v(t)) &= k_2 I_2 + \alpha T - (\delta_1 + d)A, \\ g_5(t, v(t)) &= k_1 I_1 + k_3 I_2 - (\alpha + a_2 + \delta_2 + d)T, \\ g_6(t, v(t)) &= \mu_1 S - dR. \end{aligned} \tag{13.88}$$

Implementing fractional integral defined in Eq.(13.68), to both sides of Eq.(13.86), we gain

$$v(t) - v(0) = \frac{1-\gamma}{E(\gamma)} g(t, v(t)) + \frac{\gamma}{E(\gamma)} \int_0^t g(s, v(s))\, ds. \tag{13.89}$$

Utilizing the numerical technique in Eq.(13.89), we have the following iterative formula:

$$\begin{aligned} \nu_{j+1} = v_j &+ \frac{1}{E(\gamma)} \left[\frac{23}{12} h\gamma + (1-\gamma) \right] g(t_j, v_j) - \frac{1}{E(\gamma)} \left[\frac{4}{3} h\gamma + (1-\gamma) \right] g(t_{j-1}, v_{j-1}) \\ &+ \frac{5h\gamma}{12E(\gamma)} g(t_{j-2}, v_{j-2}), \end{aligned} \tag{13.90}$$

Where, $\nu_{j+1} = v(t_{j+1}), \quad v_j = v(t_j), \quad v_{j-1} = v(t_{j-1}), \quad v_{j-2} = v(t_{j-2})$, and

$$v_0 = v(t_0) = \left[S(t_0), I_1(t_0), I_2(t_0), A(t_0), T(t_0), R(t_0) \right]^T.$$

The IC's are as $S(0) = 35, I_1(0) = 25, I_2(0) = 35, A(0) = 15, T(0) = 8, R(0) = 0$. Hence we have $E^0 = (S^0, I_1^0, I_2^0, A^0, T^0, R^0) = (0.0887, 0, 0, 0, 0, 16.9725), \quad R_0 = 0.00284 < 1.\%$ We established the fractional orders in the system in Eq.(13.11) for computational ease, as $\gamma_1 = \gamma_2 = \gamma_3 = \gamma_4 = \gamma_5 = \gamma_6 = \gamma$, and we select $E(\gamma) = 1$. Scheme in Eq.(13.90,) is used to generate numerical simulations that are intended to illustrate the behaviours for $\gamma = 0.6, 0.8, 0.95$. For our estimation, we have utilized the following initial values and numerical parameter:

Parameters	Description	Values
Λ	The population's rate at which susceptible individuals are recruited	0.55
β_1	The transmission coefficient of I_1	0.0023
β_2	The transmission coefficient of I_2	0.0033
α_1	The rapid pace of shifting individuals from the infectious class to having full-blown AIDS	0.08
α_2	Rate at which I_1 population receive treatment	0.03
k_1	Progress rate from infected (I_1) to T	0.15
k_2	Progress rate from infected (I_2) to A	0.35
k_3	Progress rate from I_2 to T	0.05
μ_1	The rate of change of susceptible whose alter the sexual habits	0.03
d	Physical mortality rate	0.0196
δ_1	The deaths caused by AIDS	0.0909
δ_2	The mortality rate of treated	0.0667

Table 13.1: Initial values and numerical parameters.

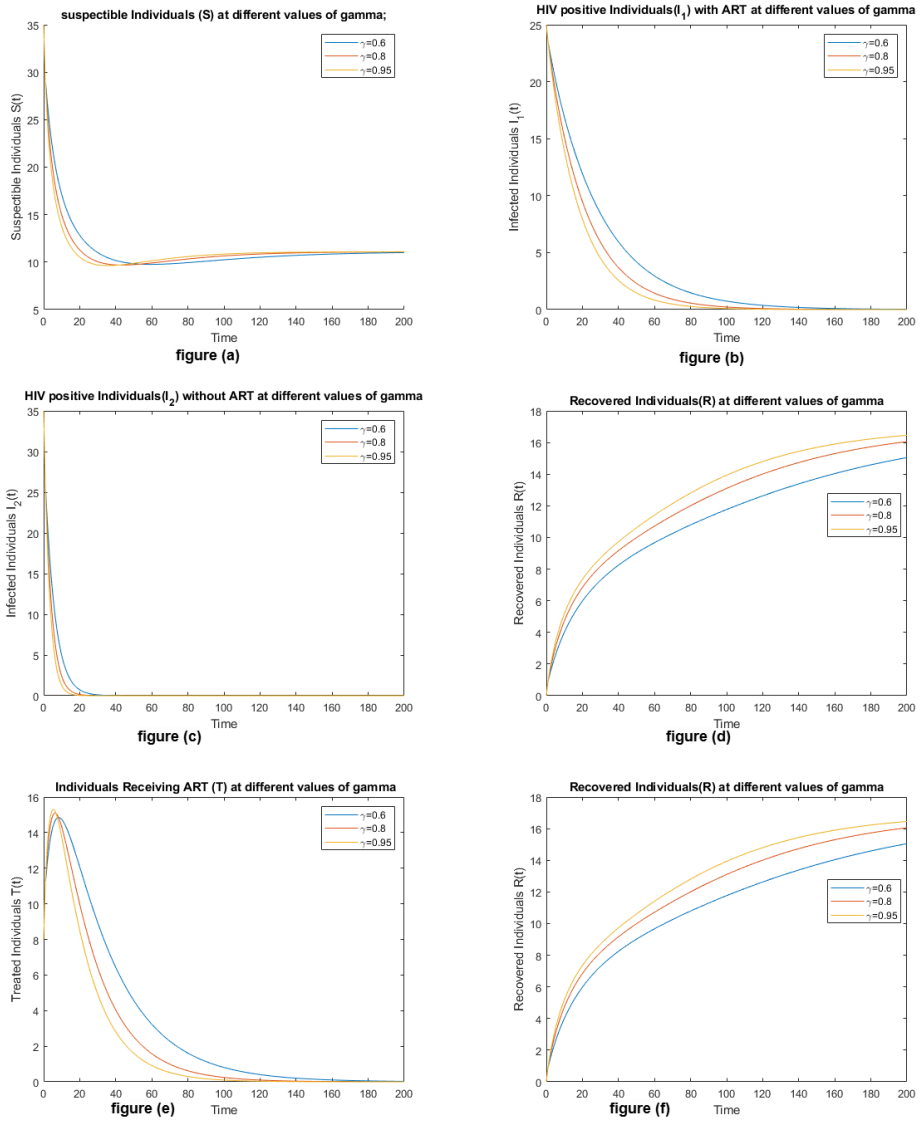

Figure 13.2: The time series plot for each state variable in model Eq.(13.11), for different values of $\gamma = 0.6$, $\gamma = 0.8$, and $\gamma = 0.95$.

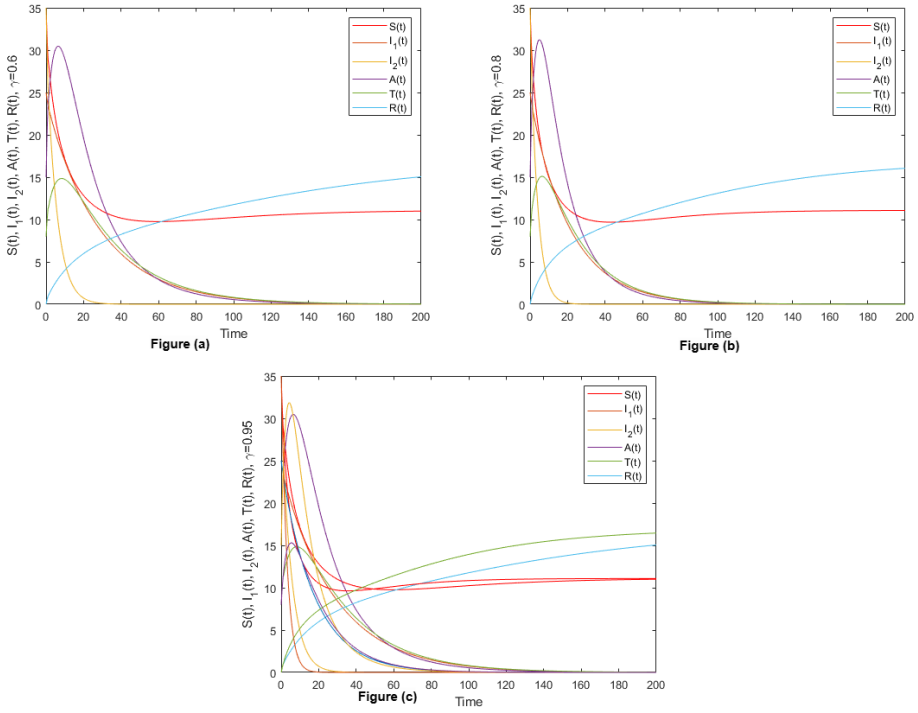

Figure 13.3: The time series plot for each state variable in model Eq.(13.11), for different values of $\gamma = 0.6$, $\gamma = 0.8$, and $\gamma = 0.95$.

The mathematical calculations have been conducted with the intention of analyzing the numerical results of various parametric merit employed in the current study for the pandemic behaviour of different populations of HIV along with the distinctive values of order. The order of the model lies between 0 and 1. Different parameters show the pandemic behavior of the disease. In order to have a detailed quantitative analysis occurred due to variations in the numerical values of. The Figure 13.2(a) shows that the state variable exposes its dynamic behaviour of HIV infection with respect to time, as we have order of the state variable model. Initially the value of state variable increases but with time the value decreases and tends to the value 11.0887 which is the point at which the disease free equilibration exists. Similarly, the Figure 13.2(b), Figure 13.2(c), Figure 13.2(d), Figure 13.2(e) exhibit that the state variables show, at initial time, an increase but with time the value of variables decreases and tends to zero which is the point at which the disease free equilibration exists. The Figure 13.2(f) exhibits that the state variable shows an increase with passage of time and its increasing value approaches to 16.9725 which is the point at which the disease free equilibration exists. The information which are utilized for the Figure 14.2 (a), (b), (c) are I.C's which are given as $S(t) = 35,\ I_1(t) = 25,\ I_2(t) = 35,\ A(t) = 15,\ T(t) = 8,\ R(t) = 0$, and the order of the model $\gamma = 0.6$. The behaviour of the graph shows that with the change of time the all compartmental values shows its dynamic behaviour with respect to the value of order of model i.e $\gamma = 0.6, 0.8, 0.95$. Initially the all state variables increase and approaches to its initial conditions then with the passage of time the all state variables approaches to its equilibrium points i.e $E^0 = (11.0887, 0, 0, 0, 0, 16.9725)$.

13.7 Conclusion

Using the transfer diagram designed for this study, the SI_1I_2ATR model is formulated, comprising compartments of susceptibles, infected patients with ART (I_1), infected patients without ART (I_2), advanced AIDS cases (A), treated individuals (T), and recovered individuals (R). The model demonstrates the uniqueness and existence of solutions. Both disease-free and endemic equilibria are obtained. Numerical simulations using the three-step fractional Adams–Bashforth method highlight the influence of fractional orders γ on the system's dynamics.

Bibliography

[1] Corbett, E. L., Watt, C. J., Walker, N., Maher, D., Williams, B. G., Raviglione, M. C., & Dye, C. (2003). The growing burden of tuberculosis: global trends and interactions with the HIV epidemic. *Archives of Internal Medicine*, 163(9), 1009–1021.

[2] Surur, A. S., Teni, F. S., Wale, W., Ayalew, Y., & Tesfaye, B. (2017). Health related quality of life of HIV/AIDS patients on highly active anti-retroviral therapy at a university referral hospital in Ethiopia. *BMC Health Services Research*, 17, 1–8.

[3] Pandey, A., & Galvani, A. P. (2019). The global burden of HIV and prospects for control. *The Lancet HIV*, 6(12), e809–e811.

[4] Wang, H., Wolock, T. M., Carter, A., Nguyen, G., Kyu, H. H., Gakidou, E., ... & Fürst, T. (2016). Estimates of global, regional, and national incidence, prevalence, and mortality of HIV, 1980–2015: the Global Burden of Disease Study 2015. *The Lancet HIV*, 3(8), e361–e387.

[5] Frank, T. D., Carter, A., Jahagirdar, D., Biehl, M. H., Douwes-Schultz, D., Larson, S. L., ... & Hosseinzadeh, M. (2019). Global, regional, and national incidence, prevalence, and mortality of HIV, 1980–2017, and forecasts to 2030, for 195 countries and territories: a systematic analysis for the Global Burden of Diseases, Injuries, and Risk Factors Study 2017. *The Lancet HIV*, 6(12), e831–e859.

[6] World Health Organization. (2017). Antiretroviral therapy (ART) coverage among all age groups. *World Health Organization*. Available from: https://www.who.int/data/gho/hiv/epidemic_response/ART/en.

[7] Dimitrov, D., Wood, D., Ulrich, A., Swan, D. A., Adamson, B., Lama, J. R., ... & Duerr, A. (2019). Projected effectiveness of HIV detection during early infection and rapid ART initiation among MSM and transgender women in Peru: a modeling study. *Infectious Disease Modelling*, 4, 73–82.

[8] Espitia, C. C., Botina, M. A., Solarte, M. A., Hernandez, I., Riascos, R. A., & Meyer, J. F. (2022).

Mathematical model of HIV/AIDS considering sexual preferences under antiretroviral therapy, a case study in San Juan de Pasto, Colombia. *Journal of Computational Biology*, 29(5), 483–493.

[9] Ahmed, I., Tariboon, J., Muhammad, M., & Ibrahim, M. J. (2025). A mathematical and sensitivity analysis of an HIV/AIDS infection model. *International Journal of Mathematics and Computer in Engineering*, 3(1), 35-46.

[10] Kretzschmar, M. (2019). Disease modeling for public health: added value, challenges, and institutional constraints. Journal of public health policy, 41(1), 39-51

[11] Gurmu, E. D., Bole, B. K., & Koya, P. R. (2020). Mathematical modelling of HIV/AIDS transmission dynamics with drug resistance compartment. *American Journal of Applied Mathematics*, 8(1), 34–45.

[12] Smith, R. J., Li, J. I. N. G., Mao, J., & Sahai, B. E. N. I. (2013). Using within-host mathematical modelling to predict the long-term outcome of human papillomavirus vaccines. *Canadian Applied Mathematics Quarterly*, 21(2). 281-299

[13] Jan, R., Khan, A., Boulaaras, S., & Ahmed Zubair, S. (2022). Dynamical behaviour and chaotic phenomena of HIV infection through fractional calculus. *Discrete Dynamics in Nature and Society*, 2022(1), 5937420.

[14] Alzaid, S. S., Alkahtani, B. S. T., Sharma, S., & Dubey, R. S. (2021). Numerical solution of fractional model of HIV-1 infection in framework of different fractional derivatives. *Journal of Function Spaces*, 2021, 1–10.

[15] Cheneke, K. R. (2023). Optimal Control and Bifurcation Analysis of HIV Model. *Computational and Mathematical Methods in Medicine*, 2023, 1–21.

[16] Arafa, A. A. M., Rida, S. Z., & Khalil, M. (2014). A fractional-order model of HIV infection with drug therapy effect. *Journal of the Egyptian Mathematical Society*, 22(3), 538–543.

[17] Bachar, M., & Dorfmayr, A. (2004). HIV treatment models with time delay. *Comptes Rendus Biologies*, 327(11), 983–994.

[18] Khalaf, S. L., & Lazim, Z. A. (2020). Stability Analysis of Caputo Fractional Model for HIV Infection. *Journal of Al-Qadisiyah for Computer Science and Mathematics*, 12(4), 1–16.

[19] Khan, M. A., & Odinsyah, H. P. (2020). Fractional model of HIV transmission with awareness effect. *Chaos, Solitons & Fractals*, 138, 109967.

[20] Okosun, K. O., Makinde, O. D., & Abiodun, G. J. (2012). Transmission dynamics of HIV/AIDS with optimal control in the presence of carefree susceptibles and treatment. In *BIOMAT 2011*, 131–152.

[21] Moore, E. J., Sirisubtawee, S., & Koonprasert, S. (2019). A Caputo–Fabrizio fractional differential equation model for HIV/AIDS with treatment compartment. *Advances in Difference Equations*, 2019(1), 1–20.

[22] Habibah, U., Pradana, Y. L., & Villadystian, W. (2021). Mathematical model of HIV/AIDS with two different stages of infection subpopulation and its stability analysis. *Engineering Letters, 29*(1), 1–9. Available from:https://www.engineeringletters.com/issues_v29/issue_1/EL_29_1_01.pdf

CHAPTER 14

Topological Indices and Statistical Modeling of Drugs Targeting Bone-Cancer

Nazeran Idrees[†], Fatima Saeed [†], Muhammad Imran[†] and Fozia Bashir Farooq[‡]

[†]*Department of Mathematics, GC University, Faisalabad, Pakistan.*

[‡]*Department of Mathematics and Statistics, College of Science, Imam Mohammad Ibn Saud Islamic University (IMSIU), Saudi Arabia.*

Corresponding Author: Nazeran Idrees: nazeranidrees@gcuf.edu.pk

Abstract: *A topological descriptor serves as a mathematical function that converts a chemical structure into a numeric value, proving invaluable in Quantitative Structure-Property Relationship (QSPR) analysis of various drugs. Degree-based topological indices are particularly utilized to ascertain the physical and chemical properties of drugs because they provide valuable insights into molecules' structural and physicochemical properties, critical for understanding their activity in biological systems and optimizing their pharmacological qualities. Bone cancer is characterized by uncontrolled cell growth in the bones. QSPR provides a design paradigm that demonstrates the precise connection between molecular physicochemical qualities and their biological impact on a drug's response. Using QSPR models, researchers can create and optimize drug candidates with improved efficacy, safety, and physiological features, boosting the probability of success in clinical trials. This study focuses on QSPR analysis applied to drugs used for treating bone cancer, including Doxorubicin, Ifosfamide, Gemcitabine, Etoposide, Methotrexate, Cisplatin, Zoledronic, Sunitinib, and Regorafenib. The investigation reveals a significant correlation between topological indices imposed on these drugs and their physical properties.*

Keywords: chemical graph, drugs; linear QSPR model; degree-based topological indices.

14.1 Introduction

The main types of bone cancers are Ewing sarcoma, osteosarcoma, and chondrosarcoma. Bone cancers that directly arise from bone are rare. Less than 1% of all diagnosed bone cancers are malignant, but their morbidity and mortality are important [1]. Among two-thirds of bone cancers, Osteosarcoma is the most important bone cancer [2]. In the US almost 1,200 patients are diagnosed with osteosarcoma annually. This cancer originated from primitive mesenchymal cells that undergo that malignant change, which in turn produces a malignant osteoid matrix. No doubt that osteosarcomas can originate in any bone, but mainly develops in the metaphysis part of long bones. Almost 60% of osteosarcoma occur in the proximal tibia, distal femur, and the proximal humerus [3]. The second most common type of bone cancer is Ewing sarcoma. It is thought to have originated from primitive stem cells, and the extent of malignancy depends on the stage at which stem cells are arrested during differentiation [4]. It primarily affects children and adults of an average age of 15 years. Ewing tumors can metastasize the lungs and other bones. Among cartilage-producing bone tumors of malignant nature is chondrosarcoma. Its incidence is one in 200,000 persons means that it is the least common bone tumor [5]. It mostly occurs in the central skeleton, arising from the pelvic girdle, vertebrae, and proximal long bones [6]. The symptoms of bone cancer are pain in bones which are immovable and inflammation in the affected area. These symptoms are mainly due to pressure effects on near nerves or organs. The treatment modality is based on the type and stage of bone cancer, its spread, and the patient's health and age. Treatment options are available surgery, chemotherapy, radiation, or a combination. In Chemotherapy, we use antimetabolites that kill cancer cells. They work by decreasing or inhibiting cancer cells which are growing and dividing quickly. However, these drugs also had adverse effects on normal cells. Such as disrupting mucosa of GIT and hair loss. In chemotherapy, some drugs work to kill cancer cells some work by slowing their divisions and some prevent them from spreading in nearby areas. Some of these drugs include vincristine sulfate, doxorubicin hydrochloride, cyclophosphamide, ifosfamide, and etoposide. Some bone tumors can also be treated by using drugs affecting normal cells of bones (osteoblasts and osteoclasts). These are mainly used for primary bone cancer, but we can also use these drugs for bone cancers that are spread.

Drug discovery passes from various steps i.e., identification of cases, synthesis, characterization, validation, optimization, screening, and assays for therapeutic efficacy. These steps aim to identify a compound that is either therapeutically useful in curing and treating diseases or not. In the development of new drugs used for treating diseases drug discovery is also important as it allows researcher and identify new targets for drugs and to develop new drugs that are more effective therapeutically and has fewer complications. Now researchers are using the QSPR approach to predict drug properties [7]. A design tool known as QSRP shows a clear connection between molecular physicochemical properties and their biological effects on medication responsiveness. Topological indices are numerical parameters of a graph that characterize its topology and are usually graph invariant. Topological indices are used for example in the development of quantitative structure-activity relationships (QSARs) in which the biological activity or other

properties of molecules are correlated with their chemical structure [8]. Degree-based topological indices of various chemical graphs are being studied by many researchers [26, 27, 28, 29, 30, 31, 32, 34, 35, 36]. S, Zamen provided structural modelling of dendrimers and some Networks in [37]. The researcher can read more about QSPR analysis on cancer diseases [17, 18, 19, 20, 21] and various drugs and diseases [22, 23, 24, 25]. The majority of the researchers investigated these features because of their effect on bioactivities and drug transportation in human tissue. In this research paper, we are computing therapeutic indices for drugs used in bone cancer treatment. This paper investigates nine anticancer drugs, Zoledronic , Ifosfamide, Gemcitabine, Methotrexate, Doxorubicine , Cisplatin, Sunitinib, Regorafenib, and Etoposide, that are secure and reliable remedies for the community heath. Figure 14.1 displays the chemical structure of these medicines.

14.2 Material and Methods

In drug structure Elements are represented as vertices, and the interconnected bonds of these atoms are represented by edges. Let G(V, E) be represented as a graph of drug structure, V represents a vertex set, while E represents an edge set of chemical graphs. The vertex degree of a graph G is represented by du and is the number of vertices adjacent to u. Degree-based topological indices which are used for our calculation are given below.

Definition 10: Randic's index [9] was established by Milan Randič and is stated as

$$\chi(G) = \sum_{uv \in E} \frac{1}{\sqrt{d_u d_v}}.$$

Definition 11: Estrada et al. in [10] proposed a degree-based topology index ABC and defined as.

$$ABC(G) = \sum_{uv \epsilon G} \sqrt{\frac{d_u + d_v + 2}{d_u d_v}}.$$

Definition 12: The Sum Connectivity index introduces by Zhou and Trinjstic [11] defined as

$$SCI(G) = \sum_{uv \in E} \frac{1}{\sqrt{d_u + d_v}}.$$

Definition 13: The GA index is designed by Vukicevic et al. [12] as

$$GA(G) = \sum_{uv \in E} \frac{2\sqrt{d_u d_v}}{d_u + d_v}.$$

Definition 14: First and the Second Zagreb indices are designed by Trinajestic and Gutman [13],

defiened as

$$M_1(G) = \sum_{uv \in E} [d_u + d_v],$$

$$M_2(G) = \sum_{uv \in E} [d_u d_v].$$

Definition 15: Harmonic index is designed by Fajtlowicz in [14] as

$$H(G) = \sum_{uv \in E} \frac{2}{[d_u + d_v]}.$$

Definition 16: The Hyper Zagreb index was proposed by Shirdel et al. [15] as,

$$HM\left(C[G\,]\right) = \sum_{uv \in E} \left(d_u + d_v\right)^2.$$

Definition 17: Forgotten topological index defined by Furtula et al. in [16] as,

$$F(G) = \sum_{uv \in E} \left({d_u}^2 + {d_v}^2\right).$$

Physical property values are obtained from Chemspider. The data in Table. 14.2 shows that they are normally distributed. The topological indices for chemical structures shown in Fig. **??**, are stated in Table. 14.1. As a result, the linear regression model is best to examine and use in this analysis. Fig. 14.1 depicts the association between topological indices and drugs.

The molecular formula related to Doxorubicine is $C_{27}H_{29}NO_{11}$. It is a chemotherapeutic medication used for cancer therapy. Doxorubicin is utilized to treat Hodgkin's lymphoma and leukemias, along with cancers or other origins bladder, stomach, breast, ovaries, lung, soft tissue, thyroid, sarcoma, and multiple myeloma. The Chemical formula related to Ifosfamide is $C_7H_{15}C_{12}N_2O_2P$. it is utilized for the therapy of Breast testicular cancer and some Lymphoma (Hodgkin and non-Hodgkin), bone tumor, soft tissue sarcoma, female reproductive cancer, and Lung cancer. The molecular formula related to Gemcitabine is $C_9H_{11}F_2N_3O_4$. Gemcitabine is used to treat different carcinomas. It is commonly used to treat cholangiocarcinoma and some other kinds of biliary tract cancers. It is given by intravenous intake at a chemotherapy clinic. The molecular formula related to Etoposide is $C_{29}H_{32}O_{13}$. It is utilized as a chemotherapy format for cancers such as Ewing's sarcoma, Kaposi's sarcoma, testicular cancer, lung cancer, glioblastoma multiforme, lymphoma and nonlymphocytic leukaemia. Etoposide is often used in a conditioning regimen before a blood stem cell or bone marrow transplant. Methotrexate has its molecular formula as $C_{20}H_{22}N_8O_5$. Methotrexate is being used for the therapy of several cancers. The molecular formula related to Cisplatin is $[Pt(NH_3)2Cl_2]$. It is being used to cure various types of cancers, including

bladder cancer, sarcomas, some carcinomas lymphomas, germ cell tumors, and cervical cancer. Zoledronic has its molecular formula $C_5H_{10}C_{12}N_2O_7P_2$. Zoledronic acid is being used to control bone fractures in patients with cancers such as multiple myeloma prostate cancer and osteoporosis. It is also used to treat hypercalcemia and can be useful for treating aches from bone metastases. The molecular formula related to Sunitinib is $C_{22}H_{27}FN_4O_2$. Sunitinib is being used in Meningioma, Gastrointestinal stromal tumors, Renal cell carcinoma, and Pancreatic neuroendocrine tumors. Regorafenib has its molecular formula as $C_{21}H_{15}ClF_4N_4O_3$. Regorafenib is being used for the treatment of advanced gastrointestinal stromal tumors, colorectal cancer and in hepatocellular carcinoma which were treated before with sorafenib.

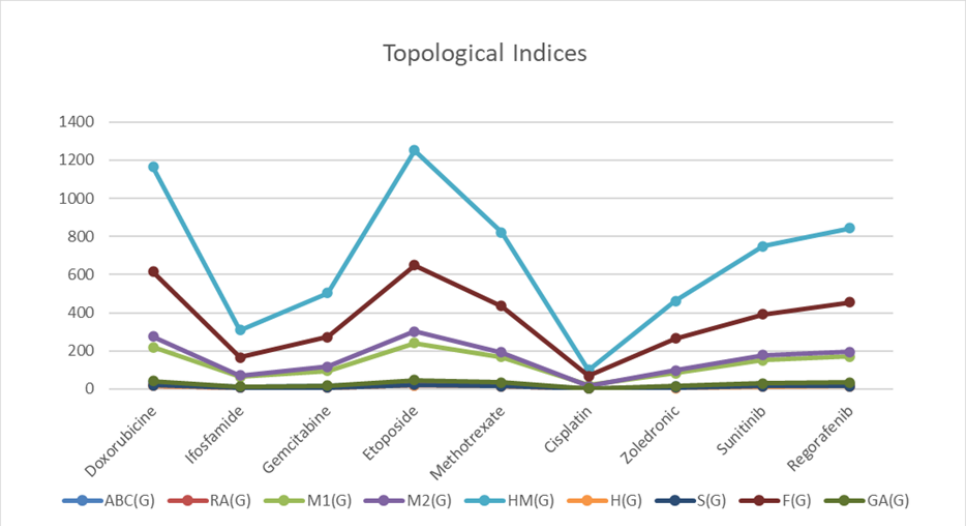

Figure 14.1: 2D graph of TIs with drugs

Name of Drug	ABC(G)	RA(G)	M_1(G)	M_2(G)	HM(G)	H(G)	SCI(G)	F(G)
Doxorubicine	30.772	18.427	220	275	1164	17.485	19.286	614
Ifosfamide	9.996	6.7265	64	72	310	6.4857	6.6908	166
Gemcitabine	13.836	8.3743	96	116	504	7.8381	8.5829	272
Etoposide	33.882	20.283	242	302	1252	19.634	21.617	648
Methotrexate	25.422	15.634	168	193	822	14.867	16.091	436
Cisplatin	3.464	2	20	16	100	1.6	1.7888	68
Zoledronic	12.236	7.0783	84	98	462	6.334	7.0875	266
Sunitinib	22.184	13.849	150	178	748	13.267	14.274	392
Regorafenib	25.480	15.562	170	195	844	14.753	16.018	454

Table 14.1: Topological indices associated to the bone-cancer drugs.

Name of Drug	Boiling Point	Refractive index	Flash point	Molar volume	complexity	Enthalpy	Molar refractivity
Doxorubicin	810.3	1.710	443.8	336.6	977	123.5	131.5
Ifosfamide	336.1	1.506	157.1	195.7	218	57.9	58.1
Gemcitabine	482.7	1.652	245.7	142.3	426	86.2	52.1
Etoposide	798.1	1.662	263.6	378.5	969	121.7	140.1
Methotrexate	823	1.738	-	295.7	704	-	119.0
Cisplatin	270	-	-	-	7.6	-	-
Zoledronic	764.0	1.719	415.8	127.4	327	116.7	50.3
Sunitinib	572.1	1.611	299.8	324.1	636	85.8	112.5
Regorafenib	513.4	1.616	264.3	323.7	686	78.5	113.1

Table 14.2: Physical properties related to drugs used for the treatment of Bone Cancer.

14.3 Regression Models and Calculation of Statistical Parameters

Seven physical characteristics of the nine medications being used to treat bone cancer are modelled using the nine topological indices previously described. The following is the value of the physical properties of different drugs used to treat bone cancer. For defined degree-based topological indices and physiochemical properties, the linear regression model is formulated as.

$$P = A + b(TI) \tag{14.1}$$

Where P indicates the physicochemical property of the drug, A is denoted by a constant, b is a regression coefficient, and TI is a topological index. Constant A and regression coefficient b are calculated from SPSS [31] software for seven physical properties and nine topological indices of the molecular structure of 9 drugs. In this part, the QSPR model is utilized to determine a relationship between the physical properties and the calculation of statistical parameters for anti-bone cancer medications. Topological indices are taken as independent variables with b, r, and N as dependent variables represented as regression model constants, correlation coefficients, and sample size, respectively. Tables 14.3, 14.4, 14.5, 14.6, 14.7, 14.8, 14.9, 14.10, 14.11 include the statistical parameters of the linear regression model of topological indices.

14.3.1 Regression models for the Atom Bond Connectivity index.

Boiling Point = 349.278 + 13.264 [ABC(G)]

Refractive index = 1.577 + .003 [ABC(G)]

Flash Point = 229.842 + 3.243 [ABC(G)]

Molar volume = 48.208 + 10.001 [ABC(G)]

Complexity = -59.350 + 31.171 [ABC(G)]

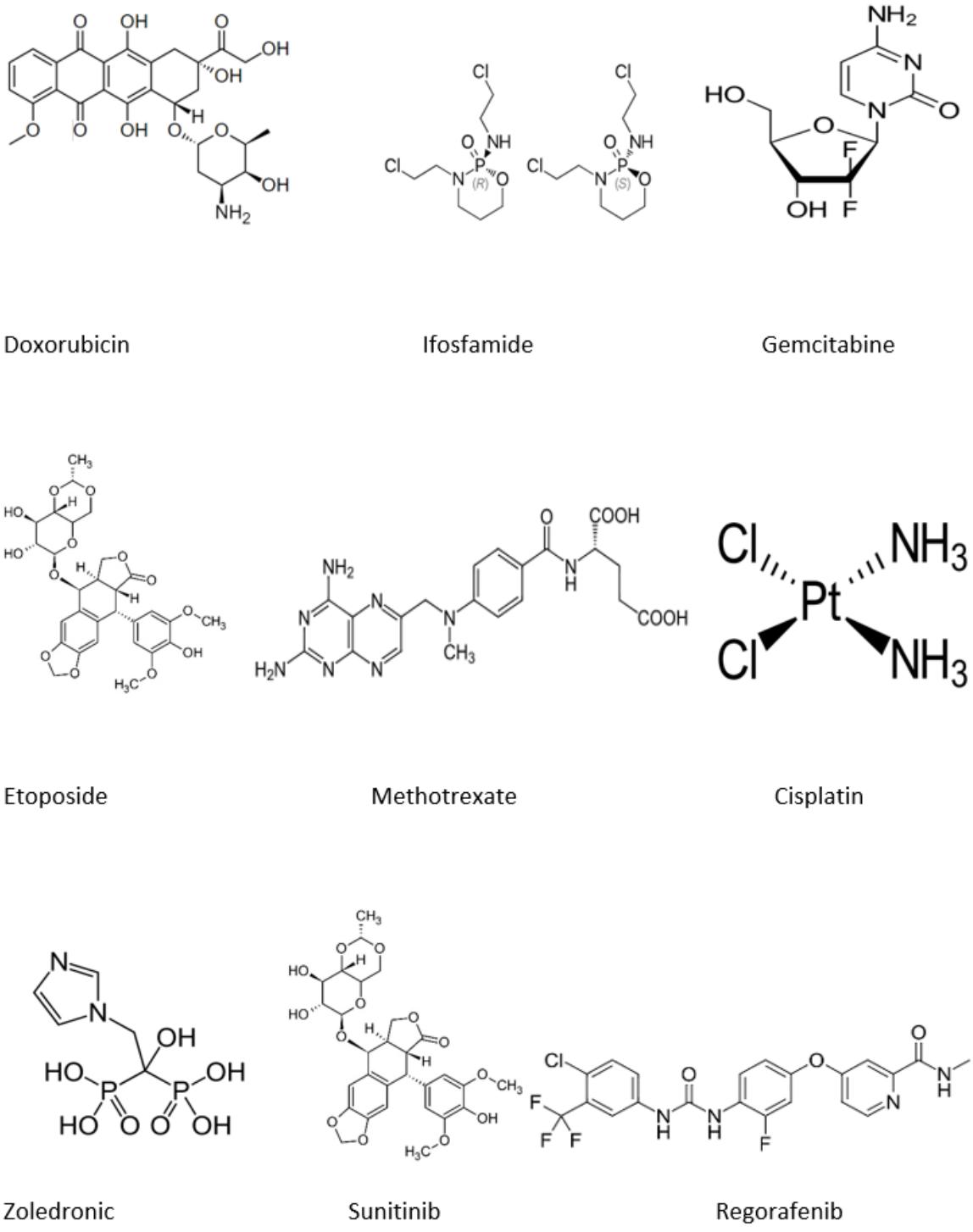

Figure 14.2: Drugs with their Molecular structure.

Enthalpy = 63.164 + 1.538 [ABC(G)]

Molar refractivity = 8.244 + 4.089 [ABC(G)]

Physiochemical property	N	A	b	r	r^2	F	P
Boiling point	8	349.278	13.264	.633	.400	4.007	.092
Refractive index	8	1.577	.003	.405	.164	1.177	.320
Flash point	7	229.842	3.243	.305	.093	.514	.506
Molar Volume	8	48.208	10.001	.920	.847	33.107	.001
Complexity	8	-59.350	31.171	.987	.974	226.382	.000
Enthalpy	7	63.164	1.538	.575	.331	2.469	.177
Molar Refractivity	8	8.244	4.089	.969	.940	93.458	.000

Table 14.3: Statistical parameters for the linear QSPR model for topological index ABC(G).

14.3.2 Regression models for Randic index RA(G)

Boiling Point = 356.146 + 21.244 [RA(G)]

Refractive index = 1.582 + .005 [RA(G)]

Flash Point = 237.069 + 4.769 [RA(G)]

Molar volume = 37.104 + 17.248 [RA(G)]

Complexity = -74.428 + 52.281 [RA(G)]

Enthalpy = 64.849 + 2.396 [RA(G)]

Molar refractivity = 4.594 + 6.985 [RA(G)]

Physiochemical property	N	A	b	r	r^2	F	P
Boiling point	8	356.146	21.244	.600	.360	3.380	.116
Refractive index	8	1.582	.005	.365	.133	.921	.374
Flash point	7	237.069	4.769	.265	.070	.378	.566
Molar Volume	8	37.104	17.248	.940	.883	45.474	.001
Complexity	8	-74.428	52.281	.981	.962	150.181	.000
Enthalpy	7	64.849	2.396	.529	.280	1.945	.222
Molar Refractivity	8	4.594	6.985	.981	.962	151.836	.000

Table 14.4: Statistical parameters for the linear QSPR model for topological index RA(G)

14.3.3 Regression models for first Zagreb index M1(G)

Boiling Point = 358.919 + 1.866 [M1(G)]

Refractive index = 1.579 + .000 [M1(G)]

Flash Point = 228.541 + .478 [M1(G)]

Molar volume = 63.824 + 1.351 [M1(G)]

Complexity = -27.387 + 4.323 [M1(G)]

Enthalpy = 62.807 + .225 [M1(G)]

Molar refractivity = 14.286 + .555 [M1(G)]

Physiochemical property	N	A	b	r	r^2	F	P
Boiling point	8	358.919	1.866	.645	.416	4.279	.084
Refractive index	8	1.579	.000	.413	.171	1.233	.309
Flash point	7	228.541	.478	.328	.108	.604	.472
Molar Volume	8	63.824	1.351	.901	.812	25.857	.002
Complexity	8	-27.387	4.323	.992	.984	376.580	.000
Enthalpy	7	62.807	.225	.614	.377	3.023	.143
Molar Refractivity	8	14.286	.555	.953	.908	59.523	.000

Table 14.5: Statistical parameters for the linear QSPR model for topological index M1(G)

14.3.4 Regression models for the second Zagreb index M2(G)

Boiling Point = 374.829 + 1.470 [M2(G)]

Refractive index = 1.584 + .000 [M2(G)]

Flash Point = 230.051 + .388 [M2(G)]

Molar volume = 80.534 + 1.035 [M2(G)]

Complexity = 13.072 + 3.386 [M2(G)]

Enthalpy = 63.339 + .184 [M2(G)]

Molar refractivity = 20.952 + .426 [M2(G)]

Physiochemical property	N	A	b	r	r^2	F	P
Boling point	8	374.829	1.470	.648	.420	4.352	.082
Refractive index	8	1.584	.000	.410	.168	1.213	.313
Flash point	7	230.051	.388	.342	.117	.661	.453
Molar Volume	8	80.534	1.035	.881	.775	20.720	.004
Complexity	8	13.072	3.386	.991	.982	330.921	.000
Enthalpy	7	63.339	.184	.642	.413	3.511	.120
Molar Refractivity	8	20.952	.426	.934	.872	41.006	.001

Table 14.6: Statistical parameters for the linear QSPR model for topological index M1(G)

14.3.5 Regression models for hyper Zagreb index HM(G)

Boiling Point = 352.877 + .373 [HM(G)]

Refractive index = 1.576 + (9.946E-5) [HM(G)]

Flash Point = 219.250 + .105 [HM(G)]

Molar volume = 73.491 + .252 [HM(G)]

Complexity = -18.361 + .834 [HM(G)]

Enthalpy = 60.540 + .047 [HM(G)]

Molar refractivity = 17.525 + .104 [HM(G)]

Physiochemical property	N	A	b	r	r^2	F	P
BP	8	352.877	.373	.668	.447	4.846	.070
Refractive index	8	1.576	9.946E-5	.439	.193	1.434	.276
FP	7	219.250	.105	.376	.141	.824	.406
Molar Volume	8	73.491	.252	.870	.756	18.633	.005
Complexity	8	-18.361	.834	.992	.984	366.980	.000
Enthalpy	7	60.540	.047	.664	.440	3.932	.104
Molar Refractivity	8	17.525	.104	.929	.862	37.592	.001

Table 14.7: {Statistical parameters for the linear QSPR model for topological index HM(G)

14.3.6 Regression models for Harmonic index H(G)

Boiling Point = 371.141 + 21.166 [H(G)]

Refractive index = 1.589 + .005 [HM(G)]

Flash Point = 245.049 + 4.368 [HM(G)]

Molar volume=41.630 + 17.792 [HM(G)]

Complexity = -53.607 + 53.365 [HM(G)]

Enthalpy = 66.663 + 2.374 [HM(G)]

Molar refractivity = 6.896 + 7.168 [HM(G)]

14.3.7 Regression models for sum Connectivity index SCI(G)

Boiling Point = 367.232 + 19.716 [SCI(G)]

Refractive index = 1.586 + .005 [SCI(G)]

Flash Point = 240.750 + 4.327 [SCI(G)]

Physiochemical property	N	A	b	r	r^2	F	P
Boiling point	8	371.141	21.166	.584	.341	3.099	.129
Refractive index	8	1.589	.005	.340	.116	.786	.409
Flash point	7	245.049	4.368	.237	.056	.298	.609
Molar Volume	8	41.630	17.792	.946	.895	51.168	.000
Complexity	8	-53.607	53.365	.977	.954	124.254	.000
Enthalpy	7	66.663	2.374	.512	.262	1.776	.240
Molar Refractivity	8	6.896	7.168	.982	.965	163.278	.000

Table 14.8: Statistical parameters for the linear QSPR model for topological index H(G)

Molar volume = 47.680 + 15.892 [SCI(G)]

Complexity = -46.102 + 48.444 [SCI(G)]

Enthalpy = 65.669 + 2.251 [SCI(G)]

Molar Refractivity = 8.871 + 6.436 [SCI(G)]

Physiochemical property	N	A	b	r	r^2	F	P
Boiling point	8	367.232	19.716	.602	.363	3.413	.114
Refractive index	8	1.586	.005	.363	.132	.910	.377
Flash point	7	240.750	4.327	.261	.068	.364	.572
Molar Volume	8	47.680	15.892	.936	.876	42.412	.001
Complexity	8	-46.102	48.444	.982	.964	162.391	.000
Enthalpy	7	65.669	2.251	.539	.290	2.045	.212
Molar Refractivity	8	8.871	6.436	.977	.954	124.675	.000

Table 14.9: Statistical parameters for the linear QSPR model for topological index SCI(G)

14.3.8 Regression models for forgotten index F(G)

Boiling Point = 332.127 + .752 [F(G)]

Refractive index = 1.568 + .000 [F(G)]

Flash Point = 208.495 + .224 [F(G)]

Molar volume = 67.734 + .487 [F(G)]

Complexity = -46.029 + 1.635 [F(G)]

Enthalpy = 57.886 + .094 [F(G)]

Molar refractivity = 14.599 + .203 [F(G)]

Physiochemical property	N	A	b	r	r^2	F	P
Boiling point	8	332.127	.752	.686	.471	5.346	.060
Refractive index	8	1.568	.000	.466	.218	1.668	.244
Flash point	7	208.495	.224	.409	.167	1.002	.363
Molar Volume	8	67.734	.487	.857	.735	16.650	.006
Complexity	8	-46.029	1.635	**.991**	.981	316.792	.000
Enthalpy	7	57.886	.094	.683	.466	4.362	.091
Molar Refractivity	8	14.599	.203	.921	.849	33.770	.001

Table 14.10: Statistical parameters for the linear QSPR model for topological index F(G)

14.3.9 Regression models for Arithmetic-geometric index GA(G)

Boiling Point = 376.743 + 9.033 [GA(G)]

Refractive index = 1.588 + .002 [GA(G)]

Flash Point = 242.979 + 1.972 [GA(G)]

Molar volume = 57.548 + 7.205 [GA(G)]

Complexity = -21.014 + 22.135 [GA(G)]

Enthalpy = 66.247 + 1.047 [GA(G)]

Molar refractivity = 12.813 + 2.920 [GA(G)]

Physiochemical property	N	A	b	r	r^2	F	P
Boiling point	8	376.743	9.033	.605	.366	3.462	.112
Refractive index	8	1.588	.002	.363	.131	.908	.377
Flash point	7	242.979	1.972	.261	.068	.366	.571
Molar Volume	8	57.548	7.205	.930	.866	38.660	.001
Complexity	8	-21.014	22.135	**.**984	.968	181.381	.000
Enthalpy	7	66.247	1.047	.551	.304	2.179	.200
Molar Refractivity	8	12.813	2.920	.972	.944	101.093	.000

Table 14.11: Statistical parameters for the linear QSPR model for topological index GA(G)

Table 14.2 lists the physicochemical properties associated with nine anti-bone-cancer drugs. On the other hand, the TI (Topological index) values reported in Table 14.1 are derived from their molecular structure. A standard error of estimate is the measure of variation for an observation calculated around the computed regression line is assesses the degree of correctness of predictions computed around the regression line as shown in Table 14.12. Table 14.13 shows the correlation coefficients between physicochemical properties and TIs. Figure 14.3 depicts a graph of the correlation coefficient of anti-bone cancer drugs. Figure 14.3 depicts the correlation of topological indices to the properties under stydy.

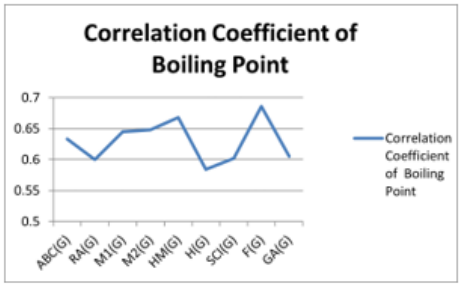

(a) Boiling point on TI

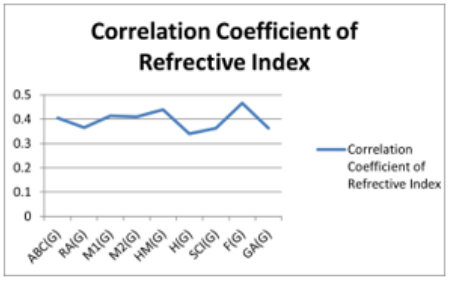

(b) Refractive index on TI

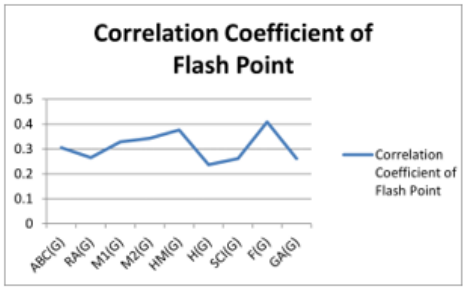

(c) Flash point on TI

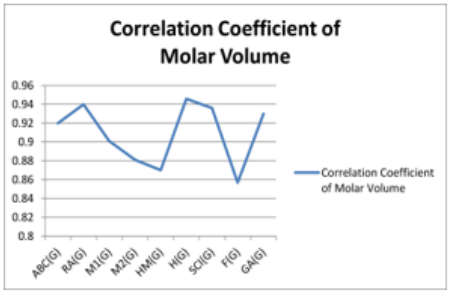

(d) Molar volume on TI

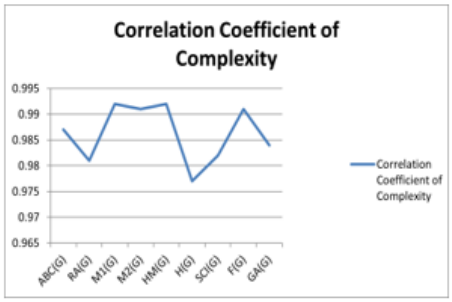

(e) Complexity on TI

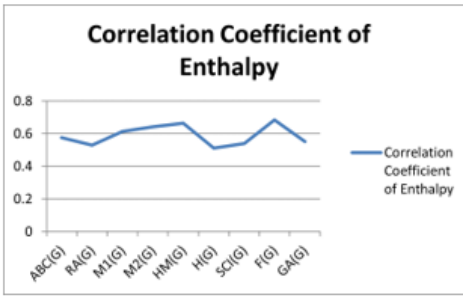

(f) Enthalpy on TI

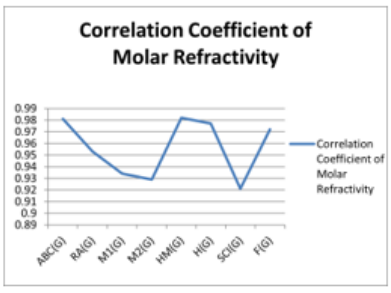

(g) Molar Refractivity on TI

Figure 14.3: Correlation coefficient graphs of physiochemical properties with topological indices.

Topological Index	Boiling point	Refractive index	Flash Point Molar Volume	Complexity	Enthalpy	Molar refractivity	P
ABC(G)	155.045	.0743	104.355	40.668	48.471	22.564	9.896
RA(G)	160.135	.0756	105.663	35.447	59.125	23.399	7.856
SCI(G)	159.862	.0757	105.795	36.552	56.941	23.232	8.634
GA(G)	159.446	.0757	105.777	38.055	53.978	23.015	9.537
M1(G)	152.973	.0740	103.506	45.059	37.776	21.777	12.193
M2(G)	152.439	.0741	102.986	49.199	40.255	21.137	14.396
F(G)	145.609	.0719	100.016	53.437	41.126	20.154	15.651
H(G)	162.593	.0764	106.458	33.636	64.743	23.689	7.5859
HM(G)	148.924	.0730	101.535	51.242	38.259	20.633	14.948

Table 14.12: Std. error of the estimate for physical properties of the drugs.

Topological index	Correlation coefficient of Boiling Point	Correlation coefficient of Refractive index	Correlation coefficient of Flash point	Correlation coefficient of Molar Volume	Correlation coefficient of complexity	Correlation coefficient of Enthalpy	Correlation coefficient of Molar refractivity
ABC(G)	.633	.405	.305	.920	.987	.575	.969
RA(G)	.600	.365	.265	.940	.981	.529	.981
M1(G)	.645	.413	.328	.901	.992	.614	.953
M2(G)	.648	.410	.342	.881	.991	.642	.934
HM(G)	.668	.439	.376	.870	.992	.664	.929
H(G)	.584	.340	.237	.946	.977	.512	.982
SCI(G)	.602	.363	.261	.936	.982	.539	.977
F(G)	.686	.466	.409	.857	.991	.683	.921
GA(G)	.605	.363	.261	.930	.984	.551	.972

Table 14.13: Correlation coefficients between physicochemical properties and Tis.

14.4 Conclusions

In this research, we constructed a QSPR model for bone cancer medications using topological indices generated from medicinal chemical structures. The QSPR prediction model identified a link between the chosen topological indices and the drug's physical properties. According to the statistical and topological index used in the linear QSPR model, ABC index, Randic index, first Zagreb index, second Zagreb index, hyper Zagreb index, harmonic index, sum Connectivity, forgetting index and arithmetic geometry index give the highest correlation values for complexity are r = 0.987, 0.981, 0.992, 0.991, 0.992, 0.977, 0.982, 0.991, and 0.984, respectively. The Randic index defines the highest correlation value for a molar refractivity of r = 0.981. Topological indices of drug chemistry were calculated and correlated with linear QSPR models of drugs used to treat bone cancer. The results thus obtained provide a cost-effective and theoretical basis for the development of new drugs with similar patterns for effective and therapeutic results. Correlation coefficients of regression models can be useful in examining the properties of newly

developed drugs. The results presented in the paper may be useful to researchers in drug research and may help influence the phsico-chemical properties of new drugs designed to treat other specific diseases.

Bibliography

[1] Cokkinides, V., Albano, J., Samuels, A., Ward, M., & Thum, J. (2005). American cancer society: Cancer facts and figures. *Atlanta: American Cancer Society*, 2017.

[2] Board, P. P. T. E. (2021). Ewing Sarcoma Treatment (PDQ®). In PDQ Cancer Information Summaries [Internet]. *National Cancer Institute (US)*.

[3] Marina N. Malignant bone tumors. In: Lanzkowsky P, ed. Manual of Pediatric Hematology and Oncology. 5th ed. London, UK: Academic Press; 2010:739–757.

[4] Rajwanshi, A., Srinivas, R., & Upasana, G. (2009). Malignant small round cell tumors. *Journal of Cytology/Indian Academy of Cytologists*, 26(1), 1.

[5] Giuffrida, A. Y., Burgueno, J. E., Koniaris, L. G., Gutierrez, J. C., Duncan, R., & Scully, S. P. (2009). Chondrosarcoma in the United States (1973 to 2003): an analysis of 2890 cases from the SEER database. *JBJS*, 91(5), 1063-1072.

[6] Wold, L. E., Adler, C. P., Sim, F. H., & Unni, K. K. (2003). Atlas of orthopedic pathology. WB Saunders Company.

[7] Deore, A. B., Dhumane, J. R., Wagh, R., & Sonawane, R. (2019). The stages of drug discovery and development process. *Asian Journal of Pharmaceutical Research and Development*, 7(6), 62-67.

[8] Kier, L. (2012). Molecular connectivity in chemistry and drug research (Vol. 14). *Elsevier*.

[9] M. Randic, "Characterization of molecular branching," *Journal of the American Chemical Society*, vol. 97, no. 23, pp. 6609–6615, 1975.

[10] E. Estrada, L. Torres, L. Rodriguez, and I. Gutman, "An atombond connectivity index: modelling the enthalpy of formation of alkanes," *Indian Journal of Chemistry*, vol. 37A, 1998.

[11] B. Zhou and N. Trinajstic, "On general sum-connectivity ´ index," *Journal of Mathematical Chemistry*, vol. 47, no. 1, pp. 210–218, 2010.

[12] D. Vukicevi ˇ c and B. Furtula, "Topological index based on the ´ ratios of geometrical and arithmetical means of end-vertex degrees of edges," *Journal of Mathematical Chemistry*, vol. 46, no. 4, pp. 1369–1376, 2009.

[13] I. Gutman, "Degree-based topological indices," *Croatica Chemica Acta*, vol. 86, no. 4, pp. 351–361, 2013.

[14] Fajtlowicz, S. (1987). On conjectures of Graffiti-II. *Congr. Numer*, 60, 187-197.

[15] G. H. Shirdel, H. Rezapour, and A. M. Sayadi, ",e hyperzagreb index of graph operations," *Iranian Journal of Mathematical Chemistry*, vol. 4, 2013.

[16] B. Furtula and I. Gutman, "A forgotten topological index," *Journal of Mathematical Chemistry*, vol. 53, no. 4, pp. 1184– 1190, 2015.

[17] Jahanbani, A., Shao, Z., & Sheikholeslami, S. M. (2021). Calculating degree based multiplicative topological indices of Hyaluronic Acid-Paclitaxel conjugates' molecular structure in cancer treatment. *Journal of Biomolecular Structure and Dynamics*, 39(14), 5304-5313.

[18] Shanmukha, M. C., Usha, A., Praveen, B. M., & Douhadji, A. (2022). Degree-Based Molecular Descriptors and QSPR Analysis of Breast Cancer Drugs. *Journal of Mathematics*, 2022.

[19] Shanmukha, M. C., Basavarajappa, N. S., Shilpa, K. C., & Usha, A. (2020). Degree-based topological indices on anticancer drugs with QSPR analysis. *Heliyon*, 6(6), e04235.

[20] Nasir, S., Farooq, F. B., & Parveen, S. (2022). Topological indices of novel drugs used in blood cancer treatment and its QSPR modeling. *AIMS Mathematics*, 7(7), 11829-11850

[21] Zheng, L., Wang, Y., & Gao, W. (2019). Topological indices of hyaluronic acid-paclitaxel conjugates' molecular structure in cancer treatment. *Open Chemistry*, 17(1), 81-87.

[22] Kirmani, S. A. K., Ali, P., Azam, F., Kuznetsov, A. E., & Alvi, P. A. (2022). Structure and electronic properties of the HA-CUR conjugate: an insight from the DFT perspective. *Computational and Theoretical Chemistry*, 113761.

[23] Mondal, S., De, N., & Pal, A. (2022). Topological indices of some chemical structures applied for the treatment of COVID-19 patients. *Polycyclic Aromatic Compounds*, 42(4), 1220-1234.

[24] Adnan, M., Bokhary, S. A. U. H., Abbas, G., & Iqbal, T. (2022). Degree-based topological indices and QSPR analysis of antituberculosis drugs. *Journal of Chemistry*, 2022.

[25] Kumar, K. A., Basavarajappa, N. S., & Shanmukha, M. C. (2020). QSPR analysis of Alkanes with certain degree based topological indices. *Malaya Journal of Mathematik*, 8, 314-330.

[26] Jagadeesh, R.; Kanna, M.R.; Indumathi, R.S. Some results on topological indices of graphene. Nanomater. Nanotechnol. 2016, 6.

[27] Chen, S.; Jang, Q.; Hou, Y. The Wiener and Schultz index of nanotubes covered by C4. Match Commun. Math. Comput. Chem. 2008, 59, 429–435.

[28] Hayat,S.;Imran,M.Computation of certain topological indices of nano tubes covered by C5 and C7. J.Comput. Theor. Nanosci. 2015, 12, 533–541.

[29] Aslam, A.; Ahmad, S.; Gao, W. On certain topological indices of boron triangular nanotubes. *Z. Nat.* A 2017, 72, 711–716.

[30] Idrees, N.; Saif, M.J.; Sadiq, A.; Rauf, A.; Hussain, F. Topological indices of H-naphtalenic nanosheet. *Open Chem.* 2018, 16, 1184–1188.

[31] IBM Corp. Released. IBM SPSS Statistics for Windows, Version 24.0 (Armonk, NY: IBM Corp., 2016).

[32] Zhou, H., Mahboob, A., Rasheed, M. W., Ovais, A., Siddiqui, M. K., & Cheema, I. Z. (2023). On QSPR Analysis of Molecular Descriptor and Thermodynamic Features of Narcotic Drugs. *Polycyclic Aromatic Compounds*, 1-21.

[33] Rasheed, M. W., Mahboob, A., & Hanif, I. (2023). An estimation of physicochemical properties of heart attack treatment medicines by using molecular descriptor's. *South African Journal of Chemical Engineering*, 45, 20-29.

[34] Mahboob, A., Rasheed, M. W., Amin, L., & Hanif, I. (2023). A study of novel molecular descriptors and quantitative structure–property relationship analysis of blood cancer drugs. *The European Physical Journal Plus*, 138(9), 856.

[35] Mahboob, A., Waheed Rasheed, M., Hanif, I., & Siddique, I. (2024). Approximating the properties of some chemical solvents by two-dimensional molecular descriptors. *International Journal of Quantum Chemistry*, 124(1), e27305.

[36] Huang, R., Mahboob, A., Rasheed, M. W., Alam, S. M., & Siddiqui, M. K. (2023). On molecular modeling and QSPR analysis of lyme disease medicines via topological indices. *The European Physical Journal Plus*, 138(3), 243.

[37] Zaman, S., Ullah, A., & Shafaqat, A. (2023). Structural modeling and topological characterization of three kinds of dendrimer networks. *The European Physical Journal E*, 46(5), 36.

CHAPTER 15

Strongly Starlikeness and Strongly Convexity of q-Bessel function

Mohsan Raza [†], **and Muhammad Ahsan Binyamin** [†]

[†] *Department of Mathematics, Government College University Faisalabad, Pakistan.*

Corresponding Author: Muhammad Ahsan Binyamin: ahsanbanyamin@gmail.com

Abstract: *The main objective of this research is to examine a specific sufficiency criterion for strongly starlikeness, strongly convexity for q-Bessel functions. In particular, we provide sufficient conditions for Jackson's second and third q-Bessel functions to be strongly starlike and strongly convex functions of order* κ.

Keywords: q-Bessel functions; Jackson q Bessel functions, strongly starlike functions, strongly convex functions

15.1 Introduction

Bessel functions are used in physics to solve problems with cylindrical or circular symmetry, such as wave motion, heat conduction, and vibrations. In applied mathematics and engineering disciplines, Bessel functions of the first kind are frequently utilized. Many publications and scientific investigations have examined the properties of Bessel functions. It is particular solution of the differential equation

$$z^2w''(z) + zw'(z) + (z^2 - p^2)w(z) = 0.$$

The series form representtion of this function is given by

$$\mathcal{J}_p(z) = \sum_{n=0}^{\infty} \frac{(-1)^n \left(\frac{z}{2}\right)^{2n+p}}{n!\Gamma(n+p+1)}. \tag{15.1}$$

The symbol Γ represents the Euler gamma function. For detailed information about this function, we refer [15]. The modified Bessel function of the first kind which is denoted by $\mathcal{I}_p$ is the solution of the equation

$$z^2w''(z) + zw'(z) - (z^2 + p^2)w(z) = 0.$$

Its series representation is given by

$$\mathcal{I}_p(z) = \sum_{n=0}^{\infty} \frac{\left(\frac{z}{2}\right)^{2n+p}}{n!\Gamma(n+p+1)}. \tag{15.2}$$

Another crucial aspect is the inherent generalizations of the Bessel functions. The Bessel functions have various generalizations. However, the literature has a few q-analogues of the Bessel functions. Jackson's q-Bessel functions were defined by the renowned English mathematician Frank Hilton Jackson at the start of the 19th century, using the q-calculus. The Jackson's second and third q-Bessel functions are defined as

$$\mathcal{J}_p^{(2)}(z;q) = \frac{\left(q^{p+1};q\right)_\infty}{(q;q)_\infty} \sum_{n=0}^{\infty} \frac{(-1)^n \left(\frac{z}{2}\right)^{2n+p}}{n!\,(q;q)_n \left(q^{p+1};q\right)_n} q^{n(n+p)}, \tag{15.3}$$

and

$$\mathcal{J}_p^{(3)}(z;q) = \frac{\left(q^{p+1};q\right)_\infty}{(q;q)_\infty} \sum_{n=0}^{\infty} \frac{(-1)^n (z)^{2n+p}}{n!\,(q;q)_n \left(q^{p+1};q\right)_n} q^{\frac{n}{2}(n+p)}, \tag{15.4}$$

where $z \in \mathbb{C}, p > -1,\ q \in (0,1)$ and

$$(a;q)_0 = 1, \quad (a;q)_n = \prod_{m=1}^{n} \left(1 - aq^{m-1}\right), \quad (a;q)_\infty = \prod_{m=1}^{\infty} \left(1 - aq^{m-1}\right).$$

For details, see [4, 10, 12, 13, 14]. The Jackson's third q-Bessel function $\mathcal{J}_p^{(3)}$ is also known as the Hahn-Exton q-Bessel function because of their contributions to the theory of q-Bessel functions. It can also be seen that these q-analogues satisfy the following limit relations:

$$\lim_{q\to 1^-} \mathcal{J}_p^{(2)}((1-q)z;q) = \mathcal{J}_p(z), \quad \lim_{q\to 1^-} \mathcal{J}_p^{(3)}p((1-q)z;q) = \mathcal{J}_p(2z).$$

The geometric properties of Jackson's second and third q-Bessel functions can be found in [1, 2, 3] and the references therein.

Because of its strong ties to mathematical physics, differential equations, and complex analysis, the theory of univalent functions has long been a key subject in geometric function theory. It is a study of analytic functions $f$such that $f(0) = f'(0) - 1 = 0$ in $\mathbb{D} = \{z \in \mathbb{C} : |z| < 1\}$. The class of such functions is denoted by $\mathcal{A}$. The Maclaurin series of functions f in $\mathcal{A}$ has the form

$$f(z) = z + \sum_{n=2} a_n z^n, \qquad z \in \mathbb{D}. \tag{15.5}$$

Let $\mathcal{S}$ denote the class of functions in $\mathcal{A}$ that are univalent in $\mathbb{D}$. Starlike and convex functions are two

of the numerous subclasses of univalent functions that have garnered a lot of attention due to their analytical richness and geometric interpretability. A significant portion of these classes can be found in geometric function theory. These univalent functions captivated mathematicians around the world and laid the groundwork for future research in this area.

Let the classes of strongly starlike and convex functions of order κ be represented by $\tilde{\mathcal{S}}^*(\kappa)$ and $\tilde{\mathcal{C}}(\kappa)$, respectively. The following is an analytical definition of these classes:

Definition 15.1: A function f in $\mathcal{A}$ is said to be in the class $\tilde{\mathcal{S}}^*(\kappa)$, if and only if

$$\left|arg\left(\frac{zf'(z)}{f(z)}\right)\right| < \frac{\kappa\pi}{2}, \qquad \kappa \in (0,1].$$

Definition 15.2: A function f in $\mathcal{A}$ is said to be in the class $\tilde{\mathcal{C}}(\kappa)$, if and only if

$$\left|arg\left(1+\frac{zf''(z)}{f'(z)}\right)\right| < \frac{\kappa\pi}{2}, \qquad \kappa \in (0,1].$$

We see that $\tilde{\mathcal{S}}^*(1) = \mathcal{S}^*$ and $\tilde{\mathcal{C}}(1) = \mathcal{C}$.

It is evident that the functions $\mathcal{J}_p^{(2)}(z;q)$ and $\mathcal{J}_p^{(3)}(z;q)$ given in (15.3) and (15.4) do not belong to the class $\mathcal{A}$. Thus, we take into account the normalization $\mathcal{H}_p^{(2)}(z;q)$ and $\mathcal{H}_p^{(3)}(z;q)$ with

$$\mathcal{H}_p^{(2)}(0;q) = \mathcal{H}_p^{(3)}(0;q) = \left(\mathcal{H}_p^{(2)}(0;q)\right)' - 1 = \left(\mathcal{H}_p^{(3)}(0;q)\right)' - 1 = 0$$

such that

$$\mathcal{H}_p^{(2)}(z;q) = 2^p C_p(q)\, z^{1-\frac{p}{2}} \mathcal{J}_p^{(2)}(\sqrt{z};q) = z + \sum_{n=2}^{\infty} \frac{(-1)^n q^{(n-1)(n-1+p)}}{4^{n-1}\,(q;q)_{n-1}\,(q^{p+1};q)_{n-1}} z^n, \tag{15.6}$$

and

$$\mathcal{H}_p^{(3)}(z;q) = C_p(q)\, z^{1-\frac{p}{2}} \mathcal{J}_p^{(3)}(\sqrt{z};q) = z + \sum_{n=2}^{\infty} \frac{(-1)^n q^{\frac{1}{2}(n-1)n}}{(q;q)_{n-1}\,(q^{p+1};q)_{n-1}} z^n, \tag{15.7}$$

where $C_p(q) = (q;q)_\infty / \left(q^{p+1};q\right)_\infty$. Recently, some radius problems and geometric properties of certain normalizations of the generalized q-Bessel functions have been studied in [1, 2, 3, 5, 6]. We also refer to [7, 8, 9, 16] for some recent work on Bessel functions.

In this paper, we study strongly starlikeness and convexity of functions $\mathcal{H}_p^{(2)}(z;q)$ and $\mathcal{H}_p^{(3)}(z;q)$ in $\mathbb{D}$.

15.2 Relevant Lemmas

This section contains a few lemmas that support the main conclusions.

Lemma 15.1: *[11] Consider two analytic functions in $\mathbb{D}$, g and f, such that $g(0) = f(0) = 1$. Assume that $f \prec g$ in $\mathbb{D}$ and that g is univalent and convex in $\mathbb{D}$. Then,*

$$(n+1)z^{-1-n}\int_0^z \upsilon^n f(\upsilon)d\upsilon \prec (n+1)z^{-1-n}\int_0^z \upsilon^n g(\upsilon)d\upsilon,\ \forall n \in \mathbb{N}\cup\{0\}.$$

15.3 Main Results

Theorem 15.1: *Let $p > -1, q \in (0,1)$ and $\kappa \in (0,1]$. Also suppose that*

(i) $(1-q)(1-q^p) > \sqrt{q}$,

(ii) $\left(4(1-q)(1-q^p) - q^p\right)^2 \geq q^p\left(8(1-q)(1-q^p) - q^p\right)$.

Then $\mathcal{H}_p^{(2)}(z;q) \in \tilde{\mathcal{S}}^*(\kappa)$, where

$$\kappa = \frac{2\sin^{-1}\left(a\sqrt{1-\frac{a^2}{4}} + \frac{a}{2}\sqrt{1-a^2}\right)}{\pi}$$

with

$$a = \frac{q^p\left(8(1-q)(1-q^p) - q^p\right)}{\left(4(1-q)(1-q^p) - q^p\right)^2}.$$

Proof: From

$$\begin{aligned}\left|\left(\mathcal{H}_p^{(2)}(z;q)\right)' - 1\right| &= \left|1 + \sum_{n=2}^{\infty}\frac{n(-1)^n q^{(n-1)(n-1+p)}}{4^{n-1}(q;q)_{n-1}\left(q^{p+1};q\right)_{n-1}}z^{n-1} - 1\right| \\ &= \left|\sum_{n=2}^{\infty}\frac{n(-1)^n q^{(n-1)(n-1+p)}}{4^{n-1}(q;q)_{n-1}\left(q^{p+1};q\right)_{n-1}}z^{n-1}\right| \\ &\leq \sum_{n=2}^{\infty}\frac{nq^{(n-1)(n-1+p)}}{4^{n-1}(q;q)_{n-1}\left(q^{p+1};q\right)_{n-1}}.\end{aligned}$$

By using the inequality$q^{(n-1)(n-1+p)} \leq q^{(n-1)p}$, $(q;q)_{n-1} > (1-q)^{n-1}$ and $\left(q^{p+1};q\right)_{n-1} > (1-q^p)^{n-1}$, we get

$$\begin{aligned}\left|\left(\mathcal{H}_p^{(2)}(z;q)\right)' - 1\right| &< \sum_{n=2}^{\infty} n\left(\frac{q^p}{4(1-q)(1-q^p)}\right)^{n-1} \\ &= \frac{q^p\left(8(1-q)(1-q^p) - q^p\right)}{\left(4(1-q)(1-q^p) - q^p\right)^2} = a \leq 1.\end{aligned}$$

Hence, we get

$$\left|\left(\mathcal{H}_p^{(2)}(z;q)\right)' - 1\right| < \frac{q^p\left(8(1-q)(1-q^p) - q^p\right)}{\left(4(1-q)(1-q^p) - q^p\right)^2} = a \leq 1. \tag{15.8}$$

Now for $a \in (0,1]$ and from (15.8), we conclude that

$$\left(\mathcal{H}_p^{(2)}(z;q)\right)' - 1 \prec az + 1 \Rightarrow \left|\arg\left(\left(\mathcal{H}_p^{(2)}(z;q)\right)'\right)\right| < \sin^{-1}(a). \tag{15.9}$$

By using Lemma 15.1 for $n = 0$ with

$$f(z) = \left(\mathcal{H}_p^{(2)}(z;q)\right)' \text{ along with } h(z) = az + 1,$$

we have

$$\frac{\mathcal{H}_p^{(2)}(z;q)}{z} \prec \frac{a}{2}z + 1. \tag{15.10}$$

Consequently,

$$\left|\arg\left(\frac{\mathcal{H}_p^{(2)}(z;q)}{z}\right)\right| < \sin^{-1}\frac{a}{2}.$$

Now, using (15.9) and (15.10), we get

$$\begin{aligned}
\left|\arg\left(\frac{z\left(\mathcal{H}_p^{(2)}(z;q)\right)'}{\mathcal{H}_p^{(2)}(z;q)}\right)\right| &= \left|\arg\left(\frac{z}{\mathcal{H}_p^{(2)}(z;q)}\right) + \arg\left(\left(\mathcal{H}_p^{(2)}(z;q)\right)'\right)\right| \\
&< \left|\arg\left(\frac{z}{\mathcal{H}_p^{(2)}(z;q)}\right)\right| + \left|\arg\left(\left(\mathcal{H}_p^{(2)}(z;q)\right)'\right)\right| \\
&< \sin^{-1}\frac{a}{2} + \sin^{-1}a \\
&= \sin^{-1}\left(a\sqrt{1-\frac{a^2}{4}} + \frac{a}{2}\sqrt{1-a^2}\right).
\end{aligned}$$

Therefore, we conclude that

$$\left(\mathcal{H}_p^{(2)}(z;q)\right) \in \tilde{\mathcal{S}}^*(\kappa),$$

where

$$\kappa = \frac{2\sin^{-1}\left(a\sqrt{1-\frac{a^2}{4}} + \frac{a}{2}\sqrt{1-a^2}\right)}{\pi}.$$

The proof of Theorem 15.1 is complete. □

Theorem 15.2: *Let $p > -1, q \in (0,1)$ and $\kappa \in (0,1]$. Also suppose that*

(i) $(1-q)(1-q^p) > \sqrt{q}$,

(ii) $\left((1-q)(1-q^p) - \sqrt{q}\right)^2 \geq \sqrt{q}\left(2(1-q)(1-q^p) - \sqrt{q}\right)$.

Then $\mathcal{H}_p^{(3)}(z;q) \in \tilde{\mathcal{S}}^*(\kappa)$, where

$$\kappa = \frac{2\sin^{-1}\left(a\sqrt{1-\frac{a^2}{4}} + \frac{a}{2}\sqrt{1-a^2}\right)}{\pi}$$

and

$$a = \frac{\sqrt{q}\left(2(1-q)(1-q^p) - \sqrt{q}\right)}{\left((1-q)(1-q^p) - \sqrt{q}\right)^2}.$$

Proof: From

$$\begin{aligned}\left|\left(\mathcal{H}_p^{(3)}(z;q)\right)'-1\right| &= \left|1+\sum_{n=2}^{\infty}\frac{n(-1)^n q^{\frac{1}{2}(n-1)n}}{(q;q)_{n-1}\left(q^{p+1};q\right)_{n-1}}z^{n-1}-1\right| \\ &= \left|\sum_{n=2}^{\infty}\frac{n(-1)^n q^{\frac{1}{2}(n-1)n}}{(q;q)_{n-1}\left(q^{p+1};q\right)_{n-1}}z^{n-1}\right| \\ &\leq \sum_{n=2}^{\infty}\frac{nq^{\frac{1}{2}(n-1)n}}{(q;q)_{n-1}\left(q^{p+1};q\right)_{n-1}}.\end{aligned}$$

By using the inequalities $q^{\frac{1}{2}(n-1)n}\leq q^{\frac{1}{2}(n-1)}$, $(q;q)_{n-1}>(1-q)^{n-1}$ and $\left(q^{p+1};q\right)_{n-1}>(1-q^p)^{n-1}$, we obtain

$$\begin{aligned}\left|\left(\mathcal{H}_p^{(3)}(z;q)\right)'-1\right| &< \sum_{n=2}^{\infty}n\left(\frac{\sqrt{q}}{(1-q)(1-q^p)}\right)^{n-1} \\ &= \frac{\sqrt{q}\left(2(1-q)(1-q^p)-\sqrt{q}\right)}{\left((1-q)(1-q^p)-\sqrt{q}\right)^2}=a\leq 1.\end{aligned}$$

Therefore

$$\left|\left(\mathcal{H}_p^{(3)}(z;q)\right)'-1\right|<\frac{\sqrt{q}\left(2(1-q)(1-q^p)-\sqrt{q}\right)}{\left((1-q)(1-q^p)-\sqrt{q}\right)^2}=a\leq 1. \tag{15.11}$$

Now for $\kappa\in(0,1]$ and from (15.11), we conclude that

$$\left(\mathcal{H}_p^{(3)}(z;q)\right)'-1\prec az+1\Rightarrow\left|\arg\left(\left(\mathcal{H}_p^{(3)}(z;q)\right)'\right)\right|<\sin^{-1}(a). \tag{15.12}$$

By using Lemma 15.1 for $n=0$ with

$$f(z)=\left(\mathcal{H}_p^{(3)}(z;q)\right)' \text{ along with } h(z)=az+1,$$

we have

$$\frac{\mathcal{H}_p^{(3)}(z;q)}{z}\prec\frac{a}{2}z+1. \tag{15.13}$$

Consequently,

$$\left|\arg\left(\frac{\mathcal{H}_p^{(3)}(z;q)}{z}\right)\right|<\sin^{-1}\frac{a}{2}.$$

Now, using (15.12) and (15.13), we have

$$\begin{aligned}\left|\arg\left(\frac{z\left(\mathcal{H}_p^{(3)}(z;q)\right)'}{\mathcal{H}_p^{(3)}(z;q)}\right)\right| &= \left|\arg\left(\frac{z}{\mathcal{H}_p^{(3)}(z;q)}\right)+\arg\left(\left(\mathcal{H}_p^{(3)}(z;q)\right)'\right)\right| \\ &< \left|\arg\left(\frac{z}{\mathcal{H}_p^{(3)}(z;q)}\right)\right|+\left|\arg\left(\left(\mathcal{H}_p^{(3)}(z;q)\right)'\right)\right| \\ &< \sin^{-1}\frac{a}{2}+\sin^{-1}a\end{aligned}$$

$$= \sin^{-1}\left(a\sqrt{1-\frac{a^2}{4}}+\frac{a}{2}\sqrt{1-a^2}\right).$$

Hence

$$\left(\mathcal{H}_p^{(3)}(z;q)\right) \in \tilde{\mathcal{S}}^*(\kappa),$$

where

$$\kappa = \frac{2\sin^{-1}\left(a\sqrt{1-\frac{a^2}{4}}+\frac{a}{2}\sqrt{1-a^2}\right)}{\pi}.$$

This complete the proof.

□

Theorem 15.3: *Let $p > -1, q \in (0,1)$ and $\kappa \in (0,1]$. Also suppose that*

(i) $4(1-q)(1-q^p) > q^p$,

(ii) $\left(4\left(1-q\right)\left(1-q^p\right)-q^p\right)^3 \geq q^{3p} - 12(1-q)(1-q^p)q^{2p} + 64(1-q)^2(1-q^p)^2q^p$.

Then $\mathcal{H}_p^{(2)}(z;q) \in \widetilde{\mathcal{C}}(\kappa)$, where

$$\kappa = \frac{2\sin^{-1}\left(a\sqrt{1-\frac{a^2}{4}}+\frac{a}{2}\sqrt{1-a^2}\right)}{\pi}$$

and

$$a = \frac{q^{3p} - 12(1-q)(1-q^p)q^{2p} + 64(1-q)^2(1-q^p)^2q^p}{\left(4\left(1-q\right)\left(1-q^p\right)-q^p\right)^3}.$$

Proof: We have

$$\begin{aligned}
\left|\left(z\left(\mathcal{H}_p^{(2)}(z;q)\right)'\right)' - 1\right| &= \left|\left(z+\sum_{n=2}^{\infty}\frac{n(-1)^n q^{(n-1)(n-1+p)}}{4^{n-1}\left(q;q\right)_{n-1}\left(q^{p+1};q\right)_{n-1}}z^n\right)' - 1\right| \\
&= \left|1+\sum_{n=2}^{\infty}\frac{n^2(-1)^n q^{(n-1)(n-1+p)}}{4^{n-1}\left(q;q\right)_{n-1}\left(q^{p+1};q\right)_{n-1}} - 1\right| \\
&= \left|\sum_{n=2}^{\infty}\frac{n^2(-1)^n q^{(n-1)(n-1+p)}}{4^{n-1}\left(q;q\right)_{n-1}\left(q^{p+1};q\right)_{n-1}}\right| \\
&\leq \sum_{n=2}^{\infty}\frac{n^2 q^{(n-1)(n-1+p)}}{4^{n-1}\left(q;q\right)_{n-1}\left(q^{p+1};q\right)_{n-1}}.
\end{aligned}$$

We obtain

$$\left|\left(z\left(\mathcal{H}_p^{(2)}(z;q)\right)'\right)' - 1\right| \leq \sum_{n=2}^{\infty}\frac{n^2 q^{(n-1)(n-1+p)}}{4^{n-1}\left(q;q\right)_{n-1}\left(q^{p+1};q\right)_{n-1}}.$$

By using the inequalities $q^{(n-1)(n-1+p)} \leq q^{(n-1)p}$, $\left(q;q\right)_{n-1} > (1-q)^{n-1}$ and $\left(q^{p+1};q\right)_{n-1} > (1-q^p)^{n-1}$, we have

$$\left|\left(z\left(\mathcal{H}_p^{(2)}(z;q)\right)'\right)' - 1\right| < \sum_{n=2}^{\infty} n^2\left(\frac{q^p}{4\left(1-q\right)\left(1-q^p\right)}\right)^{n-1}$$

$$= \frac{q^{3p} - 12(1-q)(1-q^p)q^{2p} + 64(1-q)^2(1-q^p)^2q^p}{\left(4\left(1-q\right)\left(1-q^p\right) - q^p\right)^3}$$
$$= a \leq 1,$$

so,

$$\left|\left(z\left(\mathcal{H}_p^{(2)}(z;q)\right)'\right)' - 1\right| < \frac{q^{3p} - 12(1-q)(1-q^p)q^{2p} + 64(1-q)^2(1-q^p)^2q^p}{\left(4\left(1-q\right)\left(1-q^p\right) - q^p\right)^3} = a \leq 1. \tag{15.14}$$

Now for $0 < a \leq 1$ and from (15.14), we get

$$\left(z\left(\mathcal{H}_p^{(2)}(z;q)\right)'\right)' \prec 1 + az \Rightarrow \left|\arg\left(z\left(\mathcal{H}_p^{(2)}(z;q)\right)'\right)'\right| < \sin^{-1} a. \tag{15.15}$$

By applying Lemma 15.1 for $n = 0$ with

$$g(z) = \left(z\left(\mathcal{H}_p^{(2)}(z;q)\right)'\right)' \text{ along with } h(z) = 1 + az,$$

we get

$$\left(\mathcal{H}_p^{(2)}(z;q)\right)' \prec \frac{a}{2}z + 1.$$

Hence

$$\left|\arg\left(\left(\mathcal{H}_p^{(2)}(z;q)\right)'\right)\right| < \sin^{-1}\frac{a}{2}. \tag{15.16}$$

Now, using (15.15) and (15.16), we obtain

$$\begin{aligned}
\left|\arg\left(\frac{\left(z\left(\mathcal{H}_p^{(2)}(z;q)\right)'\right)'}{\left(\mathcal{H}_p^{(2)}(z;q)\right)'}\right)\right| &= \left|\arg\left(\left(z\left(\mathcal{H}_p^{(2)}(z;q)\right)'\right)'\right) - \arg\left(\left(\mathcal{H}_p^{(2)}(z;q)\right)'\right)\right| \\
&< \left|\arg\left(\left(z\left(\mathcal{H}_p^{(2)}(z;q)\right)'\right)'\right)\right| + \left|\arg\left(\left(\mathcal{H}_p^{(2)}(z;q)\right)'\right)\right| \\
&< \sin^{-1} a + \sin^{-1}\frac{a}{2} \\
&= \sin^{-1}\left(a\sqrt{1-\frac{a^2}{4}} + \frac{a}{2}\sqrt{1-a^2}\right).
\end{aligned}$$

Hence

$$\mathcal{H}_p^{(2)}(z;q) \in \tilde{\mathcal{C}}(\kappa),$$

where

$$\kappa = \frac{2}{\pi}\sin^{-1}\left(a\sqrt{1-\frac{a^2}{4}} + \frac{a}{2}\sqrt{1-a^2}\right).$$

The proof of the theorem is complete.

□

Theorem 15.4: *Let $p > -1, q \in (0,1)$ and $\kappa \in (0,1]$. Also suppose that*

(i) $(1-q)(1-q^p) > \sqrt{q}$,

(ii) $\left(\sqrt{q} - (1-q)(1-q^p)\right)^3 \geq \sqrt{q}\left(-q + 3\sqrt{q}(1-q)(1-q^p) - 4(1-q)^2(1-q^p)^2\right)$.

Then $\mathcal{H}_p^{(3)}(z;q) \in \widetilde{\mathcal{C}}(\kappa)$, *where*

$$\kappa = \frac{2\sin^{-1}\left(a\sqrt{1-\frac{a^2}{4}} + \frac{a}{2}\sqrt{1-a^2}\right)}{\pi}$$

and

$$a = \frac{\sqrt{q}\left(-q + 3\sqrt{q}(1-q)(1-q^p) - 4(1-q)^2(1-q^p)^2\right)}{\left(\sqrt{q} - (1-q)(1-q^p)\right)^3}.$$

Proof: We have

$$\begin{aligned}
\left|\left(z\left(\mathcal{H}_p^{(3)}(z;q)\right)'\right)' - 1\right| &= \left|\left(z + \sum_{n=2}^{\infty} \frac{n(-1)^n q^{\frac{1}{2}(n-1)n}}{(q;q)_{n-1}\left(q^{p+1};q\right)_{n-1}} z^n\right)' - 1\right| \\
&= \left|1 + \sum_{n=2}^{\infty} \frac{n^2(-1)^n q^{\frac{1}{2}(n-1)n}}{(q;q)_{n-1}\left(q^{p+1};q\right)_{n-1}} - 1\right| \\
&= \left|\sum_{n=2}^{\infty} \frac{n^2(-1)^n q^{\frac{1}{2}(n-1)n}}{(q;q)_{n-1}\left(q^{p+1};q\right)_{n-1}}\right| \\
&\leq \sum_{n=2}^{\infty} \frac{n^2 q^{\frac{1}{2}(n-1)n}}{(q;q)_{n-1}\left(q^{p+1};q\right)_{n-1}}.
\end{aligned}$$

We obtain

$$\left|\left(z\left(\mathcal{H}_p^{(3)}(z;q)\right)'\right)' - 1\right| \leq \sum_{n=2}^{\infty} \frac{n^2 q^{\frac{1}{2}(n-1)n}}{(q;q)_{n-1}\left(q^{p+1};q\right)_{n-1}}.$$

By using the inequalities $q^{\frac{1}{2}(n-1)n} \leq q^{\frac{1}{2}(n-1)}$, $(q;q)_{n-1} > (1-q)^{n-1}$ and $\left(q^{p+1};q\right)_{n-1} > (1-q^p)^{n-1}$, we get

$$\begin{aligned}
\left|\left(z\left(\mathcal{H}_p^{(3)}(z;q)\right)'\right)' - 1\right| &< \sum_{n=2}^{\infty} n^2 \left(\frac{\sqrt{q}}{(1-q)(1-q^p)}\right)^{n-1} \\
&= \frac{\sqrt{q}\left(-q + 3\sqrt{q}(1-q)(1-q^p) - 4(1-q)^2(1-q^p)^2\right)}{\left(\sqrt{q} - (1-q)(1-q^p)\right)^3} \\
&= a \leq 1,
\end{aligned}$$

so,

$$\left|\left(z\left(\mathcal{H}_p^{(3)}(z;q)\right)'\right)' - 1\right| < \frac{\sqrt{q}\left(-q + 3\sqrt{q}(1-q)(1-q^p) - 4(1-q)^2(1-q^p)^2\right)}{\left(\sqrt{q} - (1-q)(1-q^p)\right)^3} = a \leq 1. \tag{15.17}$$

Now for $0 < a \leq 1$ and from (15.17), we get

$$\left(z\left(\mathcal{H}_p^{(3)}(z;q)\right)'\right)' \prec 1 + az \Rightarrow \left|\arg\left(z\left(\mathcal{H}_p^{(3)}(z;q)\right)'\right)'\right| < \sin^{-1} a. \tag{15.18}$$

By applying Lemma 15.1 for $n = 0$ with

$$g(z) = \left(z\left(\mathcal{H}_p^{(3)}(z;q)\right)'\right)' \text{ along with } h(z) = 1 + az,$$

we have

$$\left(\mathcal{H}_p^{(3)}(z;q)\right)' \prec \frac{a}{2}z + 1.$$

Consequently,

$$\left|\arg\left(\left(\mathcal{H}_p^{(3)}(z;q)\right)'\right)\right| < \sin^{-1}\frac{a}{2}. \tag{15.19}$$

Now, using (15.18) and (15.19), we get

$$\begin{aligned}
\left|\arg\left(\frac{\left(z\left(\mathcal{H}_p^{(3)}(z;q)\right)'\right)'}{\left(\mathcal{H}_p^{(3)}(z;q)\right)'}\right)\right| &= \left|\arg\left(\left(z\left(\mathcal{H}_p^{(3)}(z;q)\right)'\right)'\right) - \arg\left(\left(\mathcal{H}_p^{(3)}(z;q)\right)'\right)\right| \\
&< \left|\arg\left(\left(z\left(\mathcal{H}_p^{(3)}(z;q)\right)'\right)'\right)\right| + \left|\arg\left(\left(\mathcal{H}_p^{(3)}(z;q)\right)'\right)\right| \\
&< \sin^{-1}a + \sin^{-1}\frac{a}{2} \\
&= \sin^{-1}\left(a\sqrt{1-\frac{a^2}{4}} + \frac{a}{2}\sqrt{1-a^2}\right).
\end{aligned}$$

Hence

$$\mathcal{H}_p^{(3)}(z;q) \in \tilde{\mathcal{C}}(\kappa),$$

where

$$\kappa = \frac{2}{\pi}\sin^{-1}\left(a\sqrt{1-\frac{a^2}{4}} + \frac{a}{2}\sqrt{1-a^2}\right).$$

The proof is complete. □

Bibliography

[1] Aktas, I., & Baricz, A. (2017). Bounds for the radii of starlikeness of some q-Bessel functions. *Results in Mathematics, 72*, 947–963.

[2] Aktas, I., & Orhan, H. (2018). On partial sums of normalized q-Bessel functions. *Communications of the Korean Mathematical Society, 33*, 535–547.

[3] Aktas, I., & Orhan, H. (2020). Bounds for the radii of convexity of some q-Bessel functions. *Bulletin of the Korean Mathematical Society, 57*, 355–369.

[4] Annaby, M. H., & Mansour, Z. S. (2012). *q-Fractional calculus and equations* (Lecture Notes in Mathematics, Vol. 2056). Berlin: Springer-Verlag.

[5] Baricz, A., Dimitrov, D. K., & Mező, I. (2016). Radii of starlikeness and convexity of some q-Bessel functions. *Journal of Mathematical Analysis and Applications, 431*(1), 968–985.

[6] Baricz, Á., Kumar, P., & Singh, S. (2024). Asymptotic expansions for the radii of starlikeness of normalized q-Bessel functions. *Results in Mathematics, 79*, 248.

[7] Baricz, A., Deniz, E., & Yagmur, N. (2016). Close-to-convexity of normalized Dini functions. *Mathematische Nachrichten, 289*(14–15), 1721–1726.

[8] Baricz, A., & Ponnusamy, S. (2010). Starlikeness and convexity of generalized Bessel functions. *Integral Transforms and Special Functions, 21*(9), 641–653.

[9] Deniz, E., & Gören, S. (2019). Geometric properties of generalized Dini functions. *Honam Mathematical Journal, 41*(1), 101–116.

[10] Ismail, M. E. H. (2005). *Classical and quantum orthogonal polynomials in one variable*. Cambridge: Cambridge University Press.

[11] Hallenbeck, D. J., & Ruscheweyh, S. (1975). Subordination by convex functions. *Proceedings of the American Mathematical Society, 52*, 191–195.

[12] Jackson, F. H. (1905). The basic gamma-function and the elliptic functions. *Proceedings of the Royal Society of London A, 76*, 127–144.

[13] Jackson, F. H. (1905). The applications of basic numbers to Bessel's and Legendre's equations. *Proceedings of the London Mathematical Society, 3*, 1–23.

[14] Koelink, H. T., & Swarttouw, R. F. (1994). On the zeros of the Hahn–Exton q-Bessel function and associated q-Lommel polynomials. *Journal of Mathematical Analysis and Applications, 186*, 690–710.

[15] Watson, G. N. (1944). *A treatise on the theory of Bessel functions*. Cambridge: Cambridge University Press.

[16] Zayed, H. M., & Bulboacă, T. (2022). Normalized generalized Bessel function and its geometric properties. *Journal of Inequalities and Applications, 2022*, 158.

Contributing Authors

Dr. Javed Rashid; Dr. Riaz ul Amin; Dr. Bilal Shabbir Qaisar; Dr. Muhammad Shoaib Saleem; Mr. Ahsan Fareed Shah; Mr. Abdullah; Dr. Madiha Ghamkhar; Ms. Adeeba Fatima; Ms. Asra Ayub; Ms. Aamna Amer; Dr. Hamood Ur Rehman; Ms. Ifrah Iqbal; Mr. Muhammad Tehseen; Dr. Mujahid Iqbal; Dr. Muhammad Ashraf; Dr. Hameed Ashraf; Ms. Ayesha Siddiqa; Dr. Madeeha Tahir; Prof. Dr. Saima Akram; Dr. Shahla Faisal; Prof. Dr. M. Imran; Mr. Muhammad Abid; Mr. G. A. Danish; Dr. Khadija Tul Kubra; Mr. Rooh Ali; Ms. Muniba Nasir; Ms. Bushra Ujala; Ms. Samra Gulshan; Dr. Abdul Malik Sultan; Dr. Abdul Jawad; Dr. Muhammad Irfan; Ms. Tahreem Ashraf; Dr. Nazeran Idrees; Dr. Farkhanda Afzal; Dr. Akhtar Ali; Mr. Ali Raza; Ms. Fatima Saeed; Dr. Fozia Bashir Farooq; Prof. Dr. Mohsan Raza; Prof. Dr. M. Ahsan Binyamin.

ISBN: 978-627-7623-05-0

This book, Mathematical and Computational Systems: Theory, Methods, and Applications in Physics, Networking, and Intelligent Modeling, presents a collection of research studies and methodologies bridging mathematical theory and practical applications. It covers diverse topics, including machine learning for disease classification, computational intelligence, optimization algorithms, biofluid modeling, neural network paradigms in epidemiology, cosmology, topological descriptors, and fractional differential equations in HIV–AIDS dynamics. The aim is to provide readers, researchers, academicians, and graduate students, with insights into advanced computational methods and their applications across science and engineering. We hope this volume inspires new research directions and promotes the integration of theory, computation, and real-world problem-solving.